

MICRO & NANO TECHNOLOGIES

# Micromixers

Fundamentals, Design  
and Fabrication

Nam-Trung Nguyen

# MICROMIXERS

# **MICRO & NANO TECHNOLOGIES**

**Series Editor: Jeremy Ramsden**

*Professor of Nanotechnology*

*Microsystems and Nanotechnology Centre, Department of Materials*

*Cranfield University, United Kingdom*

The aim of this book series is to disseminate the latest developments in small scale technologies with a particular emphasis for accessible and practical content. These books will appeal to engineers from industry, academia and government sectors.

For more information about the book series and new book proposals please contact the Publisher, Dr. Nigel Hollingworth at [nhollingworth@williamandrew.com](mailto:nhollingworth@williamandrew.com).

<http://www.williamandrew.com/MNT>

# MICROMIXERS

Fundamentals, Design and Fabrication

Nam-Trung Nguyen

School of Mechanical and Aerospace Engineering

Nanyang Technological University, Singapore



Norwich, NY, USA

Copyright 2008 by William Andrew Inc.

No part of this book may be reproduced or utilized in any form or by any means, electronic or mechanical, including photocopying, recording, or by any information storage and retrieval system, without permission in writing from the Publisher.

ISBN: 978-0-8155-1543-2

Library of Congress Cataloging-in-Publication Data

Nguyen, Nam-Trung, 1970-

Micromixers : fundamentals, design and fabrication / Nam-Trung Nguyen.

p. cm. – (Micro & nano technology series)

ISBN 978-0-8155-1543-2 (alk. paper)

1. Fluidic devices—Congresses. 2. Microfluidics—Congresses. 3. Microelectromechanical systems—Congresses. I. Title.

TJ853.N49 2008

660'.284292—dc22

2007047527

Printed in the United States of America

This book is printed on acid-free paper.

10 9 8 7 6 5 4 3 2 1

Published by:

William Andrew Inc.

13 Eaton Avenue

Norwich, NY 13815

1-800-932-7045

[www.williamandrew.com](http://www.williamandrew.com)

## NOTICE

To the best of our knowledge the information in this publication is accurate; however the Publisher does not assume any responsibility or liability for the accuracy or completeness of, or consequences arising from, such information. This book is intended for informational purposes only. Mention of trade names or commercial products does not constitute endorsement or recommendation for their use by the Publisher. Final determination of the suitability of any information or product for any use, and the manner of that use, is the sole responsibility of the user. Anyone intending to rely upon any recommendation of materials or procedures mentioned in this publication should be independently satisfied as to such suitability, and must meet all applicable safety and health standards.

# Contents

<b>Series Editor's Preface</b> .....	<b>ix</b>
<b>Preface</b> .....	<b>xi</b>
<b>Acknowledgments</b> .....	<b>xi</b>
<b>Symbols</b> .....	<b>xiii</b>
<b>1 Introduction</b> .....	<b>1</b>
1.1 Micromixers and Mixing at the Microscale .....	1
1.2 Micromixers as Microreactors .....	4
1.3 Organization of the Book .....	6
References .....	7
<b>2 Fundamentals of Mass Transport at the Micro Scale</b> .....	<b>9</b>
2.1 Transport Phenomena .....	9
2.1.1 Molecular Level .....	9
2.1.2 Continuum Level .....	13
2.2 Molecular Diffusion .....	21
2.2.1 Random Walk and Brownian Motion .....	21
2.2.2 Stokes–Einstein Model of Diffusion .....	23
2.2.3 Diffusion Coefficient .....	24
2.3 Taylor Dispersion .....	28
2.3.1 Two-Dimensional Analysis .....	29
2.3.2 Three-Dimensional Analysis .....	35
2.4 Chaotic Advection .....	37
2.4.1 Basic Terminologies .....	37
2.4.2 Examples of Chaotic Advection .....	41
2.5 Viscoelastic Effects .....	54
2.6 Electrokinetic Effects .....	56
2.6.1 Electroosmosis .....	56
2.6.2 Electrophoresis .....	67
2.6.3 Dielectrophoresis .....	69
2.7 Magnetic and Electromagnetic Effects .....	69
2.7.1 Magnetic Effects .....	69
2.8 Scaling Laws and Fluid Flow at the Micro Scale .....	72
References .....	75

<b>3</b>	<b>Fabrication Technologies</b>	<b>79</b>
3.1	Silicon-Based Microtechnologies	79
3.1.1	Basic Technologies	80
3.1.2	Single-Crystalline Silicon	84
3.1.3	Polysilicon	95
3.1.4	Other Materials	97
3.2	Polymeric Microtechnologies	99
3.2.1	Thick-Film Polymeric Materials	100
3.2.2	Polymeric Bulk Micromachining	105
3.2.3	Polymeric Surface Micromachining	117
3.3	Metallic Microtechnologies	121
3.3.1	Metals as Substrate Materials	121
3.3.2	LIGA	122
3.3.3	Micro Electro Discharge Machining	122
3.3.4	Focused Ion Beam Micromachining	123
3.3.5	Powder Blasting	123
3.3.6	Ultrasonic Micromachining	124
3.4	Packaging	124
3.4.1	Anodic Bonding	124
3.4.2	Direct Bonding	125
3.4.3	Adhesive Bonding	126
3.4.4	Eutectic Bonding	127
3.5	Conclusions	127
	References	127
<b>4</b>	<b>Micromixers Based on Molecular Diffusion</b>	<b>135</b>
4.1	Parallel Lamination	135
4.1.1	Mixers Based on Pure Molecular Diffusion	135
4.1.2	Mixers Based on Inertial and Viscoelastic Instabilities	141
4.2	Sequential Lamination	144
4.3	Sequential Segmentation	146
4.4	Segmentation Based on Injection	147
4.5	Focusing of Mixing Streams	150
4.5.1	Streams with the Same Viscosity	150
4.5.2	Streams with Different Viscosities	153
4.5.3	Combination of Hydrodynamic Focusing and Sequential Segmentation	155
	References	160
<b>5</b>	<b>Micromixers Based on Chaotic Advection</b>	<b>163</b>
5.1	Chaotic Advection at High Reynolds Numbers	163
5.1.1	T-Mixer at High Reynolds Numbers	163
5.1.2	Passive Mixers with Obstacles in the Mixing Channel	166
5.1.3	Dean Flow with Repeated Turns in Mixing Channel	168

5.2	Chaotic Advection at Intermediate Reynolds Numbers . . . . .	170
5.2.1	Chaotic Advection with 90° Turns . . . . .	170
5.2.2	Chaotic Advection with Other Channel Designs . . . . .	172
5.3	Chaotic Advection at Low Reynolds Numbers . . . . .	176
5.3.1	Chaotic Advection with Dean Vortices And Complex 3-D Channels . . . . .	176
5.3.2	Chaotic Advection with Flow-Guiding Structures on Channel Walls . . . . .	180
5.4	Chaotic Advection in Multiphase Flow . . . . .	186
5.4.1	Multiphase Systems at the Micro Scale . . . . .	186
5.4.2	Mixing in Microdroplets . . . . .	198
	References . . . . .	203
<b>6</b>	<b>Active Micromixers . . . . .</b>	<b>207</b>
6.1	Flow Instability in Microchannels . . . . .	207
6.2	Pressure-Driven Disturbance . . . . .	207
6.2.1	Actuation Concepts for Pressure Generation . . . . .	207
6.2.2	Hydrodynamic Instability . . . . .	215
6.2.3	Pulsed Source-Sink Chaotic Advection . . . . .	217
6.2.4	Design Examples . . . . .	221
6.3	Electrohydrodynamic Disturbance . . . . .	227
6.4	Dielectrophoretic Disturbance . . . . .	231
6.5	Electrokinetic Disturbance . . . . .	233
6.5.1	Instability Caused by a Conductivity Gradient . . . . .	233
6.5.2	Instability Caused by Variation of Electric Field . . . . .	237
6.5.3	Instability Caused by Variation of Zeta Potentials . . . . .	238
6.5.4	Design Examples . . . . .	240
6.6	Magnetohydrodynamic Disturbance . . . . .	244
6.6.1	Straight Channel Configuration [43] . . . . .	244
6.6.2	Curved Channel Configuration [44] . . . . .	246
6.6.3	Design Examples . . . . .	250
6.7	Acoustic Disturbance . . . . .	251
6.7.1	Vibration of a Rectangular Membrane [49] . . . . .	252
6.7.2	Vibration of a Circular Membrane [49] . . . . .	255
6.7.3	Design Examples . . . . .	258
6.8	Thermal Disturbance . . . . .	261
	References . . . . .	262
<b>7</b>	<b>Characterization Techniques . . . . .</b>	<b>267</b>
7.1	Imaging Techniques . . . . .	267
7.1.1	Two-Dimensional Optical Microscopy . . . . .	267
7.1.2	Two-Dimensional Fluorescence Microscopy . . . . .	271
7.1.3	Confocal Laser Scanning Microscopy . . . . .	273
7.1.4	Acquisition and Processing of Digital Images . . . . .	275



7.2	Measurement Using Optical Microscopy . . . . .	280
7.2.1	Measurement of Velocity Field . . . . .	280
7.2.2	Measurement of Concentration Field . . . . .	283
7.3	Quantification Methods for Micromixers . . . . .	285
7.3.1	Direct Statistical Methods . . . . .	285
7.3.2	Indirect Methods . . . . .	288
	References . . . . .	291
<b>8</b>	<b>Applications of Micromixers . . . . .</b>	<b>293</b>
8.1	Chemical Industry . . . . .	293
8.1.1	Micromixers as Microreactors . . . . .	293
8.1.2	Homogeneous Reactions . . . . .	293
8.1.3	Heterogeneous Reactions . . . . .	294
8.1.4	Enhancement of Chemical Selectivity . . . . .	295
8.2	Applications in Chemical and Biochemical Analysis . . . . .	296
8.2.1	Concentration Measurement . . . . .	296
8.2.2	Improving Chemical and Biochemical Analysis . . . . .	297
8.2.3	Purification and Pre-Concentration . . . . .	301
8.3	Outlook . . . . .	302
	References . . . . .	304
	<b>Index . . . . .</b>	<b>307</b>

# Series Editor's Preface

Although micro- and nanotechnologies were born in the realm of mechanical engineering, modern electronics, especially that embodied by the very large scale integrated circuit, is also now considered to be very much a part of miniature and ultraprecision engineering, and especially when thinking of electronics as the applications of controlled flows of electrons, it is natural and inevitable to extend the world of micro-and nanotechnologies into fluidics.

The microfluidics with which this book is concerned is very much the miniature end of chemical engineering, and since chemistry would be very dull indeed non-existent if it only dealt with a single variety of entity, right from the start we are confronted with two or more different substances, either pure liquids of different natures, or different solutes dissolved in a common solvent, that must be brought together and allowed to react. Mixing can therefore lay claim to be the most fundamental concept of the field, since without mixing there can be no reaction, and without reaction there can be no product.

Micromixing as a phenomenon has of course long been a preoccupation of chemical engineers such as John Bourne as a major problem influencing reaction rates and product distributions to be contended with in macroscopic reactors. Some of the difficulties of controlling the microscale while operating at the macroscale are well-nigh insuperable however, and miniaturizing reactors offers a very attractive way out of the difficulties. At the same time, new ones are created, not least that of scale-up. That problem in particular cannot yet be said to have been solved, which perhaps explains why microfluidic reactors have until now been largely confined to analytical applications, where it is a positive advantage, especially in biology and medicine, where the volumes of the samples to be analysed may be very small.

Interestingly, the historical development of microfluidics has come not from mainstream chemical engineering and its preoccupation with micromixing, but rather through fluidics as an adjunct to other, established, fields of microtechnology, notably miniature rocket motors, and the inkjet printer as an accessory to the electronic computer. This means that the community of engineers and scientists now engaged in developing microfluidic devices may not necessarily have a classical chemical engineering background. Indeed, they may have entered the field from a variety of different backgrounds, and even if they did come from chemical engineering, it is very unlikely that they would

have been confronted by the problems of mass transport at the microscale. The strength of this book is that it allows this very diverse community intensively engaged in developing this rapidly expanding field to gain a thorough grounding in the necessary fundamentals of the subject, which they will find to be logically related to those areas of their fields with which they are familiar from a macroscopic viewpoint.

This book is also uniquely comprehensive insofar as it deals not only with problems that are directly related to fluidics as a discipline—aspects such as mass transport, molecular diffusion, electrokinetic phenomena, flow instabilities etc. but also the problems of fabricating micromixers, which involve quite different areas of knowledge, and which are equally crucial to the successful realization of a practical device.

Jeremy Ramsden  
Cranfield University, United Kingdom  
December 2007

# Preface

In the past decade, microfluidics has developed at a fast pace. The main driving forces for this research are applications in chemistry and biochemistry. The science and technology of microfluidics cover a wide spectrum ranging from fundamental studies to real applications in industry and laboratories. This book focuses on an important subtopic of microfluidics, namely mixing at the microscale. The science of such mixing has emerged from reports on newly fabricated devices building on an extensive collection of established knowledge. Mixing at the microscale and micromixers are important because they represent a reaction platform for chemistry at the microscale. Due to its applied nature, the book will discuss practical issues in the design, fabrication and characterization of micromixers. The book is intended most importantly as a reference for practising engineers in the chemical and biochemical industries (but is at a level of difficulty appropriate to serve as a course text for upper-level undergraduates and graduate students). With this objective in mind, the book is organized into chapters dealing with fundamentals, fabrication technologies, practical design examples, characterization techniques, and applications. The author will be grateful for any feedback and comment from engineers and researchers in the field leading to the improvement of the present book.

## Acknowledgments

This book was written under an extreme time constraint. Over a span of twelve months, besides numerous duties in teaching, research, and service, I needed to find the time to compile the existing material and to write the text. Fortunately, after two semesters of heavy teaching duties the Spring semester 2007 was without major teaching commitments. I would like to thank my school management for this precious free time from January to April 2007. Without this time slot, I would not have been able to complete this book according to plan. I would like to express my gratitude to the many colleagues, research staff, and graduate students for their support and inspiration. Parts of the published works of my former and current PhD students Wu Zhigang and Jiao Zhenjun have been included in this book. I really appreciate their hard

work and collaboration. I would like to thank all my colleagues from the microfluidics community, whose works have been cited as examples in this book. Due the huge amount of available literature, I could not cite and review everyone's work, and apologies to colleagues who do not find their works reviewed here. I would like to thank Dr Nigel Hollingworth, Publisher of the Micro and Nano Technologies Series of William Andrew Inc. for his constant support during this book project. Last but not least, I would like to express my love and gratitude to my wife Thuy-Mai and my two children Thuy-Linh and Nam-Tri, for their unconditional love, support, patience and sacrifice. The book indeed took up a large amount of my time at home, where I should be spending quality time with my family. I promise my family that this book project shall be the last one for a while.

Nam-Trung Nguyen  
Singapore, December 2007

# Symbols

## Dimensionless Groups

Bo	Bond number
Ca	Capillary number
Da	Damköhler number
De	Dean number
El	elasticity number
Fo	Fourier number
Kn	Knudsen number
Le	Lewis number
Pe	Peclet number
Pr	Prandtl number
Ra	Rayleigh number
Re	Reynolds number
Sc	Schmidt number
We	Weber number
Wi	Weissenberg number

## Greek Symbols

$\alpha$	flow rate ratio (Section 5.4.1.1)
$\alpha_{\text{th}}$	thermal expansion coefficient
$\alpha, \beta$	geometry parameters (Section 4.5)
$\alpha, \beta$	switching ratio and focusing ratio (Section 4.5.3)
$\beta$	friction coefficient (Section 2.2.2)
$\beta$	thermal expansion coefficient
$\beta$	viscosity ratio (Section 2.1.2.2)
$\dot{\gamma}$	shear rate
$\gamma$	flow rate ratio
$\delta$	Dirac function

$\Delta\Phi$	angular displacement
$\varepsilon$	characteristic energy (Sections 2.1.1 and 2.2.3)
$\varepsilon$	dielectric constant
$\kappa$	curvature (Section 2.4.2.3)
$\lambda$	Lyapunov exponent (Section 5.4.2)
$\lambda$	geometry parameter (Section 2.4.2.3)
$\lambda$	mean free path
$\lambda$	optical wavelength (Chapters 3 and 7)
$\lambda_{\text{D}}$	Debye length
$\eta$	efficiency
$\mu$	dynamic viscosity
$\nu$	kinematic viscosity
$\Phi$	dissipation function
$\rho$	density
$\Psi$	electric potential
$\psi$	stream function
$\sigma$	characteristic diameter of a molecule (Section 2.1.1)
$\tau$	characteristic time
$\theta$	angle, azimuthal angle
$\theta$	relative temperature (Section 5.4.1.3)
$\theta$	variable used in Fourier series (Sections 2.1.2.2 and 4.5.2)
$\rho_{\text{el}}$	charge density
$\sigma$	area density (Section 6.7.1)

$\sigma$	surface tension, interfacial tension	$\mathbf{m}$	dipole moment
$\sigma_{\text{el}}$	electric conductivity	$M$	molecular mass
$\chi$	susceptibility	NA	numerical aperture
$\tau$	torsion (Section 2.4.2.3)	$n$	number density
$\Omega$	collision integral	$n$	refractive index (Chapter 7)
$\Omega$	strength function of Dean vortices (Section 5.2.1)	$N_{\text{A}}$	Avogadro number
$\omega$	angular frequency	$\mathbf{P}$	polarization field
$\zeta$	zeta potential	$p$	pressure
<b>Latin Symbols</b>		$\dot{Q}$	volumetric flow rate
$A$	surface area	$q$	electric charge
$\mathbf{B}$	magnetic flux density field	$R$	fluidic resistance (Section 4.5)
$c$	concentration	$R$	radius of curvature (Section 5.2.2)
$c$	propagation speed of a wave (Section 7.7.1)	$r$	distance between the two molecules (Section 2.1.1)
$c_p$	specific heat	$r$	interface position between two streams (Section 2.1.2.2)
$\mathbf{D}$	displacement field	$r$	pressure ratio (Section 4.5)
$D$	diffusion coefficient	$r$	production rate of the species per volume (Section 2.1.2.4)
$e$	elementary charge	$r$	radial variable, radius
$E_{\text{el}}$	electric field strength	$T$	absolute temperature
$E_{\text{mech}}$	Young's modulus	$T$	surface tension of a thin membrane (Section 6.7.1)
$\mathbf{f}$	force vector	$t$	time
$F$	Faraday constant (Section 2.6.1.6)	$\bar{u}$	mean velocity
$F$	force	$u, v, w$	velocity components
$f$	frequency	$\mathbf{v}$	velocity vector
$\mathbf{g}$	gravity vector	$x, y, z$	spatial variables
$I$	intensity value	$z$	ionic charge (Section 2.2.3.3)
$\mathbf{J}$	current density field		
$J$	mass flux		
$k_{\text{B}}$	Boltzmann constant		

# 1 Introduction

---

## 1.1 Micromixers and Mixing at the Microscale

This book discusses the design, fabrication and characterization of micromixers, which are defined as miniaturized mixing devices for at least two different phases that can be liquids, solids or gases. The structures of a micromixer are fabricated partially or wholly using microtechnology or precision engineering. The characteristic channel size of micromixers is in the submillimeter range. Common channel widths are on the order of 100 to 500  $\mu\text{m}$ , while channel length could be a few millimeters or more. The channel height is on the order of the channel width or smaller. The overall volume defined by a micromixer is from microliters to milliliters. Compared to molecular size scales, the length scale and volume scale of micromixers are very large. This fact leads to two key characteristics of micromixers. Firstly, designing micromixers relies on manipulating the flow using channel geometry or external disturbances. Secondly, while micromixers bring advantages and new features into chemical engineering, molecular level processes such as reaction kinetics remain almost unchanged.

Mixing is a transport process for species, temperature, and phases to reduce inhomogeneity. Mixing leads to secondary effects such as reaction and change in properties. In conventional macroscale mixing techniques, there are three established terminologies for mixing: macromixing, mesomixing, and micromixing [1]. *Macromixing* refers to mixing governed by the largest scale of fluid motion. For instance, the scale of macromixing corresponds to the diameter of the mixing tank. *Micromixing* is mixing at the smallest scale of fluid motion and molecular motion. In conventional macroscale mixing, the smallest scale of fluid motion is the size of turbulent eddies, also called the Kolmogorov scale. *Mesomixing* is in the scale between macromixing and microscale. Although micromixers may have dimensions on the order of micrometers, transport process in micromixers may still be classified as mesomixing. Since structures in micromixers may have a size approaching the Kolmogorov scale, this book avoids the use of micromixing for describing mixing processes.

There are many different ways to provide mixing in macroscale such as molecular diffusion, eddy diffusion, advection, and Taylor dispersion. Eddy diffusion is the transport of large groups of species and requires a turbulent flow. Because of the dominant viscous effect at the microscale, turbulence is not possible in micromixers. Mixing based on eddy diffusion is therefore not relevant for micromixers. Thus, the main transport phenomena in micromixers are molecular diffusion, advection and Taylor dispersion. Molecular diffusion is caused by the random motion of molecules. This transport mechanism is characterized by the molecular diffusion coefficient. Advection is the transport



phenomenon caused by fluid motion. A simple Eulerian velocity can lead to a chaotic distribution of the mixed species. A stable and laminar flow can also lead to chaotic advection. Thus, chaotic advection would be ideal for the laminar flow condition in micromixers. Taylor dispersion is advection caused by a velocity gradient. Axial dispersion occurs due to advection and interdiffusion of fluid layers with different velocities. Due to this effect, mixing based on Taylor dispersion can be two or three orders faster than mixing based on pure molecular diffusion.

Designing micromixers is a completely new engineering discipline, because existing designs in macroscale can not simply be scaled down for microscale applications. One of the main challenges related to miniaturization is the dominance of surface effects over volume effects. Actuation concepts based on volume forces working well at the macroscale may have problems at the microscale. A magnetic stirrer is a typical example for the ratio between surface forces and volume forces. A magnetic stirrer consists of a bar magnet and a rotating magnet or stationary electromagnets creating a rotating magnetic field. The driving magnetic force is proportional to the volume of the bar magnet, while the friction force is proportional to its surface. Scaling down the stirrer follows the so-called cube-square law. That means, shrinking down the stir bar 10 times would roughly decrease its volume by 1000 times and its surface only by 100 times. With its original size, the external magnetic field can generate a force of the same order of the friction force and causes the stir bar to move. Scaling down the size 10 times in the same magnetic field would create a small driving force, which is only 1/10th of the friction force. As a consequence, the stir bar can not move. A surface force-based actuation concept would allow scaling down because the ratio between driving force and friction force would remain unchanged.

The dominant surface phenomena at the microscale also affect mixing processes with immiscible interfaces. For a *solid-liquid* system, mixing starts with a suspension of the solid particles. The dissolving process follows suspension. The large surface to volume ratio at the microscale is an advantage for the dissolving process, making it easily achievable. Thus, the main challenge is the suspension process. Because of their relatively large sizes and the correspondingly small diffusion coefficient, particles can only be suspended at the microscale with the help of chaotic advection. Therefore, the quality of solid-liquid mixing in microscale is determined by the suspension process.

In a system of *immiscible liquids*, additional energy is needed to overcome interfacial tension. On the one hand, dispersing the immiscible phases is a difficult task. On the other hand, surface tension breaks the stretched fluid into segments and forms microdroplets. The advantage of the microscale is that the formation process can be controlled down to each individual droplet. Therefore, emulsions with a homogenous droplet size can be achieved in micromixers.

Gas-liquid systems are other systems that are affected by the dominant surface phenomena. Some applications such as hydrogenation, oxidation,

carbonation and chlorination require *gas-liquid* dispersion. Unlike a liquid-liquid emulsion, gas molecules can be absorbed into the liquid phase. The gas-liquid mixing process consists of two processes: dispersion of the gas bubble and absorption of gas molecules. While absorption is promoted due to the larger available interfacial area, dispersion of tiny gas bubbles is the main challenge in designing micromixers for a gas-liquid system.

Besides surface phenomena, the laminar flow condition is another challenge for designing micromixers. The problems in micromixers are similar to those in macroscale laminar mixers. Laminar mixers exist in many processes of the food, biotechnological and pharmaceutical industries because of the high viscosity and the slow flow velocity involved. For many applications, the flow velocity in micromixers can not be too high. The small size of micromixers leads to an extremely large shear stress in mixing devices, even at relatively slow flow velocities. This shear stress may damage cells and other sensitive bioparticles. In complex fluids with large molecules and cells, the fluid properties become non-Newtonian at high shear stress. On the one hand, the high shear compromises both the metabolic and physical integrity of cells. On the other hand, viscoelastic effects under this condition may lead to flow instability, which can be well utilized for improving mixing.

The time scale of mixing processes changes with miniaturization. Most micromixers are used as a reaction platform for analysis or synthesis. Mixing and chemical reaction are interrelated [2]. While reaction kinetics and reaction time do not change with miniaturization, mixing time can be significantly affected by the mixer design as well as by the mixer type. This fact leads to two important issues related to chemical reaction: measurement of real reaction kinetics and control over reaction products.

At the macroscale, mixing time is usually much larger than reaction time. The reaction rate is therefore mostly determined by the mixing time. At the microscale, mixing time can be reduced to the same order as or even less than the reaction time. Measurement of real reaction kinetics is therefore possible at the microscale.

Mixing time and consequently the reaction products can be possibly controlled at the microscale. If the reaction results in only one product, mixing time can only affect the reaction rate. If there is more than one product, mixing time determines the product composition and distribution. The following example shows the impact of mixing type on reaction results. Assume a reaction between the substrate S and reagent R:



where  $P_1$  is the desired reaction product. However,  $P_1$  can react with R to form a undesired product  $P_2$ :



If mixing relies on the relatively slow process of molecular diffusion as in the case of a parallel lamination micromixer,  $P_1$  has enough time to react with R.

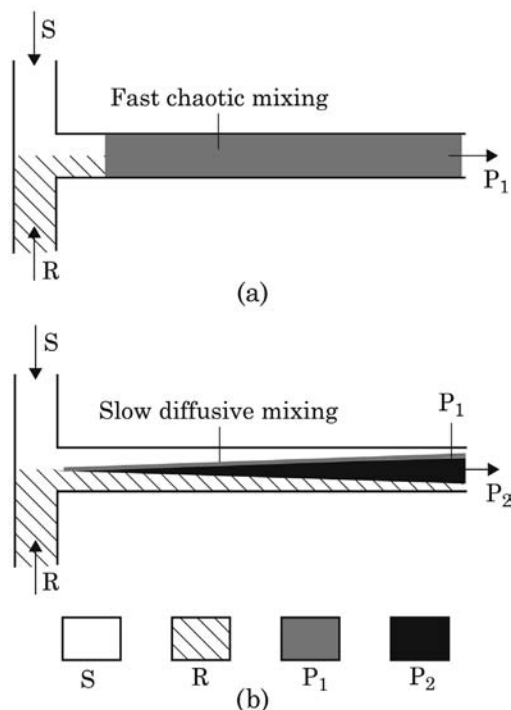


**Figure 1.1** Effect of micromixer type on a chemical reaction with more than one product: (a) fast mixing with chaotic advection, (b) slow mixing with molecular diffusion.

Therefore, the main product of the reaction process is P<sub>2</sub>. If mixing occurs quickly, for instance through chaotic advection, all molecules of R are utilized in the first reaction to form P<sub>1</sub>, not many R molecules are left for the secondary reaction. Thus, the main product of the reaction is P<sub>1</sub>. Fig. 1.1 illustrates this problem.

## 1.2 Micromixers as Microreactors

The last decade has witnessed increasing activities in the use of microfluidic technology in analytical chemistry and chemical production. Mixing is the central process of most microfluidic devices for medical diagnostics, genetic sequencing, chemistry production, drug discovery, and proteomics. The impact of micromixers on microfluidic systems for chemical analysis and synthesis is similar to that of transistors in integrated circuits. Although micromixers for analysis and synthesis are different, some applications require both classes. For instance, in combinatorial chemistry and screening microdevices, micromixers are analytical tools for information gathering and synthetic tools for providing minute quantities of products.

In micromixers for analysis, information gained from this product is the purpose of the mixing process and the reaction. The amount of the reaction product only needs to fulfill the detectability requirements. In contrast, reaction products in synthesis applications are used to make materials with improved properties at the favorable conditions given by the micromixers. A large amount of the product may be needed. Thus, the design of micromixers for synthesis should be ready for numbering up in the case of large-scale production [3].

Micromixers as microreactors will potentially have a big impact in chemical technologies. Because of the small size, micromixers allow the control over a number of production process parameters in chemistry and pharmaceutical industries. Reaction conditions that are unusual at the macroscale are technically possible in micromixers. The advantages of reactions in micromixers are the small thermal inertia, the uniform temperature, the high gradient of the different physical fields, the short residence time, and the high surface to volume ratio. The small thermal inertia allows fast and precise temperature control in micromixers. Miniaturization leads to higher rates of heat and mass transfer. Compared to their macroscale counterparts, micromixers can offer more aggressive reaction conditions. The large surface to volume ratio allows effective suppression of homogenous side reactions in heterogeneously catalyzed gas phase reactions. The small size makes reaction in micromixers safe because of the suppression of flames and explosions. Explosions can be suppressed by using mixing channels with a hydraulic diameter less than the quenching distance [4]. For instance, the fluorination of toluene can be carried out at  $-10\text{ }^{\circ}\text{C}$  in micromixers. Conventional reactors would require a temperature of  $-70\text{ }^{\circ}\text{C}$  due to the explosive nature of the reaction [4]. In case of accidents, the small amounts of hazardous reaction products are easy to contain.

Micromixers as microreactors enable a faster transfer of research results into production. Since scaling up the mixer design is not possible, a lab setup can immediately be transferred into large scale production by numbering up. Since numbering up is the only option for micromixers, the scaling law leads to high device material to reaction volume ratio. That means fixed production costs will increase with miniaturization because of the higher costs of materials and infrastructure. If microreactors deliver a similar performance as their conventional macroscale counterparts, the higher production costs will make micromixers unprofitable for chemical production. However, for some particular products the smaller production capacity may save cost through other factors such as replacing a batch process by a continuous process. For instance, due to slow mass and heat transfer in macroscale reactors, reaction time for fine chemicals is determined by mixing and is much longer than needed for reaction kinetics. Replacing a batch-based macroscale reactor by a continuous-flow microreactor can significantly reduce the reaction time. The reactor volume is smaller, but the total throughput per unit time is higher. As a result, for the same amount of products the reaction process would be carried out faster in microreactors.

In addition, as illustrated in Fig. 1.1, selectivity of reaction may increase with micromixers. Production yields of microreactors could exceed that of batch-based macroscale reactors. The next cost saving factor of micromixers for chemical production is the intensification process. The larger surface to volume ratio provides more surface for catalyst incorporation. Compared to its macroscale counterpart, the amount of catalyst needed in a microreactor can be decreased by a factor of 1000. If the cost of the catalyst is significant in the overall production, saving catalyst can compensate the large amount of construction materials needed for numbering up microreactors.

Micromixers have an indirect impact on national security due to the possibility of on-site portable detection systems for chemical weapons and explosives. However, due to their portability micromixers could be misused by criminals and terrorists [4]. A miniaturized chemical plant fitted into a suitcase could be misused for the production of drugs and hazardous gases. Raw chemicals may not be detectable prior to reactions in the miniature plants. Lethal nerve gases could be formed by two primary less-toxic compounds in a micromixer. Detection facilities should be extended to these precursor compounds to counter this potential misuse.

### 1.3 Organization of the Book

This book offers a wide spectrum for the study of the mixing processes at the microscale, from fundamental transport effects to a variety of designs to specific applications in chemistry and the life sciences. After the introduction in Chapter 1, Chapter 2 provides readers with the basic terminology and fundamental physics of transport effects that will be used for designing micromixers. Chapter 2 discusses in details the three key mass transport effects often used in micromixers: molecular diffusion, Taylor dispersion and chaotic advection. The challenges and advantages of miniaturization in mixing are highlighted in this chapter with the help of scaling laws. The scaling laws are discussed based on non-dimensional numbers, which represent relationships between different transport effects.

Chapter 3 gives an overview of available microtechnologies for making micromixers. Basic techniques of conventional silicon-based microtechnologies will be covered. Since polymers are chemically and biologically compatible, polymeric micromachining will be the focus of this chapter. Technologies for making mixing channel, for bonding and sealing are necessary for making a micromixer. This chapter also discusses the design and fabrication of fluidic interconnects that are needed for interfacing micromixers to larger-scale devices and equipment.

Different concepts and designs for micromixers are discussed in Chapters 4 to 6. Although all mixing concepts involve molecular diffusion, Chapter 4 only discusses concepts where molecular diffusion is the primary mass transfer

process. Based on the arrangement of the mixed phases, the four mixer types discussed in this chapter are parallel mixer, serial mixer, sequential mixer and injection mixer.

Chapter 5 is dedicated to micromixers based on chaotic advection. In contrast to the micromixers discussed in Chapter 4, this class of micromixers relies on bulk mass transport for mixing. The general concepts for generating chaotic advection are stretching and folding of fluid streams. These stretching and folding actions can be implemented in a planar design or in a complex three-dimensional channel structure. A special case of chaotic advection is mixing in microdroplets. Manipulation of the flow field inside a droplet can lead to the same stretching and folding effects achieved in a continuous-flow platform.

Chapter 6 discusses active mixers, where mixing is achieved with energy induced by an external source. Active mixers are similar to conventional macroscale mixers, where fluid motion is driven by an impeller. However as discussed in Section 1.1, miniaturization of the impeller concept would not work because of the dominant viscous force at the microscale. This chapter discusses different concepts for inducing a disturbance in the flow field. The use of electrohydrodynamic, dielectrophoretic, electrokinetic, magnetohydrodynamic, acoustic and thermal effects in micromixers is discussed here.

Chapter 7 summarizes key diagnostics techniques for characterization of micromixers. Since both velocity and concentration fields are important for good mixing, diagnostics techniques for these fields will be at the center of this chapter. The quantification of the extent of mixing is important for evaluation of performance as well as for design optimization of micromixers.

Chapter 8 discusses the current applications of micromixers. Different applications need different design requirements. The chapter discusses applications from the two major areas: labs-on-a-chip for chemical and biochemical analysis, and for chemical production. This chapter also recommends materials and mixer types for each application area.

## References

1. E.L. Paul, V.A. Atiemo-Oberg and S.M. Kresta, *Handbook of Industrial Mixing*, Wiley, New York, 2004.
2. J.R. Bourne, "Mixing and the Selectivity of Chemical Reactions," *Organic Process Research & Development*, Vol. 7, pp. 471–508, 2003.
3. K.F. Jensen, "The Impact of MEMS on the chemical and pharmaceutical industries," Technical Digest of the IEEE Solid State Sensor and Actuator Workshop, Hilton Head Island, SC, 4–8 June, 2000, pp. 105–110.
4. H. Löwe, V. Hessel and A. Müller, "Microreactors. prospects already achieved and possible misuse," *Pure Applied Chemistry*, Vol. 74, pp. 2271–2276, 2002.



## 2 Fundamentals of Mass Transport at the Micro Scale

---

### 2.1 Transport Phenomena

Transport phenomena in micromixers can be described theoretically at two basic levels: molecular level and continuum level. The two different levels of description correspond to the typical length scale involved. Continuum model can describe most transport phenomena in micromixers with a length scale ranging from micrometers to centimeters. Most micromixers for practical applications are in this range of length scale. Molecular models involve transport phenomena in the range from one nanometer to one micrometer. Mixers with length scale in this range should be called “nanomixer”. The term “micromixer” in this book will cover devices with submillimeter length dimension.

At continuum level, the fluid is considered as a continuum. Fluid properties are defined continuously throughout the space. At this level, fluid properties, such as viscosity, density, and conductivity, are considered as material properties. Transport phenomena can be described by a set of conservation equations for mass, momentum, and energy. These equations of changes are partial differential equations, which can be solved for physical fields in a micromixer, such as concentration, velocity, and temperature.

Miniaturization technologies have pushed the length scale of microdevices further. Upon the advent of nanotechnology, scientists and engineers will encounter more phenomena at the molecular level. At this level, transport phenomena can be described through molecular structure and intermolecular forces. Because many micromixers are used as microreactors, fundamental understanding of molecular processes is important for designing devices with a length scale in the micrometer to centimeter range.

#### 2.1.1 Molecular Level

At molecular level, the simplest description of transport phenomena is based on the kinetic theory of diluted monatomic gases, which is also called the Chapman–Enskog theory. The interaction between nonpolar molecules is represented by the Lennard-Jones potential, which has an empirical form of:

$$\phi_{ij}(r) = 4\varepsilon \left[ c_{ij} \left( \frac{\sigma}{r} \right)^{12} - d_{ij} \left( \frac{\sigma}{r} \right)^6 \right], \quad (2.1)$$

where  $\sigma$  is the characteristic diameter of the molecule,  $r$  is the distance between the two molecules, and  $\varepsilon$  is the characteristic energy, which is the maximum



**Table 2.1** Lennard-Jones Characteristic Energies and Characteristic Diameters of Common Gases [1]

Gas	Characteristic energy ( $\varepsilon/k_B$ )	Characteristic diameter $\sigma$ (nm)
Air	97.0	0.362
N <sub>2</sub>	91.5	0.368
CO <sub>2</sub>	190.0	0.400
O <sub>2</sub>	113.0	0.343
Ar	124.0	0.342

Boltzmann constant:  $k_B = 1.38 \times 10^{-23}$  J/K,  $d_{ij} = c_{ij} = 1$ .

energy of attraction between the molecules. In (2.1), the term  $(\sigma/r)^{12}$  represents the repulsion potential, while the term  $(\sigma/r)^6$  represents the attraction potential between the pair of molecules. The coefficients  $c_{ij}$  and  $d_{ij}$  are determined by molecule types and often assumed to be 1. Table 2.1 lists the parameters of some common gases. With the Lennard-Jones potential, the force between the molecules can be derived as:

$$F_{ij} = -\frac{d\phi_{ij}(r)}{dr} = \frac{48\varepsilon}{\sigma} \left[ c_{ij} \left( \frac{\sigma}{r} \right)^{13} - d_{ij} \left( \frac{\sigma}{r} \right)^7 \right]. \quad (2.2)$$

The Lennard-Jones model results in the characteristic time:

$$\tau = \sigma \sqrt{M/\varepsilon} \quad (2.3)$$

where  $M$  is the molecular mass. This characteristic time corresponds to the oscillation period between repulsion and attraction. Furthermore, the model allows the determination of the dynamic viscosity of a pure monatomic gas [2]:

$$\mu = \frac{2.68 \times 10^{-26} \sqrt{MT}}{\sigma^2 \Omega} \quad (2.4)$$

where the collision integral  $\Omega$  is a function of the dimensionless temperature  $k_B T/\varepsilon$  describing the deviation from rigid sphere behavior.  $k_B$  is the Boltzmann constant. Fig. 2.1 depicts the function of  $\Omega$ . The value of the collision integral  $\Omega$  is of the order of 1. The above equation allows the determination of Lennard-Jones parameters  $\sigma$  and  $\varepsilon$  from the measurement of viscosity  $\mu$ , a macroscopic continuum property.

**Example 2.1** (*Estimation of gas viscosity using kinetic theory*). Estimate the viscosity of pure nitrogen at 25 °C.

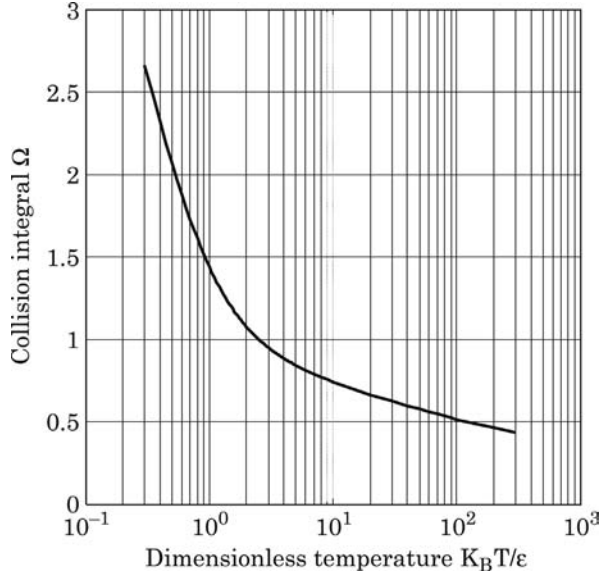


**Figure 2.1** Collision integral  $\Omega$  as a function of dimensionless temperature  $k_B T / \varepsilon$ .

**Solution.** Using the Lennard-Jones parameters of nitrogen listed in Table 2.1, the dimensionless temperature is:

$$\frac{k_B T}{\varepsilon} = \frac{25 + 273}{91.5} = 3.26.$$

According to the diagram in Fig. 2.1, the collision integral of  $N_2$  at 25 °C is 0.95. The estimated viscosity is then:

$$\begin{aligned} \mu &= \frac{2.68 \times 10^{-26} \sqrt{MT}}{\sigma^2 \Omega} \\ &= \frac{2.68 \times 10^{-26} \sqrt{28 \times (25 + 273)}}{(0.368 \times 10^{-9})^2 \times 0.95} = 1.90 \times 10^{-5} \text{ Pas.} \end{aligned}$$

The most important characteristic length scale in gas dynamics is the *mean free path*, which is the average distance traveled by a molecule between successive collisions:

$$\lambda = \frac{1}{\sqrt{2} \pi \sigma^2 n} \quad (2.5)$$

where  $n$  is the number density (number of molecules per unit volume):

$$n = \frac{p}{k_B T}. \quad (2.6)$$

The ratio between the mean free path and the characteristic length of the device, for instance the channel diameter is called the Knudsen number:

$$\text{Kn} = \frac{\lambda}{L}. \quad (2.7)$$

Because the Knudsen number represents the link between the length scale of a device and the interaction between fluid molecules, it can be used to estimate the right model for describing the transport phenomena. For  $\text{Kn} < 10^{-3}$ , the fluid is a continuum. For  $10^{-3} < \text{Kn} < 10^{-1}$ , a continuum model with modified boundary conditions is appropriate. For  $\text{Kn} > 10$ , the fluid can only be described by a free molecular flow model.

Kinetic theory can be applied to liquid as well. In this model, the motion of liquid molecules is confined within a space limited by its neighboring molecules. Based on this theory, the viscosity of a liquid can be estimated as:

$$\mu = \frac{N_A \hbar}{\bar{v}} \exp(3.8T_b/T) \quad (2.8)$$

where  $N_A = 6.023 \times 10^{23}$  is the Avogadro number or the number of molecules in one mole;  $\hbar = 6.626068 \times 10^{-34} \text{ m}^2 \text{ kg/s}$  is the Planck constant;  $\bar{v}$  is the molar volume;  $T_b$  is the boiling temperature; and  $T$  is the temperature of the liquid.

The models of viscosity for gas (2.4) and for liquid (2.8) show opposite temperature dependency. While the viscosity of gases increases with higher temperature, the viscosity of liquids decreases.

**Example 2.2** (*Dynamic viscosity of water*). If the molar volume of water at 25 °C is  $18 \times 10^{-6} \text{ m}^3/\text{mol}$ , determine the viscosity of water at this temperature.

**Solution.** The boiling temperature of water under atmospheric pressure is assumed to be 100 °C. According to (2.8), the viscosity of water can be estimated as:

$$\begin{aligned} \mu &= \frac{N_A \hbar}{\bar{v}} \exp(3.8T_b/T) \\ &= \frac{6.023 \times 10^{23} \times 6.626068 \times 10^{-34}}{18 \times 10^{-6}} \exp[3.8(100 + 273)/(25 + 273)] \\ &= 2.58 \times 10^{-3} \text{ Pas.} \end{aligned}$$

The equation overestimates the viscosity of water.

In the previous discussion, continuum properties are derived from the molecular model using statistical methods. If there are not enough molecules for good statistics, numerical tools are needed for modeling transport phenomena at the molecular level. There are two numerical methods: molecular dynamics (MD) and direct simulation Monte Carlo (DSMC). While MD is a deterministic method, DSMC is a statistical method.

Molecular dynamics is a numerical method for modeling the motion of single molecules. The interactions between the molecules can be described by the classical second Newton's law. The simplest model of a molecule is a hard sphere of a mass  $m$ . The binary interaction between two molecules is determined by the Lennard-Jones force (2.2):

$$\mathbf{f}_{ij}(r) = -\mathbf{f}_{ji}(r) \quad (2.9)$$

where  $r = |\mathbf{r}_i - \mathbf{r}_j|$  is the distance between the molecules. The bold letter indicates a vectorial variable. The dynamics of molecule  $i$  can be described by the second Newton law:

$$m \frac{d\mathbf{r}_i}{dt} = \sum_{j=1, j \neq i}^N \mathbf{f}_{ij} \quad (2.10)$$

where  $N$  is the total number of molecules in the modelled system. The basic steps of a MD-simulation are:

- Determination of initial conditions and geometry parameters,
- Determination of interaction force (2.2), and
- Integration of equation of motion (2.10).

Because of its deterministic nature, MD is extremely expensive in terms of computational resources. Less resources would be needed if the system is modelled with a statistical method.

Direct simulation Monte Carlo is a statistical method for modeling at the molecular level. In DSMC, many molecules are modeled as a single particle. The interactions between the molecules of each particle are determined statistically, while the motion of the particle is modeled deterministically. The basic steps of DSMC are [3]:

- Determination of particle motion,
- Indication and cross referencing of particles,
- Simulation of particle collision, and
- Sampling of macroscopic properties.

### 2.1.2 Continuum Level

At the continuum level, transport phenomena are described with a set of conservation equations. Because flow in micromixers is laminar, we don't need to deal with turbulent flow, which is impossible to solve analytically. The three basic conservation equations are:

- Conservation of mass: continuity equation,

- Conservation of momentum: Newton's second law or Navier–Stokes equation, and
- Conservation of energy: first law of thermodynamics or energy equation.

Solving these three equations will result in three basic variables: the velocity field  $\mathbf{v}$ , the pressure field  $p$ , and the temperature field  $T$ . Fluid properties, depending on the thermodynamic state (pressure  $p$  and temperature  $T$ ) such as density, viscosity, thermal conductivity, and enthalpy, can be derived from these variables and fed back into the conservation equations. The above three equations are formulated for a single phase of homogenous composition. In micromixers, most fluids carry one or more species other than the carrying fluids. If the mixers are used as microreactors, chemical reactions also need to be considered. Thus, in addition to the above three conservation equations, two further equations are needed to describe the transport of species in micromixers:

- Conservation of species: convective/diffusive equation and
- Laws of chemical reactions.

### 2.1.2.1 Conservation of Mass

The continuity equation has the general form:

$$\frac{D\rho}{Dt} + \rho \operatorname{div} \nabla = 0 \quad (2.11)$$

where  $\nabla$  is the nabla operator and  $\frac{D}{Dt}$  is the total derivative operator, which is defined as:

$$\frac{D}{Dt} = \frac{\partial}{\partial t} + u \frac{\partial}{\partial x} + v \frac{\partial}{\partial y} + w \frac{\partial}{\partial z} = \frac{\partial}{\partial t} + (\mathbf{v} \cdot \nabla) \quad (2.12)$$

where  $\mathbf{v} = (u, v, w)$  is the velocity vector.

### 2.1.2.2 Conservation of Momentum

Conservation of momentum is described by Newton's second law:

$$\rho \frac{D\mathbf{v}}{Dt} = \mathbf{f} = \mathbf{f}_{\text{body}} + \mathbf{f}_{\text{surface}}. \quad (2.13)$$

The left-hand side of the above equation represents the acceleration force, while the right hand-side consists of forces per unit volume acting on the fluid particle. The force  $\mathbf{f}$  may consist of body force and surface forces. At the microscale, surface forces such as viscous force, electrostatic force, or surface

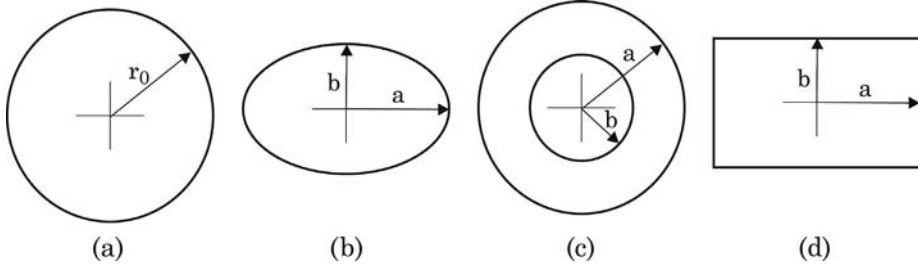


**Figure 2.2** Cross section of channels considered in Table 2.2: (a) circle; (b) ellipse; (c) concentric annulus; (d) rectangle.

stress are dominant over bulk forces such as gravity. If the only bulk force is gravity and surface forces are caused by a pressure gradient and viscous force, and both density and viscosity are constant, the Navier–Stokes equation can be derived from the general conservation equation (2.13):

$$\rho \frac{D\mathbf{v}}{Dt} = \rho \mathbf{g} - \nabla p + \mu \nabla^2 \mathbf{v} \quad (2.14)$$

where  $\rho$  and  $\mu$  are the density and the dynamic viscosity of the fluid respectively. In micromixers, we often encounter a pressure-driven flow in a straight microchannel. If the flow in the axial  $x$ -direction is fully developed, the continuity equation is automatically satisfied with  $v = w = 0$  and  $du/dx = 0$ . The Navier–Stokes equation (2.14) can then be further simplified to the two-dimensional form:

$$\frac{\partial^2 u}{\partial y^2} + \frac{\partial^2 u}{\partial z^2} = \frac{1}{\mu} \frac{dp}{dx} \quad (2.15)$$

where the right-hand side is a constant. Applying the no-slip boundary condition at the channel wall, an analytical solution can be obtained for channels with simple cross-section geometry, such as circle, ellipse, concentric annulus, rectangle, and equilateral triangle, Fig. 2.2. Table 2.2 shows and Fig. 2.3 lists the typical solution of the distribution of the dimensionless velocity  $u^*(y, z) = u(y, z)/\bar{u}$  and the mean velocity  $\bar{u}$  in the channel.

Many micromachining technologies result in microchannels with a rectangular cross section. The following examples investigate the flows of a single phase and multiple phases in rectangular microchannels.

**Example 2.3** (*Single-phase flow in a rectangular microchannel*). A liquid flows in a rectangular microchannel of width  $W$  and height  $H$ . The viscosity liquid is  $\mu$ . Determine the velocity distribution in this microchannel and the flow rate if a pressure difference of  $\Delta p$  is applied across the channel length of  $L$ .

**Table 2.2** Analytical Solution for Velocity Field Inside a Straight Channel

Channel type	Solution
Circle	$u^*(r) = 2 \left( 1 - \frac{r^2}{r_0^2} \right)$ $\bar{u} = \frac{1}{8\mu} \left( -\frac{dp}{dx} \right) r^2$
Ellipse	$u^*(y, z) = 2 \left( 1 - \frac{y^2}{a^2} - \frac{z^2}{b^2} \right)$ $\bar{u} = \frac{1}{4\mu} \left( -\frac{dp}{dx} \right) \frac{a^2 b^2}{a^2 + b^2}$
Concentric annulus	$u^*(r) = 2 \left[ a^2 - r^2 + (a^2 - b^2) \frac{\ln(a/r)}{\ln(b/a)} \right] / \left[ a^2 + b^2 - \frac{a^2 - b^2}{\ln(a/b)} \right]$ $\bar{u} = \frac{1}{8\mu} \left( -\frac{dp}{dx} \right) \left[ a^2 + b^2 - \frac{a^2 - b^2}{\ln(a/b)} \right]$
Rectangle	$u^*(y, z) = \frac{48}{\pi^3} \sum_{n=1}^{\infty} (-1)^{n-1} \left[ \left\{ 1 - \frac{\cosh[(2n-1)\pi z/2a]}{\cosh[(2n-1)\pi b/2a]} \right\} \right.$ $\times \frac{\cos[(2n-1)\pi y/2a]}{(2n-1)^3} / \left\{ 1 - \frac{192a}{\pi^3 b} \sum_{n=1}^{\infty} \frac{\tanh[(2n-1)\pi b/2a]}{(2n-1)^5} \right\}$ $\left. \bar{u} = \frac{a^2}{3\mu} \left( -\frac{dp}{dx} \right) \left\{ 1 - \frac{192a}{\pi^3 b} \sum_{n=1}^{\infty} \frac{\tanh[(2n-1)\pi b/2a]}{(2n-1)^5} \right\} \right]$

**Solution.** The fully developed flow in the microchannel is governed by Navier–Stokes equations:

$$\frac{\partial^2 u}{\partial y^2} + \frac{\partial^2 u}{\partial z^2} = \frac{1}{\mu} \frac{dp}{dx} \quad (2.16)$$

where  $\mu$  is the dynamic viscosity of the fluid, and  $dp/dx$  is the pressure gradient along the  $x$ -axis. Normalizing the coordinate system by the channel width  $W$  ( $y^* = y/W$ ,  $z^* = z/W$ ) and the velocity by a reference velocity  $u_0$  ( $u^* = u/u_0$ ), the dimensionless Navier–Stokes equation for the hatched regions in Fig. 2.4 is:

$$\frac{\partial^2 u^*}{\partial y^{*2}} + \frac{\partial^2 u^*}{\partial z^{*2}} = P' \quad (2.17)$$

where  $P' = W^2/(\mu_1 u_0) dp/dx$  represents the constant pressure gradient along the channel with the reference velocity  $u_0$ . The no-slip conditions at the wall result in:

$$\begin{aligned} u^*(1, z^*) &= 0 \\ u^*(0, z^*) &= 0 \\ u^*(y^*, \pm h/2) &= 0 \end{aligned}$$

where  $h = H/W$  is the dimensionless height of the channel. Using Fourier series analysis, the dimensionless velocity has the form ( $0 < y^* < 1$ ,  $0 < z^* < h/2$ ):

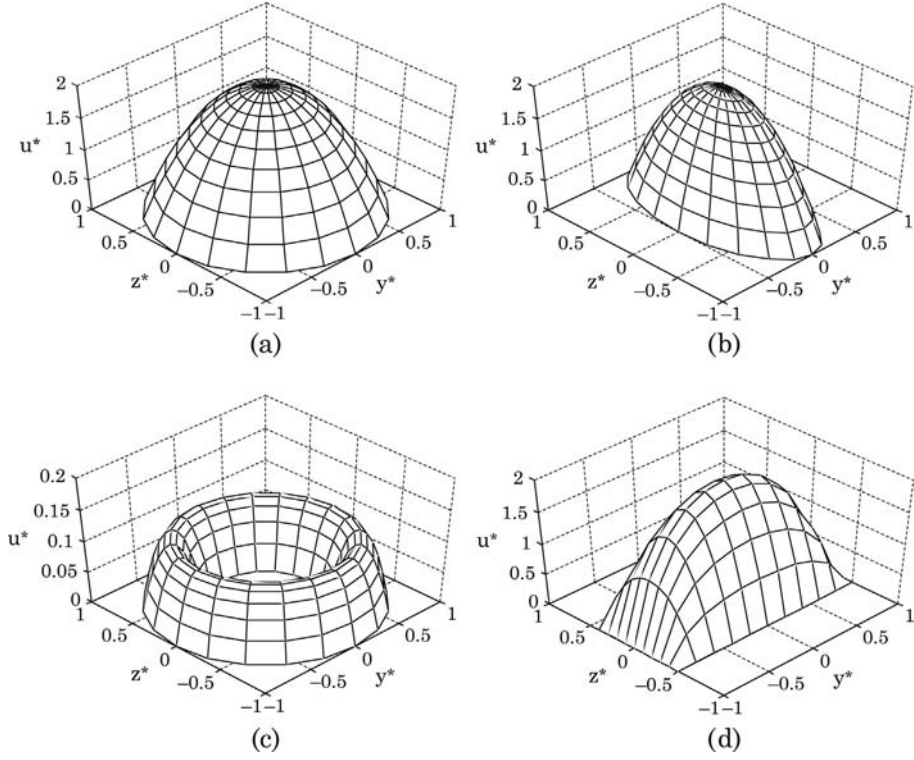


**Figure 2.3** Distribution of dimensionless velocity according to Table 2.2 ( $y^* = y/a$ ,  $z^* = z/a$ ): (a) circle; (b) ellipse ( $a = 2b$ ); (c) concentric annulus ( $a = 2b$ ); (d) rectangle ( $a = 2b$ ).

$$u^* = \frac{48 \sum_{n=1}^{\infty} \frac{1}{(2n-1)^3} \left\{ 1 - \frac{\cosh[(2n-1)\pi z^*]}{\cosh[(2n-1)\pi h/2]} \right\} \sin[(2n-1)\pi y^*]}{\pi^3 \left( 1 - \sum_{n=1}^{\infty} \frac{192}{\pi^5 (2n-1)^5 h} \tanh \left[ \frac{(2n-1)\pi h}{2} \right] \right)}.$$

If a pressure difference of  $\Delta p$  is applied across the channel length of  $L$ , the flow rate is:

$$\dot{Q} = \frac{H^3 W \Delta p}{12 \mu L} \left\{ 1 - \sum_{n=1}^{\infty} \frac{192 H}{(2n-1)^5 \pi^5 W} \tanh \left[ \frac{(2n-1)\pi H}{2W} \right] \right\}.$$

For a microchannel with low aspect ratio ( $h = H/W \rightarrow 0$ ), the flow rate can be estimated as:

$$\dot{Q} \approx \frac{H^3 W \Delta p}{12 \mu L} (1 - 0.630h).$$



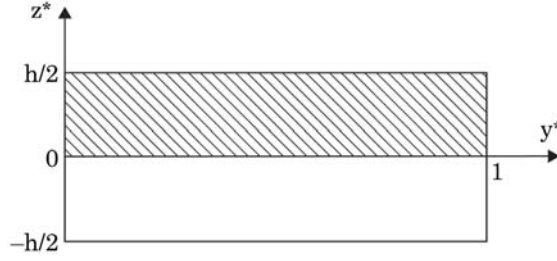


**Figure 2.4** Dimensionless model of single-phase flow in a rectangular microchannel, only half of the channel cross section (hatched areas) is considered in the analytical model.

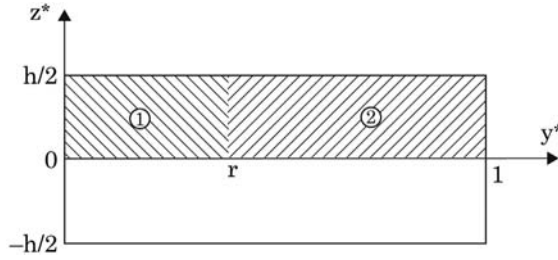


**Figure 2.5** Dimensionless model of two immiscible streams for estimating the velocity distribution inside the mixing channel, only half of the channel cross section (hatched areas) is considered in the analytical model.

**Example 2.4** (*Velocity distribution of streams with different viscosities in a rectangular microchannel*). Two immiscible fluids flow side-by-side in a rectangular microchannel of width  $W$  and height  $H$ . The viscosity ratio and flow rate ratio of the two fluids are  $\beta = \mu_2/\mu_1$  and  $\gamma = \dot{Q}_2/\dot{Q}_1$  respectively. Determine the velocity distribution in this microchannel [4].

**Solution.** The fully developed flow in the microchannel is governed by Navier–Stokes equations:

$$\begin{aligned}\frac{\partial^2 u_1}{\partial y^2} + \frac{\partial^2 u_1}{\partial z^2} &= \frac{1}{\mu_1} \frac{dp}{dx} \\ \frac{\partial^2 u_2}{\partial y^2} + \frac{\partial^2 u_2}{\partial z^2} &= \frac{1}{\mu_2} \frac{dp}{dx}\end{aligned}$$

where  $\mu_1$  and  $\mu_2$  are the viscosities of the two streams, and  $dp/dx$  is the pressure gradient along the  $x$ -axis. Normalizing the coordinate system by the channel  $W$  ( $y^* = y/W$ ,  $z^* = z/W$ ) and the velocity by a reference velocity  $u_0$  ( $u^* = u/u_0$ ), the dimensionless Navier–Stokes equations for the regions 1 and 2 in Fig. 2.5 are:

$$\frac{\partial^2 u_1^*}{\partial y^{*2}} + \frac{\partial^2 u_1^*}{\partial z^{*2}} = P'$$

$$\frac{\partial^2 u_2^*}{\partial y^{*2}} + \frac{\partial^2 u_2^*}{\partial z^{*2}} = \frac{P'}{\beta}$$

where  $P' = W^2/(\mu_1 u_0) dp/dx$  represents the constant pressure gradient along the channel with the reference velocity  $u_0$  and the ratio of viscosities  $\beta = \mu_2/\mu_1$ . The no-slip conditions at the wall result in:

$$\begin{aligned} u_2^*(1, z^*) &= 0 \\ u_1^*(0, z^*) &= 0 \\ u_1^*, u_2^*(y^*, h) &= 0 \end{aligned}$$

where  $h = H/W$  is the dimensionless height of the channel. At the interface position  $r$  between the two streams, the velocity and the shear stress are continuous:

$$\begin{aligned} u_2^*(r, z^*) &= u_1^*(r, z^*) \\ \frac{\partial u_1^*}{\partial y^*} \Big|_{y^*=r} &= \beta \frac{\partial u_2^*}{\partial y^*} \Big|_{y^*=r}. \end{aligned}$$

For a flat channel ( $h \ll 1$ ) and a constant fluid density, the interface position of the two streams can be estimated based on mass conservation as:

$$r = \frac{1}{1 + \beta\gamma}.$$

The solutions have the Fourier forms ( $0 < y^* < 1$ ,  $0 < z^* < h/2$ ):

$$\begin{aligned} u_1^*(y^*, z^*) &= P' \left[ \frac{z^{*2} - h^2/4}{2} + \sum_{n=1}^{\infty} \cos \theta z^* (A_1 \cosh \theta y^* + B_1 \sinh \theta y^*) \right] \\ u_2^*(y^*, z^*) &= \frac{P'}{\beta} \left[ \frac{z^{*2} - h^2/4}{2} + \sum_{n=1}^{\infty} \cos \theta z^* (A_2 \cosh \theta y^* + B_2 \sinh \theta y^*) \right] \end{aligned}$$

where  $\theta = (2n - 1)\pi/h$ . The coefficients  $A_1$ ,  $A_2$ ,  $B_1$ ,  $B_2$  can be obtained by solving the Fourier series with the previous boundary conditions:

$$\begin{aligned} A_1 &= (-1)^{n+1} \frac{4h^2}{(2n - 1)^3 \pi^3} \\ B_1 &= A_1 \frac{(1 - \beta)(1 - \cosh \theta) \sinh^2 r\theta + (1 - \beta) \cosh r\theta \cosh \theta + \beta \sinh^2 r\theta}{(1 - \beta) \sinh r\theta \cosh r\theta \cosh \theta - \sinh \theta (\cosh^2 r\theta - \beta \sinh^2 r\theta)} \\ &\quad - A_1 \frac{(1 - \cosh \theta) \sinh r\theta \sinh \theta (\cosh^2 r\theta - \beta \sinh^2 r\theta) + \cosh^2 r\theta}{(1 - \beta) \sinh r\theta \cosh r\theta \cosh \theta - \sinh \theta (\cosh^2 r\theta - \beta \sinh^2 r\theta)} \end{aligned}$$

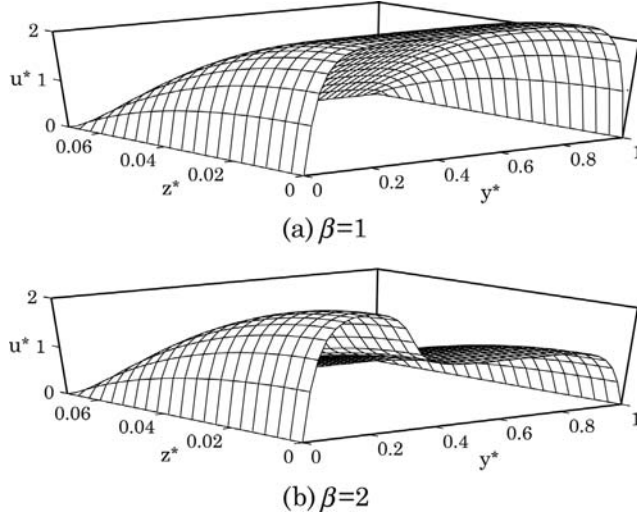


**Figure 2.6** Velocity distribution in a rectangular mixing channel ( $h = 0.14$ ): (a) with the same viscosity  $\beta = 1$ ; (b) with different viscosities  $\beta = 2$ .

$$\begin{aligned}
 A_2 &= A_1 \frac{(1 - \beta) \sinh r\theta \cosh r\theta \cosh \theta - \sinh \theta (\cosh^2 r\theta - \beta \sinh^2 r\theta)}{(1 - \beta) \sinh r\theta \cosh r\theta \cosh \theta - \sinh \theta (\cosh^2 r\theta - \beta \sinh^2 r\theta)} \\
 &\quad + A_1 \frac{-\beta \cosh \theta + (\beta - 1) \cosh r\theta \cosh \theta - \beta \sinh^2 r\theta + \cosh^2 r\theta}{(1 - \beta) \sinh r\theta \cosh r\theta \cosh \theta - \sinh \theta (\cosh^2 r\theta - \beta \sinh^2 r\theta)} \\
 B_2 &= A_1 \frac{\beta \cosh \theta + (\beta - 1) \cosh r\theta \cosh \theta + \beta \sinh^2 r\theta - \cosh^2 r\theta}{(1 - \beta) \sinh r\theta \cosh r\theta \cosh \theta - \sinh \theta (\cosh^2 r\theta - \beta \sinh^2 r\theta)}.
 \end{aligned}$$

Fig. 2.6 shows the typical velocity distribution in a rectangular channel for streams with different flow rates. For streams with the same viscosity, the velocity distribution is flat.

### 2.1.2.3 Conservation of Energy

The conservation of energy is governed by the first law of thermodynamics:

$$dQ + dW = dE_{\text{total}} \quad (2.18)$$

which means, the change of the total energy in a system is equal to the sum of the heat and work added to the system. The energy equation can then be formulated for the absolute temperature  $T$  as

$$\rho c_p \frac{DT}{Dt} = \beta T \frac{Dp}{Dt} + \text{div}(k \nabla T) + \Phi \quad (2.19)$$

where  $c_p$  is the specific heat at constant pressure,  $\beta = -\frac{1}{\rho} \left( \frac{\partial \rho}{\partial T} \right)_p$  is the thermal expansion coefficient,  $k$  is the thermal conductivity, and  $\Phi$  is the dissipation function. For Newtonian fluid the dissipation function caused by viscous stress is:

$$\begin{aligned} \Phi = \mu & \left[ 2 \left( \frac{\partial u}{\partial x} \right)^2 + 2 \left( \frac{\partial v}{\partial y} \right)^2 + 2 \left( \frac{\partial w}{\partial z} \right)^2 + \left( \frac{\partial v}{\partial x} + \frac{\partial u}{\partial y} \right)^2 \right. \\ & \left. + \left( \frac{\partial w}{\partial y} + \frac{\partial v}{\partial z} \right)^2 + \left( \frac{\partial u}{\partial z} + \frac{\partial w}{\partial x} \right)^2 \right] + \frac{2}{3} \mu \left( \frac{\partial u}{\partial x} + \frac{\partial v}{\partial y} + \frac{\partial w}{\partial z} \right)^2. \end{aligned} \quad (2.20)$$

Assuming an incompressible flow, a constant thermal conductivity and ignoring the kinetic energy change, the energy equation can be simplified to the heat-convection equation:

$$\rho c_p \frac{DT}{Dt} = k \nabla^2 T. \quad (2.21)$$

#### 2.1.2.4 Conservation of Species

The conservation of species leads to the diffusion/convection equation:

$$\frac{Dc}{Dt} = D \nabla^2 c + r_g, \quad (2.22)$$

where  $c$  is the concentration of the species,  $D$  is the diffusion coefficient of the species (solute) in the carrier fluid (solvent) and  $r_g$  is the generation rate of the species per volume. The above equation assumes a constant, isotropic diffusion coefficient. The left site of (2.22) represents the accumulation and convection of species. The first term on the right site represents molecular diffusion, while the last term is the generation of species.

The above conservation equations can also be formulated for the cylindrical and the spherical coordinate systems.

## 2.2 Molecular Diffusion

### 2.2.1 Random Walk and Brownian Motion

A random walk is the path traced by a particle taking successive steps, each in a random direction. The construction of a simple random walk follows the three basic rules:

- The particle starts at a predefined point,

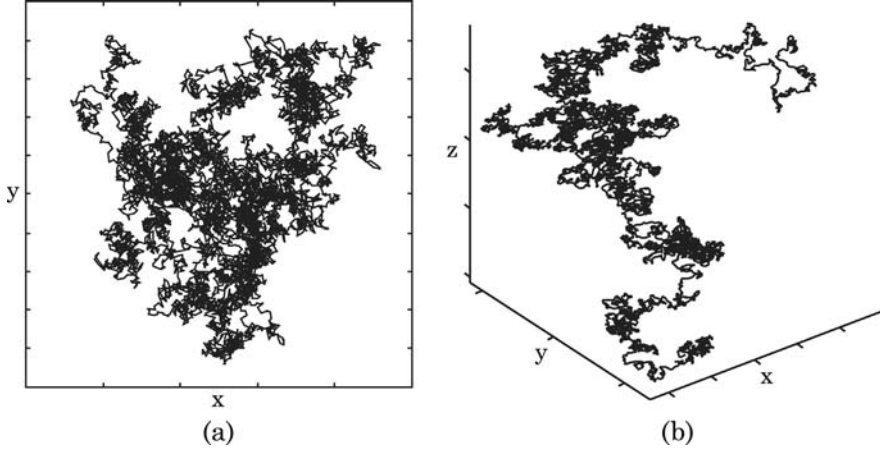


**Figure 2.7** Random walk of a particle: (a) two-dimensional; (b) three-dimensional.

- The distance done by each step is equal, and
- The direction from one point to the next is random.

Following these rules, a random walk of a particle can be realized with a simple program. Considering a one-dimensional random walk on a line, the particle has a random choice of two directions for each of its steps. The distance done by each step is assumed to be  $s$ . The position  $x(n)$  at a step  $n$  can be described as

$$x(n) = \sum_{i=1}^n s_i \quad (2.23)$$

where  $s_i$  is a random step, which can take a value of either  $+s$  or  $-s$ . The squared value of the position  $x(n)$  is:

$$x(n)^2 = \sum_{i=1}^n s_i^2 = ns^2 \propto Dt. \quad (2.24)$$

The proportionality comes from the assumption that the same amount of time is take to make each step ( $t \propto n$ ). The proportionality factor determines how fast the particle walks, which actually is the diffusion coefficient. Brownian motion is the random walk with very small steps. Fig. 2.7 shows the random walk of a particle calculated for 10,000 steps in two and three dimensions.

Jan Ingenhousz, a Dutch doctor, was the first to observe the irregular motion of coal dust particles on the surface of alcohol in 1785 [5]. However, this motion is regarded as discovered by the botanist Robert Brown, who observed in 1827 pollen particles floating in water under the microscope [6]. The Brownian

motion of particles in a liquid is due to the instantaneous imbalance in the forces exerted by the small liquid molecules on the particle. Thus, the diffusion coefficient of this particle can be derived from the force balance equation.

### 2.2.2 Stokes–Einstein Model of Diffusion

The time evolution of the position of the Brownian particle itself can be described approximately by the force balance equation where the random force of the liquid molecules represents one term in the balance. This equation is called the Langevin equation:

$$m \frac{d\mathbf{v}}{dt} = \beta \mathbf{v} + F(t) \quad (2.25)$$

where  $m$  is the mass of the particle,  $\beta$  is the friction coefficient and  $F(t)$  is the random force of the liquid molecules. On small timescales, inertial effects are dominant in the Langevin equation. The friction coefficient can be calculated using Stokes drag on a spherical particle with a radius of  $\sigma_p$ :

$$\beta = 3\pi\mu\sigma_p, \quad (2.26)$$

where  $\mu$  is the viscosity of the surrounding liquid. The force  $F(t)$  is random in time, thus its autocorrelation function should represent the delta function:

$$\langle F(t)F(t') \rangle = A\delta(t - t'), \quad (2.27)$$

where  $\delta$  is the Dirac (delta) function. Solving (2.25) for the one-dimensional case leads to the particle velocity:

$$u(t) = u_0 \exp(-\beta t/m) + \exp(-\beta t/m) \int_0^t \exp(\beta t'/m) dt'. \quad (2.28)$$

The variance of the displacement  $x(t)$  can subsequently be determined as [8]:

$$\frac{dx^2}{dt} = 2x(t)u(t) = 2 \int_0^t u(t)u(t')dt' = 2\langle u^2 \rangle \int_0^t \exp(-\beta t'/m)dt' \quad (2.29)$$

where  $\langle u^2 \rangle$  is the variance of the particle velocity. For time scale much larger than  $m/\beta$ :

$$\langle x^2(t) \rangle = 2Dt. \quad (2.30)$$

Thus, the diffusion coefficient of the particle can be determined as:

$$D = \langle u^2 \rangle m / \beta. \quad (2.31)$$

The kinetic energy of the particle is related to the temperature as:

$$\frac{1}{2} m \langle u^2 \rangle = \frac{1}{2} k_B T. \quad (2.32)$$

Substituting  $\langle u^2 \rangle = k_B T / m$  in (2.31) results in the Stokes–Einstein equation of the diffusion coefficient [9]:

$$D = \frac{k_B T}{3\pi\mu\sigma_p}. \quad (2.33)$$

## 2.2.3 Diffusion Coefficient

### 2.2.3.1 Diffusion Coefficient in Gases

Using the kinetic theory discussed in Section 2.1.1, diffusion coefficient in meters squared per second between two gases  $i$  and  $j$  can be formulated as [7]:

$$D = D_{ij} = D_{ji} = \frac{1.86 \times 10^{-27} T^{3/2} \sqrt{1/M_i + 1/M_j}}{p \sigma_{ij}^2 \Omega} \quad (2.34)$$

where  $M_i$  and  $M_j$  are the molecular weights of the gases,  $T$  is the absolute temperature, and  $p$  is the pressure. The collision diameter  $\sigma_{ij}$  is the arithmetic average of the characteristic diameter of the gas molecules  $\sigma_i$  and  $\sigma_j$ :

$$\sigma_{ij} = \frac{\sigma_i + \sigma_j}{2}. \quad (2.35)$$

The collision integral  $\Omega$  can be taken from the diagram depicted in Fig. 2.1. In this diagram, the dimensionless temperature is calculated based on the interaction energy, which is the geometric average of the individual characteristic energies:

$$\varepsilon_{ij} = \sqrt{\varepsilon_i \varepsilon_j}. \quad (2.36)$$

**Example 2.5** (*Estimation of diffusion coefficient of gases*). Estimate the diffusion coefficient of hydrogen in air at 282 K. Lennard-Jones potential

parameters of air and hydrogen are  $\sigma_1 = 0.3711$  nm,  $(\epsilon/k_B)_1 = 78.6$  and  $\sigma_2 = 0.2827$  nm,  $(\epsilon/k_B)_2 = 59.7$ , respectively. The molecular weights of air and hydrogen are 29 and 2, respectively. The experimental value is  $0.710 \times 10^{-4}$  m<sup>2</sup>/sec.

**Solution.** Although air consists mainly of oxygen and nitrogen we assume air is a gas molecule. According to (2.35), the collision diameter between air and hydrogen is:

$$\sigma_{12} = (\sigma_1 + \sigma_2)/2 = (0.3711 + 0.2827)/2 = 0.3269 \times 10^{-9} \text{ m.}$$

According to (2.36), the dimensionless temperature is:

$$\begin{aligned} \frac{k_B T}{\epsilon_{12}} &= \frac{k_B T}{\sqrt{\epsilon_1 \epsilon_2}} = \frac{T}{\sqrt{(\epsilon_1/k_B)(\epsilon_2/k_B)}} \\ &= \frac{282}{\sqrt{78.6 \times 59.7}} = 4.12. \end{aligned}$$

According to Fig. 2.1, the collision potential is approximately 0.88. Thus, the diffusion coefficient of hydrogen in air at 282 K is:

$$\begin{aligned} D &= \frac{1.86 \times 10^{-27} T^{3/2} \sqrt{1/M_i + 1/M_j}}{p \sigma_{ij}^2 \Omega} \\ &= \frac{1.86 \times 10^{-27} 282^{3/2} \sqrt{1/29 + 1/2}}{1(0.3269)^2 (0.88)} = 4.76 \times 10^{-5} \text{ m}^2/\text{s}. \end{aligned}$$

The estimated diffusion coefficient is 33% lower than the measured data.

### 2.2.3.2 Diffusion Coefficient in Liquids

While diffusion coefficients of gases are of the order of  $10^{-5}$  m<sup>2</sup>/sec, diffusion coefficients in liquids are of the order of  $10^{-9}$  m<sup>2</sup>/s. The diffusion coefficients of large molecules can be of the order of  $10^{-11}$  m<sup>2</sup>/sec. Diffusion coefficient of a molecule  $i$  in a solute  $j$  with a viscosity of  $\mu_j$  can be estimated with the Stokes–Einstein equation:

$$D_{ij} = \frac{k_B T}{3\pi\mu_j\sigma_i}, \quad (2.37)$$

where  $\sigma_i$  is the diameter of the molecule  $i$ . In the above equation, the term in the numerator represents the kinetic energy of the molecule, while the denominator represents the friction force acting on the molecule. Equation (2.37) breaks down if the size of the solute  $i$  is 5 times less than that of the solvent. For small solutes, the factor  $3\pi$  in (2.37) can be replaced by the factor  $2\pi$  due to less friction due to slip on the surface of the solute molecule. If the



solute is not spherical but ellipsoidal with dimensions  $a$  and  $b$ , the characteristic diameter can be estimated as:

$$\sigma_i = 2\sqrt{a^2 - b^2} / \ln \left( \frac{a + \sqrt{a^2 - b^2}}{b} \right). \quad (2.38)$$

**Example 2.6** (*Diffusion coefficient of a large molecule in water*). Fibrinogen is a protein that plays a key role in blood clotting. Fibrinogen significantly increases the risk of stroke. This protein molecule has a rod shape, 67 nm in length and 2.2 nm in diameter. Estimate the diffusion coefficient of fibrinogen in water at 25 °C. The dynamic viscosity of water at this temperature is  $\mu = 0.903 \times 10^{-3} \text{ Pa} \cdot \text{s}$ .

**Solution.** The long molecule can be assumed to have an ellipsoidal shape with  $a = 67 \times 10^{-9} \text{ m}$  and  $b = 2.2 \times 10^{-9} \text{ nm}$ . According to (2.38), the characteristic diameter of a fibrinogen molecule is:

$$\sigma = \frac{2\sqrt{a^2 - b^2}}{\ln \left( \frac{a + \sqrt{a^2 - b^2}}{b} \right)} \quad (2.39)$$

$$\sigma = \frac{2\sqrt{(67 \times 10^{-9})^2 - (2.2 \times 10^{-9})^2}}{\ln \left( \frac{67 \times 10^{-9} + \sqrt{(67 \times 10^{-9})^2 - (2.2 \times 10^{-9})^2}}{2.2 \times 10^{-9}} \right)} = 6.72 \times 10^{-9} \text{ m}.$$

Thus, based on the Stokes–Einstein equation (2.37) the diffusion coefficient of fibrinogen is:

$$D = \frac{k_B T}{3\pi\mu_{\text{water}}\sigma_{\text{fibrinogen}}}$$

$$= \frac{1.38 \times 10^{-23} \times (25 + 273)}{3\pi \times 0.903 \times 10^{-3} \times 6.72 \times 10^{-9}} = 7.19 \times 10^{-11} \text{ m}^2/\text{s}.$$

The diffusion of a large molecule in water is about 6 orders slower than that of gases.

### 2.2.3.3 Diffusion Coefficient of Electrolytes

Salts and many other molecules dissolve in water to form cations and anions. Thus they do not diffuse as a single molecule, because different ions have different diffusion coefficients. Tables 2.3 and 2.4 show the diffusion coefficients of typical cations and anions in water at 25 °C. However, both anion and cation together should have the same diffusion coefficient to maintain charge neutrality. It's interesting to observe from Table 2.3 that the diffusion coefficient of a proton ( $\text{H}^+$ ) is about five times larger than other ions. Since

**Table 2.3 Diffusion Coefficients of Typical Cations in Water at 25 °C (in  $10^{-9} \text{ m}^2/\text{s}$ ) [7]**

$\text{H}^+$	$\text{Li}^+$	$\text{Na}^+$	$\text{K}^+$	$\text{Rb}^+$	$\text{Cs}^+$	$\text{Ag}^+$	$\text{NH}_4^+$	$\text{Ca}^{2+}$	$\text{Mg}^{2+}$	$\text{La}^{3+}$
9.31	1.03	1.33	1.96	2.07	2.06	1.65	1.96	0.79	0.71	0.62

**Table 2.4 Diffusion Coefficients of Typical Anions in Water at 25 °C (in  $10^{-9} \text{ m}^2/\text{s}$ ) [7]**

$\text{OH}^-$	$\text{F}^-$	$\text{Cl}^-$	$\text{Br}^-$	$\text{I}^-$	$\text{NO}_3^-$	$\text{CH}_3\text{COO}^-$	$\text{B}(\text{C}_6\text{H}_5)_4^-$	$\text{SO}_4^{2-}$	$\text{CO}_3^{2-}$
5.28	1.47	2.03	2.08	2.05	1.90	1.09	0.53	1.06	0.92

the size difference between  $\text{H}^+$  and the other ion is not significant,  $\text{H}^+$  should have a different diffusion mechanism in water.  $\text{H}^+$  actually does not move through water but reacts with a water molecule and releases a proton on the other side. This new proton can cause another reaction. This chain reaction speeds up the transport process and leads to a much higher diffusion coefficient of  $\text{H}^+$  in water [7].

The diffusion coefficient of a molecule consisting of a cation of charge  $z_1$  and an anion of charge  $z_2$  is:

$$D = \frac{|z_1| + |z_2|}{\frac{|z_2|}{D_1} + \frac{|z_1|}{D_2}} \quad (2.40)$$

where  $D_1$  and  $D_2$  are the diffusion coefficients of the cation and the anion, respectively. According to (2.40), the overall diffusion coefficient is determined by the slower ion. Since the diffusion coefficients are weighted by the charge, the faster ion with a much smaller charge can dominate the overall diffusion coefficient.

**Example 2.7** (*Diffusion coefficient of sodium chloride*). Determine the diffusion coefficient of sodium chloride at 25 °C.

**Solution.** From Tables 2.3 and 2.4, the diffusion coefficients of sodium cation and chloride anion are  $D_1 = 1.33 \times 10^{-9} \text{ m}^2/\text{s}$  and  $D_2 = 2.03 \times 10^{-9} \text{ m}^2/\text{s}$ , respectively. Applying  $z_1 = +1$  and  $z_2 = -1$  in (2.40) results in the diffusion coefficient of sodium chloride:

$$\begin{aligned} D &= \frac{|z_1| + |z_2|}{\frac{|z_2|}{D_1} + \frac{|z_1|}{D_2}} \\ &= \frac{1 + 1}{\frac{1}{1.33 \times 10^{-9}} + \frac{1}{2.03 \times 10^{-9}}} = 1.61 \times 10^{-9} \text{ m}^2/\text{s}. \end{aligned}$$

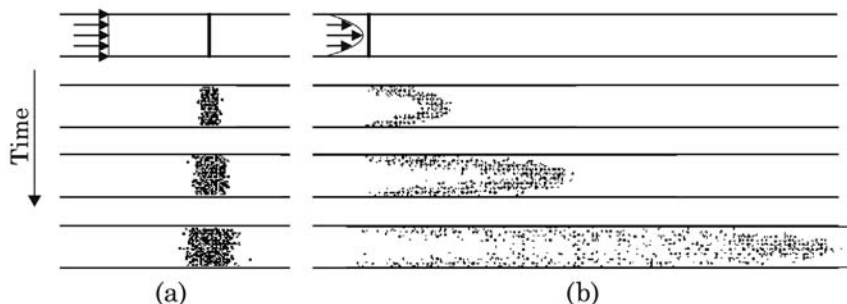


**Figure 2.8** Particle distribution in a microchannel: (a) with an uniform velocity profile, (b) with a parabolic velocity profile.

The diffusion coefficients of electrolytes in water are about 4 orders smaller than that of gases and about 2 orders larger than that of large molecules.

In many lab-on-a-chip applications, micromixers are needed for mixing proteins. The behavior of proteins is very complex. A protein molecule consists of chains of amino acids. The molecular weight is very large and can be of the order of  $10^5$ . A protein molecule has a large number of side chains that end in amino ( $-\text{NH}_2$ ) or carboxylic acid ( $-\text{COOH}$ ) groups. Depending on the pH amino groups can be positively charged to become  $-\text{NH}_3^+$ ; and carboxylic acid groups become negatively charged ( $-\text{COO}^-$ ). Therefore, the net charge of a protein can be either positive or negative. Further, depending on pH the protein chains can be folded differently resulting in different sizes and shapes. The different charges and shapes make the diffusion coefficient of proteins depend on the pH concentration. Furthermore, the diffusion coefficient of a protein also strongly depends on its concentration and the concentration of electrolytes, such as NaCl.

Many solute molecules, such as surfactant, also have diffusion coefficients that depend on the solute concentration. At high concentrations the molecules can aggregate to form micelles. The aggregation and the electrostatic interaction cause the strong concentration dependency of the diffusion coefficient.

## 2.3 Taylor Dispersion

Taylor dispersion is an effective mechanism for mixing of a solute in a distributed velocity field, such as pressure-driven flow in a microchannel. This axial effect arises from a coupling between molecular diffusion in the transverse direction and transverse distribution of the flow velocity. Fig. 2.8 illustrates the difference between molecular diffusion in a plug-like flow and Taylor dispersion in a distributed flow. In a uniform flow field, such as the plug-like electroosmotic flow, advection and diffusion are independent. Axial diffusion is the same as

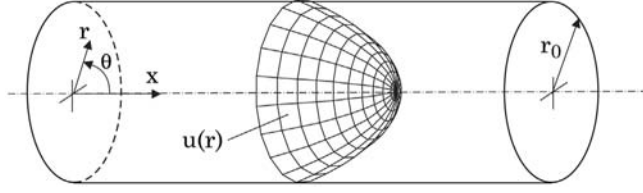


**Figure 2.9** Model for determination of Taylor dispersion in a circular channel.

molecular diffusion, Fig. 2.8 (a). In a distributed flow field, such as the pressure-driven flow with a parabolic velocity distribution, the solvent is stretched more in the middle of the channel than near the wall due to axial convective transport. The resulting concentration gradient between the different fluid layers are then blurred by diffusion in the transverse direction, see Fig. 2.8 (b). As a result, the solute appears to be “diffusing” in the axial direction at a rate that is much faster than what would be predicted by ordinary molecular diffusion.

### 2.3.1 Two-Dimensional Analysis

In the following, dispersion coefficients are derived by a two-dimensional model involving one axial and one transversal spacial dimension. G. I. Taylor was the first to present a working model for the transverse average that managed to capture the influences of both transverse diffusion and the transverse variations of the fluid velocity field. The analysis of Taylor [10] is based on the model of a long cylindrical capillary with a radius of  $r_0$  (Fig. 2.9). The following derivation of the dispersion coefficient follows Brenner and Edwards [11]. According to Table 2.2, the velocity distribution in the capillary cross section is:

$$u^* = \frac{u(r)}{\bar{u}} = 2 \left[ 1 - \left( \frac{r}{r_0} \right)^2 \right] \rightarrow u(r) = 2\bar{u} \left[ 1 - \left( \frac{r}{r_0} \right)^2 \right] \quad (2.41)$$

where  $\bar{u}$  is the mean velocity as listed in Table 2.2. For this capillary, the general equation for conservation of species (2.22), also called the convective-diffusive equation, can be formulated in the cylindrical coordinate system with no species generation ( $r_g = 0$ ) as:

$$\frac{\partial c}{\partial t} + u(r) \frac{\partial c}{\partial z} = D \nabla^2 c \quad (2.42)$$

where

$$\nabla^2 = \frac{1}{r} \frac{\partial}{\partial r} \left( r \frac{\partial}{\partial r} \right) + \frac{1}{r^2} \frac{\partial^2}{\partial \theta^2} + \frac{\partial^2}{\partial x^2}. \quad (2.43)$$

The boundary and initial conditions of (2.42) are:

$$\begin{aligned} \left. \frac{dc}{dr} \right|_{r=r_0} &= 0 \\ c|_{x \rightarrow \infty} &= 0 \\ c|_{t=0} &= c_0(r, \theta, x). \end{aligned} \quad (2.44)$$

Equation (2.42) can be solved numerically with the above boundary and initial condition for  $c(r, \theta, x, t)$ . Taylor derived an analytical asymptotic solution for (2.42) as follows:

If the observer moves along the flow with the mean velocity  $\bar{u}$ , we can consider a new axial coordinate  $x^*$ :

$$x^* = x - \bar{u}t. \quad (2.45)$$

Substituting  $x = x^* + \bar{u}t$  into (2.42) results in:

$$\frac{\partial c}{\partial t} + [u(r) - \bar{u}] \frac{\partial c}{\partial x^*} = D \left[ \frac{1}{r} \frac{\partial}{\partial r} \left( r \frac{\partial c}{\partial r} \right) + \frac{1}{r^2} \frac{\partial^2 c}{\partial \theta^2} + \frac{\partial^2 c}{\partial x^{*2}} \right]. \quad (2.46)$$

For (2.46) the previous boundary and initial conditions with the new spacial variable  $x^*$  apply. In order to solve (2.46) analytically, the following asymptotic assumptions are made:

- Radial diffusion is complete ( $t \gg r_0^2/D$ ), thus  $\frac{\partial c}{\partial t} \approx 0$ ,
- Axial diffusion is negligible compared to axial convection ( $[u(r) - \bar{u}] \frac{\partial c}{\partial x^*} \gg D \frac{\partial^2 c}{\partial x^{*2}}$ ), thus  $D \frac{\partial^2 c}{\partial x^{*2}} = 0$ ,
- Any inhomogeneity in  $\theta$  is ignored, thus  $D \frac{\partial^2 c}{\partial \theta^2} = 0$ , and
- The solute has the same velocity as the solvent.

Next, an average species concentration is introduced:

$$\bar{c}(x^*, t) = \frac{1}{\pi r_0^2} \int \int c(r, \theta, x, t) dr d\theta. \quad (2.47)$$

With the assumption of the long-time behavior, the axial concentration gradient is independent of  $r$  ( $\partial c / \partial x^* \approx \partial \bar{c} / \partial x^*$ ). Thus, (2.46) can be reduced to:

$$[u(r) - \bar{u}] \frac{\partial \bar{c}}{\partial x^*} = D \frac{1}{r} \frac{\partial}{\partial r} \left( r \frac{\partial c}{\partial r} \right). \quad (2.48)$$

The above equation can be solved for  $c$  by integration with respect to  $r$ :

$$c = C(x^*, t) + \frac{r_0^2 \bar{u}}{4D} \left[ \left( \frac{r}{r_0} \right)^2 - \frac{1}{2} \left( \frac{r}{r_0} \right)^4 \right] \frac{\partial \bar{c}}{\partial x^*} \quad (2.49)$$

where  $C(x^*, t)$  is the function of integration. Substituting (2.49) into (2.47) results in the  $r$ -independent function of the integration constant:

$$C(x^*, t) = \bar{c} - \frac{r_0^2 \bar{u}}{12D} \frac{\partial \bar{c}}{\partial x^*}. \quad (2.50)$$

Now, the axial concentration (2.49) can be expressed in terms of the average concentration:

$$c \approx \bar{c} + \frac{r_0^2 \bar{u}}{4D} \left[ -\frac{1}{3} + \left( \frac{r}{r_0} \right)^2 - \frac{1}{2} \left( \frac{r}{r_0} \right)^4 \right] \frac{\partial \bar{c}}{\partial x^*}. \quad (2.51)$$

In order to introduce the dispersion coefficient or the so-called effective diffusion coefficient  $D^*$ , the conservation of species (2.46) is written in the flux form as:

$$\frac{\partial \bar{c}}{\partial t} + \frac{\partial J^*}{\partial x^*} = 0 \quad (2.52)$$

where  $J^*$  is the area-averaged axial flux, which consists of both diffusive and convective components:

$$J^* = \underbrace{-D \frac{\partial \bar{c}}{\partial x^*}}_{\text{diffusive}} + \underbrace{J_{\text{conv}}}_{\text{convective}}. \quad (2.53)$$

The convective flux  $J_{\text{conv}}$  can be evaluated as:

$$J_{\text{conv}} = \frac{1}{\pi r_0^2} \int \int [u(r) - \bar{u}] c \, dr d\theta. \quad (2.54)$$

Substituting (2.51) in (2.54) results in:

$$J_{\text{convection}} = -\frac{r_0^2 \bar{u}^2}{48D} \frac{\partial \bar{c}}{\partial x^*}. \quad (2.55)$$

The area-averaged axial flux now can be expressed as:

$$J^* = -D \frac{\partial \bar{c}}{\partial x^*} - \frac{r_0^2 \bar{u}^2}{48D} \frac{\partial \bar{c}}{\partial x^*} = - \left[ D + \frac{r_0^2 \bar{u}^2}{48D} \right] \frac{\partial \bar{c}}{\partial x^*}. \quad (2.56)$$

According to Fick law, the term in the square bracket of the above equation can be called the effective diffusion coefficient or more accurately the dispersion coefficient:

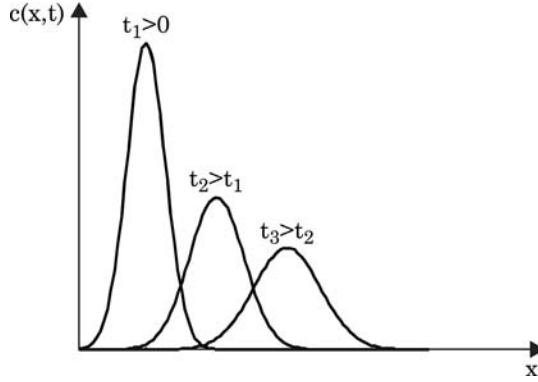


**Figure 2.10** One-dimensional dispersion, typical concentration distribution at different epochs.

$$D^* = D + \frac{r_0^2 \bar{u}^2}{48D}. \quad (2.57)$$

The species conservation equation can now be formulated as:

$$\frac{\partial \bar{c}}{\partial t} + \bar{u} \frac{\partial \bar{c}}{\partial x} = D^* \frac{\partial^2 \bar{c}}{\partial x^2}. \quad (2.58)$$

The above partial differential equation can be solved analytically. For instance, if the initial condition of the species concentration is a pulse  $\bar{c}(x, t = 0) = \bar{C}_0 \delta(x)$ , where  $\delta(x)$  is the Dirac (delta) function, the transient one-dimensional solution of the average concentration is:

$$\bar{c}(x, t) \approx \frac{\bar{C}_0}{\sqrt{4\pi D^* t}} \exp \left[ -\frac{(x - \bar{u}t)^2}{4D^* t} \right]. \quad (2.59)$$

Fig. 2.10 shows the typical concentration distribution of the one-dimensional dispersion at different epochs.

A few years after Taylor's publication, Aris provided a firmer theoretical framework for this theory by using a moment analysis [12]. He also generalized the problem to handle time-periodic flows [13]. Following the works of Taylor and Aris are several other contributions to the theory of deriving effective transport models for the transverse averages of solutes flowing through channels with more general cross-sectional geometries and flow properties. The common techniques are the use of asymptotic analysis [14–17], the theory of projection operators [18], and the center manifold theory [19]. All the above works only dealt with non-reactive problems. Johns and DeGance considered the influences of a system of linear reactions upon Taylor dispersion [20]. Yamanaka and Inui used their projection operator theory to solve problems involving a single irreversible reaction [21]. The following example by Bloechle [22] demonstrates

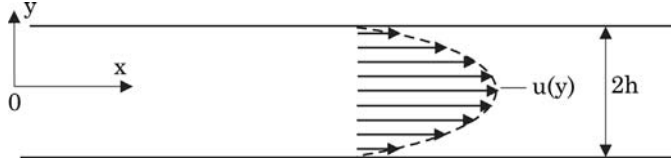


**Figure 2.11** Model for determination of Taylor dispersion in Poiseuille flow between two parallel plates.

an intuitive approach similar to that of Taylor [10]. The approach is called the mean-fluctuation method commonly used in turbulent flow.

**Example 2.8** (*Taylor dispersion in Poiseuille flow between two parallel plates [22]*). Determine the dispersion coefficient of a Poiseuille flow between two parallel plates with a gap of  $2h$  as depicted in Fig. 2.11.

**Solution.** Because of the symmetric geometry, only half of the model is considered ( $-\infty < x < \infty$ ,  $0 < y < h$ ). The governing equation (2.22) reduces to the two-dimensional form of the parallel plates model ( $t < 0$ ):

$$\frac{\partial c}{\partial t} + u(y) \frac{\partial c}{\partial x} = D \left( \frac{\partial^2 c}{\partial x^2} + \frac{\partial^2 c}{\partial y^2} \right) \quad (2.60)$$

where  $u(y)$  is the velocity distribution [2]:

$$u(y) = \frac{3\bar{u}}{2} \left( 1 - \frac{y^2}{h^2} \right). \quad (2.61)$$

The boundary and initial condition for (2.60) are:

$$\text{Symmetry condition : } \frac{\partial c}{\partial y} \Big|_{y=0} = 0$$

$$\text{Wall condition : } \frac{\partial c}{\partial y} \Big|_{y=h} = 0$$

$$\text{Initial condition : } c|_{t=0} = c_0(x, y).$$

The concentration and velocity can be formulated as the sum of an average component and a fluctuating component:

$$c(x, y, t) = \bar{c}(x, t) + c'(x, y, t) \quad (2.62)$$

$$u(y) = \bar{u} + u'(y)$$

where

$$\bar{c}(x, t) = \frac{1}{a} \int_0^a c(x, y, t) dy \quad \frac{1}{a} \int_0^a c'(x, y, t) dy = 0$$

$$\bar{u} = \frac{1}{a} \int_0^a u(y) dy \quad \frac{1}{a} \int_0^a u'(y) dy = 0.$$



Substituting (2.62) into (2.60) results in:

$$\frac{\partial \bar{c}}{\partial t} + \frac{\partial c'}{\partial t} + (\bar{u} + u') \left( \frac{\partial \bar{c}}{\partial x} + \frac{\partial c'}{\partial x} \right) = D \left( \frac{\partial^2 \bar{c}}{\partial x^2} + \frac{\partial^2 c'}{\partial x^2} + \frac{\partial^2 \bar{c}}{\partial y^2} \right) \quad (2.63)$$

with

$$\text{Symmetry condition : } \frac{\partial c'}{\partial y} \Big|_{y=0} = 0$$

$$\text{Wall condition : } \frac{\partial c'}{\partial y} \Big|_{y=h} = 0$$

$$\text{Initial condition : } \bar{c} + c'|_{t=0} = c_0(x, y).$$

Averaging (2.63) from 0 to  $h$  leads to:

$$\frac{\partial \bar{c}}{\partial t} + \bar{u} \frac{\partial \bar{c}}{\partial x} + \frac{1}{h} \int_0^h \left( u' \frac{\partial c'}{\partial x} dy \right) = D \frac{\partial^2 \bar{c}}{\partial x^2}. \quad (2.64)$$

The initial condition for the above equation is:

$$\bar{c}|_{t=0} = \frac{1}{h} \int_0^h f(x, y) dy. \quad (2.65)$$

Similar to Taylor's original approach, the dispersion coefficient can be derived from the above equation if the fluctuation concentration  $c'$  is known. Subtracting (2.64) from (2.63) leads to the partial differential equation for  $c'$ :

$$\frac{\partial c'}{\partial t} + \bar{u} \frac{\partial c'}{\partial x} + u' \frac{\partial \bar{c}}{\partial x} + \left[ u' \frac{\partial c'}{\partial x} - \frac{1}{h} \int_0^h \left( u' \frac{\partial c'}{\partial x} dy \right) \right] = D \left( \frac{\partial^2 c'}{\partial x^2} + \frac{\partial^2 c'}{\partial y^2} \right) \quad (2.66)$$

with

$$c'|_{t=0} = c_0(x, y) - \frac{1}{h} \int_0^h c_0(x, y) dy. \quad (2.67)$$

Assuming that

$$\frac{\partial \bar{c}}{\partial t} \gg \frac{\partial c'}{\partial t}, \quad \frac{\partial \bar{c}}{\partial x} \gg \frac{\partial c'}{\partial x}, \quad \frac{\partial^2 \bar{c}}{\partial x^2} \gg \frac{\partial^2 c'}{\partial x^2}, \quad (2.68)$$

equation (2.66) reduces to:

$$D \frac{\partial^2 c'}{\partial y^2} = \frac{\partial \bar{c}}{\partial t} + \bar{u} \frac{\partial \bar{c}}{\partial x} - D \frac{\partial^2 \bar{c}}{\partial x^2} + u' \frac{\partial \bar{c}}{\partial x} \quad (2.69)$$

with

$$u'(y) = \bar{u} \left( \frac{1}{2} - \frac{3y^2}{2h^2} \right). \quad (2.70)$$

Next, (2.69) can be integrated with respect to  $y$ :

$$D \frac{\partial c'}{\partial y} = y \left( \frac{\partial \bar{c}}{\partial t} + \bar{u} \frac{\partial \bar{c}}{\partial x} - D \frac{\partial^2 \bar{c}}{\partial x^2} \right) + \bar{u} \left( \frac{y}{2} - \frac{y^3}{2h^2} \right) \frac{\partial \bar{c}}{\partial x} + C_0(x, t). \quad (2.71)$$

The symmetry and wall conditions imply that  $C_0(x, t) = 0$  and

$$\frac{\partial \bar{c}}{\partial t} + \bar{u} \frac{\partial \bar{c}}{\partial x} - D \frac{\partial^2 \bar{c}}{\partial x^2} = 0, \quad (2.72)$$

respectively. Integrating (2.71) with respect to  $y$  results in:

$$c' = \frac{\bar{u}}{D} \left( \frac{y^2}{4} - \frac{y^4}{8h^2} \right) \frac{\partial \bar{c}}{\partial x} + C_1(x, t). \quad (2.73)$$

$C_1(x, t)$  can be determined by solving the condition:

$$\frac{1}{h} \int_0^h c'(x, y, t) dy = 0. \quad (2.74)$$

The final expression for the fluctuating component of the concentration is:

$$c' = \frac{\bar{u}}{D} \left( \frac{y^2}{4} - \frac{y^4}{8h^2} - \frac{7h^2}{120} \right) \frac{\partial \bar{c}}{\partial x}. \quad (2.75)$$

Substituting (2.75) in (2.64) leads to:

$$\frac{\partial \bar{c}}{\partial t} + \bar{u} \frac{\partial \bar{c}}{\partial x} - \left( D + \frac{2h^2 \bar{u}^2}{105D} \right) \frac{\partial^2 \bar{c}}{\partial x^2} = 0. \quad (2.76)$$

Thus, the dispersion coefficient in a Poiseuille flow between two parallel plates is:

$$D^* = D + \frac{2h^2 \bar{u}^2}{105D}, \quad (2.77)$$

where  $2h$  is the gap between the two parallel plates.

### 2.3.2 Three-Dimensional Analysis

For axial-symmetric channel geometry, such as a cylindrical capillary, the two-dimensional analysis described in the above subsection is appropriate. For a real channel geometry the cross-sectional velocity profile and consequently the dispersion coefficient also depend on the channel shape. In another words, the second transversal spacial dimension needs to be considered in the analysis.

Dutta et al. [23] introduce a factor  $f$  into (2.77) to consider the three dimensional effect of Taylor dispersion:

$$D^* = D + \frac{d^2 \bar{u}^2}{210D} f, \quad (2.78)$$

where  $d = 2h$  and  $f = 1$  for the case of the parallel plates model. The factor  $f$  is a function of the aspect ratio  $d/W$ , where  $d$  is the characteristic length of the shallow channel height and  $W$  is the channel width. Based on this definition, the longer cross-sectional dimension is considered as channel width, thus  $d/W \leq 1$ . Using the Aris approach [12] and numerical simulation, the factor  $f$  can be determined for different geometries. Fig. 2.12 shows the dispersion factors of typical channel geometries as functions of the aspect ratio  $d/W$ .

Because of the velocity gradient at the sharp corners of a rectangular channel, the factor  $f$  increases from  $f = 1.76$  in the case of a square channel cross section ( $d/W = 1$ ) to  $f = 7.95$  in the case of a shallow channel ( $W \gg d$ ). The factor of an elliptical channel cross section can be calculated explicitly as:

$$f = \frac{210}{192} \left( \frac{W}{d} \right)^2 \left( \frac{24 - 24\varepsilon^2 + 5\varepsilon^4}{24 - 12\varepsilon^2} \right), \quad (2.79)$$

where  $\varepsilon = \sqrt{1 - d^2/W^2}$  is the eccentricity of the geometry.

Ajdari et al. [24] argued that for a shallow channel  $W \gg d$  with a continually varying height, the dispersion coefficient is not determined by the channel height and the aspect ratio. The channel width  $W$  is the only geometric parameter that determines the dispersion coefficient. For instance, the dispersion coefficients for channels with triangle, parabolic, and elliptical cross sections are:

$$D_{\text{triangle}}^* = D + 0.0052 \frac{W^2 \bar{u}}{D}, \quad (2.80)$$

$$D_{\text{parabolic}}^* = D + 0.0031 \frac{W^2 \bar{u}}{D}, \quad (2.81)$$

$$D_{\text{elliptical}}^* = D + 0.0022 \frac{W^2 \bar{u}}{D}, \quad (2.82)$$

respectively.

In the case of an elliptical cross section, a low aspect ratio  $W \gg d$  means an eccentricity of unity,  $\varepsilon = 1$ . Substituting  $\varepsilon = 1$  in (2.79) results in a factor

$$f = \frac{210}{192} \frac{5}{12} \frac{W^2}{d^2}. \quad (2.83)$$

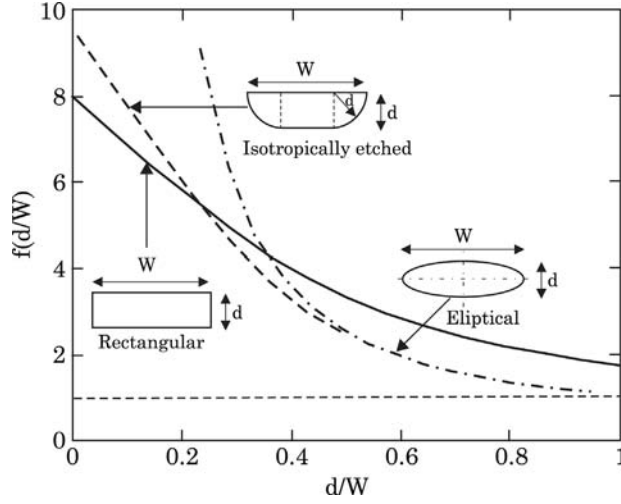


**Figure 2.12** Dispersion factor  $f$  for typical channel geometries versus aspect ratio  $d/W$  (after [23]).

Substituting (2.83) in (2.78) leads to the equation:

$$D_{\text{elliptical}}^* = D + \frac{5}{192 \times 12} \frac{W^2 \bar{u}}{D}. \quad (2.84)$$

Because  $5/(192 \times 12) \approx 0.0022$ , the approaches of Dutta [23] and Ajdari [24] agree in the case of a shallow elliptical cross section.

## 2.4 Chaotic Advection

### 2.4.1 Basic Terminologies

The term *chaotic advection* refers to the phenomenon where a simple Eulerian velocity field leads to a chaotic response in the distribution of a Lagrangian marker, such as a tracing particle [25]. Advection refers to species transport by the flow. A flow field can be chaotic even in the laminar flow regime. Chaotic advection can be created in a simple two-dimensional flow with time-dependent disturbance or in a three-dimensional flow even without time-dependent disturbance. It is important to note that chaotic advection is not turbulence. For a flow system without disturbance, the velocity components of chaotic advection at a point in space remain constant over time, while the velocity components of turbulence are random. The streamlines of steady chaotic advection flow across each other causing the particles to change their paths. Under chaotic advection, the particles diverge exponentially and enhance

mixing between the solvent and solute flows. In a time-periodic system, the condition for chaos is that streamlines cross at two consecutive epochs.

There are few terminologies related to visualization of an Eulerian velocity field. The first and most common terminology is the *pathline*, also called *trajectory* of a fluid particle in the flow field. In experiments, pathlines, orbits, or trajectories can be obtained by a long time exposure image of a fluorescent fluid particle.

If the particles are idealized so that they are small enough not to disturb the flow, but large enough so that molecular diffusion is neglected, they can move passively with the flow. The particle transport mechanism can simply be described by the advection equations:

$$\begin{cases} dx/dt = u(x, y, z, t) \\ dy/dt = v(x, y, z, t) \\ dz/dt = w(x, y, z, t). \end{cases} \quad (2.85)$$

Mathematically, pathlines or trajectories can be obtained by solving (2.85) with the initial condition at  $t = 0$  ( $x = x_0$ ,  $y = y_0$ ,  $z = z_0$ ). Numerical integration methods, such as the Runge–Kutta method, can be used for determining the positions of the particles.

In a two-dimensional flow, *streamlines* are given by the solution of:

$$\begin{cases} dx/ds = u(x, y, z, t) \\ dy/ds = v(x, y, z, t) \end{cases} \quad (2.86)$$

where  $t$  is treated as a constant and  $s$  is the independent variable. Streamlines build the image of the flow field at an epoch. In experiments, streamlines can be constructed from the two images recorded with particle image velocimetry (PIV). The flow is traced with fluorescent particles. Particle images are recorded at two successive time instances  $t$  and  $t + \Delta t$ . The particle velocities are determined by the recorded particle displacement and the time delay  $\Delta t$ . The streamlines are tangential to the velocity at each point. The streamlines can be depicted as level sets of the stream function  $\psi$ , which is defined as:

$$\begin{cases} dx/dt = u(x, t) = \partial\psi/\partial y \\ dy/dt = v(x, t) = -\partial\psi/\partial x. \end{cases} \quad (2.87)$$

A *streakline* through a point  $(x, y, z)$  at epoch  $\tau$  is the curve formed by all particles that previously ( $t < \tau$ ) passed through this point. In experiments, the streakline is the tracing curve of a non-diffusive tracer injected into the flow at the given point.

**Example 2.9** (*Trajectories and streamlines*). An Eulerian velocity field is given as:

$$\begin{cases} dx/dt = x \sin(at) \\ dy/dt = y \sin(bt + c). \end{cases}$$

All variables and constants are dimensionless. Determine the trajectories and streamlines of particles initially at  $(x_0 = 1, y_0 = 1)$ ,  $(x_0 = 1, y_0 = 2)$ , and  $(x_0 = 1, y_0 = 3)$ .

**Solution.** Solving the differential equations with the initial condition  $(x_0, y_0)$  results in the position of the fluid particle as a function of time:

$$\begin{cases} x = x_0 \left[ \cosh\left(\frac{1}{a}\right) + \sinh\left(\frac{1}{a}\right) \right] \exp\left[-\frac{1}{a} \cos(at)\right] \\ y = y_0 \left\{ \cosh\left[\frac{\cos(c)}{b}\right] + \sinh\left[\frac{\cos(c)}{b}\right] \right\} \exp\left[-\frac{1}{b} \cos(bt + c)\right]. \end{cases}$$

Fig. 2.13 shows graphically the above pathlines with the three initial particle positions,  $a = 1$ ,  $b = 2$ , and  $c = \pi/2$ .

The stream function  $\psi$  can be solved in explicit form using the equation system (2.87). Taking the time  $t$  as constant,  $u(x, y, t) = x \sin(at)$  and  $v(x, y, t) = y \sin(bt + c)$ , we have:

$$\begin{aligned} \psi(x, y, t) &= \int u(x, y, t) dy - \int v(x, y, t) dx - \int \int \frac{du(x, y, t)}{dx} dy dx \\ \psi(x, y, t) &= -xy \sin bt + c. \end{aligned}$$

It is apparent that streamlines are time-dependent. Fig. 2.14 shows the streamlines as the level sets of stream function  $\psi$ .

Equation (2.85) represents a system of coupled ordinary differential equations (ODEs). Similar dynamical systems in engineering and physics have shown a strong chaotic behavior. Poiseuille flow in a straight microchannel is considered as a one-dimensional incompressible flow at low Reynolds number. The dynamics of this flow are simple and non-chaotic. In the case of two-dimensional flow, the dynamic behavior of the flow is more interesting. The two-dimensional continuity equation:

$$\frac{\partial u}{\partial x} + \frac{\partial v}{\partial y} = 0, \quad (2.88)$$

is fulfilled by the stream function  $\psi$ (2.87). Equation system (2.87) has the same form of the Hamilton equation of motion, where the stream function  $\psi$  plays the role of the Hamiltonian. Thus, *steady* two-dimensional incompressible flow and *time-independent* Hamiltonians with one degree of freedom are integrable and

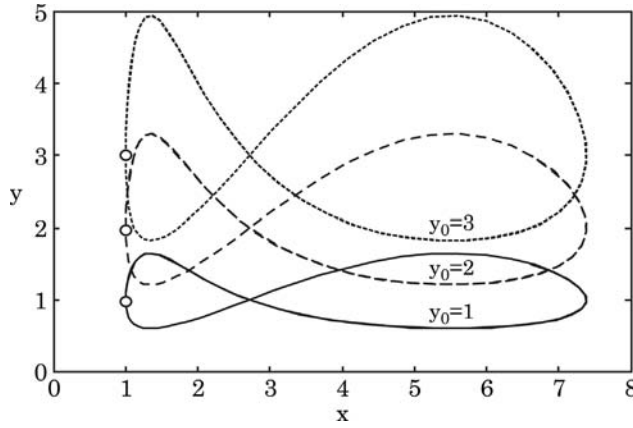


**Figure 2.13** Example 2.9: Pathlines of three particles with initial position at  $(x_0 = 1, y_0 = 1)$ ,  $(x_0 = 1, y_0 = 2)$ , and  $(x_0 = 1, y_0 = 3)$  ( $a = 1$ ,  $b = 2$ , and  $c = \pi/2$ ).

result in deterministic dynamics. Adding one more dimension to the systems, such as *unsteady* two-dimensional incompressible flow and *independent* Hamiltonians, makes the equations nonintegrable and causes chaotic dynamics.

The terminologies for chaotic advection can be borrowed from the more established field of dynamical systems theory. The advection equations (2.85) can be solved explicitly for the fluid particle position  $(x, y, z)$  at a given time  $t$ . The solution of  $(x, y, z)$  is then used for describing the motion of fluid particles in a region  $R$ , such as a channel cross section, and thus can be called a *mapping* function  $S$  [26]. From an initial condition  $(t = 0)$   $R$  can be transformed into a new region using  $S$ . This *transformation* or mapping can mathematically be described as  $S(R)$ . Each transformation is called an *advection cycle*, which corresponds to a mixing element in different micromixer designs such as the sequential lamination discussed later in this book. Repeating these mixing elements  $n$  times means repeated application of  $S$  to  $R$ , or  $S^n(R)$ . With the discrete number of advection cycles, the transformation  $S$  is understood as a discrete operation and not continuous as in the case of the time function.

If the fluid is assumed to be incompressible, then the volume (in a three-dimensional case) or the area (in a two-dimensional case) is preserved after each transformation. Thus the above mapping function  $S$  is called a *volume-preserving* transformation or an *area-preserving* transformation.

A trajectory of a point after applying many discrete transformations is called an *orbit*. If a point  $p$  returns to the same place after  $N$  transformations, the orbit is periodic with a period  $N$ . The two typical periodic orbits are the stable *elliptic* orbit and the unstable *hyperbolic* orbit. Elliptic orbits lead to a region that does not mix with the surrounding fluid, and thus are bad for mixing. Hyperbolic orbits lead to squeezing and stretching of fluid regions, and thus are good for mixing. In an unstable orbit, if the fluid particle changes its path at the

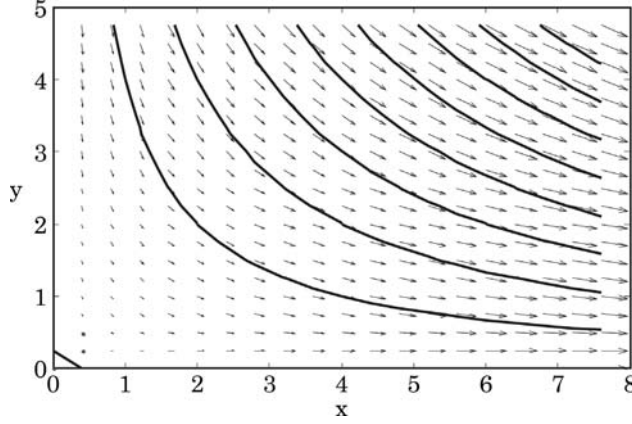


**Figure 2.14** Example 2.9: Velocity field and streamlines at  $t = 2$  ( $a = 1$ ,  $b = 2$ , and  $c = \pi/2$ ).

intersection of the same orbit, the orbit is called *homoclinic*. If the fluid particle changes its path at the intersection with another orbit, the orbit is called *heteroclinic*.

The trajectories of a chaotic three-dimensional flow are complicated. The three-dimensional positions of fluid particles can be reduced into a two-dimensional map called the *Poincaré section*. In a time-periodic system, the Poincaré section is a collection of intersections of trajectories with a plane. The continuous trajectories become discrete points of the transformations  $P_n \rightarrow P_{n+1}$ . The time needed between two points  $P_n$  and  $P_{n+1}$  does not need to be the period of the system. In three-dimensional space-periodic systems, the plane is taken at the same position of the repeated spacial structure. A trajectory will intersect all these periodic planes at several points. The collection of these points forms the Poincaré section. In this case, the transformation  $P_n \rightarrow P_{n+1}$  is the advection cycle.

## 2.4.2 Examples of Chaotic Advection

### 2.4.2.1 Lorentz's Convection Flow

For a three-dimensional system, the equations in (2.85) are more than enough to create a nonintegrable or chaotic dynamics. Lorenz [27] derived a simplified system of equations for convection rolls in the atmosphere:

$$\begin{cases} dx/dt = \text{Pr}(y - x) \\ dy/dt = x \left( \frac{\text{Ra}}{\text{Ra}_c} - z \right) - y \\ dz/dt = xy - \beta z \end{cases} \quad (2.89)$$



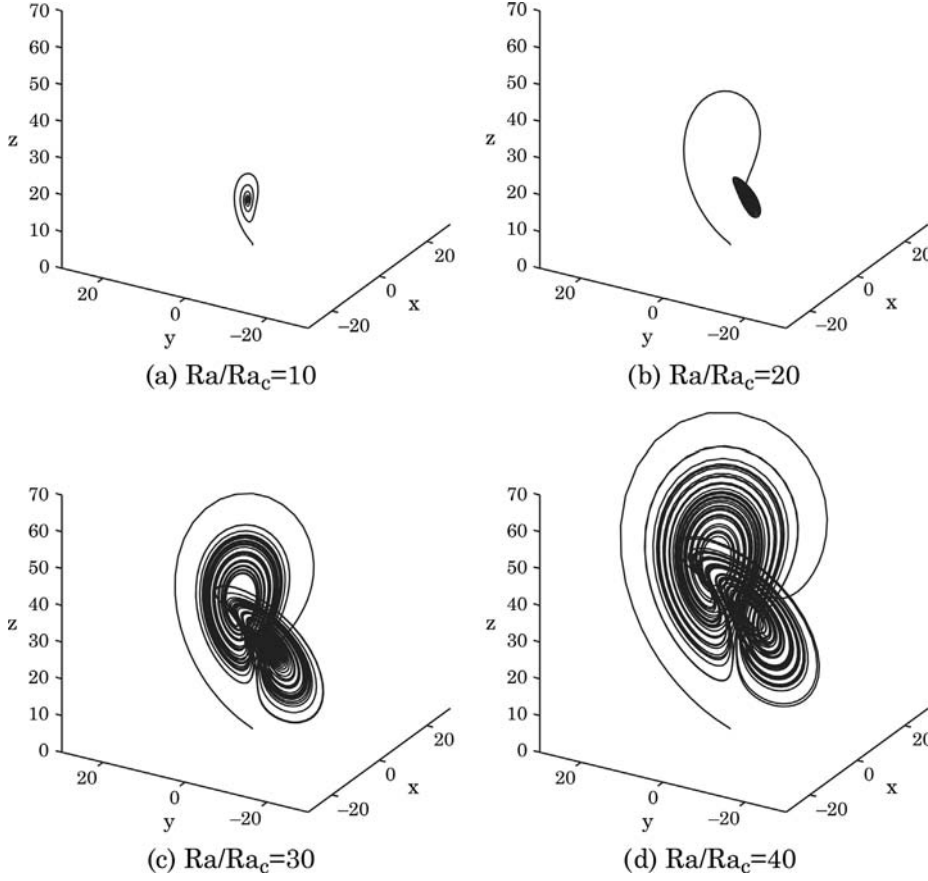


**Figure 2.15** Solution of Lorenz's equations for different Rayleigh numbers ( $Pr=10$  and  $\beta = 8/3$ ): (a)  $Ra/Ra_c=10$ ; (b)  $Ra/Ra_c=20$ ; (c)  $Ra/Ra_c=30$ ; (d)  $Ra/Ra_c=40$ .

where the variable  $x$  is proportional to convective intensity,  $y$  is proportional to the temperature difference between descending and ascending currents, and  $z$  is proportional to the difference in vertical temperature profile from linearity in this system of equations.  $Pr$ ,  $Ra$ ,  $Ra_c$ , and  $\beta$  are the Prandtl number, Rayleigh number, critical Rayleigh number and the geometric factor respectively. Fig. 2.15 shows the solution of (2.89) for different Rayleigh numbers. A small change in Rayleigh number leads to a large change in the solution.

#### 2.4.2.2 Dean Flow in Curved Pipes

The flow field inside a curved pipe was first derived by Dean [28]. For a more detailed review of flow in curved pipes, see [29]. The following detailed derivation was given by Gratton [30]. The model for the flow in a toroidal pipe is depicted in Fig. 2.16. The pipe has the form of a toroid of a radius of  $R$ . The pipe

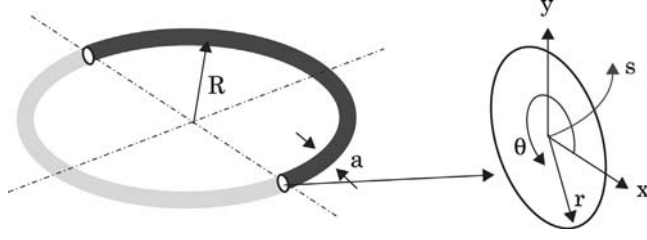


**Figure 2.16** Model of Dean flow in a toroidal pipe.

diameter is  $a$ . The coordinate system for this model is based on cylindrical coordinates, where  $s$  is the coordinate of the toroid's centerline  $\mathbf{q}$ . The metric of this coordinate system is:

$$(dq)^2 = \left(1 + \frac{r}{R} \sin \theta\right)^2 (ds)^2 + (dr)^2 + (r)^2 (d\theta)^2. \quad (2.90)$$

With the assumption of a laminar flow, the change in  $s$  is zero. With  $u$ ,  $v$ , and  $w$  are velocity components in  $s$ ,  $r$ , and  $\theta$ . The continuity equation (2.11) and Navier–Stokes equations (2.14) have the following forms in the new coordinate system:

$$\frac{\partial v}{\partial r} + \frac{1}{r} \frac{\partial w}{\partial \theta} + \frac{v}{r} + \frac{v \sin \theta + w \cos \theta}{R + r \sin \theta} = 0, \quad (2.91)$$

$$\begin{aligned} v \frac{\partial u}{\partial r} + \frac{w}{r} \frac{\partial u}{\partial \theta} + \frac{u(v \sin \theta + w \cos \theta)}{R + r \sin \theta} = & -\frac{1}{\rho} \left( \frac{R}{R + r \sin \theta} \right) \frac{\partial p}{\partial s} \\ & + \nu \left[ \frac{\partial^2 u}{\partial r^2} + \frac{1}{r^2} \frac{\partial^2 u}{\partial \theta^2} - \frac{u}{R + r \sin \theta} + \frac{1}{r} \frac{\partial u}{\partial r} \right. \\ & \left. + \frac{1}{R + r \sin \theta} \left( \sin \theta \frac{\partial u}{\partial r} + \frac{\cos \theta}{r} \frac{\partial u}{\partial \theta} \right) \right], \end{aligned} \quad (2.92)$$

$$\begin{aligned} v \frac{\partial v}{\partial r} + \frac{w}{r} \frac{\partial v}{\partial \theta} - \frac{w^2}{r} - \frac{u^2 \sin \theta}{R + r \sin \theta} = & -\frac{1}{\rho} \frac{\partial p}{\partial r} + \nu \left[ \frac{\partial^2 v}{\partial r^2} + \frac{1}{r} \frac{\partial v}{\partial r} \right. \\ & + \frac{v}{r^2} + \frac{1}{r^2} \frac{\partial^2 v}{\partial \theta^2} - \frac{2}{r^2} \frac{\partial w}{\partial \theta} + \frac{1}{R + r \sin \theta} \left( \sin \theta \frac{\partial v}{\partial r} + \frac{\cos \theta}{r} \frac{\partial v}{\partial \theta} - \frac{w \cos \theta}{r} \right) \\ & \left. - \frac{\sin \theta}{(R + r \sin \theta)^2} (v \sin \theta + w \cos \theta) \right] \end{aligned} \quad (2.93)$$

$$\begin{aligned}
v \frac{\partial w}{\partial r} + \frac{w}{r} \frac{\partial w}{\partial \theta} - \frac{vw}{r} - \frac{u^2 \cos \theta}{R + r \sin \theta} = & -\frac{1}{r\rho} \frac{\partial p}{\partial \theta} + \nu \left[ \frac{\partial^2 w}{\partial r^2} + \frac{1}{r} \frac{\partial w}{\partial r} + \frac{w}{r^2} \right. \\
& + \frac{1}{r^2} \frac{\partial^2 w}{\partial \theta^2} - \frac{2}{r^2} \frac{\partial v}{\partial \theta} + \frac{\sin \theta}{R + r \sin \theta} \frac{\partial w}{\partial r} + \frac{\cos \theta}{R + r \sin \theta} \left( \frac{1}{r} \frac{\partial w}{\partial \theta} + \frac{v}{r} \right) \\
& \left. - \frac{\cos \theta}{R + r \sin \theta} (v \sin \theta + w \cos \theta) \right], \tag{2.94}
\end{aligned}$$

where  $p$  is the pressure and  $\nu$  is the kinematic viscosity. Assuming that the radius of curvature is much larger than the pipe diameter ( $R \gg a$ ), the solution of the above four equations can be derived based on Poiseuille flow:

$$\begin{cases} u = A(a^2 - r^2) + \tilde{u} \\ v = \tilde{v} \\ w = \tilde{w} \\ \frac{p}{\rho} = Cs + \frac{\tilde{p}}{\rho}, \end{cases} \tag{2.95}$$

where  $A$  and  $C$  are the constants for the velocity and pressure gradients, respectively. The tilde-marked variables are the small perturbations. Rewriting the equations and ignoring the small products of the tilde-marked variables leads to:

$$\frac{\partial \tilde{v}}{\partial r} + \frac{\tilde{v}}{r} + \frac{1}{r} \frac{\partial \tilde{w}}{\partial \theta} = 0, \tag{2.96}$$

$$\begin{aligned}
-2Ar\tilde{v} = (1 - r\epsilon \sin \theta) \left( C + \frac{1}{\rho} \frac{\partial \tilde{p}}{\partial s} \right) + \nu \left( \frac{\partial^2}{\partial r^2} + \frac{1}{r} \frac{\partial}{\partial r} \frac{1}{r^2} \frac{\partial^2}{\partial \theta^2} \right) [A(a^2 - r^2) + \tilde{u}] \\
+ \nu \epsilon \left[ \left( \frac{\partial}{\partial r} + \frac{1}{r} \right) A(a^2 - r^2) \sin \theta + \frac{1}{r} \frac{\partial}{\partial \theta} A(a^2 - r^2) \cos \theta \right] \tag{2.97}
\end{aligned}$$

$$-\epsilon A^2 (a^2 - r^2)^2 \sin \theta = \frac{1}{\rho} \frac{\partial \tilde{p}}{\partial r} - \frac{\nu}{r} \frac{\partial}{\partial \theta} \left( \frac{\partial \tilde{w}}{\partial r} + \frac{\tilde{w}}{r} - \frac{1}{r} \frac{\partial \tilde{v}}{\partial \theta} \right), \tag{2.98}$$

$$-\epsilon A^2 (a^2 - r^2)^2 \cos \theta = -\frac{1}{r} \frac{1}{\rho} \frac{\partial \tilde{p}}{\partial \theta} + \nu \frac{\partial}{\partial r} \left( \frac{\partial \tilde{w}}{\partial r} + \frac{\tilde{w}}{r} - \frac{1}{r} \frac{\partial \tilde{v}}{\partial \theta} \right), \tag{2.99}$$

where  $\epsilon = a/R$  is the ratio between pipe diameter and the radius of curvature, and all the higher orders of the tilde-marked terms as well as of  $\epsilon$  are neglected. Setting the small terms in (2.97) to zero

$$0 = C - 2A\nu - 2A\nu \tag{2.100}$$

and rearranging for  $C$ :

$$C = -4A\nu. \tag{2.101}$$

equation (2.97) then has the form:

$$-2Ar\tilde{v} = \frac{1}{\rho} \frac{\partial \tilde{p}}{\partial s} - 6\epsilon\nu Ar \sin \theta + \nu \left( \frac{\partial^2 \tilde{u}}{\partial r^2} + \frac{1}{r} \frac{\partial \tilde{u}}{\partial r} + \frac{1}{r^2} \frac{\partial^2 \tilde{u}}{\partial \theta^2} \right). \quad (2.102)$$

Separating variables according to  $r$  and  $\theta$  and substituting the separated variables:

$$\tilde{u} = \hat{u}(r) \sin \theta, \tilde{v} = \hat{v}(r) \sin \theta, \tilde{w} = \hat{w}(r) \cos \theta, \tilde{p} = \rho \hat{p}(r) \sin \theta, \quad (2.103)$$

in (2.96), (2.98), (2.99), and (2.102), normalizing the velocities by  $\bar{w} = C/(4\nu)$  and spacial variables by  $a$ , and applying the no-slip boundary condition at  $r = 0$  result in the dimensionless velocity components:

$$\begin{cases} u = 2(1 - r^2) \left[ 1 - \epsilon \frac{3}{4} r \sin \theta + \epsilon \frac{\text{Re}}{1152} r \sin \theta (19 - 21r^2 + 9r^4 - r^6) \right] \\ v = \epsilon \frac{\text{Re}}{144} \sin \theta (4 - r^2)(1 - r^2)^2, \\ w = \epsilon \frac{\text{Re}}{144} \cos \theta (1 - r^2)(4 - 23r^2 + 7r^4), \end{cases} \quad (2.104)$$

where  $\text{Re} = \bar{w}a/\nu$  is the Reynolds number. Using Cartesian coordinates ( $x = r \sin \theta$ ,  $y = r \cos \theta$ ) the three velocity components have the form:

$$\begin{cases} \frac{dx}{dt} = \frac{\epsilon \text{Re}}{144} \left[ h(r) + \frac{y^2}{r} h'(r) \right], \\ \frac{dy}{dt} = -\frac{\epsilon \text{Re}}{144} \frac{xy}{r} h'(r) \\ \frac{ds}{dt} = 2(1 - r^2). \end{cases} \quad (2.105)$$

For the  $s$  component, all the  $\epsilon$  terms are cancelled from the expression of  $u$  in (2.104). The functions  $h(r)$  and  $h'(r)$  are:

$$h(r) = \frac{1}{4} (4 - r^2)(1 - r^2)^2, \quad (2.106)$$

$$h'(r) = -\frac{3}{2} r (1 - r^2)(3 - r^2).$$

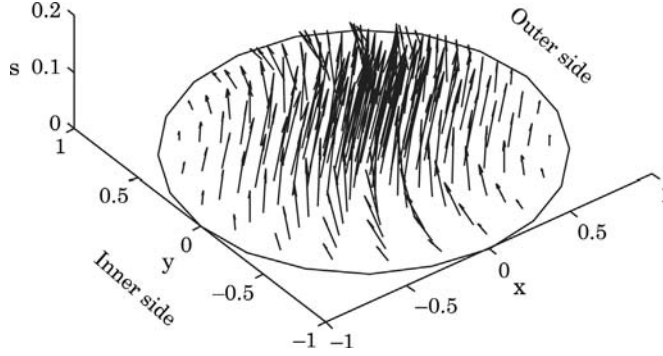


**Figure 2.17** The dimensionless velocity field of a pipe cross section.

Further normalizing of the time and  $s$  by  $\text{Re}\epsilon/144$  and  $\text{Re}\epsilon/288$  results in the dimensionless velocity components:

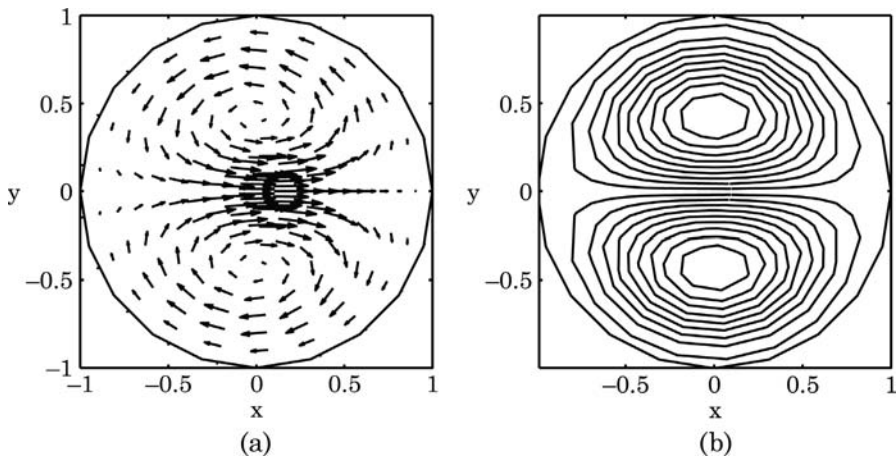
$$\begin{cases} \frac{dx}{dt} = h(r) + \frac{y^2}{r} h'(r), \\ \frac{dy}{dt} = -\frac{xy}{r} h'(r) \\ \frac{ds}{dt} = 1 - r^2. \end{cases} \quad (2.107)$$

Fig. 2.17 shows graphically the dimensionless three-dimensional velocity field (2.107) of a pipe cross section. The effect of the centrifugal force can be seen clearly. The stream function can be determined in the same way as shown in Example 2.9:

$$\begin{aligned} \psi &= \int \left( h + \frac{h'}{r} y^2 \right) dx + \int \left( \frac{h'}{r} xy \right) dy - \iint \frac{\partial}{\partial x} \left( h + \frac{h'}{r} y^2 \right) dy dx \\ &= \frac{y}{4} (4 - r^2) (1 - r^2)^2 = yh. \end{aligned} \quad (2.108)$$

Fig. 2.18 (a) shows the secondary velocity field of the pipe cross section. The inner side of the torus is on the left. Centrifugal force causes the fluid to move outward. The stream lines depicted in Fig. 2.18 (b) show the two vortices in the lower and upper halves of the pipe.

The trajectories of the fluid particles are calculated using the velocity solutions (2.107) and numerical integration (Runge–Kutta method). Projecting the particle position on a single two-dimensional cross section results in the Poincaré section. Fig. 2.19 shows the trajectories and Poincaré sections of the Dean flow where the  $s$ -axis is straightened for clarity. The results clearly show that independent of the orientation seeding lines, the Poincaré



**Figure 2.18** Dean vortices: (a) secondary velocity field; (b) streamlines of the secondary velocity field.

sections follow the streamlines as depicted in Fig. 2.18 (b). If this flow is used in a micromixer, the solvent and solute should be introduced on the left and right of the cross section or the outer and inner sides of the curved channel (Fig. 2.18), so that the trajectories of the fluid particle can sample both sides of the channel. If the solvent and solute are introduced in the upper and lower halves of the channel, the trajectories will keep them in their respective channel sections and advective mixing will not happen. Even if the solvent and solute enter at the outer and inner side of the curved channel, the trajectories are stable, elliptic, and homoclinic. Transversal transport is advective but not chaotic. That means they do not cross each other. Chaotic advection can therefore not be realized with the original Dean flow.

The above analysis assumes a small ratio between pipe diameter and radius of curvature  $a/R \ll 1$ . For realistic channel designs, this ratio can be approximately unity, and the secondary flows are more obvious. In this case, the flow is characterized by the Dean number:

$$\text{De} = \text{Re} \sqrt{\frac{a}{R}} \quad (2.109)$$

where  $\text{Re}$  is the Reynolds number. The Dean number represents the ratio between centrifugal force and inertial force. There exists a critical Dean number  $\text{De}_{\text{cr}} = 150$  where the secondary flow pattern changes. For  $\text{De} < 150$ , there is only one pair of counter-rotating vortices as analyzed above. At higher Dean numbers  $\text{De} > 150$ , the centrifugal force is dominant leading to the formation of two additional vortices at the outer channel wall. This effect and its application for mixing at a high Dean number or high Reynolds number will be discussed later in Section 5.1.

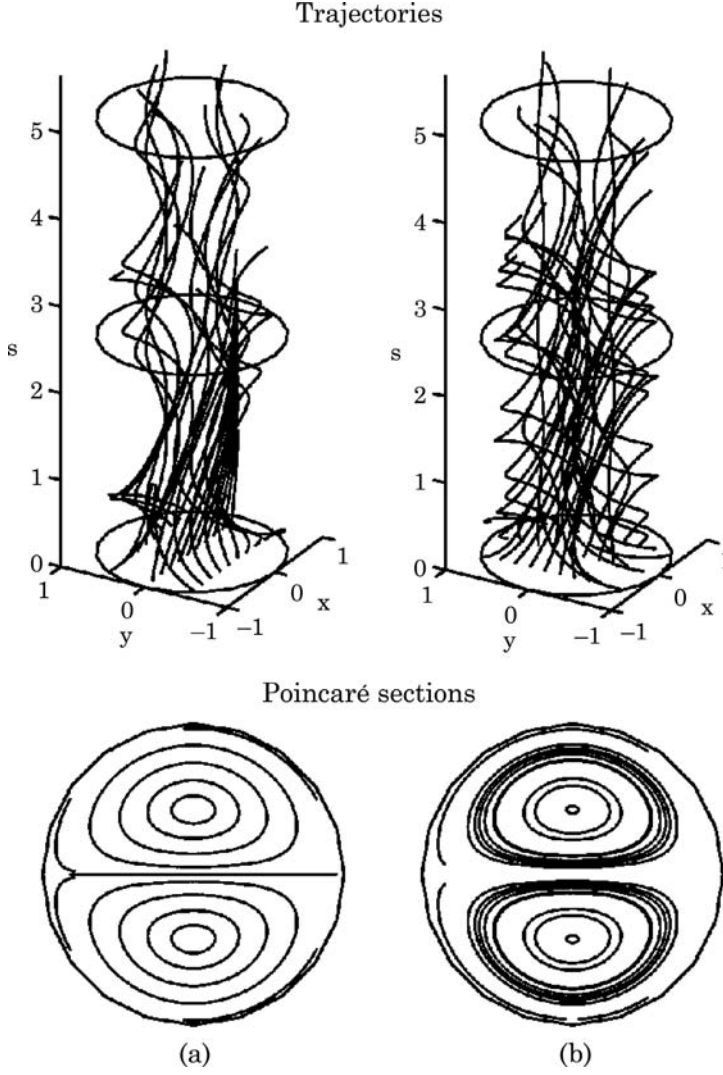


**Figure 2.19** Trajectories and Poincaré sections for fluid particles in a Dean flow: (a) seeding line parallel to the  $x$ -axis and (b) seeding lines parallel to the  $y$ -axis.

#### 2.4.2.3 Flow in Helical Pipes [32]

In helical pipes, the cross section rotates around the pipe center line  $\mathbf{q}$  (Fig. 2.20). Assuming a constant torsion of  $\tau$ , the rotation at  $s$  is  $\tau s$ . Further, a constant curvature  $\kappa = d\Phi/ds$  is assumed. Based on this assumption, Germano [31] derived the metric:

$$(dq)^2 = [1 - \kappa r \sin(\theta + \tau s)](ds)^2 + (dr)^2 + r^2(d\theta)^2. \quad (2.110)$$

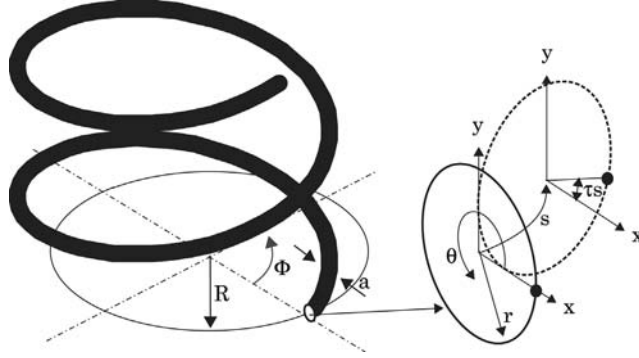


**Figure 2.20** Model of a helical pipe.

The flow in this coordinate system has only a second-order dependence on  $\tau$ . Thus the solution (2.107) can be used for helical pipes by changing the basis to the new coordinate system (2.110). The solution for the velocity field is then:

$$\begin{cases} \frac{dx}{dt} = h \cos(\lambda s) + \frac{h'}{r} y x \sin(\lambda s) + \frac{h'}{r} y^2 \cos(\lambda s), \\ \frac{dy}{dt} = - \left[ h \sin(\lambda s) + \frac{h'}{r} x y \cos(\lambda s) + \frac{h'}{r} x^2 \sin(\lambda s) \right], \\ \frac{ds}{dt} = 1 - r^2, \end{cases} \quad (2.111)$$

where the curvature and torsion are combined in the geometry parameter:

$$\lambda = \frac{144\nu}{\bar{u}} \frac{\tau}{\kappa}, \quad (2.112)$$

where  $\bar{u}$  is the mean velocity in the  $s$  direction. The stream function of (2.111) has the form:

$$\psi = \frac{\lambda r^2}{2} \left( \frac{r^2}{2} - 1 \right) + \frac{y}{4} (4 - r^2) (1 - r^2)^2. \quad (2.113)$$

Fig. 2.21 shows the streamlines calculated using (2.113). The initial positions of the particles on the depicted trajectories are on a seeding line parallel to the  $y$ -axis. The results show that at increasing torsion, the secondary flow transforms from two counter-rotating vortices into a single vortex.

The Poincaré sections of flow in helical pipes with different geometry parameters are shown in Fig. 2.22. The flow is initially sampled with a seeding line parallel to the  $y$ -axis. At  $\lambda = 0$ , there is no torsion and the pipe is a torus.



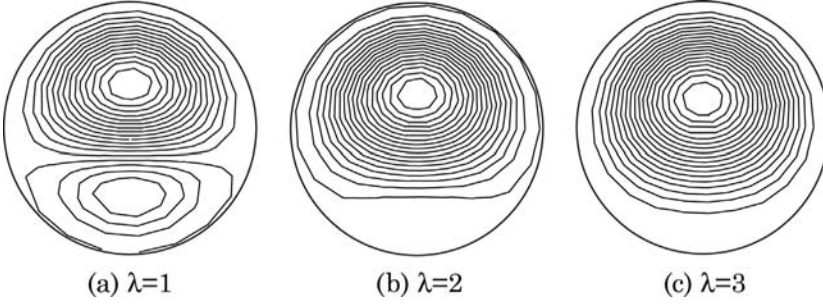


**Figure 2.21** Streamlines of the flow inside a helical pipe of different geometry parameters: (a)  $\lambda = 1$ ; (b)  $\lambda = 2$ ; and (c)  $\lambda = 3$ .

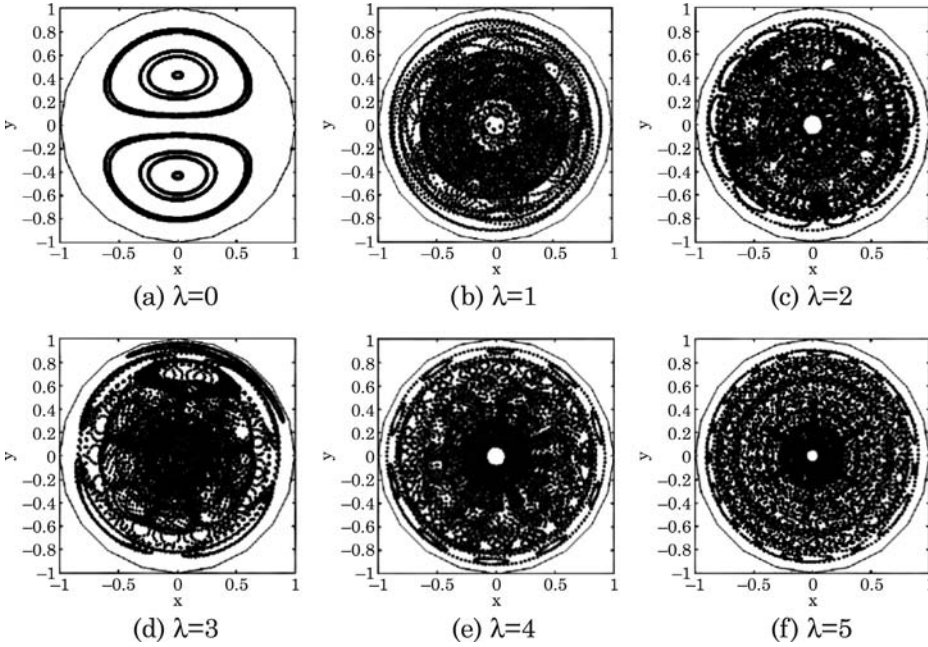


**Figure 2.22** Poincaré sections with different geometry parameters: (a)  $\lambda = 0$ ; (b)  $\lambda = 1$ ; (c)  $\lambda = 2$ ; (d)  $\lambda = 3$ ; (e)  $\lambda = 4$ ; and (f)  $\lambda = 5$ .

The flow is clearly not chaotic, the particles follow the streamlines. At  $\lambda < 0$ , chaotic advection is apparent.

#### 2.4.2.4 Flow in Twisted Pipes [32]

While a straight channel is one-dimensional, a three-dimensional flow (transverse cross-sectional plane and longitudinal axis) can be created in

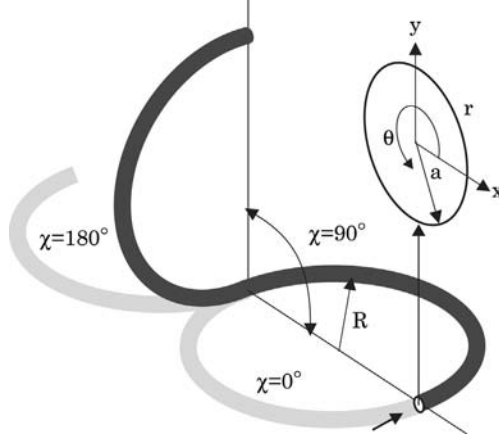


**Figure 2.23** The basic unit of a twisted pipe consisting of two C-shaped sections.

curved channels. In such curved channels, secondary vortices in the transverse cross-sectional plane can move fluid particles between the center of the channel and its wall. A unit of the simplest configuration for chaotic advection is depicted in Fig. 2.23. The secondary flow in a twisted pipe causes the so-called Dean vortices. The fluid particles rotate with an angle of  $\chi$  between the successive units. The following analysis was reported by Jones et al. [32].

Using the polar coordinate system  $(\theta, r)$  in the transverse  $x, y$  plane, the stream function  $\psi$  and the axial velocity  $u$  are determined through the following dimensionless equation system:

$$\begin{cases} \nabla^2 u = \frac{1}{r} \left( \frac{\partial \psi}{\partial r} \frac{\partial u}{\partial \theta} - \frac{\partial \psi}{\partial \theta} \frac{\partial u}{\partial r} \right) - C \\ \nabla^2 \psi = \frac{1}{r} \left( \frac{\partial \psi}{\partial r} \frac{\partial}{\partial \theta} - \frac{\partial \psi}{\partial \theta} \frac{\partial}{\partial r} \right) \nabla^2 \psi + 2\text{De}^2 u \left( \frac{\sin \theta}{r} \frac{\partial u}{\partial \theta} - \cos \theta \frac{\partial u}{\partial r} \right), \end{cases} \quad (2.114)$$

where  $\text{De}$  is the Dean number,  $a$  is the pipe radius, and  $R$  is the radius of curvature of the C-shape bend. The Dean number describes the ratio between the centrifugal force and the viscous force. From (2.109), the Dean number is proportional to the Reynolds number. The dimensionless pressure gradient is defined as:

$$C = -\frac{a^2}{R\bar{u}\mu} \frac{\partial p}{\partial \theta}, \quad (2.115)$$

where  $\bar{u}$  is the average axial velocity. In (2.114), the lengths and velocities are normalized by the pipe radius  $a$  and the average axial velocity  $\bar{u}$ , respectively.

The first-order perturbation solution results in the following equations of the particle motion [32]:

$$\begin{cases} \frac{dx}{dt} = \frac{\alpha}{1152} \left[ h(r) + y^2 \frac{h'(r)}{r} \right] \\ \frac{dy}{dt} = -\frac{\alpha}{1152} \frac{xy}{r} h'(r) \\ \frac{d\theta}{dt} = \frac{1}{4} \beta (1 - r^2) \end{cases} \quad (2.116)$$

where  $\alpha = \text{De}C^2$ ,  $\beta = \text{De}C/\text{Re}$ .

Using the angle  $\theta$  to describe the three-dimensional motion of the fluid particles, the velocity components in  $x - y$  plane can be formulated as [32]:

$$\begin{cases} \frac{dx}{d\theta} = \frac{\alpha}{1152\beta} (4 - 5x^2 - 23y^2 + x^4 + 8x^2y^2 + 7y^4) \\ \frac{dy}{d\theta} = \frac{\alpha}{192\beta} xy(3 - x^2 - y^2). \end{cases} \quad (2.117)$$

This solution results in chaotic advection for a combination of  $\alpha/\beta$  and  $\chi$ . For instance, the most chaotic pattern is achieved with  $\alpha/\beta = 100$  and  $\chi = 90^\circ$ . The condition for chaotic advection to occur in this configuration is:

$$\chi \leq 2 \arctan \left( \sinh \frac{\pi\alpha}{192\beta} \right). \quad (2.118)$$

Figs. 2.24–2.26 show the Poincaré sections with the different model parameters.

#### 2.4.2.5 Flow in a Droplet

With the increasing popularity of droplet-based microfluidics, mixing in droplets becomes a crucial task in designing a droplet-based lab-on-a-chip. The analytical solution for the internal flow inside a droplet was first reported by Hadamard [33]. Consider a spherical microdroplet with a radius  $a$ . The droplet experiences a uniform shear flow of a velocity  $\bar{u}$  in the  $z$  axis. We now consider the viscosity ratio  $\beta = \mu_1/\mu_2$ , where  $\mu_1$  is the viscosity of the droplet fluid and  $\mu_2$  is the viscosity of the surrounding fluid. Normalizing the spacial variables by the droplet radius  $a$ , the velocity by  $\bar{u}$  and the time by  $a/\bar{u}$  results in the dimensionless equations of particle motion inside the droplet [34]:

$$\begin{cases} \frac{dx}{dt} = \frac{zx}{2(1+\beta)} \\ \frac{dy}{dt} = \frac{zy}{2(1+\beta)} \\ \frac{dz}{dt} = \frac{1 - z^2 - 2y^2 - 2x^2}{2(1+\beta)}. \end{cases} \quad (2.119)$$

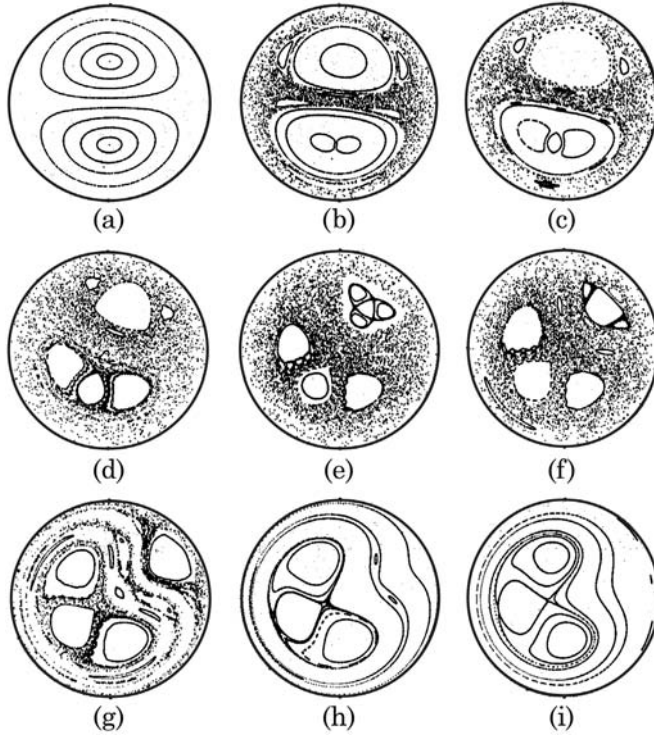


**Figure 2.24** Poincaré sections of twisted pipes with different twisting angles  $\chi$  ( $\alpha/\beta = 100$ ): (a)  $\chi = 0$ ; (b)  $\chi = \pi/16$ ; (c)  $\chi = \pi/8$ ; (d)  $\chi = \pi/4$ ; (e)  $\chi = 3\pi/8$ ; (f)  $\chi = \pi/2$ ; (g)  $\chi = 5\pi/8$ ; (h)  $\chi = 3\pi/4$ ; (i)  $\chi = 7\pi/8$  (reproduced from [32] by permission of Cambridge University Press).

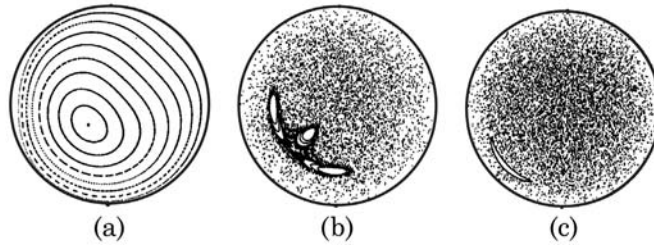


**Figure 2.25** Poincaré sections of twisted pipes with different twisting angles  $\chi$  ( $\alpha/\beta = 200$ ): (a)  $\chi = \pi/4$ ; (b)  $\chi = \pi/2$ ; (c)  $\chi = 3\pi/4$  (reproduced from [32] by permission of Cambridge University Press).

The flow described by (2.119) is actually one-dimensional and not chaotic because it has two invariants [35]:

$$I_0 = \frac{z}{y} \quad (2.120)$$

$$J_0 = z^2(1 - x^2 - y^2 - z^2).$$

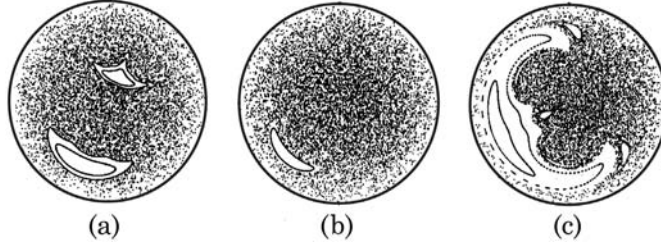


**Figure 2.26** Poincaré sections of twisted pipes with different ratios  $\alpha/\beta$  ( $\chi = \pi/2$ ): (a)  $\alpha/\beta = 50$ ; (b)  $\alpha/\beta = 150$ ; (c)  $\alpha/\beta = 250$  (reproduced from [32] by permission of Cambridge University Press).

In order to create chaotic advection, an external shear flow  $u = Gy$  is superimposed on the uniform flow  $\bar{u}$ . Defining the dimensionless parameter  $\alpha = Ga/\bar{u}$  results in the following equations of particle motion inside the droplet under the shear flow only:

$$\begin{cases} \frac{dx}{dt} = \frac{\alpha}{2(1+\beta)} \left[ (5r^2 - 3) \frac{y}{2} - 2x^2y \right] + \alpha \frac{y}{2} \\ \frac{dy}{dt} = \frac{\alpha}{2(1+\beta)} \left[ (5r^2 - 3) \frac{x}{2} - 2y^2x \right] - \alpha \frac{x}{2} \\ \frac{dz}{dt} = -\frac{\alpha xyz}{1+\beta} \end{cases} \quad (2.121)$$

where  $r = \sqrt{x^2 + y^2 + z^2}$  is the radial variable in the spherical coordinate system. Superposition of (2.119) and (2.121) results in the equations of motions of a fluid particle inside a droplet immersed in a combined shear and uniform flow, shown in Fig. 2.27.

## 2.5 Viscoelastic Effects

In most analysis and design considerations of micromixers, the solute and solvent are assumed to be Newtonian fluids. In these fluids, the viscosities do not depend on the velocity gradient or the shear stress. That means at a given temperature and pressure, the viscosity is a constant and the velocity gradient is linearly proportional to the shear stress. The Newtonian assumption is true for solvents and solutes that have small molecules. However, if they have large molecules such as long polymers, the viscosity is also a function of the shear stress. Since the shear stress and viscosity gradient at the micro scale increase with miniaturization, nonlinear effects can be expected and exploited for mixing applications.

At the molecular level, viscoelastic fluids can be described by two models: network model and single-molecule model [2]. The network model is based on

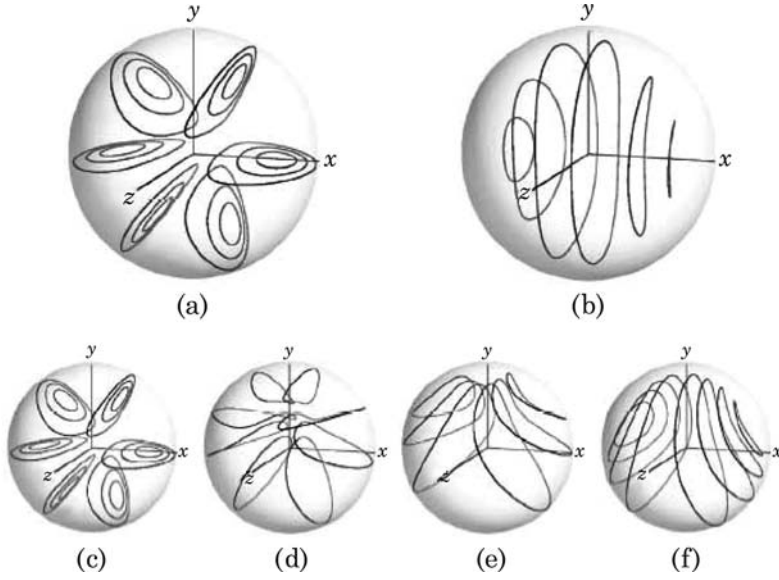


**Figure 2.27** Streamlines of flow inside a spherical droplet, the flow direction of the surrounding fluid is along the  $z$ -axis : (a) external uniform flow; (b) external shear flow; (c) superposition flow with  $\alpha = 0$ ,  $\beta = 1$ ; (d) superposition flow with  $\alpha = 0.2$ ,  $\beta = 1$ ; (e) superposition flow with  $\alpha = 0.4$ ,  $\beta = 1$ ; (f) superposition flow with  $\alpha = 0.6$ ,  $\beta = 1$  (reprinted with permission from [34]).

the formation and rupture of junctions between polymer molecules. The network model is suitable for solutions with high polymer concentration. Dilute solutions are better described with a single-molecule model, where interactions between the molecules are not frequent. The polymer molecule is represented by a “dumbbell” or “bead-on-a-string” model, where two spheres are connected by a spring. Kinetic theory with Stokes drag theory and Brownian motion can be used with this model for deriving macroscopic properties.

Fluids having large molecules display elastic behavior due to the stretching and coiling of the polymer chain. These fluids and their behavior are called here viscoelastic fluids and viscoelastic effects, respectively. The most apparent viscoelastic effect is the change of velocity profile in a channel. The dimensionless velocity profile of a viscoelastic fluid in a circular capillary can be approximated as [2]:

$$u^* = \frac{u}{u_{\max}} \approx 1 - \left( \frac{r}{r_0} \right)^{1+\frac{1}{n}} \quad (2.122)$$

where  $0 < n < 1$  is a parameter unique for the fluid, and  $r_0$  is the radius of the capillary. If  $n = 1$  the fluid becomes Newtonian and the velocity profile is parabolic.

The next viscoelastic effect, which is relevant to mixing at the microscale, is the entry flow at a contraction. The operation point of a viscoelastic flow is

represented by the Wi–Re diagram, where Wi is the Weissenberg number and Re is the Reynolds number. With a characteristic length scale  $L_c$ , mean velocity  $\bar{u}$ , density  $\rho$  and zero-stress viscosity  $\mu_0$ , the Reynolds number is defined here as:

$$\text{Re} = \frac{\rho \bar{u} L_c}{\mu_0}. \quad (2.123)$$

The Weissenberg number represents the elastic character of the fluid by using the ratio between the relaxation time  $\lambda$  of the fluid and the characteristic residence time  $\tau_{\text{flow}}$ :

$$\text{Wi} = \frac{\lambda}{\tau_{\text{flow}}}. \quad (2.124)$$

The characteristic residence time is the inverse of the characteristic shear rate  $\dot{\gamma}$  and is defined as:

$$\tau_{\text{flow}} = \frac{1}{\dot{\gamma}} = \frac{L_c}{\bar{u}}. \quad (2.125)$$

Because both Reynolds number and Weissenberg number are proportional to the average velocity  $\bar{u}$ , it's useful to define the elasticity number, which is independent from the flow velocity:

$$\text{El} = \frac{\text{Elastic effect}}{\text{Inertial effect}} = \frac{\text{Wi}}{\text{Re}} = \frac{\lambda \mu_0}{\rho L_c^2}. \quad (2.126)$$

The elasticity number represents the importance of elastic effect over inertial effect. For small Reynolds number in microfluidics, the inertial effect is negligible. However, if the elasticity number of the fluid is large enough, the elastic effect may be large enough to compete with the dominant viscous effect. Fig. 2.28 shows the typical operation region of a possible micromixer based on viscoelastic instabilities arising from a 4-to-1 contraction. Shear-thinning viscoelastic fluids are, for instance, concentrated polymer solutions. Boger fluids are dilute solutions of a polymer and a solvent. The slopes of the curves represent the elasticity numbers [36].

## 2.6 Electrokinetic Effects

### 2.6.1 Electroosmosis

Electrokinetic effects are based on an electric double layer at the interface between a solid and a liquid or between two liquids. This double layer is also

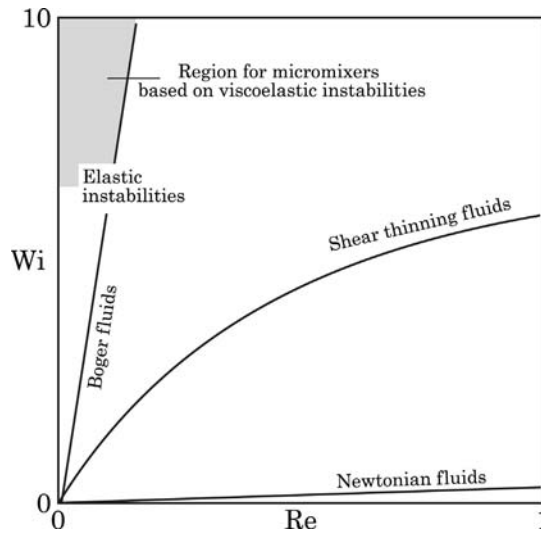


**Figure 2.28** The  $Wi$ – $Re$  diagram (based on a planar 4:1 contraction flow), the gray area represents the operating region of micromixers based on viscoelastic instabilities.

called the Debye layer. This section focuses on the interface between a solid and a liquid. In general, there are four basic electrokinetic effects:

- *Electroosmosis* is the flow of a liquid in an electric field relative to a stationary charged surface.
- *Electrophoresis* is the motion of a charged particle in an electric field relative to the surrounding liquid.
- *Streaming potential* is the opposite effect of electroosmosis. An electric potential is created when a liquid is forced to flow relative to a charged surface.
- *Sedimentation potential* is the opposite effect of electrophoresis. An electric potential is created when charged particles are forced to flow relative to a surrounding liquid.

### 2.6.1.1 The Debye Layer

The Debye layer is an electric double layer, which occurs due to interaction between an electrolyte and a charged solid surface. Ions in an electrolyte solution are attracted to the charged surface and form a thin charged layer, which is called the Stern layer. The Stern layer is attracted to the surface due to the electrostatic force. The Stern layer leads to the formation of a thicker charge layer in the solution. This diffuse and mobile layer is called the Gouy–Chapman layer. The Stern layer and the Gouy–Chapman layer together form the Debye layer, Fig. 2.29 (a). Because the Gouy–Chapman layer is mobile, it can move if an electric field is applied. The interface between the Stern layer and the



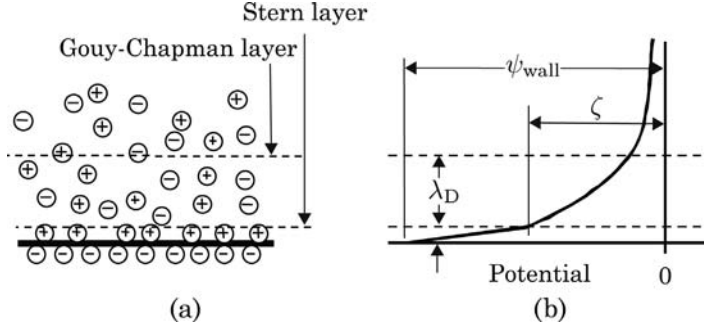


**Figure 2.29** The Debye layer: (a) the Stern layer and the Gouy–Chapman layer; (b) the potential distribution near the wall.

Gouy–Chapman layer is called the shear surface. The potential of the charged solid surface is called the wall potential  $\Psi_{\text{wall}}$ . The potential of the shear surface is called the zeta potential, Fig. 2.29 (b). The potential distribution in the electrolyte solution can be described by the one-dimensional Poisson equation:

$$\frac{d^2\Psi}{dy^2} = -\frac{\rho_{\text{el}}(y)}{\varepsilon}, \quad (2.127)$$

where  $\rho_{\text{el}}$  and  $\varepsilon = \varepsilon_0\varepsilon_r$  are the electric charge density and the dielectric constant of the electrolyte. Assuming the Boltzmann distribution for the charge density, the ion concentration in the electrolyte solution can be determined as:

$$n_i = n_{i\infty} \exp\left(-\frac{z_i e \Psi}{k_B T}\right), \quad (2.128)$$

where  $n_{i\infty}$  is the ion concentration of the electrolyte with a unit of  $1/\text{m}^3$ ,  $z_i$  is the ionic valence,  $e = 1,602 \times 10^{-19}$  is the elementary charge. Thus, the total charge in the double layer is:

$$\rho_{\text{el}} = \sum_i^{\infty} n_i z_i e. \quad (2.129)$$

The charge density  $\rho_{\text{el}}$  in an symmetric electrolyte is proportional to the concentration difference between cations and anions:

$$\begin{aligned} \rho_{\text{el}} &\sim ze(n_+ - n_-) \\ \rho_{\text{el}} &= -2zen_{\infty} \sinh\left(\frac{ze}{k_B T} \Psi\right). \end{aligned} \quad (2.130)$$

Combining (2.127) and (2.130) results in the Poisson–Boltzmann equation:

$$\frac{d^2\Psi}{dy^2} = \frac{2ze n_\infty}{\varepsilon} \sinh\left(\frac{ze\Psi}{k_B T}\right). \quad (2.131)$$

Under conditions such as a large characteristic length compared to the double layer thickness or a high ion concentration in the electrolyte, the right side of (2.131) can be linearized by the relation  $\sinh(x) = x$ :

$$\frac{d^2\Psi}{dy^2} = \frac{\Psi}{\lambda_D^2}, \quad (2.132)$$

where  $\lambda_D$  is the double layer thickness, which is called the Debye length:

$$\lambda_D = \sqrt{\frac{\varepsilon k_B T}{2z^2 e^2 n_\infty}}. \quad (2.133)$$

Solving (2.132) results in the potential distribution:

$$\Psi = \Psi_{\text{wall}} \exp\left(-\frac{y}{\lambda_D}\right). \quad (2.134)$$

### 2.6.1.2 Electroosmotic Transport Effect

Continuum models using the mass and energy conservation equations can be used for describing the electroosmotic transport effects. The conservation of momentum needs to consider the electrostatic force created by the electric field:

$$\rho \frac{D\mathbf{v}}{Dt} = -\nabla p + \mu \nabla^2 \mathbf{v} + \rho_{\text{el}} \mathbf{E}_{\text{el}} = -\nabla p + \mu \nabla^2 \mathbf{v} + \varepsilon \mathbf{E}_{\text{el}} \nabla^2 \Psi. \quad (2.135)$$

If there is no pressure gradient applied to the flow, (2.135) has the one-dimensional form:

$$-\mu \frac{d^2 u_{\text{eo}}}{dy^2} = \varepsilon E_{\text{el}} \frac{d^2 \Psi}{dy^2}. \quad (2.136)$$

With the assumption of a thin Debye length compared to the channel diameter, the electrokinetic velocity is:

$$u_{\text{eo}} = -\frac{\varepsilon E_{\text{el}} \zeta}{\mu}. \quad (2.137)$$

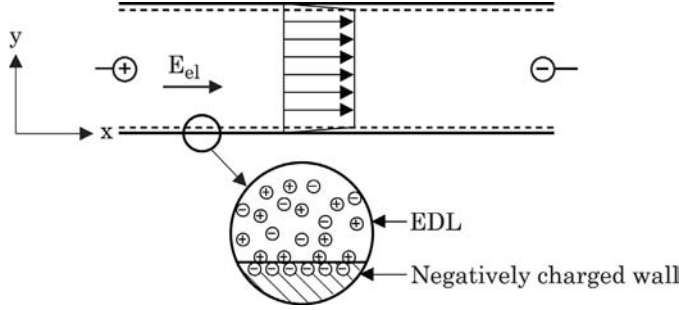


**Figure 2.30** Electroosmotic flow in a capillary with a negatively charged wall.

The velocity  $u_{eo}$  is also called the Smoluchowski velocity. If the Debye length is negligible compared to other channel dimensions, the electrokinetic flow can be modelled with slip boundary condition, where the slip velocity is the Smoluchowski velocity, Fig. 2.30.

With a constant viscosity  $\mu$  and a constant zeta potential  $\zeta$ , the electroosmotic velocity is proportional to the electric field strength  $E_{el}$ . The negative sign shows that the flow direction is opposite to the field direction. The proportionality factor is called the electroosmotic mobility:

$$\mu_{eo} = \frac{u_{eo}}{E_{el}} = \frac{\varepsilon\zeta}{\mu}. \quad (2.138)$$

Equation (2.137) shows that the analysis of electrokinetic flows in a microchannel network can be replaced by the analysis of a resistance network. Electric currents and potentials can be calculated based on the basic Kirchhoff laws:

- The sum of all currents at a node is zero,
- The sum of all voltages in a closed loop is zero.

After determining the potentials at the nodes of the network, field strengths in each microchannel can be calculated. The velocity can then be determined by the given electroosmotic mobility.

### 2.6.1.3 Electrokinetic Flow Between Two Parallel Plates

Fig. 2.31 shows the model of electrokinetic flow between two parallel plates. The velocity distribution  $U(y)$  of an electrokinetic flow between two parallel plates can be derived from the Navier–Stokes equation. For further simplicity, the variable  $U(y)$  is introduced:

$$u(y) = U(y) - \frac{u_{eo}\Psi(y)}{\zeta}. \quad (2.139)$$

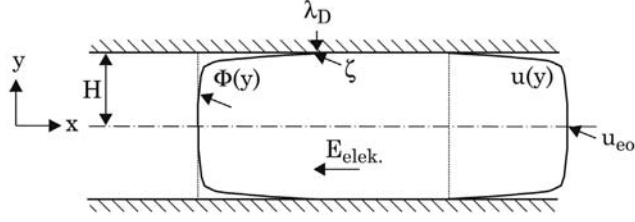


**Figure 2.31** Model for electrokinetic flow between two parallel plates.

Equation (2.136) has then the homogenous form:

$$\frac{d^2 u(y)}{dy^2} = 0. \quad (2.140)$$

With the boundary conditions:

$$\begin{aligned} \left. \frac{du}{dy} \right|_{y=0} &= 0 \\ u|_{y=h} &= -u_{eo}, \end{aligned}$$

the solution of (2.140) is:

$$u(y) = u_{eo} \left[ \frac{\Psi(y)}{\zeta} - 1 \right]. \quad (2.141)$$

Introducing the dimensionless velocity  $u^*$ , dimensionless potential  $\Psi^*$ , dimensionless zeta potential  $\zeta^*$  and the dimensionless spatial variable  $y^*$ :

$$u^* = \frac{u}{u_{eo}}; \quad \Psi^* = \frac{ze\Psi}{k_B T}; \quad \zeta^* = \frac{ze\zeta}{k_B T}; \quad y^* = \frac{y}{h}. \quad (2.142)$$

The solution (2.141) and the Poisson–Boltzmann equation (2.132) have the dimensionless forms:

$$u^*(y^*) = \frac{\Psi^*(y^*)}{\zeta^*} - 1, \quad (2.143)$$

$$\frac{d\Psi^{*2}}{d^2 y^*} = \left( \frac{h}{\lambda_D} \right)^2 \Psi^*. \quad (2.144)$$

The boundary conditions for (2.144) are:

$$\begin{aligned} \Psi^*|_{y^*=1} &= \zeta^* \\ \left. \frac{d\Psi^*}{dy^*} \right|_{y^*=0} &= 0. \end{aligned}$$

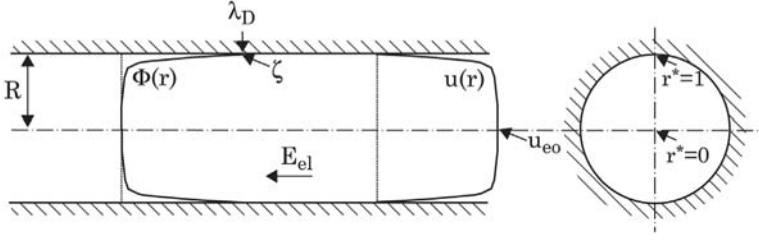


**Figure 2.32** Model of electrokinetic flow in a cylindrical capillary.

The solution of (2.144) is:

$$\Psi^* = \zeta^* \frac{\cosh\left(\frac{h}{\lambda_D} y^*\right)}{\cosh(h/\lambda_D)}. \quad (2.145)$$

Substituting (2.145) into (2.143) results in the dimensionless velocity distribution of a electrokinetic flow between two parallel plates:

$$u^*(y^*) = \frac{\cosh\left(\frac{H}{\lambda_D} y^*\right)}{\cosh(H/\lambda_D)} - 1. \quad (2.146)$$

#### 2.6.1.4 Electrokinetic Flow in a Cylindrical Capillary

Fig. 2.32 shows the model of electrokinetic flow in a cylindrical capillary. The Navier–Stokes equation and the Poisson–Boltzmann equation are formulated for the cylindrical coordinate system:

$$-\mu \frac{1}{r} \frac{d}{dr} \left( r \frac{du}{dr} \right) = \varepsilon E_{el} \frac{1}{r} \frac{d}{dr} \left( r \frac{d\Psi}{dr} \right), \quad (2.147)$$

$$\frac{1}{r} \frac{d}{dr} \left( r \frac{d\Psi}{dr} \right) = \frac{2ze n_\infty}{\varepsilon} \sinh\left(\frac{ze}{k_B T} \Psi\right). \quad (2.148)$$

For simplicity, the following dimensionless variables are introduced:

$$u^* = \frac{u}{u_{eo}}; \quad \Psi^* = \frac{ze\Psi}{k_B T}; \quad \zeta^* = \frac{ze\zeta}{k_B T}; \quad r^* = \frac{r}{R}, \quad (2.149)$$

where  $R$  is the capillary radius. Equations (2.147) and (2.148) then have the dimensionless forms:

$$-\frac{1}{r^*} \frac{d}{dr^*} \left( r^* \frac{du^*}{dr^*} \right) = \frac{1}{\zeta^*} \Psi^*, \quad (2.150)$$

$$\frac{1}{r^*} \frac{d}{dr^*} \left( r^* \frac{d\Psi^*}{dr^*} \right) = \left( \frac{R}{\lambda_D} \right)^2 \Psi^*, \quad (2.151)$$

$$\frac{d^2\Psi^*}{dr^{*2}} + \frac{1}{r^*} \frac{d\Psi^*}{dr^*} = \left( \frac{R}{\lambda_D} \right)^2 \Psi^*.$$

The dimensionless boundary conditions are:

$$\left. \frac{du^*}{dr^*} \right|_{r^*=0} = 0; \quad u^*|_{r^*=1} = 0. \quad (2.152)$$

Solving (2.150) results in:

$$u^*(r^*) = \frac{2(R/\lambda_D)^2}{\zeta^*} \sum_{n=1}^{\infty} \frac{C_n J_0(\lambda_n r^*)}{\lambda_n^2 J_1^2(\lambda_n)}, \quad (2.153)$$

where  $J_0$  and  $J_1$  are the Bessel functions of first kind and zero as well as first order, respectively.  $\lambda_n$  is the  $n$ th positive zero value of the Bessel function  $J_0(\lambda_n) = 0$ .  $C_n$  is a function of the dimensionless potential  $\Psi^*$ :

$$C_n = \int_{x=0}^1 x J_0(\lambda_n x) \Psi^*(x) dx. \quad (2.154)$$

The boundary conditions for (2.151) are:

$$\Psi^*|_{r^*=1} = \zeta^*; \quad \left. \frac{d\Psi(r^*)}{dr^*} \right|_{r^*=0} = 0. \quad (2.155)$$

The solution for the dimensionless potential is:

$$\Psi^*(r^*) = \zeta^* \frac{I_0\left(\frac{R}{\lambda_D} r^*\right)}{I_0\left(\frac{R}{\lambda_D}\right)}, \quad (2.156)$$

where  $I_0(x) = i^{-n} J_0(ix)$  are the modified Bessel functions of the first kind and zero order. Substituting (2.156) in (2.154) results in:

$$C_n = \frac{\zeta^*}{I_0\left(\frac{R}{\lambda_D}\right)} \frac{J_1(\lambda_n) I_1(R/\lambda_D)}{\lambda_n \left[ 1 + \left( \frac{R/\lambda_D}{\lambda_n} \right)^2 \right]}. \quad (2.157)$$

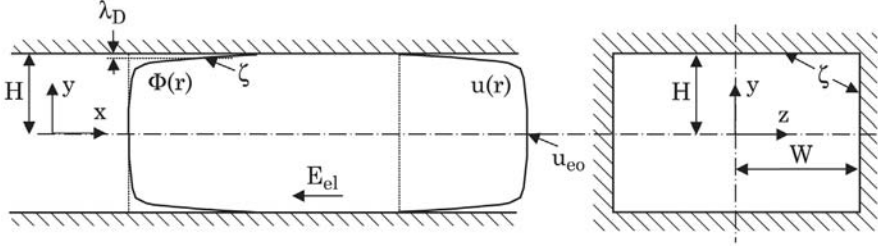


**Figure 2.33** Model for electrokinetic flow in a rectangular microchannel.

The dimensionless velocity distribution in a cylindrical capillary is then:

$$u^*(r^*) = 2 \left( \frac{R}{\lambda_D} \right)^2 \frac{I_1 \left( \frac{R}{\lambda_D} \right)}{I_0 \left( \frac{R}{\lambda_D} \right)} \sum_{n=1}^{\infty} \frac{1}{\lambda_n} \frac{J_0(\lambda_n r^*)}{J_1(\lambda_n)} \left[ \frac{1}{\lambda_n^2 + \left( \frac{R}{\lambda_D} \right)^2} \right]. \quad (2.158)$$

### 2.6.1.5 Electrokinetic Flow in a Rectangular Microchannel

Due to the characteristics of microtechnology, many micromixers have a rectangular cross section. Fig. 2.33 shows the model of electrokinetic flow in a rectangular microchannel. The Navier–Stokes equation and the Poisson–Boltzmann equation are formulated in the Cartesian coordinate system as:

$$-\mu \left( \frac{\partial^2 u}{\partial z^2} + \frac{\partial^2 u}{\partial y^2} \right) = \varepsilon E_{el} \left( \frac{\partial^2 \Psi}{\partial z^2} + \frac{\partial^2 \Psi}{\partial y^2} \right) = \frac{2ze n_{\infty}}{\varepsilon} \sinh \left( \frac{ze\Psi}{k_B T} \right). \quad (2.159)$$

The following dimensionless variables are introduced:

$$u^* = \frac{u}{u_{eo}}; \quad \Psi^* = \frac{ze\Psi}{k_B T}; \quad \zeta^* = \frac{ze\zeta}{k_B T}; \quad z^* = \frac{z}{D_h}; \quad y^* = \frac{y}{D_h}, \quad (2.160)$$

where  $D_h = 4WH/(W + H)$  is the hydraulic diameter of the microchannel. For simplicity, the approximation of  $\sinh(x) = x$  is used. As mentioned above, this assumption is correct if the hydraulic diameter  $D_h$  is much larger than the Debye length  $\lambda_D$  or if the ion concentration is dilute. At the molecular scale, this assumption means that the electric energy of the ions is much smaller than their thermal energy. Using the above dimensionless variables, the Navier–Stokes equation and the Poisson–Boltzmann equation have their dimensionless forms:

$$\frac{\partial^2 u^*}{\partial z^{*2}} + \frac{\partial^2 u^*}{\partial y^{*2}} = \frac{1}{\zeta^*} \left( \frac{D_h}{\lambda_D} \right)^2 \Psi^* = -\Upsilon \Psi^*, \quad (2.161)$$

$$\frac{\partial^2 \Psi^*}{\partial z^{*2}} + \frac{\partial^2 \Psi^*}{\partial y^{*2}} = \left( \frac{D_h}{\lambda_D} \right)^2 \Psi^*. \quad (2.162)$$

The dimensionless number

$$\Upsilon = \frac{1}{\zeta^*} \left( \frac{D_h}{\lambda_D} \right)^2 \quad (2.163)$$

describes the relation between the electrokinetic force and the friction force. Using the dimensionless boundary conditions

$$\begin{aligned} \frac{\partial u^*}{\partial z^*} \Big|_{z^*=0} &= 0, & \frac{\partial u^*}{\partial y^*} \Big|_{y^*=0} &= 0 \\ u \Big|_{z^*=W/D_h} &= 0, & u \Big|_{y^*=H/D_h} &= 0 \end{aligned}$$

and solving (2.161) lead to the dimensionless velocity distribution of the electrokinetic flow:

$$\begin{aligned} u^* &= \frac{4\Upsilon D_h^2}{WH} \sum_{n=1}^{\infty} \sum_{m=1}^{\infty} \frac{\cos(\alpha_n z^*) \cos(\beta_m y^*)}{\alpha_n^2 + \beta_m^2} \\ &\times \int_0^{z^*=W/D_h} \int_0^{y^*=H/D_h} \cos(\alpha_n z^*) \cos(\beta_m y^*) \Psi^* dz^* dy^*, \end{aligned} \quad (2.164)$$

where

$$\begin{aligned} \alpha_n &= \frac{(2n-1)\pi D_h}{2W} \quad \text{for } n = 1, 2, 3, \dots \\ \beta_m &= \frac{(2m-1)\pi D_h}{2H} \quad \text{for } m = 1, 2, 3, \dots \end{aligned}$$

The potential distribution:

$$\begin{aligned} \Psi^* &= 4\zeta^* \left\{ \sum_{n=1}^{\infty} \frac{(-1)^{n+1} \cosh \left( \sqrt{1 + \frac{(2n-1)^2 \pi^2 D_h^2}{4(W/\lambda_D)^2} \frac{D_h}{\lambda_D}} y^* \right)}{(2n-1)\pi \cosh \left( \sqrt{1 + \frac{(2n-1)^2 \pi^2 D_h^2}{4(W/\lambda_D)^2} \frac{H}{\lambda_D}} \right)} \cos \left[ \frac{(2n-1)\pi D_h}{2W} z^* \right] \right. \\ &\quad \left. + \frac{(-1)^{n+1} \cosh \left( \sqrt{1 + \frac{(2n-1)^2 \pi^2 D_h^2}{4(H/\lambda_D)^2} \frac{D_h}{\lambda_D}} z^* \right)}{(2n-1)\pi \cosh \left( \sqrt{1 + \frac{(2n-1)^2 \pi^2 D_h^2}{4(H/\lambda_D)^2} \frac{W}{\lambda_D}} \right)} \cos \left[ \frac{(2n-1)\pi D_h}{2H} y^* \right] \right\}, \end{aligned}$$



is obtained by solving the Poisson–Boltzmann equation (2.162) with the boundary conditions

$$\begin{aligned} \frac{\partial \Psi^*}{\partial z^*} \Big|_{x^*=0} &= \frac{\partial \Psi^*}{\partial y^*} \Big|_{y^*=0} \\ \Psi^*(z^*, H/D_h) &= \Psi^*(W/D_h, y^*) = \zeta^*. \end{aligned}$$

### 2.6.1.6 Ohmic Model for Electrolyte Solutions

In this section, a model for electrolyte solutions is derived. This model is useful for formulating mixing problems in an electrokinetic system. The model was formulated by Chen et al. [37], who followed the approach of Levich [38]. We consider here a monovalent binary electrolyte ( $|z_+| = |z_-| = 1$ ), where the subscripts  $+$  and  $-$  denote the cation and anion, respectively. The local charge density and conductivity  $\sigma_{\text{el}}$  are determined as:

$$\begin{aligned} \rho_{\text{el}} &= F(c_+ - c_-) \\ \sigma_{\text{el}} &= F^2(c_+ m_+ + c_- m_-) \end{aligned}$$

where  $F$  is the Faraday constant,  $m$  is the ionic mobility and  $c$  is the concentration. Electroneutrality can be evaluated based on the ratio between the concentration difference of cations and anions and the total concentration of ions.

$$\Theta = F m_+ \frac{\rho_{\text{el}}}{\sigma_{\text{el}}} = \frac{c_+ - c_-}{c_+ + (m_-/m_+)c_-}. \quad (2.165)$$

While the concentration difference contributes to the charge density, the total ion concentration contributes the electrical conductivity. Thus, electroneutrality can be assumed if the above ratio is very small,  $\Theta \ll 1$ . Under electro-neutrality, the concentrations of both ion types are the same  $c_+ = c_- = c$ , which is called the reduced concentration. The conductivity is then:

$$\sigma_{\text{el}} = F^2(m_+ + m_-)c. \quad (2.166)$$

The conservation of species can be formulated for the ions as:

$$\frac{Dc}{Dt} = D\nabla^2 c \quad (2.167)$$

$$\nabla \cdot \mathbf{i} = 0, \quad (2.168)$$

where  $D$  is the effective diffusion coefficient. According to (2.40), the diffusion coefficient of the ion with  $|z_+| = |z_-| = 1$  is:

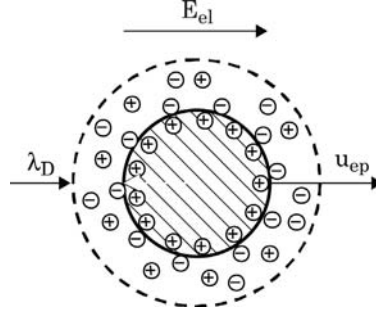


**Figure 2.34** Electrophoretic motion of a positively charged sphere.

$$D = \frac{2D_+D_-}{D_+ + D_-} \quad (2.169)$$

where  $D_+$  and  $D_-$  are the diffusion coefficients of the cations and anions, respectively. Since the convection current is zero ( $\mathbf{i}_C = \rho_{el}\mathbf{E}_{el}$ ) due to electro-neutrality, the electrical current in the electrolyte is caused by electromigration and diffusion:

$$\mathbf{i} = \mathbf{i}_O + \mathbf{i}_D = F^2(m_+ + m_-)c\mathbf{E}_{el} - F(D_+ - D_-)\nabla c, \quad (2.170)$$

where  $\mathbf{E}$  is the electric field strength. Diffusive current  $\mathbf{i}_D$  is usually much smaller than the electromigration current  $\mathbf{i}_O$ , thus  $\mathbf{i}_O = \sigma_{el}\mathbf{E}_{el}$ . The conservation of ionic species and currents can be formulated for the conductivity as:

$$\frac{D\sigma}{Dt} = D\nabla^2\sigma \quad (2.171)$$

$$\nabla \cdot (\sigma_{el}\mathbf{E}_{el}) = 0. \quad (2.172)$$

With Gauss's law  $\nabla(\varepsilon\mathbf{E}_{el}) = \rho_{el}$ , the current continuity equation can be written as:

$$\rho_{el} = -\varepsilon\mathbf{E}_{el} \cdot \nabla\sigma/\sigma \quad (2.173)$$

where  $\varepsilon$  is the permittivity of the liquid.

### 2.6.2 Electrophoresis

Electrophoresis is the motion of a charged particle relative to the surrounding liquid in an electric field, Fig. 2.34. Because of the small size and the low Reynolds number involved, the Stokes model can be assumed for the motion of the particle:

$$q_{\text{surf}} E_{\text{el}} = 6\pi \bar{u}_{\text{ep}} r_{\text{p}}, \quad (2.174)$$

where  $q_{\text{surf}}$ ,  $\bar{u}_{\text{ep}}$ , and  $r_{\text{p}}$  are the surface charge, the particle velocity and the radius of the particle. The charge density on the particle surface is:

$$\frac{q_{\text{surf}}}{A_{\text{surf}}} = -\varepsilon \frac{d\Psi}{dr} \Big|_{r=r_{\text{p}}} = \frac{\varepsilon \zeta}{r_{\text{p}}} \left( 1 + \frac{r_{\text{p}}}{\lambda_{\text{D}}} \right). \quad (2.175)$$

If the radius of the particle is much larger than the Debye length ( $r_{\text{p}}/\lambda_{\text{D}} \gg 1$ ), the surface charge can be calculated as follows:

$$q_{\text{surf}} = 4\pi r_{\text{p}}^2 \frac{\varepsilon \zeta}{r_{\text{p}}} \left( 1 + \frac{r_{\text{p}}}{\lambda_{\text{D}}} \right) = 4\pi \varepsilon r_{\text{p}} \zeta. \quad (2.176)$$

Combining (2.174) and (2.176) results in the velocity of the particle:

$$u_{\text{ep}} = \frac{q_{\text{surf}} E_{\text{el}}}{6\pi \mu r_{\text{p}}} = \frac{2 \varepsilon \zeta E_{\text{el}}}{3 \mu}. \quad (2.177)$$

At a constant dynamic viscosity  $\mu$  and a constant zeta potential  $\zeta$ , the electrophoretic velocity is proportional to the field strength  $E_{\text{el}}$ . The proportionality factor is called the electrophoretic mobility:

$$\mu_{\text{ep}} = \frac{u_{\text{ep}}}{E_{\text{el}}} = \frac{2\varepsilon \zeta}{3\mu}. \quad (2.178)$$

If the particle radius is much smaller than the Debye length ( $r_{\text{p}}/\lambda_{\text{D}} \ll 1$ ), the electrophoretic mobility approaches the electroosmotic mobility along a flat wall:

$$\mu_{\text{ep}} = \frac{u_{\text{ep}}}{E_{\text{el}}} = \frac{\varepsilon \zeta}{\mu}. \quad (2.179)$$

The electrophoretic mobility of a particle can generally be formulated as follows:

$$\mu_{\text{ep}} = \frac{2\varepsilon \zeta}{3\mu} \cdot C(r_{\text{p}}/\lambda_{\text{D}}), \quad (2.180)$$

where the correction factor  $C$  is a function of the ratio  $r_{\text{p}}/\lambda_{\text{D}}$ :

$$C = 1 + \frac{(r_{\text{p}}/\lambda_{\text{D}})^2}{16} - \frac{5(r_{\text{p}}/\lambda_{\text{D}})^3}{48} - \frac{(r_{\text{p}}/\lambda_{\text{D}})^4}{96} + \frac{(r_{\text{p}}/\lambda_{\text{D}})^5}{96} - \left[ \frac{(r_{\text{p}}/\lambda_{\text{D}})^4}{8} - \frac{(r_{\text{p}}/\lambda_{\text{D}})^6}{96} \right] \exp(r_{\text{p}}) \int_{\infty}^{r_{\text{p}}} \frac{\exp(-x)}{x} dx$$

for  $\frac{r_{\text{p}}}{\lambda_{\text{D}}} < 1$  (2.181)

$$C = \frac{3}{2} - \frac{9}{2r_p/\lambda_D} + \frac{75}{2(r_p/\lambda_D)^2} - \frac{330}{(r_p/\lambda_D)^3} \quad \text{for } \frac{r_p}{\lambda_D} < 1.$$

### 2.6.3 Dielectrophoresis

Dielectrophoresis (DEP) is the motion of a dielectric particle in a dielectric fluid. Because the particle is charge neutral, dielectric force is caused by the inhomogeneity of the electric field. Assuming a homogenous linear dielectric fluid with a susceptibility of  $\chi$ , the polarization field  $\mathbf{P}$  of the fluid is given as:

$$\mathbf{P} = \varepsilon_0 \chi \mathbf{E}_{\text{el}}. \quad (2.182)$$

The displacement field  $\mathbf{D}$  of the fluid is:

$$\mathbf{D} = \varepsilon_0 \mathbf{E}_{\text{el}} + \mathbf{P} = \varepsilon_0 \mathbf{E}_{\text{el}} + \varepsilon_0 \chi \mathbf{E}_{\text{el}} = \varepsilon_f \mathbf{E}_{\text{el}} \quad (2.183)$$

where  $\varepsilon_f = \varepsilon_0(1 + \chi)$  is the permittivity of the fluid. The relation between the displacement field and the charge density is:

$$\rho_{\text{el}} = \nabla \cdot \mathbf{D} = \nabla \cdot \varepsilon_f \mathbf{E}_{\text{el}}. \quad (2.184)$$

The dielectric force acting on a dipole moment in an inhomogeneous electric field is:

$$\mathbf{f} = (\mathbf{m} \cdot \nabla) \mathbf{E}_{\text{el}}. \quad (2.185)$$

For a spherical particle with permittivity  $\varepsilon_p$ , the polarization leads to a dipole moment  $\mathbf{m}$ :

$$\mathbf{m} = 4\pi\varepsilon_f \frac{\varepsilon_p - \varepsilon_f}{\varepsilon_p + 2\varepsilon_f} r_p^3 \mathbf{E}_{\text{el}}. \quad (2.186)$$

## 2.7 Magnetic and Electromagnetic Effects

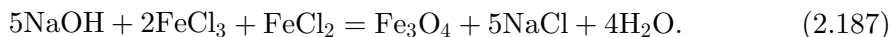
### 2.7.1 Magnetic Effects

Although magnetic forces are bulk forces and therefore do not scale favorably in micromixers, high field gradients can be achieved with integrated microcoils. The use of liquids with magnetic properties and an external actuating magnetic field promises to be a niche for inducing transversal transport and chaotic advection in micromixers. The best candidates for this concept are ferrofluids.

Pure substances such as liquid oxygen also behave like a magnetic liquid or ferrofluid. However, the term ferrofluid is commonly used to mean colloidal ferrofluid. The magnetic property of this fluid is due to ferromagnetic nanoparticles, usually magnetite, hematite, or some other compound containing iron 2+ or 3+. These nanoparticles are solid, single-domain magnetic particles suspended in a carrier fluid. The particles are typically coated with a monolayer of surfactant molecules to avoid them sticking to each other. Because the size of the particles is on the order of nanometers, Brownian motion, which represents the kinetic or thermal energy of the particles, is able to disperse them homogeneously in the carrier fluid. The dispersion is enough so that the solid particles do not agglomerate even under strong magnetic fields. A typical ferrofluid is opaque to visible light. Note that the term magnetorheological fluid (MRF) refers to liquids similar in structure to ferrofluids but different in behavior. MRF particle sizes are of the order of micrometers, that is 1 to 3 orders of magnitude larger than those of ferrofluids. MRFs also have a higher volume fraction, of the order of 20% to 40%. Exposing an MRF to a magnetic field can transform it from a light viscous fluid to a thick solid-like material [39].

Ferromagnetic nanoparticles are fabricated based on size reduction through ball milling, chemical precipitation, and thermophilic iron-reducing bacteria. In ball milling, magnetic material of several micrometers in size such as magnetite powder is mixed with the carrier liquid and the surfactant. The ball milling process takes approximately 1000 hours. Subsequently, the product mixture undergoes centrifugal separation to filter out oversize particles. The purified mixture can be concentrated or diluted into the final ferrofluid.

Synthesis by chemical precipitation is the more common approach, in which the particles precipitate out of solution during chemical processes. A typical reaction for magnetite precipitation is:



The reaction product is subsequently coprecipitated with concentrated ammonium hydroxide,  $\text{NH}_4\text{OH}$ . Next, a peptization process transfers the particles from the water-based phase to an organic phase, such as kerosene with a surfactant such as oleic acid. The oil-based ferrofluid can then be separated by a magnetic field.

Another approach for fabrication of ferrofluids is based upon thermophilic bacteria that reduce amorphous iron oxyhydroxides to nanometer-sized iron oxides. The thermophilic bacteria are able to reduce a number of different metal ions. Thus, this approach allows incorporating other compounds such as Mn (II), Co(II), Ni(III), Cr(III)) into magnetite. Varying the composition of the nanoparticles can change magnetic, electrical, and physical properties of the substituted magnetite and consequently of the ferrofluid. Ferromagnetic particles with extremely low Curie temperatures can be designed with this

method. Most of the particle materials commonly used in ferrofluids have much higher Curie temperatures. The temperature dependency of magnetic properties can be used for micromixing applications.

At the typical channel size of microfluidics (about  $100\ \mu\text{m}$ ), ferrofluid flow in a microchannel can be described as a continuum flow. The governing equations are based on conservation of mass and conservation of momentum. In the case of temperature-dependent magnetic properties, the conservation of energy may be needed for calculating the temperature field. The Navier–Stokes equation for a ferrofluid has the following form:

$$\rho \frac{D\mathbf{v}}{Dt} = -\nabla p + \mu \nabla^2 \mathbf{v} + \rho \mathbf{g} + \mathbf{f}_{\text{mag}}. \quad (2.188)$$

Compared to other types of fluid, ferrofluid flow in microchannel has an additional term for the magnetic force [39]:

$$\mathbf{f}_{\text{mag}} = -\nabla \left[ \mu_0 \int_0^H \left( \frac{\partial \mathbf{M}v}{\partial v} \right)_{H,T} d\mathbf{H} \right] + \mu_0 \mathbf{M} \nabla \mathbf{H} \quad (2.189)$$

where  $\mu_0 = 4\pi \times 10^{-7}\ \text{Hm}^{-1}$  is the permeability of space,  $\mathbf{M}$  is the intensity of magnetization,  $v$  is the specific volume, and  $\mathbf{H}$  is the magnetic field strength in A/m. The magnetic term can be grouped together with the static pressure to form an apparent pressure. Thus the conservation of momentum can be reduced to the conventional Navier–Stokes equation. Because the magnetic force is a bulk force, ferrofluid flow in microchannel should have the same velocity distribution as a pressure-driven flow.

The first term in (2.189) shows that the magnetic force is a bulk force, which is proportional to the volume. According to the scaling law, or the so-called cube-square law, the magnetic force will be dominated by viscous force at the micro scale. However, the second term in (2.189) may have advantages at the microscale due to the high magnetic field gradient that is achievable with integrated microcoils. As mentioned previously, ferrofluids with low Curie temperature are readily available. Magnetization can be adjusted by temperature from room temperature to an acceptably low Curie temperature. The temperature dependency of magnetization can be implemented in the first term of (2.189), the magnetic force then has the form [40]:

$$\mathbf{f}_{\text{magnetic}} = \frac{1}{2} \mu_0 \left( \mathbf{H} \frac{\partial \mathbf{M}}{\partial T} \right) \nabla T + \mu_0 \mathbf{M} \nabla \mathbf{H}. \quad (2.190)$$

It's clear from (2.190), that the high temperature gradient  $\nabla T$  at the microscale can be another advantage for driving ferrofluids in microchannels. Thus besides microcoils, microheaters can be another tool for controlling ferrofluid-based micromixers.

### 2.7.1.1 Electromagnetic Effects

Electromagnetic effects or magnetohydrodynamics (MHD) deal with the behavior of electrically conducting fluids in a magnetic field. A magnetic field induces currents in a moving conductive fluid. A current passing through a conductive fluid can create forces on the fluid and affects the magnetic field. Similar to electrokinetics, MHD effects represent multi-physics problems, which require the coupling of the different fields. MHD effects can be described by the Navier–Stokes equations of fluid dynamics and Maxwell’s equations of electromagnetism.

The Navier–Stokes equation of a MHD flow has the form:

$$\rho \frac{D\mathbf{v}}{Dt} = \mathbf{J} \times \mathbf{B} - \nabla p + \mu \nabla^2 \mathbf{v} \quad (2.191)$$

where  $\mathbf{v}$  is the velocity vector,  $\mathbf{B}$  is the magnetic field of flux density, and  $\mathbf{J}$  is the current density. The term  $\mathbf{J} \times \mathbf{B}$  represents the Lorentz force. The relation between the current density field, the electric field, the velocity field, and the magnetic field is:

$$\mathbf{J} = \sigma(\mathbf{E}_{\text{el}} + \mathbf{v} \times \mathbf{B}) = \sigma(-\nabla\Psi + \mathbf{v} \times \mathbf{B}) \quad (2.192)$$

where  $\mathbf{E}_{\text{el}}$  is the electric field and  $\Psi$  is the electric potential.

## 2.8 Scaling Laws and Fluid Flow at the Micro Scale

The diffusion coefficient  $D$ , the kinematic viscosity  $\nu$ , and the thermal diffusivity  $\alpha = k/\rho c$ —where  $k$ ,  $\rho$ , and  $c$  are thermal conductivity, density, and specific heat, respectively—are transport properties and all have the same unit of  $\text{m}^2/\text{s}$ . The ratios between these properties represent a group of dimensionless numbers characteristic for the ratios between the competing transport processes. These dimensionless numbers help to compare molecular diffusion with other transport processes in microfluidics.

The Schmidt number is the ratio between momentum transport and diffusive mass transport:

$$\text{Sc} = \frac{\text{momentum transport}}{\text{diffusive mass transport}} = \frac{\nu}{D} = \frac{\mu}{\rho D}. \quad (2.193)$$

For most liquids and gases, the Schmidt number is larger than unity,  $\text{Sc} \geq 1$ .

The Lewis number is the ratio between heat transport and diffusive mass transport:

$$\text{Le} = \frac{\text{heat transport}}{\text{diffusive mass transport}} = \frac{\alpha}{D} = \frac{k}{\rho c D}. \quad (2.194)$$

The ratio between advective transport and momentum transport is called the Reynolds number:

$$\text{Re} = \frac{\text{advective mass transport}}{\text{momentum transport}} = \frac{\rho \bar{u} L_{\text{ch}}}{\mu} = \frac{\bar{u} L_{\text{ch}}}{\nu} \quad (2.195)$$

where  $\bar{u}$  is the mean velocity in the flow direction and  $L_{\text{ch}}$  is the characteristic length of the considered channel. In many cases, the hydraulic diameter of the channel is taken as the characteristic length  $L_{\text{ch}}$ . For typical values of  $L_{\text{ch}} = 100 \mu\text{m}$ ,  $\bar{u} = 1 \text{ mm/s}$ ,  $\nu = 10^{-5} \text{ cm}^2/\text{s}$ , the Reynolds number is  $\text{Re} = 0.01$ . This small number typically means that laminar flow exists in almost all microfluidic applications.

The Peclet number is the ratio between advective mass transport and diffusive mass transport:

$$\text{Pe} = \frac{\text{advective mass transport}}{\text{diffusive mass transport}} = \frac{\bar{u} L_{\text{ch}}}{D}. \quad (2.196)$$

The ratio between the Peclet number and the Reynolds number is actually the ratio between momentum transport and diffusive mass transport, i.e. the Schmidt number above. For diffusion coefficients ranging from  $10^{-5} \text{ m}^2 \text{ s}^{-1}$  to  $10^{-7} \text{ cm}^2 \text{ s}^{-1}$ , the Peclet numbers for the typical values in the above example are  $100 < \text{Pe} < 10,000$ . That means advective mass transport dominates over diffusive transport in almost all microfluidic applications.

The average diffusion time  $t$  over the characteristic mixing length  $L_{\text{mixing}}$ , also called the striation thickness, is represented by the Fourier number [7]:

$$\text{Fo} = \frac{Dt_{\text{diff}}}{L_{\text{mixing}}^2}. \quad (2.197)$$

The Fourier number is usually in the range between 0.1 and 1. For a simple T-mixer with two streams in a microchannel of a length  $L_{\text{mixer}}$  and a width of  $W$ , the residence time should be the same as the average diffusion time:

$$t_{\text{res}} = t_{\text{diff}} \quad (2.198)$$

$$\frac{L_{\text{mixer}}}{U} = \frac{\text{Fo} L_{\text{mixing}}^2}{D} = \frac{\text{Fo} W^2}{D}.$$



Thus, the ratio between the channel length and channel width is:

$$\frac{L_{\text{mixer}}}{W} = \text{Fo} \frac{\bar{u}W}{D} = \text{FoPe}_W. \quad (2.199)$$

For the above typical values of Fourier number  $0.1 < \text{Fo} < 1$  and Peclet number based on the channel width  $10 < \text{Pe}_W < 10,000$ , the range of this ratio is  $10 < L_{\text{mixer}}/W < 10,000$ . For some applications, the required mixing channel is unacceptably long.

If the inlets are split and rejoined as  $n$  pairs of solute/solvent streams, the mixing length is reduced to  $L_{\text{mixing}} = W/n$ . The ratio of the required channel length and channel width then becomes:

$$\frac{L_{\text{mixer}}}{W} = \text{Fo} \frac{\bar{u}W}{D} = \frac{1}{n^2} \text{FoPe}_W. \quad (2.200)$$

This concept is called parallel lamination, where the channel length can be reduced by a factor of  $n^2$ .

If the inlets are stretched and folded in  $n$  cycles, the mixing length is reduced to  $L_{\text{mixing}} = W/b^n$ . The base  $b$  depends on the type of the mixer. In case of sequential lamination as discussed in the next section, the base is for instance  $b = 2$ . The base could have a different value in the case of mixing based on chaotic advection. The ratio between the required channel length and the channel width is:

$$\frac{L_{\text{mixer}}}{W} = \frac{1}{b^{2n}} \text{FoPe}_W. \quad (2.201)$$

The above equation reveals that a very compact micromixer can be designed using sequential lamination or chaotic advection.

In general, fast mixing can be achieved with smaller mixing path and larger interfacial area. If the channel geometry is very small, the fluid molecules collide most often with the channel wall and not with other molecules. In this case, the diffusion process is called Knudsen diffusion [7]. The ratio of the distance between molecules to the channel size is characterized by the dimensionless Knudsen number:

$$\text{Kn} = \frac{\lambda}{D_h} \quad (2.202)$$

where  $\lambda$  is the mean free path and  $D_h$  is the hydraulic diameter of the channel structure. The mean free path for gases is given by (see Section 2.1.1):

$$\lambda = \frac{k_B T}{\sqrt{2} \pi \sigma_m^2 p} \quad (2.203)$$

where  $k_B$  is the Boltzmann constant ( $k_B = 1.38066 \times 10^{-23}$  J/K),  $T$  is the absolute temperature,  $p$  is the pressure, and  $\sigma_m$  is the molecular diameter of the diffusing species. The Knudsen number for a liquid is small, because the mean free path of a liquid is on the order of a few ångströms. Thus, Knudsen diffusion may occur only in pores with nanometer sizes. In gases, the mean free path is of the order of a hundred nanometers to several micrometers. For example, under room conditions, the mean free path of hydrogen is  $0.2 \mu\text{m}$ . Knudsen diffusion may occur in microchannels with diameters of the order of a few micrometers.

Among the above dimensionless numbers, the Reynolds number  $Re$  represents the flow behavior in the microchannel, while the Peclet number ( $Pe$ ) represents the ratio between advection and diffusion. Thus, these two numbers are suitable for characterizing the operation point of a micromixer. From the definitions (2.195) and (2.196), the relation between  $Pe$  and  $Re$  is:

$$\frac{Pe}{Re} = \frac{\bar{u} L_{\text{mixing}}/D}{\bar{u} D_h/\nu} = \frac{L_{\text{mixing}}}{D_h} \frac{\nu}{D} = \frac{L_{\text{mixing}}}{D_h} Sc \quad (2.204)$$

where  $\bar{u}$ ,  $D$ ,  $\nu$ , and  $Sc$  are the mean velocity, the diffusion coefficient, the kinematic viscosity and the Schmidt number (2.193), respectively. The hydraulic diameter  $D_h$  and the mixing path  $L_{\text{mixing}}$  are usually on the same order; therefore, we can assume  $L_{\text{mixing}}/D_h \approx 1$ . The kinematic viscosity of liquids and the diffusion coefficient is of the order of  $\nu = 10^{-6}$  m<sup>2</sup>/s, while the diffusion coefficient ranges from  $D = 10^{-9}$  m<sup>2</sup>/s to  $D = 10^{-11}$  m<sup>2</sup>/s. The Schmidt number is about  $10^3 < Sc < 10^5$ . On a  $Pe$ – $Re$  diagram, the area between the two lines  $Pe \approx 1000Re$  and  $Pe \approx 100,000Re$  represents the operation range of micromixers. Operation points of micromixers are expected to be in this area.

In micromixers, the process of mixing and chemical reaction are related. Initially, mixing occurs first and is then followed by the chemical reaction. Subsequently, both mixing and chemical reaction occur in parallel. The ratio between the characteristic mixing time  $t_{\text{mixing}}$  and reaction time  $t_{\text{reaction}}$  is called the Damköhler number:

$$Da = \frac{\text{mixing time}}{\text{reaction time}} = \frac{t_{\text{mixing}}}{t_{\text{reaction}}}. \quad (2.205)$$

A small Damköhler number means reaction is much slower than mixing. Thus, the reaction rate is determined by  $t_{\text{mixing}}$ . A large Damköhler number means reaction is faster than mixing. The extent of mixing determines the rate of reaction.

## References

1. J.C. Hirschfelder, J.C. Gurtiss and R.M. Bird, *Molecular Theory of Gases and Liquids*, Wiley, New York, 1954.

2. R.B. Bird, W.E. Stewart and E.N. Lightfoot, *Transport Phenomena*, 2nd edition, Wiley, New York, 2001.
3. A.L. Garcia, *Numerical Methods for Physics*, 2nd edition, Prentice Hall, Englewood Cliffs, 2000.
4. Z. Wu and N.T. Nguyen, "Convective-diffusive transport in parallel lamination micromixers," *Microfluidics and Nanofluidics*, Vol. 1, pp. 208–217, 2004.
5. W. Bown, "Brownian motion sparks renewed debate," *New Scientist*, Vol. 133, p. 25, 1992.
6. R. Brown, "A brief account of microscopical observations made in the months of June, July and August, 1827, on the Particles contained in the pollen of plants; and on the general existence of active molecules in organic and inorganic bodies," *Philosophy Magazine*, Vol. 4, pp. 161–173, 1828.
7. E.L. Cussler, *Diffusion: Mass Transfer in Fluid Systems*, 2nd edition, Cambridge University Press, 1997.
8. G.I. Taylor, "Diffusion by continuous movements," *Proceedings of the London Mathematical Society*, Vol. A20, p. 196, 1921.
9. A. Einstein, *Investigation on the Theory of Brownian Movement*, Dover, New York, 1956.
10. G.I. Taylor, "Dispersion of soluble matter in solvent flowing slowly through a tube," *Proceedings of the Royal Society A*, Vol. 219, pp. 186–203, 1953.
11. H. Brenner and D.A. Edwards, *Macrotransport Processes*, Butterworth-Heinemann, Boston, 1993.
12. R. Aris, "On the dispersion of a solute in a fluid flowing through a tube," *Proceedings of the Royal Society A*, Vol. 235, pp. 67–77, 1956.
13. R. Aris, "On the dispersion of a solute in a pulsating flow through a tube," *Proceedings of the Royal Society A*, Vol. 259, pp. 370–376, 1960.
14. P. Fife, "Singular perturbation problems whose degenerate forms have many solutions," *Applicable Analysis*, Vol. 1, pp. 331–358, 1972.
15. P. Fife and K. Nicholes, "Dispersion in flow through small tubes," *Proceedings of the Royal Society A*, Vol. 344, pp. 131–145, 1975.
16. W.N. Gill, "A note on the solution of transient dispersion problems," *Proceedings of the Royal Society A*, Vol. 298, pp. 335–339, 1967.
17. W.N. Gill and R. Sankarasubramanian, "A note on the solution of transient dispersion problems," *Proceedings of the Royal Society A*, Vol. 316, pp. 341–350, 1970.
18. T. Yamanaka, "Projection operator theoretical approach to unsteady convective diffusion phenomena," *Journal of Chemical Engineering of Japan*, Vol. 16, pp. 29–35, 1983.
19. S.D. Watt and A.J. Roberts, "The accurate dynamic modelling of contaminant dispersion in channels," *SIAM Journal of Applied Mathematics*, Vol. 55, pp. 1016–1038, 1995.
20. L.E. Johns and A.E. Degance, "Dispersion approximations to the multicomponent convective diffusion equation for chemically active systems," *Chemical Engineering Science*, Vol. 30, pp. 1065–1067, 1975.
21. T. Yamanaka and S. Inui, "Taylor dispersion models involving nonlinear irreversible reactions," *Journal of Chemical Engineering of Japan*, Vol. 27, pp. 434–435, 1994.
22. B.W. Bloechle, On Taylor Dispersion of Reactive Solutes in a Parallel-Plate Fracture-Matrix System, PhD Thesis: University of Colorado, 2001.
23. D. Dutta, A. Ramachandran and D.T. Leighton Jr., "Effect of channel geometry on solute dispersion in pressure-driven microfluidic systems," *Microfluidics and Nanofluidics*, Vol. 2, pp. 275–290, 2006.
24. A. Ajdari, N. Bontoux and H.A. Stone, "Hydrodynamic dispersion in shallow microchannels: the effect of cross-section shape," *Analytical Chemistry*, Vol. 78, pp. 387–392, 2006.
25. H. Aref, "Stirring by chaotic advection," *Journal of Fluid Mechanics*, Vol. 143, pp. 1–21, 1984.
26. S. Wiggins and J.M. Ottino, "Foundations of chaotic mixing," *Proceedings of the Royal Society A*, Vol. 362, pp. 937–970, 2004.

27. E.N. Lorenz, "Deterministic nonperiodic flow," *Journal of the Atmospheric Sciences*, Vol. 20, pp. 130–141, 1963.
28. W.R. Dean, "Note on the motion of a fluid in a curved pipe," *Philosophy Magazine*, Vol. 4, pp. 208–223, 1927.
29. S.A. Berger, L. Talbot and L.S. Yao, "Flow in curved pipes," *Annual Reviews of Fluid Mechanics*, Vol. 15, pp. 461–512, 1983.
30. M.B. Gratton, The Effects of Torsion on Anomalous Diffusion in Helical Pipe, Thesis, Department of Mathematics, Harvey Mudd College, 2002.
31. M. Germano, "On the effect of torsion on helical pipe flow," *Journal of Fluid Mechanics*, Vol. 203, pp. 1–8, 1982.
32. S.W. Jones, O.M. Thomas and H. Aref, "Chaotic advection by laminar flow in a twisted pipe," *Journal of Fluid Mechanics*, Vol. 209, pp. 335–367, 1989.
33. J. Hadamard, "Mouvement permanent lent d'une sphere liquide et visqueuse dans un liquide visqueux," *Comptes Rendus*, Vol. 152, p. 1735, 1911.
34. Z.B. Stone and H.A. Stone, "Imaging and quantifying mixing in a model droplet micromixer," *Physics of Fluids*, Vol. 17, pp. 1–11, 2005.
35. R.O. Grigoriev, M.F. Schatz and V. Sharma, "Chaotic mixing in microdroplets," *Lab Chip*, Vol. 6, pp. 1369–1372, 2006.
36. L.E. Rodd, T.P. Scott, D.V. Boger, J.J. Copper-White and G.H. McKinley, "The inertio-elastic planar entry flow of low-viscosity elastic fluids in micro-fabricated geometries," *Journal of Non-Newtonian Fluid Mechanics*, Vol. 129, pp. 1–22, 2005.
37. C.H. Chen, H. Lin, S.K. Lele and J.G. Santiago, "Convective and absolute electrokinetic instability with conductivity gradients," *Journal of Fluid Mechanics*, Vol. 524, pp. 263–3003, 2005.
38. V.G. Levich, *Physicochemical Hydrodynamics*, Prentice-Hall, Englewood Cliffs, 1962.
39. R.E. Rosenzweig, *Ferrohydrodynamics*, Cambridge University Press, Cambridge, 1985.
40. L.J. Love, J.F. Jansen, T.E. McKnight, Y. Roh and T.J. Phelps, "A magnetocaloric pump for microfluidic applications," *IEEE Transactions on Nanobioscience*, Vol. 3, pp. 101–110, 2004.



## 3 Fabrication Technologies

---

Micromixers can be fabricated using micro technologies that were previously developed for micro electromechanical systems (MEMS). Microdevices have feature sizes ranging from 1  $\mu\text{m}$  to 1 mm. In most cases, these devices are fabricated in a batch process with techniques such as photolithography or imprinting. In the early development stage, most of these devices were fabricated based on established technologies from microelectronics, where thousands of devices can be fabricated on a single silicon wafer. Miniaturization increases the functionality significantly and decreases the fabrication cost. Micromixers can benefit from increasing functionality through the integration of electronic, mechanical, optical, fluidic, and other technologies in a single device. This functionality may lead to new applications especially in the life sciences.

The micromixer is one of many micromachined devices that were reported in the past. With almost 30 years of development, micromachined devices are numerous and cover a wide range of applications. While in the 1980s and early 90s, the development of microdevices was focused on physical sensors such as pressure sensor, accelerometer and gyroscope, recent developments point to research areas such as radio frequency (RF) MEMS, optical MEMS and bioMEMS for biochemical and chemical applications [1]. Most of the microdevices in the past were fabricated either in single crystalline silicon with bulk micromachining or in polycrystalline silicon using surface micromachining. Silicon has the advantages of established technologies coming from the decades-long development of microelectronics. However, silicon has poor mechanical and tribological properties, can not withstand extremely high operation temperature, and in some cases is not bio- nor chemically compatible. The need of other materials with properties suitable for applications in the chemical industry or life sciences lead to the development of micro technologies based on other materials, such as diamond thin film, silicon carbide, polymers, and metals.

### 3.1 Silicon-Based Microtechnologies

The history of silicon-based micromachining dates back to the 1960s, when thin silicon membranes were etched to make pressure sensors. Bulk micromachining subsequently has been used for making inkjet print heads, accelerometers, gyroscopes, and other sensors as well as actuators. Based on CMOS (Complementary Metal-Oxide-Semiconductor) technology, free-standing polysilicon structures were fabricated by etching a sacrificial layer. This technique laid the foundation for the so-called silicon surface micromachining technology, which was widely adopted in the industry for making accelerometers, gyroscopes, and comb-drive actuators. The most famous

applications of surface micromachining technologies are accelerometers made by Analog Devices and digital mirror displays made by Texas Instruments.

### 3.1.1 Basic Technologies

#### 3.1.1.1 Photolithography

The batch fabrication for the majority of micro devices is based on photolithography, a technology adapted from microelectronics. The different lithography techniques are photolithography, electron lithography, X-ray lithography, and ion lithography [2]. Among them photolithography and X-ray lithography for LIGA<sup>1</sup> are the most relevant techniques for the fabrication of micromixers. Since photolithography requires a mask to transfer patterns to a substrate, this technique and almost all other microtechniques are limited to the fabrication of two-dimensional structures. There is little control over the third dimension. The pattern of microstructures is transferred through the mask to a photosensitive emulsion layer called photo resist. The mask is a transparent glass plate. The patterns are made of a metal layer such as chromium to block light. A mask printed on a plastic transparent film by high-resolution laser printer is popular in the microfluidics community due to its low cost and fast prototyping. The relatively large size of microfluidic components, such as micromixers, allows the use of this low-cost mask.

The photolithography process consists of three basic steps: positioning, exposure, and development. In the first step, the mask is positioned laterally on a substrate, such as a silicon wafer. The substrate is coated with a resist, which will carry the pattern after the subsequent exposure step. After lateral positioning, the distance between the mask and substrate is adjusted. The exposure step transfers the pattern on the mask into the photoresist layer. Energy from the exposure source, such as ultraviolet (UV) light or X-rays, changes the properties of exposed photoresist. In the development step, unexposed negative resist is dissolved, while the exposed area remains due to crosslinking. In contrast, exposed positive resist is etched away in the developer solution.

According to the relative position between the mask and the photoresist layer, photolithography is categorized as contact printing, proximity printing, and projection printing. In contact printing and proximity printing, the mask is brought close to the substrate. The resolution  $b$  of proximity printing is determined by the wavelength  $\lambda$  and the distance  $s$  between the mask and the photoresist layer [2]:

$$b = 1.5\sqrt{\lambda s}. \quad (3.1)$$

---

<sup>1</sup>German acronym for “Lithographie, Galvanoformung, Abformung.”

Contact printing and projection printing can reach a resolution, of the order of 1  $\mu\text{m}$ . Due to the gap  $s$ , proximity printing has a lower resolution on the order of several microns.

The resolution of a projection printing system can be estimated as:

$$b = \frac{\lambda}{2\text{NA}} \quad (3.2)$$

where NA is the numerical aperture of the imaging lens system. Most photolithography systems use a mercury lamp as a light source. Mercury lamp wavelengths of the I-line, H-line, G-line, and E-line are 365 nm, 404.7 nm, 435.8 nm, and 546.1 nm, respectively.

Because of its simplicity and fast prototyping capability, photolithography of thick resists is a favored technology for the fabrication of micromixers. Thick resists structured by photolithography can be used as a template for molding polymeric devices or for electroplating metallic parts. For the molding application the resist structure should have a high aspect ratio, which is suitable for making microchannels. The high aspect ratio requires special resists, such as SU-8, or a high-energy beam, such as X-rays. If a conventional UV source is used for the exposure, a thick resist layer may degrade the resolution because the best depth of focus offered by proximity printing is only of the order of 5  $\mu\text{m}$ . For a simple estimation, the resolution is approximately one third of the resist thickness. Fig. 3.1 shows the typical steps for patterning a silicon oxide layer on a silicon substrate using photolithography.

### 3.1.1.2 Chemical Vapor Deposition

The patterns transferred from the glass mask to the photoresist are often further copied to a functional layer by etching. The functional layer is deposited before applying the photoresist. Chemical vapor deposition (CVD) is one of the many techniques for creating material films on a substrate. CVD utilizes chemical reaction between gaseous reactants to form a single solid product. The solid product is formed as a thin film on a heated substrate surface. The other reaction products should be in of gaseous form so that they can leave the reaction chamber. CVD processes are categorized based on reaction conditions. The common processes are atmospheric pressure chemical vapor deposition (APCVD), low-pressure chemical vapor deposition (LPCVD), and plasma-enhanced chemical vapor deposition (PECVD).

APCVD and LPCVD processes require relatively high temperatures ranging from 500  $^{\circ}\text{C}$  to 800  $^{\circ}\text{C}$ . The high process temperatures causes metals with low eutectic temperature with silicon, such as gold (380  $^{\circ}\text{C}$ ) or aluminum (577  $^{\circ}\text{C}$ ) to melt. Thus metals with high eutectic temperatures, such as tungsten, are suitable for deposition before APCVD or LPCVD processes. The alternative for a low-temperature substrate material is PECVD, which only requires



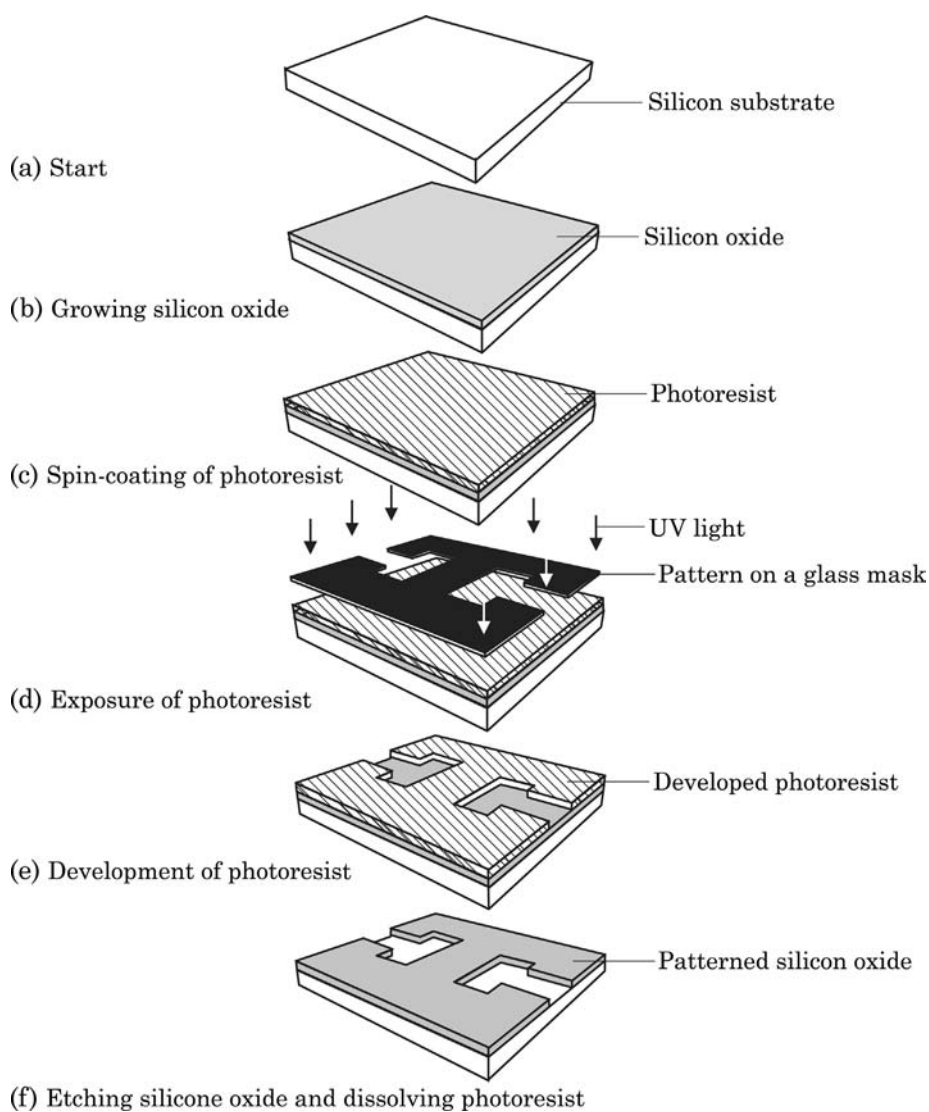


**Figure 3.1** Typical steps of pattern transfer using photolithography.

temperatures typically of the order of 100 °C to 300 °C. Table 3.1 lists common chemical reactions used in CVD of different material films and their corresponding process parameters.

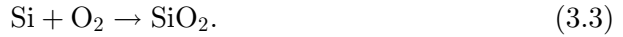
### 3.1.1.3 Thermal Oxidation

Silicon dioxide can be deposited with CVD if the substrate is a material other than silicon. If the substrate is silicon, thermal oxidation is the simplest technique to create a silicon dioxide layer. Based on the type of oxidizer,

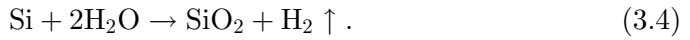
**Table 3.1 Chemical Reactions used in CVD of Different Material Films (after [3])**

Material	Chemical Reactions
Silicon	$\text{SiH}_4 \rightarrow \text{Si} + 2\text{H}_2\uparrow$ $\text{SiH}_2\text{Cl}_2 \rightarrow \text{SiCl}_2 + 2\text{H}_2\uparrow$ $\text{SiCl}_2 + \text{H}_2 \rightarrow \text{Si} + 2\text{HCl}\uparrow$
Polysilicon	$\text{SiH}_4 \xrightarrow{630^\circ\text{C}, 60\text{Pa}} \text{Si} + 2\text{H}_2\uparrow$
Silicon dioxide	$\text{SiH}_4 + \text{O}_2 \xrightarrow{430^\circ\text{C}, 1\text{bar}} \text{SiO}_2 + 2\text{H}_2\uparrow$
	$\text{SiH}_4 + \text{O}_2 \xrightarrow{430^\circ\text{C}, 40\text{Pa}} \text{SiO}_2 + 2\text{H}_2\uparrow$
	$\text{Si}(\text{OC}_2\text{H}_5)_4 \xrightarrow{700^\circ\text{C}, 40\text{Pa}} \text{SiO}_2 + \text{Gas}\uparrow$
	$\text{Si}(\text{OC}_2\text{H}_5)_4 + \text{O}_2 \xrightarrow{400^\circ\text{C}, 0.5\text{bar}} \text{SiO}_2 + \text{Gas}\uparrow$
	$\text{SiH}_2\text{Cl}_2 + 2\text{N}_2\text{O} \xrightarrow{900^\circ\text{C}, 40\text{Pa}} \text{SiO}_2 + \text{Gas}\uparrow$
Silicon nitride	$\text{SiH}_4 + 4\text{N}_2\text{O} \xrightarrow{350^\circ\text{C}, \text{plasma}, 40\text{Pa}} \text{SiO}_2 + \text{Gas}\uparrow$
	$\text{SiH}_2\text{Cl}_2 + 4\text{NH}_3 \xrightarrow{750^\circ\text{C}, 30\text{Pa}} \text{Si}_3\text{N}_4 + \text{Gas}\uparrow$
	$3\text{SiH}_4 + 4\text{NH}_3 \xrightarrow{700^\circ\text{C}, \text{plasma}, 30\text{Pa}} \text{Si}_3\text{N}_4 + \text{Gas}\uparrow$
	$3\text{Si} + 4\text{NH}_3 \xrightarrow{300^\circ\text{C}, \text{plasma}, 30\text{Pa}} \text{Si}_3\text{N}_4 + 6\text{H}_2\uparrow$
Silicide	$4\text{SiH}_4 + 2\text{WF}_6 \xrightarrow{400^\circ\text{C}, 30\text{Pa}} 2\text{WSi}_2 + 12\text{HF}\uparrow + 2\text{H}_2\uparrow$
	$4\text{SiH}_2\text{Cl}_2 + 2\text{TaCl}_5 \xrightarrow{600^\circ\text{C}, 60\text{Pa}} 2\text{TaSi}_2 + 18\text{HCl}\uparrow$
	$2\text{SiH}_4 + \text{TiCl}_4 \xrightarrow{450^\circ\text{C}, \text{plasma}, 30\text{Pa}} 2\text{TiSi}_2 + 4\text{HCl}\uparrow + 2\text{H}_2\uparrow$

thermal oxidation is categorized as dry oxidation or wet oxidation. Dry oxidation utilizes pure oxygen to form silicon oxide at high temperatures from about 800 °C to 1,200 °C:



The oxidant in wet oxidation is water vapor:



Since the thickness of the silicon oxide layer can be controlled in an oxidation process, thermal oxidation can be used for accurately adjusting gaps in microfluidic devices with submicron precision.

#### 3.1.1.4 Physical Vapor Deposition

In contrast to CVD and thermal oxidation, physical vapor deposition (PVD) creates material films on a substrate directly from a solid source. PVD is suitable for the deposition of electrically conducting layers such as metals or

silicides. The technique covers two physically different methods: evaporation and sputtering.

Evaporation deposits a thin film on a substrate by sublimation of a heated source material in a vacuum. According to the different heating techniques, evaporation can be categorized as vacuum thermal evaporation (VTA), electron beam evaporation (EBE), molecular beam epitaxy (MBE), or reactive evaporation (RE). The first two methods are the most common. Resistive heating, laser heating, or magnetic induction are used in VTA. EBE utilizes an electron beam focused on the target. Alloys can be deposited by evaporation using two or more material sources. However, sputtering is more stable than evaporation in the case of alloy deposition.

Sputtering utilizes a strong electromagnetic field to ionize a chemically inert gas, such as argon, and makes it become a plasma. The positively charged argon atoms are accelerated and bombard the target material. The bombardment knocks out target atoms, which are then condensed on the substrate surface as a thin film. Sputtering can deposit all kinds of materials, such as alloys, insulators, or piezoelectric ceramics. Sputtering is less directional than EBE but has higher deposition rates.

#### **3.1.1.5 Spin Coating**

Spin coating is the simplest method for fabricating a film on a substrate. Thin resist layers for photolithography are coated with this technique. The spin coating process starts with the dilution of the material to be deposited in a solvent. The solution is subsequently dispensed on the substrate surface. The wafer is then spun at a high speed. The thickness of the film is determined by the spinning speed, surface tension, and viscosity of the solution. The solvent is removed partly during the spinning process due to evaporation and partly by subsequent baking at an elevated temperature. Spin coating results in a relatively planar surface. This technique is often used for planarization purposes. Spin coating can be used for the deposition of sol-gels. In this process, solid particles of a polymer compound dissolved in a solvent are spin-coated on the substrate surface. The process forms a gelatinous network on the substrate surface. Subsequent removal of the solvent solidifies the gel, resulting in a solid film. This technique can be used for the deposition of various ceramics, such as lead zirconate titanate (PZT). Besides spin coating, dry lamination, dip coating, spray coating, and electrodeposition can be used for transferring a resist layer to the substrate surface.

### **3.1.2 Single-Crystalline Silicon**

Because micromachining technologies have emerged from microelectronics, silicon remains as the most important electrical and mechanical material for microsystems and microfluidics. The technology is established, and single

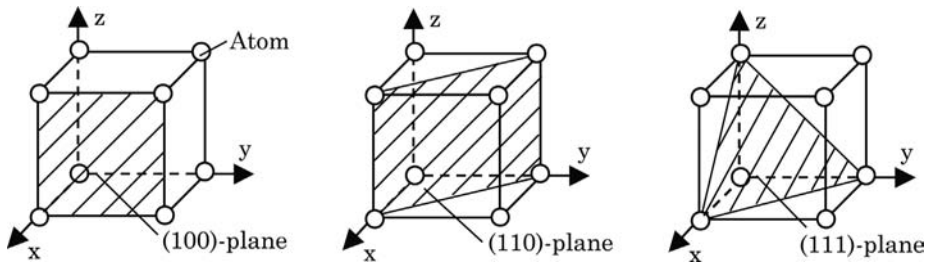


**Figure 3.2** Different crystal planes in a cubic lattice of silicon atoms.

crystalline silicon wafers with high purity are commercially available at a relatively low cost. In the early development, most micromixers were fabricated in silicon. In general, silicon-based technologies are categorized as bulk silicon micromachining and silicon surface micromachining. Bulk micromachining utilizes the single crystalline silicon substrate as the device material. Microchannels are etched directly into the silicon substrate. Surface micromachining can utilize both single-crystalline and polycrystalline silicon as device materials. The single crystalline silicon wafer only acts as a carrier. Surface micromachining based on single-crystalline silicon is also called epi-micromachining or near-surface micromachining.

Single crystalline silicon wafers are classified by the crystalline orientation of their surfaces. The classification is based on the *Miller indices*, which are shown in Fig. 3.2. A direction is described with square brackets, such as  $[100]$ . Because of the symmetry, there are a number of  $[100]$ -directions. A set of equivalent directions is described with angular brackets, such as  $\langle 100 \rangle$ . If this direction is the normal vector of a plane, the plane is denoted with parentheses such as  $(100)$ . The set of equivalent planes is denoted by braces, such as  $\{100\}$ . Single crystalline silicon is mostly fabricated with the *Czocharalski method* (CZ-method). This method starts with a small seed crystal, which determines the orientation of the silicon substrate. The seed crystal is dipped into a highly purified silicon melt and slowly pulled out of the melt while the crucible containing the melt is rotated. Silicon crystals are grown along the selected orientation of the seed to form a rod. The *floating zone method* (FZ-method) is the other method for fabricating silicon crystals. Instead of a silicon melt, a polysilicon rod is used as the starting material. A seed crystal at the end of the rod defines the orientation. The polysilicon rod is locally melted by radio-frequency heating. Crystal growth starts from the end with the seed. After the crystal growth process, the silicon rod is then sawed and polished into wafers.

### 3.1.2.1 Wet Etching

Wet etching refers to an etching process of solid materials in a chemical solution. During such processes, the substrate is dipped in the solution or the

**Table 3.2 Recipes for Isotropic Wet Etching (After [3])**

Material	Etchants	Selective against
Si	HF, HNO <sub>3</sub> , CH <sub>3</sub> COOH	SiO <sub>2</sub>
Si	KOH	SiO <sub>2</sub>
SiO <sub>2</sub>	NH <sub>4</sub> , HF	Si
SiO <sub>2</sub>	HF, NHO <sub>3</sub> , H <sub>2</sub> O	Si
SiO <sub>2</sub>	H <sub>3</sub> PO <sub>4</sub> , NHO <sub>3</sub> , H <sub>2</sub> O	Si
Si <sub>3</sub> N <sub>4</sub>	H <sub>3</sub> PO <sub>4</sub>	SiO <sub>2</sub>
Al	H <sub>3</sub> PO <sub>4</sub> , HNO <sub>3</sub> , H <sub>2</sub> O	SiO <sub>2</sub>

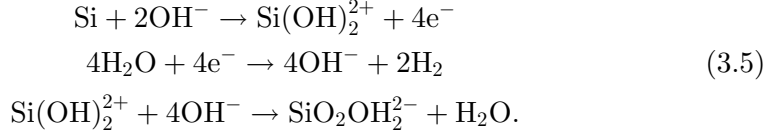
solution is sprayed on the substrate. Wet etching processes are mostly isotropic, independent of crystalline orientation. However, as discussed later in this section, etching of single crystalline silicon in KOH depends on the crystal orientation. For the fabrication of micromixers, wet etching is often used for making the microchannel network.

Isotropic etching has drawbacks in the fabrication of precise lateral structures because of underetching. If the etch solution is well stirred, the isotropic etch front has almost a spherical form. If a microchannel is fabricated with isotropic etching, the channel width also depends on the channel depth and need to be considered in the mask design. The major advantages of wet etching are the high selectivity, a relatively planar etching surface, a high repeatability, and the controllable etch rate. Isotropic wet etching is often used for removing thin layers or thinning a film. Due to possible bubble formation on the etched front, well-stirred etch solution is crucial for the process quality. Isotropic wet etching of silicon can be achieved using a mixture of acids such as hydrofluoric (HF) and nitric acids (HNO<sub>3</sub>). The etching process consists of two steps: oxidation of silicon by nitric acid and dissolution of formed silicon oxide by hydrofluoric acid. The disadvantage of isotropic etching is its poor controllability; very small structures can not be fabricated by this technique. Table 3.2 lists some common recipes for isotropic wet etching.

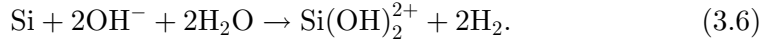
Anisotropic etching of silicon is usually achieved with KOH. The etch rate of KOH in single-crystalline silicon depends on the crystal orientation. The (111) plane of the silicon crystal has a two-orders-of-magnitude slower etch rate than the (100) plane, so single-crystalline structures etched in KOH are defined by the (111)-plane. Because of this fact, the etching process in KOH is also called anisotropic etching. Since this technology is a wet etching process, the equipment is simple and easy to implement. Because KOH is a source of mobile ion contamination, anisotropic etching in KOH is not compatible with standard CMOS processes. The problem of metal ions can be avoided by using a barrier layer or a metal-ion free etchant such as TMAH. While the standard CMOS process allows the fabrication of a number of microsensors, more complex devices can be fabricated by a combination of the standard CMOS process and

an additional micromachining process. The additional process can precede (pre-CMOS), follow (post-CMOS), or lie between the steps (intermediate-CMOS) of the standard CMOS process.

In an anisotropic wet etching process, hydroxides react with silicon in the following steps [9]:



The overall reaction is:



In the steps of (3.5), four electrons are transferred from each silicon atom to the conduction band. The presence of electrons is important for the etching process. Manipulating the availability of electrons makes a controllable etch stop possible. Silicon etchants, which can provide hydroxide groups, are categorized as [9]:

- Alkali hydroxide etchants: KOH, NaOH, CsOH, RbOH, or LiOH;
- Ammonium hydroxide etchants: ammonium hydroxide  $\text{NH}_4\text{OH}$ , tetramethyl ammonium hydroxide (TMAH)  $(\text{CH}_3)_4\text{NOH}$ ;
- Ethylenediamine pyrochatechol (EDP, which is hazardous and causes cancer, and should be accompanied by safety measures): a mixture of ethylenediamine  $\text{NH}_2(\text{CH}_2)_2\text{NH}_2$ , pyrochatechol  $\text{C}_6\text{H}_4(\text{OH})_2$ , and water; and
- Other etchants: hydrazine/water, amine gallate etchants.

Silicon atoms in  $\{111\}$ -planes have stronger binding forces, which make it more difficult to release electrons from this plane. This fact leads to the low etch rates of  $\{111\}$ -planes. Anisotropy or orientation dependency is caused by the different etch rates in different crystal planes. Table 3.3[10,20] compares the most important parameters of common anisotropic etchant solutions. KOH offers the best selectivity between the  $\{100\}$ -plane and the  $\{111\}$ -plane. However, KOH attacks aluminum structures on the wafer. TMAH etches faster in the  $\{111\}$ -plane but does not attack aluminum. All etchants are selective against silicon nitride and silicon dioxide. Thus, these two materials can be used as masks for anisotropic etching processes.

Controlled etch-stop is an important technique for precise fabrication with anisotropic wet etching. Different methods to slow down or eliminate the etch rate are:

- Using selectivity of etchants, coating silicon surfaces with a protective layer such as nitride or oxide;

**Table 3.3 Characteristics of Different Anisotropic Wet Etchants**

Characteristics	KOH	NH <sub>4</sub> OH	TMAH	EDP	Hydrazine
References	[10,13]	[14,15]	[16,17]	[12]	[18,19]
Concentration (weight %)	40–50	1–18	10–40	See <sup>a</sup>	See <sup>b</sup>
Temperature (°C)	80	75–90	90	70–97	100
{111} etch rate (nm/min)	2.5–5	—	20–60	5.7–17	2
{100} etch rate (mm/min)	1–2	0.1–0.5	0.5–1.5	0.2–0.6	2
{110} etch rate (mm/min)	1.5–3	—	0.1	—	—
Si <sub>3</sub> N <sub>4</sub> etch rate (nm/min)	0.23	—	1–10	0.1	—
SiO <sub>2</sub> etch rate (nm/min)	1–10	—	0.05–0.25	0.2	0.17
Al attack	Yes	No	No	Yes	—

<sup>a</sup> 1 L ethylene diamine NH<sub>2</sub>–CH<sub>2</sub>–CH<sub>2</sub>–NH<sub>2</sub>, 160 g pyrocatechol C<sub>6</sub>H<sub>4</sub>(OH)<sub>2</sub>, 6 g pyrazine C<sub>4</sub>H<sub>4</sub>N<sub>2</sub>, 133 mL H<sub>2</sub>O.

<sup>b</sup> 100 mL N<sub>2</sub>H<sub>4</sub>, 100 mL H<sub>2</sub>O (explosive, very dangerous!).

**Table 3.4 Characteristics of Different Anisotropic Wet Etchants**

Parameters	KOH	NaOH	TMAH	EDP
Boron concentration (cm <sup>-3</sup> )	>10 <sup>20</sup>	>3×10 <sup>20</sup>	>10 <sup>20</sup>	>3×10 <sup>19</sup>
Etch rate ratio Si/Si <sup>4+</sup>	20–500	10	40–100	10

- Using orientation dependency of etch rates; and
- By controlled hole generation.

The first method is often used for selective etching with a layer of silicon dioxide and silicon nitride as a mask. By combining multiple silicon/nitride layers, structures with different depths can be realized. Since the etch rate of the {111}-plane is two orders of magnitude slower than those of {110}- and {100}-planes, the etch front stops at the {111}-plane. This unique property can be used to fabricate microchannels with well-defined shapes.

According to (3.5), electrons are essential for a successful wet etching process. Etching away one silicon atom requires four electrons. Holes are generated when electrons are released. The holes attract more hydroxide ions to the substrate surface and speed up the etching process. There are two ways of controlling the availability of holes: via highly boron-doped p-silicon and electrochemical etching with a p-n junction.

Silicon can be doped by a solid or gaseous boron source, where silicon dioxide or silicon nitride may work as a diffusion barrier. The depth of the doped layer depends on the diffusion process and is limited by a maximum value on the order of 15 μm. Table 3.4 compares the etch rate reduction of different etchants in highly boron-doped silicon.

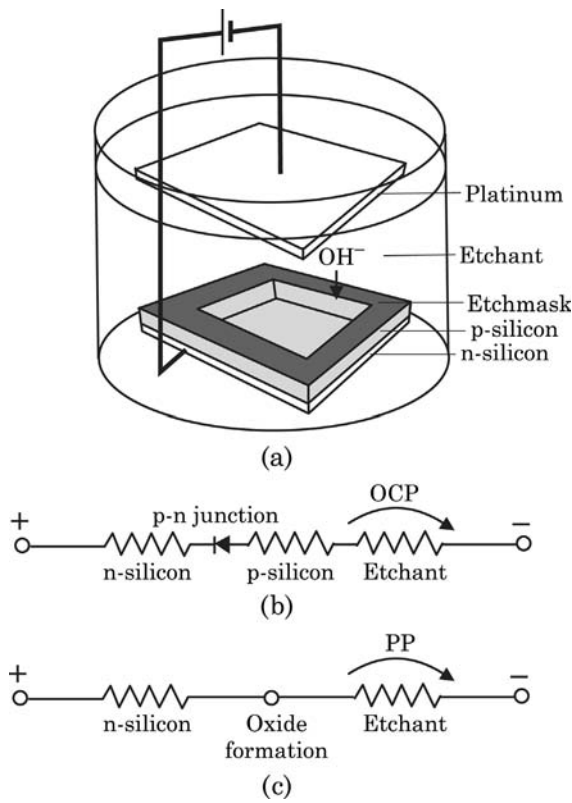


**Figure 3.3** Electrochemical etch-stop: (a) setup; (b) simplified circuit during etching; and (c) simplified circuit at etch-stop.

Etch rates can also be controlled electrochemically. If the silicon surface is biased with a positive potential relative to a platinum electrode, hydroxide ions are attracted to the substrate surface and speed up the etching process [Fig. 3.3 (a)]. There are two potential values critical for the electrochemical etch process: the open circuit potential (OCP) and the passivation potential (PP). Open circuit potential (OCP) is the potential resulting in a zero current. At this potential, no electron supply exists and the etching process works, as in the case without the circuit. OCP is on the order of 1.56 V. Decreasing the potential from OCP increases the current. The current reaches its maximum value and decreases again because of oxide formation, which prevents further etching. The potential at which oxide formation is reached is called the passivation potential. PP is of the order of 1 V.

The above-mentioned electrochemical characteristics can be used for controlling etch-stop with a p-n junction as described in Fig. 3.3 (a). Because the p-n junction is reverse-biased, most of the voltage drops at this junction. Thus, p-silicon is allowed to float at the OCP and is etched away, Fig. 3.3 (b). Etching away p-silicon destroys the p-n junction. The voltage across the two



**Table 3.5 Recipes of Dry Etchant Gases for Thin Films of Functional Materials (After [3])**

Material	Etchant Gases	Selective To
Si	BCl <sub>3</sub> /Cl <sub>2</sub> , BCl <sub>3</sub> /CF <sub>4</sub> , BCl <sub>3</sub> /CHF <sub>3</sub> , Cl <sub>2</sub> /CF <sub>4</sub> , Cl <sub>2</sub> /He, Cl <sub>2</sub> /CHF <sub>3</sub> , HBr, HBr/Cl <sub>2</sub> /He/O <sub>2</sub> , HBr/NF <sub>3</sub> /He/O <sub>2</sub> , HBr/SiF <sub>4</sub> /NF <sub>3</sub> , HCl, CF <sub>4</sub>	SiO <sub>2</sub>
SiO <sub>2</sub>	CF <sub>4</sub> /H <sub>2</sub> , C <sub>2</sub> F <sub>6</sub> , C <sub>3</sub> F <sub>8</sub> , CHF <sub>3</sub> , CHF <sub>3</sub> /O <sub>2</sub> , CHF <sub>3</sub> /CF <sub>4</sub> , (CF <sub>4</sub> /O <sub>2</sub> )	Si (Al)
Si <sub>3</sub> N <sub>4</sub>	CF <sub>4</sub> /H <sub>2</sub> , (CF <sub>4</sub> /CHF <sub>3</sub> /He, CHF <sub>3</sub> , C <sub>2</sub> F <sub>6</sub> )	Si (SiO <sub>2</sub> )
Al	BCl <sub>3</sub> , BCl <sub>3</sub> /Cl <sub>2</sub> , BCl <sub>3</sub> /Cl <sub>2</sub> /He, BCl <sub>3</sub> /Cl <sub>2</sub> /CHF <sub>3</sub> /O <sub>2</sub> , HBr, HBr/Cl <sub>2</sub> , HJ, SiCl <sub>4</sub> , SiCl/Cl <sub>2</sub> , Cl <sub>2</sub> /He	SiO <sub>2</sub>
Organics	O <sub>2</sub> , O <sub>2</sub> /CF <sub>4</sub> , O <sub>2</sub> /SF <sub>6</sub>	—

electrodes drops to the PP. The subsequent formation of silicon oxide on the surface automatically stops the etching process as schematically depicted in Fig. 3.3 (c).

A further approach to generating holes in silicon is photon pumping. Holes are generated in positively biased n-silicon by illumination. This technique was utilized for fabricating high-aspect-ratio structures [22].

### 3.1.2.2 Dry Etching

In dry etching, etchant gases or plasmas remove substrate materials. Generally, dry etching techniques are categorized as physical dry etching, chemical dry etching, and physico-chemical etching.

*Physical dry etching* utilizes the kinetic energy of particle beams, such as an ion beam, electron beam, or photon beam, to attack the substrate surface. The high-energy particles knock out substrate atoms from its surface. The knocked-out material immediately evaporates after leaving the substrate surface. Since no chemical reaction is involved in this process, almost all materials can be removed by this technique. The main drawbacks are slow etch rates, low selectivity, and trench effects caused by reflected ions.

*Chemical dry etching* uses a chemical reaction between etchant gases to attack the substrate material. Gaseous reaction products is a precondition for this etching concept because deposition of solid products will protect the surface and stop the etching process. Chemical dry etching is isotropic and exhibits relatively high selectivity. Etchant gases either can be excited in an RF field to become plasma or react directly with the etched material. Chemical dry etching is often used for cleaning wafers. For instance, photoresist and other organic layers can be removed with an oxygen plasma. Table 3.5 lists some typical recipes for dry etchant gases.

*Physico-chemical etching* is further categorized as reactive ion etching (RIE), anodic plasma etching (APE), magnetically enhanced reactive ion etching

(MERIE), triode reactive ion etching (TRIE), and transmission-coupled plasma etching (TCPE) [3]. RIE is the most important technique for micromachining. Reactant gases are excited to ions. Under low pressures and a strong electrical field, ions are directed to the substrate surface almost perpendicularly. Therefore, this method can achieve relatively high aspect ratios. The etch rates lie between the ranges of physical etching and chemical etching.

Dry etching using plasma is a better process for achieving precisely defined features. However, most conventional plasma-assisted dry etching processes are isotropic, which limits their applications to etching of thin films. The common problem of physico-chemical dry etching (or RIE) used in microelectronics is the trench effect, where etch trenches are not vertical. The trench is wider on the top because the top section of a trench is exposed longer to the etching plasma and ions. The wall should be protected during the dry etching process to keep trench walls parallel and to achieve a high aspect ratio. For microchannels, a special technique called deep reactive ion etching (DRIE) is needed for fabrication of high-aspect-ratio structures. The DRIE process does not depend on crystal orientation of the wafers. Two major approaches to DRIE are:

- Etching assisted by cryogenic cooling;
- Alternate etching and chemical vapor deposition.

In the first approach, the substrate is cooled with liquid nitrogen. The cryogenic temperatures allow reactant gas, such as  $\text{SF}_6$  or  $\text{O}_2$ , to condense on the trench surface. While the condensation film protects the sidewall from etching, it is removed at the bottom by ion bombardment. Because the trench bottom is not protected, it is etched further into the substrate, Fig. 3.4 (a).

The second approach uses chemical vapor deposition to protect sidewalls [23]. This technique was invented and patented by Robert Bosch GmbH in Reutlingen, Germany. Therefore, the technique is often called the Bosch process. The etch cycle consists of two steps: etching and deposition. In the etching step, silicon is removed by  $\text{SF}_6$ . The etching step lasts from 5 to 15 seconds, in which the etch front advances from 25 to 60 nm in silicon. In the deposition step, supply gas is switched to  $\text{C}_4\text{F}_8$ . A film of fluorocarbon polymer of about 10 nm is deposited on the trench wall. In the next cycle, the polymer film at the bottom surface is removed by ion bombardment, while the film at the sidewalls is intact and protects the sidewalls from etching. By this way, the etch front advances into the substrate at rates ranging from 1.5 to 4  $\mu\text{m}/\text{min}$ , Fig. 3.4 (b).

### 3.1.2.3 Bulk Micromachined Microchannels and Nanochannels

Microchannels are the key components of a micromixer. This section illustrates the fabrication of microchannels in bulk silicon and glass using the techniques discussed in the previous sections. Both isotropic and anisotropic etching can be used to fabricate microchannels in bulk materials. A variety of

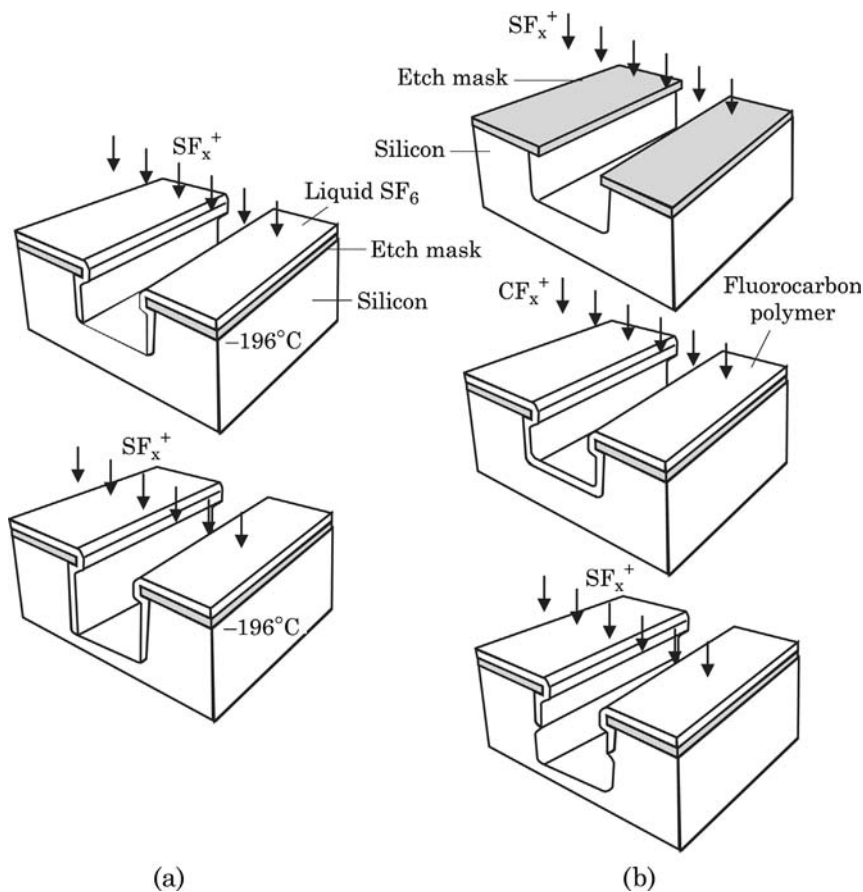


**Figure 3.4** Anisotropic dry etching: (a) cryogenic etching; and (b) alternate etching and deposition.

cross-sectional channel shapes can be achieved by combining the different micromachining techniques discussed previously.

Glass is a familiar material in chemistry and life sciences. Microchannels in glass has been used widely for applications in these fields [24,28]. Glass consists mainly of silicon dioxide and therefore can be etched with the oxide etchants listed in Table 3.2. The microchannels in glass are sealed by thermal bonding to another glass plate. Most glass types can be etched in fluoride-based solutions [25,26]. Photolithography and subsequent etching can be used for photosensitive glasses, such as Foturan, to make microchannels [27].

Isotropic etching in silicon results in semicircular channel shapes similar to those of glass etching. Microchannels with trapezoidal cross sections are formed by anisotropic etching of  $\{100\}$ - [27] or  $\{110\}$ -wafers [28]. Microchannels etched in silicon are sealed either by anodic bonding to a glass wafer or by thermal

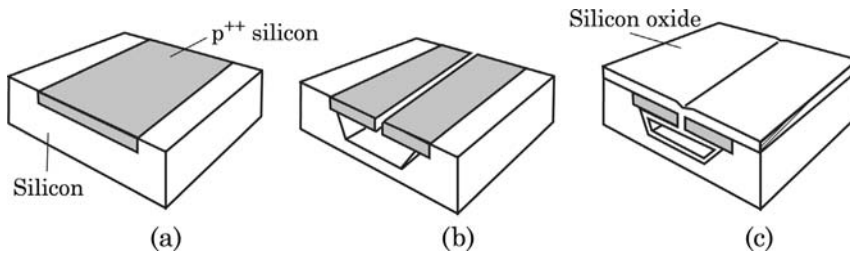


**Figure 3.5** Buried channel with highly boron-doped silicon layer as cover: (a) boron doping; (b) opening etch access, anisotropic wet etching; and (c) deposition of silicon oxide and silicon nitride.

direct bonding to another silicon wafer. A glass cover is ideal for micromixers that need optical access to the flow in the microchannel.

Sealing microchannels with anodic bonding or direct bonding has a drawback of wafer-to-wafer misalignment. Misalignments and voids trapped during bonding processes can change the desired cross-sectional shapes and consequently the function of the intended micromixer. Fabrication of covered channels in a single wafer can overcome the problems associated with misalignment and wafer bonding. Generally, these covered microchannels are fabricated and buried in a single substrate. Sealing is achieved by covering the etch access with a subsequent deposition process.

Fig. 3.5 illustrates the main steps of making a buried channel in a {100}-wafer. The process starts with a highly boron-doped silicon layer with a doping concentration higher than  $7 \times 10^{19} \text{ cm}^{-3}$ , Fig. 3.5 (a). This layer works as an etch stop and masking layer for the subsequent wet etching process. Etch accesses are opened by RIE through the highly boron-doped layer. The buried channel is formed by anisotropic etching. The boron-doped layer remains intact during the etch process, Fig. 3.5 (b). After anisotropic etching, the access gaps are sealed by thermal oxidation, Fig. 3.5 (c). The final deposition of silicon nitride covers the entire structure [29]. The burying depth of the channel described above depends on the thickness of the highly boron-doped layer, which is at most  $5 \mu\text{m}$  due to limits of diffusion processes [29,30]. The process shown in Fig. 3.6 overcomes this problem by using deep trenches etched by DRIE [31,32]. Fig. 3.6 shows the basic steps of this technique. The process starts with DRIE of a narrow trench [Fig. 3.6 (a)]. The depth of this trench defines the burying depth of the channel. In the next step, the trench wall is protected by deposition of silicon nitride or by thermal oxidation [Fig. 3.6 (b)]. The layer at trench bottom is then removed by RIE to create the etch access. Anisotropic or isotropic etching can be used to form the channel [Fig. 3.6 (c)]. After stripping the protecting layer, conformal LPCVD of silicon nitride seals the channel [Fig. 3.6 (d)]. The advantage of this technique is that a network of channels can be fabricated at different depths in bulk silicon. Complicated designs such as a the three-dimensional conduit of a micromixer based on chaotic advection can be fabricated with this technique.

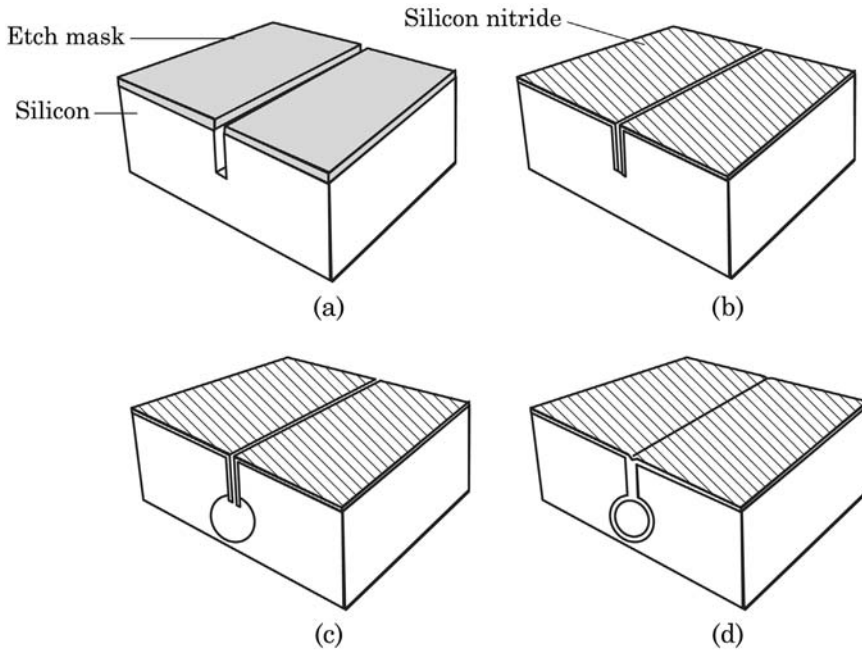


**Figure 3.6** Buried channel with an arbitrary depth: (a) DRIE; (b) deposition of silicon nitride; (c) isotropic etching; and (d) deposition of silicon nitride.

Because of the wavelengths on the order of few hundred nanometers, optical lithography cannot create nanochannels with widths on the order of several tens of nanometers. Interferometric lithography can be used for making structure sizes less than 100 nm. Some other techniques with high-energy beams can also give a higher resolution. Direct writing with scanning electron beam lithography creates structures with 10 nm resolution. However, the throughput of this technique is extremely low due to its serial nature. X-ray lithography can deliver 50 nm resolution, but the facility is expensive and impractical for mass production. Another technique for making nanostructures is called nanoimprint lithography or soft lithography. This technique uses a master, which is fabricated with the more expensive technologies such as electron beam writing. Resist patterns can be transferred by imprinting on a substrate surface. Open nanochannels can be fabricated by subsequent etching processes. The nanochannels are covered with a deposition process.

#### 3.1.2.4 Epi-Micromachining or Near-Surface Micromachining

Epi-micromachining or near-surface micromachining is a technology that allows fabricating microstructures in a thin layer of 2 to 10 micrometers on top of a silicon wafer. The general concept of epi-micromachining is similar to that of polysilicon surface micromachining. Both need a sacrificial layer beneath the

functional layer. After structuring the functional layer and etching away the sacrificial layer, a free-standing component can be released. Thus, having a sacrificial layer and ensuring selectivity against the functional layer are important for epi-micromachining.

### 3.1.3 Polysilicon

#### 3.1.3.1 Polysilicon Surface Micromachining

Polycrystalline silicon is referred to as polysilicon, which is deposited during an LPCVD process with silane. The deposition temperatures range from 575 °C to 650 °C. At temperatures below 575 °C, the silicon layer is amorphous. Above 650 °C, polycrystalline has a columnar structure. The grain size is typically between 0.03 and 0.3  $\mu\text{m}$ . After annealing at 900 °C to 1000 °C for several minutes, crystallization and grain growth occur. The grain size is then on the order of 1  $\mu\text{m}$ . Polysilicon can be doped *in situ* with the same gases used for epitaxial silicon. The deposition rates range from 10 to 20 nm/min [5].

Polysilicon layers are generally conformal. In surface micromachining, polysilicon is used directly as a mechanical material. For fabrication of micromixers, polysilicon can be used for making channel walls and sealing etched channel structures. Devices made of polycrystalline silicon (or polysilicon) are mostly fabricated with the traditional surface micromachining. The term “traditional” is used here because the same fabrication concept with a sacrificial layer has also been used recently for polymer and metallic structures. A surface micromachining process starts with the deposition of a sacrificial layer, Fig. 3.7 (a). The sacrificial layer can be structured to generate anchor points for the later functional structures. Subsequent deposition and patterning of the functional layer defines the microstructures, Fig. 3.7 (b). Removing the underlying sacrificial layer releases the free-standing microstructures, Fig. 3.7 (c).

The main advantage of surface micromachining based on polysilicon is compatibility with CMOS processes. The well established CMOS techniques, such as reactive ion etching (RIE), allow the fabrication of very small structures with sizes of the order of 1  $\mu\text{m}$ . There are a few challenges in polysilicon surface micromachining. First, a very long etching time is required for a flat and large area. Thus designing etch access into the MEMS structure is necessary for reducing the etching time. Since the sacrificial layer (commonly silicon oxide or phosphorous-doped silicon oxide) and the polysilicon layers are deposited under different conditions, it's important to deposit a stress-free polysilicon layer. The stress after deposition can be removed by subsequent annealing up to the temperature where crystallization starts.

The last problem is in the release step. The sacrificial etching process and the subsequent rinsing process are both wet processes. While drying, the liquid bridge between the free-standing structure and the substrate causes it to

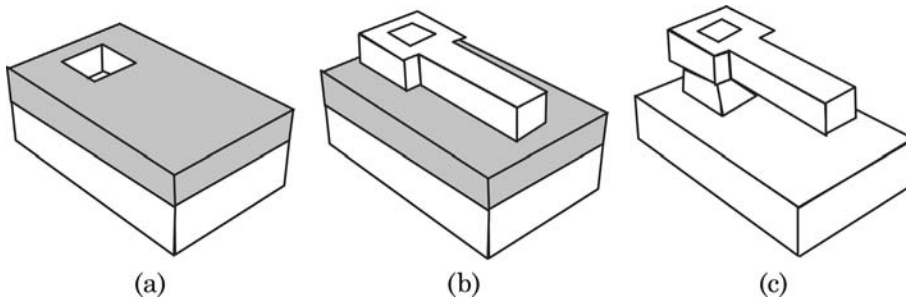


**Figure 3.7** Polysilicon surface micromachining: (a) deposition and patterning of sacrificial layer; (b) deposition and patterning of polysilicon; (c) etching of sacrificial layer.

collapse and stick to the surface. There are several solutions for this problem. Dry etchant, such as vapor phase HF, can be used to avoid the liquid phase. However gaseous HF also attacks silicon nitride. Thus, silicon nitride should not be exposed to HF during the release process. Solvents with lower surface tension, such as methanol, can be used for the rinsing process. Dimples can be introduced in the design to avoid stiction. Alternative drying techniques, such as CO<sub>2</sub> critical drying and freeze drying, can avoid the liquid phase. An organic film can work as a sacrificial layer, which only requires a dry oxygen plasma for removal. And finally, surface modification with a self-assembled monolayer (SAM) can minimize the surface energy and consequently stiction.

### 3.1.3.2 Fabrication of Microchannels with Silicon Surface Micromachining

A general surface micromachining process for microchannels starts with deposition of the sacrificial layer, Fig. 3.8 (a). The channel material is then deposited over the structured sacrificial layer. After opening etch accesses through the channel wall, the sacrificial layer is etched to hollow out the channel. A subsequent deposition of channel material seals the etch access.

Lin et al. reported the fabrication of a microchannel in a microneedle using the above technique [49]. PSG is deposited as the sacrificial layer over a ground silicon nitride layer. The structured sacrificial layer is then encapsulated by LPCVD silicon nitride. Etch access is opened with RIE of the nitride wall. After removing the sacrificial PSG, a second LPCVD process seals the empty channel with silicon nitride. In a similar process, the channel is underetched resulting in a suspended nitride channel [50].

The above approach can be further developed using a silicon substrate directly as the sacrificial material [32]. The mold is fabricated in a handle wafer with bulk micromachining. The channel wall is defined by deposition of nitride/oxide double layer, Fig. 3.8 (b). With silicon dioxide on top, the silicon wafer is bonded anodically to a glass wafer. Etching away the silicon handle wafer

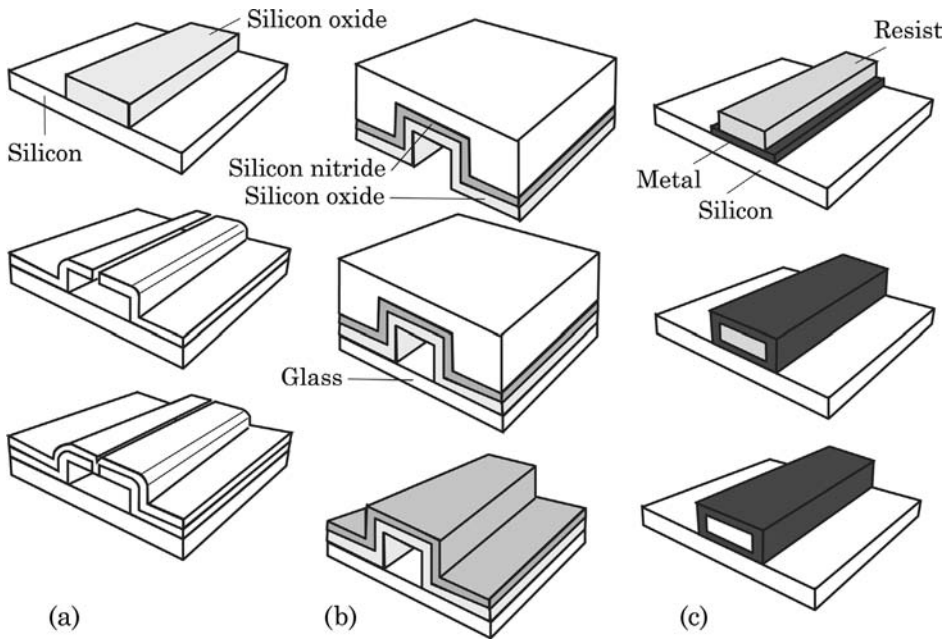


**Figure 3.8** Surface-micromachined channels: (a) polysilicon channel; (b) oxide/nitride channel; and (c) metal channel.

releases the nitride/oxide channel on glass. If the channel wall is too thin for certain applications, the surface of the structure on glass can be coated with a thick polymer layer [51].

Besides the above techniques, microchannels with reasonable heights can be fabricated in metals with the process described in [52]. The process starts with deposition of a metal seed layer on the substrate, Fig. 3.8 (c). A subsequent electroplating process defines the bottom wall of the channel. Next, a thick film photoresist, such as AZ4620, is deposited and developed to form the sacrificial structure for the channel. Gold is then sputtered on the resist structure as the second seed layer. Electroplating on this seed layer forms the side wall and top wall of the channel. Etching the gold layer exposes the sacrificial photoresist. Removing photoresist with acetone creates a hollow metal channel. A similar technique was used in [53] to fabricate more sophisticated microfluidic devices, such as microvalves.

### 3.1.4 Other Materials

#### 3.1.4.1 Diamond Thin Films

Silicon-based devices have poor mechanical and tribological properties. Due to the prominent surface effects, microdevices usually avoid large deflection and



extensive sliding as well as rolling contacts. Compared to silicon, carbon has superior properties. For instance, the coefficient of friction of single-crystal diamond is of the order of 0.01, which makes the wear life of a diamond coated surface 4 orders of magnitude higher than silicon [54]. Diamond film may be a good candidate for making micromixers for extreme conditions. Diamond microstructures can be fabricated using thin film deposition. Diamond thin films made with chemical vapor deposition methods have polycrystalline characteristics and are categorized as microcrystalline diamond (MCD) and ultrananocrystalline diamond (UNCD). The grain sizes of MCD and UNCD are of the order of several micrometers and nanometers, respectively.

The easiest method is to coat a silicon-based component with a thin diamond film. This method utilizes the well established silicon technology but provides components with superb surface properties. Microcomponents can be fabricated based on UNCD by selective deposition and lithographic patterning.

Selective deposition can be achieved by controlling the seeding layer before deposition. The growth of diamond films require a seeding layer, which is formed by exposing the substrate to a suspension of fine diamond particles. The seeding layer can be patterned by:

- Selected seeding with a photoresist mask,
- Using diamond-loaded photoresist and subsequent photolithographic patterning, and
- Selective etching of the seeding layer.

Diamond film can be doped with nitrogen to become electrically conductive. Combining with a sacrificial layer, these technologies allow making diamond-based devices in the same way as polysilicon surface micromachining. Diamond-based technologies also allow the fabrication of basic electronic components, such as diodes and transistors. Electronic components make this technology suitable for more complex diamond-based devices. A recent review of diamond-based semiconductor technology was given by Gurbuz et al. [55].

#### **3.1.4.2 Silicon Carbide**

Silicon carbide SiC poses excellent electrical, mechanical, and chemical properties. Thus, devices based on silicon carbide can be used in harsh environments at high temperature and pressure. Silicon carbide sublimates at around 2000 °C, which is much higher than the melting temperature of silicon (1410 °C). Silicon carbide is therefore suitable for making micromixers, which are used as microreactors with extremely high operation temperatures.

Silicon carbide wafers are commercially available in both single crystalline and polycrystalline forms. However, similar to polysilicon-based and diamond-based MEMS, the growth of a thin silicon carbide film is important for making SiC devices. Epitaxial SiC can be deposited in a CVD process on a SiC wafer or on a silicon wafer with a SiC seeding layer. Micromixers may not need the high

quality of epitaxial SiC, and amorphous and polycrystalline SiC film can be an economical choice for the fabrication. There are a wide range of deposition techniques for polycrystalline and amorphous SiC, such as sputtering, reactive sputtering, reactive evaporation, CVD, LPCVD, APCVD, and PECVD [56].

With the availability of SiC wafer and SiC film, both bulk micromachining and surface micromachining are possible. The extremely high temperature required for etching of SiC makes chemical etching impractical for bulkmicromachining of SiC. The only etching method available for room temperature is photoelectrochemical etching (PEC) of n-type SiC and dark electrochemical etching for p-type SiC [57]. Combining the deposition of thick-film SiC and silicon micromachining, a bulk SiC microcomponent can be fabricated. First, a mold is etched in the silicon substrate using DRIE. Next SiC is deposited to fill the mold. After polishing away excess SiC, the mold is dissolved in a silicon etchant such as KOH, releasing the SiC component [58].

Silicon carbide surface micromachining can be realized with polysilicon as sacrificial layer and RIE for etching the SiC functional layer. Plasma chemistries with fluorinated compounds, such as  $\text{CHF}_3$ ,  $\text{SF}_6$ ,  $\text{CF}_4$ ,  $\text{CBrF}_3$  and  $\text{NF}_3$ , and oxygen, are often used. Due to the high oxygen content, conventional photoresist cannot be used for masking purposes. A hard mask made of a metal, such as Al or Ni, is needed to withstand the oxygen plasma.

For application in life sciences, biocompatibility is an issue for selecting the right material for a micromixer. The biocompatibility of the materials used in silicon-based devices, such as single crystalline silicon, polysilicon, silicon dioxide, silicone nitride and silicon carbide, were evaluated according to ISO 10993 standards by Kotzar et al. [59]. Using mouse fibroblasts in the tests, none of the materials were found to be cytotoxic. An *in vivo* test based on implantation in rabbit muscle showed no sign of irritation. Only silicon nitride and SU-8 showed detectable nonvolatile residues. Further *in vivo* studies using stainless steal cages [60] and Teflon cages [61] revealed that silicon, silicon nitride, silicon dioxide, gold, and SU-8 are biocompatible. However, silicon and SU-8 have shown increased biofouling. For more details on technologies and biocompatibility issues, readers may refer to a recent review by Grayson et al. [62]. The good biocompatibility of devices made with common micromachining technologies allows the exploration of these technologies [63].

## 3.2 Polymeric Microtechnologies

Micromixers based on silicon and other inorganic materials have the drawbacks of higher cost and biocompatibility. For mass production of the relatively large devices for applications in analytical chemistry and biomedical diagnostics, polymers offer a real alternative to silicon-based substrates. Polymers are macromolecular materials, which are formed through polymerization reactions. In a polymerization reaction the monomer units

connect each other either in linear chains or in three-dimensional networks and form a macromolecule. For devices in biomedical applications, materials such as silicone rubber, polycarbonate, and polyimide are inexpensive and disposable [64]. According to the behavior of the interconnects between monomers and subsequent molding behavior, polymers are categorized as thermoplastics, elastomers, and thermosets.

Polymers as functional materials fulfill a number of requirements for devices for chemical and biomedical applications:

- Polymers are suitable for bulk and surface micromachining.
- Many polymers are optically transparent.
- Most polymers are good electrical insulators. They can also be modified to be electrically conductive.
- The surface chemistry of polymers can be easily modified for a particular application.

Shape memory polymers (SMP) are interesting materials with possible applications in active micromixers. Similar to shape memory alloys, SMPs are activated thermally. SMPs have a morphology consisting of a shape-fixing matrix phase and a shape-memorizing dispersed phase. The shape memorizing phase consists of crosslinks that remember the primary shape of the SMP. The polymer can be brought from a primary shape into a secondary shape at a temperature above the transition. The secondary shape is locked by cooling the SMP to below the transition temperature. Heating the SMP above the transition temperature brings it back to the primary shape [65].

The advances in polymeric electronics allow the integration of electronic components into an all-polymeric system. For recent works on polymeric electronics, readers may refer to the recent review by Facchetti et al. [66]. In the bioengineering field, polymeric technologies can provide scaffold structures for growing and harvesting tissues.

### **3.2.1 Thick-Film Polymeric Materials**

#### **3.2.1.1 Polymethylmethacrylate (PMMA) Resist**

Polymethylmethacrylate (PMMA) is well known by a variety of trade names such as Acrylic, Lucite, Oroglass, Perspex, and Plexiglas. PMMA can be used as a substrate material or as a thick-film resist for the LIGA technique [68].

A thick PMMA film can be deposited on a substrate by different methods: multiple spin coating, prefabricated sheets, casting, and plasma polymerization. Multilayer spin coating is achieved with several coating steps. The multiple layers cause high interfacial stresses and lead to cracks. The problem with the cracks can be avoided by using a preformed PMMA sheet, which is bonded to the substrate [69]. Monomer MMA (methylmethacrylate) can be used as the

adhesive material for the bonding process [70]. PMMA can also be polymerized in situ with casting resin [71] or with plasma [72].

Structuring PMMA requires collimated X-rays with wavelengths ranging from 0.2 to 2 nm, which are only available in synchrotron facilities. X-rays also requires special mask substrates such as beryllium and titanium, which further increases the cost of this technique. The beryllium mask with its higher Young's modulus and thickness is optimal for X-ray lithography. The absorbant material of an X-ray mask can be gold, tungsten, or tantalum. The thicker the absorber layer, the stronger the X-ray energy that can be used, and consequently the higher the aspect ratio of the structures in PMMA. The high-energy X-rays break down the polymer chains in the exposed area, which is chemically etched in the development process. The typical developer consists of a mixture of 20 vol% tetrahydro-1,4-oxazine, 5 vol% 2-aminoethanol-1, 60 vol% 2-(2-butoxy-ethoxy) ethanol, and 15 vol% water [73]. The limited access and costs of a synchrotron facility are the main drawbacks of the LIGA technique in general and PMMA as a polymeric structural material in particular. A low-cost alternative to X-ray is direct ablation using a laser. Laser micromachining of PMMA will be discussed later in this chapter. Thick film resist, such as SU-8 and the AZ-4000 series, has the advantage of requiring low-cost UV exposure. However, structure heights and aspect ratios of UV exposure cannot meet those of PMMA with X-ray exposure.

### 3.2.1.2 SU-8 Resist

In contrast to PMMA, a thick SU-8 layer can work with conventional UV light as the exposure source. SU-8 is a negative photoresist based on EPON SU-8 epoxy resin for the near-UV wavelengths from 365 to 436 nm. At these wavelengths the photoresist has very low optical absorption, which makes photolithography of thick films with high aspect ratios possible [75]. Structure heights up to 2 mm with an aspect ratio better than 20 can be achieved with standard lithography equipment [76,77]. Photoresists, such as SU-8, are epoxy resins, which are molecules with one or more epoxy groups. During the curing process, epoxy resins are converted to a thermoset form. SU-8 photoresist consists of three basic components: an epoxy resin, such as EPON SU-8; a solvent, such as gamma-butyrolactone (GBL); and a photoinitiator, such as triarylium-sulfonium salt.

SU-8 photoresists are commercially available with different viscosities. A standard SU-8 process consists of the following steps: spin coating, soft bake, exposure, post exposure bake, developing, and hard bake.

During the spin coating process, the film thickness is determined by the viscosity of the photoresist and the spin speed. Higher viscosity or lower spin speed results in a thicker resist film. After spin coating, the film is soft baked to evaporate the solvent. Soft bake can be carried out on a level hot plate or in a convection oven. Two-step temperature ramping between 65 °C and 95 °C is recommended [78,79]. SU-8 can be exposed with I-line equipment, which uses a

mercury lamp with near-UV wavelengths. Optical absorption of SU-8 increases sharply below 350 nm. Therefore, wavelengths higher than 350 nm should be used for the exposure. The thicker the film, the higher the exposure dose required. The exposed area of SU-8 film is selectively cross-linked by a post-exposure bake. The cross-link process can cause high film stress, which damages the film with cracks. To avoid this problem, a two-step ramp between 65 °C and 95 °C [78,79] or between 50 °C and 100 °C is recommended. Furthermore, rapid cooling after PEB should be avoided. Immersion processes or spray processes can be used to develop the resist. Solvent-based developers, such as ethyl lactate and diacetone alcohol, dissolve areas that are not polymerized during exposure and PEB. If necessary, the developed structure can be hard baked at elevated temperatures from 150 °C to 200 °C. However, hard baking can increase stress and cause cracks in the structures [80]. Removing a polymerized SU-8 film is the most difficult process, because SU-8 film becomes highly cross-linked after exposure and PEB. Etching with acid solutions, RIE, and laser ablation [81] are some of the methods for removing SU-8.

Because of its simple processes and the relatively good mechanical properties, SU-8 is used as the structural material for many microfluidic applications. There are many fabrication examples where SU-8 was used as spacer or directly as channel material.

The simplest technique to form a microchannel with SU-8 is using the cross-linked SU-8 structure to define the channel's sidewall. While the bottom wall is the glass or silicon substrate, the channel can be covered and sealed by another silicon or glass plate. Ayliffe et al. reported a LIGA-like process [82], Fig. 3.9 (a). Starting with a glass wafer as substrate material, a metal seed layer was deposited, Fig. 3.9 (a,1). Subsequently, SU-8 is spin-coated and structured, Fig. 3.9 (a,2). This high-aspect-ratio SU-8 structure is used as a mold for electroplating of gold or other metals, Fig. 3.9 (a,3). In the next step, SU-8 is etched in oxygen plasma using an aluminum mask to form the actual microchannel, Fig. 3.9 (a,4) and (a,5). Finally, a glass plate covers the structure using adhesive bonding.

In the above example, microchannels are etched by oxygen plasma. An alternative is patterning by photolithography and development. Fig. 3.9 (b) shows a fabrication process that uses two SU-8 layers to form a microchannel with a complex cross section [83]. To start with, the first SU-8 layer is coated and exposed with the first mask, Fig. 3.9 (b1). The next layer is spin-coated on top of the first layer, Fig. 3.9 (b2). Since the second exposure may affect the structure defined by the first mask, the mask for the second layer should cover completely the unexposed areas of the first layer to avoid double exposure, Fig. 3.9 (b3). After exposure of the second layer, the two layers are developed together to form the T-shaped microchannel. The channel is then covered by a glass plate, which has a thin unexposed SU-8 layer as the adhesive layer, Fig. 3.9 (b4). This thin adhesive layer is cross-linked by a blanket exposure through the glass plate. To form an optically transparent device, the silicon substrate can be etched away.

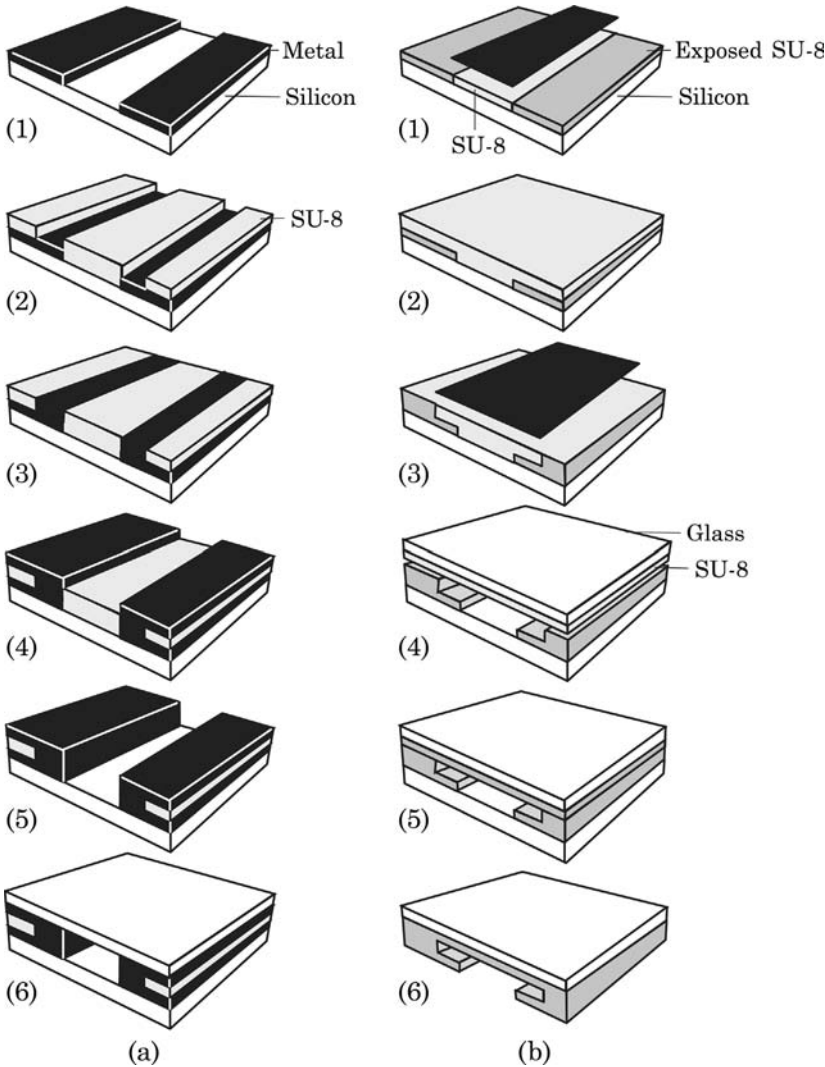


**Figure 3.9** Fabrication of microchannel with SU-8: (a) single layer combined with electroplating (after [81]); and (b) multiple layer (after [82]).

Three-dimensional structures can be constructed by multilayer exposure and embedded mask as shown in Fig. 3.9 (a). As mentioned above, the problem of multi-layer exposure is that the mask of the later layers should cover completely the previous layers to protect their unexposed areas. That means direct fabrication of a closed structure, such as a covered channel, is not possible with conventional glass masks. One solution for the double-exposure problem is the use of an embedded mask [84,85]. The process starts with the exposure of the first SU-8 layer to form the bottom of the channel, Fig. 3.10 (a,1).

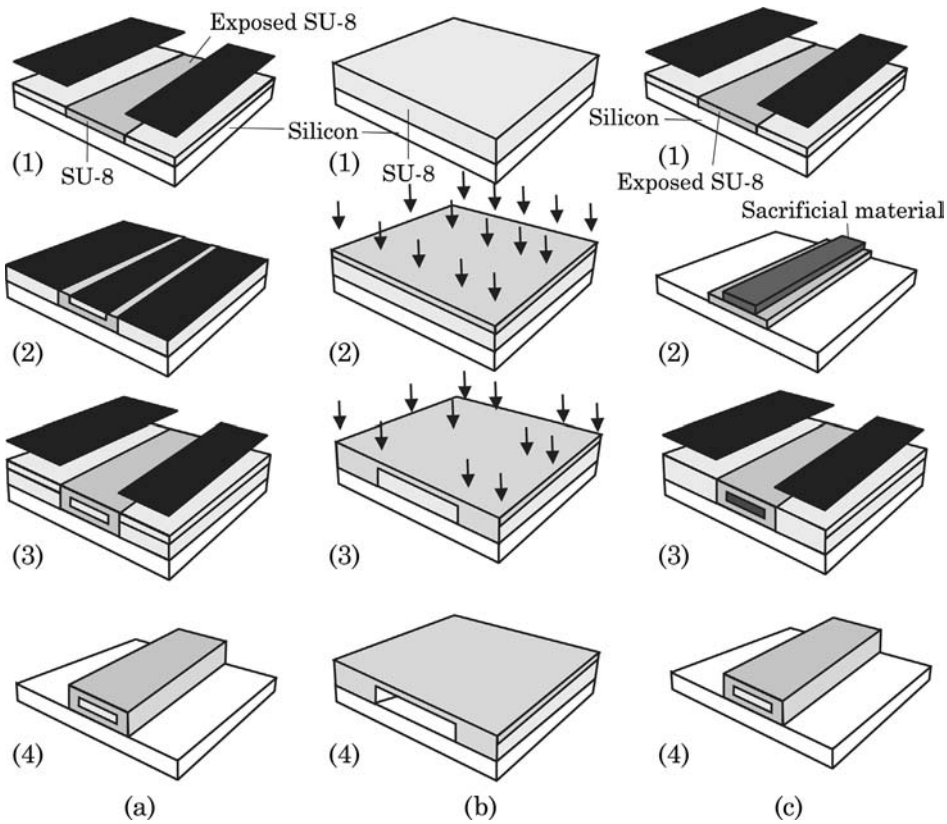


**Figure 3.10** Fabrication of covered channels with SU-8: (a) with embedded mask (after [84]); (b) selective proton writing (after [87]); and (c) with sacrificial layer (after [85]).

After the second layer is coated, the embedded mask is deposited and structured. A thin metal layer, such as gold [84], can be sputtered on the second SU-8 layer. This metal layer is patterned by ordinary photolithography and etching. The patterned metal layer is used as an embedded mask for the subsequent exposure of the second SU-8 layer, Fig. 3.10 (a,2). A third SU-8 layer is spin-coated and exposed to fabricate the top wall of the channel, Fig. 3.10 (a,3). In the final step, all three layers are developed in a single process, resulting in a covered microchannel. The embedded mask is washed away after the developing process, Fig. 3.10 (a,4). Instead of the embedded metal mask, an antireflection film, such as CK-6020L resist (FujiFilm Olin Inc., Japan), can be used for making covered SU-8 microchannels [86]. The use of an antireflection coating ensures that this coating and the structural SU-8 can be developed at the same time.

The penetration depth of a energy beam depends on its intensity and determines the thickness of the cross-linked layer. A covered channel can be fabricated with selective proton writing or proton beam micromachining [87].

Similar to near-UV exposure, a proton beam also causes polymerization of SU-8. The depth of the polymerized area depends on the proton beam energy. This feature is used to form a three-dimensional structure in SU-8. Fig. 3.10 (b) illustrates the relatively simple steps of this technique. To start with, the SU-8 layer is spin-coated on the substrate, Fig. 3.10 (b,1). Writing with low energy forms the top of the channel. With low energy, a proton beam can only penetrate shallowly into the SU-8 layer and forms a thin polymerized layer, Fig. 3.10 (b,2). Next, a proton beam with higher energy polymerizes the sidewalls of the channel. The high energy allows the beam to penetrate through the SU-8 layer down to the substrate surface, Fig. 3.10 (b,3). In the final step, the exposed SU-8 is developed, resulting in a covered microchannel, Fig. 3.10 (b,4).

Another method uses a sacrificial layer [85,86] to fabricate a closed SU-8 channel. The first SU-8 layer is coated, exposed, and developed to form the bottom of the channel, Fig. 3.10 (c1). Subsequently, a sacrificial structure is deposited and patterned, Fig. 3.10 (c2). The sacrificial material can be thermoplastic, wax, epoxy [85], or positive photoresist [87]. Because of the self-planarizing nature of an unexposed SU-8 film, the sidewalls and the channel ceiling are formed with a single coating of a second SU-8 layer, Fig. 3.10 (c3). After developing the second layer, the sacrificial material inside the channel is removed, leaving a closed SU-8 microchannel, Fig. 3.10 (c4).

### 3.2.1.3 Other Thick Film Resists

Another commercially available thick-film resist is AZ4562 (Clariant, Charlotte, North Carolina), which is a positive photoresist. This resist belongs to the Novolak resist system, in common with most commercially available positive resists. Using multilayer spin-coating, thick resist layers up to 100  $\mu\text{m}$  can be achieved. This photoresist has no oxygen sensitivity, but a high resistance to plasma etching, good adhesion properties, and high-resolution capability [88]. AZ4562 is typically used as a mold for subsequent metal electroplating [89,91] or as master templates for micromolding. Table 3.6 gives a summary of the parameters of PMMA, SU-8, and AZ4562.

AZ9260 is the other Novolak photoresist from Clariant, which exhibits a better transparency than AZ4562, and therefore promises a better aspect ratio. Aspect ratios up to 15 are achievable with a film thickness of 100  $\mu\text{m}$  [91]. A theoretical thickness of 150  $\mu\text{m}$  is expected from this photoresist.

Ma-P100 (Microresist Technology, Berlin, Germany) is the other photoresist that can give structure heights up to 100  $\mu\text{m}$ . This photoresist has aspect ratios on the order of 5, poorer than that of the AZ-family [92].

## 3.2.2 Polymeric Bulk Micromachining

In contrast to many other microdevices, micromixers are large, due to their usually long microchannels. The sample volume required for detectability needs



**Table 3.6 Properties of Common Thick Film Resists**

Resist	PMMA	SU-8	AZ4562
Exposure type	X-ray (0.2–2 nm)	UV (365, 405, 435 nm)	UV (365, 405, 435 nm)
Light source	Synchrotron facility	Mercury lamp	Mercury lamp
Mask substrate	Beryllium (100 $\mu\text{m}$ )	Quartz (1.5–3 mm)	Glass (1.5–3 mm)
Mask absorber	Titanium (2 mm)	Glass (1.5–3 mm)	Quartz (1.5–3 mm)
Maximum height	Gold (10–15 $\mu\text{m}$ )	Chromium (0.5 $\mu\text{m}$ )	Chromium (0.5 $\mu\text{m}$ )
Aspect ratio	1,000 $\mu\text{m}$	250 $\mu\text{m}$	100 $\mu\text{m}$
Youngs modulus (GPa)	~500	20–25	~10
Poissons ratio	2–3	4–5	—
Glass transition temperature ( $^{\circ}\text{C}$ )	—	0.22	—
	100	>200	—

relatively large reservoirs. Therefore, the cost of the substrate material plays an important role for large-scale production. For the same surface area and optical transparency, a glass substrate may cost 10 to 100 times more than a polymer substrate. Besides the cost advantage, polymers are available with a wide range of properties. Surface properties of polymers can be tailored for specific applications. As low-cost materials, polymers can be used directly as mechanical materials. Their electrical and chemical properties are interesting for physical, chemical, and biochemical sensing [7]. Polymer membranes and matrices are widely used at the macroscale for the separation of DNA and proteins [8].

Polymers are organic materials consisting of macromolecules, which may have more than 1000 monomeric units. The cross-linking process of the monomers is triggered chemically by an initiator substance, or physically by photons, pressure, or temperature. In a polymerization reaction, monomer units react to form linear chains or three-dimensional networks of polymer chains. If only one type of polymer is used, the material is called *homopolymer*. Polymerization of two or more monomer units results in a *copolymer*. Polymers containing specific additives are called *plastics*. Polymers exist in two basic forms: amorphous and microcrystalline. The macromolecules in a polymeric material have different lengths. Thus, there is no fixed melting temperature for polymers. Several temperatures exist in the melting process of a polymeric material. The characteristic lower and upper temperatures of a polymeric material are the *glass transition temperature* and the *decomposition temperature*. At the glass transition temperature, the material still keeps its solid shape but loses its cross-linking strength. Increasing the temperature further damages the bonds between the monomers, and the plastic will lose its

solid shape. Above the glass transition temperature, a polymeric material becomes soft and can be machined by molding or hot embossing. The glass transition temperature can be adjusted by mixing a softener with the original polymeric material. Above the decomposition temperature, the polymeric material starts to degrade and ceases to function.

Based on their molding behavior, polymers can be categorized into three groups: elastomeric materials, duroplastic materials, and thermoplastic materials. *Elastomeric materials* or elastomers have weakly cross-linked polymer chains. These polymer chains can be stretched under external stress, but regain their original state if the stress is removed. Elastomeric polymers do not melt before reaching decomposition temperature. Elastomeric materials are suitable for prototyping of microfluidic devices. The elastic property is ideal for sealing of the fluidic interfaces. In contrast to elastomeric materials, *duroplastic materials* or duroplastics have strong cross-linked polymer chains. Duroplastics do not soften much before the decomposition temperature. They are strong and brittle. The properties of *thermoplastic materials* are ranked between the above two extremes. The material consists of weakly linked polymer chains. Thus, thermoplastics can be softened and structured at temperatures between the glass transition point and the decomposition point. Due to this characteristic, thermoplastic polymers are commonly used for micromolding.

Most micromixers used for chemical analysis and the life sciences require an optically transparent material. Many polymers are self-fluorescent at low excitation wavelengths. Self-fluorescence may affect the sensitivity of microfluidic applications with fluorescent detection. The next drawback of polymers is their poor chemical resistance to solvents. With applications in the chemical industry and drug discovery, micromixers may need to handle a variety of solvents. In this case, glass and silicon are the materials of choice. Polymers are usually not the materials of great endurance. For long-term applications, aging, low chemical resistance, and low UV resistance will be the main problems of using polymers as substrate material.

Surface properties play an important role for devices utilizing electroosmotic pumping. A high charge density on the surface assures a stable and controllable electroosmotic flow. Furthermore, a surface with patterned zeta potential is vital for designing electrokinetic micromixers based on chaotic advection. Due to the lack of ionizable groups, most polymers have a low surface charge density compared to glass. Thus, for applications with electroosmotic flows such as CE separation, the surface of the polymeric substrate should be treated accordingly.

The major advantage of polymeric micromixers compared to silicon-based or glass-based counterparts is their superior biocompatibility. Polymeric devices are best for DNA analysis, polymerase chain reactions, cell handling, and clinical diagnostics. Many polymers are compatible with blood and tissue. Micromachining of these materials may make implantable microfluidic devices for applications such as drug delivery possible. Table 3.7 lists the properties of some typical polymers.

Table 3.7 Properties of Common Polymers for Bulk Micromachining

Materials	$T_g$ (°C)	$\rho$ (kg/m <sup>3</sup> )	$\kappa$ (W/K-m)	$\gamma \times 10^{-6}$ K <sup>-1</sup>
Parylene-N	410	1,100	0.13	69
Parylene-C	290	1,290	0.08	35
Parylene-D	380	1,418	—	30–80
Polyamide 6 (PA 6)	60	1,130	0.29	80
Polyamide 66 (PA 66)	70	1,140	0.23	80
Polycarbonate (PC)	150	1,200	0.21	65
Polymethylmethacrylate (PMMA)	106	1,180–1,190	0.186	70–90
Polyimide	—	1,420	0.10–0.35	30–60
Polystyrene (PS)	80–100	1,050	0.18	70

( $T_g$ : Glass Transition Temperature,  $\rho$ : Density,  $\kappa$ : Thermal Conductivity,  $\gamma$ : Thermal Expansion Coefficient)

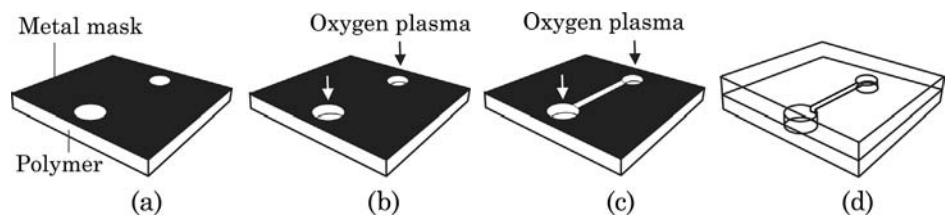


**Figure 3.11** Fabrication of a microchannel with fluidic access holes: (a) Patterning the metal masks for the access holes; (b) etching of access holes; (c) patterning the mask for the microchannel and etching until the access holes are opened; (d) etching away the mask.

There are two key approaches in polymeric bulk micromachining: dry etching with oxygen plasma and replication. Similar to silicon-based bulk micromachining, polymeric bulk micromachining uses photolithography and etching to transfer a pattern into the bulk substrate. Oxygen plasma can be used for etching polymers and other organic materials. Because photo resists are organic, a hard mask made of metals such as aluminum, nickel, or titanium should be used here. Fig. 3.11 shows an example of the fabrication of a microchannel with two access holes in a bulk polymeric material. To start with, a metal layer is deposited on the polymer surface. Sputtering is preferred because a low temperature is required for processing polymers. The metal layer is patterned and structured using conventional lithography and etching techniques, Fig. 3.11 (a). The two access holes are first etched with oxygen plasma, Fig. 3.11 (b). The metal layers are then etched to form the mask for the microchannel. Access holes and the microchannel are etched until the areas of the access holes are opened on the back side of the substrate, Fig. 3.11 (c). Finally, the mask is etched away and the microchannel can be sealed by thermal bonding to another polymer sheet, Fig. 3.11 (d).

The basic idea behind replication technologies is the combination of the more expensive silicon-based technology and the low-cost replication in polymers. The few drawbacks of replication technologies are:

- Since the master is to be removed from the molded structures, free standing structures with undercuts can not be fabricated. A combination with polymeric surface micromachining could be a solution for this problem.
- Only a few micromachining technologies can meet the required smoothness of the master mold.
- Due to contamination and fast diffusion at the micro scale, release agents used at the macro scale can not be used for the release process at the micro scale.

The mold can be fabricated in silicon with the established micromachining techniques. Conventional machining techniques such as drilling, cutting, milling, and turning can be used for structures down to several tens of microns. Bulk silicon micromachining can be used for structures with high aspect ratios. Metal mold can be electroplated with the help of a structured thick resists such as SU-8 and PMMA. For instance, the fabrication of nickel molds from structured PMMA was established and called LIGA (Lithographie-Galvanoformung-Abformung, German acronym for lithography, electroplating, and molding). In the following, three replication techniques are discussed in details: injection molding, hot embossing, and soft lithography.

### 3.2.2.1 Injection Molding

Injection molding is carried out at temperatures above the glass transition temperatures of amorphous thermoplastics such as polymethylmethacrylate (PMMA), polycarbonate (PC), and polysulfone (PSU). For semicrystalline thermoplastics, such as polyoxymethylene (POM) and polyamide (PA), the molding temperature should be higher than the crystallite melting point [105]. Table 3.8 compares the characteristics of different polymers commonly used for micromolding.

Mold inserts for injection molding can be fabricated with common microtechnologies such as bulk micromachining and LIGA. Alternatively, bulk-micromachined parts can be used as masters for electroplating [106]. After separation from the silicon part, the metal parts can be used as negative mold inserts to fabricate replicas of the silicon parts [106]. Structures in micromixers may have high-aspect ratios and very small filling channels. Together with the high viscosity of melted plastics, high pressures are required for the injection. To avoid the high pressure associated with the high viscosity, reaction injection molding (RIM) can be used. This technique involves mixing of two or more reactive chemicals. The mixture flows into the mold at relatively low temperature, pressure, and viscosity. Curing occurs in the mold at relatively

**Table 3.8 Typical Characteristics of Different Polymers for Micromolding (After [108,109])**

Polymers	PMMA	PC	PS	COC	PP
Heat resistance /°C	105	140	100	130	110
Density kg/m <sup>-3</sup>	1,190	1,200	1,050	1,020	900
Refractive index	1.42	1.58	1.59	1.53	opaque
<i>Resistant to:</i>					
Aqueous solutions	yes	limited	yes	yes	yes
Concentrated acids	no	no	yes	yes	yes
Polar hydrocarbons	no	limited	limited	yes	yes
Hydrocarbons	yes	yes	no	no	no
Suitable for micromolding	moderate	good	good	good	moderate
<i>Permeability</i>					
<i>coefficients /10<sup>-17</sup> m<sup>2</sup>s<sup>-1</sup>Pa<sup>-1</sup>:</i>					
He	5.2	7.5	—	—	—
O <sub>2</sub>	0.12	1.1	—	—	—
H <sub>2</sub> O	480–1,900	720–1,050	—	—	—
<i>Hot-embossing parameters:</i>					
Embossing temperature /°C	120–130	160–175	—	—	—
Debossing temperature /°C	95	135	—	—	—
Embossing pressure (bars)	25–37	25–37	—	—	—
Hold time /s	30–60	30–60	—	—	—

low temperatures and pressures. The excess prepolymers are fed back in a recirculation loop by pumps. The entire process, from mixing to demolding, typically takes less than one minute. The low processing viscosity allows good filling and high molding accuracy.

Fig. 3.12 shows the schematics of a typical injection molding system. The machine consists of a screw, an injection nozzle, a heater, and a mold insert. To start with, polymer pellets are loaded into the screw. The piston pumps the polymer into the accumulation zone, where it is melted by a heater. If the desired polymer amount is reached, the piston moves forward and pushes the polymeric melt into the mold cavity through the nozzle. The required pressure is typically on the order of 500 to 2,000 bars [108,109]. After cooling, the melt solidifies, and can be taken out from the mold.

### 3.2.2.2 Hot Embossing

Hot embossing was widely used for the fabrication of simple microchannels. The technique uses a master mold and a flat polymer substrate. The polymer substrate is heated above the glass transition temperature of the substrate material. The glass temperature is typically in the range from 50 °C to 150 °C. Embossing force (0.5 to 2 kN/cm<sup>2</sup>) is then applied on the substrate under vacuum conditions. Before release, the master and the substrate are cooled

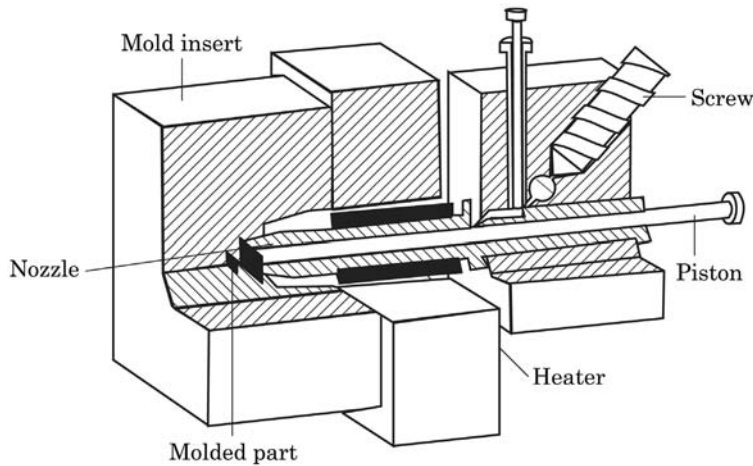


**Figure 3.12** Micro injection molding system.

under the applied embossing force. The entire hot-embossing process takes few minutes [110–112]. The vacuum is needed due to the formation of gas bubbles in the small structures. The vacuum also prevents corrosion of the master. The drawback of this technique compared to injection molding is the relatively long cycle time, of the order of several minutes.

The most important parameters of hot embossing are embossing temperature, deembossing temperature, embossing pressure, and hold time. Table 3.8 lists the typical values of these parameters for hot embossing of PMMA and PC. Hot embossing can only make open channel structures. Fabricating covered channels and fluidic interconnects need additional packaging techniques, such as thermal bonding to a sheet of the same material at temperatures above the glass temperature.

Injection compression molding combines the advantages of both injection and hot embossing. The polymer melt is first injected into the mold. The mold melt is then compressed to shape the final part. The low viscosity of the melt results in good filling in the molded part.

### 3.2.2.3 Soft Lithography

Soft lithography is a direct pattern transfer technique. The term “soft” refers to an elastomeric stamp with patterned relief structures on its surface. Polydimethylsiloxane (PDMS) has been used successfully as the elastomeric material. PDMS exhibits unique properties suitable for this purpose. PDMS has an inorganic siloxane backbone with organic methyl groups attached to silicon (see Fig. 3.13). Both prepolymers and curing agents are commercially available. PDMS has high optical transparency above a wavelength of 230 nm and low self-fluorescence. PDMS has a low interfacial free energy, which avoids

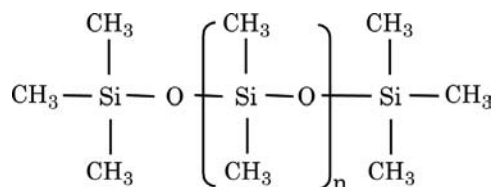


**Figure 3.13** Chemical structures of PDMS.

molecules of most other polymers sticking on or reacting with its surface. The interfacial free energy of PDMS can be manipulated with plasma treatment. The modified surface properties of PDMS are needed for certain applications. PDMS is stable against humidity and temperature. This material is optically transparent and can be cured by UV light. PDMS is an elastomer and can therefore be attached on nonplanar surfaces. PDMS is mechanically durable. These characteristics make PDMS an ideal material for soft lithography [113].

PDMS also has a number of drawbacks, such as swelling, shrinking, and elastic deformation. The design of a PDMS part should consider the shrinking effect upon curing. A number of organic solvents can swell PDMS as well. Furthermore, elastic deformation can limit the aspect ratio of the designed structure. A too-high aspect ratio leads to the pairing effect, in which two parallel structures attach to each other. An aspect ratio that is too low leads to sagging of noncontact regions, which makes further steps of soft lithography impossible. The recommended aspect ratios for PDMS structures are between 0.2 and 2 [113].

There are different techniques to transfer the pattern on the elastomeric stamp: microcontact printing and replica micromolding [113]. In many applications, the elastomeric PDMS part can be used directly as a microfluidic device with microchannels on it. Soft lithography is based on an elastomeric stamp with patterned relief structures on its surface. There are two basic techniques for transferring the micro patterns: micro contact printing and replica molding. In many polymeric devices, the elastomeric part can be used directly as the functional material. The fabrication process starts with the fabrication of a master using established technologies such as DRIE in silicon or photolithography of a thick resist film such as SU-8. Polydimethylsiloxane (PDMS) is mixed from two prepolymers. The weight ratio of the base and the curing agent could be 10:1 or 5:1. Next, the PDMS mixture is poured into the master. PDMS is then cured at a relatively low temperature from 60 °C to 80 °C for several hours. After peeling off and having surface treatment with low-temperature oxygen plasma, the structured PDMS membrane can be brought into contact with clean glass, silica, or another piece of surface-activated PDMS. The bond can withstand pressures up to five bars. Three-dimensional structures can be formed by lamination of many PDMS sheets. In this case, methanol helps to promote both bonding and self-alignment. The surface tension at superimposed holes in the PDMS sheets self-aligns them.

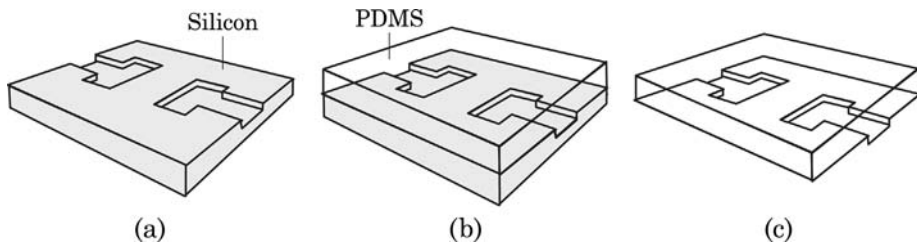


**Figure 3.14** Fabrication of PDMS stamps: (a) DRIE of silicon master; (b) coating; and (c) release.

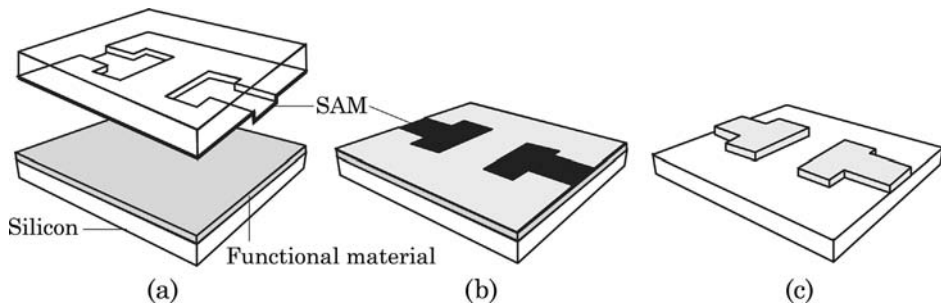


**Figure 3.15** Microcontact printing with PDMS stamps: (a) immersion; (b) stamping; and (c) etching.

Methanol prevents instant bonding between two PDMS sheets after plasma treatment. After evaporating the methanol on a hot plate, the laminated stack is bonded.

The master for a PDMS device can be fabricated with conventional silicon-based micromachining technologies. Fig. 3.14 depicts the basic steps of the fabrication of a PDMS part. The silicon master is silanized by exposure to the vapor of  $\text{CF}_3(\text{CF}_2)_6(\text{CH}_2)_2\text{SiCl}_3$  for about 30 minutes [112]. The prepolymer is coated on the silicon or glass master. After curing at an elevated temperature, the cured PDMS layer can be peeled off and is ready for use in the subsequent steps.

The master can also be fabricated with SU-8 [114]. The PDMS part is used directly as structural material. The PDMS device is bonded to a glass plate after oxidizing the surfaces with oxygen plasma. In a similar approach, three-dimensional structures are fabricated by the lamination of different structured PDMS layers. Fluidic interconnects are embedded directly in the PDMS device.

*Microcontact printing* utilizes the relief structures on the surface of the PDMS stamp to transfer a pattern of SAMs to the substrate surface by contact, Fig. 3.15 (a). SAMs can be created by immersion of the substrate in a solution containing a ligand  $\text{Y}(\text{CH}_2)_n\text{X}$ , where X is the head group and Y is the anchoring group. The head group determines the surface property of the monolayer. The stamp is wetted with the above solution and pressed on the



substrate surface, Fig. 3.15 (b). Usually the SAM layer is too thin for some applications. Thus, SAM can be used as a mask to transfer the pattern to an underlying functional layer. Because of its small thickness, SAM can be quickly destroyed by ion bombardment. Therefore, a SAM mask is not suitable for reactive ion etching, but for wet chemical etching, Fig. 3.15 (c). The thicker functional layer, in turn, can be used as a mask for the more aggressive RIE. The resolution of microcontact printing depends on the properties of the stamp material, and can reach several tens of nanometers.

Surface properties of patterned SAMs make them usable as templates for selective deposition of other materials. For example, a patterned hydrophilic SAM traps liquid prepolymer on its surface. After curing, a polymer structure is formed on top of the patterned SAM. Furthermore, patterned SAMs can be used for controlled deposition of metals and ceramics by selective CVD.

*Micromolding* with a PDMS master can be categorized as: replica molding, microtransfer molding, micromolding in capillaries, and solvent-assisted micromolding [113]. *Replica molding* uses the PDMS stamp as a replica master for a prepolymer, which is cured by UV exposure or by elevated temperature. This technique can achieve resolutions of less than 10 nm. In *microtransfer molding*, liquid prepolymer is applied on the PDMS master. The prepolymer layer is planarized by removing the excess prepolymer. Only prepolymer trapped between the relief structures remains on the surface of the PDMS master. The master is then placed on a planar substrate. UV exposure or heating solidifies the prepolymer. Peeling off the elastic PDMS master results in polymer structures on the substrate surface. This method does not remove completely the excess prepolymer on top of the PDMS stamp. A thin polymer layer of the order of 100 nm remains on the substrate surface. If the patterned polymer is to be used as a mask for subsequent etching, this thin polymer layer should be removed by oxygen plasma [113]. *Micromolding in capillaries* uses capillary forces to fill the gaps between the substrate and the PDMS master. First, the PDMS master is pressed tightly on a planar substrate. Elastic PDMS seals off walls and creates capillary channels. A drop of liquid prepolymer is placed at the ends of these channels and fills them automatically due to capillary forces. After curing and peeling off the PDMS master, polymer structures remain on the substrate surface. This technique can be used to pattern silicon and glass with different materials [113]. *Solvent-assisted micromolding* uses a solvent to wet the PDMS stamp and soften the structural polymer. The solvent only dissolves the structural polymer and not PDMS. The stamp is pressed on a polymer film, which dissolves in the solvent and fills the gaps between relief structures of the stamp. After dissipation and evaporation of the solvent, solid polymer remains on the substrate [113].

#### 3.2.2.4 Fast Prototyping of Micromixers with Soft Lithography

Soft lithography is a popular method for rapid prototyping of microfluidic devices. The majority of reported lab-scale prototypes were fabricated with this

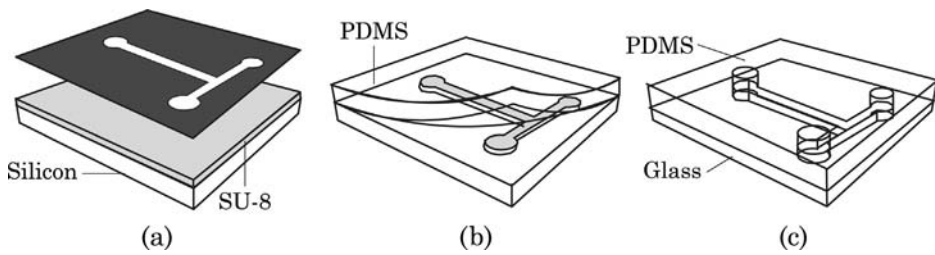


**Figure 3.16** Fabrication of microchannels with soft lithography: (a) spin coating a silicon wafer with SU-8, UV exposure with a clear field mask, development of SU-8 master; (b) pouring PDMS on the mold, curing, and peeling off the PDMS part; and (c) surface treatment of PDMS in oxygen plasma and bonding to glass.

method. PDMS is a good device material because it has a number of useful properties: low cost, low toxicity, transparency from the visible wavelengths into the near ultraviolet wavelengths, and chemical inertness. The fabrication cost is further reduced by using high-resolution laser-printed transparency masks. This type of low cost mask allows feature size of the order of  $20\ \mu\text{m}$  to be achieved.

First, PDMS is mixed from the two commercially available prepolymers. The weight ratio of the base and the curing agent is usually 10:1. A low cost and simple way is to fabricate the solid master by structuring an SU-8 layer using lithography, Fig. 3.16 (a). Glass posts are placed on the SU-8 master to define the access holes and the reservoirs. These reservoirs and access holes can also be punched later in the PDMS layer. The PDMS mixture is poured into the master and stands for a few minutes to self-level. The whole set is then cured at relatively low temperature (from  $60\ ^\circ\text{C}$  to  $80\ ^\circ\text{C}$ ) for several hours. After peeling off and having surface treatment with low-temperature oxygen plasma, Fig. 3.16 (b), the structured PDMS membrane is brought into contact with clean glass, silica, or another piece of surface-activated PDMS, Fig. 3.16 (c). The sealed channel can withstand pressures up to five bars. Without surface treatment, PDMS also forms a watertight seal when pressed against itself, glass, or most other smooth surfaces. These reversible seals are useful for detachable fluidic devices, which are often required in research and prototyping.

### 3.2.2.5 Laser Machining

Laser machining is a localized, non-contact machining technique. Machining applications of laser include drilling, cutting, engraving, marking, and texturing. Almost all types of materials, such as metals, ceramics, plastics, and wood can be used with laser machining. Most significantly, laser machining can remove materials in small amounts with a small heat-affected zone. Micromachining with controlled accuracy can be achieved. A further attractive advantage of laser machining compared to other micromachining techniques is the possibility of low cost rapid prototyping. The disadvantage of laser

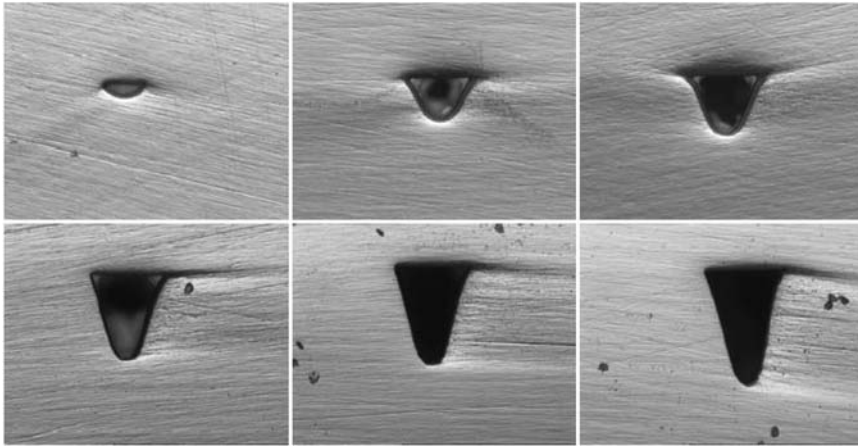


**Figure 3.17** Typical cross sections of microchannels fabricated by CO<sub>2</sub> laser.

machining is the redeposition of substrate material, which makes the quality control of the machined surfaces difficult.

UV lasers were used to realize microstructures in polymers. Although a UV laser is a good choice for laser ablation, its cost is much higher than that of a CO<sub>2</sub> laser. CO<sub>2</sub> lasers have a relatively long characteristic wavelength of 10.6  $\mu\text{m}$ . The ablation process is determined by the thermal energy of the laser beam. Therefore, the cross section of the microchannel depends on the energy distribution of the laser beam, its moving speed, the laser power, and the thermal diffusivity of substrate material. The energy of the laser beam has a Gaussian distribution, thus the cross section of the channel also has a Gaussian shape, Fig. 3.17. Three types of lasers are commonly used for laser micromachining:

- Excimer lasers with ultraviolet wavelengths (351, 308, 248, 193 nm);
- Nd:YAG lasers with near infrared (1,067 nm), visible (533 nm), and UV wavelengths (355 nm, 266 nm); and
- CO<sub>2</sub> lasers with deep infrared wavelength (10.6  $\mu\text{m}$ ).

The two major parameters of laser micromachining are wavelength and laser power. The choice of wavelength depends on the minimum structure size and the optical properties of the substrate material, such as absorption and reflection characteristics. Theoretically, the minimum achievable focal spot diameter and consequently the smallest size are about twice the laser wavelength.

The choice of power depends on the desired structure size and the ablation rate. When excimer or Nd:YAG lasers with a pulse duration of a few tens of nanoseconds are utilized, a single laser pulse will typically vaporize the surface material to a depth of 0.1 to 1  $\mu\text{m}$  (see Table 3.9). Since each pulse removes such a thin layer of material, the depth of the machined trench can be controlled

**Table 3.9 Typical Ablation Depths Per Pulse of Different Material (Nanosecond Laser)**

Material	Depth Per Pulse (μm)
Polymers	0.3–0.7
Ceramics and glass	0.1–0.2
Diamond	0.05–0.1
Metals	0.1–1.0

accurately by the number of laser pulses. Furthermore, laser pulses of very short duration eliminate heat flow to the surrounding materials. Consequently, clean and accurate structures can be achieved with short-pulsed lasers. There are two modes of laser micromachining: direct writing and using a mask [126]. In the direct writing mode, the laser beam is focused on the substrate surface. The pattern is scanned using a precision *x-y* stage or galvano scanning mirrors. In this mode, the smallest structure depends on the accuracy of the scanning system, and is of the order of 25 to 50 μm. In the masking mode, the mask determines the detailed shape of the structure. Therefore, the minimum structure size can be brought down to twice that of the laser wavelength.

Laser micromachining is suitable for fabrication of microchannels and fluidic access holes. A LIGA-like technique uses laser machining instead of X-ray lithography to machine PMMA [127]. Furthermore, the laser beam can be used for sealing polymeric devices fabricated with other techniques or making shadow masks.

**3.2.3 Polymeric Surface Micromachining**

Polymeric surface micromachining technique is similar to its silicon-based counterpart. A functional layer is structured on top of a sacrificial layer. Removing the sacrificial layer results in a freely movable structure. Polymers can work as both sacrificial layer and functional layer. With SU-8 as the functional layer, polymers, such as polystyrene, or metals, such as chromium, were used as sacrificial layers. Silicon was used directly as sacrificial material as well as the handling substrate for the fabrication of polymeric valves, polymeric micropumps, and a polymeric microgrippers.

**3.2.3.1 SU-8**

SU-8 is a thick film resist, which can be structured using UV lithography. With a Young’s modulus of 4 to 5 GPa and a Poisson’s ratio of 0.22, hardbacked

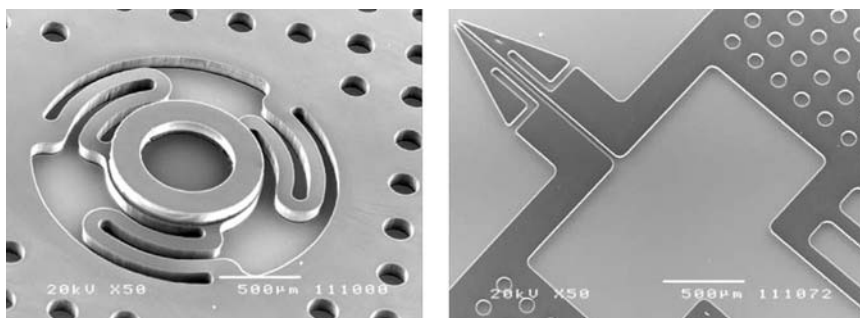


**Figure 3.18** Examples of devices made by polymeric surface micromachining: (a) microvalve, (b) microgripper.

SU-8 poses excellent mechanical properties and can be used for moveable parts. The sacrificial material for the release of the SU-8 part can be the silicon substrate, a metal layer, or a polymer layer. Fig. 3.18 (a) shows a micro check valve made with this technology [96]. The valve was first structured on silicon substrate with a two-layer process. Developing both layers results in a three-dimensional valve structure with spring beams, a valve disc, and a sealing ring. Underetching silicon with KOH releases the valve. Circular access holes were placed on the structure for faster release. The smooth contours of the design help to arrest surface stress and avoid cracks in the structure.

For many applications, a metal layer on the structural polymeric material is needed. The metal layer can be structured to form electrodes and heaters. Fig. 3.18 (b) shows a SU-8 microgripper, which has a thin metal layer on top acting as a heater [97]. Instead of silicon, a thin layer of polystyrene can be used as sacrificial layer. The polymeric sacrificial material can be dissolved by organic solvents such as toluene. In contrast to KOH for sacrificial silicon etching, solvent does not attack the thin metal layer.

### 3.2.3.2 Polyimide

Polyimide is available as photoresists such as Proimide 348 or 349 (Ciba Geigy) or PI-2732 (DuPont). Coating a single polyimide layer can result in a film thickness up to 40  $\mu\text{m}$ . This relatively thick film allows the use of photosensitive polyimide for the same purpose as other thick resists, such as SU-8 [98].

Fluorinated polyimide is optically transparent. This material can be machined by RIE. During a RIE process, fluorine radicals are released from the fluorinated polyimide and act as etchants [99].

Polyimide can work as a substrate material. Metals such as aluminum, titanium, and platinum can be sputtered on it [100]. Similar to other polymers, polyimide can be etched with RIE in oxygen plasma. Combining photolithography, RIE, and lamination, complex channel structures with metal electrodes can be fabricated in polyimide [101].

### 3.2.3.3 Parylene

Parylene is a polymer that can be deposited with CVD at room temperature. The CVD process allows coating a conformal film with a thickness ranging from several microns to several millimeters. Parylene is available as Parylene N, Parylene C, and Parylene D.

*Parylene N* is poly-paraxylylene, which is a good dielectric. Parylene N has a very low dissipation factor, high dielectric strength, and a frequency-independent dielectric constant. *Parylene C* is produced from the same monomer, modified only by the substitution of a chlorine atom for one of the aromatic hydrogens. Parylene C has a useful combination of electrical and physical properties, as well as a very low permeability to moisture and other corrosive gases. Parylene C is also able to provide a conformal insulation. *Parylene D* is modified from the same monomer by the substitution of the chlorine atom for two of the aromatic hydrogens. Parylene D is similar in properties to parylene C with the added ability to withstand higher temperatures. Deposition rates are fast, especially for Parylene C, which is normally deposited at a rate of about 10  $\mu\text{m}/\text{min}$ . The deposition rates of parylene N and Parylene D are slower. Parylene can be used in microfluidic devices as a structural material, which offers low Young's modulus. Such a soft material is needed in microvalves and micropumps. Furthermore, parylene coating can improve the biocompatibility of a microfluidic device.

Polymeric surface micromachining perfectly suits the fabrication of closed microchannels. Both the structural layer and the sacrificial layer can be made of polymers. The typical fabrication process is shown in Fig. 3.19 (a). To start with, the sacrificial polymer is spin-coated on the substrate, which can be silicon or glass. The channel height is determined by the thickness of this layer, which in turn is controlled by the viscosity of the solution and the spin speed. Since photo resist will be etched in oxygen plasma, a metal layer is sputtered over the sacrificial layer as a mask, Fig. 3.19 (a1). The metal mask allows conventional photolithography, where channel patterns are transferred to the mask, Fig. 3.19 (a2). The sacrificial layer is then structured by RIE with oxygen plasma, Fig. 3.19 (a3). After removing the metallic mask, the structural polymer is deposited over the sacrificial structures, Fig. 3.19 (a4). In the final step, the sacrificial polymer decomposes into volatile products at elevated temperatures, and leaves behind the microchannel [103].

In the above process, the sacrificial polymer should easily decompose at a temperature lower than the glass temperature of wall materials. For instance, polynorbornene (PNB) is a good sacrificial polymer [104]. The decomposition temperatures of PNB are between 370  $^{\circ}\text{C}$  and 425  $^{\circ}\text{C}$ . In this case, silicon dioxide and silicon nitride are ideal encapsulation materials at these relatively high temperatures. If polymeric channel walls are needed, polyimides, such as Amoco Ultradel 7501, Dupont PI-2611, and Dupont PI-2734, are ideal for this purpose, because of their high glass transition temperature of over 400  $^{\circ}\text{C}$  [104].

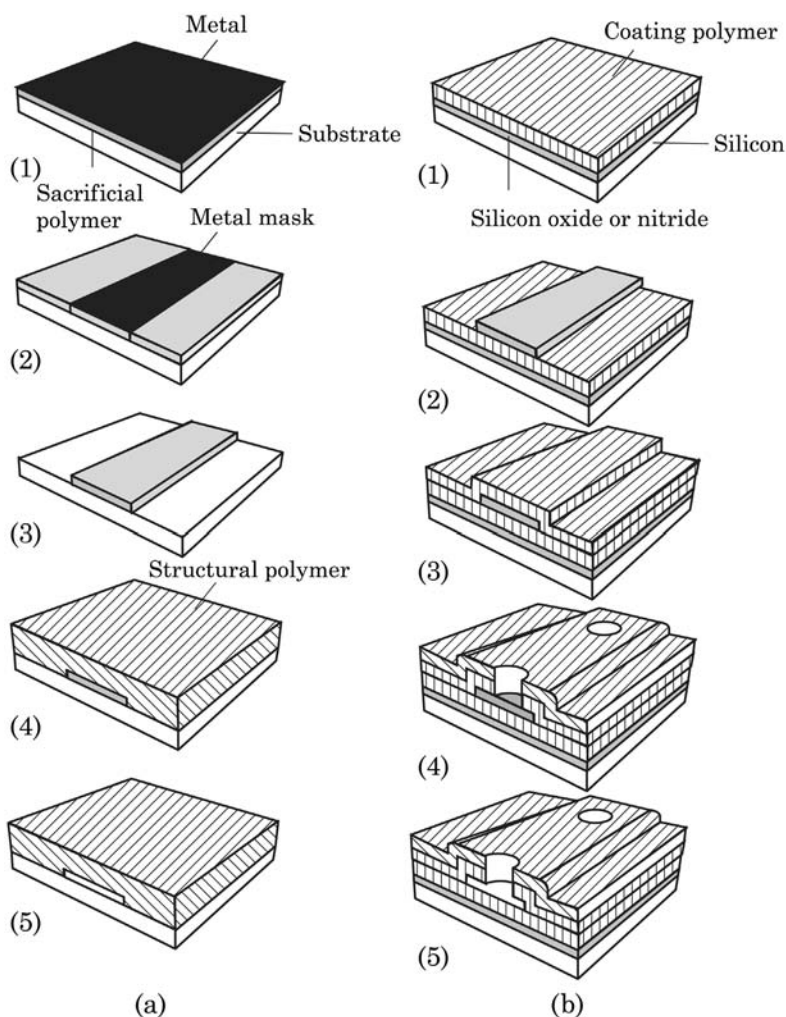


**Figure 3.19** Fabrication of microchannel with polymeric surface micromachining: (a) a simple channel (after [103]); (b) microchannel with functional coating of inner wall (after [112]).

Polycarbonates, such as polyethylene carbonate (PEC) and polypropylene carbonate (PPC), offer a relatively low decomposition temperature of the order of 200 °C to 300 °C [103]. The low decomposition temperature is needed for structural materials with less thermal stability. Inorganic glass, silicon dioxide, thermoplastic polymers, and thermoset polymers can be used as structural materials [103].

Micromixers used in the life sciences may need a biocompatible coating for their inner walls. Fig. 3.19 (b) shows the fabrication processes of such microchannels [112]. For instance, the biocompatible material can be Parylene C. First, parylene is vapor-deposited on a silicon substrate, which is covered by

a nitride/oxide barrier layer, Fig. 3.19 (b,1). Thick film resist AZ4620 is used as the sacrificial material. After photolithography, developing, and hard bake of the resist structures [Figs. 3.19 (b,2)], a second parylene layer is deposited, Figs. 3.19 (b,3). After roughening the parylene surface with oxygen plasma, photosensitive polyimide is spin-coated as a structural layer on top of the second parylene layer. Next, polyimide is exposed and developed. In order to open the fluidic access from the front side, the top parylene layer is etched in oxygen plasma with an aluminum mask, Fig. 3.19 (b,4). In the last step, the sacrificial layer is removed with acetone. The resulting microchannels are optically transparent and hermetic, Fig. 3.19 (b,5).

### 3.3 Metallic Microtechnologies

#### 3.3.1 Metals as Substrate Materials

Metals are compatible with silicon-based processes, thus metallic micromixers can be fabricated with conventional photolithography. In general, a silicon oxide layer or even the silicon wafer substrate can work as the sacrificial layer. The metallic layer can be evaporated, sputtered, or electroplated on the sacrificial material. Due to the relatively slow growth rate, evaporation and sputtering are suitable for the deposition of thin metallic films up to 10  $\mu\text{m}$  thickness. Thicker metallic layer can be achieved by electroplating. A metallic layer can be patterned by a lift-off process or by chemical etching. Subsequently, etching away the sacrificial materials releases the free-standing metallic structure.

Actuators are the key components of active micromixers. Sputtering and metallic micromachining allow the design and integration of functional smart materials, such as permanent magnet films [115,116], piezoelectric films [117,118], and shape memory alloy films [119].

Micro magnets consisting of metal alloys such as  $\text{SmCo}_5$ ,  $\text{Sm}_2(\text{Co,Fe,Zr})_{17}$ ,  $\text{Nd}_2\text{Fe}_{17}$ ,  $\text{Nd}(\text{Fe,Ti})_{12}\text{N}_x$ ,  $\text{PtCo/Ag}$ ,  $\text{Pt/Fe}$ ,  $\text{CoNiMnP}$ ,  $\text{FeCrCo}$ , an  $\text{MnAl}$  can be sputtered or electroplated on the substrate. Further, magnetic powders, such as ferrite ( $\text{Fe}_2\text{O}_3$ ), can be mixed with a polymer, such as polyimide or PDMS, to form a magnetic polymeric matrix. This magnetic polymer matrix can be structured by the common polymeric techniques discussed above or screen-printed on a substrate [115]. Magnetic materials open up potential applications in magnetic micromixers and MHD micromixers.

Piezoelectric thin films are not metallic but belong to the class of smart materials for actuation in active micromixers [117]. Piezoelectric ceramics, such as  $\text{AlN}$  and  $\text{ZnO}$ , can be sputtered. While  $\text{ZnO}$  needs to be deposited at room temperature for high resistivity,  $\text{AlN}$  with low conductivity can be deposited at high temperatures between 100  $^\circ\text{C}$  and 900  $^\circ\text{C}$ .  $\text{AlN}$  is more compatible with silicon-based technology because of the large resistivity and large band gap of 6 eV. Other popular piezoelectric materials for MEMS devices are ferroelectric



thin films, such as lead zirconate titanate (PZT). Ferroelectric thin films have the advantage of large piezoelectric coefficients. However, due to the composition of the material the deposition process is relatively complex and challenging [117]. Readers may refer to a recent review by Dorey and Whatmore for more details on fabrication issues of thick film PZT [118].

Shape memory alloy (SMA) films are another attractive metallic material for actuators in active micromixers. SMA materials, such as TiNi, can be sputtered and structured with conventional microtechniques. The main advantages of SMA are high power density, large displacement and large forces, and relatively low operation voltages. However, SMA actuators are thermal actuators that are associated with problems such as low energy efficiency, low dynamics, and large hysteresis. The hysteresis leads to nonlinear system behavior, which makes designing SMA-based micro actuators difficult. A number of microfluidic devices, such as micropumps and microvalves, have nevertheless been realized based on SMA thin films [119].

### 3.3.2 LIGA

The LIGA process is a combination of X-ray or thick resist lithography with electroplating. The metallic part usually works as the mold for further replication in polymers. However, the same process can be used for the fabrication of metallic micromixers. The process starts with applying a PMMA layer on the substrate. This process can be achieved by different methods, such as multiple spin coating, lamination of prefabricated sheets, casting, and plasma polymerization. The PMMA layer is structured by X-ray lithography. The etched PMMA part is subsequently used as a mold for electroplating the metallic structure. The metal in use is typically nickel or nickel-iron alloy.

The need for a synchrotron X-ray source and the consequent high cost prevents the widespread use of the LIGA process. The relatively high aspect ratio achievable with SU-8 allows a low cost alternative to standard LIGA. The LIGA process with SU-8 is often called UV-LIGA or “poor man’s LIGA” [120]. For more details on LIGA technology and its application, readers may refer to a recent review by Malek and Saile [121].

### 3.3.3 Micro Electro Discharge Machining

Micro electro discharge machining (micro EDM) uses erosive effects of electrostatic discharge between an electrode and an electrically conducting material. The electrostatic discharge can create locally a temperature up to 10,000 °C. Both electrode and substrate material are immersed in a dielectric fluid that also cools and removes debris from the processed location [122]. The electrode can be machined with conventional techniques. Electropolishing

usually follows EDM to improve the surface finish and to remove the heat-affected zone.

An alternative for EDM is electrochemical machining (ECM) [123]. The technique is based on the electrochemical reaction between an electrode and a workpiece. The advantage of ECM are the low mechanical stress and the non-existence of a heat-affected zone as well as tool wear. The technique utilizing both electro discharge and chemical reaction for machining nonconducting materials is called spark-assisted chemical engraving (SACE). In this technique, the substrate material does not work as an electrode. The external tool electrode and counter electrode work as the cathode and the anode, respectively. The tool electrode is placed on the substrate surface and submerged in an electrolyte solution (typically sodium hydroxide or potassium hydroxide). At first, gas bubbles are generated at the tool electrode due to electrolysis. If the voltage between the two electrodes is higher than a critical value, the gas bubbles coalesce into a gas film isolating the tool electrode from the electrolyte. At this moment, electrical discharges occur. The high temperature and probably chemical etching contribute to the eroding of the non-conducting substrate placed next to the electrode. More details about SACE are given in the recent review by Wüthrich and Fascio [124].

### 3.3.4 Focused Ion Beam Micromachining

Focused ion beam (FIB) micromachining uses highly focused ion beams such as a  $\text{Ga}^+$  beam to scan and cut the substrate surface inside a vacuum chamber. This technique was originally developed for sample preparation in electron microscopy. The spot size of FIB is less than 10 nm. The removal rates can further be improved by introducing reactive halogen gases into the processing chamber. Several effects result from the ion bombardment. First, neutral and ionized atoms are removed from the substrate, enabling micromachining of the substrate. The bombardment results in electron emission, which also allows imaging of the sample. Furthermore, the ion beam can induce damage due to the displacement of atoms and heating in the substrate. Chemical interactions, such as breaking of chemical bonds, can be used for deposition. For more details on concepts and applications of FIB micromachining, readers may refer to the recent review by Reyntjens and Puers [125].

### 3.3.5 Powder Blasting

Powder blasting is an erosion technique that uses the kinetic energy of powder particles to generate cracks in the substrate surface and consequently to remove material. The major process parameters of this technique are particle material, particle size, particle velocity, and incident angle [128]. The technique

was originally developed for metals and further extended to silicon and glass. The main advantage of powder blasting is the fast processing time. Because of this reason, the ink supply channels of inkjet print head are machined by powder blasting.

The resolution of powder blasting depends on the particle size. As a rule of thumb, the smallest cut is about three times that of the particle size [129]. High resolutions are kept by the use of a hard metal mask, which is machined by another technique, such as laser micromachining. Alternatively, masks made of thick resist foils and polyimide resist can also be used [129]. With particle velocities on the order of 80 to 200 m/s, the erosion rate is on the order of 1 mm/min [128].

Using 30- $\mu\text{m}$  alumina particles, microchannels of 100- $\mu\text{m}$  width and 10- $\mu\text{m}$  depth were fabricated in glass [128]. Changing the incident angle of the powder beam can lead to channels with slanted walls. Since glass has a relatively high zeta potential, powder blasting can be the economic way for mass fabrication of active micromixers based on electrokinetic instability. Shlautmann et al. fabricated microchannels with 85- $\mu\text{m}$  width and 22- $\mu\text{m}$  depth in glass using 9- $\mu\text{m}$  alumina particles [130]. In the fabrication of micromixers, powder blasting can be used for drilling fluidic access through a substrate.

### 3.3.6 Ultrasonic Micromachining

Another practical technique for cutting microchannels and opening access holes is ultrasonic drilling. This technique uses ultrasonically induced vibrations delivered to a tool to machine the substrate. When combined with abrasive slurry, ultrasonic abrasion can handle hard, brittle materials, such as glass and silicon.

High-frequency electrical signal is converted through a piezoelectric transducer into mechanical oscillation. The energy is acoustically transmitted to the machining tool. A piezoelectric stack actuator can work as the piezoelectric transducer. The actuation frequency is typically 20 kHz. Abrasive slurry flows around the cutting tool and causes microscopic grinding between the surfaces of the tool and the workpiece. Through this process, the machined area becomes an exact counterpart of the tool. In the fabrication process of micromixers, ultrasonic machining can be used for drilling access holes in glass and silicon. Hole diameters on the order of 100 to 200  $\mu\text{m}$  can be machined with this method.

## 3.4 Packaging

### 3.4.1 Anodic Bonding

Anodic bonding is the oldest bonding technique in silicon-based micromachining. The technique is applied to a glass wafer and a silicon wafer.

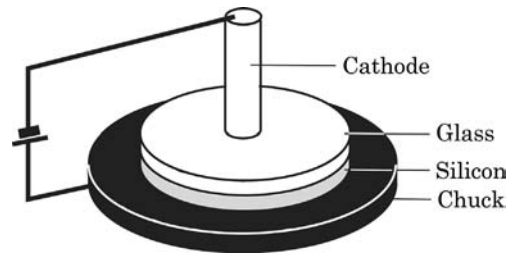


**Figure 3.20** Setup for anodic bonding.

The required conditions for the process are a bonding temperature of the order of  $400\text{ }^{\circ}\text{C}$  and a high electrical field with a bonding voltage of about  $1\text{ kV}$ . Fig. 3.20 shows the typical setup of anodic bonding. Silicon is connected to the positive electrode and works as the anode, which gives the name to this bonding technique.

Anodic bonding induces a large temperature change in the glass/silicon stack. If the thermal expansion coefficients of glass and silicon do not match, the stress upon cooling will cause cracks either in the silicon or the glass. Thus, the glass wafer should have a matching thermal expansion coefficient. Glasses suitable for this purpose are Corning 7740 (Pyrex), Corning 7750, Schott 8329, and Schott 8330. Bonding between two silicon layers can also be achieved with anodic bonding by coating a thin glass layer on one of the two wafers. The glass layer can be deposited by different techniques, such as PVD and spin-on glass. Glass material with a matching thermal expansion coefficient is used as a source or target for the evaporation or sputtering process. The bonding processes work as usual with the glass-covered silicon wafer replacing the glass wafer in Fig. 3.20. Because of the much thinner glass layer, of the order of  $0.5$  to  $4\text{ }\mu\text{m}$ , much lower bonding voltages are needed for the same field strength for bonding glass to silicon. The bonding voltage in this case is of the order of several tens of volts. A thin metal layer on glass or silicon does not affect the bonding quality. Electric interconnects can therefore survive the bonding process. Because of the optically transparent glass, this bonding technique is suitable for making micromixers for biochemical applications, where optical access for manipulation and evaluation of the fluid are required.

### 3.4.2 Direct Bonding

Direct bonding refers to the bonding process between two substrates of the same material. Direct bonding applies to a variety of materials such as silicon, glasses, polymers, ceramics, and metals.

*Silicon direct bonding*, also called *silicon fusion bonding*, seals two silicon wafers directly at high temperature. An intermediate layer makes the fabrication process more complex and more complicated. The advantage of

this technique is the lack of thermal stress because of the perfectly matching thermal expansion coefficient of the two silicon wafers. Silicon direct bonding utilizes the reaction between hydroxyl (OH) groups at the surface of the oxide layers of the two silicon wafers. These oxide layers can either be native or deposited. Hydration of the silicon wafers is achieved by immersing them in an  $\text{H}_2\text{O}_2/\text{H}_2\text{SO}_4$  mixture, boiling nitric acid, or diluted  $\text{H}_2\text{SO}_4$ . The bonding process is carried out at temperatures between 300 °C and 1000 °C. Annealing the bonded stack at high temperatures (800 °C to 1100 °C) further improves the bond quality.

Because of the optical transparency, glasses are relevant for many micromixers for life-science applications. Bonding between glasses is called *glass-glass bonding*. Many applications use soda-lime glass, which consists of  $\text{SiO}_2$ ,  $\text{Na}_2\text{O}$ ,  $\text{CaO}$ ,  $\text{MgO}$ , and a small amount of  $\text{Al}_2\text{O}_3$ . The following bonding process is used for two soda-lime glass slides. First, the glass wafers are cleaned in an ultrasonic bath and subsequently 10 minutes in a solution of [5  $\text{H}_2\text{O}$ : 1  $\text{NH}_3$  (25%): 1  $\text{H}_2\text{O}_2$  (20%)] or [6 $\text{H}_2\text{O}$ : 1  $\text{HCl}$  (37%): 1  $\text{H}_2\text{O}_2$  (20%)]. After removing moisture by annealing at 130 °C, the two wafers are thermally bonded together at 600 °C for 6 to 8 hours [132].

Many polymers are thermally bonded at temperatures above their glass transition temperatures. In cases of polymers with low surface energy, such as PDMS, a surface treatment with oxygen plasma seals the two polymer parts at room temperature. Polymer–polymer bonding can be achieved with the assistance of a solvent, which wets the bonding surfaces. Bonding is accomplished after the solvent evaporates.

Ceramic green tapes and metal sheets structured by serial techniques can be directly bonded together at high pressure and high temperatures. Ceramic green tapes are typically bonded at 138 bars, 70 °C for 10 minutes [133]. Stainless steel sheets are typically bonded at 276 bars, 920 °C for 4 hours [134].

### 3.4.3 Adhesive Bonding

Adhesive bonding uses an intermediate layer to glue the substrate. Depending on substrate materials and applications, the intermediate layer can be glasses, epoxies, photoresists, or other polymers. A thin intermediate glass layer can thermally bond silicon wafers. Glass frits with relatively low sealing temperatures ranging from 400 °C to 650 °C are commercially available. The glass layer can be sprayed, screen-printed, or sputtered on the substrate. Annealing the stack at sealing temperatures makes the glass layer melt and flow. Cooling down to room temperature results in a strong bond between two substrates [135]. A number of epoxies [136], UV-curable epoxies [137], and photoresists can be used for adhesive bonding. SU-8 is used in many microfluidic applications as both spacer and adhesive layers. The advantage of using polymers as an intermediate layer is the low process temperature. These low packaging temperatures are needed for many devices, containing metals and

alloys with low melting temperatures. The other advantage is that adhesive bonding is not limited to silicon and can be used for all kinds of substrate material.

#### 3.4.4 Eutectic Bonding

Eutectic bonding is a common packaging technique in electronics. Gold-silicon eutectic bonding is achieved at a relatively low temperature of 363 °C. A thin gold film can be sputtered on the silicon surface for this purpose. Furthermore, a gold-silicon preform with composition close to the eutectic point can also be used as the intermediate layer.

### 3.5 Conclusions

This chapter gives a short review on available micromachining technologies for silicon-based, metallic, and polymeric micromixers. Because a complete review on the technology for each type of material could cover hundreds of references, this chapter only summarizes the most important points on the topics, and in many cases cites only the topical review for each type of material. In general, silicon-based technologies are the most established techniques with commercially available equipment. Applications in rough environments and operation conditions require a tougher material than silicon. For such applications, diamond-based and silicon carbide-based devices are the better candidates. Applications in analytical chemistry and biomedical fields would require a large device area, which is not economical for silicon. Furthermore, silicon and silicon-based materials are not compatible for many chemical and biochemical applications. Polymeric devices are the real alternatives for silicon-based parts. Besides simple devices with only microchannel networks, polymeric devices with freely moveable components are also possible. Metallic devices are the other alternatives at the micro scale. The combination of all the available technologies from silicon-based to polymeric to metallic opens a huge potential and freedom for designing micromixers.

### References

1. M.J. Madou, *Fundamentals of Microfabrication: The Science of Miniaturization*, 2nd ed., CRC Press, Boca Raton, FL, 2002.
2. L.F. Thompson, C.G. Willson and M.J. Bowden, *Introduction to Microlithography*, American Chemical Society, Washington, D.C., 1994.
3. H. Friedrich, D. Widmann and H. Mader, *Technologie Hochintegrierter Schaltungen*, Springer-Verlag, Berlin, 1996.

4. C.W. Pearce, "Epitaxy," S.M. Sze, Ed., *VLSI Technology*, McGraw-Hill, New York, pp. 55–97, 1988.
5. A.C. Adams, "Dielectric and polysilicon film deposition," S.M. Sze, Ed., *VLSI Technology*, McGraw-Hill, New York, pp. 233–271, 1988.
6. H. Becker and C. Gärtner, "Polymer microfabrication methods for microfluidic analytical applications," *Electrophoresis*, Vol. 21, pp. 12–26, 2000.
7. G. Monreal and C.M. Mari, "The use of polymer materials as sensitive elements in physical and chemical sensors," *Journal of Micromechanics and Microengineering*, Vol. 7, no. 3, pp. 121–124, 1997.
8. *Polymer Applications for Biotechnology: Macromolecular Separation and Identification*, D. Soane, Ed., Prentice-Hall, Upper Saddle River, NJ, 1992.
9. G.T.A. Kovacs, N.I. Maluf and K.E. Petersen, "Bulk micromachining of silicon," *Proceedings of the IEEE*, Vol. 86, no. 8, pp. 1536–1551, 1998.
10. K.R. Williams and R.S. Muller, "Etch rates for micromachining processing," *Journal of Microelectromechanical Systems*, Vol. 5, no. 4, pp. 256–269, 1996.
11. K.E. Bean, "Anisotropic etching of silicon," *IEEE Transactions Electron Devices*, Vol. ED-25, pp. 1185–1193, 1978.
12. H. Seidel, et al., "Anisotropic etching of crystalline silicon in alkaline solutions II: Influence of dopants," *Journal of Electrochemical Society*, Vol. 137, no. 11, pp. 3626–3632, 1990.
13. G. Kaminsky, "Micromachining of silicon mechanical structures," *Journal of Vacuum Science and Technology*, Vol. B3, no. 4, pp. 1015–1024, 1985.
14. W. Kern, "Chemical etching of silicon, germanium, gallium arsenide and gallium phosphide," *RCA Review*, Vol. 39, pp. 278–308, 1978.
15. U. Schnakenberg, et al., "NH<sub>4</sub>OH Based etchants for silicon micromachining: Influence of additives and stability of passivation layers," *Sensors and Actuators A*, Vol. 25, no. 1–3, pp. 1–7, 1990.
16. O. Tabata, et al., "Anisotropic etching of silicon in TMAH solutions," *Sensors and Actuators A*, Vol. 34, no. 1, pp. 51–57, 1992.
17. U. Schnakenberg, W. Beneke and P. Lange, TMAHW etchants for silicon micromachining, Proceedings of Transducers '91, 6th International Conference on Solid-State Sensors and Actuators, San Francisco, 23–27 June, 1991, pp. 815–818.
18. K.E. Petersen, "Silicon as a mechanical material," *Proceedings of IEEE*, Vol. 70, pp. 420–457, 1982.
19. M. Mehregany and S.D. Senturia, "Anisotropic etching of silicon in hydrazine," *Sensors and Actuators*, Vol. 13, no. 4, pp. 375–390, 1988.
20. H. Linde and L. Austin, "Wet silicon etching with aqueous amine gallates," *Journal of Electrochemical Society*, Vol. 139, no. 4, pp. 1170–1174, 1992.
21. J.G. Fleming, "Combining the best of bulk and surface micromachining using Si {111} substrates," *Proceedings SPIE Micromach. Microfab. IV Tech. Conf.*, Vol. 3511, pp. 162–168, 1998.
22. V. Lehmann, Porous silicon—A new material for MEMS, Proceedings of MEMS'96, 9th IEEE international workshop micro electromechanical system, San Diego, CA, 11–15 February, 1996, pp. 1–6.
23. P. Lärmer, Method of Anisotropically Etching Silicon, German Patent DE 4 241 045, 1994.
24. D. Sobek, S.D. Senturia and M.L. Gray, Microfabricated Fused Silica Flow Chambers for Flow Cytometry, Technical digest of the IEEE solid state sensor and actuator workshop, Hilton Head Island, SC, 13–16 June, 1994, pp. 260–263.
25. D.J. Harrison et al., Miniaturized Chemical Analysis Systems Based on Electrophoretic Separations and Electroosmotic Pumping, Proceedings of Transducers '93, 7th international conference on solid-state sensors and actuators, Yokohama, Japan, 7–10 June, 1993, pp. 403–406.

26. S.C. Jacobson et al., Electrically driven separations on a microchip, Technical digest of the IEEE solid state sensor and actuator workshop, Hilton Head Island, SC, 13–16 June, 1994, pp. 65–68.
27. H. Möbius et al., Sensors controlled processes in chemical reactors, Proceedings of transducers '95, 8th international conference on solid-state sensors and actuators, Stockholm, Sweden, 16–19 June, 1995, pp. 775–778.
28. L. Jiang, M. Wong and Y. Zohar, A Micro-Channel Heat Sink with Integrated Temperature Sensors for Phase Transition Study, Proceedings of MEMS'99, 12th IEEE international workshop micro electromechanical system, Orlando, FL, 17–21 January, 1999, pp. 159–164.
29. J. Chen and K.D. Wise, "A high resolution silicon monolithic nozzle array for inkjet printing," *IEEE Transaction on Electron Devices*, Vol. 44, no. 9, pp. 1401–1409, 1997.
30. J. Chen, et al., "A multichannel neural probe for selective chemical delivery at the cellular level," *IEEE Transaction on Biomedical Engineering*, Vol. 44, no. 8, pp. 760–769, 1997.
31. R.W. Tjerkstra et al., Etching technology for microchannels, Proceedings of MEMS'97, 10th IEEE international workshop micro electromechanical system, Nagoya, Japan, 26–30 January, 1997, pp. 147–151.
32. M.J. De Boer, et al., "Micromachining of buried micro channels in silicon," *Journal of Microelectromechanical Systems*, Vol. 9, no. 1, pp. 94–103, 2000.
33. R.E. Osterbroek, et al., "Etching methodologies in <111>-oriented silicon wafers," *Journal of Microelectromechanical Systems*, Vol. 9, no. 3, pp. 390–397, 2000.
34. S.Y. Chou, P.R. Krauss and P.J. Renstrom, "Imprint of Sub-25 nm vias and trenches in polymers," *Applied Physics Letter*, Vol. 67, no. 21, pp. 2114–2116, 1995.
35. J.M. Bustillo, R.T. Howe and R.S. Muller, "Surface micromachining for microelectromechanical systems," *Proceedings of the IEEE*, Vol. 86, no. 8, pp. 1552–1574, 1998.
36. W.C. Tang, T.C.H. Nguyen and R.T. Howe, "Laterally driven polysilicon resonant microstructures," *Sensors and Actuators*, Vol. 20, pp. 25–32, 1989.
37. C. Keller and M. Ferrari, Milli-scale polysilicon structures, Technical digest of the IEEE solid state sensor and actuator workshop, Hilton Head Island, SC, 13–16 June, 1994, pp. 132–137.
38. C.G. Keller and R.T. Howe, Hexsil bimorphs for vertical actuation, Proceedings of transducers '95, 8th international conference on solid-state sensors and actuators, Stockholm, Sweden, 16–19 June, 1995, pp. 99–102.
39. A.F. Flannery, PECVD Silicon carbide for micromachined transducers, Proceedings of transducers '97, 9th international conference on solid-state sensors and actuators, Chicago, IL, 16–19 June, 1997, pp. 217–220.
40. N. Rajan, et al., "Fabrication and testing of micromachined silicon carbide and nickel fuel atomizers for gas turbine engines," *Journal of Microelectromechanical Systems*, Vol. 8, no. 3, pp. 251–257, 1999.
41. K.A. Shaw, Z.L. Zhang and N.C. MacDonald, "SCREAM-I: A single mask, single-crystal silicon, reactive ion etching process for microelectromechanical structures," *Sensors and Actuators A*, Vol. 40, no. 1, pp. 63–70, 1994.
42. Y.X. Li et al., Fabrication of a single crystalline silicon capacitive lateral accelerometer using micromachining based on single step plasma etching, Proceedings of MEMS'95, 8th IEEE international workshop micro electromechanical system, Amsterdam, The Netherlands, 29 January–2 February, 1995, pp. 398–403.
43. B. Diem et al., SOI (SIMOX) as a substrate for surface micromachining of single crystalline silicon sensors and actuators, Proceedings of transducers '93, 7th international conference on solid-state sensors and actuators, Yokohama, Japan, 7–10 June, 1993, pp. 233–236.
44. H. Jansen et al., The black silicon method IV: The fabrication of three-dimensional structures in silicon with high aspect ratios for scanning probe microscopy and other applications, Proceedings of MEMS'95, 8th IEEE international workshop micro



- electromechanical system, Amsterdam, the Netherlands, 29 January–2 February, 1995, pp. 88–93.
45. M. De Boer, H. Jansen and M. Elwenspoek, The black silicon method V: A study of the fabricating of moveable structures for micro electromechanical systems, Proceedings of transducers '95, 8th international conference on solid-state sensors and actuators, Stockholm, Sweden, 16–19 June, 1995, pp. 565–568.
  46. H. Jansen, M. de Boer and M. Elwenspoek, The black silicon method VI: High aspect ratio trench etching for MEMS applications, Proceedings of MEMS'96, 9th IEEE international workshop micro electromechanical system, San Diego, CA, 11–15 February, 1996, pp. 250–257.
  47. T.E. Bell, et al., "Porous silicon as a sacrificial material," *Journal of Micromechanics and Microengineering*, Vol. 6, pp. 361–369, 1996.
  48. S. Lee, S. Park and D. Cho, "The surface/bulk micromachining (SBM) process: A new method for fabricating released mems in single crystal silicon," *Journal of Microelectromechanical Systems*, Vol. 8, no. 4, pp. 409–416, 1999.
  49. L. Lin, A.P. Pisano and R.S. Muller, Silicon processed microneedles, Proceedings of transducers '93, 7th international conference on solid-state sensors and actuators, Yokohama, Japan, 7–10 June, 1993, pp. 237–240.
  50. S. Wu et al., A suspended microchannel with integrated temperature for high-pressure flow studies, Proceedings of MEMS'98, 11th IEEE international workshop micro electromechanical system, Heidelberg, Germany, 25–29 January, 1998, pp. 87–92.
  51. V.L. Spiering et al., Novel microstructures and technologies applied in chemical analysis techniques, Proceedings of transducers '97, 9th international conference on solid-state sensors and actuators, Chicago, IL, 16–19 June, 1997, pp. 511–514.
  52. I. Papautsky, et al., "Micromachined pipette arrays," *IEEE Transaction on Biomedical Engineering*, Vol. 47, no. 6, pp. 812–819, 2000.
  53. E.T. Carlen and C.H. Mastrangelo, Parafin actuated surface micromachined valves, Proceedings of MEMS'00, 13th IEEE international workshop micro electromechanical system, Miyazaki, Japan, 23–27 January, 2000, pp. 381–385.
  54. O. Auciello, J. Birrell, J.A. Carlisle, J.E. Gerbi, X. Xiao, B. Peng and H.D. Espinosa, "Materials science and fabrication processes for a new MEMS technology based on ultrananocrystalline diamond thin films," *Journal of Physics: Condensed Materials*, Vol. 16, pp. R539–R552, 2004.
  55. Y. Gurbuz, O. Esame, I. Tekin, W.P. Kang and J.L. Davidson, "Diamond semiconductor technology for RF device applications," *Solid-State Electronics*, Vol. 49, pp. 1055–1070, 2005.
  56. M. Mehregany, C.A. Zorman, S. Roy, A.J. Flischman, C.H. Wu and N. Rajan, "Silicon carbide for microelectromechanical systems," *International Materials Reviews*, Vol. 45, pp. 85–108, 2000.
  57. R.S. Okojie, A.A. Ned and A.D. Kurtz, "Operation of (6H)-SiC pressure sensor at 500 °C," *Sensors and Actuators A: Physical*, Vol. 66, pp. 200–204, 1998.
  58. N. Rajan, M. Mehregany, C.A. Zorman, S. Stefanescu and T.P. Kicher, "Fabrication and testing of micromachined silicon carbide and nickel fuel atomizers for gas turbine engines," *Journal of Microelectromechanical Systems*, Vol. 8, pp. 251–257, 1999.
  59. G. Kotzar, M. Freas, P. Abel, A. Fleischman, S. Roy, C. Zorman, J.M. Moran and J. Melzak, "Evaluation of MEMS materials of construction for implantable medical device," *Biomaterials*, Vol. 23, pp. 2737–2750, 2002.
  60. G. Voskerician, M.S. Shive, R.S. Shawgo, H. von Recum, J.M. Anderson, M.J. Cima and R. Langer, "Biocompatibility and biofouling of MEMS drug delivery device," *Biomaterials*, Vol. 24, pp. 1959–1967, 2003.
  61. P.R. Hernandez, C. Taboada, L. Leijia, V. Tsutsumi, B. Vazquez, F. Valdes-Perezgasga and J.L. Reyes, "Evaluation of biocompatibility of pH-ISFET materials

- during long-term subcutaneous implantation,” *Sensors and Actuators B*, Vol. 46, pp. 133–138, 1998.
62. A.C.R. Grayson, R.S. Shawgo, A.M. Johnson, N.T. Flynn, Y. Li, M.J. Cima and R.A. Langer, “BioMEMS review: MEMS technology for physiologically integrated devices,” *Proceedings of the IEEE*, Vol. 92, pp. 6–21, 2004.
  63. B. Ziaie, A. Baldi, M. Lei, Y. Gu and R.A. Sigel, “Hard and soft micromachining for BioMEMS: review of techniques and examples of application in microfluidics and drug delivery,” *Advanced Drug Delivery Reviews*, Vol. 56, pp. 145–172, 2004.
  64. G.M. Whitesides, E. Ostuni, S. Takayama, X. Jiang and D.E. Ingber, “Soft lithography in biology and biochemistry,” *Annu. Rev. Biomed. Eng.*, Vol. 3, pp. 335–373, 2001.
  65. A. Lendlein and S. Kelch, “Shape memory polymers,” *Angewandte Chemie-International Edition*, Vol. 41, pp. 2034–2057, 2002.
  66. A. Facchetti, M.H. Yoon and T.J. Marks, “Gate dielectrics for organic field-effect transistor: new opportunities for organic electronics,” *Advanced Materials*, Vol. 17, pp. 1705–1725, 2005.
  67. H. Zhang, D.W. Hutmacher, F. Chollet, A.N. Poo and E. Burdet, “Microrobotics and MEMS-based fabrication techniques for scaffold-based tissue engineering,” *Macromolecular Bioscience*, Vol. 5, pp. 477–489, 2005.
  68. E.W. Becker, et al., “Fabrication of microstructures with high aspect ratios and great structural heights by synchrotron radiation lithography, glavanofoming, and plastic moulding (LIGA Process),” *Microelectronic Engineering*, Vol. 4, pp. 35–56.
  69. H. Guckel, T.R. Christensen and K.J. Skrobis, Formation of Microstructures Using a Preformed Photoresist Sheet, U.S. Patent #5378583, January 1995.
  70. B. Chaudhuri, et al., “Photoresist application for the LIGA process,” *Microsystem Technologies*, Vol. 4, pp. 159–162, 1998.
  71. J. Mohr, et al., “Requirements on resist layers in deep-etch synchrotron radiation lithography,” *Journal of Vacuum Science and Technology*, Vol. B6, pp. 2264–2267, 1988.
  72. H. Guckel et al., Plasma polymerization of methyl methacrylate: A photoresist for 3D applications, Technical Digest of the IEEE Solid State Sensor and Actuator Workshop, Hilton Head Island, SC, 4–7 June, 1988, pp. 43–46.
  73. V. Ghica and W. Glashauser, Verfahren für die Spannungsfreie Entwicklung von Bestrahlten Polymethylmethacrylate-Schichten, German patent, #3039110, 1982.
  74. K. Lee, et al., “Micromachining applications for a high resolution ultra-thick photoresist,” *J. Vac. Scien. Technol. B*, Vol. 13, pp. 3012–3016, 1995.
  75. J.M. Shaw, et al., “Negative photoresists for optical lithography,” *IBM Journal of Research and Development*, Vol. 41, pp. 81–94, 1997.
  76. H. Lorenz, et al., “SU-8: A low-cost negative resist for MEMS,” *Journal of Micromechanics and Microengineering*, Vol. 7, pp. 121–124, 1997.
  77. H. Lorenz, et al., “Fabrication of photoplastic high-aspect ratio microparts and micromolds using SU-8 UV resist,” *Microsystem Technologies*, Vol. 4, pp. 143–146, 1998.
  78. MicroChem Corp, NANOSU-8 Negative Tone Photoresists Formulations 2-25, Data sheets, 2001.
  79. MicroChem Corp, NANOSU-8 Negative Tone Photoresists Formulations 50-100, Data sheets, 2001.
  80. H.K. Chang and Y.K. Kim, “UV-LIGA process for high aspect ratio structure using stress barrier and C-shaped etch hole,” *Sensors and Actuators A*, Vol. 84, pp. 342–350, 2000.
  81. M.K. Ghantasala, et al., “Patterning, electroplating and removal of SU-8 moulds by excimer laser micromachining,” *Journal of Micromechanics and Microengineering*, Vol. 11, pp. 133–139, 2001.
  82. H.E. Ayliffe, A.B. Frazier and R.D. Rabbitt, “Electric impedance spectroscopy using microchannels with integrated metal electrodes,” *IEEE Journal of Microelectromechanical Systems*, Vol. 8, no. 1, pp. 50–57, 1999.

83. R.J. Jackman, et al., "Microfluidic systems with on-line UV detection fabricated in photodefinable epoxy," *Journal of Micromechanics and Microengineering*, Vol. 11, pp. 263–269, 2001.
84. B.E.J. Alderman, et al., "Microfabrication of channels using an embedded mask in negative resist," *Journal of Micromechanics and Microengineering*, Vol. 11, pp. 703–705, 2001.
85. L.J. Guérin et al., Simple and low cost fabrication of embedded micro channels by using a new thick-film photoplastic, Proceedings of transducers '97, 9th international conference on solid-state sensors and actuators, Chicago, IL, 16–19 June, 1997, pp. 1419–1421.
86. Y.J. Chuang, et al., "A novel fabrication method of embedded micro-channels by using SU-8 thick-film photoresists," *Sensors and Actuators A*, Vol. 103, pp. 64–69, 2003.
87. F.E.H. Tay, et al., "A novel micro-machining method for the fabrication of thick-film SU-8 embedded micro-channels," *Journal of Micromechanics and Microengineering*, Vol. 11, pp. 27–32, 2001.
88. J. O'Brien, et al., "Advanced photoresist technologies for microsystems," *Journal of Micromechanics and Microengineering*, Vol. 11, pp. 353–358, 2001.
89. W. Qu, C. Wenzel and A. Jahn, "One-mask procedure for the fabrication of movable high-aspect-ratio 3D microstructures," *Journal of Micromechanics and Microengineering*, Vol. 8, pp. 279–283, 1998.
90. S. Roth, et al., "High aspect ratio UV photolithography for electroplated structures," *Journal of Micromechanics and Microengineering*, Vol. 9, pp. 105–108, 1999.
91. V. Conédéra, B. Le Goff and N. Fabre, "Potentialities of a new positive photoresist for the realization of thick moulds," *Journal of Micromechanics and Microengineering*, Vol. 9, pp. 173–175, 1999.
92. B. Loechel, "Thick-layer resists for surface micromachining," *Journal of Micromechanics and Microengineering*, Vol. 10, pp. 108–115, 2000.
93. D.F. Weston, et al., "Fabrication of microfluidic devices in silicon and plastic using plasma etching," *Journal of Vacuum Science and Technology B*, Vol. 19, pp. 2846–2851, 2001.
94. X. Wang, J. Engel and C. Liu, "Liquid crystal polymer (LCP) for MEMS: Processes and applications," *Journal of Micromechanics and Microengineering*, Vol. 13, pp. 628–633, 2003.
95. Y. Zhao and T. Cui, "Fabrication of high-aspect-ratio polymer-based electrostatic comb drives using the hot embossing technique," *Journal of Micromechanics and Microengineering*, Vol. 13, pp. 430–435, 2003.
96. T.Q. Truong and N.T. Nguyen, "A polymeric piezoelectric micropump based on lamination technology," *Journal of Micromechanics and Microengineering*, Vol. 14, pp. 632–638, 2004.
97. N.T. Nguyen, S.S. Ho and L.N. Low, "A polymeric microgripper with integrated thermal actuators," *Journal of Micromechanics and Microengineering*, Vol. 14, pp. 969–974, 2004.
98. A.B. Frazier and M.G. Allen, "Metallic microstructures fabricated using photosensitive polyimide electroplating molds," *Journal of Microelectromechanical Systems*, Vol. 2, no. 2, pp. 87–94, 1993.
99. T. Ito, et al., "Fabrication of microstructure using fluorinated polyimide and silicon-based positive photoresist," *Microsystem Technologies*, Vol. 6, pp. 165–168, 2000.
100. T. Stieglitz, "Flexible biomedical microdevices with double-sided electrode arrangements for neural applications," *Sensors and Actuators A*, Vol. 90, pp. 203–211, 2001.
101. S. Metz, R. Holzer and P. Renaud, "Polyimide-based microfluidic devices," *Lab on a Chip*, Vol. 1, no. 1, pp. 29–34, 2001.
102. E. Smela, "Microfabrication of Ppy microactuators and other conjugated polymer devices," *Journal of Micromechanics and Microengineering*, Vol. 9, pp. 1–18, 1999.
103. H.A. Reed, et al., "Fabrication of microchannels using polycarbonates as sacrificial materials," *Journal of Micromechanics and Microengineering*, Vol. 11, pp. 733–737, 2001.

104. D. Bhusari, et al., "Fabrication of air-channel structures for microfluidic, microelectromechanical, and microelectronic applications," *Journal of Micromechanics and Microengineering*, Vol. 10, pp. 400–408, 2001.
105. V. Piottter, et al., "Injection molding and related techniques for fabrication of microstructures," *Microsystem Technologies*, Vol. 4, pp. 129–133, 1997.
106. O. Larsson et al., Silicon based replication technology of 3D-microstructures by conventional cd-injection molding techniques, Proceedings of transducers '97, 9th international conference on solid-state sensors and actuators, Chicago, IL, 16–19 June, 1997, pp. 1415–1418.
107. M.S. Despa, K.W. Kelly and J.R. Collier, "Injection molding of polymeric LIGA HARMS," *Microsystem Technologies*, Vol. 6, pp. 60–66, 1999.
108. M. Niggemann, et al., "Miniaturized plastic micro plates for applications in HTS," *Microsystem Technologies*, Vol. 6, pp. 48–53, 1999.
109. A. Gerlach, et al., "Gas permeability of adhesives and their application for hermetic packaging of microcomponents," *Microsystem Technologies*, Vol. 7, pp. 17–22, 2001.
110. H. Becker and U. Heim, "Hot embossing as a method for the fabrication of polymer high aspect ratio structures," *Sensors and Actuators A*, Vol. 83, pp. 130–135, 2000.
111. M. Hecke, W. Bacher and K.D. Müller, "Hot embossing—the molding technique for plastic microstructures," *Microsystem Technologies*, Vol. 4, pp. 122–124, 1998.
112. P.F. Man, D.K. Jones and C.H. Mastrangelo, Microfluidic plastic capillaries on silicon substrates: A new inexpensive technology for bioanalysis chips, Proceedings of MEMS'97, 10th IEEE international workshop micro electromechanical system, Nagoya, Japan, 26–30 January, 1997, pp. 311–316.
113. Y. Xia and G.M. Whitesides, "Soft lithography," *Annual Review of Material Sciences*, Vol. 28, pp. 153–194, 1998.
114. D.C. Duffy, et al., "Rapid prototyping of microfluidic switches in poly (Dimethyl Siloxane) and their actuation by electro-osmotic flow," *Journal of Micromechanics and Microengineering*, Vol. 9, pp. 211–217, 1999.
115. T.S. Chin, "Permanent magnet films for applications in microelectromechanical systems," *Journal of Magnetism and Magnetic Materials*, Vol. 209, pp. 75–79, 2000.
116. M.R.J. Gibbs, "Applications of magMEMS," *Journal of Magnetism and Magnetic Materials*, Vol. 290–291, pp. 1298–1303, 2005.
117. S. Trolier-McKinstry and P. Muralt, "Thin film piezoelectrics for MEMS," *Journal of Electroceramics*, Vol. 12, pp. 7–17, 2004.
118. R.A. Dorey and R.W. Whatmore, "Electroceramic thick film fabrication for MEMS," *Journal of Electroceramics*, Vol. 12, pp. 19–32, 2004.
119. Y. Fu, H. Du, W. Huang, S. Zhang and M. Hui, "TiNi-based thin films in MEMS applications: a review," *Sensors and Actuators A*, Vol. 112, pp. 395–408, 2004.
120. K.Y. Lee, N. Labianca, S.A. Rishton, S. Zolgharnain, J.D. Gelorme, J. Shaw and T.H.P. Chang, "Micromachining applications of a high resolution ultra-thick photoresist," *J. Vac. Sci. Tech. B*, Vol. 13, pp. 3012–3016, 1995.
121. C.K. Malek and V. Saile, "Applications of LIGA technology to precision manufacturing of high-aspect-ratio micro-components and -systems: a review," *Microelectronics Journal*, Vol. 35, pp. 131–143, 2004.
122. A. Schoth, R. Förster and W. Menz, "Micro wire EDM for high aspect ratio 3D microstructuring of ceramics and metals," *Microsystem Technologies*, Vol. 11, pp. 250–253, 2005.
123. R. Schuster, V. Kirchner, P. Allongue and G. Ertl, "Electrochemical micromachining," *Science*, Vol. 289, pp. 98–101, 2000.
124. R. Wttrich and V. Fasciob, "Machining of non-conducting materials using electrochemical discharge phenomenon-an overview," *International Journal of Machine Tools & Manufacture*, Vol. 45, pp. 1095–1108, 2005.

125. S. Reyntjens and R. Puers, "A review of focused ion beam applications in microsystem technology," *Journal of Micromechanics and Microengineering*, Vol. 11, pp. 287–300, 2001.
126. B. Chichkov, et al., "Femtosecond, picosecond and nanosecond laser ablation of solids," *Applied Physics A*, Vol. 63, pp. 109–115, 1996.
127. R.A. Laws, A.S. Holmes and F.N. Goodall, "The formation of moulds for 3D microstructures using excimer laser ablation," *Microsystem Technologies*, Vol. 3, pp. 17–19, 1996.
128. E. Belloy, et al., "The introduction of powder blasting for sensor and microsystem applications," *Sensors and Actuators A*, Vol. 84, pp. 330–337, 2000.
129. H. Wensink, et al., "Mask materials for powder blasting," *Journal of Micromechanics and Microengineering*, Vol. 10, pp. 175–180, 2000.
130. S. Shlautmann, et al., "Powder-blasting technology as an alternative tool for microfabrication of capillary electrophoresis chips with integrated conductivity sensors," *Journal of Micromechanics and Microengineering*, Vol. 11, pp. 386–389, 2001.
131. S.H. Yeo and J.H. Choo, "Effects of rotor electrode in the fabrication of high aspect ratio microstructures by localized electrochemical deposition," *Journal of Micromechanics and Microengineering*, Vol. 11, pp. 435–442, 2001.
132. M. Stjernström and J. Roeraade, "Method for fabrication of microfluidic system in glass," *Journal of Micromechanics and Microengineering*, Vol. 8, pp. 33–38, 1998.
133. D.W. Matson et al., Laminated ceramic components for micro fluidic applications, SPIE Conference Proceeding Vol. 3877: microfluidic devices and systems II, Santa Clara, CA, 20–22 September, 1999, pp. 95–100.
134. P.M. Martin et al., Laser micromachined and laminated microfluidic components for miniaturized thermal, chemical and biological systems, SPIE Conference proceedings, Vol. 3680: Design, Test, and Microfabrication of MEMS and MOEMS, Paris, France, 30 March–1 April, 1999, pp. 826–833.
135. W.H. Ko, et al., "Bonding techniques for microsensors," Fung C.D., et al., *Micromachining and Micropackaging of Transducers*, Elsevier, Amsterdam, pp. 41–61, 1985.
136. M.V. Weckwerth, et al., "Epoxy bond and stop-etch (EBASE) technique enabling backside processing of (Al)GaAs heterostructures," *Superlattices Microstructures*, Vol. 20, no. 4, pp. 561–567, 1996.
137. H. Nguyen et al., A substrate-independent wafer transfer technique for surface-micromachined devices, Proceedings of MEMS'00, 13th IEEE international workshop micro electromechanical system, Miyazaki, Japan, 23–27 January, 2000, pp. 628–632.

## 4 Micromixers Based on Molecular Diffusion

---

The final stage in all micromixer types is molecular diffusion. This chapter discusses micromixers that rely entirely on diffusive transport. As pointed out in Chapter 2, diffusive mixing can be improved by increasing the interfacial area between the solute and solvent or by decreasing the striation thickness of these two phases. Based on the Fick's law, a large interfacial area, a large gradient, and a large diffusion coefficient can lead to a high diffusive flux. The small mixing length in micro scale actually leads to a higher concentration gradient and thus advantageous for diffusive mixing. Because the diffusion coefficient is a material constant, larger diffusion coefficients can only be achieved by a higher temperature and a lower viscosity. However, the resulting improvement in diffusive flux based on temperature and viscosity is not significant. Thus, mixing in micromixers based on molecular diffusion can only be optimized by geometrical designs for decreasing the striation thickness. The basic concepts for decreasing the striation thickness are parallel lamination, sequential lamination, sequential segmentation, segmentation based on injection, and focusing.

### 4.1 Parallel Lamination

#### 4.1.1 Mixers Based on Pure Molecular Diffusion

Parallel lamination increases the interfacial area and decreases the striation thickness by splitting the solute and solvent each into  $n$  substreams and rejoining them later in a single stream. Compared to a parallel mixer with two sub-streams, the mixing time or the required channel length can be reduced by a factor of  $n^2$ .

The simplest parallel lamination mixer is a straight channel with two inlets. The two inlets form a Y-shape or a T-shape. Thus, this mixer is often called a Y-mixer or T-mixer. The following analytical model describes the concentration distribution inside the straight channel. The model is two-dimensional and assumes that the microchannel is flat, Fig. 4.1. A flat channel has a height  $H$  much smaller than its width  $W$  ( $H \ll W$ ).

Example 2.4 already showed that different viscosities will cause different flow velocities on each side of the mixing channel. The mismatch in velocity will certainly affect the convective transport in the mixing channel. In the following model, the mixing streams are assumed to have the same viscosity and the same mean velocity  $\bar{u}$  to keep the model simple and analytically solvable. The mixer is a long channel with a width  $W$ . The inlets are defined with the inlet boundary

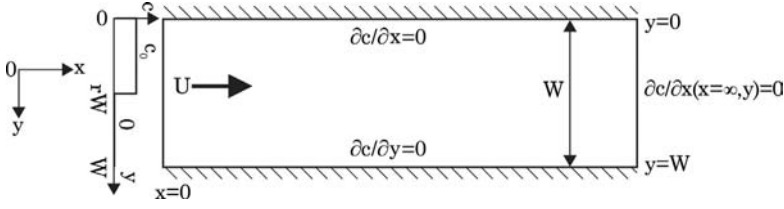


**Figure 4.1** The steady-state two-dimensional model of concentration distribution in a parallel lamination with two inlet streams.

on the left, while the outlet is defined with the exit boundary on the right side of the model. The inlets consist of a solute stream and a solvent stream. The solute stream has a concentration of  $c = c_0$  and a mass flow rate of  $\dot{m}_1$ . The solvent stream has a concentration of  $c = 0$  and a mass flow rate of  $\dot{m}_2$ . At an infinite exit position, the two streams are well mixed so that no concentration gradients exist ( $\partial c / \partial x = 0$ ,  $\partial c / \partial y = 0$ ).

With the above assumptions, the transport equation (2.22) can be reduced to the steady-state two-dimensional form:

$$\bar{u} \frac{\partial c}{\partial x} = D \left( \frac{\partial^2 c}{\partial x^2} + \frac{\partial^2 c}{\partial y^2} \right) \quad (4.1)$$

where  $D$  is the diffusion coefficient of the solute in the solvent. Assuming that both streams have the same viscosity and fluid density, the dimensionless interface location  $r$  is equal to the mass fraction  $\alpha$  of the solvent in the final mixture  $\alpha = \dot{m}_1 / (\dot{m}_1 + \dot{m}_2)$  ( $0 \leq \alpha \leq 1$ ). The mixing ratio of the solute and the solvent is therefore  $\alpha : (1 - \alpha)$ .

Introducing the dimensionless spacial variables  $x^* = x/W$ ,  $y^* = y/W$ , the dimensionless concentration  $c^* = c/c_0$ , and the Peclet number  $Pe = \bar{u}W/D$ , the transport equation has the dimensionless form:

$$Pe \frac{c^*}{\partial x^*} = \frac{\partial^2 c^*}{\partial x^{*2}} + \frac{\partial^2 c^*}{\partial y^{*2}}. \quad (4.2)$$

The corresponding boundary conditions for the inlets are:

$$c^*|_{(x^*=0, 0 \leq y^* < r)} = 1 \quad \text{and} \quad c^*|_{(x^*=0, r \leq y^* \leq 1)} = 0. \quad (4.3)$$

The exit boundary condition at  $(x^* = \infty)$  is:

$$\frac{\partial c^*}{\partial x^*} \Big|_{(x^*=\infty, 0 \leq y^* \leq 1)} = 0. \quad (4.4)$$

The wall conditions are:

$$\left. \frac{\partial c^*}{\partial y^*} \right|_{y^*=0,1} = 0. \quad (4.5)$$

The wall condition (4.5) is also the symmetry condition in the case of mixing with multiple streams. Thus this model can also be used for describing parallel lamination with more than two inlets. Using separation of variables and the corresponding boundary conditions (4.3), (4.4), and (4.5), the dimensionless concentration distribution in the mixing channel is:

$$\begin{aligned} c^*(x^*, y^*) = & \alpha + \frac{2}{\pi} \sum_{n=1}^{\infty} \frac{\sin \alpha \pi n}{n} \cos(n\pi y^*) \\ & \times \exp \left( - \frac{2n^2 \pi^2}{\text{Pe} + \sqrt{\text{Pe}^2 + 4n^2 \pi^2}} x^* \right) \\ & n = 1, 2, 3. \end{aligned} \quad (4.6)$$

The function of the concentration distribution (4.6) is described by a cosine function of the  $y^*$  axis and an exponential function of the  $x^*$  axis. It's clear that complete mixing is determined by the Peclet number in the exponential term. A large Peclet number requires a long mixing length along the  $x^*$  axis to make the exponential term approach zero. Physically, a large Peclet number means that convection dominates molecular diffusion and it would take longer for the solute to diffuse in the transversal direction across the mixing channel.

The solution of concentration distribution (4.6) clearly shows that mixing can be improved by operating the mixer at a small Peclet number. Since diffusion coefficient is a material property, a small Peclet number can be achieved with a low flow velocity or a small width. The small width and a thin striation thickness shorten the transversal transport of the solute. The simplest way to achieve thin striations is to split the solvent and solute into multiple mixing streams. As mentioned above, the solution (4.6) can also be extended to the case of multiple mixing streams. The wall boundary condition is identical to the symmetry condition in the middle of each stream. Thus, the concentration distribution (4.6) can be extended periodically along the transversal direction  $y$  or  $y^*$ . Considering the distance between two neighboring concentration extrema  $W_{\min, \max}$ , the Peclet number is evaluated as  $\text{Pe} = UW_{\min, \max}/D$ . Fig. 4.2 shows the typical theoretical and experimental results in a parallel lamination micromixer with two and three streams, respectively. The case of mixing with three streams is often referred to as hydrodynamic focusing, where the width of the middle stream and consequently the mixing time can be controlled by the sheath streams.



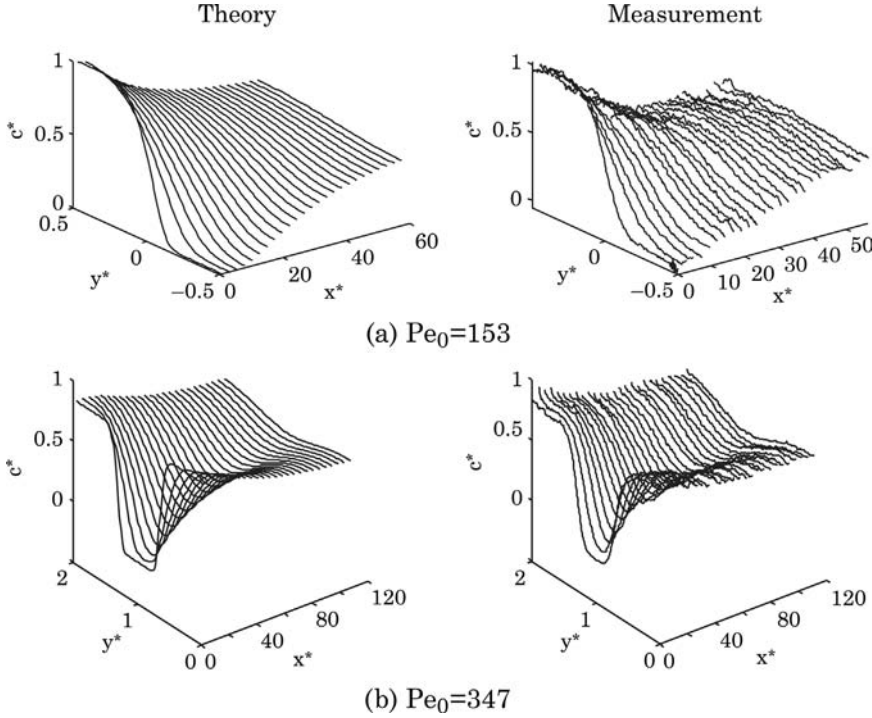


**Figure 4.2** Concentration distribution in a parallel lamination micromixer: (a) two streams; (b) three streams.

For mixing channels with aspect ratio on the order of unity, the velocity profile across the channel width is parabolic and not uniform as assumed for the analytical model. The transport equation has the form:

$$u(y, z) \frac{\partial c}{\partial x} = D \left( \frac{\partial^2 c}{\partial x^2} + \frac{\partial^2 c}{\partial z^2} \right) \quad (4.7)$$

where  $u(y, x)$  is the velocity profile of the channel cross section. Because convective transport is dominant in the flow direction  $x$ , diffusive term in  $x$  can be neglected. Equation (4.7) is nonlinear and can only be solved numerically [1].

The dispersion effect in parallel lamination is illustrated in Fig. 4.3. Due to the no-slip boundary condition, flow velocity at the channel wall grows from zero to the maximum value at the channel center. Near the channel wall, molecular diffusion dominates over convective transport leading to faster diffusion of the solvent into the solute and a cross-sectional concentration as depicted in Fig. 4.3 (a). The dispersion effect can be observed directly with confocal microscopy using Fluo-3 and calcium chloride ( $\text{CaCl}_2$ ) solution [2]. Fluo-3 is non-fluorescent, but forms a strongly fluorescent compound with calcium ions. Ismagilov et al. experimentally observed, and using dimensional analysis of equation (4.7)

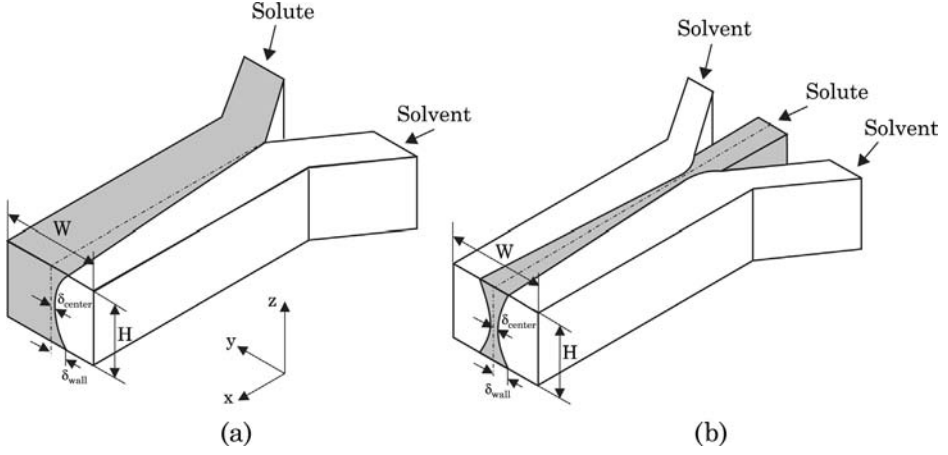


**Figure 4.3** Dispersion effect in parallel lamination (the interface is arbitrarily defined at 20% to 30% of the initial concentration): (a) Y-mixer; (b) hydrodynamic focusing.

derived, the following relation between the broadening width  $\delta$  and other parameters such as axial position  $x$ , channel height  $H$ , and the mean velocity  $\bar{u}$  at the channel center and at the channel wall, respectively:

$$\begin{aligned}\delta_{\text{center}}(x) &\propto \left(\frac{Dx}{\bar{u}}\right)^{\frac{1}{2}} \\ \delta_{\text{wall}}(x) &\propto \left(\frac{DHx}{\bar{u}}\right)^{\frac{1}{3}}.\end{aligned}\tag{4.8}$$

In equation (4.8), the term  $x/\bar{u}$  represents the mixing time. For a small channel height ( $H \ll W$ ), the difference between the broadening widths at the wall and at the channel center is quickly equalized due to diffusion in the  $z$  direction. The broadening effect is also less dramatic if the mixing time is short. Short mixing time means a high mean velocity  $\bar{u}$ , which makes convection dominate over molecular diffusion.

The same relation was obtained by Kamholz et al. based on numerical solutions of equation (4.7) [3]. The square-root relation at the center of the channel reflects the relation between the required length of the mixing channel and its width  $L_{\text{mixer}}/W \propto \text{Pe}_W$  (2.200) derived in Section 2.8. The one-third-power relation at the channel wall shows that mixing based on molecular diffusion is better in reality due to the distributed velocity profile. According to numerical results presented by Kamholz and Yager [3], the relations (4.8) are true for a short distance  $x$  near to the channel entrance. At an intermediate distance, the broadening width is proportional to the two-third-power of the distance  $x$ . At a long distance, the broadening width at both the wall and the channel center is again proportional to the square root of the distance  $x$ .

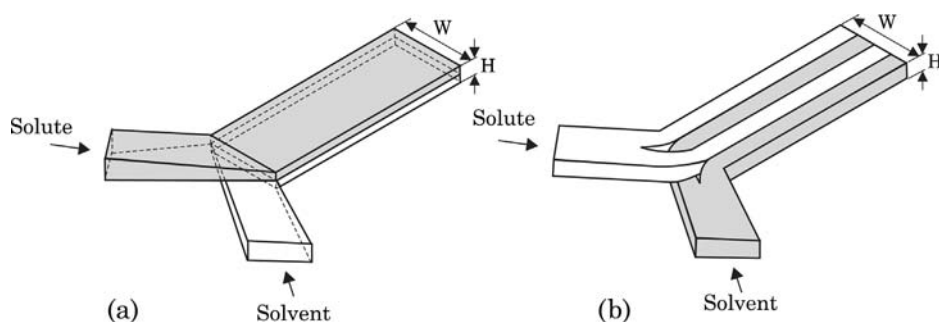


**Figure 4.4** Methods for shortening the striation thickness: (a) lamination over the channel height; (b) splitting and rejoining.

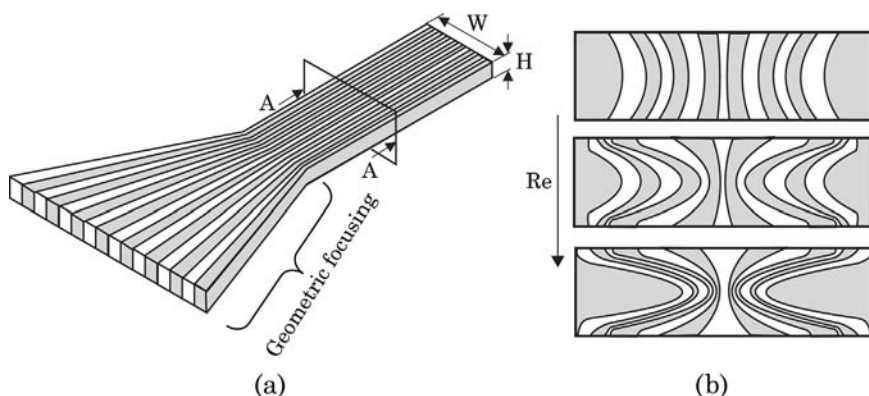


**Figure 4.5** Parallel lamination with geometric focusing: (a) concept; (b) distortion of the shape of lamellae (after [6]).

As mentioned earlier, fast mixing is achieved in parallel lamination micromixers by decreasing the mixing path and increasing the contact surface between the solvent and the solute. The simplest parallel lamination micromixers are T-mixers or Y-mixers. If the aspect ratio of the mixing channel is small ( $W \gg H$ ), the inlet streams of a T-mixer can be twisted and laminated as two thin liquid sheets to reduce the mixing path from the channel width  $W$  to the channel height  $H$  as shown in Fig. 4.4 (a). The interface between the two streams also increases by a factor of  $W/H$ . Hinsmann et al. introduced the streams into the mixing channel through a laminator consisting of many small channels [4]. The laminator keeps the flow at the entrance on track and minimizes instability.

The more common technique for shortening the striation thickness is splitting the solute and solvent into multiple streams and rejoining them through parallel lamination, Fig. 4.4. Combining parallel lamination with geometric focusing can be a powerful concept to improve micromixer's performance [5]. Fig. 4.5 (a) illustrates this concept. With a large number of streams, the outer streams may

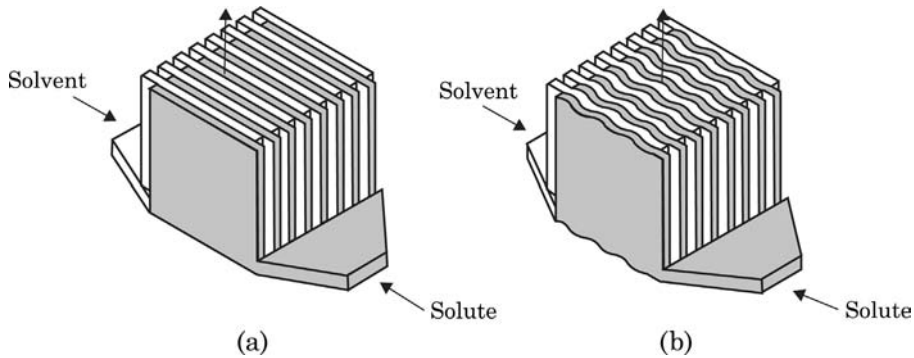


**Figure 4.6** Interdigitated parallel lamination: (a) with flat interface; (b) with corrugated interface.

experience a sharp bend during the focusing process. At small flow velocities or low Reynolds numbers, the bend has almost no effect on the shape of the lamellae. However, at high Reynolds number of the order of 10 or 100, secondary flow caused by inertial forces (see Section 2.4.2) distorts the shape of the lamellae [6]. Fig. 4.5 (b) shows schematically this change of concentration distribution at the cross section A-A in 4.5 (a). Inertial effects cause recirculation and chaotic advection, which improve mixing, and are discussed later in Section 4.1.2.

Splitting the solvent and the solute into multiple streams and rejoining them was realized in an interdigitating manner [7]. Fig. 4.6 depicts this mixing concept. Interdigitated lamination offers both thin striation thickness and a large interface between solute and solvent. The interfacial area can be further increased with the corrugated design shown in Fig. 4.6 (b). For instance, the design of Bessoth et al. can achieve full mixing with 32 streams only after a few milliseconds [8,9].

Another concept for reducing the mixing path in parallel lamination micromixers is hydrodynamic focusing. Knight et al. [10] reported a simple mixer with three inlets. The width of the solvent stream in the middle was focused by adjusting the pressure ratio between the sample flow and the sheath flow. Due to the very small focused width of the solvent stream, mixing time can be reduced to a few microseconds [12]. The same configuration of hydrodynamic focusing and mixing were used for cell infection [13]. Flow focusing will be discussed later in a separate section.

#### 4.1.2 Mixers Based on Inertial and Viscoelastic Instabilities

According to the dimensionless analysis (2.200) in Section 2.8, the required channel length is proportional to the Peclet number. In most cases, the required channel length is not practical for implementation in miniaturized platforms.

A short mixing channel can achieve full mixing at extremely high Reynolds numbers (more than 100) [14,15]. Secondary flow and chaotic advection improve mixing by further reducing the mixing path. Because of the required high Reynolds number and the high pressure, this mixing concept can only be implemented in mechanically rigid materials such as silicon, glass [15] and stainless steel. For instance, the mixer reported in [15] needs a flow velocity as high as 7.6 m/s at a pressure of up to 7 bars to achieve Reynolds numbers up to 500. The huge velocity gradient at the micro scale at high Reynolds number leads to the formation of extremely fast vortices. Improved mixing can be achieved with such vortices. Lim et al. [16] created vortices in a diamond-shaped cavity next to a straight microchannel with a flow velocity of 45 m/s. The corresponding Reynolds number in this case ( $Re = 245$ ) is very large for a typical micro scale application. Such vortex-based mixers require velocities as high as 10 m/s and pressure up to 15 bars.

Vortices caused by inertial effects can be generated at moderate Reynolds numbers with turns and geometrical obstacles. For instance, a simple  $90^\circ$  bend in the mixing channel can generate vortices at Reynolds numbers above 10 [14]. Mixing is achieved with a single bend at Reynolds numbers higher than 30. Obstacles such as structures on the channel wall [17] or throttling the channel entrance [18] can also introduce inertial instabilities into the standard T-mixer design. More details about this mixer type are discussed later in Chapter 5.

For simplification in modelling and characterization, most micromixers in this book are assumed to work with Newtonian fluids. As discussed previously, instability in Newtonian flows at high Reynolds number is caused by the competing viscous force and inertial force. Because most micromixers used for biochemical analysis work with relatively low flow rates, the Reynolds number would not be high enough for instability. Flow instabilities at low Reynolds number can be achieved using another force to replace the inertial force. In active micromixers, these forces are induced by external sources and are discussed later in Chapter 6. Diluting a small amount of highly deformable polymers would introduce elasticity to a fluid. This class of fluid is called viscoelastic and belongs to the non-Newtonian fluid family. The elastic forces caused by stretching and recoiling of the polymer molecules can work against the viscous forces to induce instabilities.

The shear stress in a viscoelastic fluid does not jump to zero after the disappearance of a driving force. Due to its elastic property, the stress decays with a characteristic time called the *relaxation time*. In macroscopic mixing devices, the relaxation time is much smaller than the characteristic residence time of the flow. Thus the elastic effect does not affect much the overall flow behavior. At the micro scale, the relaxation time and the characteristic residence time of the flow are of the same order. Thus, elastic forces become dominant.

As discussed in Section 2.5, the elastic effect of viscoelastic fluid flow can be characterized by the Weissenberg number, which is the ratio between the relaxation time and the characteristic residence time (2.125). Flows in microchannels have typically low Reynolds numbers and high Weissenberg

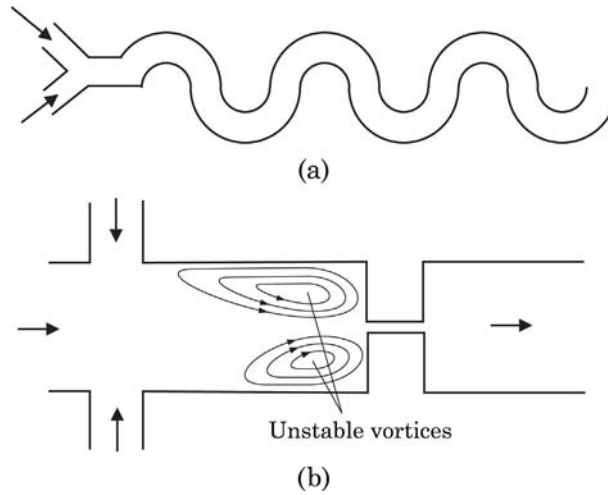


**Figure 4.7** Micromixers based on viscoelastic instability: (a) with repeated turns; (b) with a sudden contraction.

numbers. The ratio between these two numbers is called the elasticity number (2.127). Because of the low Reynolds number and the high Weissenberg number, elasticity numbers in microchannel can reach up to 100.

Groisman and Steinberg [19] use a mixer design with repeated circular turns to induce viscoelastic instability, Fig. 4.7. Because of the turn, instability is caused by a complex interplay between inertial, viscous, centrifugal, and viscoelastic forces. With a cross section of  $3 \text{ mm} \times 3 \text{ mm}$ , the mixing channel is large for common micro mixers. The viscoelastic fluid is a solution of 80 p.p.m polyacrylamide (PAA, molecular weight of  $1.8 \times 10^7$ ), 65% saccharose, and 1% NaCl in water. Good mixing was reported at an axial distance of about 41 cm from the entrance. However, with the relatively sharp turns  $W/R = 3/4.5$ , mixing can be achieved with Dean vortices as well (see Section 5.1.3).

Gan et al. [20] utilized viscoelastic instability at a sudden contraction to improve mixing. Good mixing was achieved at low Reynolds numbers ( $Re < 1$ ). The device was made of silicon. The microchannels have a depth of  $150 \mu\text{m}$ . The sudden constriction has dimensions of  $1000 \mu\text{m}:125 \mu\text{m}:1000 \mu\text{m}$ . The micromixer has the flow-focusing configuration. The fluid of the middle stream consists of 1 wt% polyethylene oxide (PEO) in 55 wt% glycerol-water. The fluid of the side streams consists of 0.1 wt% PEO in water. For a total flow rate of 12 ml/h, the corresponding Peclet number, Reynolds number, Weissenberg number, and Elasticity number are  $Pe = 49.4 \times 10^6$ ,  $Re = 0.06$ ,  $We = 278$ , and  $El = 5070$ , respectively. The very large Elasticity number shows that inertial forces are negligible compared to elastic forces. At this high elasticity number, unstable vortices appear before the constriction as depicted in Fig. 4.7 (b). The asymmetric vortices oscillate from side to side leading to

chaotic advection. Mixing was improved further by molecular-scale effects caused by stretched and collapsed polymer molecules.

## 4.2 Sequential Lamination

Sequential lamination segregates the joined stream into two channels, and rejoins them at the next transformation stage, Fig. 4.8. Because of these characteristics, sequential lamination is also called the split-and-recombine (SAR) concept [21]. Because the SAR process is similar to the stretching and folding of mixing fluids, this concept is also called the baker's transformation, or the Bernoulli transformation [22,23]. Considering the time-dependent striation thickness  $w(t)$  with the initial value  $w(0) = W$ , where  $W$  is the width of the microchannel, the decrease of striation thickness is determined by the function  $\alpha(t)$ :

$$\frac{d \ln w(t)}{dt} = -\alpha(t). \quad (4.9)$$

In chaotic advection, the function  $\alpha(t)$  is also called the stretching function and is positive. In the local coordinate system of the striation, the diffusion process is described by the normalized diffusion equation:

$$\frac{\partial c^*}{\partial t^*} = \frac{\partial^2 c^*}{\partial x^{*2}} \quad (4.10)$$

where the dimensionless space variable  $x^*$  and time  $t^*$  are defined as:

$$x^* = \frac{x}{w(t)} \quad (4.11)$$

and

$$t^* = \int_0^t \frac{D}{w(t')^2} dt'. \quad (4.12)$$

The penetration distance  $\delta$  in the  $(x^*, t^*)$  space is given by  $\delta x^* \sim t^{*1/2}$ . Thus the relation for the penetration distance  $\delta_x$  in the  $(x, t)$  space is:

$$\frac{\delta_x}{W \exp(-\alpha t)} = \left[ \frac{D}{W^2 2\alpha} (\exp 2\alpha t - 1) \right]^{\frac{1}{2}}. \quad (4.13)$$

Mixing is complete if  $\delta_x = w_{\text{final}}$ , when the diffusive penetration distance is of the same order as the striation thickness:

$$1 = \left[ \frac{D}{W^2 2\alpha} (\exp 2\alpha t - 1) \right]^{\frac{1}{2}}. \quad (4.14)$$

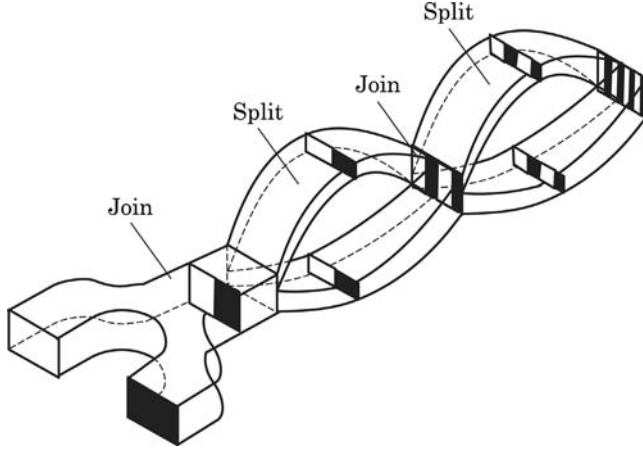


**Figure 4.8** Concept of sequential lamination.

The value of  $\alpha$  is inversely proportional to the shear rate  $\alpha \propto \bar{u}/W$ , thus  $Pe_W \propto \alpha W^2/D$ . At the fully mixed state  $[\exp(2\alpha t_{\text{final}}) \gg 1]$ , the required channel length of the mixer would be:

$$\frac{L_{\text{mixer}}}{W} \propto \ln Pe_W. \quad (4.15)$$

The transformations described above can be achieved either by sequential lamination or by chaotic advection. Sequential lamination can be implemented by forced splitting and lamination or by chaotic advection. Forced splitting and lamination are achieved at low Reynolds numbers with a complex channel design. Chaotic advection occurs at a higher Reynolds number and will be discussed later in Chapter 5. The implementation of the concept depicted in Fig. 4.8 is referred to as sequential lamination with vertical lamination and horizontal splitting. Similar transformations can be achieved with horizontal lamination and vertical splitting. This mixing concept requires relatively complicated three-dimensional fluidic structures. According to (2.201) and (2.202), the sequential concept results in much faster mixing compared to the parallel concept with the same device area. Due to their complex geometry, most of the reported sequential lamination mixers were fabricated in silicon, using bulk micromachining technologies, such as wet etching in KOH [24,25] or the deep reactive ion etching (DRIE) technique [26]. Polymeric micromachining is another alternative for making sequential lamination micromixers. Lamination of multiple polymer layers also allows making complex three-dimensional channel structures. Schoenfeld et al. [21] realized this mixing concept on PMMA. He et al. extended the concept of sequential lamination to electrokinetic flows [27].



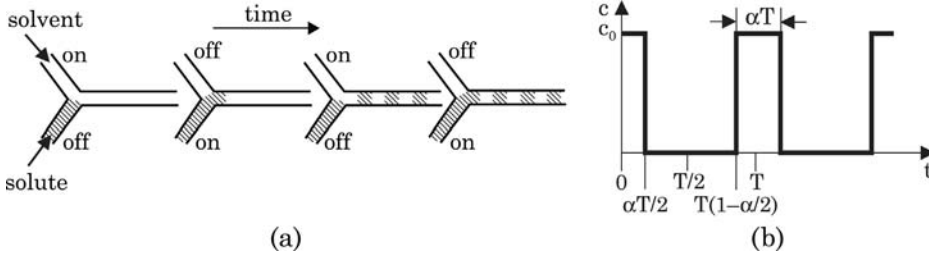


**Figure 4.9** Sequential segmentation: (a) alternate switching of the inlet streams; (b) switching ratio  $\alpha$  determines the mixing ratio.

### 4.3 Sequential Segmentation

Sequential segmentation is a process where the solvent and solute streams are broken up into segments along the axial direction. Because mixing occurs in the axial direction, axial dispersion may lead to faster mixing. According to Section 2.3, the axial dispersion coefficient may be several orders of magnitudes higher than pure molecular diffusion. Sequential segmentation is implemented by alternate switching of the inlet flows, Fig. 4.9 (a) [28]. Switching is realized by two inlet valves or by controlling the pumps of the mixing liquids. The mixing ratio can be adjusted by the switching ratio, Fig. 4.9 (b).

With a mean flow velocity  $\bar{u}$  of both fluids in the mixing channel and a switching period  $T$ , the characteristic mixing length is the segment length  $L = \bar{u}T$ , Fig. 4.10. The transport equation (2.22) can be reduced to the transient one-dimensional form [29]:

$$\frac{\partial c}{\partial t} + \bar{u} \frac{\partial c}{\partial x} = D^* \frac{\partial^2 c}{\partial x^2} \quad (4.16)$$

where  $D^*$  is the dispersion coefficient (see Section 2.3). The periodic boundary condition at the inlet ( $x = 0$ ) [Fig. 4.9 (b)] is:

$$c(t, 0) = \begin{cases} c_0 & 0 \leq t \leq \alpha T/2 \\ 0 & \alpha T/2 < t \leq T - \alpha T/2 \\ c_0 & T - \alpha T/2 < t \leq T \end{cases} \quad (4.17)$$

where  $c_0$ ,  $T$ , and  $\alpha$  are the initial concentration of the solute, the period of the segmentation, and the mixing ratio, respectively.

Normalizing the concentration by  $c_0$ , the spacial variable by  $L$ , and the time by  $T$  results in the dimensionless form of (4.16):

$$\frac{\partial c^*}{\partial t^*} = \frac{1}{Pe} \frac{\partial^2 c^*}{\partial x^{*2}} - \frac{\partial c^*}{\partial x^*} \quad (4.18)$$

where the star  $*$  denotes the dimensionless variables. The Peclet number is defined based on the characteristic mixing length  $L$  and the dispersion coefficient  $D^*$  as  $Pe = \bar{u}L/D^*$ . Because of the much higher effective diffusion coefficient at the same flow rate and Reynolds number, the Peclet number of parallel lamination is about two orders of magnitude higher than the Peclet number of a sequential segmentation. From (4.17), the corresponding dimensionless boundary condition is:

$$c^*(t^*, 0) = \begin{cases} 1 & 0 \leq t^* \leq \alpha/2 \\ 0 & \alpha/2 < t^* \leq 1 - \alpha/2 \\ 1 & 1 - \alpha/2 < t^* \leq 1. \end{cases} \quad (4.19)$$

Solving (4.18) with (4.19) and  $c^*(\infty) = \alpha$  results in the transient concentration distribution:

$$c^*(x^*, t^*) = \Re \left\langle \alpha + \sum_1^\infty \frac{2\sin(\alpha\pi n)}{\pi n} \times \left\{ \exp \left[ \frac{1}{2} (Pe - \sqrt{Pe^2 + 8\pi n Pe i}) x^* \right] \times \exp(2\pi t^* i) \right\} \right\rangle \quad (4.20)$$

where  $i$  is the imaginary unit and  $\Re$  indicates the real component of a complex number. Nguyen and Huang used piezoelectric discs as active valves [30]. The mixer was fabricated by a  $\text{CO}_2$  laser and hot lamination of the multiple polymer sheets. Hydrodynamic focusing was used to eliminate the side effect of Taylor-Aris dispersion in a rectangular microchannel.

## 4.4 Segmentation Based on Injection

Segmentation based on injection introduces the solvent into the solute flow through a nozzle array. This concept also decreases the mixing path and increases the interfacial area between the solvent and the solute. Fig. 4.11 shows a simple two-dimensional model of the concentration distribution around a single circular nozzle. The nozzle has a radius of  $R$ . The mass flow rate of the solute is  $\dot{m}_1$  (e.g., kilograms per second), while the mass flow rate of the solvent is  $\dot{m}_2$  and an inlet concentration of  $c_0$ . The solvent flow has a uniform velocity of  $\bar{u}$  and a concentration of  $c = 0$ .

Considering a steady-state, two-dimensional problem and neglecting the source term, the transport equation reduces to the form:

$$\frac{\bar{u}}{D} \frac{\partial c}{\partial x} = \frac{\partial^2 c}{\partial x^2} + \frac{\partial^2 c}{\partial y^2}. \quad (4.21)$$

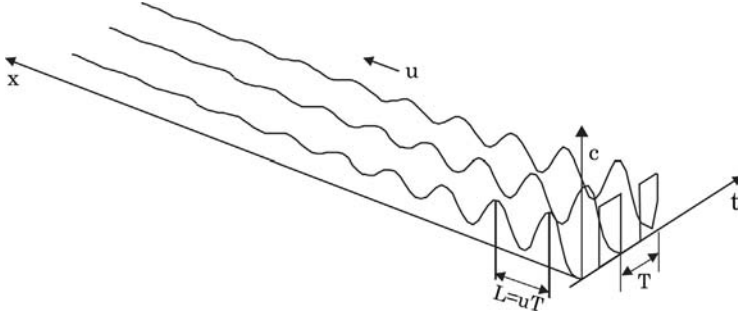


**Figure 4.10** Transient one-dimensional model of sequential segmentation.

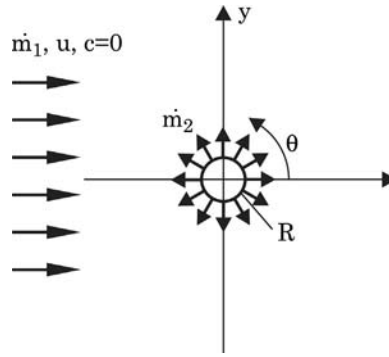


**Figure 4.11** Two-dimensional model of the concentration distribution around a circular nozzle.

The general solution of (4.21) is the product of a velocity-dependent term and a symmetric term  $\Gamma$ :

$$c = \exp\left(\frac{\bar{u}x}{2D}\right)\Gamma(x, y). \quad (4.22)$$

Substituting (4.22) in (4.21) results in:

$$\left(\frac{\bar{u}}{2D}\right)\Gamma = \frac{\partial^2 \Gamma}{\partial x^2} + \frac{\partial^2 \Gamma}{\partial y^2}. \quad (4.23)$$

Defining the variable  $r = \sqrt{x^2 + y^2}$  in the polar coordinate system shown in Fig. 4.11, the boundary condition of the solute flow is, after Fick's law:

$$\left.\frac{dc}{dr}\right|_{r=R} = -\frac{j}{D} = -\frac{\dot{m}_2}{2\pi RHD} \quad (4.24)$$

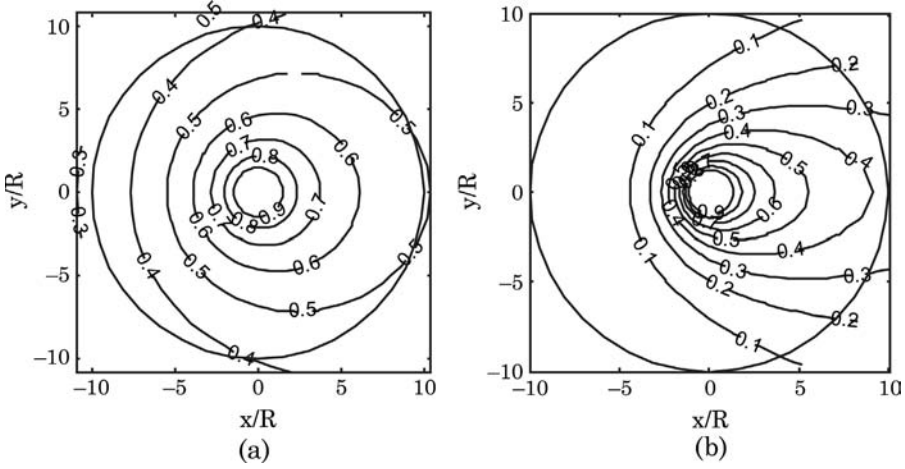


**Figure 4.12** Dimensionless concentration distribution around the injection nozzle: (a)  $Pe=0.1$ ; (b)  $Pe=1$ .

where  $H$  is the height of the mixing chamber above the injection nozzle. Assuming a small mixing ratio ( $\dot{m}_2 \ll \dot{m}_1$ ), the following boundary condition is acceptable for (4.23):

$$\left. \frac{d\Gamma}{dr} \right|_{r=\pm\infty} = 0. \quad (4.25)$$

Equation (4.23) can be rewritten for the polar coordinate system as:

$$\frac{d^2\Gamma}{dr^2} + \frac{1}{r} \frac{d\Gamma}{dr} - \left( \frac{\bar{u}}{2D} \right)^2 \Gamma = 0. \quad (4.26)$$

The solution of (4.26) is the modified Bessel function of the second kind and zero order:

$$\Gamma = K_0[\bar{u}r/(2D)]. \quad (4.27)$$

The solution of (4.21) with the previously-mentioned boundary conditions is:

$$c(r, \theta) = \frac{\dot{m}_2 D}{\pi R H} \bar{u}^{-1} \frac{K_0[\bar{u}r/(2D)]}{K_1[\bar{u}R/(2D)] - K_0[\bar{u}R/(2D)] \cos \theta} \frac{\exp[\bar{u}r \cos \theta / (2D)]}{\exp[\bar{u}R \cos \theta / (2D)]} \quad (4.28)$$

where  $\theta$  is the angular variable of the polar coordinate system.

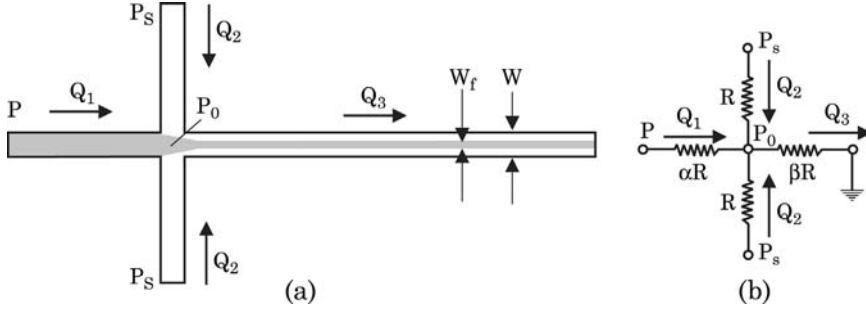


**Figure 4.13** Focusing concepts: (a) geometric focusing; and (b) hydrodynamic focusing.

Introducing the Peclet number  $Pe = 2\bar{u}R/D$ , the dimensionless radial variable  $r^* = r/R$ , and the dimensionless concentration:

$$c^* = \frac{c}{2\dot{n}_2/(\pi H)} \quad (4.29)$$

the dimensionless form of (4.28) is:

$$c^*(r^*, \theta) = \frac{K_0(Pe r^*/4)/Pe}{K_1(Pe/4) - K_0(Pe/4)\cos\theta} \{\exp[Pe(r^* - 1)/4]\}^{\cos\theta} \quad (4.30)$$

where  $K_1$  is the modified Bessel function of the second kind and first order. Fig. 4.12 shows the typical dimensionless concentration distribution around a single injection nozzle at different Peclet numbers.

## 4.5 Focusing of Mixing Streams

### 4.5.1 Streams with the Same Viscosity

Hydrodynamic focusing reduces the mixing path by decreasing the width of the solute flow. Two solvent streams work as sheath flows in this concept, Fig. 4.13 (a). Knight et al. [10] reported detailed experimental results for hydrodynamic focusing. However, the theoretical model reported in [10] was erroneous. The correct model is presented as follows:

If the sheath streams have the same viscosity as the sample flow and all liquids are incompressible, the effect of hydrodynamic focusing can be represented by a simple network model. Assuming that the flow is laminar, the pressure difference across a microchannel is proportional to the flow rate. Fig. 4.13 (b) shows the network model of hydrodynamic focusing, where microchannels are represented by fluidic resistances. For simplicity, we further assume that both sheath microchannels have the same fluidic resistance of  $R$ ,

which is defined as the quotient between the applied pressure difference and the flow rate  $R = \Delta p / \dot{Q}$ . The resistance of the inlet microchannel and the mixing microchannel are  $\alpha R$  and  $\beta R$ , respectively. The factors  $\alpha$  and  $\beta$  are determined by geometry parameters such as shape and size of channel cross section as well as channel length. Taking the exit pressure as the reference, the relations between the pressures at sample inlet, sheath flow inlets, and flow rates are given by the equation system:

$$\begin{cases} \dot{Q}_1 + 2\dot{Q}_2 = \dot{Q}_3 \\ p - p_0 = \alpha R \dot{Q}_1 \\ p_s - p_0 = R \dot{Q}_2 \\ p_0 = \beta R \dot{Q}_3 \end{cases} \quad (4.31)$$

where  $p$ ,  $p_s$ ,  $p_0$  are the pressures at the sample inlet, at the sheath flow inlet and at the junction, respectively. The flow rates through the fluidic resistances are  $\dot{Q}_1$ ,  $\dot{Q}_2$ , and  $\dot{Q}_3$ . Eliminating  $\dot{Q}_3$  from the equation system leads to:

$$\begin{cases} p = p_0 + \alpha R \dot{Q}_1 \\ p_s = p_0 + R \dot{Q}_2 \\ p_0 = \beta R \dot{Q}_3 \end{cases} \quad (4.32)$$

The ratio between the sheath flow pressure and the sample pressure  $r = p_s/p$  can be derived as follows:

$$r = \frac{p_s}{p} = \frac{\beta \dot{Q}_1 + (2\beta + 1) \dot{Q}_2}{(\beta + \alpha) \dot{Q}_1 + 2\beta \dot{Q}_2}. \quad (4.33)$$

The maximum and minimum values of the pressure ratio is subsequently determined by setting  $\dot{Q}_1 = 0$  and  $\dot{Q}_2 = 0$ , respectively:

$$\begin{aligned} r_{\max} &= \frac{2\beta + 1}{2\beta} \\ r_{\min} &= \frac{\beta}{\beta + \alpha}. \end{aligned} \quad (4.34)$$

With the focusing width  $W_f$  and the channel width  $W$ , the dimensionless focusing width  $W_f^*$  can be determined as:

$$W_f^* = \frac{W_f}{W} = \frac{\dot{Q}_1}{\dot{Q}_1 + 2\dot{Q}_2} = \frac{1}{2\dot{Q}_2/\dot{Q}_1 + 1}. \quad (4.35)$$

The ratio  $\dot{Q}_2/\dot{Q}_1$  can be solved as an explicit function of  $\alpha$ ,  $\beta$  and  $r$  from (4.32)

$$\frac{\dot{Q}_2}{\dot{Q}_1} = \frac{\beta - r(\alpha + \beta)}{2\beta r - 2\beta - 1} \quad (4.36)$$

leading to:

$$W_f^* = \frac{1 + 2\beta - 2\beta r}{1 + 2\alpha r}. \quad (4.37)$$

**Example 4.1** (*Network model for hydrodynamic focusing*). The microchannel network depicted in 4.13 is made in silicon and glass by deep reactive ion etching and anodic bonding. The microchannel has a width of 100  $\mu\text{m}$  and a height of 10  $\mu\text{m}$ . The three inlet channels are 5 mm long, while the mixing channel is 20 mm long. What is the range of pressure ratio between the sheath flow and the sample flow? What is the required pressure ratio for a focusing width of 1  $\mu\text{m}$ ?

**Solution.** With a low aspect ratio  $h = H/W = 0.1$ , the relation between the flow rate and the pressure derived in Example 2.3 can be used:

$$\dot{Q} \approx \frac{H^3 W \Delta p}{12\mu L} (1 - 0.630h).$$

Thus, the fluidic resistance of the microchannel with a length  $L$  is

$$R = \frac{\Delta p}{\dot{Q}} = \frac{12\mu L}{1 - 0.63h} \frac{H^3}{W}.$$

Because the cross section of the microchannel network remains constant, the fluidic resistance is proportional to the channel length. From the geometry of the given channel network, we have:

$$\alpha = \frac{5 \text{ mm}}{5 \text{ mm}} = 1$$

$$\beta = \frac{20 \text{ mm}}{5 \text{ mm}} = 4.$$

The maximum and minimum pressure ratios are:

$$r_{\max} = \frac{2\beta + 1}{2\beta} = \frac{2 \times 4 + 1}{2 \times 4} = 1.125$$

$$r_{\min} = \frac{\beta}{\beta + \alpha} = \frac{4}{4 + 1} = 0.8.$$

For a focusing width of  $W_f = 1 \mu\text{m}$  we have:

$$\begin{aligned} \frac{W_f}{W} &= \frac{1 + 2\beta - 2\beta r}{1 + 2\alpha r} \\ \frac{1}{100} &= \frac{1 + 2 \times 4 - 2 \times 4r}{1 + 2 \times 1r} = \frac{9 - 8r}{1 + 2r}. \end{aligned}$$

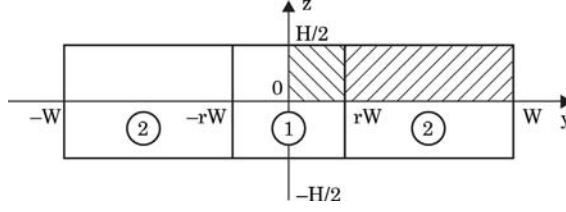


**Figure 4.14** Analytical model for two-phase focusing.

Solving the above linear equation results in the required pressure ratio for a focused width of  $1\text{ }\mu\text{m}$ :

$$r = \frac{901}{802}.$$

#### 4.5.2 Streams with Different Viscosities

The following model analyzes the effect of hydrodynamic focusing for reducing the width of the mixing streams. In the model, the sample stream is sandwiched between two identical sheath streams (Fig. 4.14). The sample stream and the sheath stream are assumed to be immiscible. Fig. 4.14 shows the geometry of the channel cross section with the above two phases. The channel has a width  $2W$  and a height  $H$ . The position of the interface is  $rW$ . Since the model is symmetrical regarding the  $y$ -axis and  $z$ -axis, only one-fourth of the cross section needs to be considered [11].

The velocity distribution  $u_1$  and  $u_2$  in the channel can be described by the Navier-Stokes equations:

$$\begin{cases} \frac{\partial^2 u_1}{\partial y^2} + \frac{\partial^2 u_1}{\partial z^2} = \frac{1}{\mu_1} \frac{\partial p}{\partial x} \\ \frac{\partial^2 u_2}{\partial y^2} + \frac{\partial^2 u_2}{\partial z^2} = \frac{1}{\mu_2} \frac{\partial p}{\partial x} \end{cases} \quad (4.38)$$

where indices 1 and 2 describe the sample flow and the sheath flow, respectively. In (4.38)  $\mu_1$  and  $\mu_2$  are the viscosities of the sample fluid and of the sheath fluid. Normalizing the velocity by a reference velocity  $u_0$ , and the coordinates by  $W$ , leads to the dimensionless model:

$$\begin{cases} \frac{\partial^2 u_1^*}{\partial y^{*2}} + \frac{\partial^2 u_1^*}{\partial z^{*2}} = P' \\ \frac{\partial^2 u_2^*}{\partial y^{*2}} + \frac{\partial^2 u_2^*}{\partial z^{*2}} = P'. \end{cases} \quad (4.39)$$



With  $P' = \frac{W}{\mu_1 u_0} \frac{\partial p}{\partial x^*}$ ,  $\beta = \mu_2/\mu_1$ , and  $\theta = (2n-1)\pi/h$ , the solutions of (4.39) have the forms ( $0 < y^* < 1$ ,  $0 < z^* < h/2$ ):

$$\begin{cases} u_1^*(y^*, z^*) = P' \left[ \frac{z^{*2} - h^2/4}{2} + \sum_{n=1}^{\infty} \cos \theta z^* (A_1 \cosh \theta y^* + B_1 \sinh \theta y^*) \right] \\ u_2^*(y^*, z^*) = \frac{P'}{\beta} \left[ \frac{z^{*2} - h^2/4}{2} + \sum_{n=1}^{\infty} \cos \theta z^* (A_2 \cosh \theta y^* + B_2 \sinh \theta y^*) \right]. \end{cases} \quad (4.40)$$

The no-slip conditions at the wall are

$$u_2^*(1, z^*) = 0. \quad (4.41)$$

The symmetry condition at the  $z^*$ -axis is:

$$\left. \frac{\partial u_1^*}{\partial y^*} \right|_{y^*=0} = 0. \quad (4.42)$$

At the interface between the sample flow and the sheath flow, the velocity and the shear rate are continuous:

$$\begin{cases} u_2^*(r, z^*) = u_1^*(r, z^*) \\ \left. \frac{\partial u_1^*}{\partial y^*} \right|_{y^*=r} = \beta \left. \frac{\partial u_2^*}{\partial y^*} \right|_{y^*=r}. \end{cases} \quad (4.43)$$

For a flat channel ( $h \ll 1$ ), the position of the interface can be estimated as:

$$r = \frac{1}{1 + 2\beta\kappa} \quad (4.44)$$

where  $\kappa = \dot{m}_2/\dot{m}_1$  is the flow rate ratio between the sheath streams and the mixing streams. A Fourier analysis with the above boundary conditions results in the coefficients of (4.40):

$$\begin{aligned} A_1 = & A_0 [\beta \sinh \theta r \cosh^2 \theta r \cosh \theta - \sinh^3 \theta r \cosh \theta \\ & - (\beta - 1) \sinh^2 \theta r \sinh \theta \cosh \theta - (\beta - 1) \sinh^2 \theta r (\cosh \theta - \cosh \theta r) \\ & + (\beta - 1) \sinh \theta r \cosh \theta r \cosh \theta (\cosh \theta - \cosh \theta r)] / \\ & [\beta \cosh^2 \theta r \sinh \theta r \cosh^2 \theta - \sinh^3 \theta r \cosh^2 \theta \\ & - (\beta - 1) \sinh^2 \theta r \cosh \theta r \sinh \theta \cosh \theta] \end{aligned}$$

$$\begin{aligned}
A_2 &= A_0 [\beta \cosh^2 \theta r \cosh \theta - \sinh^2 \theta r \cosh \theta \\
&\quad - (\beta - 1) \sinh \theta r \cosh \theta r \sinh \theta \\
&\quad - (\beta - 1) \sinh \theta r (\cosh \theta - \cosh \theta r)] / [\beta \cosh^2 \theta r \sinh^2 \theta \\
&\quad - \sinh^2 \theta r \cosh^2 \theta - (\beta - 1) \sinh \theta r \cosh \theta r \sinh \theta \cosh \theta] \\
B_1 &= 0 \\
B_2 &= A_0 [(\beta - 1) \sinh \theta r (\cosh \theta - \cosh \theta r)] / [\beta \cosh^2 \theta r \cosh \theta \\
&\quad - \sinh^2 \theta r \cosh \theta - (\beta - 1) \sinh \theta r \cosh \theta r \sinh \theta]
\end{aligned} \tag{4.45}$$

where  $A_0 = (-1)^{n+1} \frac{4h^2}{(2n-1)^3 \pi^3}$ . Fig. 4.15 shows the typical dimensionless velocity distribution inside the flow channel for the same flow rate in all streams ( $\kappa = 1$ ). The theoretical model is depicted with the solid lines in Fig. 4.15. The velocity of the sample flow is lower if the sample flow is more viscous than the sheath flow ( $\beta < 1$ ), Fig. 4.15 (a). If the sheath flows are more viscous ( $\beta > 1$ ), the sample flow is faster, Fig. 4.15 (b).

### 4.5.3 Combination of Hydrodynamic Focusing and Sequential Segmentation

Both hydrodynamic focusing and sequential segmentation can be combined to improve convective/diffusive mixing in a microchannel [29]. The concept reduces mixing paths in both transversal and axial directions. Fig. 4.16 describes this mixing concept. The micromixer has four inlets and one outlet. Two inlets are used for the sheath flows. The middle two inlets are used for sequential segmentation. Solvent and solute are switched alternately, so that segments of them are formed in the focused stream. The final mixing ratio is determined by both the focusing ratio of the inlet flows and the switching ratio of the two focused flows.

The analytical model assumes a rectangular microchannel with width  $W$  and height  $H$ . For a microchannel with low aspect ratio ( $W \gg H$ ), the flow inside the microchannel is similar to that between two parallel plates. The model assumes a uniform velocity profile in the transversal direction ( $y$ -axis) and a pressure-driven velocity profile in the channel height ( $z$ -axis):

$$u(z) = 6\bar{u} \left(1 - \frac{z}{H}\right) \frac{z}{H} \tag{4.46}$$

where  $\bar{u}$  is the mean velocity in the flow direction along the  $x$ -axis, as shown in Fig. 4.16 (a). The parabolic velocity profile causes the so-called Taylor-Aris dispersion, which can be described by an effective diffusion coefficient  $D^*$ . According to Section 2.3, the effective diffusion coefficient in the axial direction can be determined as:

$$D^* = D + \frac{H^2 U^2}{210D} \tag{4.47}$$

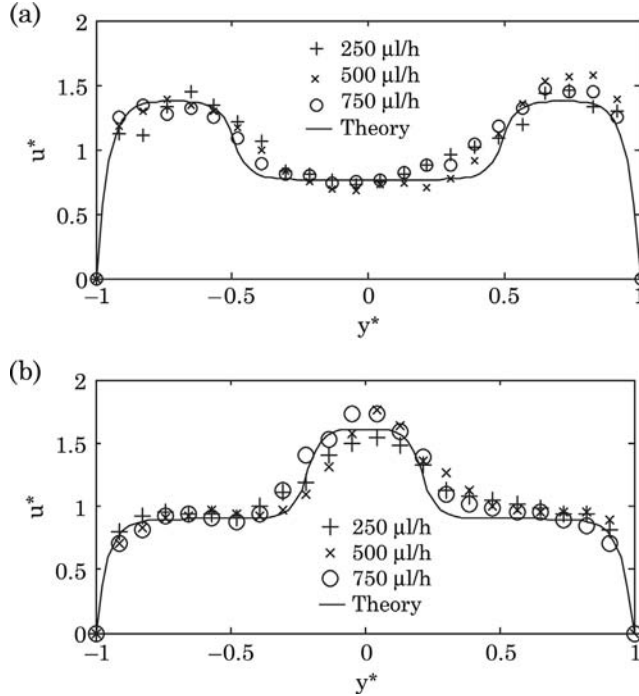


**Figure 4.15** The dimensionless velocity profile ( $h = 0.1$ ,  $\kappa = 1$ ): (a)  $\beta = 1/1.8$ ; (b)  $\beta = 1.8$ .

where  $D$  is the molecular diffusion coefficient, which is characteristic for transversal ( $y$ -axis) diffusion in our model. The dispersion model (4.47) assumes a position far away from the entrance. This assumption is only true if the position of  $x$  is long enough for completing diffusion across the channel height ( $x \gg UH^2/D$ ).

Fig. 4.16 (a) shows the two-dimensional model of the mixing concept based on hydrodynamic focusing and sequential segmentation. Assuming that all the liquids involved in the system have the same viscosity, the velocity in the mixing channel is uniform across all streams. The focusing ratio  $\beta = b/W$  can be adjusted by the flow rate ratio between the sheath streams and the focused streams. Considering the above effective diffusion coefficient in the axial direction (4.47) and the molecular diffusion coefficient in the transversal direction, the analytical model for combined hydrodynamic focusing and sequential segmentation in the domain depicted in Fig. 4.16 (a) can be described by a transient two-dimensional transport equation:

$$\frac{\partial c}{\partial t} + \bar{u} \frac{\partial c}{\partial x} = D^* \frac{\partial^2 c}{\partial x^2} + D \frac{\partial^2 c}{\partial y^2} \quad (4.48)$$

where  $c$  is the concentration of the solute. The mixing channel is assumed to be two-dimensional with width  $W$ . The width of the focused stream is  $b$ , Fig. 4.16 (a). The transient inlet conditions at ( $x = 0$ ) are depicted in Fig. 4.16 (b)

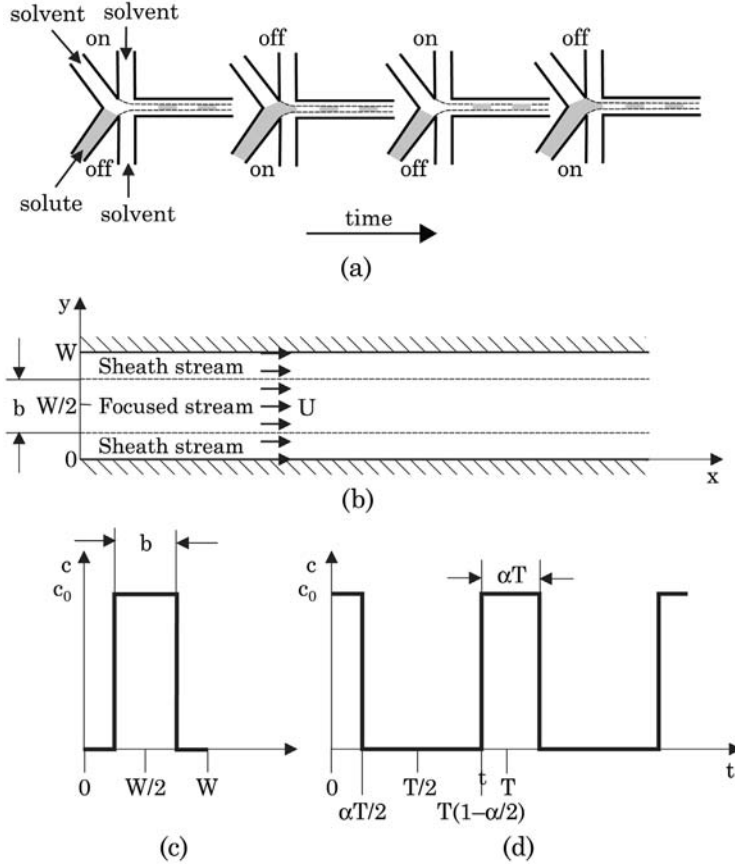


**Figure 4.16** Mixing in a microchannel based on hydrodynamic focusing and sequential segmentation: (a) the concept, (b) the two-dimensional model,  $x$  is the axial direction,  $y$  is the transversal direction; (c) the boundary conditions at  $t = 0$ ,  $x = 0$ ; (d) the transient conditions at  $x = 0$ ,  $y = W/2$ .

and (c). This condition can be formulated as a function of both  $y$  and  $t$ :

$$c(x = 0) = r(y)s(t) \quad (4.49)$$

where

$$r(y) = \begin{cases} 0, & 0 \leq y < W/2 - b/2 \\ 1, & W/2 - b/2 \leq y \leq W/2 + b/2 \\ 0, & W/2 + b/2 \leq y < W \end{cases} \quad (4.50)$$

and

$$s(t) = \begin{cases} c_0, & 0 \leq t < \alpha T/2 \\ 1, & \alpha T/2 \leq t \leq T - \alpha T/2 \\ c_0, & T - \alpha T/2 < t \leq T \end{cases} \quad (4.51)$$

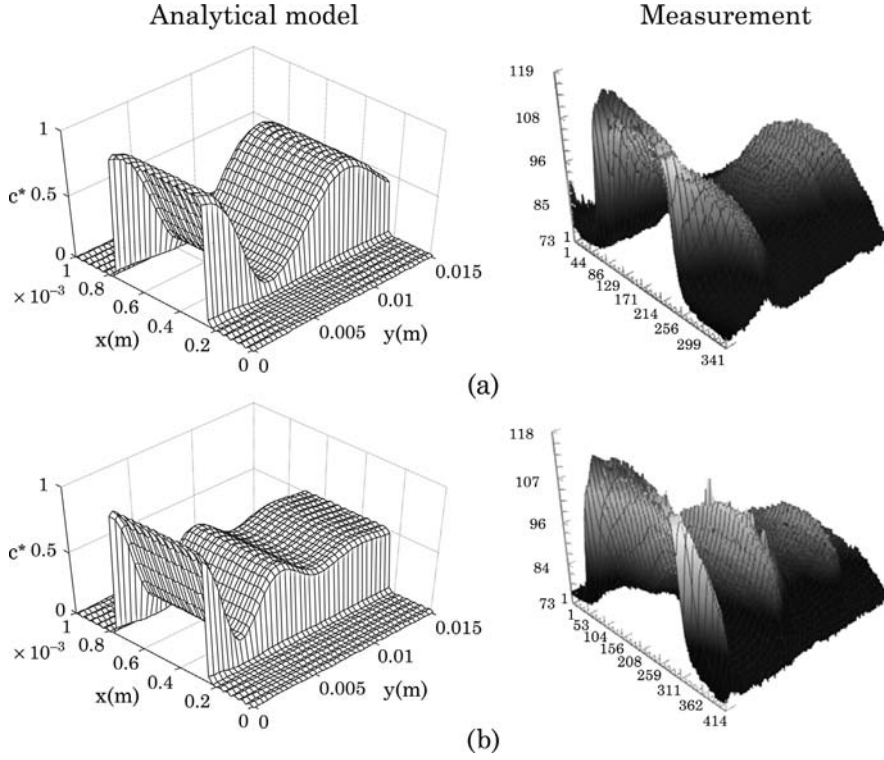


**Figure 4.17** Concentration distribution of the mixing concept based on hydrodynamic focusing and sequential segmentation: (a)  $f = 1$  Hz,  $Pe = 68,587$ ; (b)  $f = 2$  Hz,  $Pe = 34,294$ .

where  $T$  is the time period of the switching process and  $\alpha$  is the switching ratio. The switching frequency is then  $f = 1/T$ . The final mixed concentration can be adjusted by both the focusing ratio  $\beta = b/W$  and the switching ratio  $\alpha$ . The expected concentration at the end of a long mixing channel is  $c(x = \infty) = \alpha\beta c_0$ .

Normalizing spacial variables by the segment length  $L = \bar{u}T$ , the time by the switching period  $T$ , and the concentration by the initial solute concentration  $c_0$ :  $x^* = x/(UT)$ ,  $y^* = y/UT$ ,  $W^* = W/UT$ ,  $t^* = t/T$ ,  $c^* = c/c_0$ , the transport equation (4.48) has the dimensionless form:

$$\frac{\partial c^*}{\partial t^*} = \frac{1}{Pe} \left( \gamma \frac{\partial^2 c^*}{\partial x^{*2}} + \frac{\partial^2 c^*}{\partial y^{*2}} \right) - \frac{\partial c^*}{\partial x^*} \quad (4.52)$$

where  $\gamma$  is the ratio of the effective diffusion coefficient  $D^*$  in axial direction to the molecular diffusion coefficient  $D$  in the transverse direction:

$$\gamma = \frac{D^*}{D} = 1 + \frac{H^2 U^2}{210 D^2} \quad (4.53)$$

and  $Pe = UL/D = U^2T/D$  is the Peclet number defined based on the segment length  $L$ . Because the concentration field at the entrance does not meet the condition of the Taylor-Aris dispersion model, we should consider two asymptotic cases of no dispersion ( $\gamma = 1$ ) and with dispersion far away from the entrance ( $\gamma \gg 1$ ). The dimensionless inlet condition is:

$$c^*(x^* = 0) = r^*(y^*)s^*(t^*) \quad (4.54)$$

where  $r^*$  and  $s^*$  are:

$$r^*(y^*) = \begin{cases} 0, & 0 \leq y^* < W^*/2 - \beta W^*/2 \\ 1, & W^*/2 - \beta W^*/2 \leq y^* \leq W^*/2 + \beta W^*/2 \\ 0, & W^*/2 + \beta W^*/2 \leq y^* < W^* \end{cases} \quad (4.55)$$

and

$$s^*(t^*) = \begin{cases} 1, & 0 \leq t^* < \alpha/2 \\ 0, & \alpha/2 \leq t^* \leq 1 - \alpha/2 \\ 1, & 1 - \alpha/2 < t^* \leq 1. \end{cases} \quad (4.56)$$

The boundary conditions at the channel walls are:

$$\frac{\partial c^*}{\partial y^*} \Big|_{y^*=0} = \frac{\partial c^*}{\partial y^*} \Big|_{y^*=W^*} = 0. \quad (4.57)$$

Using the method of separation of variables and the above conditions, the solution of (4.52) is:

$$\begin{aligned} c^*(x^*, y^*, t^*) = & A_{00} \\ & + \sum_{n=1}^{\infty} A_{0n} \Re \left\{ \exp \left[ \frac{1}{2\gamma} (Pe - \sqrt{Pe^2 + 8\gamma Pen\pi i}) x^* \right] \exp(i2n\pi t^*) \right\} \\ & + \sum_{m=1}^{\infty} A_{m0} \left\{ \exp \left[ \frac{1}{2\gamma} \left( Pe - \sqrt{Pe^2 + 4 \left( \frac{m\pi}{W^*} \right)^2} \right) x^* \right] \cos \left( \frac{m\pi y^*}{W^*} \right) \right\} \\ & + \sum_{n=1}^{\infty} \sum_{m=1}^{\infty} A_{mn} \Re \left\{ \exp \left[ \frac{1}{2\gamma} \left( Pe - \sqrt{Pe^2 + 8\gamma Pen\pi i + \left( \frac{m\pi}{W^*} \right)^2} \right) x^* \right] \right. \\ & \quad \left. \times \cos \left( \frac{m\pi y^*}{W^*} \right) \times \exp(i2n\pi t^*) \right\} \end{aligned} \quad (4.58)$$

with

$$\begin{aligned}
 A_{00} &= \alpha\beta \\
 A_{0n} &= \frac{2\beta \sin(n\pi\alpha)}{n\pi} \\
 A_{m0} &= \frac{2\alpha}{m\pi} \left\{ \sin\left[\frac{m\pi}{2}(1+\beta)\right] - \sin\left[\frac{m\pi}{2}(1-\beta)\right] \right\} \\
 A_{mn} &= \frac{4 \sin(n\pi\alpha)}{mn\pi^2} \left\{ \sin\left[\frac{m\pi}{2}(1+\beta)\right] - \sin\left[\frac{m\pi}{2}(1-\beta)\right] \right\}
 \end{aligned} \tag{4.59}$$

where  $m$  and  $n$  are integer numbers,  $i$  is the imaginary unit, and  $\Re$  indicates the real component of a complex number. Nguyen and Huang [29] fabricated a polymeric micromixer based on this concept. Switching of solvent and solute streams was realized by piezoelectric valves. Fig. 4.17 compares the measured concentration distribution from [29] with the above analytical model. It's obvious that the assumption of the effective diffusion coefficient  $D^*$  can describe axial transport relatively well.

## References

1. A.E. Kamholz, B.H. Weigl, B.A. Finlayson and P. Yager, "Quantitative analysis of molecular interaction in microfluidic channel: The T-Sensor," *Analytical Chemistry*, Vol. 71, pp. 5340–5347, 1999.
2. R.F. Ismagilov, A.D. Stroock, P.J.A. Kenis, G. Whitesides and H.A. Stone, "Experimental and theoretical scaling laws for transverse diffusive broadening in two-phase laminar flows in microchannels," *Applied Physics Letters*, Vol. 76, pp. 2376–2378, 2000.
3. A.E. Kamholz and P. Yager, "Molecular diffusive scaling laws in pressure-driven microfluidic channels: Deviation from one-dimensional Einstein approximations," *Sensors and Actuators B*, Vol. 82, pp. 117–121, 2002.
4. P. Hinsmann, J. Frank, P. Svasek, M. Harasek and B. Lendl, "Design, simulation and application of a new micromixing device for time resolved infrared spectroscopy of chemical reactions in solutions," *Lab on a Chip*, Vol. 1, pp. 16–21, 2001.
5. V. Hessel, S. Hardt, H. Loewe and F. Schoenfeld, "Laminar mixing in different interdigital micromixers: I. Experimental characterization," *AIChE Journal*, Vol. 49, pp. 566–577, 2003.
6. S. Hardt and F. Schoenfeld, "Laminar mixing in different interdigital micromixers: II. Numerical simulations," *AIChE Journal*, Vol. 49, pp. 578–584, 2003.
7. V. Haverkamp, W. Ehrfeld, K. Gebauer, V. Hessel, H. Loewe, T. Richter and C. Wille, "The potential of micromixers for contacting of disperse liquid phases," *Fresenius Journal of Analytical Chemistry*, Vol. 364, pp. 617–624, 1999.
8. F.G. Bessoth, A.J. de Mello and A. Manz, "Microstructure for efficient continuous flow mixing," *Anal. Comm.*, Vol. 36, pp. 213–215, 1999.
9. M. Kakuta et al., "Micromixer-based time-resolved NMR: Applications to ubiquitin protein conformation," *Analytical Chemistry*, Vol. 75, pp. 956–960, 2003.
10. J.B. Knight, A.P. Vishwanath, J. Brody and R. Austin, "Hydrodynamic focusing on a silicon chip: Mixing nanoliters in microseconds," *Physical Review Letters*, Vol. 80, pp. 3863–3866, 1998.

11. Z. Wu and N.T. Nguyen, "Rapid mixing using two-phase hydraulic focusing in microchannels," *Biomedical Microdevices*, Vol. 7, pp. 13–20, 2005.
12. K. Jensen, "Chemical kinetics: Smaller, faster chemistry," *Nature*, Vol. 393, pp. 735–736, 1998.
13. G.M. Walker, M.S. Ozers and D.J. Beebe, "Cell infection within a microfluidic device using virus gradients," *Sensors and Actuators B*, Vol. 98, pp. 347–355, 2004.
14. M. Yi and H.H. Bau, "The kinematics of bend-induced mixing in micro-conduits," *International Journal of Heat and Fluid Flow*, Vol. 24, pp. 645–656, 2003.
15. S.H. Wong, M.C.L. Ward and C.W. Wharton, "Micro T-mixer as a rapid mixing micromixer," *Sensors and Actuators B*, Vol. 100, pp. 365–385, 2004.
16. D.S.W. Lim, D.S.W. Lim, J.P. Shelby, J.S. Kuo and D.T. Chiu, "Dynamic formation of ring-shaped patterns of colloidal particles in microfluidic systems," *Applied Physics Letters*, Vol. 83, pp. 1145–1147, 2003.
17. S.H. Wong, P. Bryant, M. Ward and C. Wharton, "Investigation of mixing in a cross-shaped micromixer with static mixing elements for reaction kinetics studies," *Sensors and Actuators B*, Vol. 95, pp. 414–424, 2003.
18. D. Gobby, P. Angeli and A. Gavrilidis, "Mixing characteristics of T-type microfluidic mixers," *Journal of Micromechanics and Microengineering*, Vol. 11, pp. 126–132, 2001.
19. A. Groisman and V. Steinberg, "Efficient mixing at low Reynolds number using polymer additives," *Nature*, Vol. 410, pp. 905–908, 2001.
20. H.Y. Gan, Y.C. Lam, N.T. Nguyen, C. Yang and K.C. Tam, "Efficient mixing of viscoelastic fluids in a microchannel at low Reynolds number," *Microfluidics and Nanofluidics*, Vol. 3, pp. 101–108, 2006.
21. F. Schoenfeld, V. Hessel and C. Hofmann, "An optimised split-and-recombine micro-mixer with uniform chaotic mixing," *Lab Chip*, Vol. 4, pp. 65–69, 2004.
22. S. Wiggins and J.M. Ottino, Foundation of chaotic mixing, *Phil. Trans. R. Soc. Lond. A*, Vol. 362, pp. 937–970.
23. J.M. Ottino and S. Wiggins, "Introduction: Mixing in microfluidics," *Phil. Trans. R. Soc. Lond. A*, Vol. 362, pp. 923–935, 2004.
24. J. Branebjerg, P.K.P. Gravesen, J. Nielsen and C. Rye, Fast mixing by lamination, *Proceedings of the IEEE Micro Electro Mechanical Systems (MEMS)*, 1996, pp. 441–446.
25. N. Schwesinger, T. Frank and H. Wurmus, "A modular microfluid system with an integrated micromixer," *Journal of Micromechanics and Microengineering*, Vol. 6, pp. 99–102, 1996.
26. B.L. Gray, D. Jaeggi, N.J. Mourlas, B.P. Van Driehhuizen, K.R. Williams, N.I. Maluf and G.T.A. Kovacs, "Novel interconnection technologies for integrated microfluidic systems," *Sensors and Actuators A*, Vol. 77, pp. 57–65, 1999.
27. B. He, B.J. Burke, X. Zhang, R. Zhang and F.E. Regnier, "A picoliter-volume mixer for microfluidic analytical systems," *Analytical Chemistry*, Vol. 73, pp. 1942–1947, 2001.
28. C.K.L. Tan, M.C. Tracey, J.B. Davis and I.D. Johnston, "Continuously variable mixing-ratio micromixer with elastomer valves," *Journal of Micromechanics and Microengineering*, Vol. 15, pp. 1885–1893, 2005.
29. N.T. Nguyen and X.Y. Huang, "Mixing in microchannels based on hydrodynamic focusing and time-interleaved segmentation: Modelling and experiment," *Lab Chip*, Vol. 5, pp. 1320–1326, 2005.
30. N.T. Nguyen and X.Y. Huang, "Modeling, fabrication and characterization of a polymeric micromixer based on sequential segmentation," *Biomedical Microdevices Journal*, Vol. 8, pp. 133–139, 2006.





## 5 Micromixers Based on Chaotic Advection

---

As discussed in Chapter 2, molecular diffusion and advection are the two important forms of mass transport. Advection allows improved mixing in fluid flows at low Reynolds number. In most passive micromixers based on molecular diffusion, advection is parallel to the main flow direction. Thus, transversal transport of species relies entirely on molecular diffusion. Advection with a three-dimensional orbit can cause secondary transversal transport and significantly improve mixing [1]. The basic design concept for the generation of advection is the modification of the channel shape for stretching, folding, and breaking of the laminar flow. According to [1] these processes are chaotic. The necessary condition for chaos is that the streamlines should cross each other at different times. This effect occurs in a time-periodic flow or a spatially periodic flow. While the first flow type can be implemented by motions of boundaries, periodic changes in geometry can induce the second flow type. Micromixers based on time-periodic flows are categorized as active micromixers, which are later discussed in Chapter 6. Depending on the geometrical configuration, chaotic advection was observed at different Reynolds numbers. Therefore, micromixer designs based on chaotic advection are categorized by their operating range of Reynolds numbers. A range of  $Re > 100$  is considered in this section as high. The range of  $10 < Re < 100$  is intermediate. The range of  $Re < 10$  is regarded as low. In the following, only micromixers based on passive chaotic advection are discussed.

### 5.1 Chaotic Advection at High Reynolds Numbers

#### 5.1.1 T-Mixer at High Reynolds Numbers

As described in Section 2.8, the Peclet number is about three order higher than the Reynolds number. Thus at Reynolds numbers higher than unity, convection in the flow direction dominates transversal diffusion. A simple T-mixer cannot be used for mixing at high Reynolds number.

Due to the sharp  $90^\circ$  turn at the entrance, the inertial force is large enough to cause vortices, which in turn lead to chaotic advection. In general, the laminar regime in a T-mixer consists of three subregimes: stratified, vortex, and engulfment [2,3]. In the stratified subregime ( $Re < 50$ ), the two inlet streams flow side by side. Transversal transport only occurs through molecular diffusion. Mass transport in this subregime was already analyzed in details in Chapter 4. In the vortex regime ( $50 < Re < 150$ ), Dean vortices appear, but they are symmetrical across the interface between the two streams. In the engulfment regime  $Re > 150$ , the vortices become asymmetric and real chaotic advection occurs. This regime is useful for mixing application. At a Reynolds

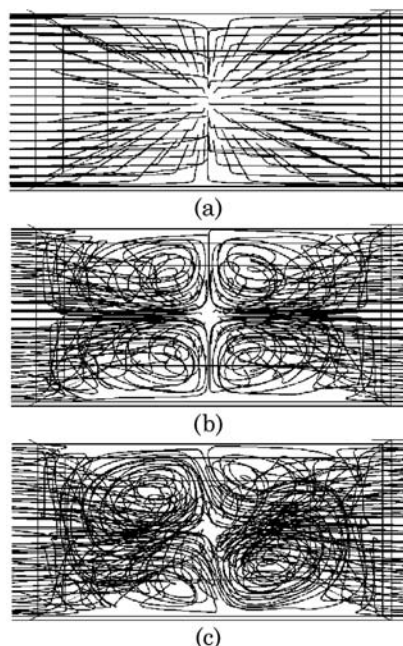


**Figure 5.1** Trajectory near the entrance of a T-mixer at different Reynolds numbers: (a)  $Re = 1.32$ ; (b)  $Re = 119$ ; and (c)  $Re = 146$  (reprinted with permission from [2]).

number of over 400, the flow becomes unsteady and the flow moves from the transition regime to turbulence. Experimental results based on hot-film measurement indicated turbulent flow at Reynolds numbers beyond 1000 [4].

Fig. 5.1 shows the numerically simulated trajectory of liquid flow at the entrance of T-mixer [2]. At Reynolds numbers on the order of unity, the flow is stable but fast enough to dominate over molecular diffusion, Fig. 5.1 (a). At high Reynolds number ( $50 < Re < 150$ ) the trajectories clearly show the existence of vortices due to secondary flow caused by centrifugal force at the  $90^\circ$  turn of the entrance. The two inlets correspond to two Dean flows (see Section 2.4.2.2). Each Dean flow has a pair of counter rotating vortices, Fig. 2.18. However, as shown in Fig. 5.1 (b), the vortices are symmetric, thus the solute and solvent still remain in their particular half. No mixing occurs at  $Re = 119$ , Fig. 5.1 (b). Increasing the Reynolds number further destroys the symmetry of the vortices, Fig. 5.1 (c). The inertial force is strong enough to make fluid streams to cross the two halves of the mixing channel. Fig. 5.3 shows the three-dimensional concentration distribution measured with confocal micro laser-induced fluorescence ( $\mu$ -LIF). The fact that the confocal measurement is slow proves that the flow and the concentration distribution are time-independent. Thus, the transport process at high Reynolds number ( $Re > 100$ ) is chaotic advection but not turbulence. Stretching and folding are clearly visible at high Reynolds numbers (Fig. 5.2). The increased interfacial area and the smaller

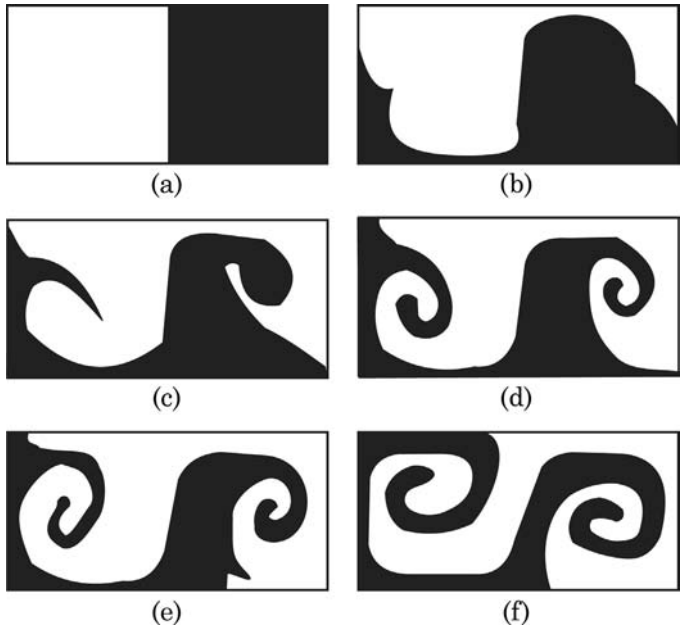


**Figure 5.2** Concentration distribution at a dimensionless position of  $x^* = 1.5$ : (a)  $Re = 119$ ; (b)  $Re = 139$ ; (c)  $Re = 146$ ; (d)  $Re = 153$ ; (e)  $Re = 159$ ; and (f)  $Re = 186$  (after [2]).

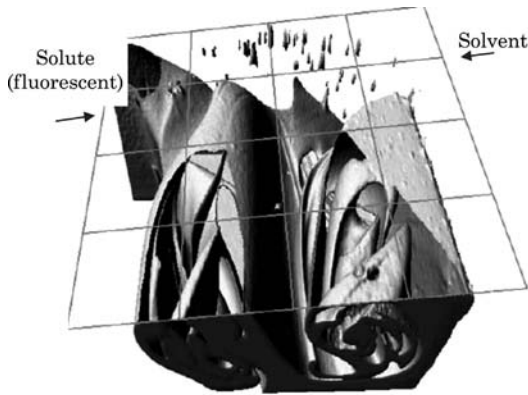


**Figure 5.3** Measured three-dimensional concentration distribution at  $Re = 160$  (reprinted with permission from [3]).

striation thickness leads to improved mixing. Fig. 5.4 shows the mixing regions and boundary layers of the engulfment subregime. These regions are clearly observed with numerical simulation and measurement [2,3]. The  $90^\circ$  turns cause the two streams to separate and follow a curved path. The separation of boundary layers leads to the formation of vortices at the top of the junction, where the two streams collide. The vortices cause mixing of the two fluids. Dean vortices occur at the curved paths of the  $90^\circ$  turns. The secondary flows in the

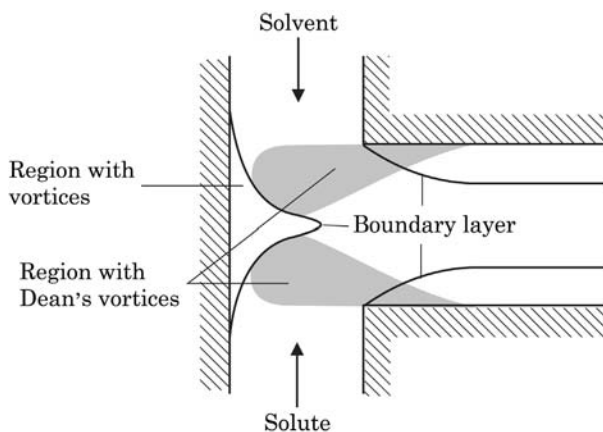


**Figure 5.4** Mixing regions and boundary layers at the entrance of a T-mixer.

curved path swept the fluids in the partially mixed region at the top of the junction into its path. This effect causes the transversal cross-flow of the fluid between the two channel halves.

The high Reynolds number required for chaotic advection needs a high driving pressure, up to 5 bars. Thus, the micromixer should be fabricated in a solid substrate. Bothe et al. [2] and Wong et al. [5] reported T-mixers made in silicon. The rectangular microchannels are etched in silicon using deep reactive ion etching. Sealing and optical access were made possible through anodic bonding to a glass wafer. Mixing channels with depths less than  $100\ \mu\text{m}$  and widths less than  $200\ \mu\text{m}$  were fabricated.

Kochmann et al. [6] presented further designs for mixing improvement at high Reynolds numbers. Additional  $90^\circ$  turns are added after the T-junction. According to numerical simulation at  $\text{Re} = 270$  [6] a single  $90^\circ$  turn would reach a mixing efficiency (see Chapter 7) of 45%, while two  $90^\circ$  turns in the S-form and U-form [Fig. 5.5 (a)] would allow the mixing efficiency to reach 65% and 70%, respectively. In the tangential shear design depicted in Fig. 5.5 (b), the T-junction inlet is replaced by a shearing design. Instead of head-on collision, the two mixing fluids enter the shear chamber at different sides and leave it perpendicularly at the bottom. The micromixers were fabricated in two layers of silicon. Microchannels were etched using DRIE technique. Optical access was achieved with a pyrex glass cover bonded anodically on top of the channel. The drawback of the additional mixing elements is the increase in applied pressure, which is already too high for the conventional T-mixer.

### 5.1.2 Passive Mixers with Obstacles in the Mixing Channel

Flows in passive mixers become unstable at high Reynolds number. Similar to the turbulators used at the macro scale, obstacles placed in the mixing channels

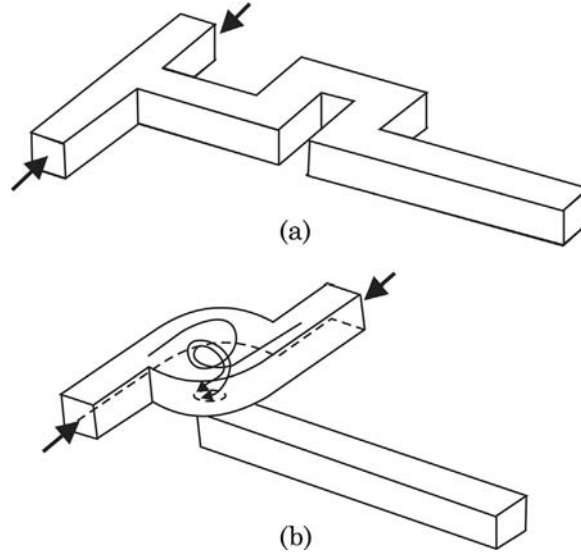


**Figure 5.5** Other mixer designs for high Reynolds numbers: (a) U-shaped channel, (b) tangential shear.

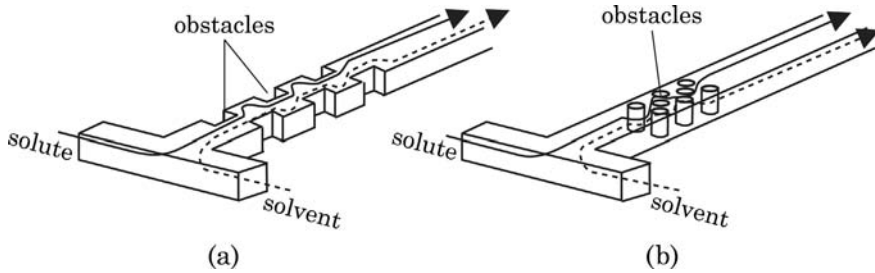


**Figure 5.6** Micromixers based on chaotic advection: (a) obstacles on walls [7]; (b) obstacles in the channel [8,9].

or repeated change can speed up this instability. Fig. 5.6 shows the two common implementation of obstacles in a mixing channel.

Wong et al. [7] investigated the effects of obstacles on the channel walls [Fig. 5.6 (a)] of the focusing design discussed previously in Section 4.5. In this design the partially mixed liquid passes a number of obstacles, which generate vortices at high Reynolds number. The vortices disrupt the laminar flow pattern and induces transversal transport. With the obstacles, flow velocities are still high enough to induce vortices in the flow. However, the drawback is the increasing pressure drop across the mixing channel. The design reported by Wong et al. [7] has a cross section of  $30\text{ }\mu\text{m} \times 30\text{ }\mu\text{m}$ . The obstacles are square protrusions of  $10\text{ }\mu\text{m}$  on the channel walls. At Reynolds numbers of the order of

200, improved mixing can be achieved right after the obstacles. Results from numerical simulations show that increasing the number of obstacles and placing them at the entrance further improve the mixing performance. Such a mixer would require a pressure of about 2 bars to reach Reynolds numbers of 200 or higher.

Wang et al. numerically investigated the role of cylindrical pillars in a mixing channel as depicted in Fig. 5.6 (b) at high Reynolds numbers [8]. The results showed that these obstacles can improve mixing at high Reynolds numbers. The obstacles and inertial forces alter the flow directions and creates transversal mass transport. In general, the more obstacles in the channel, the better is the mixing effect. However, placing the obstacle groups asymmetrically along the mixing channel results in better mixing than having a large number of obstacles.

Lin et al. [9] used cylinders placed in a narrow channel to enhance mixing, Fig. 5.6 (b). The micromixer was fabricated in silicon. Seven cylinders of 10  $\mu\text{m}$  diameter were arranged in a  $50 \times 100 \times 100$   $\mu\text{m}$  mixing chamber. The micromixer was fabricated using standard photolithographic techniques. The cylinders are etched in the same process with the mixing channel. The device was subsequently bonded to a glass wafer for sealing and enabling an optical access. The two liquids flow through the 50  $\mu\text{m}$ -wide microchannel before entering the mixing chamber. The micromixers work with Reynolds number ranging from 200 to 2000. At a flow velocity of the order of 20 m/s, vortices caused by the obstacles ensure efficient mixing at these high Reynolds numbers.

### 5.1.3 Dean Flow with Repeated Turns in Mixing Channel

As mentioned in Section 4.1.1.1, Dean vortices at the  $90^\circ$  turn on a T-mixer are responsible for chaotic advection at high Reynolds number. Thus, repeating the turns would allow the effect of Dean flow to intensify. Fig. 5.7 shows the basic concept of Dean vortex in a circular channel with a rectangular cross section. At Dean numbers above the critical number of 150 [10], two vortex pairs appear. We can use this critical Dean number to estimate the required Reynolds number for a micromixer based on Dean flow. The definition equation of the Dean number (2.110) leads to:

$$\text{Re}_{\text{cr}} = \text{De}_{\text{cr}} \sqrt{R/D_h} \quad (5.1)$$

where  $R$  is the radius of curvature and  $D_h$  is the hydraulic diameter. Thus, for the best case scenario of  $R = D_h$  the critical Reynolds number is  $\text{Re}_{\text{cr}} = \text{De}_{\text{cr}} = 150$ . For most cases, the working range of planar micromixers based on Dean flow is  $\text{Re} > 150$ .

Although the closed circular channel as depicted in Fig. 5.7 can be realized with a pumping concept based on magnetohydrodynamics as discussed later in Section 5.6, it is not realistic for pressure-driven flow. However, Dean vortices can be achieved in a planar microchannel by repeating the curved sections as

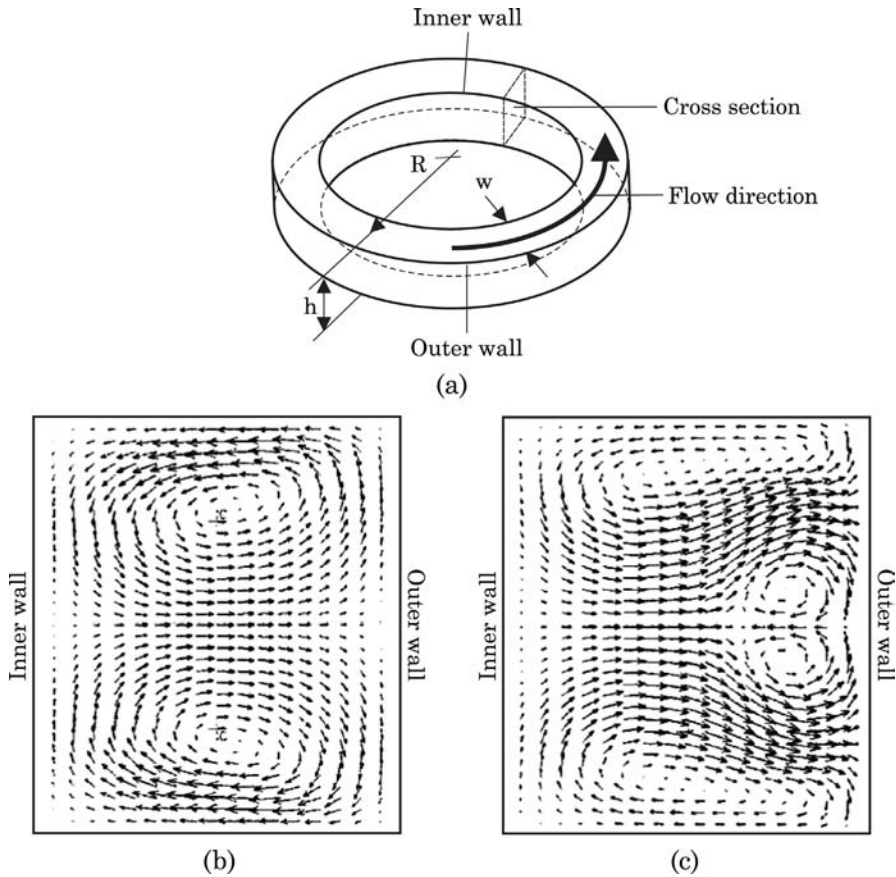


**Figure 5.7** Dean vortices at different Dean numbers: (a) the basic channel configuration; (b) secondary flow pattern at low Dean number ( $De < 150$ ); (c) secondary flow pattern at high Dean number ( $De > 150$ ).

depicted in Fig. 5.8[10]. The alternate signs of radius of curvature make the two vortices at low Dean numbers [Fig. 5.7 (a)]. This effect causes folding of fluid interfaces, but not enough for efficient mixing. At a high Dean number above the critical value of 150, a second vortex pair appears. These smaller vortices sweep from one side to the other, making the secondary flow asymmetric. This flow pattern at high Dean numbers makes chaotic advection in the micromixer possible. The mixer reported by Jiang et al. [10] was machined in a PMMA substrate. The mixing channel was sealed by solvent bonding to a PMMA layer. Because large Reynolds number and Dean number are required for the mixing concept, a relatively large channel with a  $1 \text{ mm}^2$  cross section was used. The large channel allows the realization of Dean numbers ranging from 35 to 351 or Reynolds numbers ranging from 78 to 785 at a reasonable driving pressure provided by a syringe pump. Experimental results show that mixing time is inversely proportional to the Dean number. The slope clearly changes at the



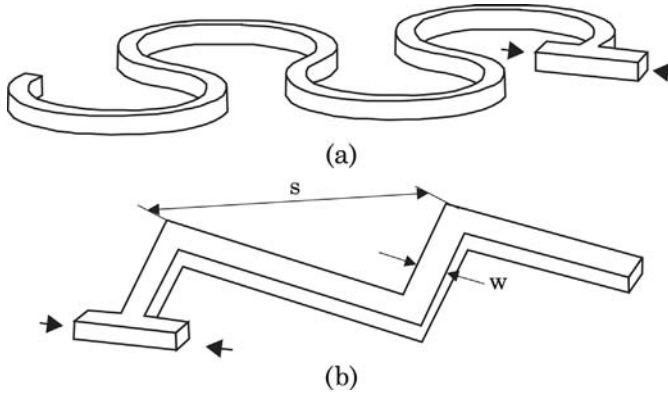


**Figure 5.8** Planar micromixers based on Dean flow: (a) curved channels (after [10]), (b) 90-degree turns.

critical Dean number of around 140 indicating the change in secondary flow pattern (Fig. 5.7).

Sharp turns or meandering mixing channels can also induce spatially periodic flows at high Reynolds numbers, Fig. 5.8 (b). Mengeaud et al. [11] used the ratio between the spatial period  $s$  and the channel width  $w$  as the optimization parameter. The periodic turns cause chaotic advection. A two-dimensional model predicts chaotic advection at Reynolds number above 80. For a given Reynolds number, there exist an optimal ratio between the spatial period and the channel width. Both small and large ratios make the mixing channel approach the asymptotic case of a straight channel. For instance, numerical results show an optimum value of 4 at  $Re = 267$ . However, the results of Mengeaud et al. [11] only consider a two-dimensional model and cannot capture the effect of Dean vortices. The micromixers were made of polyethylene terephthalate (PET). Microchannels with a width of  $100\ \mu\text{m}$ , a depth of  $48\ \mu\text{m}$ , and a length of  $2\ \text{mm}$  were fabricated using an excimer laser. Because of the extremely high pressure, only Reynolds number up to 10 can be achieved with this mixer. The high pressure above this Reynolds number will cause leaking. This example shows that mixing at high Reynolds number is only suitable for processes with available facilities and technology that can handle high pressures.

## 5.2 Chaotic Advection at Intermediate Reynolds Numbers

### 5.2.1 Chaotic Advection with $90^\circ$ Turns

Because a  $90^\circ$  turn is the key factor for mixing in a T-mixer at high Reynolds numbers, mixing can be improved if this  $90^\circ$  turn is repeated in the mixing

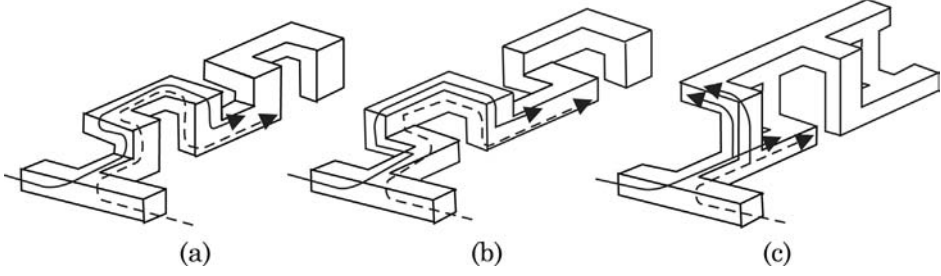


**Figure 5.9** Micromixers based on chaotic advection at intermediate Reynolds numbers: (a) C-shape[13]; (b) L-shape [14]; (c) connected out-of-plane L-shapes [15].

channel. The two vortices at Dean numbers below the critical value are still sufficient for improving mixing. Micromixers working in the Reynolds number range  $10 < \text{Re} < 100$  can well utilize Dean vortices to improve transversal transport.

Yi and Bau investigated Dean flow at a  $90^\circ$  turn in microchannels [12]. The strength of Dean vortices at an axial position  $x$  was defined as:

$$\Omega(\text{Re}, z^*) = \int \int \left( \frac{\partial u^*}{\partial y^*} - \frac{\partial v^*}{\partial x^*} \right)^2 dx^* dy^*. \quad (5.2)$$

The star indicates that the variables are dimensionless. The spacial variables are normalized by the hydraulic diameter of the channel. Fitting the numerical data results in the following function for vortex strength after a  $90^\circ$  turn [12]:

$$\Omega(\text{Re}, z^*) = \Omega(\text{Re}, 0.5) \exp[-f(\text{Re})(z^* - 0.5)] \quad (5.3)$$

with

$$f(\text{Re}) \sim 7.5\text{Re}^{-0.27} \quad (5.4)$$

$$\Omega(\text{Re}, 0.5) = \begin{cases} 7 \times 10^{-3}\text{Re}^2 + 0.058\text{Re} + 0.84 & (0 < \text{Re} < 10) \\ 0.18\text{Re} + 0.41 & (10 < \text{Re} < 80). \end{cases} \quad (5.5)$$

It is apparent from the above relations that the strength of vortices decays along the axial direction and is proportional to the Reynolds number. Good mixing can be achieved if the turns are repeated before the Dean vortices disappear. The higher the Reynolds number the stronger are the vortices and the better is the mixing. If the turns are on a plane, the vortices are symmetric. Repeating the turns out-of-plane lead to the case of a twisted pipe as discussed in Section 2.4.2. Thus, chaotic advection in three-dimensional  $90^\circ$  turns can further decrease the operational range of the mixer to  $10 < \text{Re} < 30$ .

Liu et al. [13] reported a three-dimensional serpentine mixing channel fabricated in silicon and glass. The channel was constructed as a series of C-shaped segments positioned in perpendicular planes, Fig. 5.9 (a). The mixing

channel was shaped by anisotropic etching and had a typical trapezoidal cross section with a largest width of 300  $\mu\text{m}$  and a depth of 150  $\mu\text{m}$ . The three-dimensional structure was formed by etching on both sides of a polished silicon wafer. The channels were covered on both sides of the wafer by glass plates using adhesive bonding. Mixing was evaluated based on the reaction between phenolphthalein and sodium hydroxide streams, which were introduced by syringe pumps. Chaotic advection was induced by the twisted intersecting streamlines. At a Reynolds number of 70, full mixing was achieved after only two C-shaped segments. For the same mixing length, the three-dimensional chaotic mixer produces 16 times more reaction product than a straight channel and 1.6 times more than the planar design [13].

Yi and Bau constructed three-dimensional 90° turns by laminating multiple layers of pre-fired ceramic tapes. Optical access was realized by thermal bonding of two glass slides on top and bottom of the ceramic stack. Full mixing was achieved at a Reynolds number of 20.

Vijayendran et al. reported a three-dimensional serpentine mixing channel fabricated in PDMS [14], Fig. 5.9 (b). The channel was designed as a series of L-shaped segments in perpendicular planes. The mixer was tested at the Reynolds numbers of 1, 5, and 20. Better mixing was achieved at higher Reynolds numbers.

Chen and Meiners reported another complex channel design realized in PDMS [15]. The periodic structure is formed by two connected out-of-plane L-shapes and measures about 400  $\times$  300  $\mu\text{m}$ . The microchannels are 100  $\mu\text{m}$  wide and 70  $\mu\text{m}$  deep, Fig. 5.9 (c). The mixer is based on a concept similar to sequential lamination. A number of serial mixing units split, turn, and recombine the mixing streams. The 90° turns can induce secondary flow and improve mixing. The micromixer was tested with two protein solutions. Despite the relatively small molecular diffusion coefficients of the protein ( $D = 2 \times 10^{-11} \text{ m}^2/\text{s}$ ), effective mixing was achieved with a purely laminar flow at Reynolds numbers ranging from 0.1 to 2. At these low Reynolds number, and correspondingly low Dean numbers, Dean vortices are negligible. Mixing time can be improved if the same mixer works in the intermediate Reynolds number range  $10 < \text{Re} < 100$ .

### 5.2.2 Chaotic Advection with Other Channel Designs

Mixing at intermediate Reynolds numbers can benefit from combining Taylor dispersion with Dean vortices. As discussed in Section 2.3, the effective axial dispersion coefficient is proportional to the square of the flow velocity, thus to the square of Reynolds number. According to (5.5), the strength of Dean vortices is linearly proportional to the Reynolds number as well. Thus, the higher the Reynolds number the more effective are both effects. Taylor dispersion and Dean flow can be best utilized in a micromixer design that provides curved channels or turns as well as variation in velocity distribution. A Tesla structure was usually used in micropumps as a flow rectification

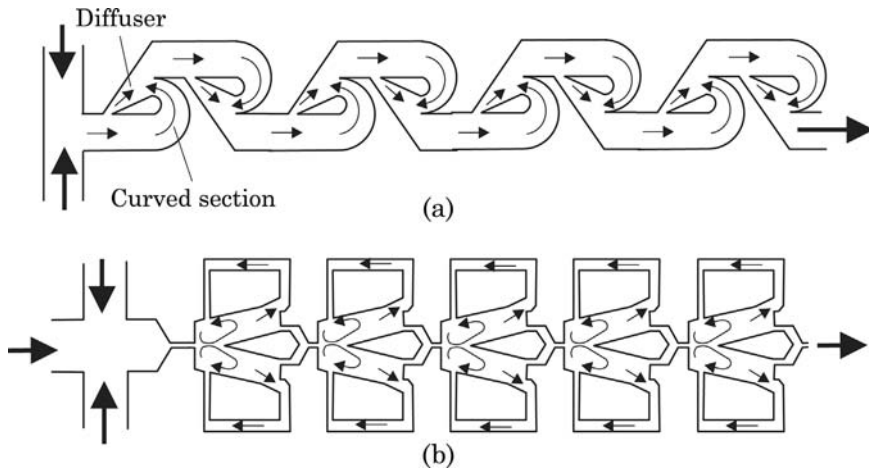


**Figure 5.10** Different micromixer designs for intermediate Reynolds number: (a) Tesla mixer with four mixing units; (b) Recycle mixer with five mixing units.

component. Hong et al. [16] demonstrated an in-plane micromixer with modified Tesla structures as depicted in Fig. 5.10 (a). The channel structures provide a curved section and a diffuser section. The curved section allows the split fluid streams to collide at angles close to  $180^\circ$ . Collision of two mixing streams was the basic concept for mixing at high Reynolds number with a simple T-mixer. The micromixer was fabricated using hot embossing. The master was fabricated using the “poor-man’s” LIGA technology (see Section 3.3.2). Nickel was electroplated in a SU-8 mold, which was structured using photolithography. The nickel mold was then used to emboss the mixer structures in a cyclic olefin copolymer (COC) substrate. After drilling the inlets and outlets, the micromixer was sealed by thermal bonding to a blank COC substrate. Complete mixing was achieved after 10 mixing units and at a Reynolds number of about 10.

Jeon et al. [18] reported a design that utilizes the instability caused by the Coanda effect. A mixing unit provides two feedback channels to remix the fluids. The mixed fluids are split into two streams before rejoining to enter the next mixing unit. Fig. 5.10 (b) shows a micromixer with five such mixing units. The micromixer was fabricated in PDMS using soft lithography. The final device was bonded to a glass slide with the help of oxygen plasma treatment. The microchannels have a depth of  $100\ \mu\text{m}$ , the width of the inlet of each mixing unit is  $50\ \mu\text{m}$ . At low Reynolds numbers, no instability occurs and the flow in the feedback arms flows in the same direction as the mean flow. At higher Reynolds numbers ( $\text{Re} > 14$ ), recirculation appears at the entrance of the mixing unit. Feedback flow follows the direction as shown in Fig. 5.10 (b). Good mixing can be achieved in the range of  $10 < \text{Re} < 100$ .

At the macro scale, chaotic advection was achieved in circular pipes using partitioned walls that rotate and split the mixing fluids [17]. Modifying the channel shapes can induce chaotic advection and improve mixing. Fig. 5.11

shows the twisted design reported by Park et al. [19]. The micromixer is constructed based on two layers of PDMS. Each layer has mixing segments that are identical in shape. The segments are joined at their ends, where the fluid goes up or down between the two layers. This channel structure allows the fluid to rotate in a helical manner, which promotes chaotic advection, Fig. 5.11. The microchannels are 100  $\mu\text{m}$  in width and 50  $\mu\text{m}$  in height. Park et al. also combined the split-and-recombine concept of sequential lamination with rotation. Five rotational mixer segments are arranged in parallel. The group of five segments are joined with the next group by a shift of half of the channel width. In this device, the fluids are first split into five streams. While rotating in the mixer segment, the streams are further divided into two groups at the entrance of the following group due to the shift of half of a channel width. The process repeats with the subsequent groups. The two layers of the micromixers were fabricated using soft lithography with masters made of silicon and SU-8. The two PDMS layers are subsequently aligned and bonded with the help of oxygen plasma treatment. Experimental results showed that best mixing was achieved with a Reynolds number of 10.

Dean vortices in curved channels can rotate mixing streams. This feature can be used to realize sequential lamination. Fig. 5.12 (a) shows the rotating characteristics of a curved channel at high Dean numbers ( $\text{De} > 10$ ). A  $180^\circ$  turn can be achieved with a curved channel of length  $L$  and a radius of curvature  $R$ , with an average velocity in the axial direction  $\bar{u}$ . The average transversal Dean velocity can be estimated as [20]:

$$\bar{v} = \text{Re} \frac{D_h}{R} \bar{u} \quad (5.6)$$

where  $D_h$  is the hydraulic diameter, which is characteristic for the transversal length scale. The ratio between the axial time scale and transversal time scale is:

$$\frac{\tau_{\text{axial}}}{\tau_{\text{trans}}} = \frac{L/\bar{u}}{D_h/\bar{v}} = \text{Re} \frac{L}{R}. \quad (5.7)$$

To complete a  $180^\circ$  turn, the axial and transversal time scales should match ( $\tau_{\text{axial}}/\tau_{\text{trans}} \approx 1$ ) leading to the required Reynolds number for a given radius of curvature  $R$  and length  $L$ :

$$\text{Re} \approx \frac{R}{L}. \quad (5.8)$$

Sudarsan and Ugaz [20] combined the characteristics of curved channel with geometric splitting to realize sequential lamination in a simple planar design. There is no need of a complex three-dimensional channel structure for geometric rotating and splitting as shown in Section 3.3. The mixing concept is depicted in

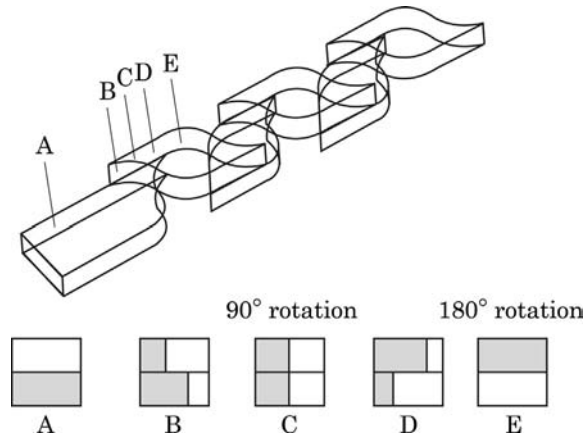


**Figure 5.11** A twisted mixer for intermediate Reynolds number.

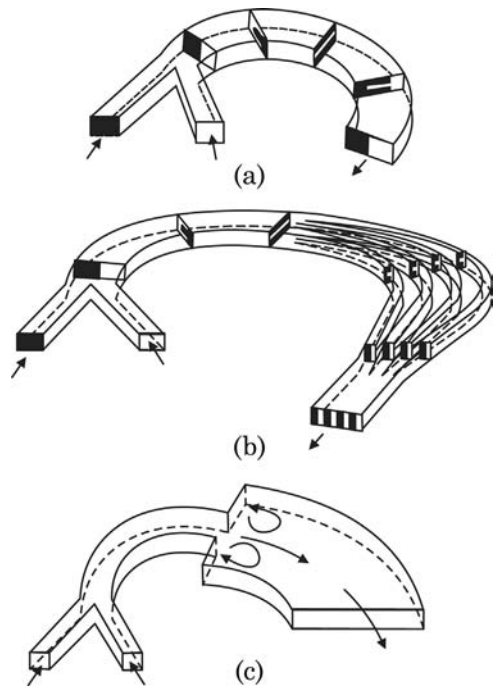


**Figure 5.12** Micromixers utilizing Dean flow for splitting: (a) a single curved channel for rotation; (b) rotation and split; (c) Dean vortex combined with recirculation at a sudden expansion (after [20]).

Fig. 5.12 (b). A mixing unit consists of a single curved channel and multiple curved channels. Fluid streams enter the mixer and flow through a  $90^\circ$  curve. The streams are simultaneously rotated by  $90^\circ$  at the end of the curved section, where they are split into multiple streams. These streams continue the curved

path for another  $90^\circ$ , so that the fluid pairs are further rotated by  $90^\circ$  in their respective streams. Lamination of multiple liquid layers is achieved, when the streams are finally rejoined. The mixing unit is repeated for complete mixing. The simpler planar design reduces pressure drop and mixing time compared to a conventional micromixer based on sequential lamination.

Vortices created by a sudden expansion was used in the design shown in Fig. 5.10 (b) to improve transversal transport. These vortices can be combined with Dean vortices to create an even better mixing effect. Sudarsan and Ugaz [20] reported the design depicted in Fig. 5.12 (c). This design combines the Dean vortices in the vertical plane with the vortices of the sudden expansion in the horizontal plane. The concept only works at a high Reynolds number ( $Re > 32$ ) where both Dean vortices and expansion vortices become significant. The design parameters of this mixer design is the position for the sudden expansion and the expansion ratio. Following (5.8), a length of  $L \approx R/(2Re)$  is required for a  $90^\circ$  rotation of the mixing fluids before the sudden expansion. Expansion ratios of 1:5 and 1:4 are common for reasonably large expansion vortices.

## 5.3 Chaotic Advection at Low Reynolds Numbers

### 5.3.1 Chaotic Advection with Dean Vortices And Complex 3-D Channels

As mentioned previously, Dean vortices induce secondary flow that improves transversal transport [20]. At lower Reynolds number ( $1 < Re < 10$ ), the small Dean numbers are large enough to create chaotic advection in the mixing channel. The design reported by Sudarsan and Ugaz utilizes spiral microchannels to induce Dean vortices in mixing channels for the Reynolds number range of ( $0.02 < Re < 18.6$ ) [21]. The spiral channel design allows the reduction of radius of curvature, thus the increase of the Dean number. Each mixing unit consists of an inlet section and outlet section. The two sections are connected by an S-shaped channel, Fig. 5.13. The spiral microchannel was designed by reducing the radius of curvature by 80% every  $90^\circ$ . In this way the radius of curvature can be reduced from the outermost arc to the innermost arc by about 10 times. Unlike a  $90^\circ$  turn (Section 5.2.1), Dean vortices in a spiral microchannel sustain along the flow path. The long channel path of the spiral microchannel also provide a sufficient residence time for the mixing fluids. Thus the design allows mixing at low Reynolds number due to molecular diffusion. While in a straight mixing channel dominant convection at high Reynolds number prevent transversal transport, Dean vortices and the resulting chaotic advection reduce the mixing length. Thus, this mixer design utilizes both molecular diffusion and chaotic advection for working under a wide range of Reynolds number. The micromixer reported in [21] was fabricated using a simple prototyping technique. The master mold was etched in the copper layer of a printed circuit board. The mixer was

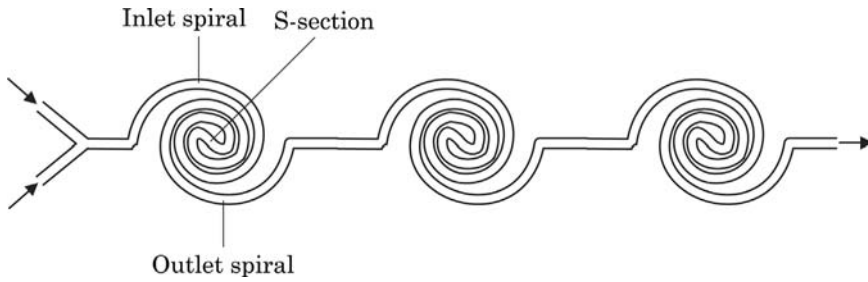


**Figure 5.13** Micromixer based on spiral microchannel (after [21]).

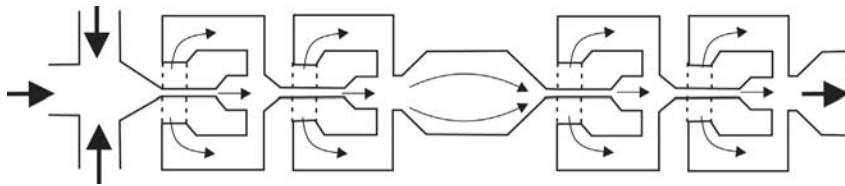


**Figure 5.14** Planar micromixer design based on splitting and recombination. The dashed lines indicate areas with shallower channels (after [22]).

made of a thermoplastic elastomer by hot embossing. The microchannels are sealed by thermal direct bonding of the molded part to a cover made of the same material.

Many sequential lamination micromixers have complex three-dimensional structures. Thus, splitting and recombination of the mixing streams can lead to chaotic advection at low Reynolds numbers. Such a mixer design was reported by Simonnet et al. [22] Fig. 5.14. The side channels are not used to return the mixing fluids but to split and rejoin it later at the exit of the mixing unit. The inlets of the side channels are shallower than the microchannels elsewhere, increasing the hydraulic resistance and avoiding back flow as in the feedback case. The mixer works with Reynolds number less than unity. Because of the required shallow side channels, the master mold was fabricated with two lithography steps. The mixer was then molded in PDMS and covered by bonding to a glass slide. Experimental results show that the required mixer length is proportional to  $Pe^{0.25}$ .

Fig. 5.15 shows a design with a three-dimensional channel network [23]. The micromixer consists of 8 mixing units. Each mixing unit is constructed from two F-shape channels machined in two sides of the device. The two F-shapes realize the splitting and recombination of mixing fluids. In contrast to conventional sequential lamination mixers, the streams are not split and recombined by channel walls but by twisted streams. Similar to micromixers based on Dean vortices, the twisted streams caused by the three-dimensional channel network also induce chaotic advection, which is effective at higher Reynolds numbers. This design can easily be implemented for mass production using hot embossing



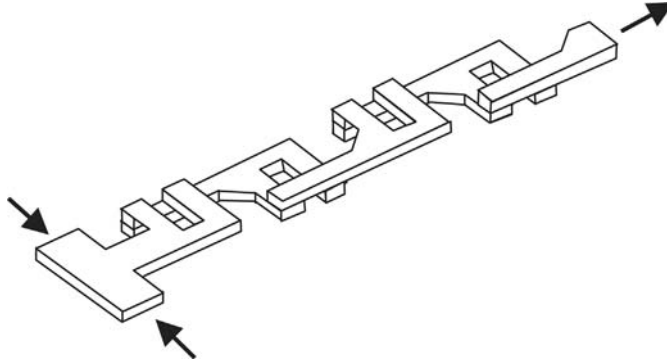


**Figure 5.15** Micromixer on based on an F-shaped microchannel (after [23]).

or injection molding. Kim et al. [23] fabricated the mold from electroplated nickel and used it as an insert for a commercial injection molding system. The micromixer was made of cyclic olefin copolymer (COC). The two polymeric parts are finally thermally bonded to form the mixing channels. The total mixer's length is 10 mm. The width and height of the main channel are  $250\ \mu\text{m}$  and  $60\ \mu\text{m}$ , respectively. The mixer works in the Reynolds number range of approximately  $1 < \text{Re} < 10$ .

Xia et al. [24] used three-dimensionally crossing channels to induce chaotic advection. Similar to the above design, the three-dimensional microchannel network was fabricated on two sides of the device. Fig. 5.16 shows the two mixer designs investigated by Xia et al. [24]. The mixers consist of mixing units that are three-dimensional X-shaped crossing microchannels. The crossing channels are perpendicular to each other and are slanted by  $45^\circ$  relative to the main flow axis. In the first design [Fig. 5.16 (a)], the two-layer channels first go across each other at A. At B, a fluid enters the top layer, while the other fluid makes a  $90^\circ$  turn. Both fluids join at C and enter the bottom layer. At the bottom layer, the mixing fluids split again. While one stream remains in the bottom layer, the other stream enters the top layer. The two streams cross each other at E and the process starts again. The second design has simpler structures. The mixing unit is shorter with joining and splitting on the two layers, Fig. 5.16 (b). Simulation results show chaotic advection at a Reynolds number as low as  $\text{Re} = 0.2$ . The mixer was tested with highly viscous glycerol solution to minimize molecular diffusion. Experimental results show that with a sufficient number of mixing units, these designs can work at Reynolds numbers of the order of 0.01.

The two-layer concept allows the fabrication of fairly complex channel structures. Chang et al. [25] used this concept to design mixing units that can rotate and laminate mixing fluid streams. Fig. 5.17 shows the two designs for realizing rotation of the mixing fluids either in a counter clockwise direction [Fig. 5.17 (a)] or a clockwise direction [Fig. 5.17 (b)]. The arrangement of channel sections in the two layers shown in Fig. 5.17 allows the fluids to rotate

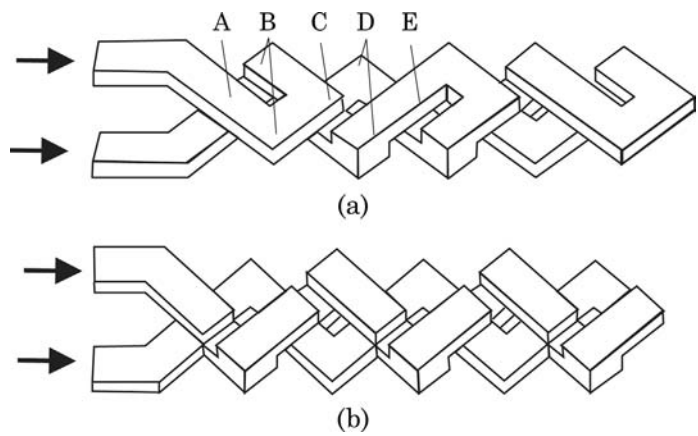


**Figure 5.16** Micromixer based on a X-shaped microchannel (after [24]).

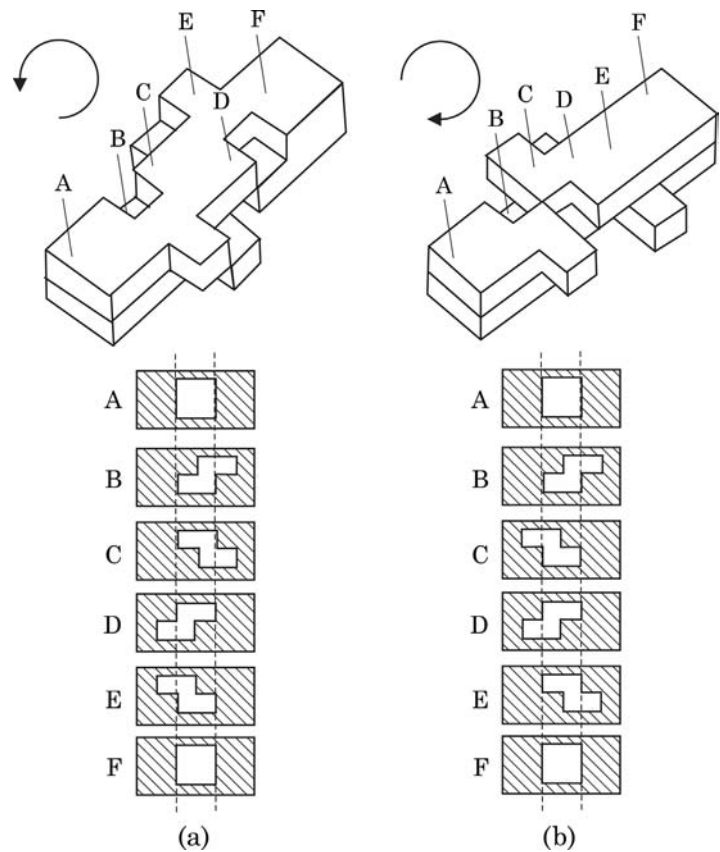


**Figure 5.17** Rotation mixer (a) counter clockwise; (b) clockwise (after [25]).

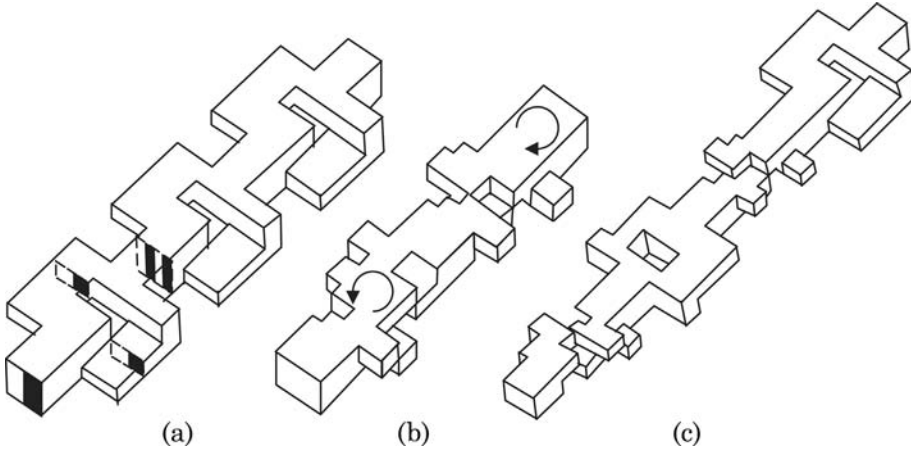


**Figure 5.18** Combination of sequential lamination and rotation: (a) sequential lamination; (b) alternate rotation; (c) alternate rotation and sequential lamination (after [25]).

while passing through the mixing channel. The concept is similar to the screw-like Kenics static mixer at the macro scale. The concept of sequential lamination is depicted in Fig. 5.18 (a). Combining the concepts of rotation and lamination can result in a very complex flow pattern. Fig. 5.18 (b) shows the combination of counter clockwise and clockwise rotation in a single device, while the design depicted in Fig. 5.18 (c) combines all three concepts of lamination, clockwise rotation and counter clockwise rotation. The micromixers were fabricated in two layers of PDMS using an SU-8 mold. Typical channel cross section is of the order of  $200\ \mu\text{m} \times 100\ \mu\text{m}$ . Experimental results show that the mixer can work well with 10 mixing units for a wide range of Reynolds numbers from 0.26 to 26. The combined designs of alternate rotation [Fig. 5.18 (b)] and lamination with alternate rotation [Fig. 5.18 (b)] give the best results. In terms of pressure drop, these two designs also require a higher driving pressure due to the pressure losses in the complex channel structure. The maximum pressure required for these mixers at  $\text{Re} = 26$  was about 7 kPa, which is reasonably low.

### 5.3.2 Chaotic Advection with Flow-Guiding Structures on Channel Walls

A secondary flow pattern similar to the Dean vortices can be generated by the axial pressure gradient if ridges are placed at the channel wall at an angle  $\theta$  with respect to the flow direction [26,27]. At low Reynolds numbers, these structures on the wall act as an anisotropic fluid resistance. The resistance is minimum if the ridges are parallel to the flow direction ( $\theta = 0^\circ$ ). The maximum resistance is achieved if the ridges are perpendicular to the flow direction  $\theta = 90^\circ$ . The anisotropic resistance guides the flow along the direction of ridges. This design

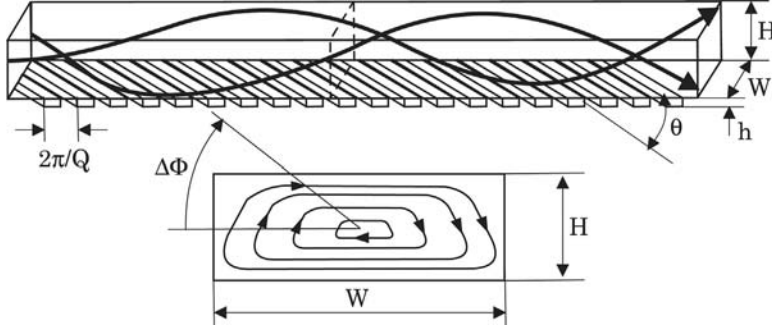


**Figure 5.19** Micromixer with bas-relief structure on the channel wall.

is called the slanted groove micromixer (SGM). Fig. 5.19 shows the typical stream lines of the secondary flow caused by an array of slanted ridges. As a result, the fluid flowing along the channel will follow a helical path Fig. 5.20. For a small ridge height ( $h/H < 0.3$ ), the shape of the trajectory is independent of the Reynolds number for a relatively wide range of Reynolds numbers ( $Re < 100$ ) [26]. For small ridges ( $h \ll H$ ) and a flat channel  $H \ll W$ , the change of angular displacement  $\Delta\Phi$  along the flow direction can be estimated as [26]:

$$\frac{d\Delta\Phi}{dx} = \alpha^2 \frac{3}{4} h^* \left[ \frac{4h^* - \sinh(2h^*) - 2(h^*)^2 \coth(h^*)}{\sinh^2(h^*) - (h^*)^2} \right] \sin \theta \cos \theta \frac{\pi}{H + W} \quad (5.9)$$

where  $\alpha = h/H$  is the ratio between the ridge height and the channel height,  $2\pi/Q$  is the distance between the two neighboring ridges,  $H$  is the channel height and  $W$  is the channel width. The dimensionless variable  $h^* = QH$  represents the ratio between the channel height and the distance between two neighboring ridges. The optimal design with the maximum angular displacement change is achieved with  $\theta = 45^\circ$  and  $h^* \approx 2$ .

Jonson et al. [29] used an excimer laser to ablate slanted grooves on the bottom wall of the mixing channel. This structure twists an electrokinetically driven flow into helical stream lines, which allow chaotic mixing at a relatively low velocity of 300  $\mu\text{m/s}$ . The substrate material of this mixer is polycarbonate (PC), which is sealed by a cover made of polyethylene terephthalate glycol (PETG). The mixing channel was 72  $\mu\text{m}$  wide at the top, 28  $\mu\text{m}$  wide at the bottom, and 31  $\mu\text{m}$  in depth. The width of an ablated groove was 14  $\mu\text{m}$ , the center-to-center spacing between the grooves was 35  $\mu\text{m}$ . The length of the region occupied by the wells from the T-junction was 178  $\mu\text{m}$ .

Secondary transverse flow generated by slanted ridges on the channel wall can be used for designing chaotic advection in microchannels. Stroock et al. [26,27] proposed a mixer design with a pair of slanted ridges called the staggered herringbone mixer (SHM), Fig. 5.21. These structures generate a pair of

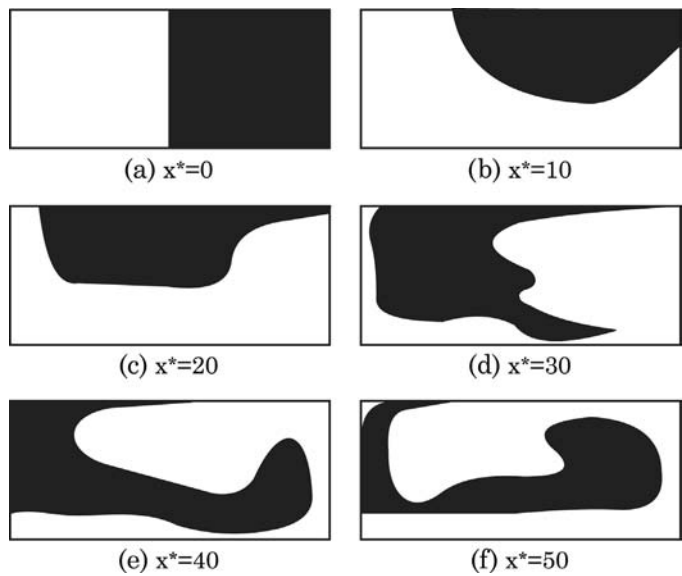


**Figure 5.20** Concentration distribution along the mixing channel in a SGM. The position is normalized by the channel width  $x^* = x/W$ . (Redrawn after numerical results of Aubin et al. [28]).

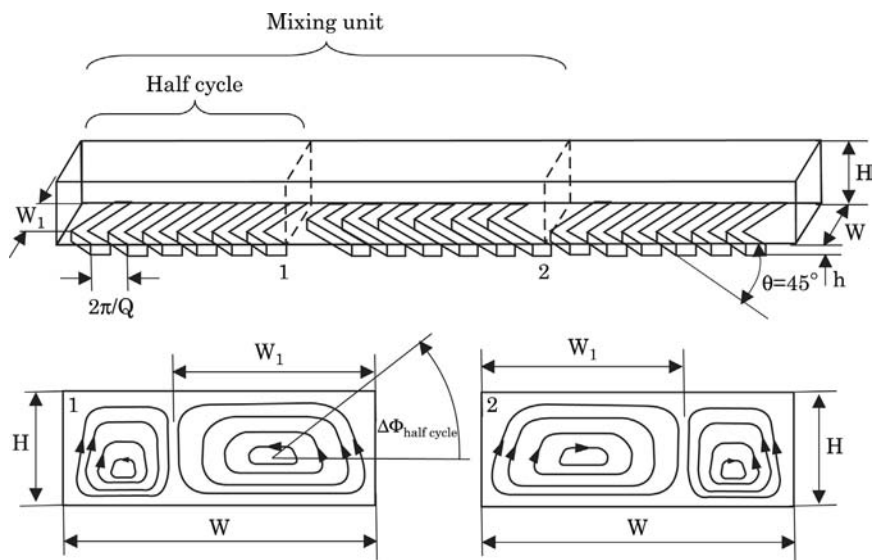


**Figure 5.21** Micromixer with staggered herringbone (SHB) structure.

counter rotating vortices. The flow pattern changes within a mixing unit, thus both rotational and extensional secondary flows are available in a mixing unit. Repeating these rotational and extensional flows leads to chaotic advection.

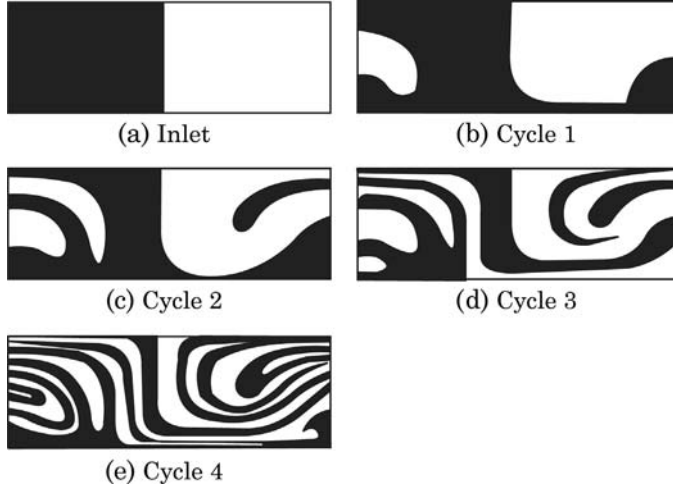


**Figure 5.22** Concentration distribution in a SHM: (a) at the inlet; (b) after the first cycle; (c) after the second cycle; (d) after the third cycle; (e) after the fourth cycle. (Redrawn after experimental results of Stroock et al. [26]).

The mixing efficiency is determined by the asymmetry of the herring bone structure  $p = W_1/W$  and the number of ridges for a particular flow pattern. At the optimal angle of  $45^\circ$ , the number of ridges determines the angular displacement per half cycle  $\Delta\Phi_{\text{half cycle}}$ . The flow in the mixing channel is not chaotic if  $p \rightarrow 1/2$  and  $\Delta\Phi_{\text{half cycle}} \rightarrow 0^\circ$ . For  $p = 2/3$  and  $\Delta\Phi_{\text{half cycle}} > 60^\circ$ , chaotic advection occurs in the mixing channel. Fig. 5.22 shows the typical concentration distribution inside a staggered herringbone mixer. The counter rotating vortices stretch and fold the mixing liquids, reducing the striation thickness significantly.

A number of numerical works have reported on the optimization of the mixers depicted in Fig. 5.19 and Fig. 5.21. Schönfeld and Hardt [30] numerically investigated the helical flows of the mixer shown in Fig. 5.19. The strength of the vortices or the change of angular displacement is proportional to the square of the relative height  $\alpha$  of the ridge height as predicted from equation (5.9). Furthermore, the simulation results confirm that the flow pattern is almost independent of the Reynolds numbers. Thus the mixing concept based on slanted ridges on a channel wall can work with a wide range of Reynolds numbers. The change of angular displacement almost doubles with ridges on both top and bottom walls of the mixing channel. Hassel and Zimmerman [31] investigated the SHM design. Kang and Kwon [32] used the so-called colored particle tracking method (CPTM) to investigate both the helical design and the SHM design. The method first runs a flow analysis to obtain the periodic velocity field. Next, particles of mixing fluids are tracked according to the predetermined velocity field (see Chapter 2). The particles are “colored” according to the type

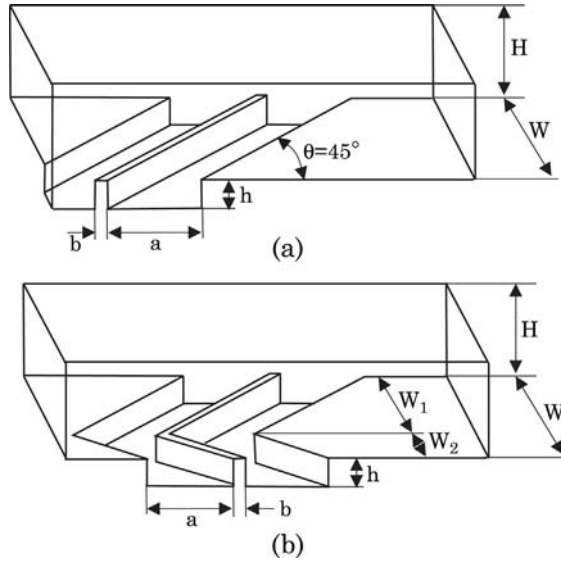


**Figure 5.23** Geometrical parameters of (a) the SGM and (b) the SHM.

of fluid. The final distribution of colored particles allows the evaluation of mixing efficiency in the micromixer. Optimization studies by Lynn and Dandy [33] lead to the following conclusions:

- Chaotic advection in SHM leads to more efficient mixing than the helical flow in SGM.
- The optimized width fraction of the herring bone structure is approximately  $p = W_1/W = 2/3$ .
- The optimized angle of grooves and ridges is  $45^\circ$ .
- The magnitude of the secondary transversal flow is weakly dependent on the channel aspect ratio  $H/W$ .
- The magnitude of helical flow is strongly dependent on the groove depth (ridge height) ratio  $h/H$ . The higher the ratio  $h/H$  the more efficient is the mixing process.

It's apparent that mixing is improved if the transversal secondary flow is strong relative to the axial flow. A strong secondary flow also increases the chance of angular displacement leading to a shorter mixing channel. A large groove would allow more mass transport in transversal direction, while the axial flow is affected by the flow within the groove. Lynn and Dandy [33] focused on the numerical optimization on the lengths  $a$  and  $b$  of the groove and the ridge, respectively (Fig. 5.23). Since the asymptotic cases of  $a/b \rightarrow 0$  and  $a/b \rightarrow \infty$  would lead to a Poiseuille flow with only axial flow component, there exists an optimum for this ratio. Most of the reported works assumed a ratio of  $a/b = 1$ . According to Lynn and Dandy, at a ratio of the period  $a + b$  and the channel

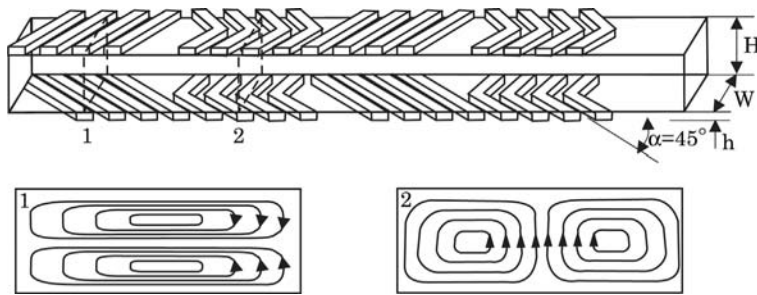


**Figure 5.24** Micromixer with both slanted and herring bone structures on both top and bottom walls.

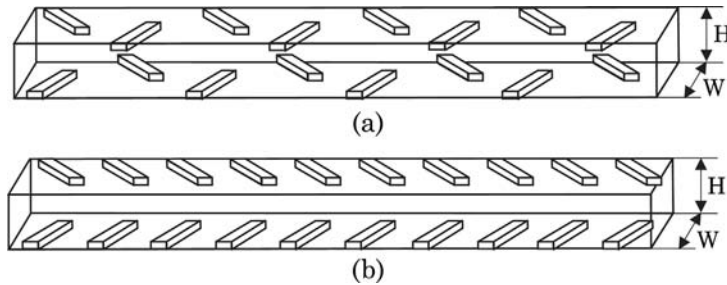


**Figure 5.25** SOR with slanted structures on both top and bottom walls.

width  $W$  of  $(a + b)/W = 1$ , there is almost no change when the ratio  $a/b$  is varied. The maximum variation is obtained with  $(a + b)/W = 1/2$ . At this period/channel width ratio, the optimum length ratio between the groove and the ridge is  $a/b \approx 1/9$ .

A number of designs were derived from the two basic concepts discussed previously. Howell and Floyd-Smith et al. [34,35] proposed a design with both types of ridges. Each mixing unit consists of four slanted ridges at an angle of  $45^\circ$  and four symmetric ( $p = 1/2$ ) herringbone ridges. This design aims to have alternate flow patterns with two vortices. As shown on Fig. 5.24, the structures on the top wall and the bottom wall allow the formation of a pair of counter rotating vortices vertically and horizontally.

Fu et al. [36] proposed the designs of staggered oriented mixers (SOR) as depicted in Fig. 5.25. The design only employs slanted structures on both top and bottom walls. The ridges on top and at the bottom cross each other allowing overlapping of the helical flows in the mixing channel. The micromixer was fabricated on two glass slides. The ridges on both sides were wet-etched using an aluminium mask. The glass slides are subsequently aligned and thermally bonded. Although the design is similar to the SHM design, this mixer only works well in the intermediate range of Reynolds number ( $10 < Re < 100$ ).

Inspired by the macro scale Kenics mixer, Kim et al. [39] improved the design of Stroock et al. [27] with embedded barriers parallel to the flow direction. This



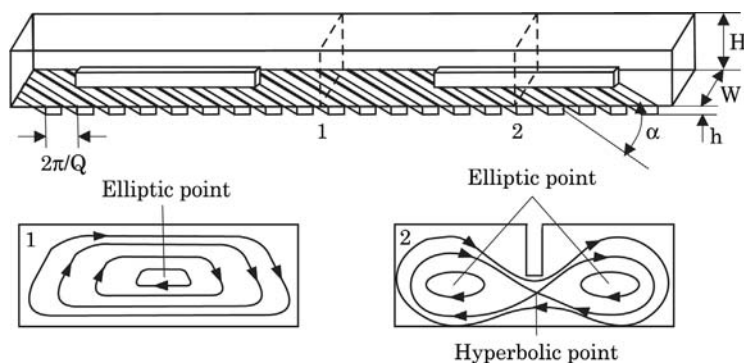


**Figure 5.26** Barrier embedded mixer (BEM).

barrier forces the flow to change the original elliptical mixing pattern [27] to a hyperbolic pattern [39], Fig. 5.26. The micromixer was fabricated in PDMS. The mixing channel of this design is 240  $\mu\text{m}$  in width, 60  $\mu\text{m}$  in depth, and 21 mm in length. The barriers have a cross section of 40  $\mu\text{m}$   $\times$  30  $\mu\text{m}$ . Experimental results show a clear improvement in mixing efficiency compared to the SGM design. Based on numerical simulation, the performance of the BEM is slightly lower than that of the SHM. A variety of designs can be derived from the basic concept shown in Fig. 5.26. Two or more barriers can be used. The barriers can be placed asymmetrically inside the mixing channel. Alternating one and two barriers may lead to an even more chaotic flow pattern.

Bertsch et al. reported a miniaturized version of the conventional Kenics static mixer with helical flow-twisting elements [38]. Two designs were tested for this concept. The first design was formed by four mixing elements, which was made of 24 rectangular bars placed at 45°. The four mixing elements were arranged at an angle of 45° in the channel. The second design consists of right-handed and left-handed helical elements containing six small-helix structures. Because of this complex geometry, the micromixer was fabricated by stereo micro lithography. The complex structure was built up layer by layer. Kim et al. [39] improved the Kenics design with embedded barriers. The rationale of the barriers is the same as in the case of the BEM discussed above. Hyperbolic points exist with the introduction of the barriers. The complex structure of the micromixer was realized by stereo micro lithography. Each unit of the design reported by Kim et al. [39] rotates the mixing streams by 180°, while the design of Bertsch et al. [38] allows a 90° rotation after each mixing unit.

## 5.4 Chaotic Advection in Multiphase Flow

### 5.4.1 Multiphase Systems at the Micro Scale

Most micromixers discussed in this book are based on single-phase miscible liquids. Multiphase systems consist of two or more partially immiscible or

immiscible fluids. Multiphase immiscible systems provide interesting microscale effects, which enhance mixing and minimize undesired effects of single-phase flows such as Taylor dispersion and absorption of species to the channel wall. Introducing a multiphase system in a microchannel results in different flow forms. Each of the forms may find its own applications in mixing at the micro scale. The forms of a multiphase system depends on the flow conditions, which dictate the balance between the several body forces and surface forces. A multiphase system in microchannels may have the forms of floating droplets, long plugs, or thin wetting films. Flow systems with droplets and plugs formed in an immiscible carrier fluid are called segmented flows and play a significant role in mixing micro scale. Segmented flows have the advantage of fast mixing due to chaotic advection and reduced axial dispersion due to the confined fluid segments [40].

#### 5.4.1.1 Passive Droplet Formation

A common system for formation of droplets consists of a solid channel wall, an aqueous phase, and an immiscible oil phase. The relation between the contact angle and the interfacial tensions in a liquid/liquid/solid system can be described by the Young equation:

$$\sigma_{sw} - \sigma_{so} = \sigma_{wo} \cos \theta \quad (5.10)$$

where  $\sigma_{sw}$ ,  $\sigma_{so}$ ,  $\sigma_{wo}$  and  $\theta$  are the interfacial tensions of solid/water, solid/oil, water/oil and the contact angle at the triphasic line. Adding a surfactant such as Span 80 to the oil decreases  $\sigma_{so}$  and  $\sigma_{wo}$ . As a result, the term  $\cos \theta$  should increase to keep the above equation in balance. If the concentration of the surfactant is high enough,  $\cos \theta$  reaches its maximum value of 1 and  $\theta = 0$ . In this case, the oil totally wets the channel wall causing the water droplet to detach from the solid surface. Adding surfactant to the oil can help to control the passive formation of aqueous droplets in an oil flow.

The forces involved in the passive formation of droplets, bubbles, plugs, and slugs are gravitational, interfacial, inertial, and viscous forces. Besides the Reynolds number often used for single-phase flows, the relation between the above forces can be represented in a multiphase flow through a number of dimensionless numbers, such as the Bond number, the capillary number, and the Weber number.

The Bond number represents the ratio between the gravitational buoyancy force and the interfacial force:

$$\text{Bo} = \frac{\text{gravitational force}}{\text{interfacial force}} = \frac{\Delta \rho g D_h^2}{\sigma} \quad (5.11)$$

where  $\Delta \rho = \rho_2 - \rho_1$  is the density difference between the two immiscible fluids 1 and 2, and  $D_h$  is the hydraulic diameter of the microchannel. The Capillary

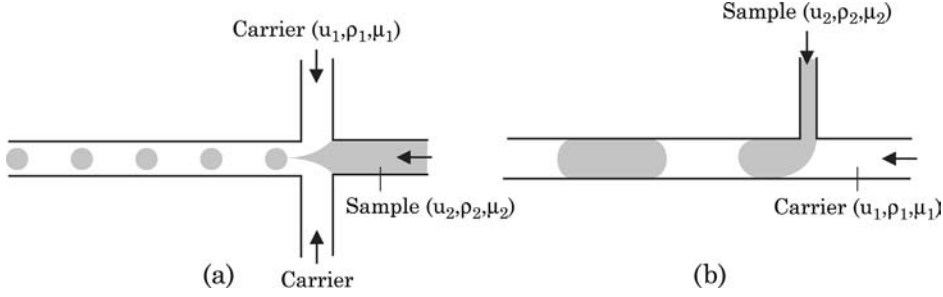


**Figure 5.27** Two basic configurations for droplet formation: (a) flow focusing configuration; (b) T-configuration.

number represents the ratio between the viscous force and the interfacial force:

$$Ca = \frac{\text{Inertial force}}{\text{Viscous force}} = \frac{\mu \bar{u}}{\sigma} \quad (5.12)$$

where  $\mu$  is the dynamic viscosity of the carrier fluid and  $\bar{u}$  is the average velocity. The Weber number represents the ratio between inertial force and interfacial force:

$$We = \frac{\text{Inertial force}}{\text{Interfacial force}} = \frac{\rho \bar{u}^2 D_h}{\sigma}. \quad (5.13)$$

Another important parameter of the formation process is the sample fraction:

$$r_{dc} = \frac{\dot{Q}_d}{\dot{Q}_d + \dot{Q}_c}, \quad (5.14)$$

and  $\dot{Q}_d$  and  $\dot{Q}_c$  are the flow rates of the droplet liquid and carrier fluid, respectively.

The physics of the formation process is determined by a critical Capillary number  $Ca_{cr} \approx 10^{-2}$ . For  $Ca > Ca_{cr}$ , the shear force plays an important role in the formation process. For  $Ca < Ca_{cr}$ , shear stress becomes insignificant and the formation process works in a squeezing regime. The formation of bubbles are typically in the squeezing regime, while the formation of droplets can be in both squeezing and shearing regime.

Fig. 5.27 shows the two basic configurations for passive droplet formation using pressure driven flows. The flow focusing configuration uses the immiscible carrier fluid as sheath flows. By approximately balancing the Laplace pressure with the shear force, the diameter of the formed droplet can be predicted as [41]:

$$D \propto \frac{\sigma}{\mu_c \dot{\gamma}}, \quad (5.15)$$

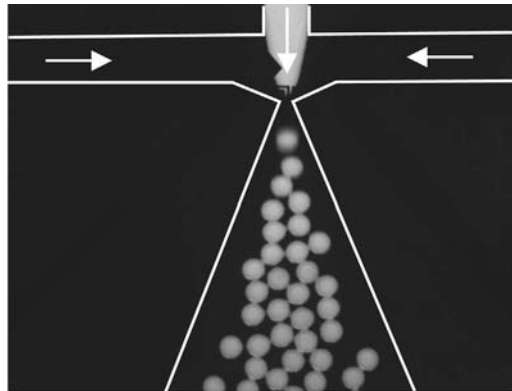


**Figure 5.28** Droplets form with flow focusing configuration.

where  $D$  is the droplet diameter,  $\sigma$  is the interfacial tension between the two immiscible faces,  $\mu_c$  is the dynamic viscosity of the carrier phase, and  $\dot{\gamma}$  is the shear rate. The shear rate is estimated as  $\dot{\gamma} \propto u/W$ , where  $u$  is the average velocity at the gap between the channel wall and the droplet and  $W$  is the width of the inlet channel, Fig. 5.28.

Alternatively, droplets can be formed with the T-configuration. Fig. 5.29 depicts a simple model of the formation process of a liquid droplet in another immiscible carrier fluid at a T-junction. Based on a simple model, the relation between the droplet diameter and other parameters can be revised. The model assumes a fixed flow rate ratio between the aqueous liquid and carrier liquid ( $\alpha = \dot{Q}_d/\dot{Q}_c$ ). For small droplet sizes, the flow rate of the carrier is significant and dominant ( $\alpha \ll 1$ ). Furthermore, mass-related forces, such as inertial force, momentum force, and buoyancy force, are neglected due to the dominance of surface-related forces, such as drag force and interfacial tension force. For simplification, the injection channel and the carrier channel are both assumed to be cylindrical in order to have the diameters as the single geometric parameters of the microchannels.

For  $Ca > Ca_{cr}$ , the droplet formation process is determined by the balance between the shear force of the carrier flow and the interfacial tension force at the injection port:

$$F_{\text{drag}} = F_{\text{interfacial tension}} \quad (5.16)$$

$$\frac{1}{2} C_D \rho_c \bar{u}_c^2 A_D = C_S \pi D_i \sigma$$

where  $\rho_c$ ,  $U_c$ ,  $A_D$ ,  $D_i$ , and  $\sigma$  are the density of the carrier fluid, the average velocity of the carrier flow, the effective drag surface, the diameter of the injection port, and the interfacial tension, respectively. In addition,  $C_D$  and  $C_S$  are the drag coefficient and the coefficient for the interfacial tension. The coefficient  $C_S$  depends on the contact angle and the shape of the injection port.

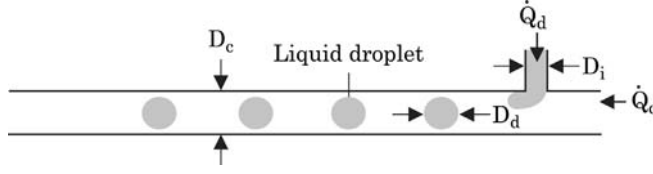


**Figure 5.29** Model of formation of liquid droplets in shearing regime.

In this model,  $C_S$  is assumed to be constant. We assume for  $C_D$  the drag coefficient of a hard sphere at a low Reynolds number  $Re$ :

$$C_D = \frac{24}{Re}. \quad (5.17)$$

The effective drag interfacial  $A_D$  grows with the droplet. Assuming that the droplet is a sphere, the effective drag surface at the detachment moment is:

$$A_D = \frac{\pi D_d^2}{2} \quad (5.18)$$

where  $D_d$  is the diameter of the generated droplet. Initially, the interfacial tension is large enough to keep the small droplet at the injection port. At the detachment moment, the continuous droplet growth makes the drag force large enough to release the droplet. Combining the above equations results in the droplet diameter:

$$D_d = 2\sqrt{\frac{C_S}{C_D} D_i \frac{\sigma}{\rho_c \bar{u}_c^2}}. \quad (5.19)$$

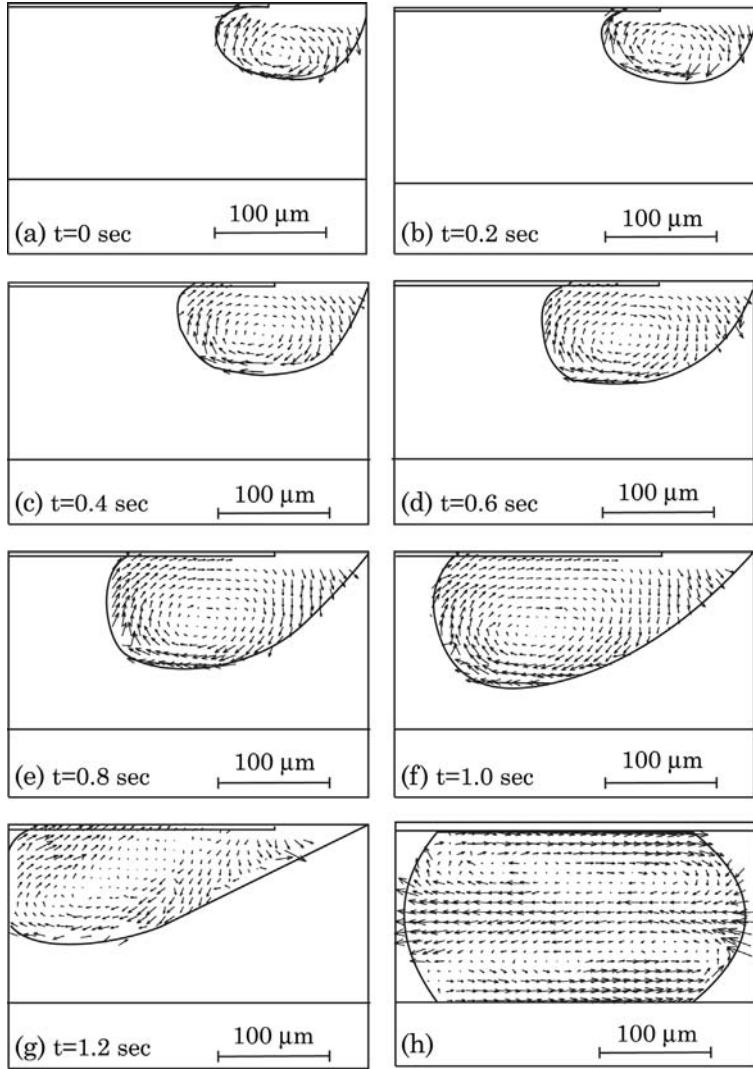
Substitute (5.17) with  $Re = \rho_c \bar{u}_c D_c / \mu_c$  into (5.19) results in:

$$D_d = 2\sqrt{\frac{\sigma}{\mu_c} \frac{D_c D_i}{\bar{u}_c}}. \quad (5.20)$$

Because the shear rate can be estimated as  $\dot{\gamma} \approx \bar{u}_c / D_c$ . The relation between droplet size and the interfacial tension, and the shear rate of a T-configuration can be estimated as:

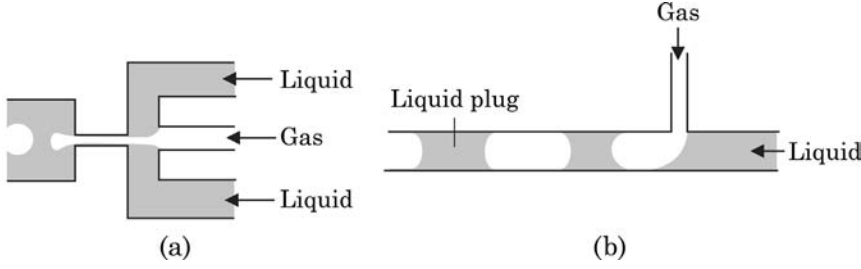
$$D_d \propto \sqrt{\frac{\sigma}{\mu_c \dot{\gamma}}}. \quad (5.21)$$

Fig. 5.30 shows the velocity field inside a droplet formed at a T-junction. The velocity field was measured using micro particle image velocimetry



**Figure 5.30** Velocity field inside a droplet during its formation (a–g) and during its passage through a microchannel (h) (measured with micro particle image velocimetry).

(see Chapter 7). The formation process illustrated in Fig. 5.30 is clearly in the shearing regime. The shearing regime is possible because of the small ratio between the widths of the injection channel and the carrier channel. The high shear stress deforms the droplet and stretches along the flow direction allowing a large gap between the droplet and the channel wall. Since the carrier fluid has enough place to flow through this large gap, the pressure drop across the droplet is small and can be neglected in the force balance. The shear stress caused by the carrier fluid leads to a single vortex in the droplet during formation [Fig. 5.30 (a–g)] (micro-PIV). The single-vortex flow pattern subsequently changes to a flow



**Figure 5.31** Bubble formation: (a) Flow-focusing configuration and (b) T-configuration.

pattern with two vortices. These flow patterns inside a droplet can be used for generating chaotic advection as elaborated later in Section 5.4.2.

#### 5.4.1.2 Passive Bubble Formations

In the case of bubble formation, the capillary number is usually extremely small due to the high gas/liquid surface tension and the smaller shear rate due to the low viscosity of the gaseous phase. Thus, shear force is negligible compared to surface tension force. A stable droplet formation process can only be achieved with a confined geometry, such as the T-configuration and the flow-focusing configuration shown in Fig. 5.31[42]. According to Garstecki et al. [42], the bubble diameter generated by the flow-focusing configuration can be adjusted by the supply pressure  $p$  of the gas phase and the flow rate  $\dot{Q}$  of the liquid phase:

$$D_{\text{bubble}} \propto \sqrt[3]{\frac{p}{\dot{Q}\mu}} \quad (5.22)$$

where  $\mu$  is the viscosity of the liquid phase. The formation process does not depend on the surface tension.

In a T-configuration, the two formation regimes are determined by the gap  $g$  between the bubble and the top channel wall. If this gap is small  $g \ll W$ , the formation process is in the squeezing regime. If the gap is large  $g \approx W$ , the formation process is in the shearing regime. The formation process in the shearing regime was already described with a simple model in Section 5.4.1.1. In a T-configuration, the ratio between the size of injection channel and carrier channel determines the formation regime, Fig. 5.29. If  $D_d/D_c \geq 1/2$ , the bubble size is large and breaks in the squeezing mode. If  $D_d/D_c < 1/2$ , the bubble is stretched by the shear stress allowing a large gap between the bubble and the top channel wall. The formation process is then in the shearing regime.

In the squeezing regime, the length  $L$  of the bubble can be estimated as [48]:

$$L = W \left( 1 + \alpha \frac{\dot{Q}_{\text{gas}}}{\dot{Q}_{\text{liquid}}} \right) \quad (5.23)$$

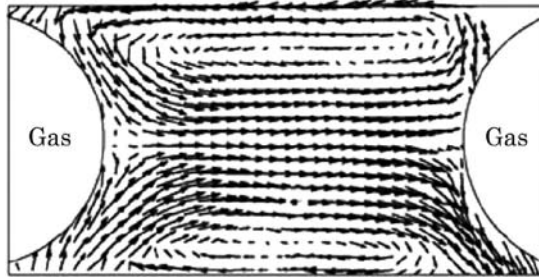


**Figure 5.32** Velocity field inside a liquid plug separated by gas bubbles (reprinted with permission from [40]).

where  $W$  is the channel width,  $\alpha$  is a constant of the order of 1,  $\dot{Q}_{\text{gas}}$  and  $\dot{Q}_{\text{liquid}}$  are the flow rates of the gas and the liquid, respectively.

In mixing applications, bubbles are used as the immiscible phase for the segmented flow. The internal flow field of the liquid plug may create chaotic advection. Fig. 5.32 shows the measured velocity field inside a liquid plug, which is separated by gas bubbles [40] (micro-PIV).

#### 5.4.1.3 Active Control of Microdroplet

Mixing in microdroplets can be realized passively in a pressure-driven continuous system. However, droplets can be manipulated individually using different actuation schemes. Chaotic advection inside a droplet can be achieved by controlling the motion of the droplet by an external actuation concept. The most common actuation concepts for active control of microdroplets are:

- Direct electrowetting;
- Electrowetting on a dielectric; and
- Thermocapillary actuation.

*Direct electrowetting* is the wetting effect between an electrolyte and the surface of an electrode. A thin electric double layer (EDL) exists between the electrolyte and the electrode [Fig. 5.33 (a)]. The EDL of a thickness  $\lambda_D$  acts as a capacitor with the capacitance per unit surface:

$$c_{\text{EDL}} = \frac{\varepsilon_0 \varepsilon_r}{\lambda_D} \quad (5.24)$$

where  $\varepsilon_0$  and  $\varepsilon_r$  are the dielectric constant of vacuum and the relative dielectric constant of the electrolyte, respectively. The higher the amount of energy stored in the capacitance, the lower is the surface energy. The relation between surface tension and the applied voltage across the interface is described by the Lippmann equation [44]:



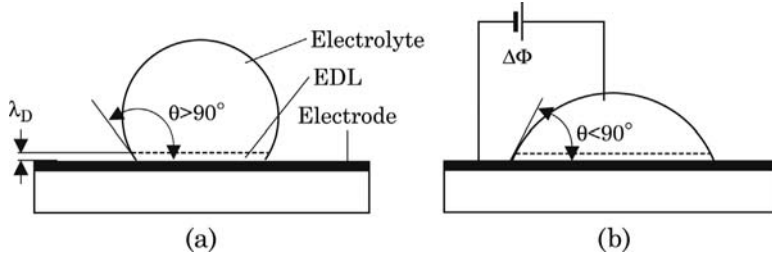


**Figure 5.33** Direct electrowetting: (a) formation of an electric double layer at the interface; and (b) an applied voltage changes the contact angle.

$$\sigma_{sl} = \sigma_{sl0} - \frac{c_{EDL} \Delta\Phi^2}{2} \quad (5.25)$$

where  $\Delta\Phi$  is the voltage across the interface, and  $\sigma_{sl0}$  is the initial surface tension at  $\Delta\Phi = 0$ . Combining the Lippmann equation (5.25) with the Young equation:

$$\sigma_{sg} - \sigma_{sl} = \sigma_{lg} \cos \theta \quad (5.26)$$

where  $\sigma_{sg}$ ,  $\sigma_{sl}$ , and  $\sigma_{lg}$  are the tensions at the solid/gas, solid/liquid, and liquid/gas interface, results in the relation between the contact angle  $\theta$  and the applied voltage  $\Delta\Phi$  [Fig. 5.33 (b)]:

$$\theta = \arccos \left( \cos \theta_0 + \frac{1}{\sigma_{lg}} \frac{c \Delta\Phi^2}{2} \right). \quad (5.27)$$

From the above equation, the condition for the applied voltage to make an originally hydrophobic surface  $\theta_0 > 90^\circ$  hydrophilic ( $\theta < 90^\circ$ ) is:

$$\Delta\Phi > \sqrt{-2\sigma_{lg} \cos \theta_0 / c}. \quad (5.28)$$

Increasing the voltage decreases the contact angle until a critical voltage is reached. At voltages higher than that critical value, the contact angle does not follow the Lippmann relation (5.25).

*Electrowetting on a dielectric.* The drawbacks of direct electrowetting are the fixed capacitance per unit surface, and the electrolysis reaction at the electrodes. If the electrode is coated with a hydrophobic and dielectric material such as Teflon, the capacitance per unit surface can be controlled by the thickness  $d$  of the dielectric coating (Fig. 5.34):

$$c = \frac{\epsilon_r \epsilon_0}{d}. \quad (5.29)$$

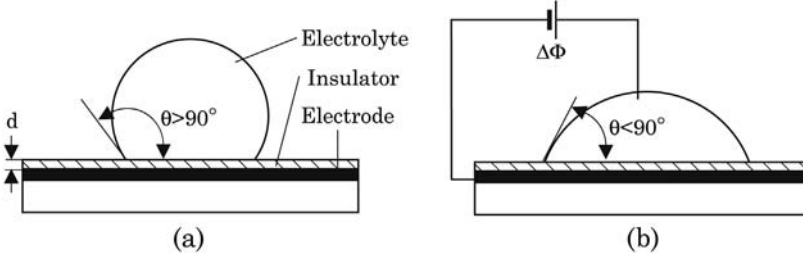


**Figure 5.34** Electrowetting on a dielectric: (a) the hydrophobic dielectric layer acts as a capacitor; and (b) an applied voltage changes the contact angle.

The relative dielectric coefficient of Teflon is approximately  $\varepsilon_r = 2$ . The contact angle can be formulated as a function of the applied voltage by combining (5.25) and (5.27).

*Thermocapillary actuation* utilizes the temperature dependency of the surface tension or the interfacial tension [45]. Fig. 5.35 depicts a simple model of this actuation concept. A liquid plug is positioned in a capillary between two external heaters. The capillary with two open ends is considered as long compared to the distance between the two heaters. The rest of the capillary is filled with air. The transient temperature distribution in the capillary can be described with a transient 1-D heat conduction equation. With the known temperature as a function of position and time, the temperature difference across the liquid plug and consequently the thermocapillary force can be determined. The velocity and the position of the plug are then determined by solving the balance equation of forces acting on the liquid plug.

Neglecting radiation and heat transfer to the liquid plug, the transient energy equation is formulated for a glass capillary as:

$$\frac{\partial \theta}{\partial t} = \alpha \frac{\partial^2 \theta}{\partial x^2} - \frac{2hR_o}{\rho c(R_o^2 - R_i^2)} \theta \quad (5.30)$$

where  $\theta$  is the temperature difference relative to the ambient temperature,  $R_o$  and  $R_i$  are the outer and inner radii of the capillary,  $\alpha$ ,  $\rho$ , and  $c$  are the thermal diffusivity, density and specific heat capacity of the capillary material, respectively. The heat transfer coefficient due to free convection at the outer surface of the capillary is estimated as  $h = 0.631k_a/(2R_o)$  with  $k_a$  being the thermal conductivity of air [45]. The periodic boundary conditions of the two heaters as depicted in Fig. 5.35 (c) are:

$$\begin{aligned} 0 \leq t < T_h/2: \quad \frac{d\theta}{dx} \Big|_{x=0} &= -\frac{q_0''}{k}; \quad \frac{d\theta}{dx} \Big|_{x=D_h} = 0 \\ T/2 < t \leq T_h: \quad \frac{d\theta}{dx} \Big|_{x=0} &= 0; \quad \frac{d\theta}{dx} \Big|_{x=D_h} = \frac{q_0''}{k} \end{aligned} \quad (5.31)$$

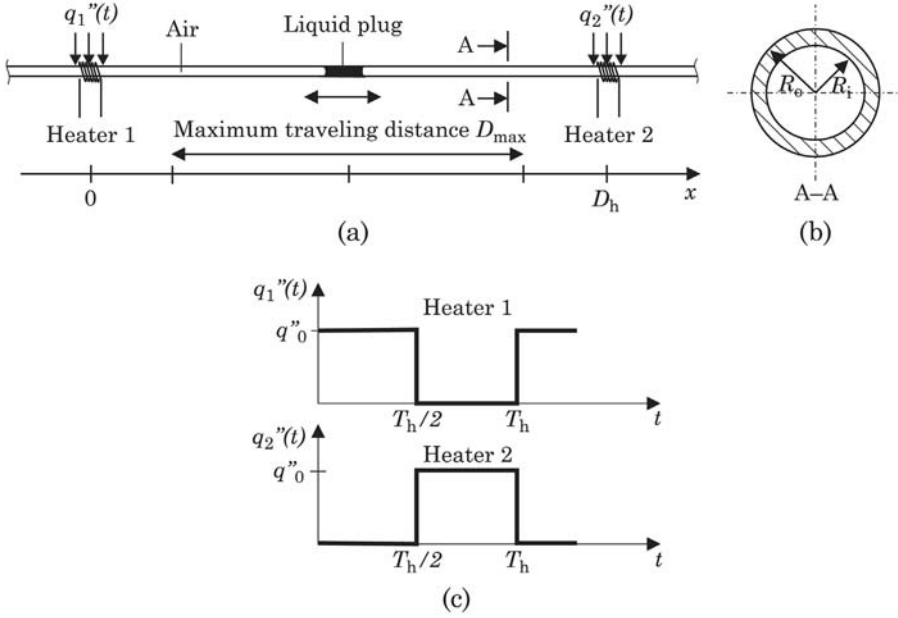


**Figure 5.35** Model of the thermocapillary actuation concept: (a) heater arrangement; (b) capillary cross section; (c) heating schemes.

where  $D_h$  is the distance between the two heaters,  $T_h$  is the heating period,  $k$  is the thermal conductivity of the capillary material, and  $q''_0$  is the heat flux inside the capillary wall. Introducing the dimensionless variables  $t^* = t/T_h$ ,  $x^* = x/D_h$  and  $\theta^* = \theta k / (q''_0 \cdot D_h)$  and solving the corresponding dimensionless energy equation results in the dimensionless temperature [45]:

$$\theta^*(x^*, t^*) = \Re \left\langle \sum_{n=-\infty}^{\infty} \frac{1}{\lambda_n} \left\{ \frac{F_{2n} \exp(\lambda_n) - F_{1n}}{\exp(2\lambda_n) - 1} \exp(\lambda_n x^*) + \left[ \frac{F_{2n} \exp(\lambda_n) - F_{1n}}{\exp(2\lambda_n) - 1} - F_{1n} \right] \exp(-\lambda_n x^*) \right\} \exp(i2\pi n t^*) \right\rangle \quad (5.32)$$

where  $\Re$  denotes the real part of a complex number,  $i$  is the imaginary unit, and

$$\begin{aligned} n = 0: & \quad \begin{cases} F_{1n} = -0.5 \\ F_{2n} = 0.5 \end{cases} \\ n \neq 0: & \quad F_{1n} = F_{2n} = \frac{1}{2\pi n} [1 - (-1)^n] \\ & \quad \lambda_n = \sqrt{\beta^2 + i2\pi n \eta} \end{aligned} \quad (5.33)$$

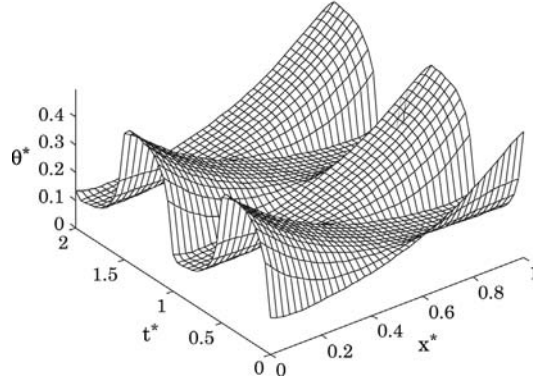


**Figure 5.36** Dimensionless temperature distribution between the two heaters as a function of dimensionless time  $t^*$  (capillary with inner radius  $R_i = 0.475$  mm and outer radius  $R_o = 0.69$  mm): (a)  $T_h = 100$  sec or  $f_h = 0.01$  Hz; (b)  $T_h = 10$  sec or  $f_h = 0.1$  Hz; (c)  $T_h = 1$  sec or  $f_h = 1$  Hz.

with  $\beta^2 = 2hD_h^2 R_o / [k(R_o^2 - R_i^2)]$ , and  $\eta = D_h^2 / (\alpha T_h)$ . Fig. 5.36 shows the temperature distribution as function of time.

Since the surface tension  $\sigma$  of the liquid depends on the temperature:

$$\sigma_{lg}(\theta) = \sigma_{lg0} + \gamma(\theta - \theta_0) \quad (5.34)$$

where  $\sigma_{lg0}$  is the surface tension at the reference temperature  $\theta_0$ , and the temperature field is a function of the position  $x$ , the surface tension is also a function of the position:

$$\sigma_{lg}(\theta) = f[\theta(x)] = g(x) = \sigma_{lg}(x). \quad (5.35)$$

The velocity  $u$  can be then determined through the force balance equation [45]:

$$\frac{du}{dt} + \left( \frac{8\nu}{R^2} \right) u + \frac{2}{\rho R_i L_{\text{plug}}} [\sigma_{lg}(x+L) \cos \phi_a - \sigma_{lg}(x) \cos \phi_r] = 0 \quad (5.36)$$

where  $L_{\text{plug}}$  is the length of the plug,  $R_i$  is the inner radius of the capillary, and  $\nu$  is the kinetic viscosity of the plug liquid. The receding and advancing contact angles are denoted with  $\phi_r$  and  $\phi_a$ . The three terms in the above represent the acceleration, the friction, and the thermocapillary force, respectively. The solution for the plug velocity is:

$$u = \frac{B}{A} [1 - \exp(-At)] \quad (5.37)$$

with

$$A = \frac{8\nu}{R_i^2} \quad (5.38)$$

$$B = \frac{2}{\rho R_i L_{\text{plug}}} [\sigma_{\text{lg}}(x + L_{\text{plug}}) \cos \phi_a - \sigma_{\text{lg}}(x) \cos \phi_r].$$

At the relatively slow velocity as observed later in the experiment, we can assume the same contact angle at the receding and advancing sides ( $\phi_r = \phi_a = \phi$ ). Applying this assumption and (5.34) into (5.38) results in

$$B = \frac{2}{\rho R_i L_{\text{plug}}} \gamma [\theta(x + L_{\text{plug}}) - \theta(x)] \cos \phi. \quad (5.39)$$

From (5.37), the position of the left side of the plug can be determined as:

$$x = \int_0^t u dt = x_0 + \frac{B}{A} t + \frac{B}{A^2} \exp(-At). \quad (5.40)$$

Fig. 5.37 depicts the typical positions and velocity of a liquid plug driven by the thermocapillary effect according to the above model.

## 5.4.2 Mixing in Microdroplets

### 5.4.2.1 Droplet-Based Mixing in a Straight Channel

Chaotic advection in the microdroplets can not be achieved in a straight microchannel. As shown in Fig. 5.30 (h) and Fig. 5.32, the flow pattern inside a droplet or a plug is steady and symmetrical. Although, during the formation process at a T-junction, the single vortex may improve transversal transport between the mixing liquids, the two symmetrical vortices in a straight channel keep them separately in each half of the droplet. In this case, the initial distribution at the instance of the break-up is crucial for good mixing during the passage of the liquid plug through the straight microchannel. If the velocity of the single vortex during the formation process is high enough, the mixing liquids can rotate at least a full  $360^\circ$ . When this plug is broken up from the injection port, the mixing fluids are equally distributed across both halves of the plugs and easily dispersed by the two internal vortices, Fig. 5.38 (a). During the passage in the straight microchannel, the number of rotations is proportional to the ratio between the travelling distance  $x$  and the plug length  $L$ . Thus, scaling of the mixing time can be estimated as:

$$t_{\text{mixing}} \propto L/x. \quad (5.41)$$

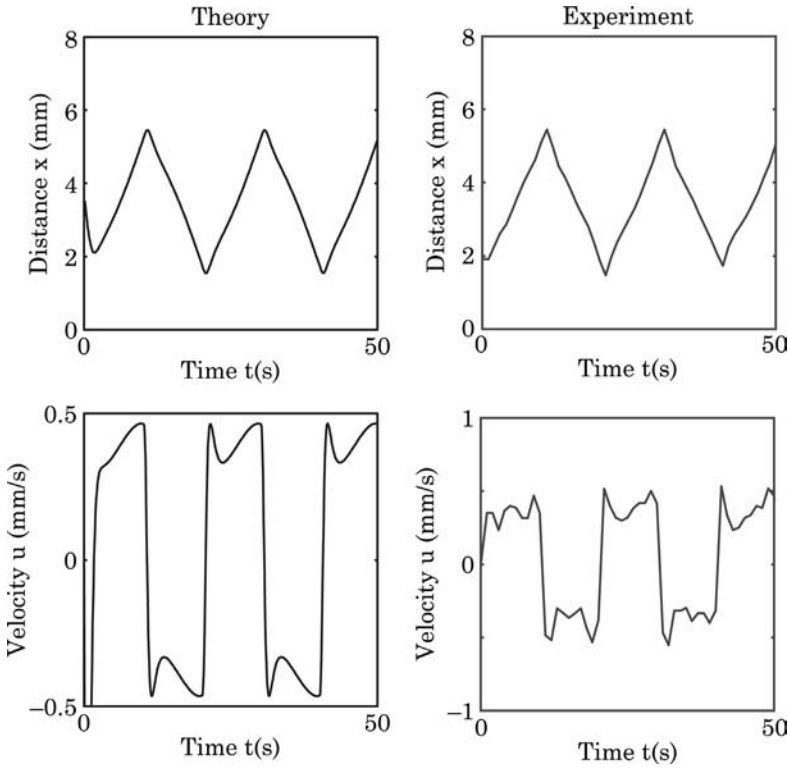


**Figure 5.37** Theoretical and experimental results of the position and the velocity of a plug as functions of time at a switching frequency of  $f_h = 0.05$  Hz (capillary with inner radius  $R_i = 0.475$  mm and outer radius  $R_o = 0.69$  mm, kinematic viscosity  $\nu = 10$  cSt, heat flux  $q'' = 2 \times 10^4$  W/m<sup>2</sup>, plug length  $L_{\text{plug}} = 1$  mm).

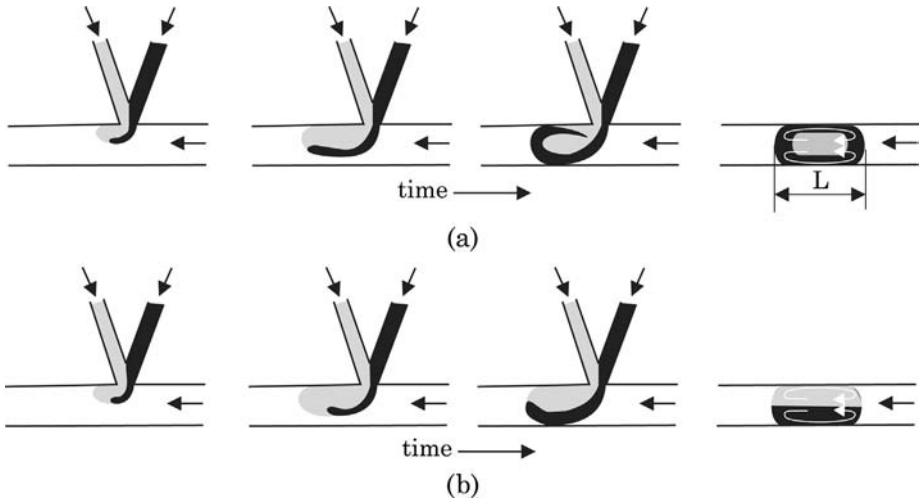


**Figure 5.38** Droplet-based micromixer in a straight channel: (a) good initial distribution; (b) bad initial distribution.

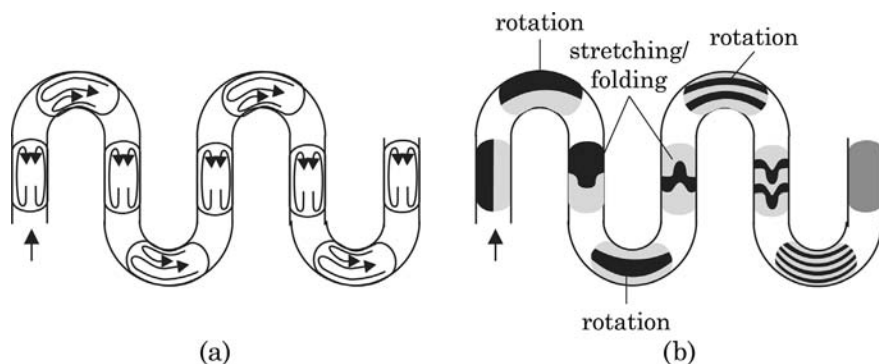


**Figure 5.39** Flow pattern in a microdroplet: (a) flow patterns inside the plugs in a microchannel with repeated turns; and (b) possible mixing pattern inside the plugs.

If the velocity of the single vortex during formation is not high enough, the mixing liquid cannot complete a  $90^\circ$  rotation. The mixing liquids are then separated in the two halves of the broken-up plug. The liquids will stay in their halves because of the symmetric vortices. The mixing condition is then similar to that of a simple T-mixer with parallel lamination, Fig. 5.38 (b).

As a rule of thumb, the initial distribution depicted in Fig. 5.38 (a) can be achieved with a high shear rate and a small plug. Thus, the higher the carrier flow rate and the smaller flow rate ratio  $r$  [see (5.14)], the better is mixing in liquid plugs, which are formed and transported in a straight channel. Since the internal velocity of the plug and the formation process itself are a complex interplay between flow rates, viscosity, interfacial tension, and channel geometry, it's difficult to achieve the right initial distribution in the plug. In the subsequent Section, different schemes for achieving chaotic advection inside the plug while it is transported in a microchannel are presented. With chaotic advection, mixing quality no longer depends on the initial distribution of the liquids.

#### 5.4.2.2 Mixing Based on Chaotic Advection Inside a Microdroplet

As mentioned previously, mixing in a microplug or a microdroplet moving in a straight channel relies much on the initial distribution of the mixing liquids. Fig. 5.39 shows the mixing concept based on a microchannel with repeated turns. The repeated turns induce periodic boundary conditions for the plugs. These periodic boundary conditions in turn induce chaotic advection. When a liquid plug is moving in a microchannel, the two counter rotating vortices stretch and fold the mixing liquids inside the plug. At each turn the vortices become asymmetric. One vortex is large and slow, while the other is small and fast. As a result, the mixing liquids experience a rotation at each turn. The time-periodic folding, stretching, and rotation leads to chaotic advection inside the plug and consequently faster mixing.

Considering a plug of a length  $L$ , a width  $W$ , and an initial striation thickness of  $s(0) \approx W$ , the striation thickness after  $n$  steps of repeated stretching, folding, and rotation is [46]:

$$s(n) = W\lambda^{-n} \quad (5.42)$$

where  $\lambda$  is the Lyapunov exponent of chaotic advection inside the plug. The exponential decrease of the striation thickness is a sign of a chaotic process. The diffusion time scale across the striation layer is:

$$t_{\text{diff}} = \frac{s(n)^2}{2D} = \frac{W^2\lambda^{-2n}}{2D} \quad (5.43)$$

where  $D$  is the molecular diffusion coefficient. Assuming that the plug travelled a distance of  $nL$  after the  $n$  steps, the residence time can be estimated as:

$$t_{\text{res}} \approx \frac{nL}{\bar{u}} \quad (5.44)$$

where  $\bar{u}$  is the velocity of the liquid plug. For complete mixing, the diffusion time should be approximately the same as the residence time:

$$\frac{W^2\lambda^{-2n}}{2D} \approx \frac{nL}{\bar{u}}. \quad (5.45)$$

Rearranging the above equation leads to:

$$2nL^*\lambda^{2n} \approx \text{Pe} \quad (5.46)$$

where  $\text{Pe} = W\bar{u}/D$  is the Peclet number, and  $L^* = L/W$  is the dimensionless droplet length normalized by the channel width. Taking the logarithm of both sides of (5.46) and assuming a large Peclet number, so that  $\log(n) \ll n \log(\lambda)$ , result in the relation [46]:

$$n \approx \log(\text{Pe}). \quad (5.47)$$

Substituting the above value of  $n$  into (5.44), results in the required residence time of the microplug:

$$t_{\text{res}} = \frac{L}{\bar{u}} \log(\text{Pe}). \quad (5.48)$$



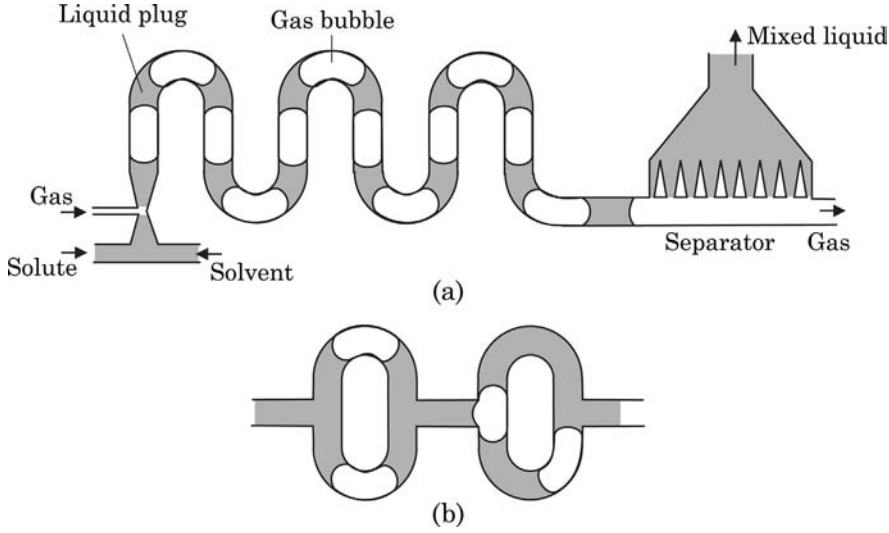


**Figure 5.40** Micromixers based on gas/liquid flow: (a) Mixer design with repeated turns; and (b) Chaotic advection with loop design.

Compared to diffusive mixing with parallel lamination, the improvement of mixing time is [46]:

$$\frac{t_{\text{lamination}}}{t_{\text{chaotic}}} = \frac{\text{Pe}}{L \cdot \log(\text{Pe})}. \quad (5.49)$$

Because of the passive microfluidic network, droplet-based micromixer can be easily implemented with any micromachining technology. Most of the reported droplet-based micromixers are made in PDMS using soft lithography [46].

If the application requires a single phase of the mixed fluid, the two immiscible phases need to be separated. One of the drawbacks of droplet-based micromixers is the difficult separation of the carrier fluid and the mixed fluid due to the lower interfacial tension. The higher surface tension of a liquid/gas system would allow easy separation by capillary effect. Günther et al. replaced the immiscible oil by a gas phase [47]. The liquid phase is separated by gas bubbles. Mixing in a liquid plug occurs in the same manner as discussed above. Curved channels induce chaotic advection and improve mixing significantly. The large surface tension of the gas/liquid system allows the design of a capillary separator at the end of the micromixer. A single mixed liquid can be collected, Fig. 5.40 (a).

Garstecki et al. [48] introduced the loop design shown in Fig. 5.40 (b). The curved sections of the loops also cause chaotic advection similar to the design shown in Fig. 5.40 (a). However, due to the increased fluidic resistance in the branch with the air bubble, the pattern of the bubbles becomes chaotic, leading to further improvement of mixing inside the liquid plug.

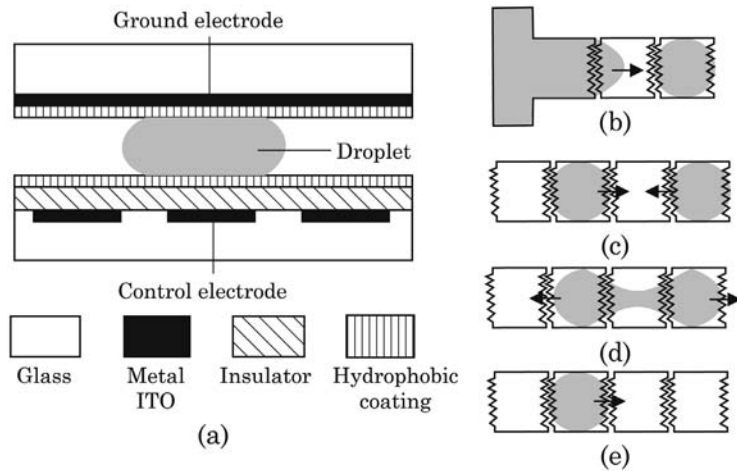


**Figure 5.41** Droplet-based micromixer based on electrowetting on a dielectric: (a) device concept; (b) droplet dispensing; (c) droplet merging; (d) droplet cutting; and (e) droplet transport.

Besides the passive formation process described above, droplets can be generated and transported actively by hydrodynamic force [49,50] or surface effects, such as thermocapillary [51] and electrowetting [52]. Hosokawa et al. [49] reported the earliest droplet-based micromixer, which was fabricated in PDMS. The concept utilized a hydrophobic microcapillary vent, which join the solute with the solvent droplet.

Paik et al. reported different droplet-based mixing schemes with the electrowetting concept [52]. The active actuation allows droplets to be merged and split repeatedly. Subsequently, the merged droplet can be transported with different motion patterns to induce chaotic mixing. Fig. 5.41 (a) depicts the device concept. The aqueous droplet is surrounded by immiscible oil. The droplet is aligned with the control electrode at the bottom. The  $1 \times 1$  mm control electrode changes the hydrophobicity of the solid/liquid interface. A 800-nm Parylene C layer works as the insulator. The ground electrode is made of transparent ITO for optical investigation. A 60-nm Teflon layer was coated over the surface to make it hydrophobic. Electrowetting allows different droplet handling operations, such as droplet dispensing [Fig. 5.41 (b)], droplet merging [Fig. 5.41 (c)], droplet cutting [Fig. 5.41 (d)], and droplet transport [Fig. 5.41 (e)]. These basic operations allow merging and fast mixing of liquid droplets.

## References

1. S. Wiggins and J.M. Ottino, "Foundation of chaotic mixing," *Phil. Trans. R. Soc. Lond. A*, Vol. 362, pp. 937–970, 2004.

2. D. Bothe, C. Stemich and H.J. Warnecke, "Fluid mixing in a T-shaped micro-mixer," *Chemical Engineering Science*, Vol. 61, pp. 2950–2958, 2006.
3. M. Hoffmann, C. Schlüter and N. Rübiger, "Experimental investigation of liquid-liquid mixing in T-shaped micro-mixers using  $\mu$ -LIF and  $\mu$ -PIV," *Chemical Engineering Science*, Vol. 61, pp. 2968–2976, 2006.
4. N.T. Nguyen, D. Bochnia, R. Kiehnscherf and W. Dötzel, "Investigation of forced convection in micro-fluid systems," *Sensors and Actuators A: Physical*, Vol. 55, pp. 49–55, 1996.
5. S.H. Wong, M.C.L. Ward and C.W. Wharton, "Micro T-mixer as a rapid mixing micro-mixer," *Sensors and Actuators B: Physical*, pp. 359–379, 2004.
6. N. Kockmann, T. Kiefer, M. Engler and P. Woias, "Silicon microstructures for high throughput mixing devices," *Microfluidics and Nanofluidics*, Vol. 4, pp. 327–335, 2006.
7. S.H. Wong, M.C.L. Ward and C.W. Wharton, "Micro T-mixer as a rapid mixing micro-mixer," *Sensors and Actuators B: Physical*, pp. 359–379, 2004.
8. H. Wang, P. Iovenitti, E. Harvey and S. Masood, "Optimizing layout of obstacles for enhanced mixing in microchannels," *Smart Materials and Structures*, Vol. 11, pp. 414–424, 2002.
9. Y. Lin, G.J. Gerfen, D.L. Rousseau and S.R. Yeh, "Ultrafast microfluidic mixer and freeze-quenching device," *Analytical Chemistry*, Vol. 75, pp. 5381–5386, 2003.
10. F. Jiang, K.S. Drese, S. Hardt, M. Küpper and F. Schöfeld, "Helical flows and chaotic mixing in curved micro channels," *AIChE Journal*, Vol. 50, pp. 2297–2305, 2004.
11. V. Mengeaud, J. Josserand and H.H. Girault, "Mixing processes in a zigzag microchannel: Finite element simulation and optical study," *Analytical Chemistry*, Vol. 74, pp. 4279–4286, 2002.
12. M.Q. Yi and H.H. Bau, "The kinematics of bend-induced mixing in micro-conduits," *International Journal of Heat and Fluid Flow*, Vol. 24, pp. 645–656, 2003.
13. R.H. Liu, M.A. Stremler, K.V. Sharp, M.G. Olsen, J.G. Santiago, R.J. Adrian, H. Aref and D.J. Beebe, "Passive mixing in a three-dimensional serpentine microchannel," *Journal of Microelectromechanical Systems*, Vol. 9, pp. 190–197, 2000.
14. R.A. Vijayendran, K.M. Motsegood, D.J. Beebe and D.E. Leckband, "Evaluation of a three-dimensional micromixer in a surface-based biosensor," *Langmuir*, Vol. 19, pp. 1824–1828, 2003.
15. H. Chen and J.C. Meiners, "Topologic mixing on a microfluidic chip," *Applied Physics Letters*, Vol. 84, pp. 2193–2195, 2004.
16. C.C. Hong, J.W. Choi and C.H. Ahn, "A novel in-plane microfluidic mixer with modified tesla structures," *Lab on a Chip*, Vol. 4, pp. 109–113, 2004.
17. Y. Mizuno and M. Funakoshi, "Chaotic mixing due to a spatially periodic three-dimensional flow," *Fluid Dynamics Research*, Vol. 31, pp. 129–149, 2002.
18. M.K. Jeon, J.H. Kim, J. Noh, S.H. Kim, H.G. Park and S.I. Woo, "Design and characterization of a passive recycle micromixer," *Journal of Micromechanics and Microengineering*, Vol. 15, pp. 346–350, 2005.
19. S.J. Park, J.K. Kim, J. Park, S. Chung, C. Chung and J.K. Chang, "Rapid three-dimensional passive rotation micromixer using the brackup process," *Journal of Micromechanics and Microengineering*, Vol. 14, pp. 6–14, 2004.
20. A.P. Sudarsan and V.M. Ugaz, "Multivortex micromixing," *PNAS*, Vol. 103, pp. 7228–7233, 2006.
21. A.P. Sudarsan and V.M. Ugaz, "Fluid mixing in planar spiral microchannels," *Lab Chip*, Vol. 6, pp. 74–82, 2006.
22. C. Simonnet and A. Croisman, "Chaotic mixing in a steady flow in a microchannel," *Physical Review Letters*, Vol. 94, p. 134501, 2005.
23. D. Kim, S.H. Lee, T.H. Kwon and C.H. Ahn, "A serpentine laminating micromixer combining splitting/recombination and advection," *Lab Chip*, Vol. 5, pp. 739–747, 2005.

24. H.M. Xia, C. Shu, S.Y.M. Wan and Y.T. Chew, "Chaotic micromixers using two-layer crossing channels to exhibit fast mixing at low reynolds numbers," *Lab Chip*, Vol. 5, pp. 748–755, 2005.
25. S.H. Chang and Y.H. Cho, "Static micromixers using alternating whirls and lamination," *Journal of Micromechanics and Microengineering*, Vol. 15, pp. 1397–1405, 2005.
26. A.D. Stroock, S.K.W. Dertinger, A. Ajdari, I. Mezic, H.A. Stone and G.M. Whitesides, "Chaotic mixer for microchannels," *Science*, Vol. 295, pp. 647–650, 2002.
27. A.D. Stroock and G.M. Whitesides, "Controlling flows in microchannels with patterned surface charge and topography," *Accounts of Chemical Research*, Vol. 36, pp. 597–604, 2003.
28. J. Aubin, D.F. Fletcher, J. Bertrand and C. Xuereb, "Characterization of the mixing quality in micromixers," *Chemical Engineering Technology*, Vol. 26, pp. 1262–1270, 2003.
29. T.J. Johnson, D. Ross and L.E. Locascio, "Rapid microfluidic mixing," *Analytical Chemistry*, Vol. 74, pp. 45–51, 2002.
30. F. Schönfeld and S. Hard, "Simulation of helical flows in microchannels," *AIChE Journal*, Vol. 50, pp. 771–778, 2004.
31. D.G. Hassel and W.B. Zimmerman, "Investigation of the convective motion through a staggered herringbone micromixer at low reynolds number flow," *Chemical Engineering Science*, Vol. 61, pp. 2977–2985, 2006.
32. T.G. Kang and T.H. Kwon, "Colored particle tracking method for mixing analysis of chaotic micromixers," *Journal of Micromechanics and Microengineering*, Vol. 14, pp. 891–899, 2004.
33. N.S. Lynn and D.S. Dandy, "Geometrical optimization of helical flow in grooved micromixers," *Lab Chip*, Vol. 7, pp. 580–587, 2007.
34. P.B. Howell, D.R. Mott, S. Fertig, C.R. Kaplan, J.P. Golden, E.S. Oran and F.S. Ligler, "A microfluidic mixer with grooves placed on the top and bottom of the channel," *Lab Chip*, Vol. 5, pp. 524–530, 2004.
35. T.M. Floyd-Smith, J.P. Golden, P.B. Howell and F.S. Ligler, "Characterization of passive microfluidic mixers fabricated using soft lithography," *Microfluidics and Nanofluidics*, Vol. 2, pp. 180–183, 2006.
36. X. Fu, S.F. Liu, X.D. Ruan and H.Y. Yang, "Research on staggered oriented ridges static micromixers," *Sensors and Actuators B*, Vol. 114, pp. 618–624, 2006.
37. D.S. Kim, S.W. Lee, T.H. Kwon and S.S. Lee, "A barrier embedded chaotic micromixer," *Journal Micromechanics and Microengineering*, Vol. 14, pp. 798–805, 2004.
38. A. Bertsch, S. Heimgartner, P. Cousseau and P. Renaud, "Static micromixers based on large-scale industrial mixer geometry," *Lab on a Chip*, Vol. 1, pp. 56–60, 2001.
39. D.S. Kim, I.H. Lee, T.H. Kwon and D.W. Cho, "A barrier embedded kenics micromixer," *Journal of Micromechanics and Microengineering*, Vol. 14, pp. 1294–1301, 2004.
40. A. Günther and K.F. Jensen, "Multiphase microfluidics: from flow characteristics to chemical and materials synthesis," *Lab on a Chip*, Vol. 6, pp. 1487–1503, 2006.
41. G.I. Taylor, "The formation of emulsions in definable fields of flow," *Proc. R. Soc. London A*, Vol. 146, p. 501, 1934.
42. P. Garstecki, H.A. Stone and G.M. Whitesides, "Mechanism for flow-rate controlled breakup in confined geometries: A route to monodisperse emulsions," *Physical Review Letters*, Vol. 94, p. 164501, 2005.
43. P. Garstecki, M.J. Fuerstman, H.A. Stone and G.M. Whitesides, "Formation of droplets and bubbles in a microfluidic T-junction—scaling and mechanism of break-up," *Lab Chip*, Vol. 6, pp. 473–446, 2006.
44. M.G. Lippmann, "Relations entre les énomènes électriques et capillaires," *Ann. Chim. Phys.*, Vol. 5, pp. 494–549, 1875.
45. Z. Jiao, N.T. Nguyen, X.Y. Huang and Y.Z. Ang, "Reciprocating thermocapillary plug motion in an externally heated capillary," *Microfluidics and Nanofluidics*, Vol. 3, pp. 39–46, 2006.

46. M. Bringer, C.J. Gerdt, H. Song, J.D. Tice and R.F. Ismagilov, "Microfluidic systems for chemical kinetics that rely on chaotic mixing in droplets," *Phil. Trans. R. Soc. Lond. A*, Vol. 362, pp. 1087–1104, 2004.
47. A. Günther, M. Jhunjhunwala, M. Thalmann, M.A. Schmidt and K.F. Jensen, "Micromixing of miscible liquids in segmented gas-liquid flow," *Langmuir*, Vol. 21, pp. 1547–1555, 2005.
48. P. Garstecki, M.J. Fuerstman, M.A. Fischbach, S.K. Sia and G.M. Whitesides, "Mixing with bubbles: a practical technology for use with portable microfluidic devices," *Lab Chip*, Vol. 6, pp. 207–212, 2006.
49. K. Hosokawa, T. Fujii and I. Endo, Droplet-based nano/picoliter mixer using hydrophobic microcapillary vent, Proceedings of the IEEE International Workshop Micro Electromechanical System, Piscataway, NJ, USA, 1999, pp. 388–393.
50. H. Song, M.R. Bringer, J.D. Tice, C.J. Gerdt and R.F. Ismagilov, "Experimental test of scaling of mixing by chaotic advection in droplets moving through microfluidic channels," *Applied Physics Letters*, Vol. 83, pp. 4664–4666, 2003.
51. K. Handique and M.A. Burns, "Mathematical modeling of drop mixing in a slit-type microchannel," *Journal of Micromechanics and Microengineering*, Vol. 11, pp. 548–554.
52. P. Paik, V.K. Pamula and R.B. Fair, "Rapid droplet mixers for digital microfluidic systems," *Lab on a Chip*, Vol. 3, pp. 253–259, 2003.

## 6 Active Micromixers

---

### 6.1 Flow Instability in Microchannels

Active micromixers are based on disturbance induced by external fields. Because flows in microchannels have Reynolds numbers far below the critical Reynolds number, transversal disturbance is needed for making the interface between the two mixed phases become unstable. A typical stability analysis consists of the following seven steps [1]:

- Formulating the governing equation and finding the basic solution to the physical effect. The stability analysis applies to the basic solution  $x_0$  of the problem. This solution can be a scalar or a vector function.
- Adding a disturbance  $x'$  to the basic solution  $x_0$  and substituting  $x_0 + x'$  into the governing equation.
- Subtracting terms that  $x_0$  satisfies. The remaining equation is the disturbance equation.
- For small disturbance analysis, ( $x' \ll x_0$ ), the higher order of  $x'$  can be neglected. The disturbance equation becomes linear.
- Further simplifying the disturbance equation by assuming a prescribed form such as a travelling wave.
- The linearized disturbance equation should be homogenous and have homogenous boundary conditions. Thus it can only be solved for specific values of the equation's parameters. The analysis becomes an eigenvalue problem.
- The eigenvalues found in the step above are examined for unstable, stable, or neutrally stable behavior. The results are shown on a chart with neutral curves, which separate the stable and the unstable regions.

### 6.2 Pressure-Driven Disturbance

#### 6.2.1 Actuation Concepts for Pressure Generation

In most cases, pressure-driven disturbance is created by an external actuator. This section reviews the most common microactuator concepts, which can be integrated in a micromixer. These concepts can be categorized according to their physical effects as:

- Pneumatic;
- Thermopneumatic;

- Thermomechanical;
- Piezoelectric;
- Electrostatic;
- Electromagnetic;
- Electrochemical and chemical;
- Capillary force;
- Centrifugal and Coriolis forces.

As explained later in Section 6.2.2, the two key parameters for hydrodynamic instability needed in active micromixers are the magnitude and the frequency of the disturbance. Thus, the pressure generated by an actuator and its dynamic response are of interest for designers of active micromixers. Fig. 6.1 shows the typical ranges of actuation pressure and actuation frequency. Because actuation magnitude is associated with the storage capacity of the microactuator, thermal concepts, such as thermopneumatic and thermomechanical, are the most powerful in term of actuation pressure. However, thermal processes are usually slow and the actuation frequencies are of the order of a few hertz. In contrast, surface-based concepts, such as electrostatic and piezoelectric microactuators, can work at a very high frequency.

Because the total energy delivered by a microactuator is proportional to its volume, a small actuator also means a small actuation energy. The energy density of actuators usually does not scale with miniaturization and can be estimated as follows.

The energy density of a thermomechanical actuator, which is based on the thermal expansion to convert electrical energy to mechanical energy through thermal energy, can be estimated as:

$$\epsilon = \frac{1}{2} E_{\text{mech}} (\alpha_{\text{th}} \Delta T)^2 \quad (6.1)$$

where  $E_{\text{mech}}$  and  $\alpha_{\text{th}}$  are the Young's modulus and the thermal expansion coefficient of the actuator's material.  $\Delta T$  is the temperature difference.

The energy density of a piezoelectric actuator is proportional to the electric field strength  $E_{\text{el}}$  and inversely proportional to the piezoelectric coefficient  $d$  and the Young's modulus  $E_{\text{mech}}$ :

$$\epsilon = \frac{1}{2} \frac{E_{\text{el}}}{(dE_{\text{mech}})^2}. \quad (6.2)$$

The energy density in an electrostatic actuator is equivalent to the electric energy stored in the capacitance between the two electrodes:

$$\epsilon = \frac{1}{2} \varepsilon E_{\text{el}}^2 \quad (6.3)$$

where  $\varepsilon$  is the permittivity of the material between the two electrodes.

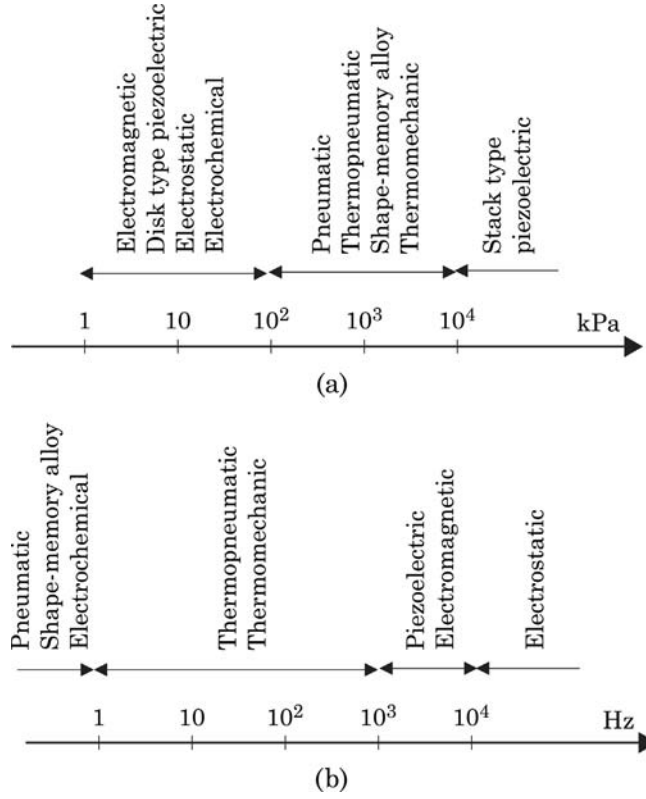


**Figure 6.1** Characteristics of microactuators used in active micromixers: (a) typical actuation magnitudes; (b) typical actuation frequency.

The energy density in an electromagnetic actuator is proportional to the square of the magnetic flux  $B$ :

$$\epsilon = \frac{1}{2} \frac{B^2}{\mu}, \quad (6.4)$$

where  $\mu$  is the permeability of the actuator's material. For a constant coil's resistance, the magnetic flux is proportional to the applied voltage. It's apparent that the energy density of most microactuators is proportional to the square of the applied voltage, which in turn generates temperature difference, electric field strength, and magnetic flux.

*Pneumatic actuators* represent the simplest actuation concept for active micromixers. Many microfluidic devices based on PDMS use pneumatic actuation for micro-pumps, microvalves, and active mixers. The advantage of this concept is that external pneumatic sources are readily available. Further, the fabrication of microchannels for the actuation pressure can follow the same steps as those of the microchannel network. Because the actuation concept



relies on an external pressure supply, the disturbance frequency depends on the external switching valves and is of the order of 0.1 Hz to 1 Hz.

*Thermopneumatic actuators* convert electric energy into heat, which in turn is converted into mechanical energy through the thermal expansion of gases. Compared to electrostatic or electromagnetic actuators, thermopneumatic actuators can offer a much larger actuation energy. Gas bubble nucleation and boiling processes cause an explosion-like phase transition at the micro scale. These processes are difficult to control, but very powerful if they are used for actuation. Thermal expansion of a single phase is often enough for actuation application. However, due to the large change in specific volume of the phase transition, the solid-to-liquid and liquid-to-gas phase change can be utilized to achieve the maximum performance.

*Thermal-expansion actuators* refer to actuators based on thermal expansion of a solid. In contrast to the thermopneumatic concept, thermal expansion of a solid results in a small volume change but a large force. The generated force is proportional to the temperature difference  $\Delta T$  between the heater and the ambient temperature:

$$f \propto \alpha_{\text{th}} \Delta T \quad (6.5)$$

where  $\alpha_{\text{th}}$  is the thermal expansion coefficient of the solid material. Careful design of heaters, their location, and thermal isolation are needed for optimal operation. The usually small deflection can be amplified by utilizing the instability of compliant structures. The high compressive stress within the structure can accumulate up to a critical value and then buckles instantaneously. The buckling stress allows a large displacement to be realized, even though the volume change is small. Because heat is conducted in the solid material, active mixer designs with this type of actuator should consider a material with low thermal conductivity.

*Bimorph actuators* use the difference in thermal coefficient of expansion of two bonded solids, also called a bimorph. Compared to thermal-expansion actuators, bimetallic actuators can generate a large stress at the interface between the two materials, thus potentially high actuation force. The actuation force is proportional to the difference between the thermal expansion coefficients of the two materials  $\alpha_{\text{th},2} - \alpha_{\text{th},1}$  and the temperature difference  $\Delta T$ :

$$f \propto (\alpha_{\text{th},2} - \alpha_{\text{th},1}) \Delta T. \quad (6.6)$$

The heat for bimorph actuators can come from any external source, such as a focused laser. For compact designs, the heat is usually generated by a microheater, which is integrated between the two solid materials or on one side of the bimorph. Because of the required deflection, most bimorph structures are thin. Thus, the temperature gradient along the thickness is small. Therefore, the position of the microheater is not significant. Bimetallic actuators offer an

almost linear deflection. This actuator type shares the same disadvantages of other thermal actuators, such as high power consumption and slow response. Because of the linear relation and small hysteresis, feedback control can be realized with an integrated temperature sensor.

*Shape-memory alloys* (SMA) are materials such as titanium/nickel alloy, which can return to their original undeformed shape upon a change of temperature. The actuation concept is based on the phase transformations of the alloy from a “soft” state (martensite) at low temperatures to a “hard” state (austenite) at higher temperatures. Because the alloy structure is electrically conductive, heat can be generated by passing a current directly through it. Titanium/nickel alloys are the most common SMA commercially available.

*Piezoelectricity* is an effect that can convert electric energy directly into mechanical energy. An applied electric field generates a mechanical strain in the material that can be translated into force or displacement. In contrast to thermal concepts, the direct electrical-mechanical conversion prevents losses and allows high energy efficiency. Piezoelectric actuators generally generate small strain (usually less than 0.1%) and high stresses (several megapascals). Therefore, they are suitable for applications that require large forces but small displacements. Large displacement can be realized by stacking many piezoelectric layers in parallel. Common piezoelectric materials that are compatible to microtechnology are polyvinylidene fluoride (PVDF), lead zirconate titanate (PZT), and zinc oxide (ZnO). PZT offers high piezoelectric coefficients but is very difficult to deposit as a thin film. PVDF and ZnO are often used in microfabrication. Thin-film piezoelectric actuators usually do not deliver enough force for pressure disturbance in active micromixers. A more economic way is using external actuators, such as piezostacks, bimorph piezocantilevers, or bimorph piezodiscs, are commercially available. Piezostack actuators can deliver a large force, while bimorph piezocantilevers allow large displacement at the expense of small actuation forces.

*Electrostatic actuators* are based on the attractive force between two oppositely charged plates. Similar to piezoelectric actuators, electrostatic actuators convert electrical energy directly into mechanical energy. There are no thermal losses in this actuation concept. The simplest approximation for the electrostatic force is the force between two plates with the overlapping plate area  $A$ , distance  $d$ , applied voltage  $V$ , relative dielectric coefficient  $\varepsilon_r$ , and the permittivity of vacuum  $\varepsilon_0 = 8.85418 \times 10^{-12}$  F/m:

$$f = \frac{1}{2} \varepsilon_r \varepsilon_0 A \left( \frac{V}{d} \right)^2. \quad (6.7)$$

The main advantage of electrostatic actuators is the fast response. However, the high voltage and small deflection make them not suitable for active micromixers with dimensions of the order of a millimeter.

*Electromagnetic actuators* are based on magnetic forces. The force can be created by electromagnets or permanent magnets that offer a large deflection.

The vertical force of a magnetic flux  $B$  in direction  $z$  acting on a magnet with magnetization  $m_m$  and volume  $V$  is given by:

$$f = m_m \int \frac{dB}{dz} dV. \quad (6.8)$$

The relation between the magnetic flux  $B$  and the magnetic field strength is:

$$B = \mu H = \mu_0 \mu_r H = \mu(1 + \chi_m)H \quad (6.9)$$

where  $\mu$ ,  $\mu_0$ ,  $\mu_r$ , and  $\chi_m$  are the permeability, permeability of free space ( $4\pi \times 10^{-7}$  H/m), relative permeability, and the magnetic susceptibility of the medium, respectively. In the case of an electromagnet, the magnetic field strength inside a solenoid with  $N$  turns, a length  $L$ , and a driving current  $I$  can be estimated as:

$$H = \frac{NI}{L}. \quad (6.10)$$

Magnetic actuators can generate large forces and large displacements. However, actuation coils are also Ohmic resistances. Joule heating of the coils leads to heat losses, and consequently lower efficiency.

*Electrochemical actuators* convert electrical energy into mechanical energy through electrochemical reaction. The reaction creates gas bubbles, which in turn generate mechanical energy through pressure or gas/liquid interfacial tensions. A common electrochemical reaction is electrolysis of water:



The reaction products are gases, thus increase the volume and pressure. The generated gases have a volume that is about 600 times of the original liquid water. This ratio exceeds that of thermopneumatic actuators. The reverse reaction makes oxygen and hydrogen turn back to water. This reversed reaction needs a catalyst, such as platinum. The catalyst is able to absorb hydrogen. The hydrogen-platinum bond is weaker than the hydrogen-hydrogen bond. Therefore, the energy barrier required for freeing hydrogen atoms from  $\text{H}_2$  and bonding with oxygen is lower than in the gas phase:



Compared to all other actuation concepts, electromechanical actuation offers the most efficient way for converting electrical energy into mechanical energy. The pressure inside the bubble is proportional to the surface tension  $\sigma$  and the radius of curvature  $R$  of the meniscus.

*Chemical actuators* convert chemical energy directly into mechanical energy. Electrical energy is not needed. Polymeric materials often swells if they are immersed in a solvent. Swelling is to be avoided if the polymer is used as the device material. However, swelling is attractive for actuation applications. Hydrogels are polymers with high water content. Hydrogel volume is sensitive to temperature, solvent concentration, and ionic strength. Thus, swelling can be controlled by diffusion of solvent and ions. Species transport based on diffusion is faster at the micro scale due to the shorter diffusion path. Because the temperature diffusivity is of the order of  $10^{-3} \text{ cm}^2/\text{s}$ , the diffusion coefficient of a solvent is of the order of  $10^{-5} \text{ cm}^2/\text{s}$ , the cooperative diffusion coefficient of polymer chains is on the order of  $10^{-7} \text{ cm}^2/\text{s}$ , and the swelling dynamics are determined by the later coefficient. The characteristic time constant of swelling response can be estimated as:

$$\tau = \frac{d^2}{D_{\text{coop}}} \quad (6.13)$$

where  $d$  is the characteristic dimension of the hydrogel, and  $D_{\text{coop}}$  is the cooperative diffusion coefficient of the polymer chains. From (6.13), the dynamics of chemical actuators depends only on the size and the bulk polymer. Using packed small particles instead of a bulk material would improve the response of the actuator. Common hydrogels are polymethacrylic acid triethyleneglycol (pMAA-g-EG), polyacrylic acid-2-hydroxymethylmethacrylate (pAA-2-HEMA), and polyacrylamide-3-methacrylamidophenylboronic acid (pAAm-3-MPBA).

*Electrocapillary actuators* relies on the change in interfacial tension between two immiscible, conductive liquids, or between a solid surface and a liquid, caused by a potential difference. The effect is also called electrowetting and is caused by the adsorption characteristics of ions at the electric double layer between the two phases. This layer is typically 1 to 10 nm thick and works as an electrical insulator between the two conductive liquids. By changing the electrical potential across this double layer, the surface tension  $\sigma$  between the two liquids becomes:

$$\sigma = \sigma_0 - \frac{C}{2} \Delta\Phi^2 \quad (6.14)$$

where  $\sigma_0$  is the maximum value of surface tension at  $V = V_0$ ,  $C$  is the capacitance per unit area of the double layer, and  $V$  is the voltage applied across the liquid interface. Electrowetting can be used for moving a droplet that leads to improved mixing either inside the droplet or in the surrounding liquid. Readers may refer to Chapter 5 for chaotic mixing in a droplet.

The *thermocapillary actuator* is another actuation concept suitable a multiphase system. The thermocapillary effect is caused by the temperature dependence of the interfacial tension between two immiscible phases. At a higher

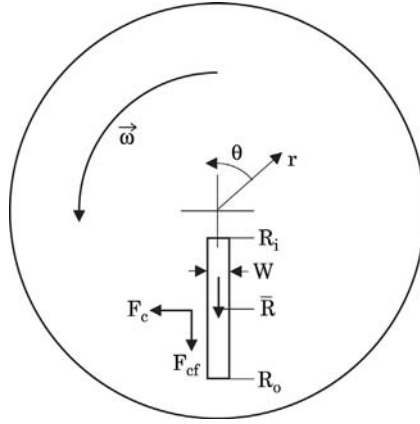


**Figure 6.2** Model of a disc spinning at an angular velocity of  $\omega$ . The liquid plug starts at the radial position  $R_i$  and ends at  $R_o$ . The average radial distance between the plug and the disc center is  $\bar{R} = (R_o - R_i)/2$ . The width of the plug is  $W$ .

temperature, the molecules in the bulk liquid move faster and their attractive force decreases. The smaller attractive force causes lower viscosity and lower interfacial tension. Thermocapillary forces cause a liquid droplet to run away from a heat source and make a bubble run towards the heat source. Since the rate of change of surface tension with temperature is not large, the effect requires considerable heating power to get the desired force. Thermocapillary actuators are suitable for droplet-based systems.

The *centrifugal/Coriolis actuator* is based on the rotational motion of a unique device platform, also called “lab-on-a-disc.” For the flow in this platform, the Navier–Stokes equation has two additional terms for the centrifugal force  $\mathbf{f}_{cf}$  and the Coriolis force  $\mathbf{f}_C$  [2]:

$$\rho \frac{D\mathbf{v}}{Dt} = -\nabla p + \mu \nabla^2 \mathbf{v} + \mathbf{f}_{cf} + \mathbf{f}_C. \quad (6.15)$$

For the model depicted in Fig. 6.2, the expression for the centrifugal force and the Coriolis force are:

$$\mathbf{f}_{cf} = -\rho \vec{\omega} \times (\vec{\omega} \times \mathbf{r}) \quad (6.16)$$

$$\mathbf{f}_C = -2\rho \vec{\omega} \times \mathbf{v},$$

where  $\vec{\omega}$  indicates the vector of the angular velocity. The Coriolis force acting on the liquid plug depicted in Fig. 6.2 can be estimated as:

$$f_C = \frac{\rho \bar{R} W^2 \omega^3}{8\mu}. \quad (6.17)$$

The Coriolis force is perpendicular to the radial direction and consequently improves transversal transport in the liquid plug. The ratio between the Coriolis force and the driving centrifugal force is:

$$\frac{f_C}{f_{cf}} = \frac{\rho W^2 \omega}{8\mu}. \quad (6.18)$$

The above relation shows that transversal transport may dominate over radial transport if the angular velocity is high enough.

*Biological actuators* are autonomous actuators at the nanometer scale using motors from biological systems [3,4]. These systems can work in an aqueous environment, which exists in many microfluidic applications. For instance, bacterial actuation can be achieved with biomolecular motors from flagellated bacteria, such as *Escherichia coli* (*E. coli*) or *Serratia marcescens*. These bacteria provide regulatory hooks on which to build and control flagella. The biomolecular motors can be switched on, and their direction as well as duration can be controlled.

The bacterial flagellar motor is about 50 nm in diameter and consists of about 20 different parts. The motor can spin at about 100 Hz in both clockwise and counterclockwise directions. The motors drive long thin helical filaments that allow cells to swim. Peritrichously flagellated cells, such as *Escherichia coli*, search for food using sensors near the surface of the cell. The sensors detect molecules of interest, such as sugars and amino acids, and control the direction of the motor. An *E. coli* cell is about 1  $\mu\text{m}$  in diameter by 2  $\mu\text{m}$  long. Each cell has on average four helical flagellar filaments. Each filament is driven by a rotary motor at its base. The motors switch rotational direction randomly. It's likely that the switch is triggered by a signaling protein. The motors are powered by protons moving down an electrochemical gradient. This type of bacterial motor can be used for stirring motion at the nanometer scale and improving transversal transport in a micromixer.

## 6.2.2 Hydrodynamic Instability

Fig. 6.3 shows the model of a typical mixer configuration with pressure disturbance. The solvent and solute flow side by side at the inlet at a constant mean velocity  $u_0$ , while the transversal disturbance flow is time-dependent  $v^* = v_0 \cos(\omega t)$ . The net transversal flow is zero. Thus the mean velocity at the outlet of the mixer is still  $u_0$ . The mixing effect in this mixer is called “spatiotemporal resonance,” a phrase coined by Okkels and Tabeling [5]. Assuming laminar flow at low Reynolds numbers and a two dimensional model, the following dimensionless control parameters are defined:

$$\alpha = \frac{v_0}{u_0}$$

$$\Omega = \omega \frac{W}{u_0}.$$

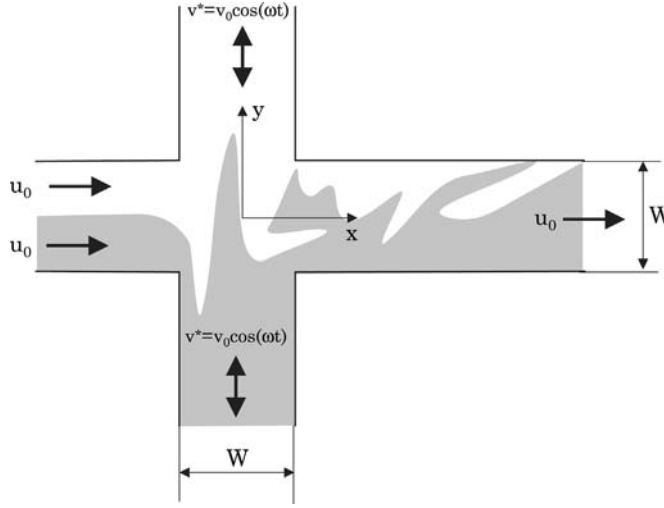


**Figure 6.3** Model of an active mixer with pressure disturbance at the inlet. The main flow has a velocity  $u_0$  while the transversal disturbance velocity is time-dependent  $v^* = v_0 \cos(\omega t)$ .

The governing equation for the stability analysis is:

$$\frac{d\mathbf{x}}{dt} = \mathbf{u} + f(t)\mathbf{v} \quad (6.19)$$

where the function  $f(t) = \alpha \cos(\Omega t)$ . Solving the Navier–Stokes equation (2.14) with the model and boundary conditions depicted in Fig. 6.3 and tracking the fluid particles according to (6.19) allow the evaluation of mixing in the microchannel. The extent of mixing is measured numerically by the folding quality:

$$f = \frac{L}{L_0} - 1 \quad (6.20)$$

where  $L$  is the length of material lines in a segment with a dimension of  $dx \times dy$ . The reference length is determined as  $L_0 = \sqrt{dx^2 + 4dy^2}$ . Fig. 6.4 shows the contour plot of folding quality  $f$ , which is calculated numerically. Generally, stretching and folding and subsequently good mixing are achieved with  $\Omega > \alpha$ . That means that low frequency with a large velocity magnitude will allow good mixing in this type of micromixer. However, there are areas of poor mixing called “spaciotemporal resonance” as depicted in Fig. 6.4 [6]. The solid line in Fig. 6.4 are the resonance lines described by the following relation between  $\alpha$  and  $\Omega$ :

$$\alpha = C^2 \Omega \sqrt{\frac{15}{16} \left[ 1 - \frac{C^2 \Omega}{2\pi(n + 1/2)} \right]}, \quad (6.21)$$

where the  $n$  are positive integers and  $C \approx 1.239$ .

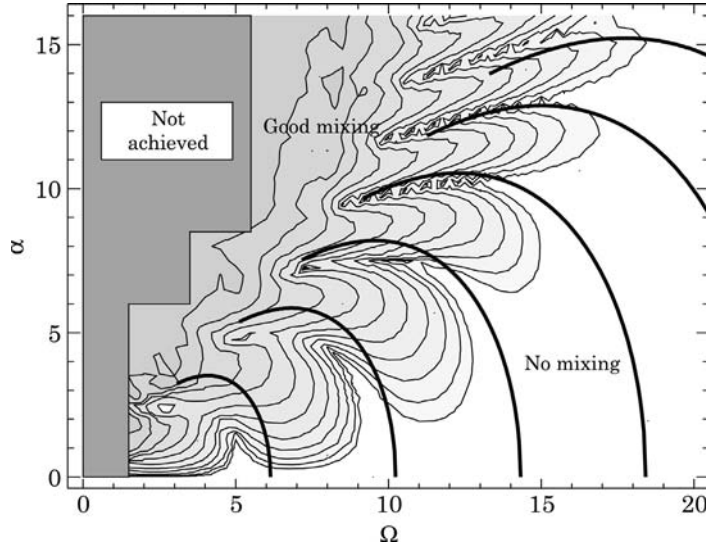


**Figure 6.4** Contour plot of mixing extent expressed as folding quality  $f$ . The solid curves are the resonance lines according to (6.21) (reprinted with permission [5]).

### 6.2.3 Pulsed Source–Sink Chaotic Advection

Passive mixers based on chaotic advection were described in the previous chapter. Hydrodynamic instability is also a form of chaotic advection caused by a periodic disturbance. This section is dedicated to a special concept for active generation of chaotic advection: the pulsed source–sink concept.

The original concept proposed by Jones and Aref [7] consider a single point source and a single point sink on an unbounded plane. This system is two-dimensional and can be used for flat microfluidic systems, which are modelled by the Hele–Shaw flow. The point source and sink represent singularities that are switched alternately with a fixed time period. Both source and sink have the same magnitude of flow rate. Thus, the net flow in the system is zero. Using Poincaré sections and Lyapunov exponents, Jones and Aref showed that this system creates chaotic advection over a wide range of operation parameters.

A two-dimensional model can be formulated for a source–sink pair. In a Cartesian coordinate system, a source and a sink are placed at  $(x_+, y_+)$  and  $(x_-, y_-)$ , respectively. The strengths of the source and the sink are  $Q$  and  $-Q$ , respectively. For the convenience of mathematical treatment, the coordinates  $x$  and  $y$  describing a point on this plane can be replaced by a complex number  $z = x + iy$ , where  $i$  is the imaginary unit. Considering the positive half of the imaginary axis and the complex position  $z_+$  of the source and the complex position  $z_-$  of the sink, the stream function of the flow system is the imaginary part of the following complex potential:

$$W(z) = \frac{Q}{2\pi} [\log(z - z_+) + \log(z - z_+^*)] - [\log(z - z_-) - \log(z - z_-^*)], \quad (6.22)$$



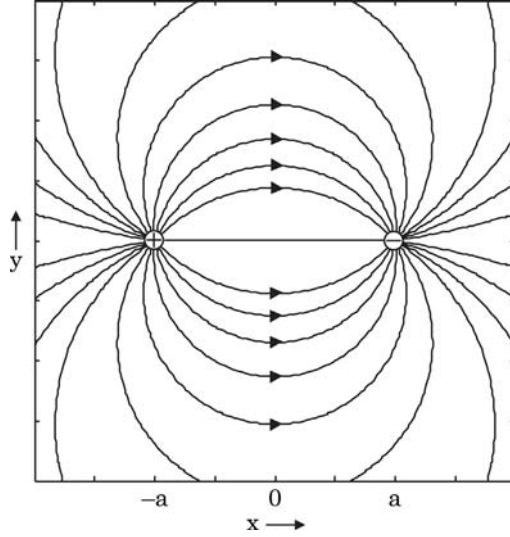


**Figure 6.5** Stream lines of a source–sink pair in an unbounded domain.

where the asterisk denotes the complex conjugate. The real part  $\phi$  of the above function is the velocity potential. The streamlines are the level sets of the imaginary part  $\psi$ . Velocity components can be subsequently evaluated using the advection equation (2.86). Integrating the velocity components over time results in positions of the fluid particles. Plotting the particle position at regular time intervals results in a Poincaré section, which is used for evaluating the degree of chaotic mixing.

The stream function of the system with  $z_+ = (-a, 0)$  and  $z_- = (a, 0)$  is the imaginary part of the following complex potential:

$$W(z) = \phi + i\psi = \frac{Q}{2\pi} [\log(z + a) - \log(z - a)]. \quad (6.23)$$

Fig. 6.5 shows this source–sink pair and their stream lines. Under steady conditions, the fluid particles move along these streamlines, which have the form of circular arcs. This flow system is determined by two parameters: the distance  $2a$  between the source and the sink, and their strength  $Q$ . The speed of evolution is controlled by  $Q$ . Normalizing the time by  $2\pi a^2/Q$  and integrating the velocity from the source to the sink along the line  $(0, y)$  results in the shortest dimensionless transfer time  $t_0^* = 2/3$ .

The mixing domain in real applications is bounded inside a mixing chamber. For a circular mixing chamber with a radius  $R$  and a center positioned between the source and the sink, the complex potential transforms to the form [8]:

$$W(z) = \frac{Q}{2\pi} [\log(z + a) - \log(z - a) + \log(R^2 + az) - \log(R^2 - az)]. \quad (6.24)$$

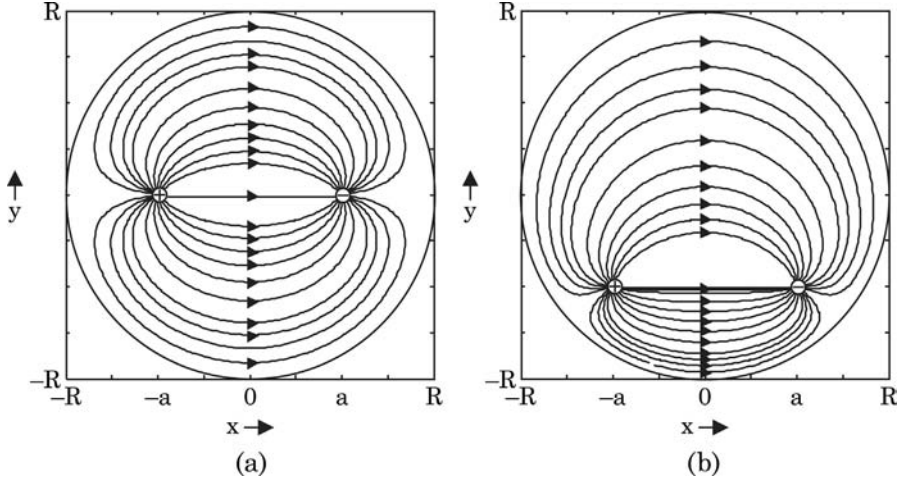


**Figure 6.6** Stream lines of a source–sink pair in an unbounded domain.

Streamlines of this system are depicted in Fig. 6.6 (a). The shortest dimensionless response time is  $t_0^* \approx 0.556$ .

A similar approach can be used to drive the complex potential with source and sink at  $(-a, -a)$  and  $(a, -a)$  as:

$$W(z) = \frac{Q}{2\pi} \{ \log(z + a + ia) - \log(z - a + ia) \\ + \log[R^2 + a(1 - i)z] - \log[R^2 - a(1 + i)z] \}. \quad (6.25)$$

Streamlines of this system are depicted in Fig. 6.6 (b). The shortest dimensionless response time is  $t_0^* \approx 0.51$ .

Another common geometry of a mixing chamber is the rectangle. Consider a rectangle with width of  $2a$  and a length of  $2\alpha a$ , where  $\alpha$  is the aspect ratio of the rectangle. The mixing domain is bounded by the four corners  $(\pm a, \pm\alpha a)$ . The complex potential of a source–sink pair inside this rectangle is [9]:

$$W(z) = \frac{Q}{2\pi} \{ \log[\sigma(z) - \sigma(z_+)] + \log[\sigma(z) - \sigma^*(z_+)] \\ \times \log[\sigma(z) - \sigma(z_-)] - \log[\sigma(z) - \sigma^*(z_-)] \} \quad (6.26)$$

where

$$\sigma(z) = \operatorname{sn} \left[ \left( \frac{z}{a} + i\alpha \right) K(k), k \right], \quad (6.27)$$

$\operatorname{sn}(z, k)$  is the Jacobian elliptic sine, and  $K(k)$  is the complete elliptic integral of the first kind. The variable  $k$  is determined from the aspect ratio by the

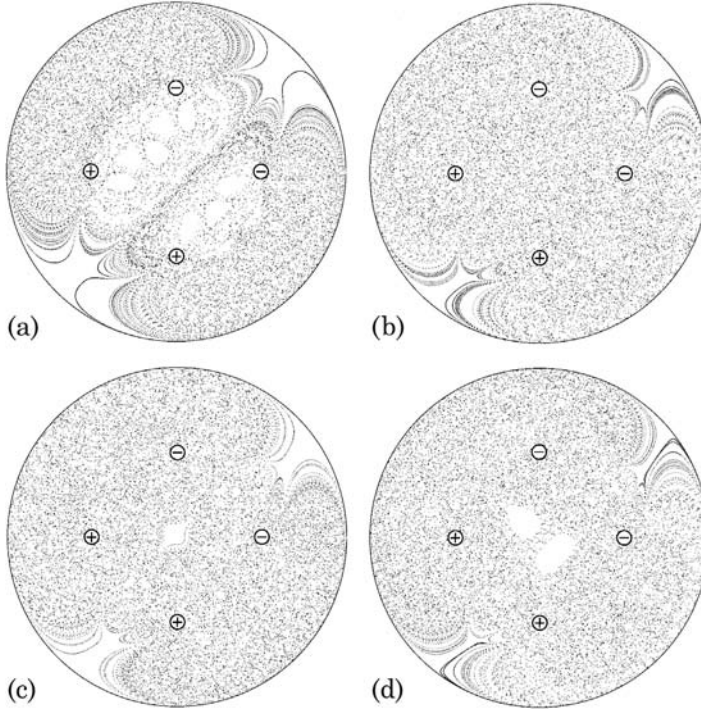


**Figure 6.7** Poincaré section of mixing with two source–sink pairs for different dimensionless times: (a)  $t^* = 0.15$ ; (b)  $t^* = 0.5$ ; (c)  $t^* = 0.556$ ; (d)  $t^* = 0.6$ . The fluid is first pumped from left to right, then from bottom to top (reprinted with permission from [8]).

following relation [9]:

$$\alpha = \frac{K(\sqrt{1-k^2})}{2K(k)}. \quad (6.28)$$

Mixing protocols based on pulsed source–sink chaotic advection are determined by the way the fluid is injected and rejected from the source and the sink, respectively. The fluid can be collected from the sink and transferred to the source according to “first in, first out” or “first in, last out” protocols. Fig. 6.7 illustrates the Poincaré section of two pairs of pulsed source–sinks. The source–sink pairs are centered at the origin of the circular boundary. At a short pumping time of  $t^* = 0.15$  the Poincaré section indicates the presence of several non-mixing islands, where fluid particles never pass. Best mixing appears to be at  $t^* = 0.5$ . This concept can be implemented using external or integrated pumps at the sources and sinks.

Fig. 6.8 shows the Poincaré sections of two source–sink pairs in a rectangular mixing chamber with an aspect ratio of 21/71 [9]. The parameter for good mixing is the switching time  $t_{\text{switch}}$  between the source–sink pairs. At a fixed

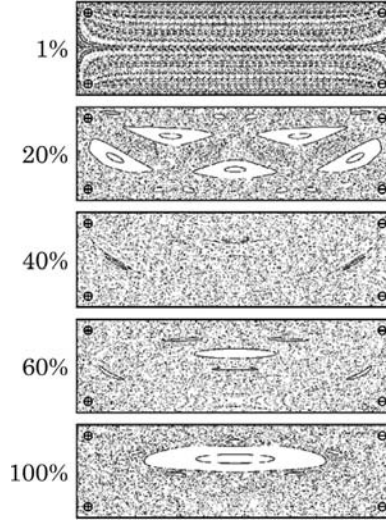


**Figure 6.8** Poincaré section of mixing with two source–sink pairs bounded by a rectangular mixing chamber at different dimensionless switching time  $t_{\text{switch}}^*$  (reprinted with permission from [9]).

source–sink strength of  $Q$ , the switching time is normalized by the maximum pumping time  $T_c$  needed for emptying the mixing chamber. The influence of this dimensionless switching time  $t_{\text{switch}}^* = t_{\text{switch}}/T_c$  on the Poincaré section is illustrated in Fig. 6.8. The Poincaré sections are created by plotting the position of a liquid particle after every pulsing period or  $2t_{\text{switch}}^*$ . The section shows zones not passed by the particle, also called elliptic islands. Particles in these zones will experience a periodic regular transport, and consequently can not be mixed.

## 6.2.4 Design Examples

Due to the established technologies and the advancement of micro electromechanical systems (MEMS), active micromixers with pressure-driven disturbance are relatively simple to realize. Fig. 6.9 shows the example of an active micromixer with integrated micropumps [10]. The disturbance is generated by two micropumps operated out of phase. The pulsatile flows cause the instability in the mixing channel improving transversal transport. Furthermore, the concept leads to the generation of fluid segments similar to sequential lamination as discussed in Chapter 3. Both transversal transport by instability and Taylor dispersion contribute to improved mixing performance. Pressure disturbance is generated by the two integrated micropumps. Each micropump consists of a thermopneumatic actuator and two micro check valves. The actuator is designed with a 400- $\mu\text{m}$  diameter actuation chamber and a connecting microchannel. Integrated microheaters evaporate liquid water creating a vapor bubble, which acts as the actuator. If the heat is removed, the

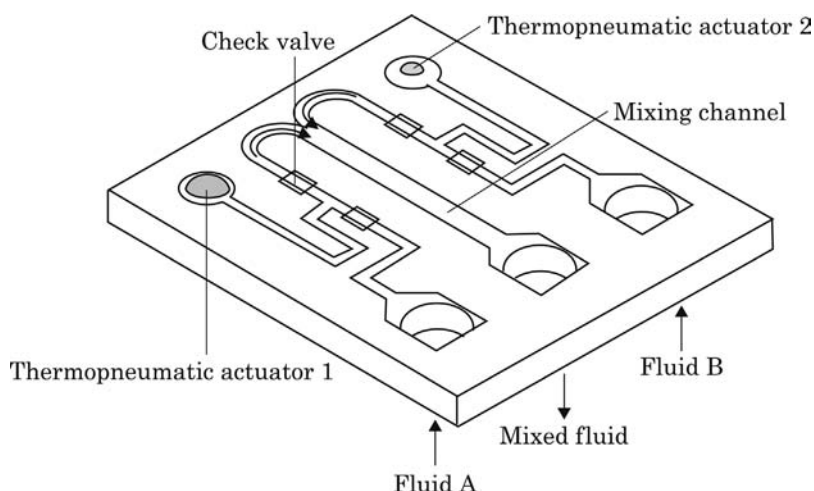


**Figure 6.9** Concept of a active micromixer based on pressure-driven disturbance. The fluids are delivered by integrated micropumps. Thermopneumatic actuators drive the pump and generate the pressure disturbance (after [10]).

bubble collapses due to condensation. A long microchannel connects the actuation chamber with the pump chamber, which is located between the two check valves. This long microchannel prevents the pumped liquid from being affected by the evaporation and condensation processes in the actuation chamber. The microchannel network depicted in Fig. 6.9 was fabricated on a planar silicon substrate using deep reactive ion etching (DRIE) and silicon-on-insulator (SOI) technology (see Chapter 6). The microheaters are made of polysilicon deposited on a quartz substrate. The check valves are freely floating silicon structures. The silicon and quartz parts are bonded by an epoxy. Subsequent treatment with oxygen plasma frees epoxy blockage in the microchannels.

Fig. 6.10 shows another design of an active micromixer based on pressure-driven disturbance. In contrast to the monolithic approach of Deshmukh et al., Fujii et al. [11] presented a hybrid approach, where silicon micropumps are combined with a microchannel network in PDMS. Both the silicon part and the PDMS part are bonded to a glass plate. Connecting holes are drilled in the glass plate and allow liquids to be delivered from the pump to the mixing channel. The micromixer has the typical Y-design with two inlets and a long mixing channel, molded in PDMS using a soft lithography technique (see Section 3.2.2.3). The silicon micropump is a valveless diaphragm pump driven by a piezoelectric actuator. The inlet and outlet of the micro pump are designed as structures with different fluidic resistances. Liquid is driven towards the direction of the outlet with lower fluidic resistance. By adjusting the actuation times of the pumping and supply modes, a bidirectional operation can be realized with this pump. The micropump can deliver a flow rate from 20 nl/s to

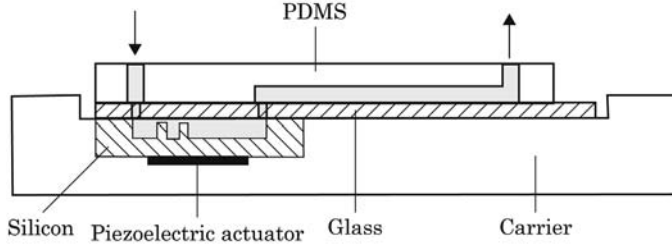


**Figure 6.10** Concept of an active micromixer based on pressure-driven disturbance. The fluids are delivered by hybrid-integrated piezoelectric micropumps (after [11]).

200 nl/s, and pressure up to 5.0 kPa. The mixing channel has a cross section of  $150 \times 150 \mu\text{m}$ . Each inlet is equipped with a passive capillary valve, which is simply a constriction. The constriction allows the synchronous introduction of the two liquids into the microchannel during priming. Similarly to the sequential segmentation concept, the two pumps at the inlet are turned on and off alternately. Mixing is achieved with both pressure-driven disturbance and Taylor dispersion.

Glasgow and Aubry [12] used disturbance generated by external peristaltic pumps to improve mixing in a T-junction configuration. The flow rates of the two inlets pulsate with a sinusoidal function. The best performance was achieved when the two flow rates are  $180^\circ$  out of phase. This confirms the alternate driving concept used by the systems depicted in Figs. 6.9, 6.10, and in sequential segmentation.

Niu and Lee [13] implemented the concept of hydrodynamic instability depicted in Fig. 6.3 with multiple side channels. The governing equation (6.19) is interpreted as:

$$\frac{dx}{dt} = \begin{cases} \bar{u}[1 - (2y/W_y)^2] & \text{if } |y| < W_y/2 \\ 0 & \text{if } |y| > W_y/2 \end{cases}$$

$$\frac{dy}{dt} = \begin{cases} \bar{v}\{1 - [2(x - x_c)/W_x]^2\}\sin(\omega t) & \text{if } |x| < x_p + W_x/2 \\ 0 & \text{if } |x| > x_p + W_x/2 \end{cases} \quad (6.29)$$

where  $x_c = x_p + W_x/2$  with  $x_p = nP$ .  $P$  is the length of each mixing unit. All other parameters are indicated in Fig. 6.11. As mentioned previously, the magnitude of the disturbance  $v_0$  and its angular frequency  $\omega$  are the parameters for the analysis of chaotic advection. In the junction area (gray in Fig. 6.11), equation (6.29) reduces to:

$$\begin{cases} \frac{dx}{dt} = \bar{u}[1 - (2y/W_y)^2] \\ \frac{dy}{dt} = \bar{v}\{1 - 2[(x - x_p)/W_x]^2\}\sin(\omega t). \end{cases} \quad (6.30)$$

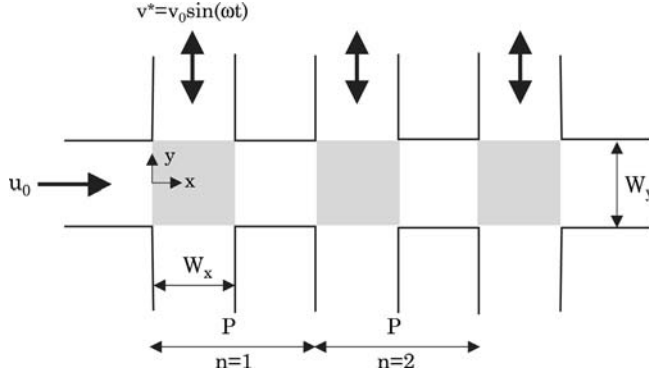


**Figure 6.11** Hydrodynamic instability with multiple side channels.

Following the analysis in Section 2.4, particle trajectories can be determined by the above velocity field. Using this analysis, an optimal frequency  $\omega_o$  and optimal velocity magnitude  $\bar{v}_o$  can be chosen for the maximum Lyapunov exponent  $\lambda$ , which characterizes the degree of chaos in the mixer. Due to stretching and folding, the penetration distance between two fluid streams can be estimated as:

$$\delta = W_y \exp(-\lambda t). \quad (6.31)$$

Thus, the required channel length for this type of micromixer can be estimated as:

$$L_{\text{mixer}} = \frac{\delta^2 \bar{u}}{2D} = W_y^2 \frac{\bar{u}}{2D} \exp(-2\lambda t). \quad (6.32)$$

Bottausci et al. [14] implemented the concept depicted in Fig. 6.11 in a silicon/glass device. Three pairs of disturbance channels were used in this design. The disturbance velocities were generated by an external pump. The mixing channel is 200  $\mu\text{m}$  wide, 100  $\mu\text{m}$  deep, and 1300  $\mu\text{m}$  long. Full mixing can be achieved within 0.1 second in this micromixer.

Tabeling et al. [15] reported a mixer with only one pair of disturbance channels. The device was fabricated in a PDMS/PDMS/glass stack. The flows in the two disturbance channels are controlled by pneumatic valves, which alternately open and close. The valve actuation induces the periodic disturbance. Pressure supply to the pneumatic valves was controlled by external valves, which determine the switching frequency of the disturbance. The same device was characterized for spatiotemporal resonances by Dodge et al. [6], but instead of using folding quality as depicted in Fig. 6.4, the time-averaged variance, which is similar to the mean square perturbation discussed later in Chapter 7, was used. A small variance means good mixing, while a large variance indicates bad

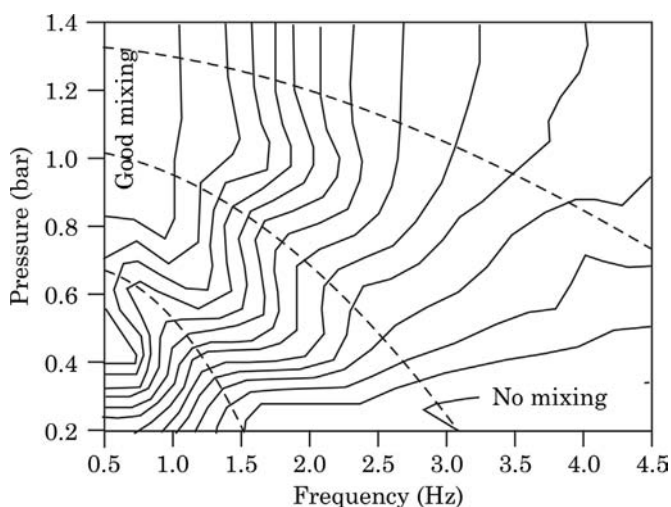


**Figure 6.12** Mean square perturbation or variance in concentration as a function of magnitude and frequency of the disturbance (from [6] with permission).

mixing. Fig. 6.12 depicts the measurement results of this variance, which is comparable to the simulation results shown in Fig. 6.4. At a fixed flow rate, good mixing can be achieved with a large disturbance magnitude and a low disturbance frequency. The spatiotemporal resonances are indicated by the dashed lines. At the resonance, the interface between the two liquids is strongly distorted, but returns straight at the intersections.

Kim and Breuer [16] utilized *E. coli* bacteria to create disturbance on the nanometer scale. The motion of the bacterium's flagella increases the apparent diffusion coefficient of the solute. Up to 4 times improvement of diffusion coefficient can be achieved. In their experiments, Kim and Breuer used a conventional focusing mixer with three inlets, where the middle stream contains large molecules with molecular weight of the order of  $2 \times 10^5$ . To improve the diffusion coefficient of these large molecules, wild type *E. coli* was mixed in the solvent stream. The apparent diffusion coefficient is then proportional to the concentration of the bacteria. Introducing chemoeffectors into the side stream can control the apparent diffusion coefficient at a fixed bacterium concentration. For instance, chemoattractants, such as L-aspartic acid, can increase diffusion into the side stream, while chemorepellants, such as nickel sulfate ( $\text{NiSiO}_4$ ), decrease it.

As analyzed in 6.2.3, the first in-last out pulsed source-sink concept is easy to implement at the micro scale. Fig. 6.13 shows the micromixer implemented by Evan et al. [17]. The mixing chamber and microchannel network were etched 100  $\mu\text{m}$  deep in silicon. The mixing channel has two inlets for the solute and solvent. The other four inlets are the two source-sink pairs. The positions of the sources and sinks are indicated in Fig. 6.13. These sources and sinks are connected to thermopneumatic micropumps. Switching between the sink-source



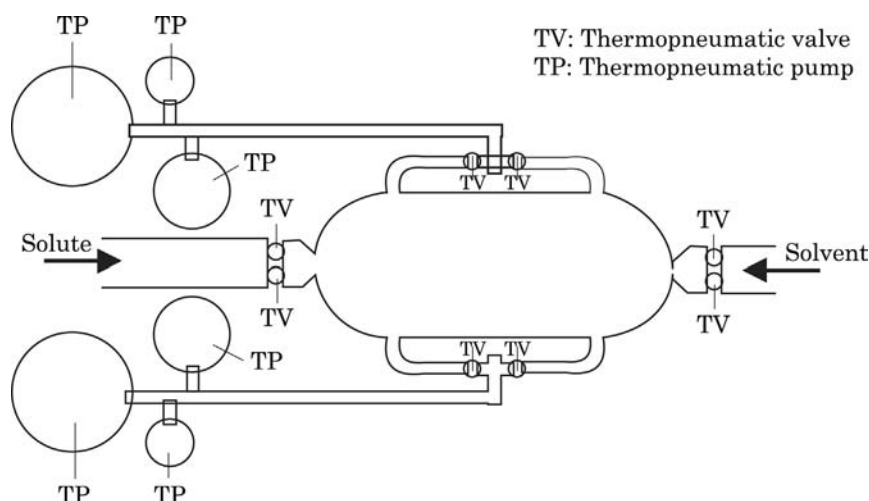


**Figure 6.13** Active micromixer based on the pulsed source-sink concept.

pairs is controlled by thermopneumatic microvalves. The liquids are first loaded into the mixing chamber. The micropumps and microvalves are synchronized so that the two source-sink pairs are activated alternately. While the first pair drives liquid from the bottom to the top, the second pair drives it from the top to the bottom. The microchannel network allows the realization of the first in-last out concept. Thermopneumatic actuators for micropumps and microvalves are implemented by polysilicon heaters on the quartz cover plate. The heaters generate vapor bubbles, which in turn drive the liquid. The micromixer is characterized by the distance  $2a$  between source and sink, the distance between the two source-sink pairs  $2b$ , the pump chamber diameter  $\sqrt{2}\lambda$ , and the source-sink strength  $Q$ . Normalizing all other lengths by  $a$  results in the aspect ratio of the mixing chamber  $\alpha = b/a$  and the dimensionless size of the pump chamber  $\beta = \lambda/a$ . A too large aspect ratio  $\alpha$  decouples the two source-sink pairs. A too small aspect ratio makes the two pairs work again each other. Both extreme cases do not lead to good mixing in the chamber.

Cola et al. [18] realized the pulsed source-sink concept in a much larger scale. The mixing chamber measures  $21 \times 71$  mm. The sources and sinks are driven by external syringe pumps. The switching valves are external solenoid pinch valves. A similar device was reported by Raynal et al. [19]. The mixing chamber measures  $15 \times 15$  mm. These relatively large pulsed source-sink mixers are needed for hybridization reactions on DNA arrays.

Moving parts in the mixing chamber or mixing channel can actively cause pressure and flow disturbance in the mixing channel. Suzuki and Ho [20] demonstrated a miniaturized version of a macro scale magnetic stirrer. An electrical conductor generates a magnetic field, which in turn attracts magnetic beads of 1 to 10  $\mu\text{m}$  in diameter. The disturbance caused by the magnetic field leads to chaotic advection in the otherwise regular flow.

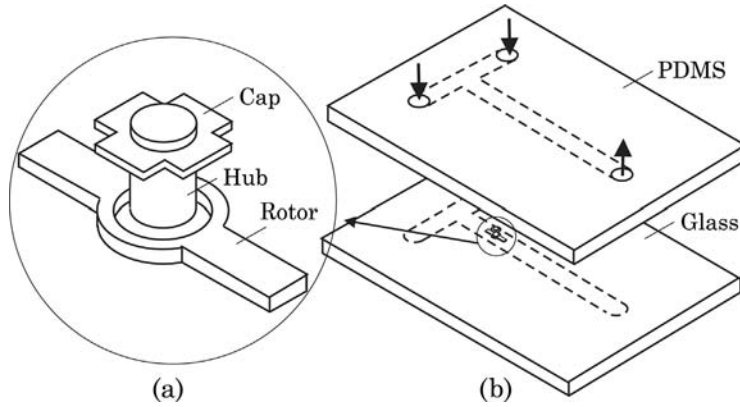


**Figure 6.14** Active micromixer with integrated micro stirrer: (a) the stirrer, (b) the micromixer.

Lu et al. integrated a magnetic micro stirrer inside the mixing channel [21]. The micro stirrer was fabricated by electroplating of iron/nickel alloy on a glass substrate. Sacrificial layers made of photoresist and copper were used for defining the rotor, the hub, and the cap. The micro stirrer is in total  $25\text{ }\mu\text{m}$  tall.  $0.5\text{ }\mu\text{m}$  Tips define a gap between the rotor and the substrate, Fig. 6.26. The microchannel network was fabricated in PDMS using soft lithography. The mixing channel had a cross section of  $70 \times 750\text{ }\mu\text{m}$ . The micromachined stirrer is placed at the interface between two liquids in a T-mixer. Stirring speeds between 100 and 600 rpm were achieved with an external magnetic field. The advantage of this design is that there is no need for electrical interconnects to the mixing device. However, a span of  $400\text{ }\mu\text{m}$  is relatively large. Magnetic force is a bulk force that is proportional to the volume of the stir bar. Further miniaturization of this concept could be problematic because magnetic force cannot overcome the dominant friction force at the micro scale.

Agarwal et al. [22] combined the magnetic stirrer with a brake based on a chemical actuator. The brake is made of hydrogel that is sensitive to temperatures and pH values. The stirrer was fabricated in nickel using a similar approach to that described above. The rotor measures about  $2 \times 0.4 \times 0.2\text{ mm}$ . Hydrogel was structured around the hub to work as a brake. Depending on the type of control (pH or temperature), different hydrogels were used. The stirrers were controlled by applying flow with corresponding pH values and temperatures.

### 6.3 Electrohydrodynamic Disturbance

Although electrokinetic effects, such as electroosmosis and electrophoresis, are subfields of electrohydrodynamics (EHD), which is the study of the

interaction between the electric field and fluid mechanics. EHD effects considered in this section only concern fluid systems with at least one dielectric fluid. In this case, the fluids are often immiscible. Thus mixing these fluids will lead to an emulsion. There are many practical applications, such as organic-aqueous liquid extraction for DNA purification. Mixing or partitioning is achieved by disturbing the liquid/liquid interface with an electrical field. The discontinuity of the electrical properties across the interface affects the force balance at the fluid/fluid interface and leads to instability.

There are two basic approaches for investigating EHD instability. The first approach is the surface-coupled model, which considers a jump in electrical conductivity at the interface of the two fluids and is suitable for modeling immiscible systems with dielectric fluids. The second approach is the bulk coupled model assuming a conductivity gradient in a thin diffusion layer between the two fluids. The second approach is suitable for modeling electrokinetic systems and will be discussed in Section 6.5.

A system of dielectric fluids can be described through the basic equations, such as the continuity equation, the Navier–Stokes equation, and the conservation equation of species. The Navier–Stokes equation has an additional term  $\mathbf{f}_{\text{el}}$  for the electrohydrodynamic forces

$$\rho \frac{D\mathbf{v}}{Dt} = -\nabla p + \mu \nabla^2 \mathbf{v} + \mathbf{f}_{\text{el}}. \quad (6.33)$$

The electrohydrodynamic force can be calculated as:

$$\mathbf{f}_{\text{el}} = \rho_{\text{el}} E_{\text{el}} - \frac{1}{2} E_{\text{el}}^2 \nabla \varepsilon - \nabla \left[ \frac{1}{2} \rho E_{\text{el}}^2 \frac{\partial \varepsilon}{\partial \rho_{\text{el}}} \Big|_T \right] \quad (6.34)$$

where  $E_{\text{el}}$  is the electric field,  $\rho_{\text{el}}$  is the charge density,  $\varepsilon$  is the permittivity, and  $T$  is the temperature. The first and second terms in (6.34) represent the electrophoretic and dielectrophoretic forces, respectively. The last term is the electrostrictive force. If the fluid is incompressible ( $\rho = \text{const.}$ ), the electrostrictive force is negligible.

The ratio between permittivity  $\varepsilon$  and the conductivity  $\sigma_{\text{el}}$  of a fluid is called the charge relaxation time  $\tau_c = \varepsilon/\sigma_{\text{el}}$ . The relaxation time of distilled water is 3.6  $\mu\text{sec}$ , while that of cooking oil is on the order of 0.5 sec. In the case of a DC electric field, the charge has time to build up at fluid interfaces, thus the electrophoretic force is dominant. In the case of an AC electric field, if the relaxation time  $\tau$  is much larger than the excitation period  $T = 1/f$ , the charge does not have time to build up. Consequently, the electrophoretic force is negligible in an AC electric field, while the dielectrophoretic force is dominant. Mixing can be realized by using fluids with different electric properties. Furthermore, electric properties, such as permittivity, are functions of temperature. Thus, a gradient of permittivity can be generated by a heater integrated in the microchannel.

In an immiscible fluid system, the interfacial tension between the two phases needs to be considered in the stress balance. Both viscous and interfacial effects are surface effects and dominant in micro scale. The ratio between the damping capability of the viscous force and the interfacial stress is characterized by the flow time scale:

$$\tau_f = \frac{\mu L}{\sigma} \quad (6.35)$$

where  $\mu$ ,  $L$ , and  $\sigma$  are the dynamic viscosity, the characteristic length, and the interfacial tension, respectively. For more details on analytical models describing electrohydrodynamic instabilities, readers may refer to the work of Thaokar and Kumaran [26] or the work of Wu and Russel [27].

El Moctar et al. reported an active micromixer with electrohydrodynamic disturbance [28]. Electrode wires are placed along the mixing channel, which is 30 mm long, 250  $\mu\text{m}$  wide, and 250  $\mu\text{m}$  deep, Fig. 6.15 (a). A number of titanium electrodes are placed in the direction perpendicular to the mixing channel. Transversal flows were induced by changing the voltage and frequency of the electrodes. The dielectric fluid in use was corn oil. Oil-miscible antistatic was added to increase conductivity and permittivity.

Hydrodynamic instability occurred at a relatively high DC field strength of  $E_{\text{el}} = 2 \times 10^5 \text{ V/m}$ . This instability threshold depends on the perturbation of the interface between the two fluids and the dynamic characteristics of the applied DC voltage. Due to the relatively small relaxation time, mixing occurs almost instantaneously after switching on the electric field. A delay time of less than 100 ms was observed. Good mixing was achieved at a Reynolds number as low as 0.02. Generally, mixing improves with increasing field strength. Mixing index is proportional to electrohydrodynamic force (6.34), and thus is proportional to the square of the electric field strength. There exists a saturation field strength, where no further mixing improvement can be observed.

The mixing concept also works with an AC voltage. For applications with water-based solution, AC has an advantage over DC because of the lack of electrolysis. Similar to the DC case, the extent of mixing is proportional to the square of the electric field. A sinusoidal electric field results in non-mixing zones when the voltage drops under the critical value for instability. A square-wave electric field results in better mixing, because there is no instance with field strength less than the critical value needed for instability. The use of several electrode pairs further improves mixing efficiency.

Ozen et al. [29] used a single pair of parallel electrodes along the mixing channel, Fig. 6.15 (b). The mixing channel has a cross section of  $1.5 \times 0.25 \text{ mm}$ . Corn oil and glycerine work as the immiscible liquids. Thus instability at the interface will lead to the formation of droplets. The droplet size can be controlled by the applied voltage. A possible application of this effect is the

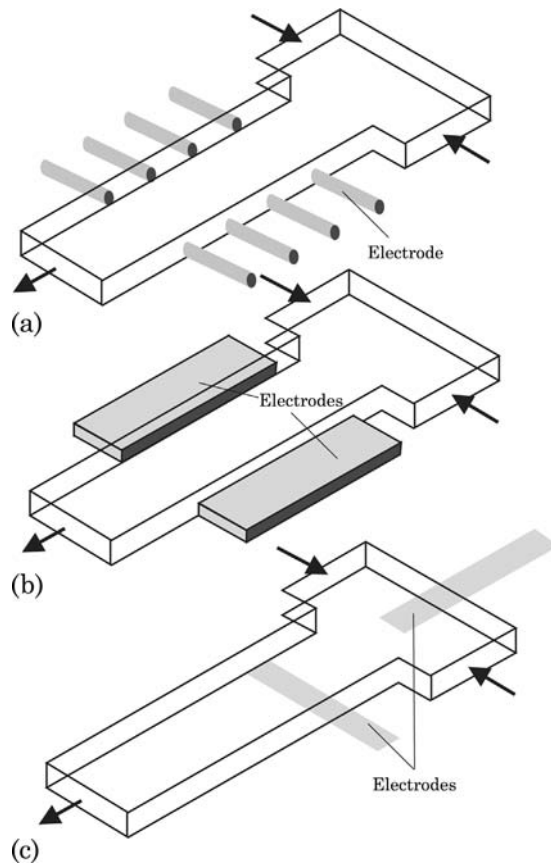


**Figure 6.15** Different electrode configurations for active micromixer based on EHD.

encapsulation of the two miscible phases in another immiscible phase, the actual mixing process that occurs in the droplet.

Zahn et al. [30] used the flow-focusing configuration with three inlets for mixing experiments with electrohydrodynamic instability. The micromixer was fabricated in PDMS using the standard soft lithography technology. The mixing channel has a cross section of  $150 \times 30 \mu\text{m}$ . Chromium/gold electrodes were patterned on the floor of the mixing channel. The electrodes are 2 mm long and  $75 \mu\text{m}$  apart. Phenol and water are the working fluids for this system. The water-phenol-water system was realized using three inlets. AC voltages with root mean square values from 0 to 45 V and frequencies ranging from 250 kHz to 10 MHz were used for disturbing the interface between phenol and water.

Tsouris et al. [31] used a different electrode configuration to disturb the interface between the two streams, Fig. 6.15 (c). The electric field was parallel to the flow direction. The mixing fluid was butanol. Rhodamine B was used as a dye for visualization of the mixing effect. With an applied voltage of 0 to 900 V and a distance between the two electrodes of  $450 \mu\text{m}$ , a field strength ranging

from 0 to  $2 \times 10^6$  V/cm was achieved. The mixing channel was fabricated in PDMS. The channel depth and width were 36.5  $\mu\text{m}$  and 78  $\mu\text{m}$ , respectively. EHD instabilities occurred at a field strength of about  $1 \times 10^6$  V/cm, which is one order of magnitude higher than that required for the configurations depicted in Figs. 6.15 (a) and (b).

## 6.4 Dielectrophoretic Disturbance

The background of DC dielectrophoresis was discussed in Section 2.6.3. Since a DC field can only trap dielectric particles and does not induce instability, mixing applications require the stirring motion of particles to be induced by AC dielectrophoretic forces. Considering an AC electric field  $\mathbf{E}_{\text{el}}(t) = \mathbf{E}_{\text{el}} \exp(-i\omega t)$  with the driving frequency  $\omega$  and a spherical dielectric particle with a radius of  $r_p$ , the dielectric force acting on the particle is:

$$\mathbf{f}_{\text{DEP}}(t) = \frac{1}{2} \Re[\mathbf{m}(\omega) \cdot \nabla \mathbf{E}_{\text{el}}^*] \quad (6.36)$$

where  $\Re$  represents the real component of a complex number and  $\mathbf{E}_{\text{el}}^*$  is the complex conjugate of  $\mathbf{E}_{\text{el}}$ . Due to the frequency dependency of the permittivities of both the fluid and the particle, the dipole moment is also frequency-dependent:

$$\mathbf{m} = 4\pi\epsilon_f r_p^3 \frac{\epsilon_p(\omega) - \epsilon_f(\omega)}{\epsilon_p(\omega) + 2\epsilon_f(\omega)} \mathbf{E}_{\text{el}} \quad (6.37)$$

where  $\epsilon_f$  and  $\epsilon_p$  are the complex permittivities of the fluid and the particle. The complex permittivity is defined as:

$$\epsilon(\omega) = \epsilon - i \frac{\sigma_{\text{el}}}{\omega} \quad (6.38)$$

where  $\sigma_{\text{el}}$  is the conductivity of the dielectric medium. The term with the complex permittivities is called the Clausius–Mossotti factor:

$$K(\omega) = \frac{\epsilon_p(\omega) - \epsilon_f(\omega)}{\epsilon_p(\omega) + 2\epsilon_f(\omega)}. \quad (6.39)$$

Integrating (6.36) over time results in the time-averaged DEP force:

$$\mathbf{f}_{\text{DEP}} = 2\pi\epsilon_f r_p^3 \frac{\epsilon_p(\omega) - \epsilon_f(\omega)}{\epsilon_p(\omega) + 2\epsilon_f(\omega)} \nabla \mathbf{E}_{\text{rms}}^2 \quad (6.40)$$

where  $\mathbf{E}_{\text{rms}} = \mathbf{E}_{\text{el}}/\sqrt{2}$  is the root-mean-square electric field. The Clausius–Mossotti factor can take any value between  $-0.5$  and  $1$ . That means, the DEP force can change its direction at a critical driving frequency  $\omega_c$ . This critical

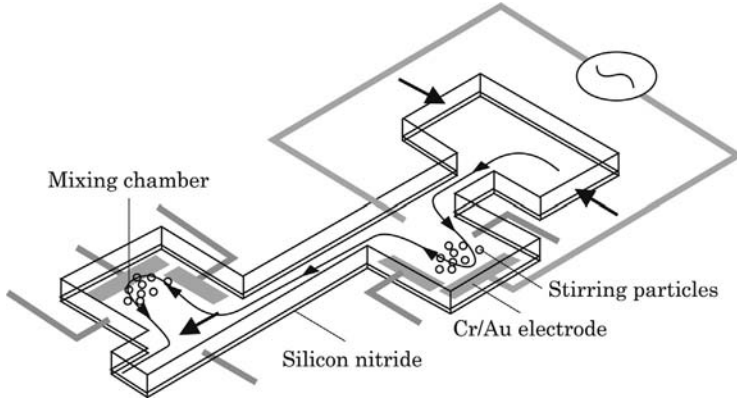


**Figure 6.16** Active micromixer based on dielectrophoretic disturbance.

frequency can be determined by setting the DEP force or the real part of  $K(\omega)$  to zero:

$$\omega_c = \sqrt{\frac{(\sigma_{el,f} - \sigma_{el,p})(\sigma_{el,p} + 2\sigma_{el,f})}{(\varepsilon_p - \varepsilon_f)(\varepsilon_p + 2\varepsilon_f)}}. \quad (6.41)$$

Deval et al. [32] used polystyrene spheres as the stirring particles for mixing in an aqueous solution with a conductivity of 10 to 20 mS/m. The mixing concept utilizes the frequency-dependency of the DEP force. At high frequencies, the DEP force is negative. The stirring particles are repelled from the electrodes. At low frequencies, the particles move toward the electrodes due to the positive DEP force. With a critical frequency of the order of a few megahertz, stirring motion was achieved by using AC with a magnitude of 10 V and a frequency changing alternately between 700 kHz (attracting mode) and 15 MHz (repelling mode). These two modes are switched with a frequency of 1 Hz. The attracting and repelling actuation modes cause stretching and folding of the fluid, thus improving mixing. The electrodes were made of a sputtered chromium/gold layer on a silicon substrate. The electrodes were insulated from the fluid by a silicon nitride layer. The mixing channel was formed by a 25  $\mu\text{m}$ -thick SU-8 layer. The mixing channel measures  $50 \times 25 \mu\text{m}$  in cross section. The mixing chamber was designed with  $100 \times 100 \mu\text{m}$  square walls. The two inlet streams were driven by syringe pumps. Fig. 6.16 shows the concept of this active micromixer.

Lee et al. [33] reported another design of the above micromixer. The mixing chamber is located symmetrically at the center. The mixing chamber measures  $200 \times 200 \times 25 \mu\text{m}$ . The driving voltage was switched between 100 kHz and 10 MHz to achieve transversal disturbance in the mixing chamber.

## 6.5 Electrokinetic Disturbance

The key parameters affecting electrokinetic flow are the electrohydrodynamic properties of the fluid, such as conductivity and permittivity, the electric field and the zeta potential at the channel walls. Disturbances introduced into these parameters will lead to instability in an electrokinetic flow. This section discusses the instability effects of a conductivity gradient, electric field or zeta potential, and their application for the mixing of electrokinetic flows.

### 6.5.1 Instability Caused by a Conductivity Gradient

Electrokinetic disturbance in a channel network driven by electroosmosis can be utilized for improving mixing. Electrokinetic instability occurs when electroosmotic forces need to work against the electroviscous forces in the flow. While the electroosmotic force is an electrostatic boundary force at the double layer, the electroviscous force is a bulk force caused by charge gradients in the bulk fluid. In general, electrokinetic instability can be classified as convective or absolute. In convective instability, the disturbance introduced at the inlet of the system propagates only downstream, in the flow direction. A convectively unstable system is physically a disturbance amplifier. In absolute instability, the disturbance spreads in both directions: downstream and upstream. An absolutely unstable system is physically an intrinsic oscillator where oscillating waves spread in both directions of the flow. Convective instability occurs under the same conditions as for temporal instability discussed previously [24,35].

Fig. 6.17 shows the two basic configurations for mixing with electrokinetic disturbance. Mixing streams with different ionic concentrations are driven by an electric field due to electroosmosis. At a high field strength, the interface between the two streams becomes unstable and mixing is achieved by transversal transport caused by electroviscous forces.

The transport effects in the previous system is based on the electrolytic ohmic model and can be described by the following governing equations:

- The species transport equation

$$\frac{D\sigma_{\text{el}}}{Dt} = D\nabla^2\sigma_{\text{el}} \quad (6.42)$$

where  $\sigma_{\text{el}}$  is the conductivity of the fluid and  $D$  is the effective diffusion coefficient of the ions according to (2.40).

- The Poisson–Boltzmann equation

$$\nabla \cdot (\sigma_{\text{el}} \nabla \Psi) = 0 \quad (6.43)$$

where  $\Psi$  is the electric potential in the fluid.



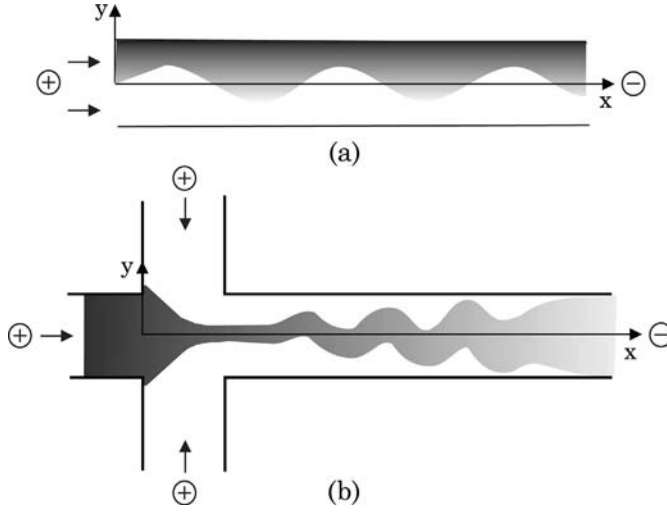


**Figure 6.17** Two basic configuration for mixing with electrokinetic disturbance: (a) parallel lamination with two streams; (b) parallel lamination or focusing with three streams.

- The continuity equation

$$\nabla \cdot \mathbf{v} = 0. \quad (6.44)$$

- The Navier–Stokes equation:

$$\rho \frac{D\mathbf{v}}{Dt} = -\nabla p + \mu \nabla^2 \mathbf{v} + \varepsilon (\nabla^2 \Psi) \nabla \Psi \quad (6.45)$$

where  $p$  is the pressure,  $\rho$  and  $\mu$  are the density and dynamic viscosity of the liquid.

The above governing equations can be used for the subsequent instability analysis of this system. For the details of this analysis, readers may refer to the original work of Chen et al. [24].

In the parallel lamination system depicted in Fig. 6.18 (a), the transversal perturbation of electrokinetic instability is proportional to  $\exp(-2K_x x^*)$ , where  $K_x$  and  $x^*$  are the dimensionless growth rate and streamwise location, respectively. The larger the growth rate, the better the mixing. Both variables are normalized by the channel half-width  $W/2$ . Similar to the case of pressure-driven disturbance, the instability is characterized by the magnitude of disturbance and the dimensionless temporal frequency  $\Omega$ :

$$\Omega = \omega \frac{W}{u_{eo}} \quad (6.46)$$

where  $u_{eo} = \varepsilon \zeta E_{el} / \mu$  is the electroosmotic velocity and  $\omega$  is the temporal frequency of the perturbed interface. The magnitude of disturbance is represented by the dimensionless electric Rayleigh number, which is the ratio between the transversal electroviscous velocity  $u_{ev}$  and the effective ion diffusion coefficient  $D$ :

$$Ra_{el} = \frac{u_{ev} W}{D} = \left( \frac{\gamma - 1}{\gamma + 1} \right)^2 \frac{W}{\delta} \frac{\varepsilon E_{el}^2 H^2}{\mu D} \quad (6.47)$$

where  $\gamma = \sigma_{el,H} / \sigma_{el,L}$  is the conductivity ratio of the two streams, and  $\delta$  is the diffusion length. The ion concentration distribution is assumed to be  $\sigma_{el}(y) = \sigma_{el,L} + \frac{\sigma_{el,H} - \sigma_{el,L}}{2} \text{erfc}(2y/\delta)$ . The ratio between electroviscous and electroosmotic velocity is another important parameter for the instability analysis:

$$R_v = \frac{u_{ev}}{u_{eo}} = \left( \frac{\gamma - 1}{\gamma + 1} \right)^2 \frac{2E_{el} H^2}{\zeta \delta}. \quad (6.48)$$

Fig. 6.18 (b) shows the behavior of convective instability. Mixing extent is expressed as the spacial growth rate of the perturbed interface. It's apparent that the threshold for the onset of convective instability is the critical electric Rayleigh number  $Ra_{E,cr} = 11$ . At high Rayleigh numbers above 50, the perturbed wave moves with the speed of the electroosmotic velocity  $u_{eo}$ . Fig. 6.18 (b) shows the onset of absolute instability indicated by the cusp point of the spatial growth rate as a function of the temporal frequency  $\Omega$ . Good mixing is achieved with a high velocity ratio or a high electric Rayleigh number.

The critical Rayleigh number depends on the definition equations for the electric Rayleigh numbers. According to Baygents and Baldessari [25], the critical Rayleigh number is  $1.4 \times 10^4$  if

$$Ra_{el} = \frac{4\varepsilon E_{el}^2 W^2}{D\mu} \frac{\Delta\sigma_{el}}{\sigma_{el,0}}$$

where  $\sigma_{el,0}$  is the average conductivity of both mixing streams. According to Lin et al. [39], the critical Rayleigh number is on the order of 1000, if:

$$Ra_{el} = \frac{\varepsilon E_{el}^2 H^2}{D\mu}.$$

The electric Rayleigh number shows the ratio between transverse transport caused by electroviscous velocity and molecular diffusion. A larger Rayleigh number means better mixing due to stronger instability. Furthermore, the electric Rayleigh number is proportional to the square of the field strength

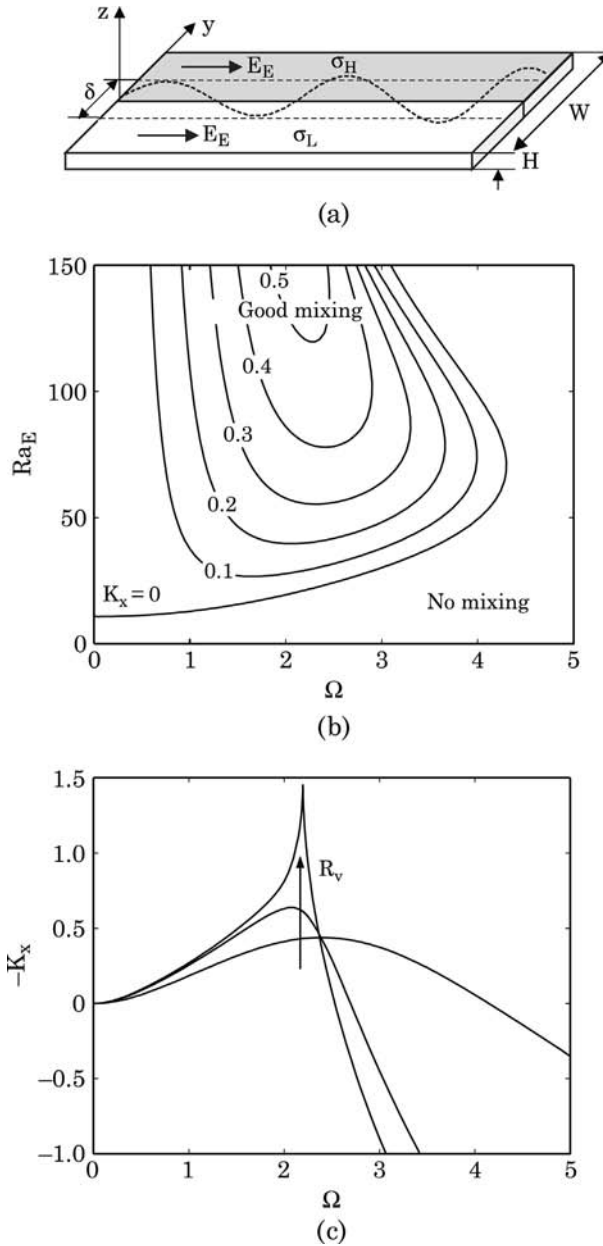


**Figure 6.18** Electrokinetic instability of two streams with different ionic concentrations: (a) the model; (b) convective electrokinetic instability: contour plot of mixing extent expressed as the spacial growth rate  $K_x$ , the instability parameters are the electric Rayleigh number and the temporal frequency  $\Omega$ ; (c) absolute electrokinetic instability: mixing extent expressed as the partial growth rate  $-K_x$  for three different velocity ratios ( $R_v = 3.0, 4.5, 4.9$ ), which corresponds to the three electric Rayleigh numbers ( $Ra_{el} = 90, 200, 240$ ) (after [24]).

( $\text{Ra}_{\text{el}} \propto E_{\text{el}}^2$ ). Thus, mixing based on electrokinetic instability is sensitive to the applied voltage.

### 6.5.2 Instability Caused by Variation of Electric Field

Besides using a gradient in conductivity, instability can be induced by a periodic transversal flow similar to the case of hydrodynamic instability depicted in Fig. 6.3. Similar to the hydrodynamic case (Fig. 6.11), a transversal disturbance flow can be introduced using one or more disturbance channels. The main mixing streams can be either pressure-driven [34] or electrokinetic [36].

For a simple two-dimensional electrokinetic disturbance flow, the Navier–Stokes equation in the  $y$  direction reduces to:

$$\rho \frac{\partial v}{\partial t} = \mu \frac{\partial^2 v}{\partial x^2}. \quad (6.49)$$

If the Debye length is assumed to be very small compared to the channel width, a slip boundary condition with Smoluchowski velocity:

$$v_{\text{wall}} = \frac{\varepsilon \zeta E_{\text{el},0}}{\mu} \exp(i\omega t) \quad (6.50)$$

where  $E_{\text{el},0} \exp(i\omega t)$  with the angular disturbance frequency  $\omega$  represents the applied disturbance electric field. For the geometry depicted in Fig. 6.11 and introducing the dimensionless variables  $x^* = x/W_x$ ,  $t^* = t\omega$  and  $v^* = v\mu/(\varepsilon \zeta E_{\text{E}0})$  the solution for the disturbance velocity is [34]:

$$v^*(x^*, t^*) = \Re \left\{ \frac{\sinh[\beta(1+i)(1-x^*)] + \sinh[\beta(1+i)x^*]}{\sinh[\beta(1+i)]} \exp(it^*) \right\} \quad (6.51)$$

where  $\Re$  and  $i$  stand for the real part and the imaginary unit, respectively. The ratio  $\beta$  is defined as:

$$\beta = \frac{W_x}{\sqrt{2\mu/\rho\omega}}. \quad (6.52)$$

The term  $\sqrt{2\mu/\rho\omega}$  is called the Stokes penetration depth. Instability was observed by Oddi et al. [34] for  $\beta$  of the order of 0.1 to 10. In a weak electric field strength, the flow described by (6.51) is stable. Fig. 6.19 shows the typical dimensionless time-dependent velocity profile at  $\beta = 5$ . At high electric field, the flow becomes unstable with three-dimensional chaotic behavior. Thus, an AC electric field can also be applied in the flow direction for creating instability and improving mixing.

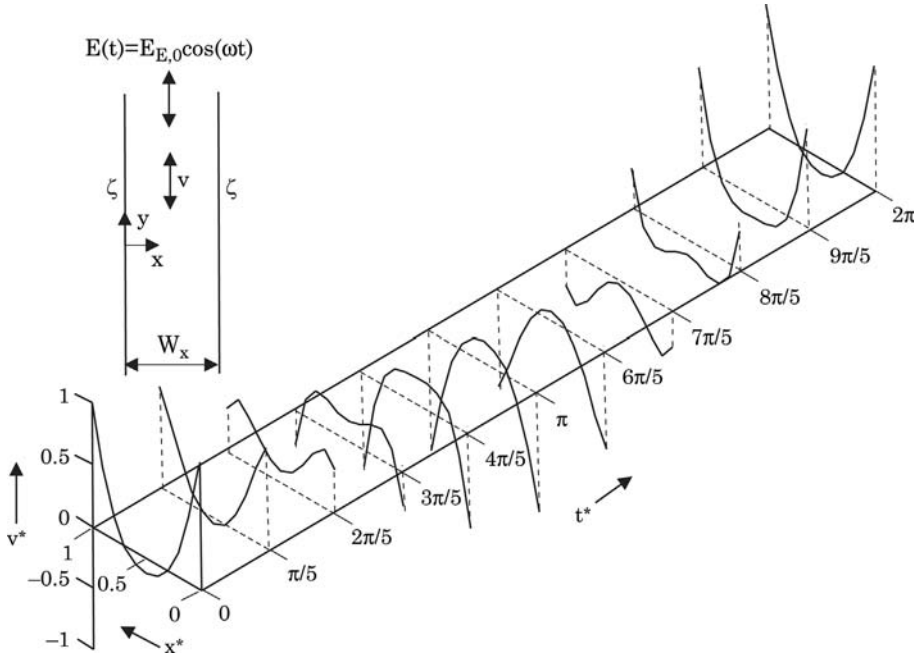


**Figure 6.19** Dimensionless time-dependent velocity profile of an electrokinetic flow in an AC electric field ( $\beta = 5$ ).

### 6.5.3 Instability Caused by Variation of Zeta Potentials

Pulsating electrokinetic flow can also be generated by keeping the electric field constant while varying the zeta potential at the channel wall. The zeta potential on the channel walls can be controlled by shielding electrodes, in the same way as field effect transistors work [23]. Controlling these shielding electrodes leads to spatiotemporal changes of zeta potential in the mixing channels, and thus instability in the flow.

The shielding electrode and the channel wall form a capacitor, where the dielectric medium is the device material. Considering a shielding electrode parallel to the channel wall under steady-state conditions, the charge density stored in the capacitor is:

$$\rho_{el,0} = \frac{\varepsilon_r \varepsilon_0 (V_c - V_i)}{d} \quad (6.53)$$

where  $\varepsilon_r$  is the relative permittivity of the device material,  $\varepsilon_0$  is the dielectric constant of vacuum, and  $d$  is the gap between the channel wall and the electrode. The initial voltage  $V_i$  corresponds to the case of zero control voltage  $V_c = 0$ , where the resulting charge density is equal to the initial charge density at the channel wall. The charge density of the capacitor formed at the electric

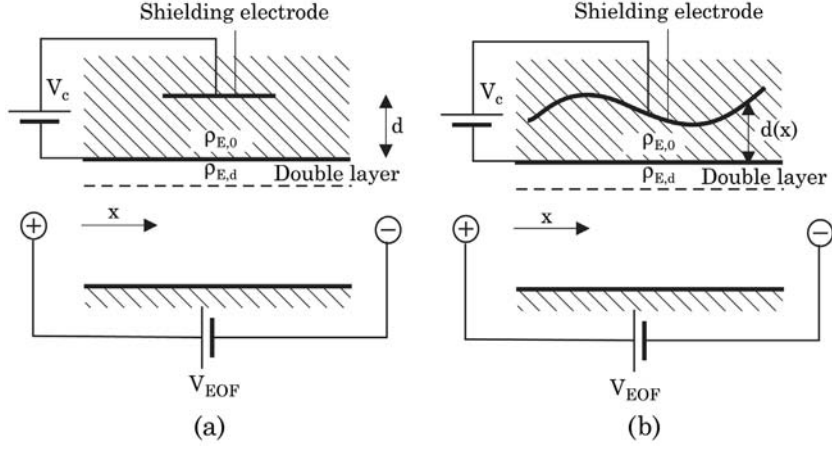


**Figure 6.20** Model of control of zeta potential: (a) parallel shielding electrode; (b) shielding electrode with an arbitrary shape.

double layer in the microchannel is:

$$\rho_{el,d} = \frac{4n_{\infty}ze}{\kappa} \sinh\left(\frac{ze\zeta}{2k_B T}\right) \quad (6.54)$$

where  $n_{\infty}$  is the ion concentration in the channel,  $e$  is the elementary charge,  $z$  is the ionic valence,  $\kappa$  is the Debye parameter,  $k_B$  is the Boltzmann constant, and  $T$  is the absolute temperature. Setting  $\rho_{el,0} = \rho_{el,d}$ , the zeta potential can be expressed explicitly as a function of the control voltage:

$$\zeta = \frac{2k_B T}{ze} \operatorname{arsinh}\left[\frac{\varepsilon_r \varepsilon_0 \kappa (V_c - V_i)}{4n_{\infty} z e d}\right]. \quad (6.55)$$

For a transient process, the charging time of the capacitors needs to be considered. Since the capacitance of the double layer is much smaller than the capacitance formed by the shielding electrode and the channel wall, the time constant is determined by the control capacitance and its resistance only:

$$\tau = RC = \frac{\rho_{ohm}}{A} \frac{\varepsilon_r \varepsilon_0 A}{d} = \frac{\varepsilon_r \varepsilon_0 \rho_{ohm}}{d} \quad (6.56)$$

where  $\rho_{ohm}$  is the specific resistance of the device material. The transient function of the zeta potential is:

$$\zeta(t) = \frac{2k_B T}{ze} \operatorname{arsinh}\left[\frac{\varepsilon_r \varepsilon_0 \kappa (V_c - V_i)}{4n_{\infty} z e d} \exp(-t/\tau)\right]. \quad (6.57)$$

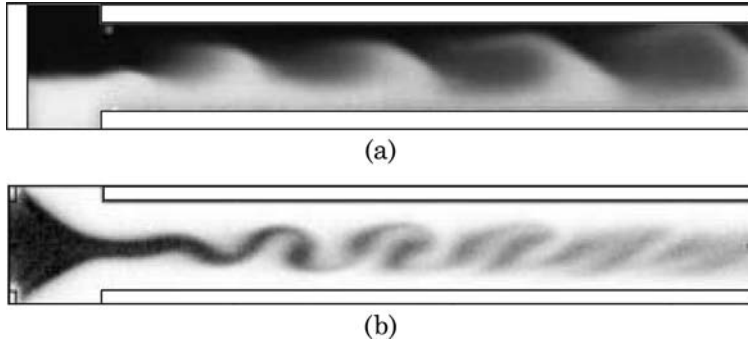


**Figure 6.21** Mixing based on electrokinetic instability: (a) two streams; (b) three streams (reprinted with permission from [24] and [35]).

In the case that the distance between the control electrode and the channel wall is a function of  $x$ , the zeta function is also a function of  $x$ :

$$\zeta(x) = \frac{2k_B T}{ze} \operatorname{arcsinh} \left[ \frac{\varepsilon_r \varepsilon_0 \kappa (V_c - V_i)}{4n_\infty z e d(x)} \right]. \quad (6.58)$$

#### 6.5.4 Design Examples

Electrokinetic instability with an ion concentration gradient can be implemented using any platform with electrokinetic flow. Chen et al. [24] and Posner et al. [35] used microchannels etched in glass. Fig. 6.21 shows electrokinetic instability between two mixing streams and three mixing streams. In the case of two mixing streams [Fig. 6.21 (a)], the channel cross section is 155  $\mu\text{m}$  in width and 11  $\mu\text{m}$  in depth. Borate buffers with concentrations of 1 mM and 10 mM are used as working fluids. The 10-mM solution was dyed with rhodamine B, which is fluorescent and neutral. The liquids are first introduced into the mixing channel using a relatively low field strength of 250 V/cm. Once the two liquids flow side by side in the channel, a high voltage is switched on to generate instability. Convective instability occurred at a field strength threshold of  $500 \pm 100$  V/cm. The unstable wave has a wavelength of approximately the channel width. The travelling speed of the convectively unstable wave is proportional to the electric field. That means electroosmotic flow is responsible for carrying the wave down stream. Absolute instability occurred at a higher field strength of 1.5 kV/cm. In the case shown in Fig. 6.21 (b), instability occurred at about 400 V/cm at about 1.5 times the channel width from the position with the smallest width. At higher field strengths, the location of the starting instability moves to the inlet of the middle stream.

Oddy et al. used electrokinetic flows as a disturbance for pressure-driven flow [34]. The micromixer depicted in Fig. 6.22 (a) was molded in PDMS, which is

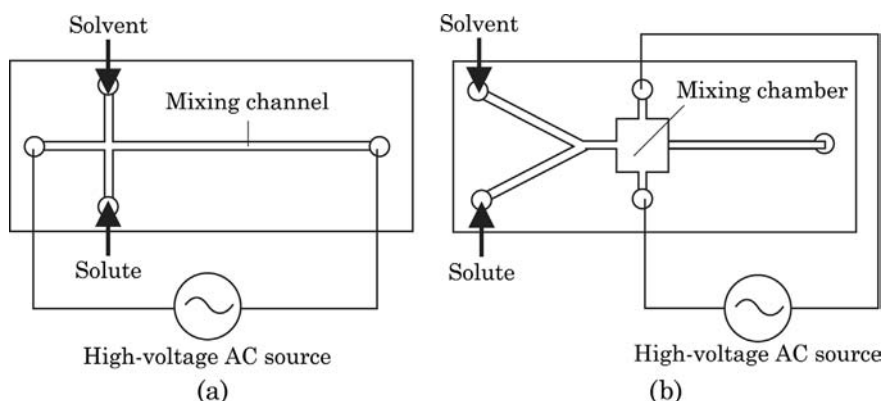


**Figure 6.22** Mixing based on electrokinetic disturbance: (a) disturbance in axial direction; (b) disturbance in transversal direction.

subsequently bonded to a glass slide using adhesive bonding with epoxy. The channels have a cross section of  $1\text{ mm} \times 300\text{ }\mu\text{m}$ . The liquid streams are introduced by syringe pumps. High-voltage AC excitation is introduced along the mixing channel by platinum electrode wires. The electrokinetic disturbance was introduced in both continuous and stop mode. The micromixer depicted in Fig. 6.22 (b) was etched in glass. The microchannels are  $300\text{ }\mu\text{m}$  wide and  $100\text{ }\mu\text{m}$  deep. Transversal electrokinetic disturbance is introduced in a square mixing chamber measuring  $1\text{ mm} \times 1\text{ mm} \times 100\text{ }\mu\text{m}$  which corresponds to a volume of  $100\text{ nL}$ . The inlet streams can be either pressure-driven or electrokinetically driven. In the later case, porous dielectric frits are used for high fluidic resistance. Thus, instability can be contained in the mixing chamber. In both mixer types, chaotic advection was observed when electrokinetic instability occurred.

Fu et al. [36] used transversal electrokinetic disturbance in their micromixer design. The microchannels were etched in glass. The mixing channel is  $100\text{ }\mu\text{m}$  wide and  $30\text{ }\mu\text{m}$  deep. The mixing streams were introduced electrokinetically. The instability was realized by periodically switching the electric field in the disturbance channels. At a relatively low switching frequency of  $1\text{ Hz}$  and a driven field of  $50\text{ V/cm}$ , full mixing was achieved at  $1\text{ mm}$  downstream from the inlet.

Sasaki et al. [37] used an electrode pair with a wavy design to create secondary electrokinetic flow in the channel cross section. An AC electric field across the mixing channel will cause transversal flows, which are confined in two recirculation vortices, Fig. 6.23 (a). With the wavy electrode designs, the two vortices have different sizes, which are controlled by the position of the gap between the two electrodes. The mixing channel was etched in glass with a width and a depth of  $120\text{ }\mu\text{m}$  and  $40\text{ }\mu\text{m}$ , respectively. The electrodes are made of platinum sputtered on a glass substrate. The mixing streams are driven by pressure. Without an applied voltage at the electrodes, no secondary flow



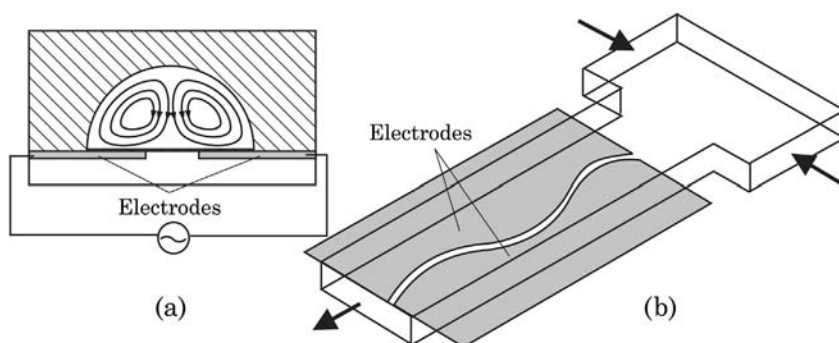


**Figure 6.23** Mixing based on electrokinetic disturbance and chaotic advection: (a) channel cross section with secondary flow; (b) concept of the micromixer.

exists. Mixing occurred with a peak-to-peak voltage of 20 V and a frequency of 1 kHz. Electroosmotic secondary flow causes chaotic advection similar to the case of passive micromixers based on chaotic advection discussed in the previous chapter. Mixing was achieved at a Peclet number as high as 2000.

The concept of sequential segmentation can also be implemented in an electrokinetic flow. Tang et al. utilized switching of electrokinetic flow to generate short segments of solvent and solute in the mixing channel [38]. Electrokinetic segmentation was capable of creating stable fluid segments in the mixing channel at a frequency between 0.01 and 1 Hz. However because of the lack of a distributed velocity profile in the channel cross section, there was no Taylor dispersion and mixing in the flow direction still relies on molecular diffusion.

The concept of controllable zeta potential was reported by Lin et al. [39,40]. Fig. 6.24 shows the different configurations of the shield electrodes. The groves for the electrodes are etched in glass with the microchannels in the same process. A gold/chromium layer was sputtered and etched to form the shield electrodes. The microchannels are sealed by another glass plate using thermal direct bonding. The mixing channel has a width of 150  $\mu\text{m}$  or 200  $\mu\text{m}$ . In the case of parallel electrodes shown in Fig. 6.24 (a), the electrodes are 200  $\mu\text{m}$  long and are placed 130  $\mu\text{m}$  from the channel wall. Inclined electrodes shown in Figs. 6.24 (b) and (c) have their distance varying linearly from 130  $\mu\text{m}$  to 520  $\mu\text{m}$ . Fig. 6.24 also shows the simulated streamlines of the electrokinetic flows with these three electrode configurations. The simulation data shows clearly that the zone with controlled zeta potentials generates a flow opposite to the main flow, leading to recirculation at these areas. While parallel electrodes lead to relatively regular streamlines, a gradient in zeta potential causes very complex streamlines, which possibly lead to chaotic advection. Experimental results showed that the configuration with zigzag electrodes shown in Fig. 6.24 (c) delivers the best mixing performance.

Wu et al. [48] controlled the zeta potential by embedded electrodes. The electrodes are made of a 200-nm thick aluminium layer and take the asymmetric

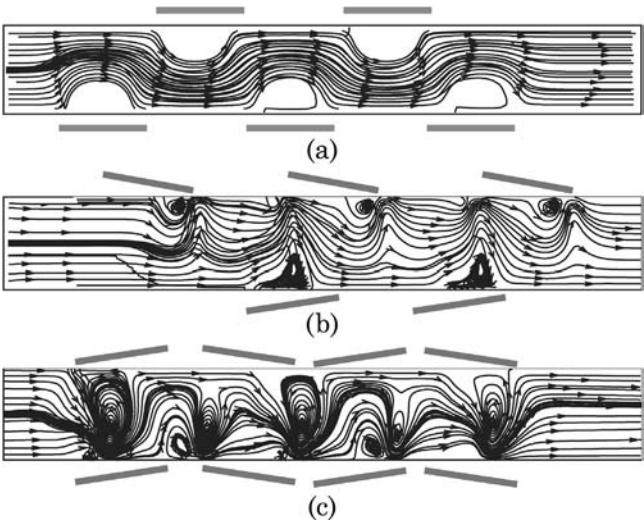


**Figure 6.24** Stream lines of electrokinetic flow with controlled zeta potentials: (a) parallel electrodes; (b) inclined electrodes; (c) zigzag electrodes (reprinted with permission from [40]).

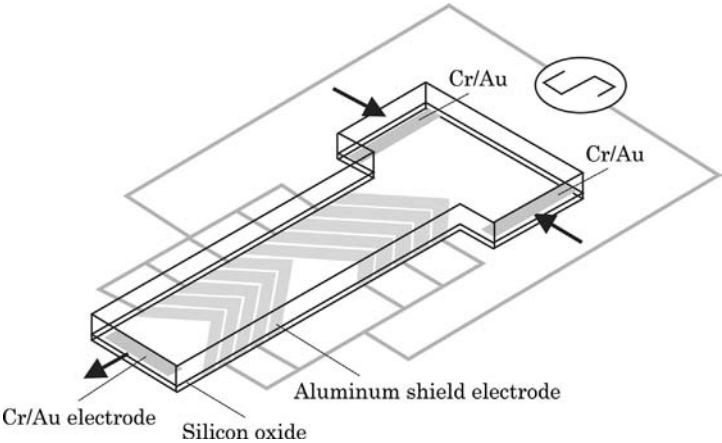


**Figure 6.25** Micromixer based on electrokinetic disturbance with staggered herringbone electrodes.

herringbone shapes, Fig. 6.25. The electrodes are insulated from the mixing liquids by a 500-nm silicon oxide layer. The driving electrodes for the mixing streams are made of a titanium/gold layer. The mixing channel was molded in PDMS, which was bonded to the silicon substrate with all the electrode structures using oxygen plasma-assisted bonding. Similar to the work of Lin et al. [39,40], the zeta potential at the bottom surface of the mixing channel can be controlled by shield electrodes made of aluminum. Mixing occurs when a square wave with peak voltages of 100 V and  $-50$  V was applied at 0.5 Hz.

Qian and Bau [41] proposed to use time-dependent control of zeta potentials using shield electrode arrays on the channel wall. The different streamline patterns were overlapped to generate chaotic advection in the mixing channel.

Zeta potential can be modified chemically using surface charge patterning [42]. Similar to chaotic advection caused by slanted grooves in hydrodynamic flow, surface charge patterning on the channel wall leads to chaotic advection in an electrokinetically driven flow. Biddiss et al. [42] used 0.1 M sodium hydroxide, deionized water, and 5% Polybrene solution to pattern a glass surface through a PDMS mask. This technique allows patterning patches with positive charges on the glass surface, which has a native negative charge. The T-type micromixer was fabricated in PDMS and bonded to the glass slide with the patterned surface charge. The mixing channel has a cross section of  $200 \times 200 \mu\text{m}$ . Numerical simulation and experimental results show that at Reynolds numbers of 0.08–0.7 and Peclet numbers of 190–1500, the liquids are fully mixed at 2.5 mm downstream from the entrance. For the same performance, mixing based on molecular diffusion would require a channel length of 22 mm. Fig. 6.26 shows the typical patterns for zeta potential modification. The gray areas represent the modified surface with positive charge, while the rest of the surface keeps its native negative charge.

## 6.6 Magnetohydrodynamic Disturbance

### 6.6.1 Straight Channel Configuration [43]

The next candidate for transversal transport of species in microchannels is the magnetohydrodynamic (MHD) effect [43]. Fig. 6.27 shows the schematic concept of an active micromixer based on MHD instability. Interdigitated electrodes are connected to a DC power supply. If the fluid is an electrolyte, there is a current density  $\mathbf{J}$  between the electrode pair. If the liquid is subjected to an external magnetic field with the density  $\mathbf{B}$  as shown in Fig. 6.27, the resulting Lorentz force is:

$$\mathbf{f} = \mathbf{J} \times \mathbf{B}d, \quad (6.59)$$

where  $d$  is the distance between the electrodes. The Lorentz force is a bulk force, thus does not scale favorably with the miniaturization. However, this force could be strong enough to induce transversal flow and improves mixing. Incorporating the Lorentz force into the Navier–Stokes equation results in the governing equation for flow in the mixing channel:

$$\rho \frac{D\mathbf{v}}{Dt} = -\nabla p + \mu \nabla^2 \mathbf{v} + \mathbf{J} \times \mathbf{B}. \quad (6.60)$$

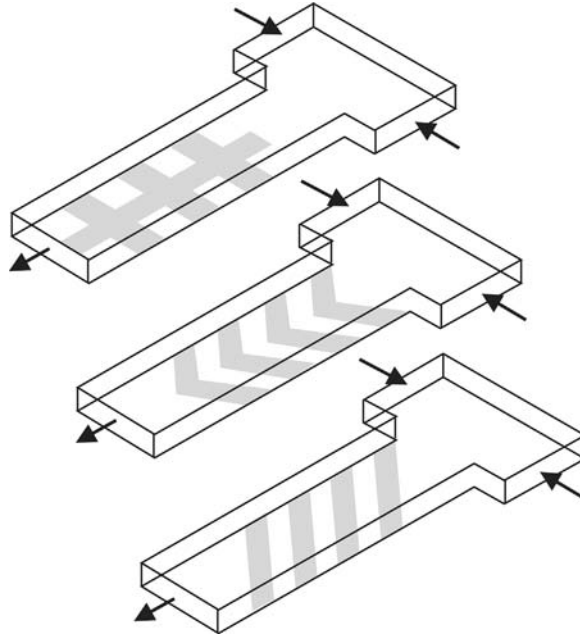


**Figure 6.26** Micromixers based on zeta potential modification.

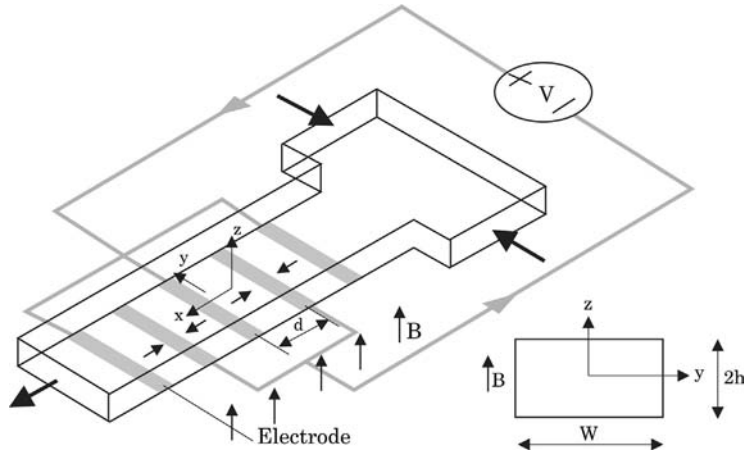


**Figure 6.27** Concept of active micromixer based on magneto hydrodynamic disturbance.

The current density can be determined based on Ohm's law:

$$\mathbf{J} = \sigma_{\text{el}}(\mathbf{E}_{\text{el}} + \mathbf{v} \times \mathbf{B}), \quad (6.61)$$

where  $\sigma_{\text{el}}$  is the conductivity of the fluid. Assuming that the channel height is much smaller than the channel width and the electrode distance  $h \ll w, d$ , the

problem can be reduced to a two-dimensional problem for the  $x$ – $y$  plane. With a velocity scale  $\bar{u} = \sigma E_{cl} B h^2 / \mu$ , the length scale, the time scale, and the pressure can be normalized by  $d$ ,  $d/\bar{u}$  and  $\mu \bar{u} d / h^2$ , respectively. Using the stream function  $\psi(x^*, y^*)$ , the steady-state Navier–Stokes equation has the form:

$$\nabla^2 \psi = -2 \sum_{n=0}^{\infty} \left\{ \cos \left[ \frac{(2n+1)\pi x^*}{2} \right] \right\} \quad (6.62)$$

with the boundary conditions  $\psi(x^*, \pm w^*/2) = 0$  and  $\psi(\pm 1, y^*) = 0$ . With the stream function from (6.62) the velocity components can be determined as:

$$u^* = -\frac{1}{2\pi} \sum_{n=0}^{\infty} (-1)^n \ln \left\{ \frac{\cosh[(-y^* + w^*/2 + nw^*)\pi] + \cos(\pi x^*)}{\cosh[(-y^* + w^*/2 + nw^*)\pi] - \cos(\pi x^*)} \right. \\ \left. \times \frac{\cosh[(y^* + w^*/2 + nw^*)\pi] - \cos(\pi x^*)}{\cosh[(y^* + w^*/2 + nw^*)\pi] + \cos(\pi x^*)} \right\} \quad (6.63)$$

$$v^* = \frac{1}{2} \text{sgn}(x) - \frac{1}{\pi} \sum_{n=0}^{\infty} (-1)^n \left[ \arctan \left\{ \frac{\sin(\pi x^*)}{\sinh[(-y^* + w^*/2 + nw^*)\pi]} \right\} \right. \\ \left. \times \arctan \left\{ \frac{\sin(\pi x^*)}{\sinh[(y^* + w^*/2 + nw^*)\pi]} \right\} \right] \quad (6.64)$$

where the sign function is defined as

$$\text{sgn}(x^*) = \begin{cases} -1 & (x^* > 0) \\ 0 & (x^* = 0) \\ 1 & (x^* < 0) \end{cases} \approx \frac{4}{\pi} \sum_{n=0}^{\infty} \frac{1}{2n+1} \sin[(2n+1)\pi x^*]. \quad (6.65)$$

The solution of the velocity field  $(u^*, v^*)$  is depicted in Fig. 6.28. The kinetic equations of a fluid particle can be formulated by superposition of the previous steady-state solution with the time-dependent switching function of the electrodes. This time-dependent flow field can lead to chaotic advection and improves mixing.

### 6.6.2 Curved Channel Configuration [44]

Fig. 6.29 shows an annular channel configuration. The electrodes are placed on the inner and outer channel walls. Assuming a two-dimensional model ( $h \ll W$ ), the Navier–Stokes equation with the MHD body force is:

$$\frac{d^2 v}{dr^2} + \frac{1}{r} \frac{dv}{dr} - \frac{v}{r^2} = -\frac{\alpha}{r} \quad (6.66)$$

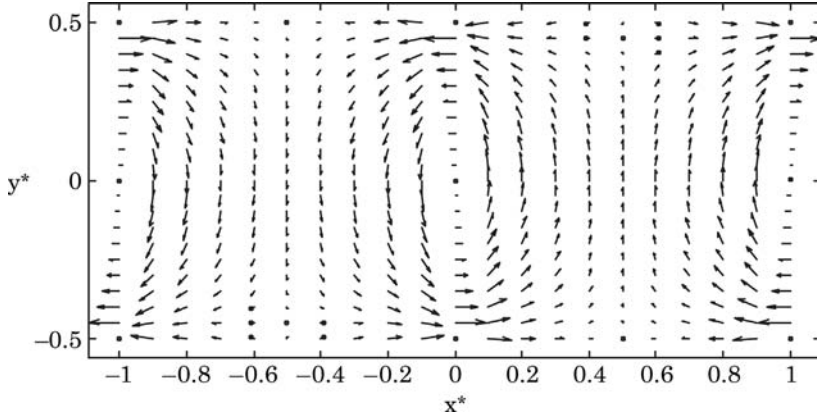


**Figure 6.28** Velocity field of the MHD system depicted in Fig. 6.27.

where  $\alpha = -BI/4\pi h\mu$  represents the EHD force.  $I$ ,  $B$ , and  $\mu$  are the current, the magnetic field strength and the dynamic viscosity of the fluid, respectively. The ratio between the channel's half width and the radius of curvature is  $\beta = W/R$ . Normalizing the radial variable by  $R$ , the velocity by  $\alpha R$  and applying the no-slip boundary conditions at  $r^* = 1 - \beta$  and  $r^* = 1 + \beta$ , results in the dimensionless velocity:

$$v^*(r^*) = \frac{1}{8\beta r^*} \left[ (1 - \beta^2)^2 \ln \frac{1 - \beta}{1 + \beta} + r^{*2} (1 - \beta)^2 \ln \frac{r^*}{1 - \beta} + r^{*2} (1 + \beta)^2 \ln \frac{1 + \beta}{r^*} \right]. \quad (6.67)$$

The average angular velocity is:

$$\omega = \alpha \left[ \frac{1}{4} - \frac{(1 - \beta^2)^2}{16\beta^2} \left( \ln \frac{1 - \beta}{1 + \beta} \right)^2 \right]. \quad (6.68)$$

The results of the velocity field can be converted into the Cartesian coordinate system using the transformations  $x^* = r^* \cos \theta$ ,  $y^* = r^* \sin \theta$ ,  $u^* = -v^* \sin \theta$  and  $v^* = v^* \cos \theta$ . Fig. 6.30 shows the typical velocity field of an MHD-driven flow in an annular microchannel.

In polar coordinates, the convective-diffusive equation has the following forms:

$$\frac{\partial c}{\partial t} + \frac{v(r)}{r} \frac{\partial c}{\partial \theta} - \frac{D}{r} \frac{\partial}{\partial r} \left( r \frac{\partial c}{\partial r} \right) - \frac{D}{r^2} \frac{\partial^2 c}{\partial \theta^2} = 0 \quad (6.69)$$

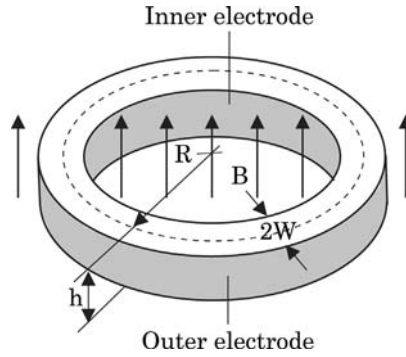


**Figure 6.29** Model of EHD flow in an annular microchannel.

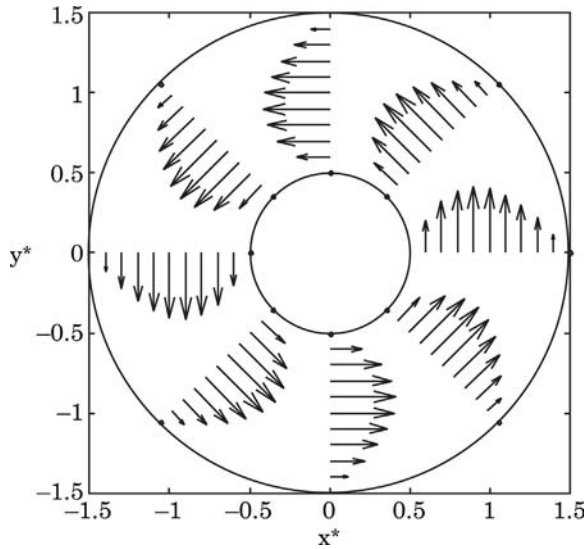


**Figure 6.30** MHD-driven velocity field inside an annular microchannel ( $\beta = 0.5$ ).

where  $D$  is the diffusion coefficient of the species. With the known velocity field, the convective-diffusive equation can be solved numerically or analytically for asymptotic cases [44]. Fig. 6.31 shows the typical concentration distribution at  $D = 0$ . The lamination effect of the two fluids can be observed clearly. To obtain analytical results, asymptotic cases are formulated for different ranges of the Peclet number:

$$\text{Pe} = \frac{\bar{v}W}{D} = \frac{\omega RW}{D}. \quad (6.70)$$

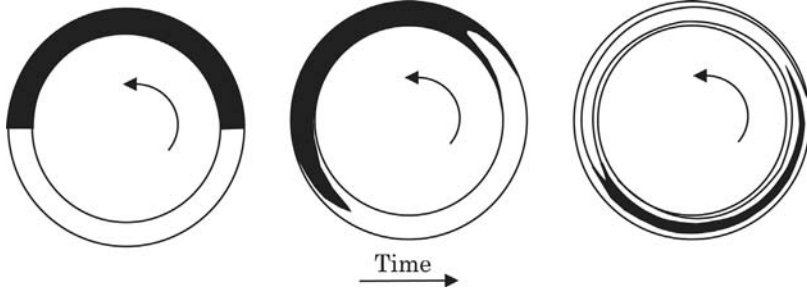


**Figure 6.31** Concentration field in an annular micromixer based on MHD flow ( $\beta = 0.5$ ,  $D = 0$ ) (after [44]).

The mixing measure at an epoch  $t$  is defined as:

$$m(t) = \frac{\int_{R-W}^{R+W} \int_0^{2\pi} [c(r, \theta, t) - \bar{c}(t)]^2}{\int_{R-W}^{R+W} \int_0^{2\pi} [c(r, \theta, 0) - \bar{c}(t)]^2} \quad (6.71)$$

where  $\bar{c}$  is the average concentration over the whole annulus channel:

$$\bar{c}(t) = \frac{1}{4\pi RW} \int_{R-W}^{R+W} \int_0^{2\pi} c(r, \theta, t) r d\theta dr. \quad (6.72)$$

Mixing measure will decrease from 1 to 0 ( $m \rightarrow 0$  when time is going to infinity,  $t \rightarrow \infty$ ). For evaluation of mixing effectiveness, a mixing time  $t_{\text{mixing}}$  is defined when the mixing measure reaches a prescribed value  $M$ :

$$m(t_{\text{mixing}}) = M. \quad (6.73)$$

The mixing time can be made dimensionless through normalizing by  $R^2/D$ :

$$t_{\text{mixing}}^* = \frac{t_{\text{mixing}}}{R^2/D}, \quad (6.74)$$

which eliminates the dependence of mixing time on radius of curvature and diffusion coefficient.

At low Peclet numbers ( $\text{Pe} \ll 7.2$ ), the mixing process is determined by molecular diffusion. The mixing time depends only on the geometry of the channel and the diffusion coefficient:

$$t_{\text{mixing}}^* \approx \frac{1}{2} \ln(M^{-1}) \left( 1 - \frac{1}{3} \beta^2 \right). \quad (6.75)$$



At intermediate Peclet numbers ( $7.2 \ll \text{Pe} \ll 15/\beta$ ), the mixing process is determined by Taylor dispersion:

$$t_{\text{mixing}}^* \approx \text{Pe}^{-2} \ln(M^{-1}) \frac{105}{4} \left( 1 - \frac{18165}{1576} \beta^2 \right). \quad (6.76)$$

At high Peclet numbers ( $\text{Pe} \gg 15/\beta$ ) and moderate  $M$  values, the process is determined by the lamination process of the mixed liquids:

$$t_{\text{mixing}}^* \approx \text{Pe}^{-\frac{2}{3}} \beta^{\frac{4}{3}} \left[ \frac{1}{6} f^{-1}(2M\sqrt{\pi}) \right]^{\frac{1}{3}} \quad (6.77)$$

where function  $f$  is defined as:

$$f(x) = x^{-1/2} \text{erf}(x^{1/2}) \quad (6.78)$$

and erf is the error function.

At high Peclet numbers ( $\text{Pe} \gg 15/\beta$ ) and small  $M$  values, the mixing time is:

$$t_{\text{mixing}}^* \approx \text{Pe}^{-\frac{1}{2}} \beta^{\frac{3}{2}} \frac{1}{4\sqrt{3}} \ln \left[ \frac{4\pi^2}{3M^4} \frac{1}{\beta \text{Pe}} \right]. \quad (6.79)$$

Fig. 6.32 shows the numerical and analytical results of the dimensionless mixing time in different regions of Peclet numbers. The three mixing regimes can be clearly observed. At a fixed geometry and constant diffusion coefficient, the Peclet number is determined by the angular velocity  $\omega$  only. In contrast to a straight channel, high Peclet numbers lead to a short mixing time because of the lamination effect shown in Fig. 6.31.

### 6.6.3 Design Examples

Bau et al. [43] fabricated their MHD mixer using cofired ceramic tapes. The ceramic tapes consist of oxide particles, glass frit, and an organic binder. The tape can be cast with a thickness of 40  $\mu\text{m}$  or more and subsequently machined by laser, milling, or lithography. Microchannels with a depth from 10  $\mu\text{m}$  to a few millimeters can be formed. Metal electrodes can be printed or sputtered on the green tape. After firing, the organic binder will disappear, leaving the sintered oxide particles and forming the solid substrate. In the micromixer reported by Bau et al. [43], electrodes were formed by printing gold paste onto the substrate. The depth, width, and length of the mixing channel are 1 mm, 4.7 mm, and 22.3 mm, respectively. A rectangular permanent magnet was positioned under the mixing channel to generate the external magnetic field. Mixing was observed when DC at 4 V was applied at the electrodes.

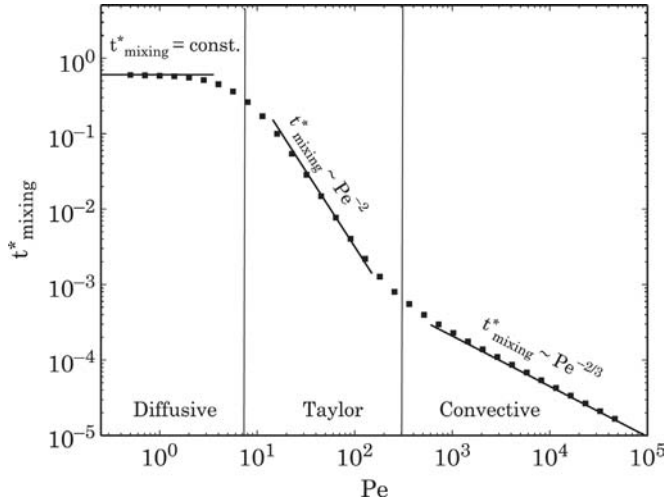


**Figure 6.32** Dimensionless mixing time as a function of Peclet number ( $\beta = 0.05$ ,  $M = 0.3$ , the rectangles shows the simulation result, the lines are analytical results) (after [44]).

Qian and Bau [45] used electrodes on the side wall of a Y-mixer to induce MHD disturbance. The electrode configuration is similar to the EHD-based active micromixer depicted in Fig. 6.15 (a). The mixing channel has a cross section of  $4 \times 2$  mm.

The annular channel configuration depicted in Fig. 6.29 was implemented by West et al. [46]. The prototype was fabricated using a brass disc positioned inside a brass ring. The radius of curvature is  $R = 5$  mm and the channel width is  $W = 2$  mm. The channel height  $h = 0.5$  mm is defined by the thickness of the brass disc and the brass ring. The device is covered on both sides by two transparent polycarbonate plates. Another version was fabricated in silicon using anisotropic etching with KOH with the same radius of curvature, but an average channel width of 1.16 mm. The electrodes are made of chromium and gold, which are sputtered on the channel side wall. Alternatively, the annular microchannel can also be made of SU-8, a negative thick resist [47]. The side-wall electrodes were sputtered over a stencil. The electrode consists of a 100-nm thick platinum layer on a 1- $\mu$ m thick copper layer. MHD actuation utilized an AC signal to avoid electrolysis and electrode degradation. These devices were successfully used for mixing and amplification of DNA samples.

## 6.7 Acoustic Disturbance

A piezoelectric bimorph disc is often the actuator of choice in microfluidic devices, due to its simplicity in implementation and the high energy efficiency. Another key advantage of the piezoelectric actuator is the high actuating

frequency. The high frequency generates acoustic energy, which in turn induces secondary flow in a mixing chamber. Acoustic disturbance can be induced by choosing an actuating frequency at the resonant modes of a membrane. In the following, models for vibration modes of rectangular and circular membranes are considered. These two basic shapes are the most often used for mixing chambers. The following analytical solutions of the membrane deflections at different vibration modes can be applied as the boundary condition for modeling the flow in a mixing chamber. The coupling of a moving wall condition to the Navier–Stokes equation can be implemented with a numerical model.

### 6.7.1 Vibration of a Rectangular Membrane [49]

We consider here a rectangular membrane with a width  $W$ , a length  $L$ , and a constant surface tension  $T$ , Fig. 6.33 (a). The edges of the membrane are fixed. Fig. 6.33 (b) depicts a small element  $dx dy$  with an area density of  $\sigma$ . The forces acting at the two edges at  $y$  and  $y + dy$  are  $-T \sin \alpha dx$  and  $T \sin \beta dx$ . For a small displacement of  $dz$  or small  $\alpha$  and  $\beta$ :

$$\begin{aligned}\sin \alpha &\approx \tan \alpha = \frac{\partial z}{\partial y} \Big|_{y+dy} \\ \sin \beta &\approx \tan \beta = \frac{\partial z}{\partial y} \Big|_y.\end{aligned}\tag{6.80}$$

Thus, the restoring forces in  $x$  and  $y$  are:

$$\begin{aligned}f_x &= -T dx \left( \frac{\partial z}{\partial y} \Big|_{y+dy} - \frac{\partial z}{\partial y} \Big|_y \right) = -T dy \frac{\partial^2 z}{\partial y^2} dx \\ f_y &= -T dy \left( \frac{\partial z}{\partial x} \Big|_{x+dx} - \frac{\partial z}{\partial x} \Big|_x \right) = -T dx \frac{\partial^2 z}{\partial x^2} dy.\end{aligned}\tag{6.81}$$

The total restoring force on the element  $dx dy$  is  $f = f_x + f_y$ . Newton's second law leads to the wave equation:

$$T dx dy \left( \frac{\partial^2 z}{\partial x^2} + \frac{\partial^2 z}{\partial y^2} \right) = \sigma dx dy \frac{\partial^2 z}{\partial t^2}\tag{6.82}$$

or

$$\frac{\partial^2 z}{\partial t^2} = \frac{T}{\sigma} \left( \frac{\partial^2 z}{\partial x^2} + \frac{\partial^2 z}{\partial y^2} \right) = c^2 \nabla^2 z\tag{6.83}$$

where  $c = \sqrt{T/\sigma}$  is the propagation velocity. The wave equation can be solved by separation of variables. Substituting

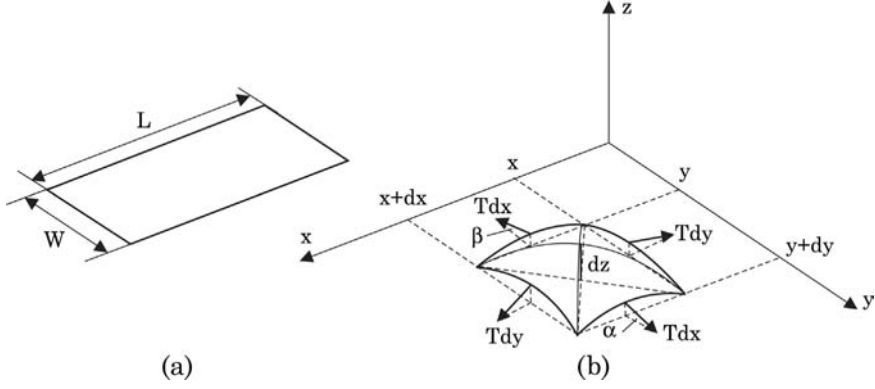


**Figure 6.33** Vibration model for a rectangular membrane: (a) membrane dimensions; (b) forces on a membrane element  $dx dy$ .

$$z(x, y, t) = X(x)Y(y)T(t) \quad (6.84)$$

into (6.83) results in:

$$\frac{1}{T} \frac{d^2 T}{dt^2} = \frac{c^2}{X} \frac{d^2 X}{dx^2} + \frac{c^2}{Y} \frac{d^2 Y}{dy^2} = \omega^2. \quad (6.85)$$

Separating and solving the temporal term:

$$\frac{d^2 T}{dt^2} + \omega^2 T = 0 \quad (6.86)$$

results in

$$T(t) = E \sin \omega t + f \cos \omega t. \quad (6.87)$$

The spacial terms become:

$$\frac{1}{X} \frac{d^2 X}{dx^2} + \frac{\omega^2}{c^2} = -\frac{1}{Y} \frac{d^2 Y}{dy^2} = k^2. \quad (6.88)$$

Solving

$$\frac{d^2 X}{dx^2} + \left( \frac{\omega^2}{c^2} - k^2 \right) X = 0 \quad (6.89)$$

results in

$$X(x) = A \sin \sqrt{(\omega/c)^2 - k^2} x + B \cos \sqrt{(\omega/c)^2 - k^2} x. \quad (6.90)$$

Solving

$$\frac{d^2 Y}{dy^2} + k^2 Y = 0 \quad (6.91)$$

results in

$$Y(y) = C \sin ky + D \cos ky. \quad (6.92)$$

Applying the boundary conditions of  $z = 0$  at  $x = 0$  and  $x = L$  leads to  $B = 0$  and

$$A \sin \sqrt{(\omega/c)^2 - k^2} L = 0. \quad (6.93)$$

Thus

$$X(x) = A \sin\left(\frac{m\pi x}{L}\right) \quad (6.94)$$

where  $\sqrt{(\omega/c)^2 - k^2} L = m\pi$  and  $m = 1, 2, \dots$ . Applying the boundary conditions of  $z = 0$  at  $y = 0$  and  $y = W$  leads to  $D = 0$  and

$$C \sin kW = 0. \quad (6.95)$$

Thus

$$Y(y) = C \sin\left(\frac{n\pi y}{W}\right). \quad (6.96)$$

Substituting  $X(x)$ ,  $Y(y)$  and  $T(t)$  back into (6.84) results in:

$$\begin{aligned} z_{mn} &= A \sin \frac{m\pi x}{L} C \sin \frac{n\pi y}{W} (E \sin \omega t + f \cos \omega t) \\ &= \sin \frac{m\pi x}{L} \sin \frac{n\pi y}{W} (M \sin \omega t + N \cos \omega t) \end{aligned} \quad (6.97)$$

with  $m = 1, 2, \dots$

The modal frequency  $f_{mn} = \omega/(2\pi)$  can be determined from:

$$\sqrt{(\omega/c)^2 - k^2} = \frac{m\pi}{L} \quad (6.98)$$

or

$$\omega^2 = \left(\frac{m\pi}{L}\right)^2 c^2 + k^2 c^2 = \left(\frac{m\pi}{L}\right)^2 c^2 + \left(\frac{n\pi}{W}\right)^2 c^2. \quad (6.99)$$

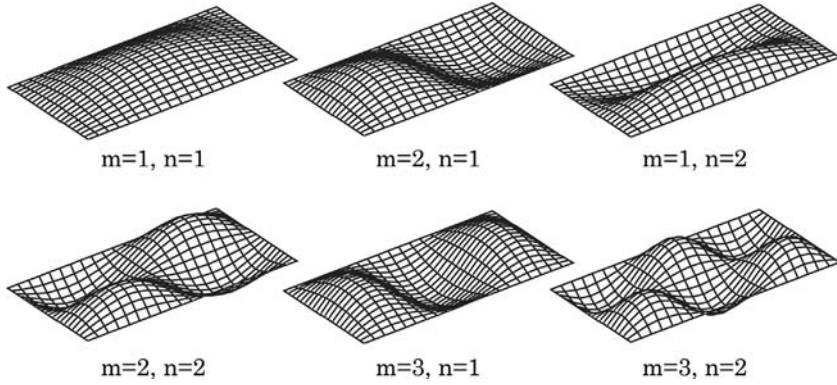


**Figure 6.34** Some vibration modes of a rectangular membrane ( $L : W = 1 : 2$ ).

Thus,

$$f_{mn} = \frac{1}{2\pi} \sqrt{\frac{T}{\sigma} \left( \frac{m^2}{L^2} + \frac{n^2}{W^2} \right)} \quad (6.100)$$

with  $m = 1, 2, \dots$ . Fig. 6.34 shows the solution for the first few vibration modes of a rectangular membrane. These vibration modes will affect the acoustically induced flow pattern inside the mixing chamber. For a square membrane ( $L = W$ ), the two modes  $mn$  and  $nm$  have the same frequency ( $f_{mn} = f_{nm}$ ). At this frequency, the membrane can vibrate with an infinite number of different shapes. The different shapes results from the combination of  $a$  and  $b$  in the equation:

$$z(x, y, t) = (az_{mn} + bz_{nm}) \cos \omega_{mn} t \quad (6.101)$$

where  $a^2 + b^2 = 1$ . These vibration modes are called degenerate modes. Fig. 6.35 shows the few possible combinations of  $z_{12}$  and  $z_{21}$ . This mode can be used for creating chaotic advection in a mixing chamber without hopping from one resonant mode to another.

## 6.7.2 Vibration of a Circular Membrane [49]

The wave equation (6.83) can be formulated for the cylindrical coordinate as:

$$\frac{\partial^2 z}{\partial t^2} = c^2 \left( \frac{\partial^2 z}{\partial r^2} + \frac{1}{r} \frac{\partial z}{\partial r} + \frac{1}{r^2} \frac{\partial^2 z}{\partial \theta^2} \right). \quad (6.102)$$

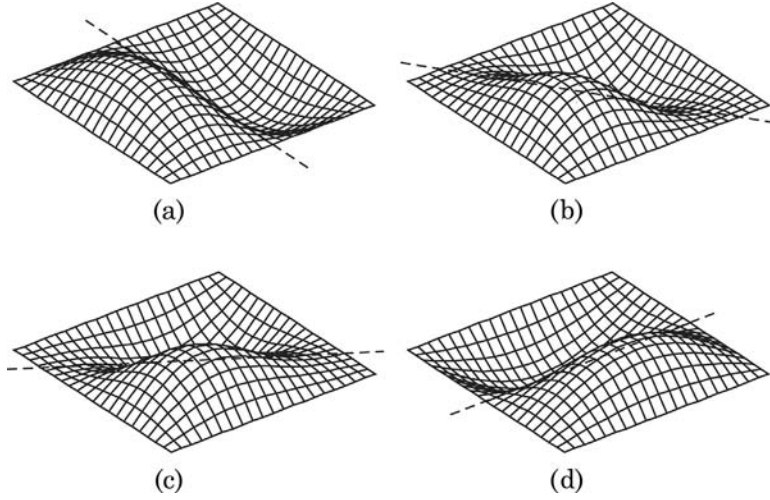


**Figure 6.35** Some degenerate vibration modes of a square membrane at  $m, n = 1, 2$  (the dashed lines are the nodal lines): (a)  $a = \sin 0$ ,  $b = \cos 0$ ; (b)  $a = \sin \pi/6$ ,  $b = \cos \pi/6$ ; (c)  $a = \sin \pi/3$ ,  $b = \cos \pi/3$ ; (d)  $a = \sin \pi/2$ ,  $b = \cos \pi/2$ .

The separated solution for the deflection  $z$  has the form:

$$z(r, \theta, t) = R(r)\Theta(\theta)\exp(i\omega t). \quad (6.103)$$

The separated equations have the forms:

$$\frac{d^2 R}{dr^2} + \frac{1}{r} \frac{dR}{dr} + \left( \frac{\omega^2}{c^2} - \frac{m^2}{r^2} \right) R = 0 \quad (6.104)$$

and

$$\frac{d^2 \Theta}{d\theta^2} + m^2 \Theta = 0. \quad (6.105)$$

The solution of the above equations are:

$$R = J_m(\omega r/c) = J_m(\omega \sqrt{\sigma/T} r) \quad (6.106)$$

$$\Theta(\theta) = A \cos m\theta \quad (6.107)$$

where  $J_m$  is the Bessel function of the first kind and order  $m$ . The  $n$ th zero  $\lambda_n = \omega \sqrt{\sigma/T} r$  of  $J_m(\omega \sqrt{\sigma/T} r)$  gives the frequency of the  $mn$ -mode. Fig. 6.36 shows the first six vibration modes of a circular membrane with a dimensionless frequency, normalized by the frequency of the first mode ( $m = 0$ ,  $n = 1$ ). The corresponding zeros are  $\lambda_n = 2.405 f_{mn}^*$ . The number 2.405 is the first zero of the

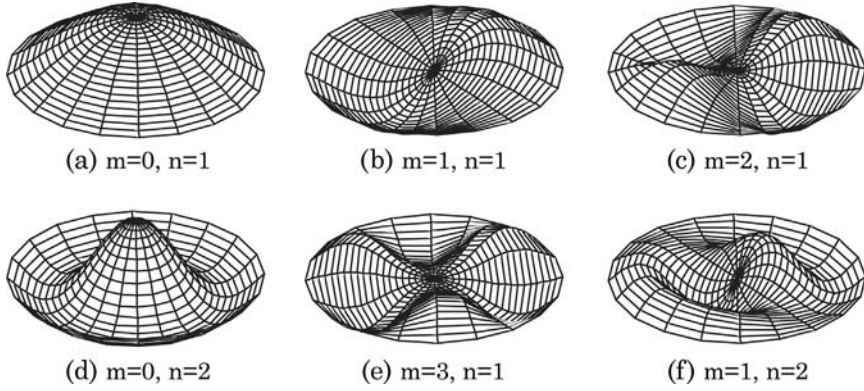


**Figure 6.36** The first six vibration modes of a circular membrane: (a)  $f^* = 1.000$ ; (b)  $f^* = 1.594$ ; (c)  $f^* = 2.136$ ; (d)  $f^* = 2.296$ ; (e)  $f^* = 2.653$ ; (f)  $f^* = 2.918$ .

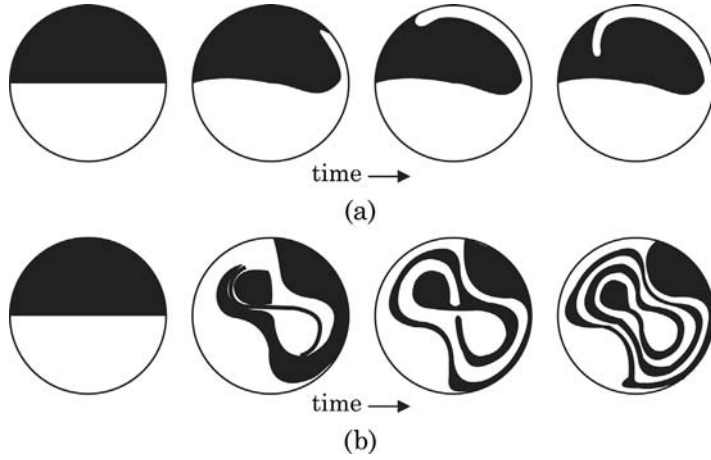


**Figure 6.37** Mixing pattern in a circular chamber: (a) first mode ( $m = 0$ ,  $n = 1$ ,  $f^* = 1.000$ ); (b) second mode ( $m = 1$ ,  $n = 1$ ,  $f^* = 1.594$ ) (redrawn after the experimental data of [50]).

Bessel function of zero order,  $J_0$ . The actual vibration frequency can be determined as:

$$f_{mn} = \frac{2.405 f_{mn}^*}{2\pi a} \sqrt{\frac{T}{\sigma}} \quad (6.108)$$

where  $a$  is the radius of the membrane. The corresponding mixing pattern with the first two modes is shown in Fig. 6.37. The pattern evolves at the same time scale. Mode two has a higher frequency and therefore induces a higher streaming velocity. The two liquids are folded and stretched leading to good mixing in the circular chamber [50].



### 6.7.3 Design Examples

Acoustically induced flow, or acoustic streaming, is an effective transport effect for improving mixing in microchannels. Moroney et al. reported the proof of concept of acoustic mixing at the micro scale [51]. The acoustic field was induced from the channel wall by flexible plate wave, Fig. 6.38 (a). When a flexural plate wave (FPW) propagates in a thin membrane, a high intensity acoustic field exists in the fluid near the membrane, Fig. 6.38 (b). This acoustic field causes net fluid flow in the direction of wave propagation. Due to viscous losses, the first-order particle velocity decays exponentially, 6.38 (c). Therefore, only a fast moving fluid layer exists next to the membrane, 6.38 (d). A basic FPW-device consists of a rectangular flow channel that has a thin membrane on the bottom. The composite membrane is made of low-stress silicon nitride, piezoelectric zinc oxide, and aluminum. Typical membrane thicknesses range from 1 to 3  $\mu\text{m}$ . The FPW has a typical frequency of 3 MHz and a wavelength of 100  $\mu\text{m}$ . Arrays of finger pairs placed at wavelength intervals on a piezoelectric film generate the flexural waves.

Rife et al. used acoustic streaming to improve mixing [52]. The actuation system is based on an array of piezoelectric actuators. The actuator consists of a  $\text{BaTiO}_3$  piezoelectric thin film. The whole piezoelectric actuator was deposited as a thin film on a silicon substrate. Electrical contacts are made with gold and platinum electrodes. The piezoelectric thin-film thickness was chosen so that the actuator works with the fundamental thickness mode resonance near a frequency of 50 MHz. The attenuation length was about 8.3 mm, which can cover the length of the mixing channel. The microchannel network is shown in Fig. 6.39 (a). The actuator array was attached to the PMMA device, which contains the microchannel network. Thus, the actuator is facing air on one side and liquid on the other side. Due to the large mismatch of acoustic impedance on each side, the acoustic energy is almost entirely reflected at the air side. Almost all of the acoustic energy is transferred into the fluid. At the resonance frequency of about 50 MHz, the actuator can induce a flow velocity of 1 mm/s.

Yang et al. reported an acoustic micromixer with an actuator membrane [53,54]. Fig. 6.39 (b) shows the schematic concept of the device. As discussed in the previous section, the different vibration modes of the actuating membrane can induce flows with different streamline patterns. The mixing chamber was fabricated in a Pyrex glass wafer, which is bonded to silicon using anodic bonding. The mixing chamber measured 6 mm on each side and is 60  $\mu\text{m}$  deep. The actuating membrane is formed in the silicon wafer using anisotropic etching with KOH. The membrane is 150  $\mu\text{m}$  thick and covers the entire mixing chamber. The titanium/platinum layer was deposited on the silicon membrane before gluing the PZT layer. The piezo disc was driven by a square wave (50 V peak-to-peak, 60 KHz).

Jang et al. [50] report a similar micromixer with a circular mixing chamber. The chamber measures 6 mm in diameter and 30  $\mu\text{m}$  in depth. The chamber was wet etched in KOH and sealed to a Pyrex glass wafer by anodic bonding.

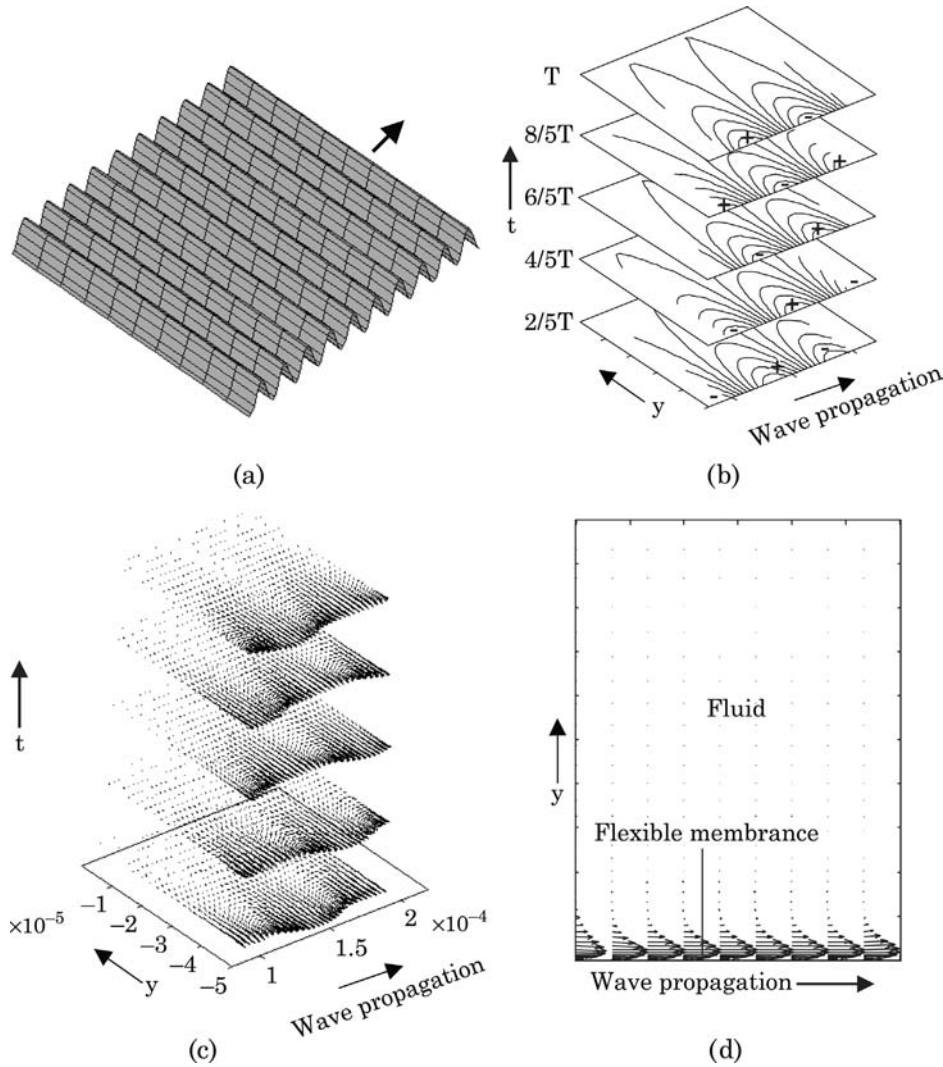


**Figure 6.38** The concept of acoustic streaming: (a) wave propagation in a flexible membrane; (b) pressure field in the fluid, positive and negative pressures are indicated; (c) the first order velocity; (d) the second order or net velocity of acoustic streaming.

A  $6 \times 6$  mm rectangular piezoelectric layer is glued to the membrane above the chamber. The bimorph of 190- $\mu\text{m}$  thick (lead-zirconate-titanate) PZT layer and 210- $\mu\text{m}$  thick silicon membrane forms the actuator for the mixing chamber. The mixer operated at resonant frequencies of the first three modes. The mixing pattern of the first two modes is depicted in Fig. 6.37. The higher the frequency the better the mixing because of the faster induced acoustic streaming. Mixing is more effective if the actuating frequency is switched between different resonant modes. The resulting chaotic mixing pattern of this “mode-hopping”

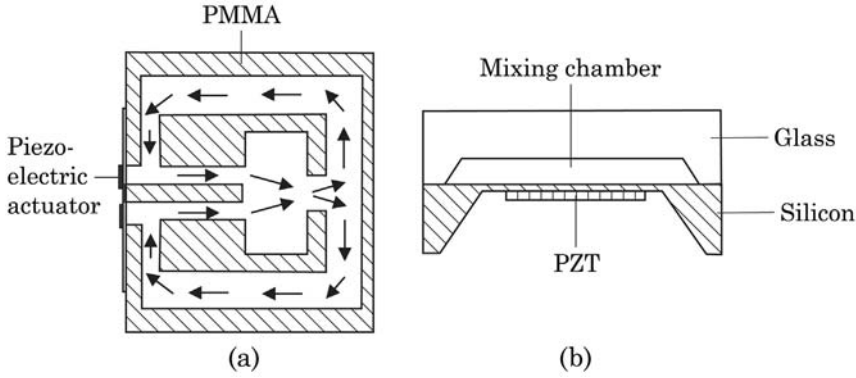


**Figure 6.39** Acoustic micromixers: (a) acoustic-streaming based micromixer (after [52]); (b) acoustic micromixer with an actuating membrane (after [53,54]).

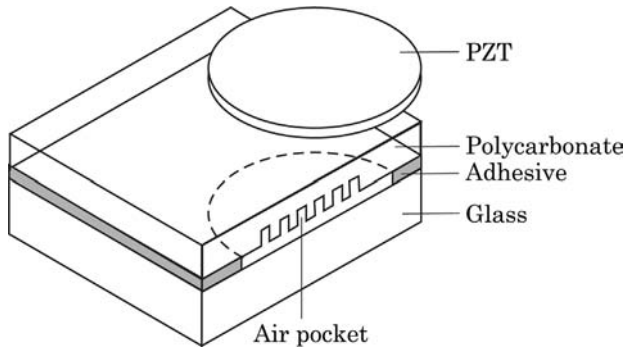


**Figure 6.40** Active micromixers based on acoustic streaming around air bubbles (after [55]).

operation leads to faster mixing compared to single-mode operation. Full mixing was generally achieved after less than 30 seconds.

Liu et al. utilized acoustic streaming induced around an air bubble for mixing [55]. In an acoustic field, the air/liquid interface of an air bubble vibrates and generates its own resonant acoustic field. The behavior of bubbles in sound fields is determined largely by their resonance characteristics. The resonant frequency of a bubble is estimated as:

$$f_{\text{res}} = \frac{1}{2\pi a} \sqrt{\frac{3kp_0}{\rho}} \quad (6.109)$$

where  $a$  is the bubble radius,  $k = c_p/c_v$  is the ratio of specific heats for the gas,  $p_0$  is the hydrostatic pressure, and  $\rho$  is the density of the liquid. Acoustic streaming is generated in the fluid surrounding an air bubble in an acoustic field. If the bubble is excited with a frequency close to its resonant frequency,

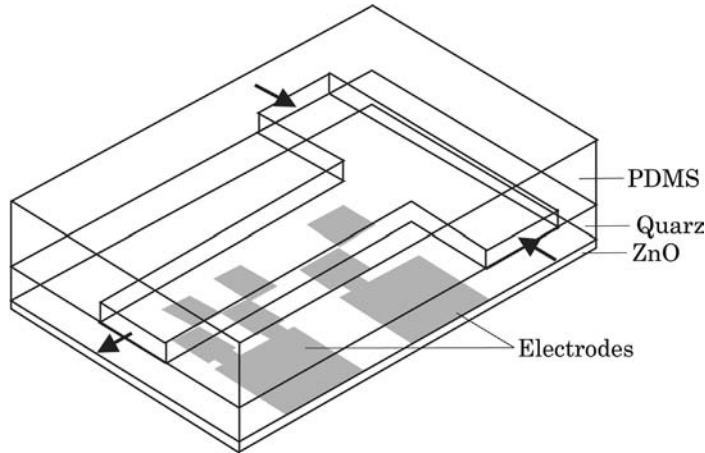


**Figure 6.41** Active micromixers based on acoustic streaming with different electrode patterns (after [57]).

acoustic streaming of recirculation flows around the bubble. This recirculation flow can be used to improve mixing. Fig. 6.40 shows the basic concept of the mixing chamber. The mixing chamber is  $300\text{ }\mu\text{m}$  deep and has a diameter of  $15\text{ mm}$ . The mixing chamber and the air pockets are machined in a polycarbonate (PC) substrate. Since PC is a hydrophobic material, air will be trapped in the pockets when the mixing chamber is filled with liquid. The piezoelectric disc is made of PZT and has a diameter of  $15\text{ mm}$ . The disc was driven by a sinusoidal  $5\text{ V}$  peak-to-peak signal at a frequency of  $2\text{ kHz}$ .

Yaralioglu et al. utilized acoustic streaming to disturb the flow in a conventional Y-mixer [57]. While the channel is made of PDMS, the piezoelectric actuator is integrated into the cover quartz wafer. The master for the PDMS channel was fabricated in silicon using deep reactive ion etching (DRIE). The piezoelectric actuators were fabricated on a quartz wafer. A  $300\text{-nm}$  thick gold layer was first deposited and patterned on the quartz wafer, Fig. 6.41. A  $8\text{-}\mu\text{m}$  thick zinc oxide was deposited on top of the gold electrodes and worked as the piezoelectric material. In the last step, a  $300\text{-nm}$  thick gold layer was deposited and worked as the top electrode. The PDMS part was then bonded to the quartz wafer with the help of surface treatment in an oxygen plasma. The induced acoustic streaming significantly enhances mixing in the microchannel.

## 6.8 Thermal Disturbance

Because molecular diffusion depends on the kinetic energy of the molecules, the diffusion coefficient highly depends on temperature. Thus, thermal energy can be used to enhance mixing. Darhuber et al. [58] proposed and numerically

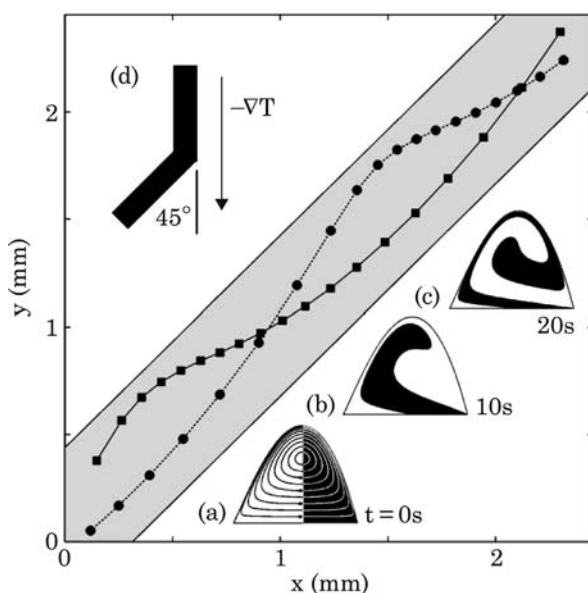


**Figure 6.42** Active micromixers based on thermally induced convection (reprinted with permission from [58]).

analyzed the thermocapillary advection induced by a transverse temperature gradient. In Fig. 6.42, two liquids are following a hydrophilic stripe. The stripe is 500  $\mu\text{m}$  wide; the liquid column is 20  $\mu\text{m}$  high. The temperature gradient in use was  $dT/dy = 4\text{ }^{\circ}\text{C}/\text{mm}$ . The lines in Fig. 6.42 are experimental results of the trajectories of two tracing particles. Figs. 6.42 (a) to (c) show the concentration distribution of the two liquids ( $D = 0$ ). The transverse motion is achieved by the thermal gradient  $dT/dy$ . According to the simulation results [58], the interfacial area between the two liquids increases 150 times in 30 seconds.

## References

1. F.M. White, *Viscous Fluid Flow*, 2nd edition, McGraw-Hill, New York, 1991.
2. J. Ducreé, S. Haeberle, T. Brenner, T. Glatzel and R. Zengerle, "Patterning of flow and mixing in rotating radial microchannels," *Microfluidics and Nanofluidics*, Vol. 2, pp. 97–105, 2006.
3. C.H. Berg, "The rotary motor of bacterial flagella," *Annual Review of Biochemistry*, Vol. 72, pp. 19–54, 2003.
4. N. Darnton, L. Turner, K. Breuer and H.C. Berg, "Moving fluid with bacterial carpets," *Biophysical Journal*, Vol. 86, pp. 1863–1870, 2004.
5. F. Okkels and P. Tabeling, "Spatiotemporal resonances in mixing of open viscous fluids," *Physical Review Letters*, Vol. 92, p. 038301, 2004.
6. A. Dodge, A. Hountondji, M.C. Jullien and P. Tabeling, "Spatiotemporal resonances in a microfluidics system," *Physical Review*, Vol. 92, p. 038301, 2004.

7. S. Jones and H. Aref, "Chaotic advection in pulsed source-sink systems," *Physics of Fluids*, Vol. 31, pp. 469–485, 1988.
8. J.M. Hertzsch, R. Sturman and S. Wiggins, "DNA microarrays: Design principles for maximizing ergodic, chaotic mixing," *Small*, Vol. 3, pp. 202–218, 2007.
9. M.A. Stremler and A.C. Baratunde, "Maximum entropy approach to optimal mixing in a pulsed source-sink flow," *Physics of Fluids*, Vol. 18, p. 011701, 2006.
10. A.A. Deshmukh, D. Liepmann and A.P. Pisano, "Continuous micromixer with pulsatile micropumps", Technical Digest of the IEEE Solid State Sensor and Actuator Workshop, Hilton Head Island, SC, 4–8 June, 2000, pp. 73–76.
11. T. Fujii, Y. Sando, K. Higashinob and Y. Fujii, "A plug and play microfluidic device," *Lab on a Chip*, Vol. 3, pp. 193–197, 2003.
12. I. Glasgow and N. Aubry, "Enhancement of microfluidic mixing using time pulsing," *Lab on a Chip*, Vol. 3, pp. 114–120, 2003.
13. X.Z. Niu and Y.K. Lee, "Efficient spatial-temporal chaotic mixing in microchannels," *Journal of Micromechanics and Microengineering*, Vol. 13, pp. 454–462, 2003.
14. F. Bottausci, I. Mezic, C.D. Meinhardt and C. Cardonne, "Mixing in the shear superposition micromixer: three dimensional analysis," *Phys. Trans. R. Soc. Lond. A*, Vol. 362, pp. 1001–1018, 2003.
15. P. Tabeling, M. Chabert, A. Dodge, C. Jullien and F. Okkels, "Chaotic mixing in cross-channel micromixers," *Phys. Trans. R. Soc. Lond. A*, Vol. 362, pp. 987–1000, 2003.
16. M.J. Kim and K.S. Breuer, "Controlled mixing in microfluidic system using bacterial chemotaxis," *Analytical Chemistry*, Vol. 79, pp. 955–959, 2007.
17. J. Evans, D. Liepmann and A.P. Pisano, Planar laminar mixer, Proc. MEMS97, 10th IEEE Int. Workshop Micro Electromechanical System (Nagoya, Japan), 1997, pp. 96–101.
18. B.A. Cola, D.K. Schaffer, T.S. Fisher and M.A. Stremler, "A pulsed source-sink fluid mixing device," *Journal of Microelectromechanical Systems*, Vol. 15, pp. 259–266, 2006.
19. F. Raynal, F. Plaza, A. Beuf and P. Carriere, "Study of chaotic mixing system for dna chip hybridization chambers," *Physics of Fluids*, Vol. 16, pp. L63–L66, 2004.
20. H. Suzuki and C.M. Ho, A magnetic force driven chaotic micro-mixer, Proceedings of MEMS'02, 15th IEEE International Workshop Micro Electromechanical System, Las Vegas, NV, 20–24 January, 2002, pp. 40–43.
21. L.H. Lu, K.S. Ryu and C. Liu, "A magnetic microstirrer and array for microfluidic mixing," *Journal of Microelectromechanical Systems*, Vol. 11, pp. 462–469, 2002.
22. A.K. Agarwal, S.S. Sridharamurthy, D.J. Beebe and H. Jiang, "Programmable autonomous micromixers and micropumps," *Journal of Microelectromechanical Systems*, Vol. 14, pp. 1409–1421, 2005.
23. R.B.M. Schasfoort, S. Schlautmann, J. Hendrikse and A. Van den Berg, "Field-effect flow control for microfabricated fluidic networks," *Science*, Vol. 286, pp. 942–945, 1999.
24. C.H. Chen, H. Lin, S.K. Lele and J.G. Santiago, "Convective and absolute electrokinetic instability with conductivity gradients," *Journal of Fluid Mechanics*, Vol. 524, pp. 263–303, 2005.
25. J.C. Baygents and F. Baldessari, "Electrohydrodynamic instability in thin fluid layer with an electrical conductivity gradient," *Physics of Fluids*, Vol. 10, pp. 301–311, 1998.
26. R.M. Thakkar and V. Kumaran, "Electrohydrodynamic instability of the interface between two fluids confined in a channel," *Physics of Fluids*, Vol. 17, p. 084104, 2005.
27. N. Wu and W.B. Russel, "Electrohydrodynamic instability of dielectric bilayers: kinetics and thermodynamics," *Ind. Eng. Chem. Res.*, Vol. 45, pp. 5455–5465, 2006.
28. A.O. ElMoctar, N. Aubry and J. Batton, "Electro-hydrodynamic micro-fluidic mixer," *Lab on a Chip*, Vol. 3, pp. 273–280, 2003.
29. O. Ozen, N. Aubry, D.T. Papageorgiou and P.G. Petropoulos, "Monodisperse drop formation in square microchannels," *Physical Review Letters*, Vol. 96, p. 144501, 2006.
30. J.D. Zahn and V. Reddy, "Two phase micromixing and analysis using electrohydrodynamic instabilities," *Microfluidics and Nanofluidics*, Vol. 2, pp. 399–415, 2006.

31. C. Tsouris, C.T. Culbertson, D.W. DePaoli, S.C. Jacobson, V.F. de Almeida and J.M. Ramsey, "Electrohydrodynamic mixing in microchannels," *AIChE Journal*, Vol. 49, pp. 2181–2186, 2003.
32. J. Deval, P. Tabeling and C.M. Ho, A dielectrophoretic chaotic mixer, Proceedings of MEMS'02, 15th IEEE International Workshop Micro Electromechanical System, Las Vegas, NV, 20–24 January, 2002, pp. 36–39.
33. Y.K. Lee, J. Deval, P. Tabeling and C.M. Ho, Chaotic mixing in electrokinetically and pressure driven micro flows, Proceedings of MEMS'01, 14th IEEE International Workshop Micro Electromechanical System, Interlaken, Switzerland, 21–25 January, 2001, pp. 483–486.
34. M.H. Oddy, J.G. Santiago and J.C. Mikkelsen, "Electrokinetic instability micromixing," *Analytical Chemistry*, Vol. 73, pp. 5822–5832, 2001.
35. J.D. Posner and J.G. Santiago, "Convective instability of electrokinetic flows in a cross-shaped microchannel," *Journal of Fluid Mechanics*, Vol. 555, pp. 1–42, 2006.
36. L.M. Fu, R.J. Yang, C.H. Lin and Y.S. Chien, "A novel microfluidic mixer utilizing electrokinetic driving forces under low switching frequency," *Electrophoresis*, Vol. 5, pp. 1814–1824, 2005.
37. N. Sasaki, T. Kitamori and H.B. Kim, "AC electroosmotic micromixer for chemical processing in a microchannel," *Lab on a chip*, Vol. 6, pp. 550–554, 2006.
38. Z. Tang, S. Hong, D. Djukic, V. Modi, A.C. West, J. Yardley and R.M. Osgood, "Electrokinetic flow control for composition modulation in a microchannel," *Journal of Micromechanics and Microengineering*, Vol. 12, pp. 870–877, 2002.
39. J.L. Lin, K.H. Lee and G.B. Lee, "Active mixing inside microchannels utilizing dynamic variation of gradient zeta potentials," *Electrophoresis*, Vol. 26, pp. 4605–4615, 2005.
40. J.L. Lin, K.H. Lee and G.B. Lee, "Active micro-mixers utilizing a gradient zeta potential induced by inclined buried shielding electrodes," *Journal of Micromechanics and Microengineering*, Vol. 16, pp. 757–768, 2006.
41. S.Z. Qian and H.H. Bau, "A chaotic electroosmotic stirrer," *Analytical Chemistry*, Vol. 74, pp. 3616–3625, 2002.
42. E. Biddiss, D. Erickson and D. Li, "Heterogeneous surface charge enhanced micromixing for electrokinetic flows," *Analytical Chemistry*, Vol. 76, pp. 3208–3213, 2004.
43. X. Yu and H.H. Bau, "Complex magnetohydrodynamic low-reynolds-number flow," *Physical Review E*, Vol. 68, p. 016312, 2003.
44. J.P. Gleeson, et al., "Modelling annular micromixers," *SIAM Journal of Applied Mathematics*, Vol. 64, pp. 1294–1310, 2004.
45. S. Qian and H.H. Bau, "Magneto-hydrodynamic stirrer for stationary and moving fluids," *Sensors and Actuators B*, Vol. 106, pp. 859–870, 2005.
46. J. West, J.P. Gleeson, J. Aldermann, J.K. Collins and H. Berney, "Structuring laminar flow using annular magnetohydrodynamic," *Sensors and Actuators B*, Vol. 96, pp. 190–199, 2003.
47. J. West, B. Karamata, B. Lillis, J.P. Gleeson, J. Alderman, J.K. Collins, W. Lane, A. Mathewson and H. Berney, "Application of magnetohydrodynamic actuation to continuous flow chemistry," *Lab Chip*, Vol. 2, pp. 224–230, 2002.
48. H.Y. Wu and C.H. Liu, "A novel electrokinetic micromixer," *Sensors and Actuators A*, Vol. 118, pp. 107–115, 2005.
49. T.D. Rossing and N.H. Fletcher, *Principles of Vibration and Sound*, Springer, New York, 1994.
50. L.S. Jang, S.H. Chao, M.R. Holl and D.R. Meldrum, "Resonant mode-hopping micromixing," *Sensors and Actuators A*, 2007. doi:10.1016/j.sna.2007.04.052.
51. R.M. Moroney, R.M. White and R.T. Howe, Ultrasonically induced microtransport, Proceedings of MEMS'91, 3th IEEE International Workshop Micro Electromechanical System, Nara, Japan, January 30–February 4, 1991, pp. 277–282.

52. J.C. Rife, M.I. Bell, J.S. Horwitz, M.N. Kabler, R.C.Y. Auyeung and W.J. Kim, "Miniature valveless ultrasonic pumps and mixers," *Sensors and Actuators A*, Vol. 86, pp. 135–140, 2000.
53. Y. Zhen, H. Goto, M. Matsumoto and R. Maeda, "Active micromixer for microfluidic systems using lead-zirconate-titanate (PZT)-generated ultrasonic vibration," *Electrophoresis*, Vol. 21, pp. 116–119, 2000.
54. Z. Yang, S. Matsumoto, H. Goto, M. Matsumoto and R. Maeda, "Ultrasonic micromixer for microfluidic systems," *Sensors and Actuators A*, Vol. 93, pp. 266–272, 2001.
55. R.H. Liu, J. Yang, M.Z. Pindera, M. Athavale and P. Grodzinski, "Bubble-induced acoustic micromixing," *Lab on a Chip*, Vol. 2, pp. 151–157, 2002.
56. J. Melin, G. Gimenez, N. Roxhed, W. Van DerWijngaart and G. Stemme, "A fast passive and planar liquid sample micromixer," *Lab on a Chip*, Vol. 3, pp. 214–219, 2004.
57. G.G. Yaralioglu, I.O. Wygant, T.C. Marentis and B.T. Khuri-Yakub, "Ultrasonic mixing in microfluidic channels using integrated transducers," *Analytical Chemistry*, Vol. 76, pp. 3694–3698.
58. A.A. Darhuber, et al., "Microfluidic actuation by modulation of surface stresses," *Applied Physics Letters*, Vol. 82, pp. 657–659.





## 7 Characterization Techniques

---

### 7.1 Imaging Techniques

#### 7.1.1 Two-Dimensional Optical Microscopy

Optical microscopy is the key tool for characterizing micromixers. Optical microscopy offers a noninvasive means of measurement at the micro scale. Together with digital cameras and digital image processing, a number of measurements in micromixers can be carried out with optical microscopy. Optical microscopy works with that part of the electromagnetic spectrum that is visible to the human eye. A typical human eye responds to wavelengths in air from 400 to 700 nm. The corresponding wavelengths in other media are reduced by a factor of the refractive index. A human eye has maximum sensitivity at about 555 nm, which is the green region. Table 7.1 shows the approximate ranges of the different spectral colors of visible light.

Because light is an electromagnetic wave, the relation between the propagation speed  $c$ , the wavelength  $\lambda$ , and the frequency  $\nu$  is:

$$c = \nu\lambda. \quad (7.1)$$

For the visible spectrum in Table 7.1 and the speed of light in space of  $c_0 = 3 \times 10^8$  m/s, the corresponding frequency of visible spectrum is 450–750 terahertz ( $10^{12}$  Hz). The propagation velocity of an electromagnetic wave is determined by the permeability  $\mu_{\text{em}}$  and the permittivity  $\varepsilon_{\text{em}}$  of the material:

$$c = \frac{1}{\sqrt{\mu_{\text{em}}\varepsilon_{\text{em}}}}. \quad (7.2)$$

The refractive index of a material is the ratio between the speed of light in space and that in the material:

$$n = \frac{c_0}{c}. \quad (7.3)$$

Because the speed of light in space is the fastest, the refractive index of materials should be more than unity. From (7.3) and (7.2) it is apparent that for the same material, the refractive index is inversely proportional to the wavelength. The refractive index determines the angle through which a planar wavefront incident on an interface between two materials will be refracted from its original direction. For instance, a light ray incident on an interface at an

Table 7.1 Spectral Colors of Visible Light

Color	Violet	Blue	Green	Yellow	Orange	Red
Wave length (nm)	380–450	450–495	495–570	570–590	590–620	620–750

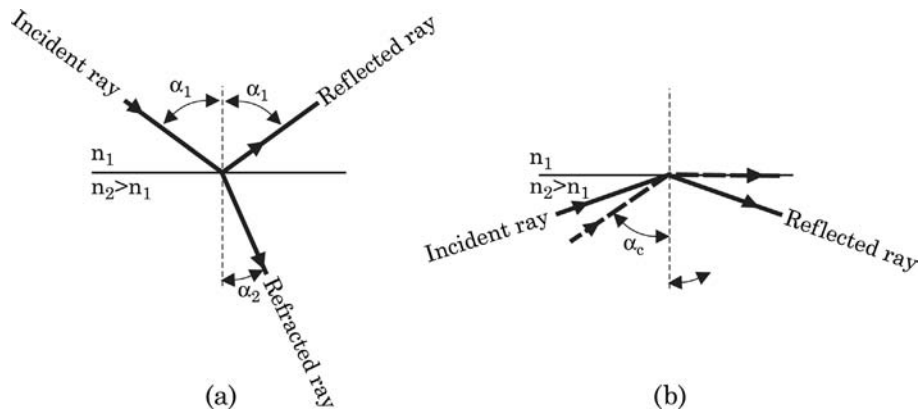


Figure 7.1 Optical effect at an interface: (a) refraction and reflection; (b) total internal reflection.

angle  $\alpha_1$  will split into a reflected ray and a transmitted ray, whose direction to the normal at the interface is  $\alpha_2$  [Fig. 7.1 (a)]:

$$n_1 \sin \alpha_1 = n_2 \sin \alpha_2. \tag{7.4}$$

The above effect of refraction is fundamental for making lenses, which are the basic components of an optical microscopy system. If light passes from a medium of higher refractive index  $n_2$  to a medium of lower refractive index  $n_1$ , the angle of refraction is larger than the angle of incidence. At a critical angle of incidence  $\alpha_c$  the angle of refraction becomes  $90^\circ$ , the light is totally internally reflected, Fig. 7.1 (b). The effect of internal reflection can be used for making mirrors and optical fibers for guiding lights. The critical angle can be derived from (7.4) as:

$$\alpha_c = \arcsin(n_1/n_2). \tag{7.5}$$

Fig. 7.2 shows a simple microscope setup with a charge coupled device (CCD) as the image sensor. Lens 1 is focused on the sample. This lens is also called the objective lens. The magnified image is projected onto the CCD sensor, which is then transferred digitally to a computer for further processing. The amount of

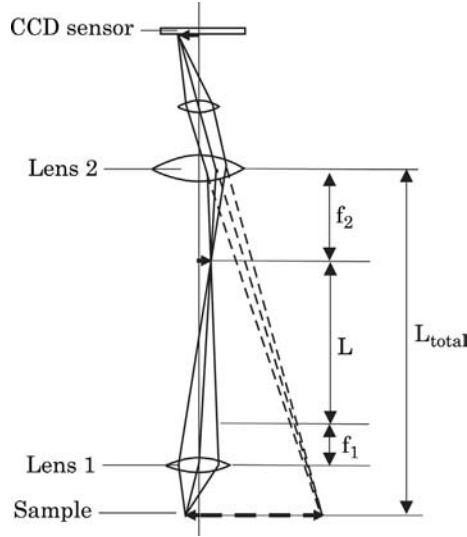


**Figure 7.2** Schematic concept of a simple microscope with a CCD sensor.

light collected by the objective lens determines the brightness of the image. The brightness of the recorded image is proportional to the square of the numerical aperture:

$$I \propto \text{NA}^2 \quad (7.6)$$

where NA is the numerical aperture of the objective lens. The numerical aperture is determined as:

$$\text{NA} = n \sin \alpha \quad (7.7)$$

where  $n$  is the refractive index of the medium in which the lens is working, and  $\alpha$  is the half-angle of the maximum cone of light that can enter or leave the lens.

The magnification of the microscope system depicted in Fig. 7.2 is the product of the magnifications of the objective lens 1 and the eyepiece lens 2:

$$M = -\frac{L L_{\text{total}}}{f_1 f_2} \quad (7.8)$$

where  $L$  is the distance between the second focal point of the objective lens (lens 1) and the first focal point of lens 2 (also called the tube length),  $L_{\text{total}}$  is the near-point distance (also called the viewing distance), and  $f_1$  and  $f_2$  are the focal lengths of the lenses 1 and 2, respectively. The brightness of the recorded

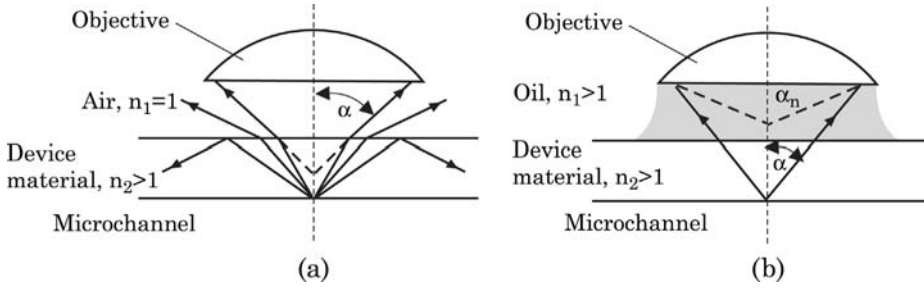


**Figure 7.3** Typical situation of a micromixer with a transparent substrate material: (a) in air; (b) immersed in oil.

image is inversely proportional to the square of the magnification:

$$I \propto \frac{1}{M^2}. \quad (7.9)$$

According to (7.7), the numerical aperture of the objective lens depends on the refractive index of the coupling medium between the lens and the device and cannot be more than unity. In order to increase the numerical aperture, oil immersion objective lenses are often used. Fig. 7.3 shows that the refractive index of the oil and the substratum material of the device increases the semi-angle of the cone of rays from the point source, leading to a higher effective NA. While the maximum achievable numerical aperture in air is about 0.85, immersion objective lenses may reach a maximum numerical aperture of 1.4. Oil immersion objective lenses are designed to work with a given oil as a working medium.

$$\alpha_c = \arcsin(n_1/n_2). \quad (7.10)$$

The effective field of view of a measurement based on a microscope/camera system depends on both the objective lens and the surface area of the sensor. For a given magnification  $M$  and sensor surface area  $A_s$ , the effective area of view is:

$$A_v = A_s/M^2. \quad (7.11)$$

Another important parameter of the microscope/camera system is the relation between the in-plane spatial resolution  $d$ , magnification  $M$ , and the pixel size of the sensor  $d_{\text{pixel}}$ . The in-plane spatial resolution is limited by the diffraction effect [1]:

$$d = 1.22M\lambda\sqrt{\left(\frac{n}{\text{NA}}\right)^2 - 1} \quad (7.12)$$

where  $n$  is the refraction index of the recording medium, and NA and  $M$  are the numerical aperture and the magnification of the microscope system, respectively. The required pixel size  $d_{\text{pixel}}$  can be estimated from the in-plane spatial resolution and the size of the sample (such as a particle)  $d_p$  as:

$$d_{\text{pixel}} = \sqrt{d^2 + M^2 d_p^2}. \quad (7.13)$$

If  $d \gg Md_p$  the required pixel size is determined by diffraction. If  $d \ll Md_p$  the required pixel size is determined by the geometric sample size,  $d_{\text{pixel}} \approx Md_p$ .

Fig. 7.2 depicts a simplified and ideal microscope system with ideal lenses. Real lenses have problems with longitudinal chromatic aberration. That means that different colors are focused at different positions along the optical axis, because the refractive index is a function of wavelength. Modern microscopes have complex achromatic lens systems, which comprise a convex crown glass lens next to a flint concave lens.

Because measurement of intensity distribution is important for quantitative characterization of micromixers, the quality of the illuminating system is important for the microscope setup. The illuminating system of a research grade microscope should fulfill three basic criteria, of:

- Allowing maximum resolution and maximum contrast,
- Being simple and easy to adjustment, and
- Having uniform illumination.

The most common illumination source of modern microscopes is a laser. The laser light produces an output beam that is both coherent and collimated, which is ideal for illumination purposes.

### 7.1.2 Two-Dimensional Fluorescence Microscopy

One solution for problems associated with chromatic aberration is using monochromatic illumination and detection. Fluorescent microscopy is based on fluorescence, which is an optical phenomenon in cold bodies. A molecule absorbs a photon, then emits another photon with a longer wavelength. The energy difference between the absorbed and emitted photons is dissipated as heat. The absorbed photon is commonly in the high-energy ultraviolet range, and the emitted light is in the visible range. However, many fluorescent dyes or fluorophores have both excitation and emission wavelengths in the visible range. The difference between the emission wavelength and the excitation wavelength is called the Stokes shift.

In a fluorescence microscope, excitation and emission wavelengths have to be separated from other wavelengths using optical filters. Fig. 7.4 (a) shows the basic concept of a fluorescence microscope system. Light from a source is directed

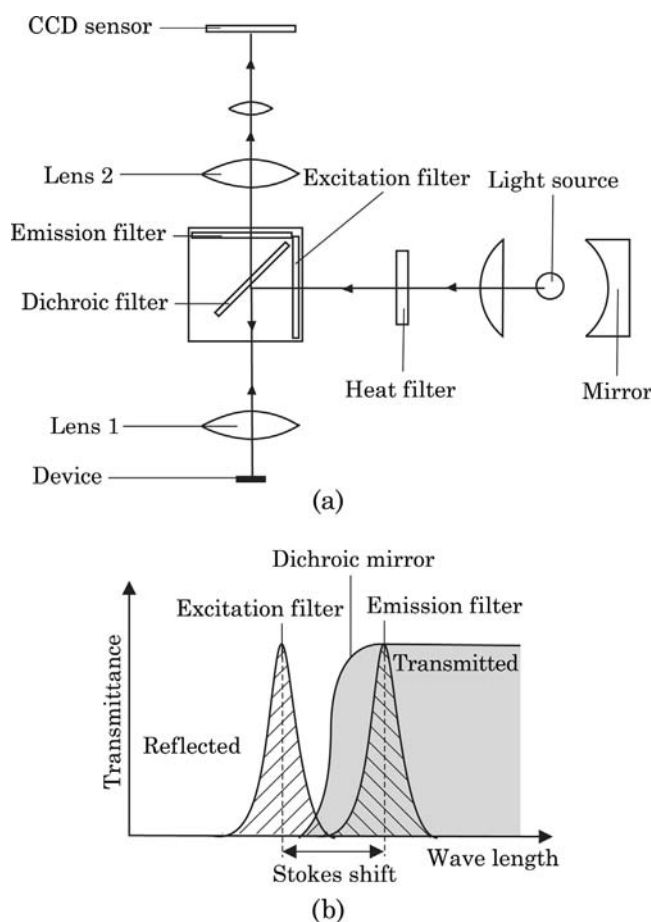


**Figure 7.4** Fluorescence microscope: (a) schematic concept; (b) transmission characteristics.

to a filter cube through a condenser lens system. Typical light sources for a fluorescence microscope system are high-pressure mercury lamps, xenon lamps, halogen lamps, or lasers. A heat filter keeps infrared wavelengths out of the optical system to avoid unnecessary heating. There are two filters in the cube. The excitation filter allows wavelengths smaller than the emitted fluorescence wavelengths, while the emission filter allows through only the longer fluorescence wavelengths. Neutral density filters are the most common types of filters used in a fluorescence microscope. Neutral density filters are usually fabricated by evaporation of a thin metal layer onto the glass surface. A fluorescence microscope can be equipped with different optical filter sets. Common fluorescent dyes have fixed wavelength pairs, and need a corresponding filter set. The filter sets are selected by a multi-position filter wheel. Because the sample only works with two wavelengths, a fluorescence microscope needs to

ensure that only shorter excitation wavelength is directed onto the sample and only longer emitted wavelength is used to form the image on the sensor.

A dichroic mirror can fulfill these two requirements. The mirror works as a high pass filter, which reflects the shorter excitation wavelength and directs it to the sample, while letting the longer emitted wavelength go through, Fig. 7.4 (b). The intensity of the emitted signal is extremely weak compared to the excitation intensity. Thus, the excitation light and the emitted light must be completely separated by using narrow-band filters or fluorescent dyes with a large Stokes shift.

### 7.1.3 Confocal Laser Scanning Microscopy

Confocal laser scanning microscopes allow the three-dimensional reconstruction of semitransparent microstructures using two-dimensional sections of the object. The two-dimensional image is formed by scanning a focused point across the imaged section. This imaging concept requires that both the condenser lens of the illumination and the objective lens have the same point of focus or are confocal. Strictly speaking, standard optical microscopes also use high NA lenses to both illuminate and image the sample and are therefore also confocal. However, the terminology of the confocal microscope as a synonym for the confocal laser scanning microscope is well established in the literature. A confocal microscope allows imaging a particular plane without information about the out-of-focus planes. To avoid the accurate alignment needed for the condenser and objective lenses, a single lens can be used for both illumination and imaging. Modern confocal microscopes use a laser beam to generate a focused spot on the imaged section. The laser beam is scanned through the objective in a raster pattern. The reflected light is collected on the image sensor through the same optical system and a pinhole. The speed of the confocal microscope depends on the scanning speed of the light spot.

Fig. 7.5 shows the schematic concept of an epifluorescence confocal laser scanning microscope with two pinholes for illumination and imaging. The illumination system consists of a laser source, a pinhole, and a beam expander. Because the laser source provides a single wavelength, the excitation filter may not be needed. The laser should have a stable intensity during the scanning period, because a change in source intensity will lead to error in the measured image. In a confocal microscope, the objective lens is used for both illumination and receiving the reflected light. Thus, the effect of aberration is very crucial for the objective lens. The light passes the objective lens and is focused at the sampling point. The stage holding the device is scanned in an raster pattern to form the two-dimensional image point by point. The scanning stage should have high speed, positioning accuracy, and stability. The scanning level in the  $z$  direction is usually controlled by a piezoelectric transducer.

The pinholes determine both the axial and transverse resolution of the confocal measurement. A large pinhole allows more light to pass through,



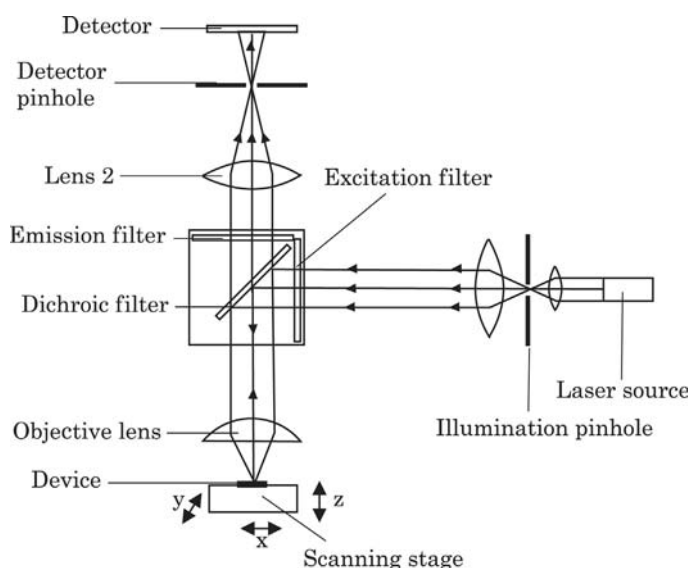


**Figure 7.5** Schematic concept of a confocal laser scanning microscope with two pinholes and a scanning stage.

leading to a stronger signal but lower resolution. A small pinhole results in a higher resolution but weaker signals with lower signal-to-noise ratio.

Light from the sampling point passes through the detector pinhole and impinges on the detector. The optical detector can be a photodiode or a photomultiplier tube. A relay lens between the pinhole and the detector can be used for imaging the pinhole on the detector surface. Furthermore, a narrow-band filter can be used to reduce the noise level caused by stray light. The detected signal is recorded together with the  $x$ ,  $y$  position of the sampling point to form the two-dimensional image.

Stage scanning has the advantage of simplicity. The beam is stationary and the objective is used on-axis. Thus, aberration correction is easy. However, the scanning speed is limited by the relatively large weight of the scanning stage. Most commercial confocal microscopy systems use beam scanning techniques because of their speed advantage. Scanning in  $x$ - and  $y$ -directions is realized by combining beam steering devices, such as galvanometer mirrors and acousto-optic deflectors. Using an  $x$ -slit instead of the pinhole, a CCD line array can be used for recording the image line by line. If the  $x$ -line image is descanned by a  $y$ -scanning mirror, an apparent two-dimensional image can be generated and observed by eye or recorded by a two-dimensional CCD sensor.

Direct-view confocal microscopy can also be realized by the rotating Nipkow disk, which was originally used for mechanically scanned television. Fig. 7.6 shows the schematic concept of a real-time scanning optical microscope. The pinholes in the disk are used for both illumination and imaging. The disk is tilted slightly by about  $5^\circ$ . The tilted disk reflects light away from the eyepiece.

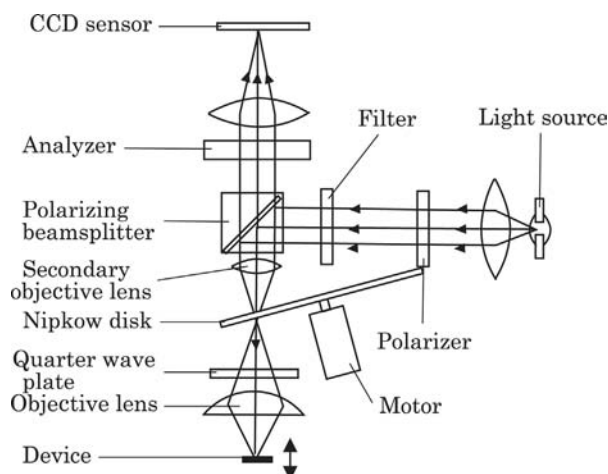


**Figure 7.6** Schematic concept of a real-time, direct view scanning optical microscope.

An optical insulator also deflects a part of light reflected from the top of the disk back to the light source.

The disk has several thousand pinholes arranged in interleaved spirals. Several hundred pinholes are illuminated at the same time, in order to increase the light efficiency and scanning speed. With this disk design, a rate of several hundred frames per second and several thousand lines per frame can be achieved. The pinholes on the disk are fabricated using photolithography techniques as discussed in Chapter 3. The typical pinhole size is about 20  $\mu\text{m}$ .

## 7.1.4 Acquisition and Processing of Digital Images

### 7.1.4.1 Image Sensors

Characterization of micromixers requires accurate measurement of the intensity field, which is equivalent to the concentration field of a fluorescent dye. Besides the requirements for the light source and the optical system discussed in the previous sections, the optical detector should also offer good properties, such as linearity, dynamic range, and sensitivity. Fluorescence imaging is often the main task in many experiments related to micromixers. Because fluorescence signals coming from fluorescence microscope and confocal microscope are low, high sensitivity and low noise level are the key parameters for selecting an optical detector for characterization experiments of micromixers.

Currently, two types of high-resolution solid state imaging devices are commercially available: charge-coupled devices (CCDs) and complementary metal oxide semiconductor (CMOS) image sensors. Both imaging sensors were developed between the early and late 1970s, but CMOS sensors have only

gained attention since the early 1990s due to advances in CMOS technology. Both CCD and CMOS sensors detect light based on the photoelectric effect, where photons interact with silicon to move electrons from the valence band into the conduction band. These electrons are called photoelectrons. The number of photoelectrons generated is a function of the wavelength and the light intensity. Photoelectrons are collected in a potential well until the exposure period is completed. These charges are then either converted into a voltage (in a CMOS sensor) or transferred to a register (in a CCD sensor). The sensor's pixel is a photodiode. The pixels are typically organized in an orthogonal matrix ranging from  $128 \times 128$  pixels to a more common  $1280 \times 1024$  pixels. Both CCD and CMOS sensors are black and white devices, responding only to the light intensity and not the color of the light. Color is detected by using a sequential series of red, green, and blue filters, or polymeric thin-film filters deposited in a mosaic pattern over the pixel array.

The quantum efficiency  $\eta$  is defined as the ratio between the number of generated photoelectrons  $N_{pe}$  and the number of arriving photons  $N_p$ :

$$\eta = \frac{N_{pe}}{N_p}. \quad (7.14)$$

An ideal detector should have 100% quantum efficiency and zero sensor noise. A CCD sensor has a typical quantum efficiency in the range of 30% to 50%. Special CCD sensors with thinned back-illuminated CCD arrays may have a quantum efficiency up to 80%.

In a CCD image sensor, each pixel element of a CCD sensor is defined by a set of electrodes, which are made of doped polysilicon on top of the photosensitive silicon. The electrodes and the photosensitive silicon are separated by a thin layer of silicon dioxide. The electrodes define a potential well (the pixel) on the silicon substrate. Photoelectrons generated by incident light are stored inside these potential wells. The charges in each pixel are transferred serially from pixel to pixel until the whole column is transferred into a register. The transferred charges are converted and amplified into voltages. An analog-to-digital converter and a line driver transfers the image signal to a the frame grabber, which stores the image data. Figure 7.7 depicts the schematic concept of a CCD image sensor and its external circuit.

The dark current is caused by thermally-generated electrons. This current leads to noises in the detected signal. Thus, noise will be minimized if the temperature of the sensing material is reduced. Noise level can be significantly decreased using cooling methods such as liquid nitrogen or thermoelectric cooling.

The spacial resolution of a CCD sensor is determined by the sensor width, height, and its pixel size. All CCD chips have defects, which are regions either with reduced sensitivity or with increased dark current. CCD sensors are graded according to the number of defects.

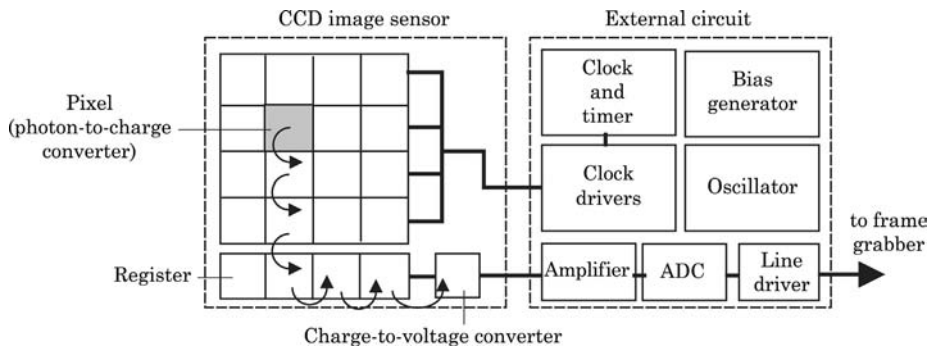


**Figure 7.7** Schematic concept of a CCD image sensor and the external circuit.

In a CMOS image sensor, each pixel has its own charge-to-voltage conversion. Voltage amplifiers, noise correction, and analog-to-digital converters are integrated in a single chip. The integration of all these components makes the chip design complex and reduces the available surface area for detection. With each pixel doing its own conversion, the image's uniformity is lower. But the chip can be built to require less off-chip circuitry for basic operation, Fig. 7.8. Because CMOS technologies are available at low cost, CMOS image sensors can be fabricated at a lower cost than a CCD image sensor. Compared to a CCD sensor, a CMOS sensor has a lower sensitivity because part of each pixel is covered with circuitry that filters out noise and performs other functions. The ratio between the sensing surface area and the total pixel area is called the fill factor. The fill factor of a CMOS image sensor ranges from 30% to 80%. Because the rest of the pixel area is shielded by transistors and metallic bus lines, which are optically opaque, these structures absorb or reflect a majority of the incident photons. These metal layers can also lead to undesirable effects, such as vignetting, pixel crosstalk, light scattering, and diffraction, causing a higher overall noise level. A CMOS image sensor uses digital signal processing (DSP) to reduce or eliminate the noise, thus the dynamics of a CMOS sensor are also inferior to those of a CCD sensor.

#### 7.1.4.2 Digital Images

An image captured with an optical instrument is a continuously varying array of shades and color tones. Images captured on films for instance are referred to as continuous-tone because the shades and hues blend together without disruption. Continuous-tone images are captured with analog optical and electronic devices. Optical signals are converted to analog electrical signals or to continuous change of the chemical properties. In the world of digital systems, these continuous-tone images need to be converted to digital format. In this case, the continuous tones of an analog image are divided into individual intensity values. Similar to the

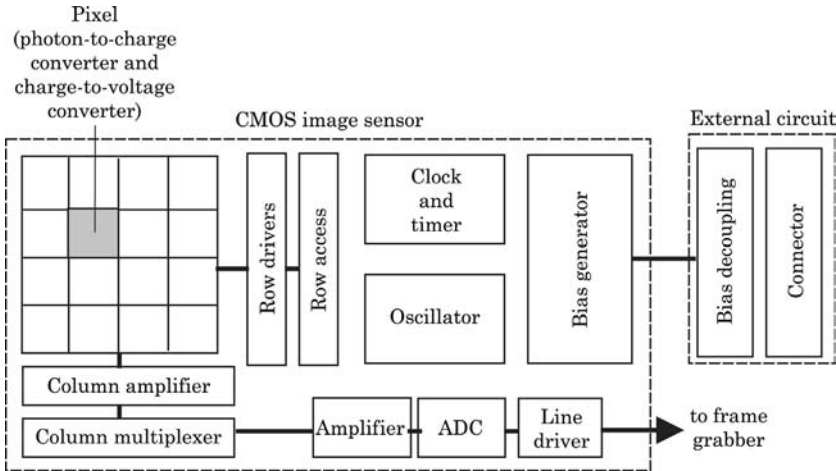


**Figure 7.8** Schematic concept of a CMOS image sensor and the external circuit.

analog-to-digital converting process in electronics, the conversion to a digital image requires two steps: sampling and quantization. With the pixel array, sampling and quantization occur in a CCD or CMOS image sensor automatically. Each pixel contains specific information about intensity and can be described by a specific digital data value in a precise location.

Each image pixel is represented by the intensity value and a coordinate-pair with specific  $x$  and  $y$  values arranged in a Cartesian coordinate system. In many cases, the  $x$  location is referred to as the pixel number, and the  $y$  location is known as the line number. A digital image is therefore a two-dimensional array of intensity values. For an image with a size of  $M$  pixels by  $N$  pixels, the pixel positioned at coordinates  $(1,1)$  is located in the upper left-hand corner of the array, while a pixel located at  $(M,N)$  would be positioned at the lower right-hand corner of the array. Fig. 7.9 shows a schematic representation of the intensity array  $I(x,y)$  of a  $M \times N$  digital image.

The *aspect ratio* of a digital image is the ratio between the width and the height of the image  $M/N$ . For instance, the recommended NTSC (National Television Systems Committee) commercial broadcast standard aspect ratio for television and video equipment is  $M/N = 4/3$ . The standard aspect ratio for digital high-definition television (HDTV) is  $M/N = 16/9$ , sometimes referred to as widescreen format.

The *image resolution* determines the quality of a digital image. The image resolutions are referred to as spacial resolution and gray scale resolution. The spacial resolution is determined by the number of pixels  $M \times N$ . Within a given physical dimension, a digital image with a higher number of pixels will have a higher spacial resolution. The gray scale resolution is directly proportional to the bit depth of the digitizing device. A bit depth of  $n$  can generate  $2^n$  different gray scales. Most common CCD and CMOS sensors provide bit depths of 8, 10,

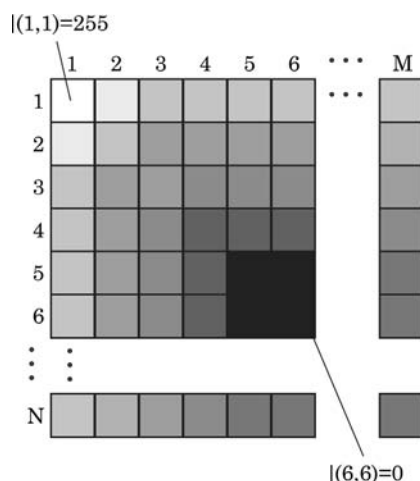


**Figure 7.9** Schematic representation of the intensity array of a  $M \times N$  digital image.

or 12. An 8-bit, 10-bit, and 12-bit depth can describe 256, 1024, and 4096 different gray levels, respectively. If the image shown in Fig. 7.9 has a bit depth of 8, the value of the white pixel (1,1) is 255, while the value of the black pixel (6,6) is 0. The human eye can better discriminate between different shades of color than between varying shades of gray. Therefore, gray scale images are often rendered in pseudocolor by assigning specific gray level ranges to particular color values. This technique is useful for highlighting regions of interest, especially concentration fields in micromixers. Pseudocolor imaging is widely employed in fluorescence microscopy to display merged monochrome images obtained at different wavelengths utilizing multiple stained specimens. Often, the color assigned to individual fluorophore images in a collage assembly is close in color to that naturally emitted by the fluorescent dye.

The intensity of the pixels in a digital image can be graphically depicted in a gray scale histogram, which maps the number of pixels at each gray level present in the image. The histogram can be used directly for evaluating the extent of mixing. The gray scale histogram of a well mixed concentration field shows a single peak, while the histogram of a not mixed concentration field shows two intensity peaks corresponding to the two liquids.

A digital image can be stored in a single file. Intensity values are stored in a single vector. The coordinate of the pixel does not need to be stored because it can be derived from the known image's spacial resolution and incremental counting of the pixels. The horizontal and vertical dimension of an image is often stored in the header of the image file. Reading the files with known dimension can restore the two-dimensional matrix for further processing. The size of a digital image file depends on the pixel dimension, format (compression algorithms), and bit depth of the image. Uncompressed file formats, such as tagged image file format (TIFF) and Windows image bitmaps (BMP) results in

the largest file sizes. Using compression algorithms, such as the popular Joint Photographic Experts Group (JPEG) technique, can reduce the file size significantly, while the image quality is reasonably maintained.

Digital images of optical sections obtained through confocal laser scanning microscopy can be rendered to make a three-dimensional image. Two popular rendering techniques of an image set for display in three-dimensions are volume rendering and surface rendering. In volume rendering, the two-dimensional pixel geometry and intensity information is combined with the known focal displacements to generate volume elements, termed voxels. The resulting voxels are then appropriately shaded and projected to produce a view of the specimen volume with associated perspective and lighting to produce a three-dimensional representation. In surface rendering, only the surface pixels are utilized, representing the outside surface of the specimen, and the interior structure is not visible because of the surface opacity. Lighting, perspective, and depth cues subsequently help to generate a three-dimensional representation of the image set.

## 7.2 Measurement Using Optical Microscopy

### 7.2.1 Measurement of Velocity Field

The most common technique for measuring the velocity field inside a micromixer is micro particle image velocimetry (micro-PIV). PIV was originally developed for the measurement of two-dimensional velocity fields at the macro scale. The flow is first traced with particles. The measurement is carried out by recording two digital images of particles at two different time instances. The digital images are then divided into smaller interrogation windows, where particle displacements are evaluated. The displacement is evaluated using a two-dimensional cross correlation of the two corresponding interrogation windows. Because the cross correlation can only resolve one pixel, different curve fitting algorithms can be used. The same technique can be applied to micro scale velocity fields using a fluorescent microscope system coupled with laser illumination.

If the intensity matrices of the two corresponding interrogation windows are  $I_1(i, j)$  and  $I_2(i, j)$ , the cross correlation function  $R(m, n)$  is determined as:

$$R(m, n) = \sum_{j=1}^{N^*} \sum_{i=1}^{M^*} I_1(i, j) I_2(i + m, j + n) \quad (7.15)$$

where  $M^* \times N^*$  is the size of the interrogation window measured in pixels. The position of a pixel in the matrix is denoted with the coordinates  $m$  and  $n$ . The displacement vector of the particles in the interrogation window is the vector

between the origin of the coordinate system and the peak of the cross correlation function  $R(m, n)$ . The quotient between the displacement vector and the known time delay between the acquisitions of the two images is the velocity vector of the interrogation window. Repeating this algorithm across the entire particle image results in the whole velocity field of the flow.

Utilizing fast Fourier transform FFT and inverse fast Fourier transform  $\text{FFT}^{-1}$ , equation (7.15) can be formulated as follows:

$$R(m, n) = \text{FFT}^{-1}\{\text{FFT}[I_1(i, j)] \times \overline{\text{FFT}[I_2(i, j)]}\} \quad (7.16)$$

where  $\overline{\text{FFT}[I_2(i, j)]}$  is the conjugate of the complex array  $\text{FFT}[I_2(i, j)]$ .

With the matrix  $R(m, n)$ , the correlation peak can be identified and refined with subpixel accuracy. The peak and its two neighboring points in the matrix  $R(m, n)$  are needed for the different subpixel algorithms. The peak is detected by determining the maximum value  $R(x, y)$  in the correlation matrix  $R(m, n)$ . Subsequently, the position  $(x, y)$  of the peak is stored. The four neighboring points  $R(x-1, y)$ ,  $R(x+1, y)$ ,  $R(x, y-1)$ , and  $R(x, y+1)$ , as well as their positions, are also stored. Three points in each direction are needed for the estimation of the peak position  $(x_0, y_0)$ . The algorithms for estimating the position  $(x_0, y_0)$  are called three-point estimators. The three basic estimators are the middle-point estimator, the parabolic estimator, and the Gaussian estimator.

The *middle-point estimator* assumes the following fitting function:

$$f(x) = \frac{\text{First order momentum}}{\text{Second order momentum}}. \quad (7.17)$$

The corresponding refined position of the peak is

$$\begin{aligned} x_0 &= x + \frac{(x-1)R(x-1, y) + xR(x, y) + (x+1)R(x+1, y)}{R(x-1, y) + R(x, y) + R(x+1, y)}, \\ y_0 &= y + \frac{(y-1)R(x, y-1) + yR(x, y) + (y+1)R(x, y+1)}{R(x, y-1) + R(x, y) + R(x, y+1)}. \end{aligned} \quad (7.18)$$

The *parabolic estimator* assumes a parabolic fitting function for the correlation peak:

$$f(x) = Ax^2 + Bx + C. \quad (7.19)$$



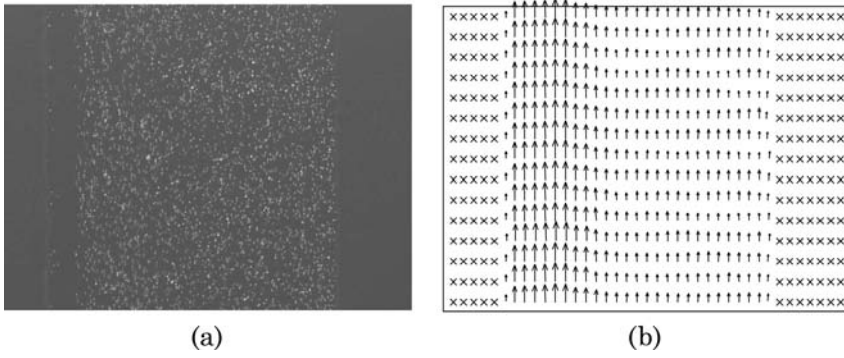


**Figure 7.10** Typical results of a micro-PIV measurement: (a) particle image (single frame, double exposure); (b) evaluated velocity field.

In this case, the refined position of the peak is:

$$x_0 = x + \frac{R(x-1, y) - R(x+1, y)}{2R(x-1, y) - 4R(x, y) + 2R(x+1, y)}, \quad (7.20)$$

$$y_0 = y + \frac{R(x, y-1) - R(x, y+1)}{2R(x, y-1) - 4R(x, y) + 2R(x, y+1)}.$$

The *Gaussian estimator* assumes a Gaussian distribution of the correlation peak:

$$f(x) = C \exp \left[ \frac{-(x_0 - x)^2}{k} \right]. \quad (7.21)$$

The position of the peak can be estimated as:

$$x_0 = x + \frac{\ln R(x-1, y) - \ln R(x+1, y)}{2\ln R(x-1, y) - 4\ln R(x, y) + 2\ln R(x+1, y)}, \quad (7.22)$$

$$y_0 = y + \frac{\ln R(x, y-1) - \ln R(x, y+1)}{2\ln R(x, y-1) - 4\ln R(x, y) + 2\ln R(x, y+1)}.$$

Fig. 7.10 shows a typical particle image and the corresponding evaluated velocity field (micro-PIV).

The results of micro-PIV can be improved by several techniques, such as removing the background, improving the particle density, and reducing the noise in the correlation matrix.

The background of a digital image for micro-PIV measurement can be determined by averaging a number of  $N$  particle images. Because the particles of the flow field are stochastically distributed and therefore removed through

the integration, the background image remains:

$$\bar{I}(i, j) = \frac{1}{L} \sum_{k=1}^N I_k(i, j). \quad (7.23)$$

The background can be removed by subtracting  $\bar{I}(i, j)$  from the measured particle image:

$$I(i, j) = I(i, j) - \bar{I}(i, j). \quad (7.24)$$

In many cases the tracing particles are not dense enough for an accurate evaluation of the velocity field. A method for increasing the number of particles in the image is overlapping several recorded images:

$$I_0(i, j) = \max[I_k(i, j)]_{k=1}^N. \quad (7.25)$$

Noise may lead to a wrong correlation peak in the matrix  $R(m, n)$ . Thus integration over several correlation matrices can form a sharp correlation peak for subsequent subpixel refinement:

$$\bar{R}(m, n) = \frac{1}{N} \sum_{k=1}^N R_k(m, n). \quad (7.26)$$

## 7.2.2 Measurement of Concentration Field

The intensity of a fluorescent dye solution is proportional to the concentration of the dye molecules. Thus, the concentration field can be measured indirectly as the intensity field of a fluorescent dye. This measurement is easily achieved with a CCD camera attached to a fluorescence microscope. The following example demonstrates the use of image processing functions for evaluating the digital image of a concentration field of a fluorescent dye. The functions are available in the Image Processing Toolbox of MATLAB (MathWorks, Inc.).

**Example 7.1** (*Measurement of concentration field based on a digital image*). Fig. 7.11 shows a digital image of a fluorescent dye stored in the Windows bitmap format. The evaluation of this image with MATLAB is described in the following steps. For more details on digital image processing with MATLAB, readers may refer to the book by Gonzalez et al. [2].

The following command reads a bitmap image stored in the file `FieldExample.bmp` and converts it to a two-dimensional array of intensity values  $I$ :

```
I = imread('FieldExample', 'bmp');
```

The information about the image file can be obtained using:

```
imfinfo FieldExample.bmp
```

The image can be displayed in the default 256 gray levels with the following command:

```
imshow(I);
```

As shown in Fig. 7.11 (a), there is a high level of noise, especially in the areas with high intensity. To reduce the level of noise, spacial filtering can be applied to each point of the intensity array. Spacial filtering is implemented in the following steps:

- Defining the processed point,
- Applying the filtering algorithm to a window around the above point (the result is the intensity value of the processed point), and
- Repeating the process for all points of the intensity array.

Depending on the type of the filtering algorithm, linear and nonlinear spacial filtering is available. MATLAB provides `imfilter` and `fspecial` for filtering and selecting the algorithm, respectively [2]. One of the effective noise canceling filtering algorithms is Wiener filtering. Applying Wiener filtering to the original intensity array  $I$  and a processing window of  $5 \times 5$  pixels:

```
I=wiener2(I,[5 5])
```

results in the image shown in Fig. 7.11 (b). Noise is significantly reduced. The concentration profile across the channel can be normalized and evaluated as follows:

```
image_handle=figure;
%Select a line for evaluation
[x,y]=getline(image_handle);
x=round(x);
y=round(y);
%Getting intensity values in vector c
c=improfile(I,x,y); c=c';
%Getting the total number of pixel in the line
L=length(c);
%Normalizing the spacial variable
%and the concentration
for i=1:L
    ystar(i)=(i-1)/L;
    c(i)=(c(i)-cmin)/(cmax-cmin);
end figure
%Plotting the dimensionless concentration distribution
plot(ystar,c,'-');
```

In the above MATLAB code, `cmax` and `cmin` are intensity values of unmixed fluids. The line of interest is selected from the displayed image using the computer mouse. The resulting concentration profiles are similar to those in the lower part of Fig. 7.11.

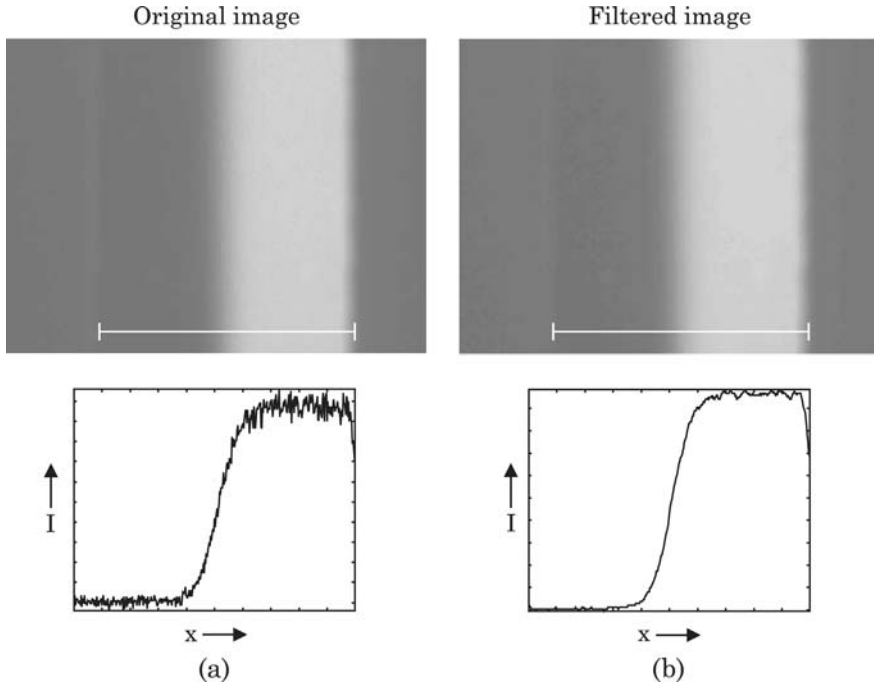


**Figure 7.11** Intensity images: (a) original; (b) filtered.

## 7.3 Quantification Methods for Micromixers

### 7.3.1 Direct Statistical Methods

There are several quantification methods for micromixers. Because good mixing is understood as the homogeneity of the mixed results, the distribution of the intensity values or the histogram  $H(I)$  of an image can be used for evaluating the degree of mixing. As mentioned in the previous section, intensity values are proportional to the concentration of the fluorescent dye molecules. The gray scale histogram actually represents the probability distribution function (PDF) of the concentration. The normalized concentration is assumed to be the same as the normalized intensity values of the recorded image:

$$c^* = I^* = \frac{I - I_{\min}}{I_{\max} - I_{\min}}. \quad (7.27)$$

The probability values can be obtained by normalizing the pixel number of each intensity value by the total number of the pixels in the evaluated region:

$$P(c^*) = P(I^*) = P(I) = \frac{N(I)}{\sum_{I_{\min}}^{I_{\max}} N(I)}. \quad (7.28)$$

The following example shows the implementation of PDF in MATLAB for evaluating the concentration field:

**Example 7.2** (*Measurement of Probability Distribution Function of the Concentration Field*). Using the intensity array  $I$  as shown in Example 7.1, the PDF of a region of interest is obtained by the following MATLAB code:

```
%Defining the region of interest
rect=getrect(image_handle);
%Reducing the image to the region of interest
ROI= imcrop(I,rect);
%Open a new window
figure
%Display the region of interest
imshow(ROI,[cmin cmax]);
%Obtaining the normalized concentration field
ROI_norm=(double(ROI)-double(cmin))/(double(cmax)-double(cmin));
%Determine the number of discrete values
N=double(cmax)-double(cmin);
for i=1:N+1
    edges(i)=(i-1)/N;
end
%Determining the distribution function
imagesize=size(ROI_norm);
Cnorm=reshape(ROI_norm,imagesize(1)*imagesize(2),1);
distribution=HISTC(Cnorm,edges)/imagesize(1)/imagesize(2);
%Plotting the probability distribution function
plot(edges,distribution);
```

In the above example, the region of interest is selected by a mouse click as a rectangle in the displayed image. Subsequently, probabilities for the different concentration values are calculated and plotted. Fig. 7.12 shows the typical results of the PDFs of a micromixer. In a region such as the entrance region, where the two fluids are not mixed, there exist two predominant concentration values of 0 and 1 resulting in two separate peaks as shown in Fig. 7.12 (a). In a region of well-mixed fluids, the predominant concentration is 0.5 resulting in a single peak as shown in Fig. 7.12 (b).

The homogeneity can be expressed as the standard deviation of the concentrations or the intensity values:

$$\sigma_{st} = \sqrt{\frac{1}{N} \sum_{i=1}^N (c_i^* - \bar{c}^*)^2} \quad (7.29)$$

where  $c^*$  is the normalized concentration, which is calculated according to (7.27). If the expected normalized concentration is  $\bar{c}^* = 0.5$ , the standard derivations are 0.5 and 0 for the unmixed case and mixed case, respectively.

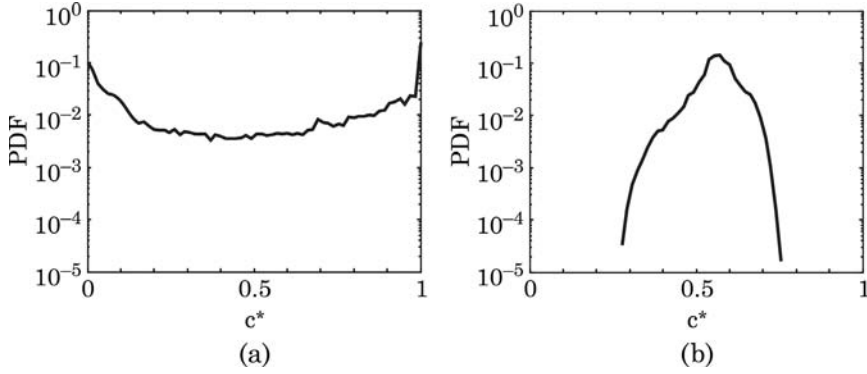


**Figure 7.12** Probability intensity function of: (a) a not-mixed region and (b) a well-mixed region.

The standard deviation can be normalized again by the mean concentration to get the mixing index:

$$\text{MI} = \sqrt{\frac{1}{N} \sum_{i=1}^N \left( \frac{c_i^* - \bar{c}^*}{\bar{c}^*} \right)^2} = \sqrt{\frac{1}{N} \sum_{i=1}^N \left( \frac{I_i - \bar{I}}{\bar{I}} \right)^2} \quad (7.30)$$

where  $I_i$  is the intensity value at a given position (pixel) of the region of interest. The mixing index therefore varies from 1 to 0. For convenience, mixing efficiency can also be defined based on the mixing index:

$$\eta_{\text{mixing}} = 1 - \text{MI} = 1 - \sqrt{\frac{1}{N} \sum_{i=1}^N \left( \frac{I_i - \bar{I}}{\bar{I}} \right)^2}. \quad (7.31)$$

Mixing efficiency is 1 if the two fluids are fully mixed. In the published literature, mixing efficiency is sometimes referred to as the mixing index.

For time-dependent concentration fields of active micromixers, a single image has little information about the mixing performance. The extent of the disturbance can be evaluated by averaging a large number  $N$  of image frames [3]:

$$\overline{I(x, y)} = \frac{\sum_{i=1}^{N+1} I_i(x, y)}{N} \quad (7.32)$$

where  $I_i(x, y)$  is the intensity matrix of each image, which is equivalent to the concentration field. The extent of the disturbed concentration is indicated by the dispersion of the averaged field. For evaluation of the energy content of the

disturbance, the mean square perturbation field can be used [3]:

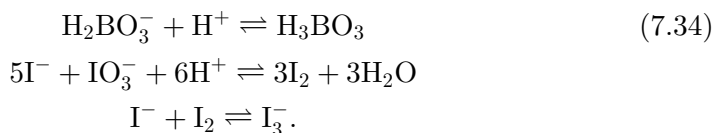
$$\overline{I'(x,y)}^2 = \frac{\sum_{i=1}^{N+1} \left[ I_i(x,y) - \overline{I(x,y)} \right]^2}{N}. \quad (7.33)$$

Fig. 7.13 shows a typical time-dependent concentration field. The images were recorded from the micromixer based on viscoelastic instability depicted in Figure 4.7(b) (Section 4.1.2). The white lines indicate the channel wall. The time-averaged concentration field depicted in Fig. 7.14 (a) is evaluated from 20 images. The result shows the extent of instability by the gray area around the middle stream. Imaging the concentration field with a long exposure time results in the same image shown in Fig. 7.14 (a). The mean square perturbation field depicted in Fig. 7.14 (b) represents the perturbation energy of the instability. The results show that a large area between the side streams and the middle stream is highly perturbed. The maximum perturbation can be seen just before the constriction.

### 7.3.2 Indirect Methods

Indirect methods measure the extent of mixing based on the products of chemical reactions or a change in fluorescent intensity due to a change of pH level in the mixed fluids.

Parallel competing reactions can be used for evaluating mixing efficiency. For instance, when a mixture of iodate, iodine, sodium hydroxide, and boric acid is mixed with sulfuric acid, the so-called Dushman reaction occurs [4]:



The first reaction is a neutralization reaction, which is very fast compared to the second reaction. If mixing is good, there is no acid left for the second reaction to form iodine. In other words, the amount of iodine produced depends on the efficiency of the mixing process. The concentration of  $\text{I}_3^-$  in the mixing product indicates the degree of mixing. The concentration of  $\text{I}_3^-$  can be measured via the absorbance at 353 nm. Using this method, the mixing efficiency can be determined as:

$$\eta_{\text{mixing}} = \frac{\text{ABS}}{\text{ABS}_{\infty}} \quad (7.35)$$

where ABS is the result of the absorbance measurement and  $\text{ABS}_{\infty}$  is the absorbance of the fully mixed solution. The disadvantage of this technique is

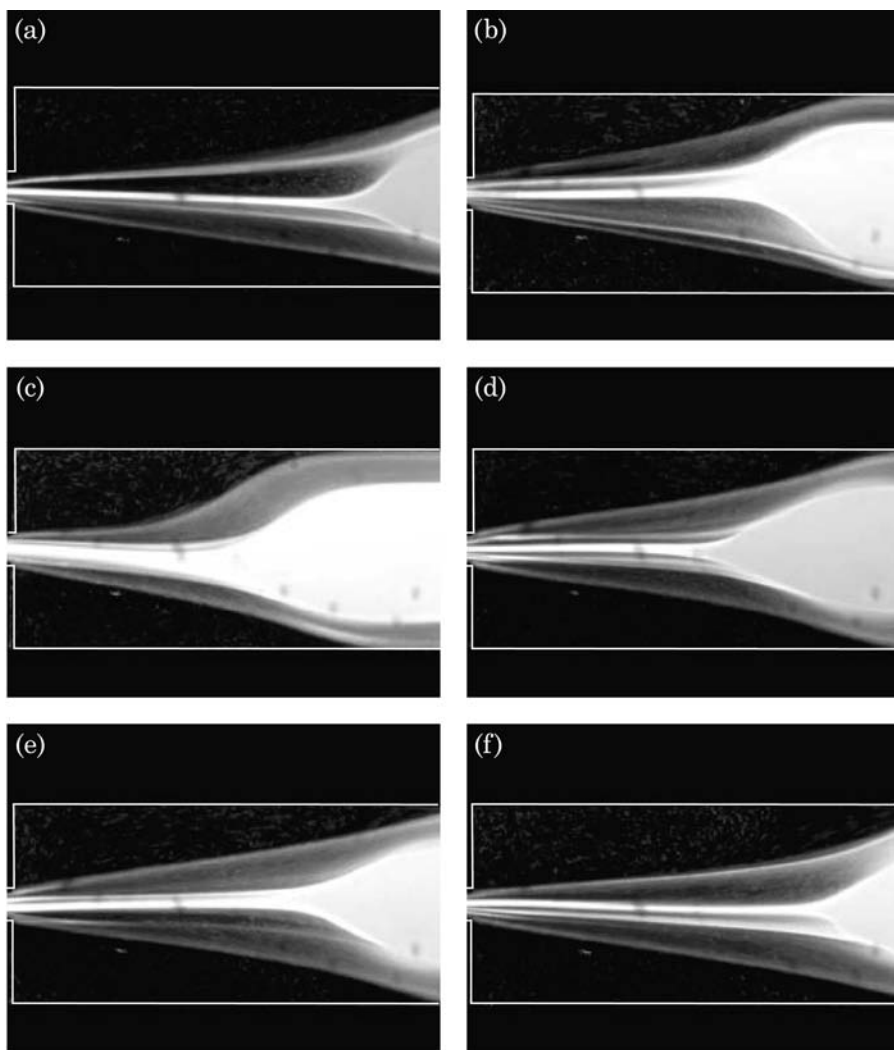


**Figure 7.13** Image sequence of a time-dependent concentration field (courtesy of Mr. Gan Hiong Yap, Nanyang Technological University).

that the absorbance measurement would normally need to be carried out off the chip. The integration of fiber optics for on-chip measurement would be expensive and impractical.

One of the main challenges in characterizing micromixers is due to the two-dimensional nature of fluorescent measurement with a camera/microscope system. The use of mixing index and PDF are based on statistical evaluation of tracing fluorescent dyes. These methods are suitable for micromixers with flat channels, where the concentration distribution along the view direction is negligible. Thus, the use of two-dimensional camera/microscope system is



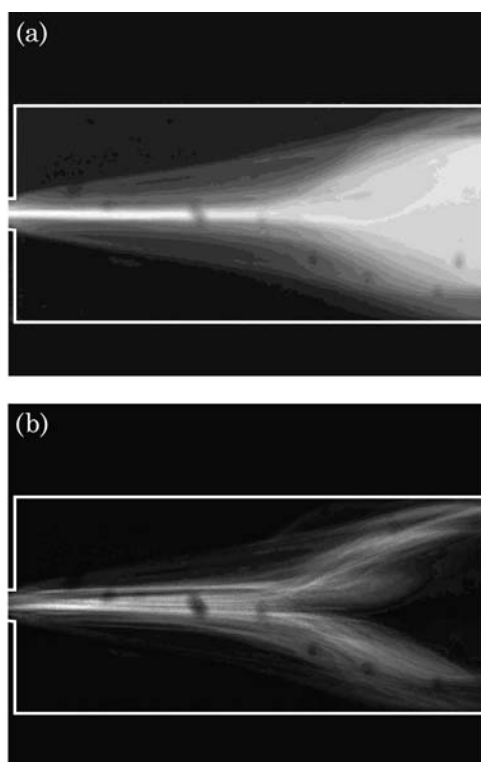


**Figure 7.14** Evaluation of time-dependent concentration fields: (a) time-averaged concentration field from the images in Fig. 7.13; (b) mean square perturbation field from the images in Fig. 7.13.

justified, Fig. 7.15 (a). For cases with a concentration distribution along the view direction, measurement would only be possible with the more expensive laser scanning confocal microscope system. A two-dimensional camera/microscope system would record the image of a fully-mixed region, Fig. 7.15 (b). Munson and Yager [5] proposed a fluorescent detection techniques based on the pH sensitivity of a fluorophore. The two fluids are mixed with an equal concentration ( $10\text{ }\mu\text{M}$ ) of fluorescein. They only differ in the pH levels. One fluid consists of a  $1\text{ mM}$  phosphate buffer at a pH of 5.15. At this pH level, 13.7% of the fluorescein molecules are in the dianionic state, which is much brighter than the monoanionic form. The other fluid consists of  $14\text{ nM}$  phosphate buffer at a pH of 8.18. At this pH level, 99.7% of fluorescein are in the bright dianionic state. If the two solutions completely mix, the resulting buffer will have a pH level of 8.0 with 97.8% of fluorescein in the bright dianionic state. Thus, the increase from 13.7% to 97.8% of the first fluid will overwhelm the decrease from 99.7% to 97.8% of the second fluid. If the fluids are fully mixed at a ratio of 1:1, the total fluorescence will increase by a factor of 2. Because the two fluids have different ionic concentrations, a liquid junction potential may form at the interface of the

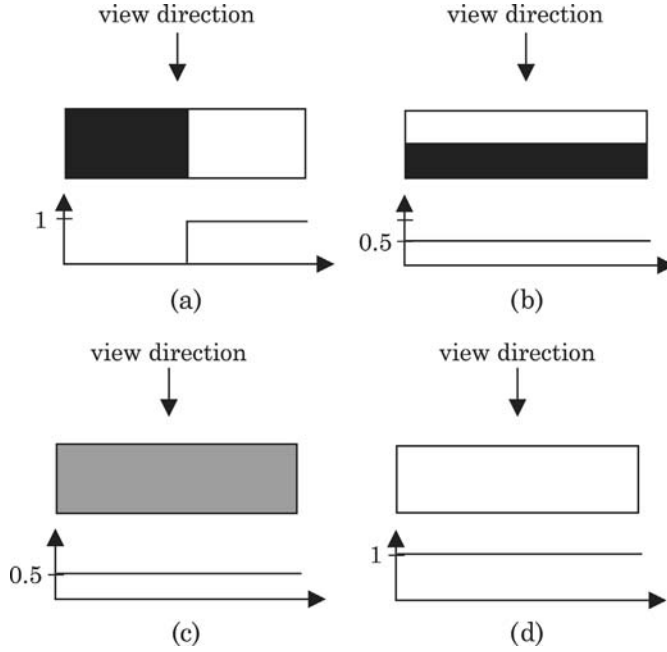


**Figure 7.15** Mixing evaluation using fluorescent dye: (a) before mixing, view direction parallel to fluid interface, techniques with mixing index and PDF based on two-dimensional optical microscopy can be used; (b) before mixing, view direction perpendicular to fluid interface, only measurement with confocal microscopy is possible; (c) results of mixing using conventional fluorescent technique; (d) results of mixing using fluorescent technique based on pH sensitivity.

two fluids. The potentials may cause electroosmotic transport across the interface. To suppress the junction potential and to abolish the electroosmotic component, Munson and Yager added 0.5M NaCl to both fluids. Given the average intensity measured across both fluids at the inlet  $I_0$  and the intensity of the fully mixed solution  $I_\infty$ , the mixing efficiency can be evaluated as:

$$\eta_{\text{mixing}} = \frac{I - I_0}{I_\infty - I_0} \quad (7.36)$$

where  $I$  is the averaged intensity of the region of interest.

## References

1. N.T. Nguyen and S.T. Wereley, *Fundamentals and Applications of Microfluidics*, 2nd edition, Artech House, New York, 2006.
2. R.C. Gonzalez, R.E. Woods and S.L. Eddins, *Digital Image Processing using MATLAB*, Pearson Prentice Hall, Upper Saddle River, New Jersey, 2004.

3. J.D. Posner and J.G. Santiago, "Convective instability of electrokinetic flows in a cross-shaped microchannel," *Journal of Fluid Mechanics*, Vol. 555, pp. 1–42, 2006.
4. M.-C. Fournier, L. Falk and J. Villermaux, "A new parallel competing reaction system for assessing micromixing efficiency-determination of micromixing time by a sample mixing model," *Journal of Fluid Mechanics*, Vol. 555, pp. 5187–5192, 1996.
5. M.S. Munson and P. Yager, "Simple quantitative optical method for monitoring the extent of mixing applied to a novel microfluidic mixer," *Analytical Chimica Acta*, Vol. 507, pp. 63–71, 2004.

## 8 Applications of Micromixers

---

### 8.1 Chemical Industry

#### 8.1.1 Micromixers as Microreactors

Micromixers play an important role in the chemical industry because of their unique features as highlighted in Chapter 1. Generally, the fast mixing process is the key advantage of micromixers. Micromixers allow the formation of new products, which are not possible in large-scale reactors. Considering a simple reaction between two species A and B to form a product C. The reaction rate  $r$  is defined as the generation rate of the product under an isothermal condition:

$$r = \frac{dc_C}{dt} = -kc_A^a c_B^b \quad (8.1)$$

where  $c_A$ ,  $c_B$  and  $c_C$  are the concentration of A, B and C, respectively. The factors  $k$ ,  $a$ , and  $b$  are called the rate constants and the reaction orders of A and B, respectively. The rate constant  $k$  is a function of temperature  $T$ :

$$k(T) = k_0 \exp\left(\frac{-E_0}{k_B T}\right) \quad (8.2)$$

where  $k_0$  is a constant,  $E_0$  is the activation energy of the reaction, and  $k_B$  is the Boltzmann constant. The rate constant represents the number of collisions between reactant molecules A and B. According to (8.2), the reaction rate increases if the activation energy decreases or the temperature increases.

For reactions with very fast reaction kinetics, the reaction rate is determined by diffusion,  $k \propto D$ . Because diffusion is the final stage in all micromixer types, the efficiency of a micromixer determines the reaction rate. Thus, the reaction rate can be controlled by careful micromixer design.

#### 8.1.2 Homogeneous Reactions

Due to the high demand for applications in chemical and biochemical analysis, most micromixers were designed for the liquid phase. Thus, all these micromixers can be directly used as micro reactors for homogenous liquid phase reactions. All basic micromixer designs are suitable for single-step reactions. Using many micromixers in series would allow multi-step reactions.

Sand et al. used a simple T-mixer as a microreactor for the synthesis of enamines. Cyclohexanone and dicyclohexylcarbodiimide (DCC) as drying agents are mixed with pyrrolidine in anhydrous methanol to form enamine [1].

Whiles et al. used a micromixer to demonstrate the synthesis of 1,3-dicarbonyl compounds [2]. Garcia-Egido et al. [3] used a T-mixer made in glass and a Peltier heater to synthesize 2-aminothiazoles by means of a Hantzsch reaction of ring-substituted 2-bromoacetophenones and 1-substituted-2-thioureas. During the synthesis process, the microreactor was kept at 70 °C. Fernandez-Saurez et al. [4] realized multi-step reactions in a series of T-mixers to form a number of tri- and tetra- cyclic heterocycles.

Micromixers are suitable for combinatorial chemistry, especially the synthesis of proteins for drug discovery. Watts et al. [5] used micromixers to create a synthetic  $\beta$ -dipeptide from  $\beta$ -alanine. The multi-step reactions in micromixers allow the isolation of intermediate products. Thus, condensation chemistry, protection, and deprotection of intermediate products can be realized on a single chip.

Micromixers are good reaction platforms for the synthesis of solid micro particles. Micromixers allow the control over the size and shape of the solid particles. “Drowning-out” crystallization technology is one of the methods for controlling the characteristics of particles in a solution. By adding anti-solvent into the solution, the solubility of a solute can be reduced, leading to nucleation and crystal formation. Kim et al. [6] used a T-mixer to generate high supersaturation, where the solid formation occurs rapidly at the same time scale of the extent of mixing. The mixing efficiency affects the final crystal size distribution. Sodium chloride (NaCl) was formed in a NaCl/methanol/water system, where methanol is mixed with saturated aqueous NaCl solution to form salt crystals. By adjusting the flow rates and consequently the residence time between 0.32 and 0.61 seconds, crystal sizes ranging from 7 to 29  $\mu\text{m}$  can be achieved.

Köhler et al. [7] used micromixers for the synthesis of metallic nanoparticles. Gold/silver nano particles were formed by mixing the solutions of the two salts  $\text{HAuCl}_4$  and  $\text{AgNO}_3$  and ascorbic acid. Because the optical properties of the Au/Ag particles depend on their compositions, tailored Au/Ag particles are needed. The micromixer allows the precise control of the particles composition. The ratio between gold and silver in the composite particle can be adjusted with the concentration of the salt solution and the mixing ratio.

### 8.1.3 Heterogeneous Reactions

Heterogeneous reaction occurs between two or more phases. In industrial processes, catalytic reactions are usually carried out heterogeneously. The reactants are mostly in the liquid or gas phases, while catalysts are in the solid phase. The catalyst should not dissolve in the reactants solvents.

The solid catalyst can be deposited directly on the micromixers wall or packed as beads or as a porous material in the mixing channel. The micromixer should bring the reactants in the liquid phase close to the solid catalyst.

Solid oxide-supported reactions are suitable for fuel reforming applications. Wilson and McGreedy [8] realized the dehydration of alcohols using sulfated zirconia as catalyst. In the microreactor at 150 °C, ethanol is converted into ethene, ethane, and methane.

A popular heterogeneous synthesis reaction is the Suzuki reaction, which is a organic reaction of an aryl- or vinyl-boronic acid with an aryl- or vinyl-halide catalyzed by palladium. It is widely used to synthesize polyolefins, styrenes, and substituted biphenyls. Greenwat et al. [9] realized the Suzuki reaction in a micromixer made in glass. A mesoporous silicate frit with about 1.8% palladium as catalyst was deposited on the channel wall. Compared to conventional batch reactions, the conversion yield improves 7 times (from 10% to 68%). The residence time was reduced from hours to minutes.

In a liquid/liquid reaction system, a large interfacial area can be obtained with the formation of micro droplets. Using the microdroplets, synthesis reactions based on organic and aqueous phases can be performed with high yields. Ueno et al. [10] realized several fundamental carbon-carbon bond-forming reactions in a glass micromixer using the formation of aqueous droplets in the organic phase.

#### 8.1.4 Enhancement of Chemical Selectivity

The relation between mixing and reaction was already highlighted at the beginning of this book (see Section 1.1). Micromixers can control the chemical selectivity, which is the relative tendency to form different products [11]. The chemical selectivity is determined by competing reactions, which occur either in a parallel or a sequential manner. The competing reactions are controlled by reaction kinetics or thermodynamics. If the reaction is controlled by kinetics, the selectivity is simply determined by the reaction rate  $k$  because no equilibrium between the products is needed. If the products require a thermodynamic equilibrium, the selectivity is determined by the thermodynamic stability of the products. Micromixers can control selectivity of kinetics-based competing reactions but can not affect the thermodynamics-based selectivity.

In parallel competing reactions, the substrate  $S$  reacts with different reagents ( $R_1$ ,  $R_2$ ) to form different products ( $P_1$ ,  $P_2$ ):



The selectivity in this case is determined by the reaction rate and concentration of the reagents. If the reagents have the same concentrations, the ratio of formation rates of  $P_1$  and  $P_2$  is the same as the ratio of the rate constants  $k_1 k_2$ . Thus, if one reaction rate is known, the rate of the other competing reaction

can be measured by simply determining the ratio of the products. Similarly, if the reaction rates are known, the concentration of the reactants can be determined by measuring the products as discussed in Section 8.2.1. Another application of parallel competing reactions in a micromixer is the measurement of the extent of mixing (see Section 7.3.2).

In sequential or consecutive reactions, the substrate  $S$  reacts with the reagent  $R$  to form the first product  $P_1$ . Subsequently, the product  $P_1$  reacts with the same reagent  $R$  to form the second product  $P_2$ . Both reactions have their own rate constants  $k_1$  and  $k_2$ , respectively.



The yield of the first product  $P_1$  is high if the substrate  $S$  and the reagent  $R$  are mixed quickly or  $k_1 \gg k_2$ . Micromixers can enhance the product selectivity of a number of competing sequential reactions such as Friedel-Crafts reactions, the phenyl boronic acid process,  $[4 + 2]$  cycloadditions and carboanionic polymerization [11]. In polymerization reactions, the substrate  $S$  is the initiator and the reagent  $R$  is the monomer. Controlling the number of reactions leads to the precise control of the number of monomers in a single chain and consequently the molecular weight of the polymer.

## 8.2 Applications in Chemical and Biochemical Analysis

### 8.2.1 Concentration Measurement

Micromixers are widely used in the chemical, biological, and medical analysis fields. Almost every chemical assay requires mixing of reagents with a sample. The basic T-mixer was used in the work of Kamholz et al. [12] for measurement of analyte concentration in a continuous flow. The concentration of a target analyte is measured with the fluorescence intensity in the region where the analyte and a fluorescent indicator have interdiffused [12]. Using this concept, the measurement of an analyte concentrations can be carried out on a continuous basis. This device is referred to as a T-sensor. The concept of a T-sensor is depicted in Fig. 8.1. Kamholz et al. [12] used the T-sensor for measurement of the concentration of human serum albumin (HSA) in a sample. The fluorescein is Albumin Blue 580 (AB580), which has high affinity for HSA but low affinity for other types of proteins. AB580 has an excitation wavelength of 580 nm and emits photons with a wavelength of 606 nm. The stream containing AB580 has low native fluorescence. However, the fluorescent intensity increase by a few orders of magnitude when AB580 binds to HSA. In a T-sensor, the solution of interest, such as HSA sample, and the binding

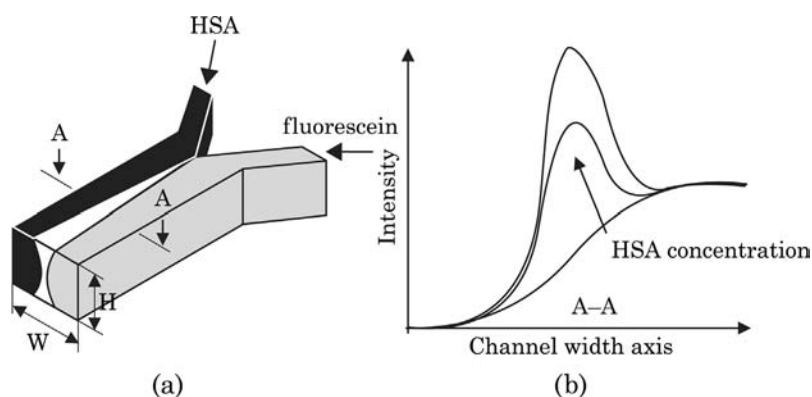


**Figure 8.1** The concept of a T-sensor. (a) The microfluidic design; (b) fluorescence intensity near the outlet.

fluorescein, such as AB580, are introduced at the inlet. If the two streams have the same flow rate and the same viscosity, the interface of the two streams will be in the middle of the mixing channel, Fig. 8.1 (a). The native fluorescein has an initial low level of intensity, while the intensity at the interface increases due to diffusion and the subsequent binding reaction between the fluorescein and the protein. The higher the concentration of the protein, the higher is the intensity peak at the interface, Fig. 8.1 (b).

Veenstra et al. used a micromixer for detection of ammonia in aqueous solutions [13]. The Berthelot reaction was used for the detection. Ammonia in an aqueous solution was converted into indophenol-blue using a two-step reaction. The first step is the chlorination of ammonia to produce monochloramine,  $\text{NH}_2\text{Cl}$ . In the second step, two phenol molecules bind to form monochloramine, resulting in indophenol blue. Indophenol blue can be detected with an absorption measurement because it has a peak at 625 nm in the absorption spectrum. Because the kinetics of formation of indophenol blue is relatively slow, the micromixer should allow a residence time of the order of 1 minute for the complete conversion of all ammonia molecules in the solution into indophenol blue.

### 8.2.2 Improving Chemical and Biochemical Analysis

Protein folding is controlled by the solvent composition of a protein solution. The changes in protein conformation as a response to changes in solvent composition can be measured using time-resolved nuclear magnetic resonance NMR spectroscopy. Time-resolved measurement of reaction kinetics using nuclear magnetic resonance (NMR) can benefit from the fast mixing time in a micromixer [14]. The solvent/protein interaction time depends on the mixing length and the flow rates of the mixed streams. Adjusting these two parameters



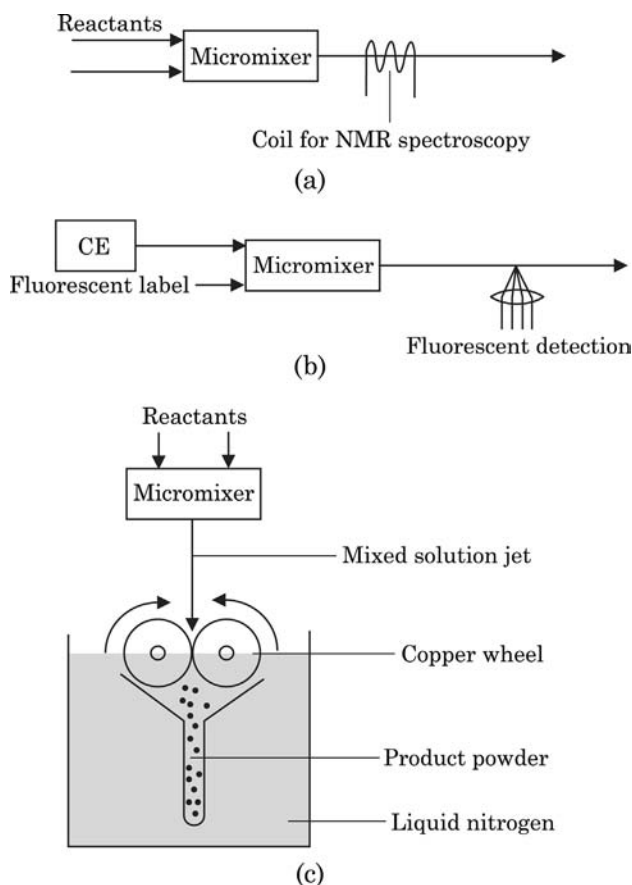


**Figure 8.2** Schematic concepts of micromixer applications in chemical analysis: (a) NMR measurement; (b) CE measurement; and (c) freeze-quenching reactions.

allows the measurement of NMR spectra at a precise epoch. Microcoils for NMR can be integrated with the micromixer to facilitate on-chip measurement, Fig. 8.2 (a). The integration of an array of microcoils would allow simultaneous measurement of multiple detection points. Such micromixers with integrated microcoils for NMR spectroscopy can be used for investigations of reaction intermediates and molecular interactions. Kakuta et al. used ubiquitin as the test protein. Ubiquitin changes its conformation from native to A-state at low pH and in 40% or higher methanol/water solvents. The micromixer was used for mixing the ubiquitin solution with the methanol solution. The concentration of the A-state increases with better mixing. Because the micromixer used was a Y-mixer with parallel lamination (Chapter 2), good mixing was achieved at low Peclet number or low flow rates. The reported NMR measurement can resolve the changes in a time scale of seconds.

Another application of micromixers is the labeling reaction of molecules after their separation using techniques such as capillary electrophoresis (CE). Because a fluorescence measurement is commonly used for detecting such molecules, they must be derivatized with a fluorescent label. Micromixers can be integrated in a CE chip as postcolumn reactors. Because the reactants and the products continue to be separated in the mixing channel, micromixers for this purpose should be efficient enough to allow rapid reaction. Slow reaction may lead to band-broadening caused by the different mobilities of reactants and products. Fluri et al. [15] combined capillary electrophoresis (CE) separation with a T-shaped intersection for the reaction of amino acids with the labeling reagent *o*-phthaldialdehyde (OPA), Fig. 8.2 (b). Fluid flows in this system were electrokinetically driven.

Fast mixing with a micromixer was used for the freeze-quenching technique, which is useful for trapping metastable intermediates during fast chemical or biochemical reactions [16]. The determination of the molecular properties of these intermediates leads to further understanding of chemical and biochemical reactions. The freeze-quenching technique ejects the mixed solution from a continuous-flow mixer through a small nozzle into an isopentane bath at a low temperature ( $-130^{\circ}\text{C}$ ). The frozen samples contain trapped reaction intermediates that can be conveniently investigated without the time constraints, Fig. 8.2 (c). At the macro scale, the application of the freeze-quenching technique is limited because of the long mixing time and the slow freezing time of cryogenic fluids. The delay time is generally of the order of milliseconds. Before the spectroscopic investigation, the reaction should be initiated in a way such that all the molecules are in phase. A mixer should work as a microreactor for this purpose. The earliest time allowed by conventional mixers for detection of the intermediates is of the order of milliseconds. Although the time limit can be solved by lowering the reaction temperature and fast spectroscopic tools, it is easier to reduce the mixing dead time using micromixers. The micromixer reported by Lin et al. [16] allows freeze-quenching within 20  $\mu\text{s}$  resulting in an ultrafine frozen powder with excellent spectral quality and high packing factor.

Enzyme assays are the basic techniques in clinical and bioanalytical chemistry. Micromixers can promote the reactions between the enzyme and the substrate. These devices often use electrokinetic transport to deliver analyte and enzyme into the chip and to the detector. An electrokinetically-driven T-mixer was used in [18] for performing enzyme assays. Substrate, buffer, enzyme, and inhibitor were mixed in two stages. The amount of each reagent was controlled by the applied voltages. Hadd et al. [18] used resorufin  $\beta$ -D-galactopyranoside (RBG),  $\beta$ -galactosidase ( $\beta$ -Gal), and phenylethyl  $\beta$  4-D-thiogalactoside (PETG) as the substrate, enzyme and inhibitor, respectively. The reaction forms resorufin, a fluorescent product with an emission wavelength of 585 nm. The system allows the measurement of reaction kinetics by varying the concentration of substrate and monitoring the amount of resorufin using fluorescent detection. The assay performed with the micromixers consumed about 4 orders of magnitude less

reagent compared to a conventional assay. Micromixers can therefore help to reduce the cost of enzyme assays, especially those with expensive reagents. Burke and Regnier [17] reported a microfabricated enzyme assay system with a micromixer to perform stopped-flow reactions. The device was tested with galactosidase as the enzyme and fluorescein monod-galactopyranoside (FMG) as the substrate.

Micromixers can work as a reaction platform for drug production using recombinant protein production. The production process consists of several steps. In the first step, the DNA sequence of the protein to be produced is inserted into the DNA of viruses. The viruses in turn are mixed with a cell culture to allow the infection cycle to proceed. After a certain amount of time, all cells are infected with the virus and the recombinant protein can be collected. The infection process can be optimized by the right concentration of the virus. Thus determining the right concentration of virus is crucial for protein production. In conventional reactors, virus is diluted to various concentrations and used for infecting separate batches of cells. The optimum virus concentration is then determined by evaluating the amount of proteins harvested in each cell batch. Diffusion transport in a lamination micromixer could allow the formation of a concentration gradient, where cell infection at different concentrations can be realized concurrently. Protein expression based on fluorescent measurement can be carried out on a chip. The short mixing length of a cross mixer with hydrodynamic focusing makes fast infection of a cell with viruses possible. Walker et al. [19] reported the infection of cells by viruses at different concentrations in a cross mixer. The cells are attached to the bottom of the mixing channels. A concentration gradient of virus particles was created by diffusive mixing in a flow-focusing configuration, where the middle stream contains virus particles. The cells were monitored with green fluorescent protein.

In biochemical sensors, the analyte often needs to be transported to immobilized receptors to make binding and subsequent detection possible. Receptors are surface-immobilized biomolecules that are complementary to the biomolecules to be detected. Vijayendran et al. used micromixers based on chaotic advection to promote analyte transport to receptors immobilized on a surface [20]. Soluble rabbit IgG antibodies were passed through the micromixer allowing them to bind to protein A immobilized on one microchannel wall. The binding reactions were detected using surface plasmon resonance (SPR). Since the binding kinetics are two or three orders higher than the diffusion of analytes, the quality of detection depends on the extent of chaotic advection. Experiments showed that compared to a simple T-mixer, a chaotic mixer can double the rate of analyte detection.

Kim et al. [21] used the F-shaped chaotic micromixer depicted in Fig. 5.15 for blood typing on a disposable chip. Blood typing is an important blood test because transfusion of incompatible blood groups (A, B, AB, and O) may lead to intravascular hemolysis in the recipient. The blood group is determined by

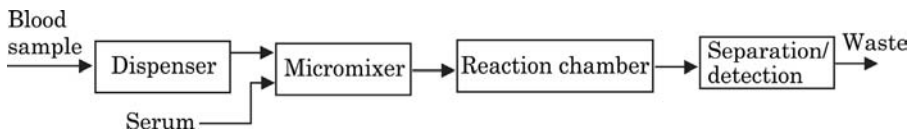


**Figure 8.3** Schematic concept of a lab-on-a-chip for blood typing.

the agglutination results of red blood cells reacting with the corresponding blood serum. The reaction shows the presence of antigens (agglutinogens) on the red blood cells corresponding to antibodies (agglutinins) in the serum. The sera, Anti-A, Anti-B, and Anti-AB, are obtained from the sera of blood group B persons, A persons, and O persons, respectively. The micromixers work as reactors for the agglutination process. The small size of the device allows blood typing with a very small sample blood volume (of the order of  $1\ \mu\text{L}$ ). Besides the chaotic micromixers, the reported lab-on-a-chip device also contained flow-splitting microchannels, reaction chambers, and detection microfilters (Fig. 8.3). The blood sample was divided into multiple equal volumes through the flow splitting microchannel so that multiple tests can be performed in parallel. The reaction chambers were used to keep the mixture of the blood and serum for a few minutes before filtering. The gradually decreasing multi-step detection microfilters were designed for separation of the reacted agglutinated red blood cells. The separation result allows the visual detection of blood groups A, B, and AB.

### 8.2.3 Purification and Preconcentration

Sensitive detection is crucial for biochemical analysis. The sample condition may affect the quality of processes such as the polymerase chain reaction (PCR). To improve the accuracy of pathogen detection, preconcentration and purification of a DNA sample are necessary before PCR. Furthermore, higher sample concentration also leads to better detection sensitivity. Depending on the filtering or trapping concept, micromixers can be used for controlling buffer concentration or generating chaotic advection as described in the following two examples.

Lee et al. [22] used a serpentine chaotic micromixer for DNA purification. Because DNA has a negative charge, it is strongly adsorbed by the glass surface under high-salt buffer conditions. The binding forces to glass of other contaminants, such as proteins or sugars, are relatively weak. Thus packed beads can be used for DNA purification. The adsorbed DNA can subsequently be released and collected if a low-salt buffer is introduced into the packed chamber. A micromixer can realize the stepwise change of salt concentration in a buffer solution before flushing it through the packed chamber. Lee et al. used

the micromixer to change the concentration of  $\text{MgCl}_2$  500 mmolL to 15 mmolL. For this purpose, the mixing ratios were controlled at 1:1 and 1:66.

Dielectrophoresis (DEP) can be utilized for trapping, manipulating, and separating bioparticles, such as viruses, DNA molecules, bacteria, and cells. Planar interdigitated electrodes (IDEs) can be used to generate the nonuniform electric field required for dielectrophoresis. However, the electrophoretic force is only effective if the sample particles are brought close to the surface with the IDEs, similar to the case with surface-immobilized receptors. Lee and Voldman [23] used the micromixers depicted in Figs. 5.19 and 5.21 to bring more sample particles closer to the IDEs. Chaotic advection in the flow increases the amount of particles trapped at the surface. Using the mixer, the amount of trapped particles increased by 50% compared to the case of a straight and smooth channel.

### 8.3 Outlook

Micromixers continue to receive the attention of the research community, because of the huge potential and impact in chemical analysis and the chemical industry. Fig. 8.4 shows the statistics of the number of published research works on micromixers and their citations until 2006. After the initial surge of interest, one can expect that the research output on micromixers will stabilize at 100 to 150 papers per annum in the years to come. This impressive number proves the importance of micromixers in the quest for miniaturization in chemical and biochemical analysis and the chemical industry.

The recent trend points to the development of micromixers without moving parts. Passive and active micromixers with chaotic advection are preferred due to their effectiveness in microscale. Mixing based on chaotic advection caused by flow-guiding structures could be the focus of future research works on passive micromixers. With technologies such as hot embossing or molding, the flow-guiding structures and the mixing channel can be fabricated in the same process. Mixing based on electrokinetic disturbance could be the favorite one among the active mixing concepts because of the simplicity in the fabrication. Only electrodes are needed for actuation. As described in Section 6.5, mixing based on electrokinetic instability would require a relatively strong DC electric field and consequently a high voltage. Electrokinetic mixing based on an AC field could have the potential for creating chaotic advection at a much lower electric field and supply voltage.

In industrial applications, solid and reliable designs for high throughput are required. Pressure-driven passive mixers made in materials such as ceramics and stainless steel are suitable for this purpose. For aggressive conditions such as high temperature and high pressure, materials such as silicon carbide may be needed for the fabrication of the micromixers. However, finding a suitable micromachining technology for these materials could be a challenge.

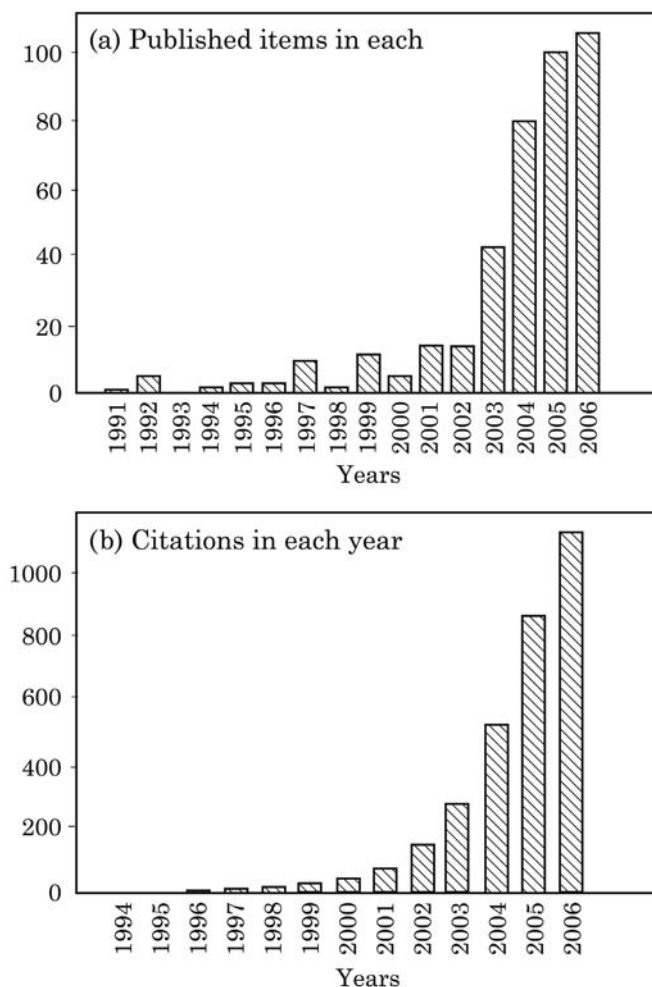


**Figure 8.4** Statistics of published works on micromixers (source of data: ISI Web of Science, Thomson Scientific): (a) number of publications; (b) number of citations. Note that the data source does not cover all journals.

Furthermore, the micromixers for chemical production may need to fulfill other requirements such as energy consumption and fouling resistance. Besides mixing function, microreactors should be able to provide a controlled environment for the industrial production of chemicals. Additional functions such as heating and temperature sensing would be needed for controlling the temperature of the reaction. For a wide adoption of micromixers as platforms for microreactor technology, issues related to intellectual property and the cost to the first user should be considered. A high cost for setting up a production process based on microreactor technology may hinder or delay the transfer of this technology from academic research to industrial production [24].

## References

1. M. Sands, et al., "The investigation of an equilibrium dependent reaction for the formation of enamines in a microchemical system," *Lab Chip*, Vol. 1, pp. 64–65, 2001.
2. C. Wiles, et al., "The aldol reaction of silyl enol ethers within a micro reactor," *Lab Chip*, Vol. 1, pp. 100–101, 2001.
3. E. Garcia-Egido, S.Y.F. Wong and B.H. Warrington, "A hantzsch synthesis of 2-aminothiazoles performed in a heated microreactor system," *Lab Chip*, Vol. 2, pp. 100–101, 2002.
4. M. Fernandez-Suarez, S.Y.F. Wong and B.H. Warrington, "Synthesis of a three-member array of cycloadducts in a glass microchip under pressure driven flow," *Lab Chip*, Vol. 2, pp. 170–174, 2002.
5. P. Watts, C. Wiles, S.J. Haswell, E. Pombo-Villar and P. Styring, "The synthesis of peptides using micro reactors," *Chemical Communications*, Vol. 11, pp. 990–991, 2001.
6. K.J. Kim, "Crystal growth in drowning-out crystallization using a T-mixer," *Chemical Engineering and Technology*, Vol. 29, pp. 1267–1272, 2006.
7. J.M. Köhler, M. Held, U. Hübner and J. Wagner, "Formation of Au/Ag nanoparticles in a two step micro flow-through process," *Chemical Engineering and Technology*, Vol. 30, pp. 347–354, 2007.
8. N.G. Wilson and T. McCreedy, "On-chip catalysis using a lithographically fabricated glass microreactor the dehydration of alcohols using sulfated zirconia," *Chemical Communications*, Vol. 9, pp. 733–734, 2000.
9. G.M. Greenway, S.J. Haswell, D.O. Morgan, V. Skelton and P. String, "The use of novel microreactor for high throughput continuous flow organic synthesis," *Sensors and Actuators B*, Vol. 63, pp. 153–158, 2000.
10. M. Ueno, H. Hisamoto, T. Kitamori and S. Kobayashi, "Phase-transfer alkylation reactions using microreactors," *Chemical Communications*, Vol. 11, pp. 936–937, 2003.
11. J. Yoshida, A. Nagaki, T. Iwasaki and S. Suga, "Enhancement of chemical selectivity by microreactors," *Chemical Engineering and Technology*, Vol. 28, pp. 259–265, 2005.
12. A.E. Kamholz, et al., "Quantitative analysis of molecular interactive in microfluidic channel: the T-sensor," *Analytical Chemistry*, Vol. 71, pp. 5340–5347, 1999.
13. T.T. Veenstra, "Characterization method for a new diffusion mixer applicable in micro flow injection analysis systems," *Journal of Micromechanics and Microengineering*, Vol. 9, pp. 199–202, 1999.
14. M. Kakuta, et al., "Micromixer-based time-resolved NMR: Applications to ubiquitin protein conformation," *Analytical Chemistry*, Vol. 75, pp. 956–960, 2003.
15. K. Fluri, et al., "Integrated capillary electrophoresis devices with an efficient postcolumn reactor in planar quartz and glass chips," *Analytical Chemistry*, Vol. 68, pp. 4285–4290, 1996.
16. Y. Lin, et al., "Ultrafast microfluidic mixer and freeze-quenching device," *Analytical Chemistry*, Vol. 75, pp. 5381–5386, 2003.
17. B.J. Burke and F.E. Regnier, "Stopped-flow enzyme assays on a chip using a microfabricated mixer," *Analytical Chemistry*, Vol. 75, pp. 1786–1791, 2003.
18. A.G. Hadd, et al., "Microchip device for performing enzyme assays," *Analytical Chemistry*, Vol. 69, pp. 3407–3412, 1997.
19. G.M. Walker, M.S. Ozers and D.J. Beebe, "Cell infection within a microfluidic device using virus gradients," *Sensors and Actuators B*, Vol. 98, pp. 347–355, 2004.
20. Vijayendran, et al., "Evaluation of a three-dimensional micromixer in a surface-based biosensor," *Langmuir*, Vol. 19, pp. 1824–1828, 2003.
21. D.S. Kim, S.H. Lee, C.H. Ahn, J.Y. Leed and T.H. Kwon, "Disposable integrated microfluidic biochip for blood typing by plastic microinjection moulding," *Lab Chip*, Vol. 6, pp. 794–802, 2006.

22. N.Y. Lee, M. Yamada and M. Seki, "Development of a passive micromixer based on repeated fluid twisting and flattening, and its application to DNA purification," *Analytical and Bioanalytical Chemistry*, Vol. 5, pp. 776–782, 2005.
23. H.Y. Lee and J. Voldman, "Optimizing micromixer design for enhancing dielectrophoretic microconcentrator performance," *Analytical Chemistry*, Vol. 79, pp. 1833–1839, 2007.
24. D.M. Roberge, L. Durcy, N. Bieler, P. Cretton and B. Zimmermann, "Microreactor technology: a revolution for the fine chemical and pharmaceutical industries?," *Chemical Engineering and Technology*, Vol. 28, pp. 318–322, 2005.





# Index

- acoustic impedance, 258
- acoustic streaming, 258, 260
- Acrylic, 100
- actuator
  - piezoelectric
  - piezocantilever, 211
  - piezodisc, 211
  - piezostack, 211
- thermopneumatic, 212
- advection cycle, 40
- anion, 26
- anisotropy, 87
- anodic bonding, 124
- APCVD, 81
- APE, 90
- aspect ratio, 91, 101, 105, 112, 122, 138, 140, 155, 219, 220, 226, 278
- Avogadro number, 12
- AZ4562, 105
- AZ9260, 105
  
- BEM, 186
- Bessel function, 63, 149, 150, 256, 257
- biochemical sensor, 300
- biocompatibility, 107
- blood group, 301
- blood typing, 300
- Boltzmann constant, 10, 75, 239, 293
- Bond number, 187
- bonding
  - adhesive, 126
  - direct
    - ceramics and metals, 126
    - glass, 126
    - polymer, 126
    - silicon, 125
  - eutectic, 127
  - fusion, 125
- Bosch process, 91
- Brownian motion, 22
- Brownian particle, 23
- bubble, 86, 123, 187, 192, 193, 202, 212, 214, 222, 260, 261
  
- capillary electrophoresis, 299
- cation, 26
- CCD, 268, 269, 274, 276, 277
- chaotic advection, 2, 7, 37, 74, 93, 107, 141, 142, 144, 145, 163, 164, 167, 169–171, 173, 176–178, 182, 192, 200–202, 217, 223, 242, 244, 300
- Chapman–Enskog theory, 9
- charge density, 58, 66, 68, 69, 107, 228, 238
- chemical reaction, 14
- chemical vapor deposition, 81
- Clausius–Mossotti factor, 231
- CMOS, 86, 95, 275–278
- COC, 173, 178
- collision diameter, 24
- collision integral, 24
- conductivity, 9, 66, 67, 72, 121, 228, 229, 231, 233, 235, 245
  - gradient, 228
  - thermal, 195, 210
- conservation
  - of energy, 14, 20
  - of mass, 13
  - of momentum, 14, 59, 71

- of species, 14, 21, 31
- conservation equation, 13
- continuity equation, 13, 14
- continuum level, 9, 13
- correlation peak, 281
- cross correlation, 280, 281
- cube-square law, 2, 71
- CVD, 81, 83, 114
- Czochralski method, 85
- Damköhler number, 75
- Dean flow, 42, 43, 46–48, 164, 168, 170–172, 175
- Dean number, 47, 51, 168, 169, 171, 174, 176
- Dean vortex, 47, 51, 143, 163, 168, 170–172, 174, 176, 180
- Debye length, 59, 64, 68, 237
- density, 15
- DEP, 302
- developing, 102
- dielectrophoresis, 69, 70, 231, 302
- diffusion
  - Knudsen, 75
  - molecular, 21
- diffusion coefficient, 1, 21, 22, 24–27, 155, 156, 160, 213, 233, 249
- Dirac function, 23, 32
- direct bonding, 125
- dispersion, 2, 138, 146, 187, 287
  - coefficient, 31, 35
  - Taylor, 28
  - Taylor-Aris, 155
- dispersion coefficient, 29, 146, 147
- disturbance
  - acoustic, 251
  - dielectrophoretic, 70, 231
  - electrohydrodynamic, 228
  - electrokinetic, 233, 237, 238, 240, 241
  - magnetohydrodynamic, 244
  - pressure-driven, 208, 217
  - thermal, 261
- DNA, 106, 226, 251, 300–302
  - analysis, 107
  - purification, 228, 301
- DRIE, 91, 145, 166, 222, 261
- droplet, 7, 52, 187, 193, 198, 200, 295
- droplet-based, 52, 202, 203, 214
- drug delivery, 107
- drug production, 300
- DSMC, 12
- E. coli, 215, 225
- EBE, 84
- EHD, 227, 228, 231, 247
- elasticity number, 56, 143
- elastomer, 107
- electro-osmotic pumping, 107
- electrokinetic effect, 56
- electroosmosis, 57, 227, 233
- electrophoresis, 57, 67
- electroplating, 97
- electrowetting
  - direct, 193
  - on dielectric, 193, 194
- emulsion, 2
- energy equation, 20
- equation
  - continuity, 13, 14
  - diffusion/convection, 21, 29
  - energy, 20
  - Navier–Stokes, 14–16, 18
  - Poisson–Boltzmann, 59, 61, 64, 66, 233
  - Stokes–Einstein, 25, 26
- etch rate, 89
- etching
  - anisotropic, 87
  - chemical dry, 90
  - dry, 90
  - isotropic, 86, 90
  - physical dry, 90
  - physical-chemical, 90
  - wet, 85
- Eulerian velocity field, 39
- evaporation, 84
- exposure, 80, 101

- ferrofluid, 69–71
- floating zone method, 85
- flow
  - Dean, 42, 43, 46–48, 164, 168, 170–172, 175
  - electroosmotic, 28
  - ferrofluid, 71
  - plug-like, 28
  - Poiseuille, 33, 35
  - pressure-driven, 29
  - viscoelastic, 55
- fluid
  - Newtonian, 21, 54, 55, 142
  - non-Newtonian, 3, 142
- focusing, 150
  - geometric, 140, 150
  - hydrodynamic, 150
- Foturan glass, 92
- Fourier analysis, 154
- Fourier number, 73
- Fourier series, 16, 19
- friction coefficient, 23
- fuel reforming, 295
- Gouy–Chapman layer, 57
- Hamilton equation, 39
- Hamiltonian, 39
- hard bake, 102
- hydrodynamic focusing, 137, 141, 150, 153, 157, 158, 300
- hydrogel, 213
- immersion objective, 270
- instability
  - electrohydrodynamic, 228
  - electrokinetic, 233, 238, 240, 241
  - hydrodynamic, 208, 217
  - magnetohydrodynamic, 244
  - viscoelastic, 56, 143, 288
- Kirchhoff law, 60
- Knudsen number, 12, 74
- KOH, 87
- lamination, 145
  - parallel, 135
  - sequential, 135, 144
- Laplace pressure, 188
- laser
  - excimer, 116
  - Nd:YAG, 116
- laser micromachining, 116
- lead zirconate titanate (PZT), 211
- Lennard-Jones force, 13
- Lennard-Jones model, 10
- Lennard-Jones parameter, 10
- Lewis number, 73
- LIGA, 80, 102
- liquid plug, 193, 195, 198, 200–202, 214
- lithography, 80
  - electron, 80
  - ion, 80
  - X-ray, 80, 101
- LPCVD, 81, 93, 95
- Lucite, 100
- Lyapunov exponent, 201, 217, 224
- Ma-P 100, 105
- macromixing, 1
- macroscale, 1, 5
- magnetohydrodynamics, 72
- mapping function, 40
- MATLAB, 283, 284, 286
- MBE, 84
- MD, 12
- mean free path, 11
- mean square perturbation field, 288
- MERIE, 91
- mesomixing, 1
- MHD, 72, 121, 244, 246, 250, 251
- micro-PIV, 191, 193, 280, 282
- microchannel, 102, 121
  - C-shaped, 51, 171
  - F-shaped, 300
  - L-shaped, 171, 172
  - X-shaped, 178, 179
- microdroplet, 7, 52, 187, 193, 198, 200, 295

- microgripper, 118
- micromixer
  - active
    - acoustic, 251
  - passive
    - chaotic advection, 163
    - dielectrophoretic, 231
    - electrokinetic, 233
    - parallel lamination, 139
    - pressure-driven, 221
- micromixing, 1
- micromolding, 114
- micropump, 119
- microreactor, 5
- microscope, 271
  - confocal, 273, 275
  - confocal laser scanning, 273
  - fluorescence, 271, 272
  - optical, 268
- microvalve, 97, 119
- Miller indices, 85
- mixing efficiency, 166, 184, 229, 287, 288, 294
- mold insert, 109
- molding
  - compression, 110
  - in capillaries, 114
  - injection, 109
  - microtransfer, 114
  - reaction injection, 109
  - replica, 114
  - solvent-assisted, 114
- molecular diffusion, 21, 38
- molecular dynamics, 12
- molecular level, 9
- molecular weight, 24
- multi-phase system, 187
- multiple streams, 137, 141, 175
- 
- nanochannel, 94
- nanoimprint, 94
- nanostructure, 94
- national security, 6
- 
- Navier–Stokes equation, 14–16, 18, 43, 60, 62, 64, 71, 72, 153, 214, 216, 228, 234, 237, 244, 246, 252
- Newton second law, 14
- no-slip condition, 15, 19, 45, 138, 154, 247
- numerical aperture, 269–271
- 
- OCP, 89
- orbit, 38, 40
  - elliptic, 40
  - heteroclinic, 41
  - homoclinic, 41
  - hyperbolic, 40
- Oroglas, 100
- 
- PA, 109
- particle image velocimetry, 38, 191, 193, 280, 282
- parylene, 119, 121
  - C, 119
  - D, 119
  - N, 119
- pathline, 38
- PC, 109
- PCR, 301
- PDF, 285
- PDMS, 111, 112, 115, 180, 186, 203, 209, 222, 224, 230, 243, 261
- PEB, 102
- PEC, 120
- Peclet number, 73, 136, 137, 143, 147, 150, 163, 201, 244, 249, 250, 298
- PECVD, 81
- permittivity, 228
- permittivity, 67, 208, 228, 231, 238, 267
- Perspex, 100
- photolithography, 80, 84, 119
- physical vapor deposition, 83
- PI-2611, 119
- PIV, 38, 191, 193, 280, 282
- planarization, 84
- Planck constant, 12

- plastics, 106
- Plexiglas, 100
- PMMA, 100, 109, 145, 169, 258
- Poincaré section, 41, 48, 49, 217
- Poisson–Boltzmann equation, 59, 61, 64, 66, 233
- polyimide, 118
  - fluorinated, 118
  - photosensitive, 118
- polymer, 105
  - co-, 106
  - homo-, 106
- polymeric micromachining surface, 117, 119
- polysilicon, 95
- polyvinylidene fluoride (PVDF), 211
- POM, 109
- positioning, 80
- potential
  - attraction, 10
  - Lennard-Jones, 9, 24
  - repulsion, 10
- powder blasting, 123
- PPC, 120
- Prandtl number, 42
- printing
  - contact, 80
  - projection, 80
  - proximity, 80
- probability distribution function, 285
- protein, 26
- proton, 27
- proton writing, 104
- PSG, 96
- PSU, 109
- pulsed source–sink, 217, 220, 226
- PVD, 83, 125
- PVDF, 211
- PZT, 84, 211
- radius of curvature, 174
- random walk, 21
- Rayleigh number, 42
  - electric, 235
- RE, 84
- reaction, 14
  - biochemical, 299
  - chemical, 3, 4, 14, 75, 82, 90, 123, 212, 288
  - polymerization, 106
- relaxation time, 142
- remove, 102
- repeatability, 86
- residence time, 5, 56, 142, 176, 201, 294, 297
- resist, 84, 101, 126
  - thick, 81
- resolution, 278
- Reynolds number, 39, 45, 47, 51, 56, 67, 73, 75, 141–143, 145, 147, 163, 164, 166–173, 175–177, 187, 190, 244
- RIE, 90, 91, 119
- Runge–Kutta method, 38
- sacrificial layer, 96
- SAM, 113
- Schmidt number, 72, 73, 75
- sedimentation potential, 57
- segmentation
  - focusing, 135
  - injection, 135
  - sequential, 135, 146
- selectivity, 86, 87
- SGM, 181, 182, 184, 186
- SHB, 181, 182, 243
- silicon
  - polycrystalline, 85, 95
  - single crystalline, 85
- silicon dioxide, 82
- silicon etchant, 87
- slanted groove, 181
- Smoluchowski velocity, 60, 237
- soft bake, 101
- soft lithography, 111, 114
- sol-gel, 84
- SOR, 185
- spin coating, 84, 101
- sputtering, 84

- staggered herring bone, 181, 182
- staggered herringbone, 243
- staggered oriented mixers, 185
- Stern layer, 57, 58
- Stokes–Einstein equation, 24, 25
- streakline, 38
- streaming potential, 57
- streamlines, 38
- striation thickness, 73, 135, 140, 141, 144, 165, 183, 201
- SU-8, 81, 101, 115, 117
  
- T-junction, 166, 181, 190, 198
- T-mixer, 73, 135, 140, 163, 164, 166, 170, 200, 227, 294, 299, 300
- T-sensor, 296
- Taylor dispersion, 1, 28, 32, 36, 172, 221, 223, 250
- TCPE, 91
- temperature
  - absolute, 20
  - melting, 106
- thermal diffusivity, 72, 116, 195
- thermal oxidation, 83
  - dry, 83
  - wet, 83
- thermocapillary, 193, 195, 197, 203, 262
- TMAH, 87
- toroid, 42
- trajectory, 38
- transformation, 40
  - area-preserving, 40
  - volume-preserving, 40
- transport phenomena, 9, 12
- TRIE, 91
- turbulence, 37
- twisted pipe, 51, 53, 54, 171
  - of a rectangular membrane, 252
- viscoelastic
  - effect, 3, 55
  - fluid, 54, 55, 142, 143
- viscosity
  - dynamic, 15, 16
  - kinematic, 44, 72, 75, 199
- VTA, 84
  
- Weber number, 187, 188
- Weissenberg number, 56
  
- Y-mixer, 135, 139, 251, 261, 298
  
- zeta potential, 58, 60, 61, 68, 107, 124, 233, 238, 239, 242, 244, 245
  
- ultrasonic drilling, 124
- underetching, 86, 96, 118
  
- vibration, 124
  - modes, 255, 256
  - of a circular membrane, 255

## MICRO & NANO TECHNOLOGIES

### PUBLISHED 2008

1. *Microdrops and Digital Microfluidics* · Jean Berthier · 978-0-8155-1544-9
2. *Micromixers: Fundamentals, Design and Fabrication* · Nam-Trung Nguyen · 978-0-8155-1543-2

### FORTHCOMING 2008

- Fabrication and Design of Resonant Microdevices* · Behraad Bahreyni · 978-0-8155-1577-7
- Hot Embossing: Theory and Technology of Microreplication* · Matthias Worgull · 978-0-8155-1579-1
- Introduction to Quantum Information Processing (QIP)* · Timothy P. Spiller and William J. Munro · 978-0-8155-1575-3
- Nanotechnology Applications: Solutions for Improving Water Quality* · Edited by Mamadou Diallo, Jeremiah Duncan, Nora Savage, Anita Street, Richard Sustich · 978-0-8155-1578-4
- Micro-machining Using Electrochemical Discharge Phenomenon: Fundamentals and Application of Spark Assisted Chemical Engraving* · Rolf Wüthrich · 978-0-8155-1587-6
- Industrial Micro and Nano Fabrication* · J.G.E. Gardeniers and R. Luttge · 978-0-8155-1582-1
- Physics of Carbon Nanotube Devices* · François Léonard · 978-0-8155-1573-9
- Small Scale Mechanics: Principles and Applications* · David Mendels · 978-0-8155-1590-6
- Emerging Nanotechnologies for Manufacturing* · Edited by Waqar Ahmed and M.J. Jackson · 978-0-8155-1583-8
- Risk Governance of Nanotechnology: Environmental, Health and Safety Concerns About Nanotechnology and Their Implication for the Nanotechnology Industry* · Edited by Steffi Friedrichs · 978-0-8155-1586-9
- Handbook of MEMS Materials and Technologies* · Edited by Veikko Lindroos, Markku Tilli, Ari Lehto, and Teruaki Motooka · 978-0-8155-1594-4
- Micromanufacturing Engineering and Technology* · Edited by Yi Qin · 978-0-8155-1545-6

### OF RELATED INTEREST

- MEMS: A Practical Guide to Design, Analysis and Applications* · Edited by Jan Korvink and Oliver Paul · 978-0-8155-1497-8 · 2006
- Nanostructured Materials: Processing, Properties and Applications, 2nd Edition* · Edited by Carl C. Koch · 978-0-8155-1534-0 · 2007
- Ultrananocrystalline Diamond: Synthesis, Properties, and Applications* · Edited by Olga A. Shenderova and Dieter M. Gruen · 978-0-8155-1524-1 · 2006

For the latest information on related titles visit [www.williamandrew.com/MNT/](http://www.williamandrew.com/MNT/)